University of Novi Sad

Faculty of Technical Sciences

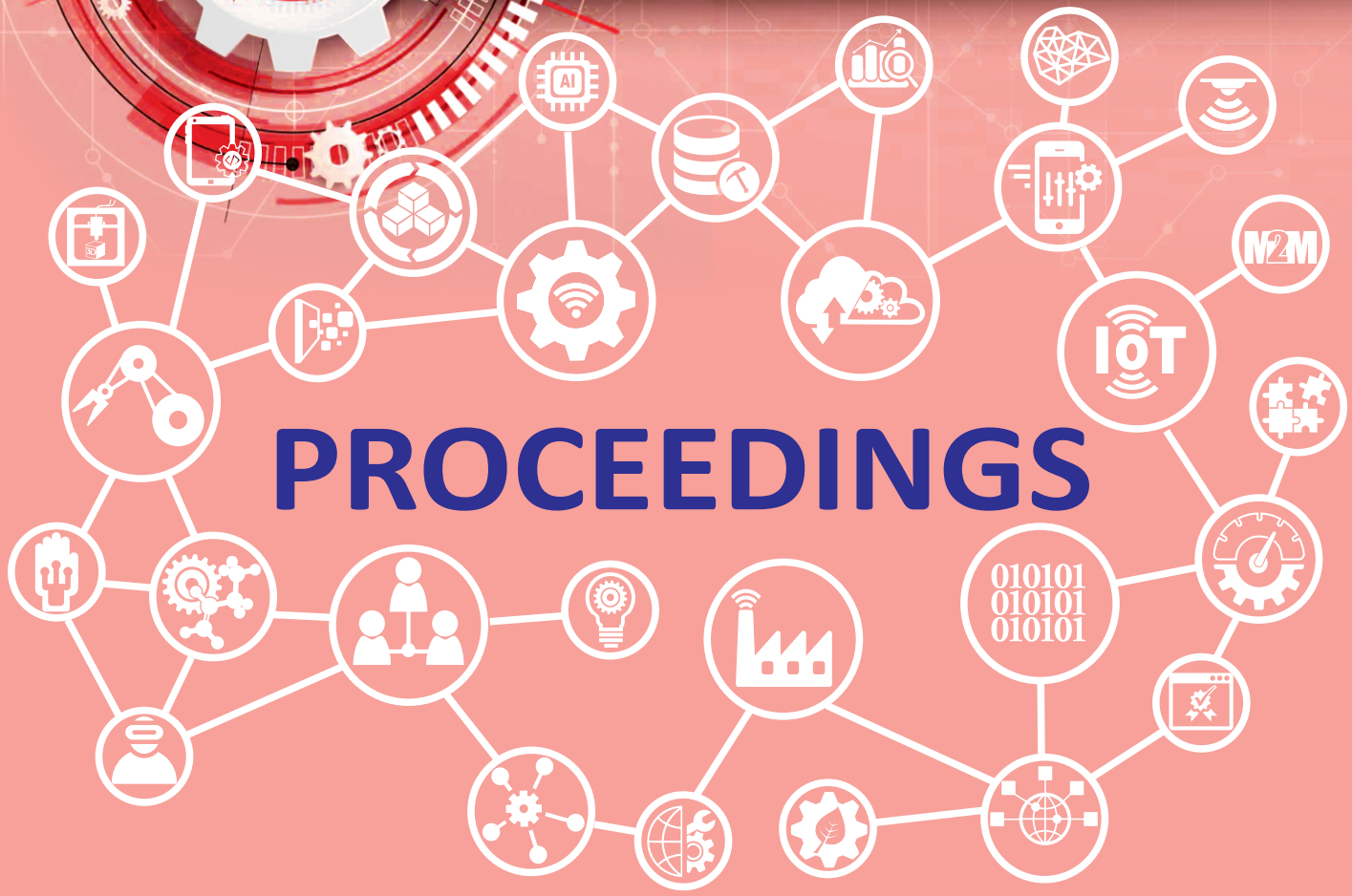
Department of Production Engineering

Science and Technology Park Novi Sad

15TH International Scientific Conference

MMA 2024

FLEXIBLE TECHNOLOGIES



PROCEEDINGS

Novi Sad, Serbia

September 24-26, 2024

UNIVERSITY OF NOVI SAD
FACULTY OF TECHNICAL SCIENCES
DEPARTMENT OF PRODUCTION ENGINEERING
NOVI SAD, SERBIA

15th INTERNATIONAL SCIENTIFIC CONFERENCE
MMA 2024 - FLEXIBLE TECHNOLOGIES

MMA 2024
FLEXIBLE TECHNOLOGIES

PROCEEDINGS

Novi Sad, September 24-26, 2024

Proceedings of the 15th International Scientific Conference
MMA 2024 - FLEXIBLE TECHNOLOGIES
Novi Sad, 2024

Publisher: **FACULTY OF TECHNICAL SCIENCES**
DEPARTMENT OF PRODUCTION ENGINEERING
21000 NOVI SAD, Trg Dositeja Obradovica 6
SERBIA

Organization of this Conference was approved by Educational-scientific Council of Faculty of Technical Sciences in Novi Sad

Editor: Dr Boris Dumnić, full professor, dean

Technical treatment and design: Dr Đorđe Vukelić, full professor
Dr Milana Ilić Mićunović, assistant professor
MSc Aleksandar Milošević, assistant

Manuscript submitted for publication: September 2024
Printing: 1st
Circulation: 150 copies

CIP classification:

CIP - Каталогизација у публикацији
Библиотеке Матице српске, Нови Сад

621.7/.9(082)
621.9(082)

INTERNATIONAL Scientific Conference MMA - Flexible Technologies (15 ; 2024 ; Novi Sad)
Proceedings [Elektronski izvor] / 15th International Scientific Conference MMA 2024 - Flexible Technologies, Novi Sad, September 24-26, 2024 ; [editor Boris Dumnić]. - Novi Sad : Faculty of Technical Sciences, Department of Production Engineering, 2024

Način pristupa (URL): http://mma.ftn.uns.ac.rs/mma_history.html. - Opis zasnovan na stanju na dan 27.8.2024. - Bibliografija uz svaki rad. - Registar.

ISBN 978-86-6022-681-7

а) Производно машинство -- Зборници б) Метали -- Обрада -- Зборници

COBISS.SR-ID 151010569

Printing by: Faculty of Technical Sciences, Graphic Centre GRID, Novi Sad

Financing of the Proceedings was sponsored by the Ministry of Science, Technological Development and Innovation of the Republic of Serbia and by the Provincial Secretariat for Higher Education and Scientific Research of AP Vojvodina.

MMA 2024
FLEXIBLE TECHNOLOGIES

15th INTERNATIONAL SCIENTIFIC CONFERENCE
NOVI SAD, SERBIA, SEPTEMBER 24-26, 2024

CONFERENCE ORGANIZER

University of Novi Sad, Faculty of Technical Sciences
Department of Production Engineering, Novi Sad, Serbia

INTERNATIONAL SCIENTIFIC COMMITTEE

- Miodrag Hadžistević, Chairman, University of Novi Sad, SRB
- Bojan Ačko, University of Maribor, SVN
- Boris Agarski, University of Novi Sad, SRB
- Sergei Alexandrov, Russian Academy of Sciences, RUS
- Aco Antić, University of Novi Sad, SRB
- Jan C. Aurich, Technical University Kaiserslautern, GER
- Sebastian Baloš, University of Novi Sad, SRB
- Jelena Baralić, University of Kragujevac, SRB
- Stevo Borojević, University of Banja Luka, BIH
- Miran Brezočnik, University of Maribor, SVN
- Borut Buchmeister, University of Maribor, SVN
- Erhan Budak, Sabanci University, TUR
- Igor Budak, University of Novi Sad, SRB
- Emanuele Carpanzano, University of Applied Sciences and Arts of Southern Switzerland, CHE
- Jasmina Čaloska, Ss. Cyril and Methodius University in Skopje, MKD
- Robert Čep, Technical University of Ostrava, CZE
- Ilija Ćosić, University of Novi Sad, SRB
- Joao Paulo Davim, University of Aveiro, PRT
- Goran Devedžić, University of Kragujevac, SRB
- Zoran Dimić, Lola Institute, SRB
- Lubomir Dimitrov, Technical University of Sofia, BGR
- Miroslav Dovica, University of Kosice, SVK
- Viorel Mircea Dragoi, Transilvania University of Brasov, ROU
- Igor Drstvenšek, University of Maribor, SVN
- Boris Dumnić, University of Novi Sad, SRB
- Numan M. Durakbasa, Vienna University of Technology, AUT
- Goran Đukić, University of Zagreb, CRO
- Kornel Ehmann, Northwestern University, USA
- Sabahudin Ekinović, University of Zenica, BIH
- Milan Erić, University of Kragujevac, SRB
- Luigi Maria Galantucci, Politecnico di Bari, ITA
- Adam Gaska, Cracow University of Technology, POL
- Valentina Gečevska, Ss. Cyril and Methodius University in Skopje, MKD
- Gordana Globočki Lakić, University of Banja Luka, BIH
- Dušan Golubović, University of East Sarajevo, BIH
- Marin Gostimirović, University of Novi Sad, SRB
- Predrag Janković, University of Niš, SRB
- Živana Jakovljević, University of Belgrade, SRB
- Sabahudin Jašarević, University of Zenica, BIH
- Zoran Jurković, University of Rijeka, CRO
- Simon Klančnik, University of Maribor, SVN
- Milan Kolarević, University of Kragujevac, SRB
- Lazar Kovačević, University of Novi Sad, SRB
- Borut Kosec, University of Ljubljana, SVN
- Snežana Ćirić Kostić, University of Kragujevac, SRB
- Aleksandar Košarac, University of East Sarajevo, BIH
- Milija Kraišnik, University of East Sarajevo, BIH
- Peter Krajnik, Chalmers University of Technology, SWE
- Davorin Kramar, University of Ljubljana, SVN
- Ivan Kuric, University of Zilina, SVK
- Dragan Lazarević, University of Priština in Kosovska Mitrovica, SRB
- Dejan Lukić, University of Novi Sad, SRB
- Ognjan Lužanin, University of Novi Sad, SRB
- Srećko Manasijević, Lola Institute, SRB
- Miodrag Manić, University of Niš, SRB
- Mijodrag Milošević, University of Novi Sad, SRB
- Mladomir Milutinović, University of Novi Sad, SRB
- Zoran Miljković, University of Belgrade, SRB
- Slobodan Mitrović, University of Kragujevac, SRB
- Slobodan Morača, University of Novi Sad, SRB
- Dejan Movrin, University of Novi Sad, SRB
- Dimitris Mourtzis, University of Patras, GRE
- Bogdan Nedić, University of Kragujevac, SRB
- Duško Pavletić, University of Rijeka, CRO
- Mladen Perinić, University of Rijeka, CRO
- Darko Petković, University of Zenica, BIH
- Petar B. Petrović, University of Belgrade, SRB

- Franci Pušavec, University of Ljubljana, SVN
- Radovan Puzović, University of Belgrade, SRB
- Dragan Rajnović, University of Novi Sad, SRB
- Biserka Runje, University of Zagreb, CRO
- Borislav Savković, University of Novi Sad, SRB
- Milenko Sekulić, University of Novi Sad, SRB
- Plavka Skakun, University of Novi Sad, SRB
- Denijal Sprečić, University of Tuzla, BIH
- Darko Stefanović, University of Novi Sad, SRB
- Miladin Stefanović, University of Kragujevac, SRB
- Antun Stoić, University of Slavonski Brod, CRO
- Tibor Szalay, Budapest University of Technology and Economics, HUN
- Tomislav Šarić, University of Slavonski Brod, CRO
- Goran Šimunović, University of Slavonski Brod, CRO
- Branko Škorić, University of Novi Sad, SRB
- Ľubomír Šooš, Slovak University of Technology, SVK
- Dušan Šormaz, Ohio University, USA
- Branko Štrbac, University of Novi Sad, SRB
- Slobodan Tabaković, University of Novi Sad, SRB
- Zorana Tanasić, University of Banja Luka, BIH
- Pal Terek, University of Novi Sad, SRB
- Radoslav Tomović, University of Montenegro, MNE
- Alan Topčić, University of Tuzla, BIH
- Nicolae Ungureanu, North University of Baia Mare, ROU
- Joško Valentinčič, University of Ljubljana, SVN
- Marko Vilotić, University of Novi Sad, SRB
- Đorđe Vukelić, University of Novi Sad, SRB
- Lihui Wang, KTH Royal Institute of Technology, SWE
- Wojciech Zebala, Cracow University of Technology, POL
- Saša Živanović, University of Belgrade, SRB
- Aleksandar Živković, University of Novi Sad, SRB

HONORARY COMMITTEE

- Slavko Arsovski, University of Kragujevac, SRB
- Pavao Bojanić, University of Belgrade, SRB
- Franc Čuš, University of Maribor, SVN
- Dragan Domazet, Metropolitan University, SRB
- Milenko Jovičić, University of Belgrade, SRB
- Vid Jovišević, University of Banja Luka, BIH
- Milisav Kalajdžić, University of Belgrade, SRB
- Janez Kopač, University of Ljubljana, SVN
- Pavel Kovač, University of Novi Sad, SRB
- Miodrag Lazić, University of Kragujevac, SRB
- Ljubomir Lukić, University of Kragujevac, SRB
- Vidosav Majstorović, University of Belgrade, SRB
- Dragoje Milikić, University of Novi Sad, SRB
- Dragan Milutinović, University of Belgrade, SRB
- Ratko Mitrović, University of Kragujevac, SRB
- Miroslav Plančak, University of Novi Sad, SRB
- Miroslav Radovanović, University of Niš, SRB
- Mirko Soković, University of Ljubljana, SVN
- Bogdan Sovilj, University of Novi Sad, SRB
- Branko Tadić, University of Kragujevac, SRB
- Ljubodrag Tanović, University of Belgrade, SRB
- Velimir Todić, University of Novi Sad, SRB
- Dragiša Vilotić, University of Novi Sad, SRB
- Milan Zeljković, University of Novi Sad, SRB

ORGANIZING COMMITTEE

- Đorđe Vukelić, Chairman, University of Novi Sad, SRB
- Anđelko Aleksić, University of Novi Sad, SRB
- Dejan Božić, University of Novi Sad, SRB
- Miroslav Dramićanin, University of Novi Sad, SRB
- Milana Ilić Mićunović, Secretary, University of Novi Sad, SRB
- Miloš Knežev, University of Novi Sad, SRB
- Aleksandra Kosanović, University of Novi Sad, SRB
- Dejan Marinković, University of Novi Sad, SRB
- Ivan Matin, University of Novi Sad, SRB
- Cvijetin Mlađenović, University of Novi Sad, SRB
- Aleksandar Milošević, University of Novi Sad, SRB
- Miloš Ranisavljev, University of Novi Sad, SRB
- Dragan Rodić, University of Novi Sad, SRB
- Željko Santoši, University of Novi Sad, SRB
- Mario Šokac, University of Novi Sad, SRB

ACKNOWLEDGEMENT

Organisation of 15th International Scientific Conference MMA 2024 – Flexible Technologies was made possible with understanding and financial help of following sponsors and donators:

- **Ministry of Science, Technological Development and Innovation of the Republic of Serbia,**
- **Provincial Secretary for Higher Education and Scientific Research of AP Vojvodina,**
- **University of Novi Sad,**
- **Faculty of Technical Sciences,**
- **Department of Production Engineering at the Faculty of Technical Sciences,**
- **Science and Technology Park Novi Sad,**
- **Lola Institute Ltd Belgrade,**
- **Tehnoexport Indjija,**
- **Mecafor Products Kikinda.**

FOREWORD

Continuing a long tradition of more than 45 years, the Department of Production Engineering of the Faculty of Technical Sciences in cooperation with Science and Technology Park Novi Sad organizes the 15th International Scientific Conference MMA 2024 – Flexible Technologies.

The conference will cover current issues in the field of production engineering as well as multidisciplinary fields of mechanical engineering, information technologies, environmental engineering, bio-medical engineering and other related engineering fields, that play a significant role in successful functioning of manufacturing industry, agriculture, transport, electric power industry, oil industry, military industry, health care and other branches of economy and society.

The conference, with its long tradition and regular organization since 1976, aims to gather and exchange experience of researchers and experts from faculties, institutes and industry, and thus wants to contribute to more intensive scientific and economic development.

The 15th International Scientific Conference MMA 2024 - Flexible Technologies is being held for the eleventh time as an international conference. By the number of papers, their quality and participation of domestic and foreign authors achieved so far, the Conference has gained an enviable reputation among scientific and professional employees from both faculty and industry.

The content of the International Scientific Conference MMA 2024 – Flexible Technologies involves the following areas:

- Material Removal Technologies,
- Machine Tools and Automatic Flexible Technological Systems, CAx and CIM Procedures and Systems,
- Metrology, Quality, Fixtures, Cutting Tools and Tribology,
- Process Planning, Optimization, Logistics and Internet Technologies in Production Engineering,
- Materials, Metal Forming, Casting and Welding,
- Mechanical Engineering and Environmental Protection,
- Bio-Medical Engineering,
- Additive Manufacturing Technologies.

With 61 scientific papers the 15th International Scientific Conference MMA 2024 - Flexible Technologies keeps the pace of previous conferences. The participation of numerous national and foreign authors from 11 countries, as well as the topics covered in the papers, confirm the efforts put into the organization of the conference, thus contributing to the exchange of knowledge, research results and expert experiences from industry, research institutions and universities working in the field of production engineering.

We would like to thank all domestic and foreign authors, reviewers, as well as institutions and individuals who contributed to the realization of high-quality program of the International Scientific Conference MMA 2024 - Flexible Technologies.

Novi Sad, September 2024

International Scientific and Organizing Committee

MMA 2024
FLEXIBLE TECHNOLOGIES

15th INTERNATIONAL SCIENTIFIC CONFERENCE
NOVI SAD, SERBIA, SEPTEMBER 24-26, 2024

CONTENTS

Section A:
MATERIAL REMOVAL TECHNOLOGIES

Rodić, D., Gostimirović, M., Sekulić, M., Savković, B., Aleksić, A., Kosanović, A.:
CIRCULARITY ANALYSIS OF LASER-DRILLED HOLES USING THE TAGUCHI METHOD 1

Madić, M., Trifunović, M., Janković, P.:
DEVELOPMENT AND ANALYSIS OF ANN MODEL FOR TOOL LIFE PREDICTION
IN DRY TURNING OF S355JR UNALLOYED STEEL 5

Baralić, J., Nedić, B., Jovičić, A.:
MULTILAYER CUTTING WITH ABRASIVE WATER JET 9

Kovac, P., Taric, M., Rodic, D., Savkovic, B., Dudic, B., Jesic, D.:
NEURO-FUZZY SYSTEMS MODELING OF HARD STEEL SURFACE
ROUGHNESS PARAMETERS 13

Vorkapic, N., Kokotovic, B., Zivanovic, S.:
COMPARATIVE ANALYSIS OF STATISTICAL FEATURES OF SIGNALS
IN THE TIME DOMAIN IN INTERNAL TURNING OPERATIONS 17

Aleksić, A., Rodić, D., Gostimirović, M., Sekulić, M., Savković, B., Kosanović, A.:
RELIMINARY INVESTIGATION OF THE IMPACT OF MQL ON SURFACE
ROUGHNESS DURING THE TURNING ALUMINUM ALLOY 6082 21

Savkovic, B., Rodic, D., Sekulic, M., Kovac, P., Aleksic, A., Kosanovic, A.:
DEVELOPMENT OF A MEASUREMENT-ACQUISITION SYSTEM FOR MEASURING
CUTTING FORCES AND TEMPERATURES USING VIRTUAL INSTRUMENTATION 25

Section B:
MACHINE TOOLS AND AUTOMATIC FLEXIBLE TECHNOLOGICAL SYSTEMS, CAx AND CIM PROCEDURES AND SYSTEMS

Karabegović, I., Husak, E., Mahmić, M., Karabegović, E.:
CHINA IS THE LEADING COUNTRY IN THE WORLD DEVELOPING AND IMPLEMENTING
ROBOT TECHNOLOGY IN ALL INDUSTRY BRANCHES 31

Marinković, D., Živković, A., Mlađenović, C., Knežev, M., Mejić, L., Savković, B.:
ANALYSIS OF THE INFLUENCE OF THE CUTTING REGIMES ON THE QUALITY
OF THE MACHINING SURFACE IN TURNING PROCESS 35

Devic, A., Vidakovic, J., Zivkovic, N., Stepanovic, A.:
ADVANCEMENT OF THE INDUSTRIAL ROBOT PROGRAMMING
LANGUAGE L-IRL USING AUGMENTED REALITY 39

Matin, I., Strbac, B., Ranisavljev, M., Hadzistevic, M., Vukelic, D.:
RESEARCH OF THE DEVIATION BETWEEN NUMERICAL SIMULATION AND EXPERIMENTS IN PLASTIC INJECTION MOLDING....43

Anišić, Z., Peić Tukuljac, E.:
DEVELOPMENT OF AN ELECTRONIC TOOL (ESAL – ELECTRONIC SHAFT ADJUSTER AND LOCKER) FOR DIRECT INJECTION PUMPS....47

Devedzic, G., Kocovic, V., Djordjevic, A., Jovanovic Pesic, Z., Dzunic, D., Vukelic, D., Petrovic Savic, S.:
RECONSTRUCTION AND OPTIMIZATION OF COMPLEX GEOMETRIC PARTS THROUGH REVERSE ENGINEERING....51

Živković, N., Pavlović, D., Ponjavić, M., Krošnjar, A., Stepanović, A.:
DESIGN OF COOLING SYSTEM FOR TWO POWER TRANSISTOR MODULES....55

Šulc, J., Reljić, V., Dakić, N., Jurošević, V.:
INTEGRATION OF ONE PNEUMATIC SOLUTION WITH A CNC DEVICE FOR THE REALIZATION OF THE PERFORATION PROCESS....59

Budimir Buda, A., Tabaković, S., Zeljković, M., Živanović, S., Dimić, Z.:
STRAIGHTNESS ANALYSIS OF MACHINE TOOL WITH NON-LINEAR KINEMATICS....63

Tabaković, S., Zeljković, M., Živanović, S.:
METHODS OF MONITORING AND APPLYING ENERGY BALANCE PARAMETERS IN THE EXPLOITATION OF MODERN MACHINE TOOLS....67

Jokić, A., Jevtić, Đ., Brenjo, K., Petrović, M., Miljković, Z.:
DEEP LEARNING-BASED VISUAL SERVOING ALGORITHM FOR WHEELED MOBILE ROBOT CONTROL....71

Knežev, M., Mlađenović, C., Marinković, D., Calin, A., Živković, A.:
FINITE ELEMENT ANALYSIS OF TURNING CUTTING TOOL....75

Nešovanović, Lj., Živanović, S., Konjević, P.:
INACCURACY ANALYSIS OF CHEBYSHEV'S MECHANISM....79

Suvajac, Z., Nedeljkovic, D., Jakovljevic, Z.:
OBJECT POSITION AND ORIENTATION DETECTION IN ASSEMBLY TASKS – AN APPROACH BASED ON YOLOV8 ALGORITHM....83

Maletić J., Vorkapic, N., Živanović S.:
PROGRAMMING AND VERIFICATION OF THE MACHINING PROGRAM FOR A TEST WORKPIECE FOR A MACHINE WITH A HORIZONTAL ROTARY AXIS....87

Section C:
METROLOGY, QUALITY, FIXTURES, CUTTING TOOLS AND TRIBOLOGY

Tanasić, Z., Vuković, M., Panić, M., Janjić, G.:
IMPROVEMENT ASSEMBLY PROCESS USING LEAN MANUFACTURING METHODS AND TOOLS....91

Milosevic, A., Kocovic, V., Santosi, Z., Sokac, M., Simunovic, G., Tadic, B., Vukelic, D.:
MODELLING THE BORING PROCESS ON THE BASIS OF CENTRIFUGAL FORCE
USING A SPECIALLY DESIGNED TOOL HOLDER....95

Vidakovic I., Simunovic, K., Pacarek, G., Barac, Z., Rozing, G.:
APPLICATION OF NiCrBSi AND NiCrBSi-WC COATINGS AS WEAR PROTECTION
FOR PARTS OF AGRICULTURAL TECHNIQUE....99

Jotic, G., Strbac, B., Sokac, M., Tanasic, Z., Runje, B., Acko, B., Hadzistevic, M.:
OPTIMIZATION OF THE MEASUREMENT PROCESS USING A 3D LASER SCANNER....103

Ognjenčić, K., Šimunović, G.:
MEASUREMENT TECHNIQUES FOR REDUCING WATER LOSS IN SUPPLY
SYSTEMS: FLOW, PRESSURE, AND NOISE ASSESSMENT....107

Bozic, D., Runje, B., Razumic, A., Lisjak, D., Strbac, B.:
RISK ASSESSMENT FOR NON-CENTERED MODELS IN METROLOGY....111

Rodinger, T., Lukšić, H., Ćorić, D., Rede, V.:
THE INFLUENCE OF ARTIFICIAL AGING PARAMETERS ON THE ABRASIVE
WEAR RESISTANCE OF AN Al-Zn-Mg ALLOY....115

Kasalica, V., Zivanovic, S., Stojadinovic, S.:
SIMULATION OF MEASUREMENT ON CMM BY IMPLEMENTING A DIGITAL TWIN MODEL....119

Santosi, Z., Sokac, M., Milosevic, A., Ivanov, V., Vukelic, D.:
3D RECONSTRUCTION OF MACHINE VISE BY APPLICATION OF PHOTOGRAMMETRY
AND REVERSE ENGINEERING....123

Bozic, D., Runje, B., Razumic, A., Lisjak, D., Strbac, B.:
RISK ASSESSMENT FOR LINEAR REGRESSION MODELS IN
METROLOGY: HYPOTHETICAL CASES....127

Section D:
PROCESS PLANNING, OPTIMIZATION, LOGISTICS AND INTERNET TECHNOLOGIES IN PRODUCTION ENGINEERING

Makovec, I.:
GENERATIVE ARTIFICIAL INTELLIGENCE IN COLABORATIVE MANUFACTURING....131

Bozic, D., Lukic, D., Milosevic, M., Spaic, O., Marinovic, B., Radovanovic, M.:
OPTIMIZATION OF MACHINING PROCESS PLANNING – CASE STUDY
OF A PRISMATIC PART....135

Trstenjak, M., Opetuk, T., Cajner, H., Đukić, G., Mustapić, M.:
METHODS AND TOOLS FOR ERGONOMIC ASSESSMENT IN MODERN
INDUSTRIAL ENVIRONMENT....139

Vukelic, Z., Cajner, H., Trstenjak, M.:
THE ASPECT OF TECHNOLOGICAL HUMANISM IN THE IMPLEMENTATION OF
ROBOTIC SYSTEMS (RS) AND ARTIFICIAL INTELLIGENCE (AI) IN INDUSTRY 5.0....143

Štrbac, G., Štrbac, B., Milošević, M., Ranisavljev, M., Hadžistević, M.:
IMPORTANCE OF 3D CAD SEARCH ENGINES IN GEAR MAINTENANCE 147

Vukman, J., Milošević, M., Borojević, S., Ungureanu. N., Božić, D., Lukić, D.:
OPTIMIZATION OF THE MACHINING PARAMETERS OF ALUMINUM PARTS
AS A FUNCTION OF THE PERPENDICULARITY DEVIATION OF THIN-WALLED SURFACES 151

Ćurčić, S., Milovančević, M., Savković, B.:
IMPROVING THE SAFETY OF THE TRANSPORT ZONE USING
THE MAKIGAMI METHODOLOGY 155

Section E:
MATERIALS, METAL FORMING, CASTING AND WELDING

Lukšić, H., Rede, V.:
EFFECT OF LASER WELDING PARAMETERS ON THE WELDED JOINT IN BATTERY
SYSTEMS OF ELECTRIC VEHICLES: A REVIEW 161

Terek, V., Kovačević, L., Škorić, B., Drnovšek, A., Čekada, M., Bobić, Z.,
Zagoričnik, M., Terek, P.:
TRIBOLOGICAL TESTING OF MULTILAYER TiAlSiN COATING AT HIGH TEMPERATURES 165

Panić, M., Smiljić, Đ., Movrin, D., Milutinović, M.:
ANALYSIS OF THE INFLUENCE OF RING DIMENSION RATIO
ON FRICTION IN UPSETTING TESTS 169

Timotijević, M., Erić Cekić O., Janjatović, P., Rajnović, D.:
THE INFLUENCE OF OVERHEATING TEMPERATURE ON THE MICROSTRUCTURE
OF HP40 ALLOY 173

Skakun, P., Janjatović, P., Dramićanin, M., Rajnović, D.:
AN EXPERIMENTAL ASSESMENT OF DEFORMATION IN METAL FORMING PROCESSES 177

Trivkovic, M., Maksimovic, N., Pecanac, M., Stojisic, N., Dramicanin, M.,
Rajnovic D., Balos, S.:
LASER SHOCK PEENING OF AISI 316L AUSTENITIC STAINLESS STEEL WITH
VARIOUS CONFINEMENTS 181

Vilotić, M., Dačević, N., Li, Y., Rynkovskaya, M., Alexandrov, S.:
THE PREDICTION OF A STRAIN STATE IN THE MULTISTAGE SEVERE
PLASTIC DEFORMATION 185

Petrovic, B., Pecanac, M., Hauck, A., Stojisic, N., Savkovic, B., Rajnovic, D., Balos S.:
RESISTANCE ELEMENT WELDING OF AW6060 AND STRUCTURAL STEEL 189

Kostić, N., Ranđelović, S., Perić, M.:
FEM SIMULATION AND VERIFICATION OF MECHANICAL PROPERTIES
OF NONSYMMETRIC HOT FORGED PART 193

Maksimovic, N., Hauck, A., Janjatovic, P., Pecanac, M., Savkovic, B., Rajnovic, D., Savic, V., Balos, S.:
INFLUENCE OF BASE METAL ROUGHNESS ON ADHESION-JOINED ALUMINIUM ALLOY AND STEEL....197

Karpe, B., Kosec, B., Gojic, M., Ivanic, I., Nagode, A., Cigic, L., Bizjak, M.:
HEAT TRANSFER IN CHILLING WHEEL IN MELT-SPINNING PROCESS....201

Section F:
MECHANICAL ENGINEERING AND ENVIRONMENTAL PROTECTION

Stanivuk, T., Dujmovic, M., Muslim, N., Dujmovic, M.:
ELECTRICAL MACHINES AND CONTROLL SYSTEM FOR MANAGING BALLAST WATER OF SHIP....207

Jovanovic, S., Ranisavljev, M., Milosevic, A., Ilic Micunovic, M., Vukelic, D., Agarski, B.:
LIFE CYCLE ASSESSMENT OF MACHINING PROCESSES: TURNING, MILLING, AND DRILLING 211

Bošković, G., Stepanov, B., Bošković. M., Todorović, M., Čepić, Z.:
THE PROCEDURE FOR CALCULATING INPUT PARAMETERS IN THE PROCESS OF DETERMINING POTENTIAL RISK ZONES IN WAREHOUSES 215

Ćurčić, S., Milovančević, M., Šarenac, S.:
APPLICATION OF MECHATRONIC STRUCTURES FOR THE PURPOSE OF ENVIRONMENTAL PROTECTION....219

Krstanoski, M.:
STRATEGIES THAT CONTRIBUTE TO THE SUSTAINABLE DESIGN IN HURRICANE PRONE ENVIRONMENTS....223

Section H:
ADDITIVE MANUFACTURING TECHNOLOGIES

Vasileska E., Pandilov Z., Gecevska V., Tomov M.:
EXPERIMENTAL DETERMINATION OF FLUENCE THRESHOLD AND MELT SIZE WITH D-SQUARED METHOD IN LASER POWDER BED FUSION....227

Cerjak, A., Fink, A., Jurečič, J., Zaviršek, N., Žalec, U., Hozdić, E., Rogelj, A., Hozdić, E.:
EFFECT OF INFILL STRUCTURE SHAPE ON THE MECHANICAL PARAMETERS OF FDM 3D PRINTED PETG AND PETG+CF MATERIALS 231

Ilić, K., Banjanin, B., Spasojević, S., Adamović, S., Dramićanin, M.:
EFFECT OF INFILL PATTERN ON THE TENSILE STRENGTH OF FDM 3D PRINTED PLA MATERIAL 235

Tuteski, O., Kochov, A.:
OVERVIEW OF THE APPLICATION OF STEREOLITHOGRAPHY IN ADDITIVE MANUFACTURING OF INJECTION MOLDING TOOL INSERTS....239

Trontelj, K., Slak, D., Primožič, J., Božič, A., Hozdić, E., Rogelj, A., Hozdić, E.:
IMPACT OF INFILL DENSITY ON THE MECHANICAL PROPERTIES OF FDM
3D PRINTED PETG AND PETG+CF MATERIALS 243

Bogojević, N., Ćirić-Kostić, S., Sinđelić, V., Olmi, G., Croccolo, D.:
EFFECTS OF AGING AND SURFACE TREATMENTS ON THE FATIGUE STRENGTH
OF STEEL COMPONENTS PRODUCED BY DMLS 247

MMA 2024
FLEXIBLE TECHNOLOGIES

Section A:
MATERIAL REMOVAL TECHNOLOGIES

MMA 2024
FLEXIBLE TECHNOLOGIES

15th INTERNATIONAL SCIENTIFIC CONFERENCE
NOVI SAD, SERBIA, SEPTEMBER 24-26, 2024

Original research paper https://doi.org/10.24867/MMA-2024-01-001

Rodić, D., Gostimirović, M., Sekulić, M., Savković, B., Aleksić, A., Kosanović, A.

CIRCULARITY ANALYSIS OF LASER-DRILLED HOLES USING THE TAGUCHI METHOD

Abstract: *Achieving a high circularity in laser drilled holes is critical for many industrial applications. In this study, the circularity of laser-drilled holes is analyzed using the Taguchi method. An orthogonal L9 array is used to investigate the effects of input parameters, including laser power, cutting speed and gas pressure, on the circularity of the holes. Circularity is measured as the ratio between the minimum and maximum diameter of the holes. The aim is to determine the influence of these parameters on circularity. The analysis shows that the gas pressure has the greatest influence, followed by the cutting speed and the laser power. These results provide information on the optimization of laser drilling processes to improve hole quality. The results suggest that careful control of gas pressure is critical to achieving high circularity and that adjustments to cutting speed and laser power can further improve hole quality.*

Key words: *Circularity, hole, laser power, cutting speed, gas pressure.*

1. INTRODUCTION

Laser drilling is widely used in industry to drill precise holes in a variety of materials, including metals, ceramics and composites. This advanced technique is highly regarded for its ability to produce high quality holes with minimal thermal damage and exceptional repeatability. One of the main advantages of laser drilling is the precise control of drilling parameters, which results in excellent hole characteristics, especially circularity [1]. Circularity, an important quality criterion for laser drilled holes, is often assessed by the ratio between the minimum and maximum diameter of the hole. This precise control ensures that the holes are consistent and meet the stringent quality standards required in various industries, from aerospace to medical device manufacturing [2]. The ability to maintain such high precision and quality makes laser drilling a preferred choice for applications that require exceptional accuracy and reliability [3].

Numerous research papers have dealt with the analysis of the circular shape of laser bores. Ghoreishi and Low (2002) analyzed the statistical aspects of hole circularity in laser drilling and emphasized the importance of optimizing the laser parameters [4]. Their study shows how different laser parameters affect the quality and precision of the drilled holes. The results of the study point to improvements in manufacturing processes through precise control of the laser parameters. Tiwari et al. (2005) investigated the influence of laser cutting parameters on the circularity of holes drilled in nickel-based superalloys [5]. Their study investigated how different laser parameters can affect the quality and precision of hole circularity. The results suggest that optimizing these parameters is crucial to achieve the desired results when cutting nickel-based superalloys. Muthuramalingam et al (2021) focused on the optimization of surface quality and circularity in CO_2 laser drilling of titanium alloys [6]. They investigated how different CO_2 laser parameters affect the surface quality and circularity of the drilled holes. The study concluded that careful optimization of these parameters is essential to improve the overall quality and precision of titanium alloy drilling. Chatterjee et al (2019) investigated the performance characteristics of micro-holes drilled with pulsed Nd lasers in titanium alloys [7]. Their study focused on evaluating the efficiency, precision and quality of microholes produced under different laser parameters. The results underline the crucial role of pulsed Nd laser settings in optimizing the performance of microhole drilling in titanium alloys. Kuar et al (2006) used response surface methodology to improve hole circularity in laser micromachining of composite materials [8]. In this study, a statistical approach was used to determine optimal laser parameters to improve hole circularity. The results showed that the response surface method is effective in refining laser micromachining processes to achieve better circularity in composite materials. Ghoreishi (2006) provided a comparative statistical analysis of hole circularity in laser percussion drilling [9]. The study compared different laser parameters and their effects on the circularity of drilled holes. By analyzing the statistical data, the study provided insights into the best practices for achieving high circularity in laser percussive drilling. The problem of circularity in laser drilled holes has not yet been sufficiently researched due to the complexity of the process, the large number of influencing factors and their interactions. Despite various studies focusing on the optimization of laser parameters, achieving a consistent and precise circularity in laser drilling remains a challenge.

In this study, the Taguchi L9 orthogonal array design is used to investigate the effect of three important input parameters - laser power, cutting speed and gas pressure - on the circularity of laser drilled holes. Circularity is measured as the ratio between the minimum and maximum diameter of the holes. The analysis shows that gas pressure has the greatest influence on hole circularity, followed by cutting speed and laser power.

This study contributes to the body of knowledge by providing insight into optimizing parameters to achieve high quality laser drilled holes, supporting advanced manufacturing processes. By understanding and controlling the key factors that affect hole circularity, manufacturers can improve the precision and quality of laser drilled holes, increasing the performance and reliability of their products.

2. MATERIAL AND METHODS

The cut was made using the "Bystar 3015" laser machine, which is renowned in the industry for its precision and efficiency. The machine's key features include a laser power of 3500 W and the ability to process large workpiece weights and thicknesses. The machine works on the basis of fiber technology, which differs from the traditional method of directing the laser to the melting point via mirrors. Instead, this technology works by reflecting the beam off the walls within an optical cable.

The experiments were carried out with low carbon hot rolled steel sheet, commonly known in practice as black steel, designated S235JR (1.0330) according to SRPS EN 10130:2011. The main mechanical properties of this steel are Tensile strength of 360-510 MPa, yield strength of 235 MPa, hardness of 104-154 HB and a modulus of elasticity of 210 GPa. The basic chemical composition is: Fe (≤98.5%), C (0.17-0.20%), Mn (≤1.4%), Si (≤0.035%), P (≤0.045%), S (≤0.045%).

Due to the complexity of the laser cutting process, several factors influence the cut quality. Based on the literature and user experience, the most important parameters were identified: Laser power, cutting speed and gas pressure. The values for these parameters were selected taking into account manufacturer recommendations, machine limitations and material properties. Assuming complex non-linear relationships between the input parameters and the hole circularity, three levels of variation were selected for each factor to ensure that a complete cut of a 3 mm thick workpiece is achieved with each combination (see Table 1).

Factors	Unit	Level		
		1	2	3
Cutting speed	(mm/min)	3000	3400	3800
Laser power	(kW)	1	1.5	2
Gas pressure	(MPa)	0.5	0.7	1.0

Table 1. Factors and levels used in experiments

The Taguchi L9 orthogonal array is a robust design of experiments (DOE) method that can be used to study the effects of multiple factors on a process with minimal trial runs [10]. It is particularly useful for optimizing processes where the relationship between variables and outcomes is complex. In this research, "higher is better" refers to the goal of maximizing a desired performance characteristic. The Taguchi method helps determine the optimal values of each factor to achieve the best performance while reducing variability. The Taguchi method helps to determine the optimal values for each factor to achieve the best performance while reducing variability. This makes it a valuable tool, especially in the area of impact analysis. This approach is reflected in the division of the optimization problem into two categories, using the logarithmic function of the observed response as the target optimization function, known as the signal-to-noise ratio (S/N).

One of the ways to measure the circular shape is the ratio between the smaller and the larger diameter, equation 1. This measurement technique is mainly used to determine roundness in small diameter openings. The circularity at entry and exit has been measured by using the ratio of minimum to maximum Feret's diameters of the hole, which is a commonly accepted method for assessing the quality of small diameter holes [1].

$$C = \frac{Dmin}{Dmax} \quad (1)$$

To investigate the influence of factors such as laser power, cutting speed, and auxiliary gas pressure on circularity, measurements were conducted using a Euromex NexiusZoom EVO microscope with a CMEX-5 Pro digital camera. The measurement accuracy was 0.01 mm, using a scale of 1 DIV 0.01 mm.

This approach emphasizes the relevance and timeliness of research in this area, as precise control of hole geometry is critical in many advanced manufacturing applications. Table 2 shows the Taguchi plan of the experiment with the measurement results and the hole circularity evaluation.

No.	Factors			Diameters		*C* [/]	*S/N*
	C1	C2	C3	*Dmin* (mm)	*Dmax* (mm)		
1.	1	1	1	2.59	2.9	0.89	19.74
2.	1	2	2	2.65	2.92	0.91	20.86
3.	1	3	3	2.74	2.88	0.95	20.59
4.	2	1	2	2.83	3.19	0.89	23.12
5.	2	2	3	2.65	2.84	0.93	19.82
6.	2	3	1	2.67	3.13	0.85	22.83
7.	3	1	3	2.68	3.02	0.89	20.43
8.	3	2	1	2.68	2.9	0.92	20.03
9.	3	3	2	2.8	3.09	0.91	22.92

Table 2. Taguchi L9 orthogonal array, measured values, circularity ratio and S/N ratio

3. RESULTS AND DISCUSSION

The results of the study on the circularity of laser-drilled holes using the Taguchi method are presented, focusing on the effects of laser power, cutting speed, and gas pressure. The circularity of the holes was evaluated using the ratio of minimum to maximum diameter. Circularity is a crucial parameter in determining the quality of the hole. Fig. 1 shows drilled holes with different laser parameters.

Taguchi orthogonal array L9(3^4) was applied during laser cutting of 3 mm thick hot rolled sheet in order to optimize and analyze the influence of circularity hole input parameters in more detail. Based on the measured values of C, the S/N ratio was calculated for all 9 experimental points. The values of the S/N ratio for all output performances are calculated based on the Taguchi quality characteristic "larger is better", Table 2.

The analysis of S/N values, in order to determine the approximately optimal values of the factors of the laser cutting process for each objective function, was performed using the analysis of mean values. According to Table 2, the effects of the input factors of the laser cutting process on the S/N value of the circularity hole were obtained, which were first presented in tabular form (Table 3) and then in the form of a graph of the main effects in Fig. 2.

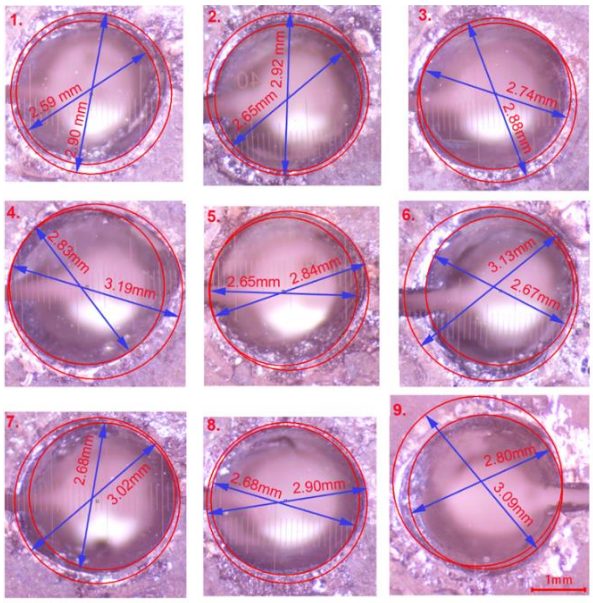


Fig. 1. Optical images showing circularities of drilled holes with different laser parameters

No.	Factor	*S/N* Level			Delta	Rang
		1	2	3		
1.	C1	-0.759	-1.018	-0.851	0.259	1
2.	C2	-1.012	-0.724	-0.892	0.287	2
3.	C3	-1.049	-0.883	-0.696	0.353	3

Table 3. The effects of the input factors of the laser cutting process on the S/N value

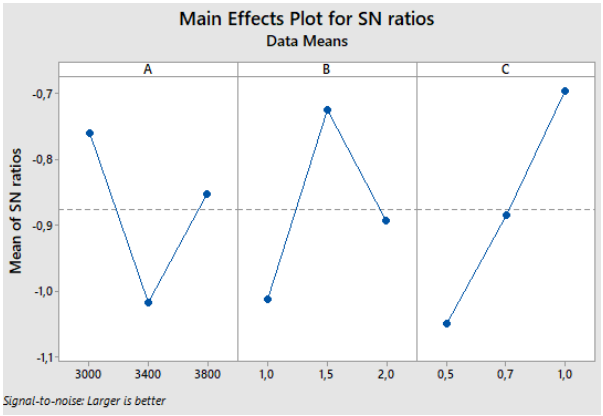


Fig. 2. Effect of process parameters on circularity hole

According to the obtained results from Table 3 and Fig. 2, it can be concluded that the optimal combination of factor levels that maximizes the ratio of the diameters is C1 (level 1) C2 (level 2) C3 (level 3). When evaluating these parameters, the study found a S/N ratio (signal-to-noise ratio) of -0.43 and a ratio of lower to upper diameter of 0.95. The closer the ratio of lower to upper diameter is to 1, the better the circularity of the hole. A ratio close to 1 indicates a minimal deviation between the minimum and maximum diameter, which indicates a high-quality circular shape and consequently better precision when drilling. This is an important indicator of the overall quality and consistency of the laser drilling process.

To influence the circularity of laser-drilled holes, adjustments to laser power, cutting speed, and gas pressure can be made.

A higher laser power can significantly improve material removal during the drilling process. This higher power facilitates efficient cutting of the material and results in cleaner and more precise holes. However, if the laser power is set too high, it can lead to excessive melting or vaporization of the material. This excess heat can lead to irregular hole shapes, such as tapering or uneven edges, which negatively affects the circularity of the hole. On the other hand, lower laser power may not provide enough energy to penetrate the material effectively. This can result in incomplete holes where the hole does not go all the way through the material or has an uneven depth. Insufficient power can also lead to inconsistent material removal, resulting in rough and irregular edges, further compromising the desired circularity.

Therefore, it is important to carefully balance the laser power to achieve optimal circularity. The power must be high enough to ensure clean cuts and efficient material removal, but not so high as to cause deformation due to excessive heat. Finding this balance is key to maintaining the integrity and precision of the drilled holes.

Higher cutting speeds can reduce the amount of heat input into the material during the drilling process, which helps minimize thermal deformation and maintain the integrity of the hole's shape. This reduction in heat input can improve circularity by preventing the material from warping or distorting, resulting in more uniform and precise holes. However, if the cutting speed is too high, it can lead to incomplete cuts or uneven edges. The material may not have enough time to be fully removed or melted away, leading to irregularities in the hole's shape and negatively impacting circularity.

On the other hand, lower cutting speeds allow more time for heat to accumulate in the material, which can lead to excessive melting and potential distortion of the hole's shape. This can cause the edges to become rounded or uneven, reducing the overall circularity of the hole. Additionally, slower speeds can lead to a buildup of molten material and debris around the cutting area, which can further degrade the quality and precision of the hole. Therefore, it is essential to optimize cutting speed to balance heat input and material removal. The goal is to achieve a speed that minimizes thermal deformation while ensuring complete and clean cuts, resulting in holes with high circularity and precision.

Using a higher gas pressure during laser drilling can help remove molten material and debris from the cutting area. This removal is critical to maintaining clean cuts and achieving a better circular shape, as it prevents the

accumulation of unwanted particles that can affect the path of the laser and the final shape of the hole. A consistent and sufficient gas flow can blow away the molten material, ensuring a clear cut area and a smoother, more precise hole edge.

However, if the gas pressure is set too high, this can lead to turbulence and uneven cooling in the cutting area. This turbulence can cause the molten material to spread unevenly or cool unevenly, resulting in distortions in the shape of the hole. Such distortions can lead to a deviation from the desired circular shape, so that the hole has uneven edges or a non-uniform diameter. On the other hand, the lower gas pressure may not be enough to remove all of the molten material and debris from the cutting area. This insufficient removal can lead to a buildup of debris around the hole, resulting in rough or irregular edges. The accumulation of such material can also cause incomplete cuts or clogging, further affecting the quality and circularity of the hole. Therefore, it is important to carefully control the gas pressure to achieve optimal results. The pressure should be high enough to effectively clear the cutting area, but not so high that it causes turbulence and uneven cooling. The correct balance of gas pressure is critical to producing holes with high circularity and minimal defects.

4. CONCLUSION

The study focused on analyzing the circularity of laser-drilled holes by investigating the effects of laser power, cutting speed, and gas pressure using the Taguchi method. Circularity, evaluated as the ratio of minimum to maximum diameter, is a critical quality parameter for drilled holes. The Taguchi orthogonal array L9 was used to analyze these factors, and the signal-to-noise ratio (S/N) was calculated based on the "larger is better" quality characteristic. The analysis revealed that the optimal combination of factor levels to maximize circularity is: 3000 mm/min, 1,5 kW and 1 MPa resulting a diameter ratio of 0.95, indicating good circularity. Higher laser power can improve material removal but can lead to irregular shapes if the power is too high, while lower power can lead to incomplete holes. Higher cutting speeds can minimize thermal deformation and thus improve circularity, but too high speeds can result in incomplete cuts. Lower speeds can lead to excessive melting and deformation. Finally, adequate gas pressure helps to remove debris and maintain circularity. However, too high or insufficient pressure can lead to deformation or irregular edges.

5. REFERENCES

[1] Biswas, R., A. Kuar, S. Biswas, and S. Mitra: *Characterization of hole circularity in pulsed Nd: YAG laser micro-drilling of TiN–Al 2 O 3 composites*. The International Journal of Advanced Manufacturing Technology, Vol. 51: pp. 983-994, 2010.

[2] Sztankovics, I.: *Cylinder accuracy analysis of tangential turning of disk-like workpieces with increased cutting speed*. Journal of Production Engineering.Vol. 27(1): pp. 22-29, 2024.

[3] Meijer, J.: *Laser beam machining (LBM), state of the art and new opportunities*. Journal of materials processing technology, Vol. 149(1-3): pp. 2-17, 2004.

[4] Ghoreishi, M., D. Low, and L. Li: *Comparative statistical analysis of hole taper and circularity in laser percussion drilling*. International Journal of Machine Tools and Manufacture, Vol. 42(9): pp. 985-995, 2002.

[5] Thawari, G., J. S. Sundar, G. Sundararajan, and S. Joshi: *Influence of process parameters during pulsed Nd: YAG laser cutting of nickel-base superalloys*. Journal of Materials Processing Technology, Vol. 170(1-2): pp. 229-239, 2005.

[6] Muthuramalingam, T., R. Akash, S. Krishnan, N. H. Phan, V. N. Pi, and A. H. Elsheikh: *Surface quality measures analysis and optimization on machining titanium alloy using CO_2 based laser beam drilling process*. Journal of Manufacturing Processes, Vol. 62: pp. 1-6, 2021.

[7] Chatterjee, S., S. S. Mahapatra, V. Bharadwaj, A. Choubey, B. N. Upadhyay, and K. S. Bindra: *Quality evaluation of micro drilled hole using pulsed Nd: YAG laser: a case study on AISI 316*. Lasers in Manufacturing and Materials Processing, Vol. 5: pp. 248-269, 2018.

[8] Kuar, A., G. Paul, and S. Mitra: Nd: *YAG laser micromachining of alumina–aluminium interpenetrating phase composite using response surface methodology*. International Journal of Machining and Machinability of Materials, Vol. 1(4): pp. 432-444, 2006.

[9] Ghoreishi, M.: *Statistical analysis of repeatability in laser percussion drilling*. The International Journal of Advanced Manufacturing Technology, Vol. 29: pp. 70-78, 2006.

[10] Kramar, D., M. Sekulić, D. Rodić, and V. Pejić: *Optimizing main cutting force in high-pressure jet-assisted turning using Taguchi method*. Journal of Production Engineering, Vol. 27(1): pp. 1-4, 2024.

ACKNOWLEDGMENTS

This research has been supported by the Ministry of Science, Technological Development and Innovation (Contract No. 451-03-65/2024-03/200156) and the Faculty of Technical Sciences, University of Novi Sad through project “Scientific and Artistic Research Work of Researchers in Teaching and Associate Positions at the Faculty of Technical Sciences, University of Novi Sad” (No. 01-3394/1).

Authors:

PhD Dragan Rodić, PhD Marin Gostimirović, PhD Milenko Sekulić, PhD Borislav Savković, MSc Anđelko Aleksić, BSc Aleksandra Kosanović, University of Novi Sad, Faculty of Technical Sciences, Trg Dositeja Obradovica 6, 21000 Novi Sad, Serbia, Phone.: +381 21 485-23-24.

E-mail: rodicdr@uns.ac.rs; maring@uns.ac.rs; milenkos@uns.ac.rs; savkovic@uns.ac.rs; andjelkoa@uns.ac.rs; kosanovic@uns.ac.rs

MMA 2024 FLEXIBLE TECHNOLOGIES

15th INTERNATIONAL SCIENTIFIC CONFERENCE
NOVI SAD, SERBIA, SEPTEMBER 24-26, 2024

Original research paper https://doi.org/10.24867/MMA-2024-01-002

Madić, M., Trifunović, M., Janković, P.

DEVELOPMENT AND ANALYSIS OF ANN MODEL FOR TOOL LIFE PREDICTION IN DRY TURNING OF S355JR UNALLOYED STEEL

Abstract: *Assessment of tool life is of prime importance in machining process planning. The present study is focused on the development of tool life prediction model using artificial neural network (ANN). Data for model development were obtained using a tool and cutting data recommendation system of the cutting tool manufacturer and by applying full factorial design. The ANN prediction model was developed in terms of five input parameters, three parameters related to the machining process (depth of cut, feed rate and cutting speed) and two related to the cutting tool geometry (rake angle and cutting edge angle). Dry longitudinal single-pass turning of S355JR unalloyed steel using coated carbide tools was considered in the analysis. The adequacy of the developed ANN model was confirmed by considering the estimation of mean absolute percentage error and correlation coefficient, as well as residual analysis. In order to analyse and evaluate effects of considered input parameters on the tool life, sensitivity analysis of developed ANN model was conducted. Additional cutting data proved the generalization capability of the developed ANN model and its high prediction accuracy.*

Key words: *tool life, turning, ANN, sensitivity analysis, S355JR unalloyed steel, coated carbide tool*

1. INTRODUCTION

Tool life is one of the most significant criteria for assessment of cutting tool performance and machinability of materials [1]. It may be defined as the ability to preserve the tool cutting characteristics in certain operating conditions, while its assessment can be made with respect to effective cutting time, volume of removed chips, number of machined workpieces or total cutting length [2]. Most standard tool life tests use flank wear as criterion to define the end of tool life [1].

Reliable and accurate predictions of tool life is essential in manufacturing practice given that knowledge of tool wear and life can be helpful in multiple ways, such as process optimization regarding productivity, costs and scheduling, fulfilment of required tolerances, decrease of scrap, energy consumption [3,4,5]. In open literature and industrial practice one can find different methods and approaches for estimation of the tool wear and tool life. Among these, one can distinguish between model-based and data-driven methods (empirical mathematical modelling and use of AI), which belong to the in-direct methods, and direct methods, which use image recognition and deep learning to predict remaining tool life [6].

Choudhury and El-Baradie [7] applied experimental design method to develop first- and second-order tool-life models. Rao et al. [8] developed the extended Taylor model to predict tool life. Qehaja et al. [9] developed power model in terms of cutting speed, feed rate, depth of cut and tool flank wear. Laghari et al. [10] developed ANN model to predict tool life in SiCp/Al turning in terms of cutting speed, feed rate and depth of cut. Ojha and Dixit [11] proposed an economical and reliable procedure for the estimation of the tool life including the methodology for tool usage monitoring based on the shopfloor feedback, and approach for updating Taylor's tool life exponents. Królczyk et al. [12] proposed a second-order polynomial model to study the effects of depth of cut, feed rate and cutting speed on tool life. An approach for prediction of tool life in turning based on ANN models, which uses wear parameters, obtained by image processing, as model inputs was presented by Mikołajczyk et al. [5]. Bagga et al. [3] proposed a computer vision-based tool wear monitoring and tool life prediction system using machine learning methods. Gradient-boosted trees and support vector machine methods were also used for the prediction of tool life. Gao et al. [13] proposed reliability Taylor tool life equation in which approximate Bayesian theory was used to update reliability model parameters. Albertelli et al. [14] developed a generalized tool life model for considering non-stationary cutting conditions. A stochastic Markov model for prediction of remaining tool life was discussed by Mishra and Bhardwaj [15]. Hage et al. [16] proposed a novel combination of a tabu search algorithm with the regression analysis for the development of tool life prediction models in terms of spindle speed, depth of cut and feed rate. Karkalos and Markopoulos [17] analysed applicability of different experimental designs and ANN for prediction of tool life using CBN tools for a wide range of cutting speeds.

Given that the determination of the effect of each parameter on tool life is of crucial importance when designing the manufacturing process of a product in order to select suitable process parameter values and tool types [17], the present research deals the analysis of the effects of three parameters related to the machining process (depth of cut, feed rate and cutting speed) and two related to the cutting tool geometry (rake angle and cutting edge angle) on the tool life in dry longitudinal single-pass turning of S355JR unalloyed steel using coated carbide tools. Data for the analysis were obtained using a tool and cutting data recommendation system of the cutting tool manufacturer [18] and were modelled using ANN.

2. EXPERIMENTAL DATA

The start diameter for longitudinal single-pass turning was 120 mm, while the machined length was 60 mm. The workpiece material was S355JR unalloyed medium-carbon structural steel (hardness 161 HB). It is used for medium to high strength non-vital machine parts, with good toughness and easy formability. The machine tool was the CNC lathe with the motor power of P_m = 37 kW, the maximum spindle speed of n_{max} = 2000 rpm, and the maximum torque of M_{cmax} = 4200 Nm.

Walter was selected as cutting tool manufacturer. The cutting tools were toolholders DDJNR2525M15 (cutting edge angle of κ = 93°, rake angle of γ_{oh} = -6°) and DDNNN2525M15 (κ = 62.5°, γ_{oh} = -6°), with DNMG150612-MP3 WPP10G (γ_{oi} = 22.5°) and DNMG150612-MP5 WPP10G (γ_{oi} = 15°) coated carbide inserts for medium machining. Cutting parameter ranges and levels were selected considering availability and capabilities of the tool and cutting data recommendation system of the cutting tool manufacturer and recommended cutting conditions for the inserts. For the DNMG150612-MP3 WPP10G insert, the minimal and maximal depth of cut values were set to 1.2 and 3.5 mm, respectively, the minimal and maximal feed rate values were set to 0.16 and 0.40 mm/rev, respectively, while the cutting tool rake angle was 16.5°. For the DNMG150612-MP5 WPP10G insert, the minimal and maximal depth of cut values were set to 1.2 and 5.0 mm, respectively, the minimal and maximal feed rate values were set to 0.20 and 0.40 mm/rev, respectively, while the cutting tool rake angle was 9°. The cutting speed values for both inserts were selected considering availability and capabilities of the tool and cutting data recommendation system of the cutting tool manufacturer. It allows selection of values for the cutting speed from ranges that are different for different feed rate values, due to power limitation (e.g., for the feed rate value of f = 0.16 mm/rev the cutting speed value can be selected from the range of 351 – 550 m/min, while for the feed rate value of f = 0.40 mm/rev the cutting speed value can be selected from the range of 269 – 421 m/min). For the DNMG150612-MP3 WPP10G insert, the minimal and maximal selected cutting speed values were 269 and 550 m/min, respectively. For the DNMG150612-MP5 WPP10G insert, the minimal and maximal selected cutting speed values were 269 and 525 m/min, respectively. The cutting edge angles were 62.5° and 93° for both inserts. Data for the analysis were obtained using a tool and cutting data recommendation system of the cutting tool manufacturer [18]. The total number of different cutting conditions that were attempted in the virtual experiment was 108.

3. TOOL LIFE MODEL

To establish mathematical relationship between inputs and output, a multi layer perceptron (MLP) ANN architecture was chosen for its exceptional ability to approximate arbitrary functional dependencies. The number of hidden neurons was determined considering the number of ANN hyper-parameters (weights and biases) to be determined in the training process, and the number of available data. Linear transfer function and tangent sigmoid transfer function were used in the output and hidden layer, respectively. The entire set of cutting data was randomly divided into the data set for training (60% of data), used to develop ANN model, the data set for validation (20% of data), used to handle bias-variance trade-off and validate developed ANN model, and testing set (20% of data), for statistical assessment of the generalization capability of the developed model. The specified ANN model was trained using Levenberg-Marquardt algorithm due to its high accuracy and fast convergence [19]. Only fourteen epochs were sufficient for training process as no further improvement in ANN model performance was achieved. The mean absolute percentage error between ANN model predictions and the tool life values on the entire set of data was found to be 1.85%, which indicated the validity of the developed model. ANN model prediction results in relation to the experimental data are given in Figure 1. As could be observed, there exists perfect correlation for the entire set of gathered cutting data, thus confirming high performance capability of the developed ANN model. Residual analysis was also performed in order to further validate the appropriateness of the developed model for the prediction tool life (Figure 2). Residuals are scattered around zero with mean value close to zero, indicating closeness of predicted and observed values and unbiased prediction capability of the ANN model. Absence of obvious patterns also confirms the adequacy of the proposed prediction model. Finally, approximately even spread of the residuals across fitted values of tool life means that the model fits consistently in all regions of the covered experimental hyper-space.

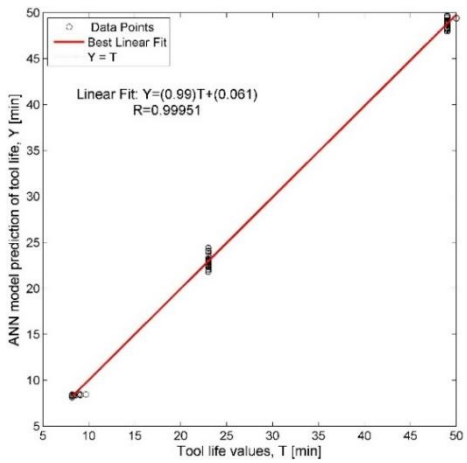


Fig. 1. Performance of ANN tool life prediction model

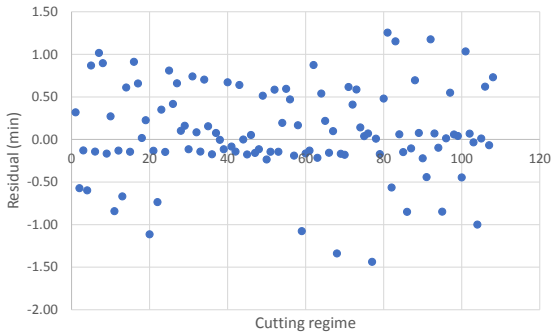


Fig. 2. Scatter plot of ANN models' residuals

4. RESULTS AND DISCUSSION

Sensitivity analysis is a very popular approach for knowledge extraction when using ANN. The idea of this approach is to simulate trained ANN model with different input data patterns and record how inputs affect output values over a range of values [20]. In the present study, four parameters were kept constant (at low, medium, and high level), while the fifth input parameter was varied at three levels (low, medium, and high). Subsequently, by ANN model simulation it was possible to observe the change in tool life values as the difference between maximal and minimal values (Figure 3).

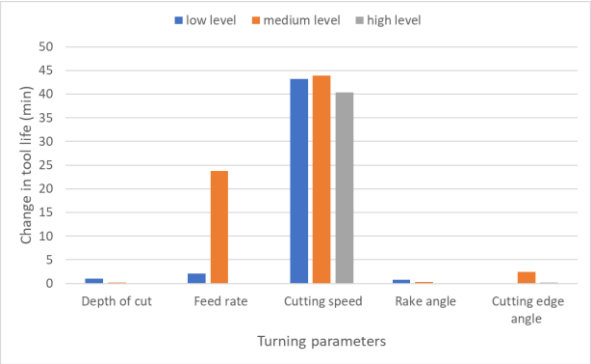


Fig. 3. Main effects of turning parameters on tool life

As could be observed, irrespective of whether other turning parameters are set at low, medium, or high level, cutting speed has the most significant effect on tool life. The effect of feed rate is also pronounced, particularly when all other turning parameters are set at medium level. Effects of cutting edge angle, depth of cut and rake angle on tool life are negligible. Based on performed analysis in general, there exist indirect relationships between feed rate, cutting speed, rake angle, cutting edge angle and resulting tool life. It is interesting to note that with an increase in depth of cut, one may observe insignificant change in tool life or even a slight increase. In sum, if one tends to extend tool life, cutting tool with rake angle of 16.5° and cutting edge angle of 93° is to be used under the following cutting conditions: depth of cut 5 mm, feed rate 0.16 mm/rev and cutting speed of 269 m/min. Under this cutting regime ANN model predicts tool life of 51.28 min.

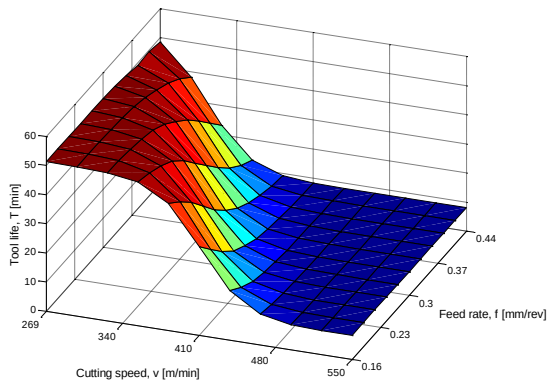


Fig. 4. Interaction effect of two most significant parameters on tool life (constant parameters: a_p = 5 mm, κ = 93°, γ = 16.5°)

Given that cutting speed and feed rate are the most significant turning parameters affecting tool life, it was decided to analyse their combined effect by developing 3D surface plot (Figure 4). As could be observed from Figure 4, there is no significant interaction effect, however, one can observe that at high feed rates, an increase in cutting speed leads to a faster decrease in tool life. It is interesting to note that for maximization of the tool utilization cutting regime with the highest possible tool life may not be, as a rule, the best solution, given that resulting material removal rates may differ for the same value of the tool life.

Given the high dimensionality of the input data, novel data from the tool and cutting data recommendation system of the cutting tool manufacturer [18], which were not used previously, were used to further assess model performance generalization capability. Four cutting regimes and tool geometry specifications were considered, as given in Table 1. With a mean absolute percentage error below 5% one can argue that ANN model proved to be able to adequately model tool life in five-dimensional hyper-space.

Cutting data	Trial 1	Trial 2	Trial 3	Trial 4
f (mm/rev)	0.34	0.22	0.25	0.36
a_p (mm)	1.8	3	2.1	4
v (m/min)	317	468	408	305
γ_o (°)	16.5	16.5	9	9
κ (°)	93	62.5	93	62.5
T (min) [18]	33	13	18	42
T (min) ANN model	34.76	13.75	17.5	39.59

Table 1. Additional cutting data for assessment of ANN model performance

5. CONCLUSION

The present study was focused on the development of ANN model for tool life prediction in dry longitudinal single-pass turning of S355JR unalloyed steel using coated carbide tools. Unlike traditional and extended Taylor's tool life models, the derived model was developed in terms of three parameters related to the machining process (depth of cut, feed rate and cutting speed) and two related to the cutting tool geometry (rake angle and cutting edge angle). It was observed that ANN model with 5-4-1 architecture, trained with Levenberg-Marquardt algorithm, proved to be able to capture the underlying dependencies between inputs and output with high accuracy and also showed very good generalization capability. Analysis of obtained results indicated the dominant effect of cutting speed on tool life, followed by the effect of feed rate, while the effects of cutting edge angle, depth of cut and rake angle on tool life are negligible. Analysis of interaction effect of the two most significant parameters (cutting speed and feed rate) indicated that there is no qualitative change in parameter effects. However, more comprehensive analysis, which included the consideration of MRR, indicated that some cutting conditions having lower tool life may be preferable given that these conditions enable removal of higher volume of material (chip).

The derived prediction model can be used in formulation of turning optimization problems to select

the most appropriate cutting parameter values with respect to different objective functions, such as machining time, production costs, etc. Future work will consider application of connection weight approach for ranking the importance of considered input variables and dual-response approach for simultaneous analysis of tool life and material removal rates.

6. REFERENCES

[1] Stephenson, D.A., Agapiou, J.S.: *Metal Cutting Theory and Practice, Third Edition*, CRC Press, Boca Raton, 2016.

[2] Radovanović, M.: *Tehnologija mašinogradnje: Obrada rezanjem*, Univerzitet u Nišu, Mašinski fakultet u Nišu, Niš, 2002.

[3] Bagga, P.J., Patel, K.M., Makhesana, M.A., Şirin, S., Khanna, N., Krolczyk, G.M., Pala, A.D., Chauhan, K.C.: *Machine vision‐based gradient‐boosted tree and support vector regression for tool life prediction in turning*, The International Journal of Advanced Manufacturing Technology, Vol. 126, No. 1-2, pp. 471-485, 2023.

[4] De Barrena, T.F., Ferrando, J.L., García, A., Badiola, X., de Buruaga, M.S., Vicente, J.: *Tool remaining useful life prediction using bidirectional recurrent neural networks (BRNN)*, The International Journal of Advanced Manufacturing Technology, Vol. 125, No. 9-10, pp. 4027-4045, 2023.

[5] Mikołajczyk, T., Nowicki, K., Bustillo, A., Yu Pimenov, D.: *Predicting tool life in turning operations using neural networks and image processing*, Mechanical Systems and Signal Processing, Vol. 104, pp. 503-513, 2018.

[6] Bazaz, S.M., Lohtander, M., Varis, J.: *The prediction method of tool life on small lot turning process – Development of Digital Twin for production*, Procedia Manufacturing, Vol. 51, pp. 288-295, 2020.

[7] Choudhury, I.A., El-Baradie, M.A.: *Tool-life prediction model by design of experiments for turning high strength steel (290 BHN)*, Journal of Materials Processing Technology, Vol. 77, No. 1-3, pp. 319-326, 1998.

[8] Rao, C.J., Sreeamulu, D., Mathew, A.T.: *Analysis of Tool Life during Turning Operation by Determining Optimal Process Parameters*, Procedia Engineering, Vol. 97, pp. 241-250, 2014.

[9] Qehaja, N., Abdullahu, F., Zhujani, F.: *Multifactorial mathematical models of tool life for turning operation based on tool wear and cutting parameters*, International Journal of Mechanical Engineering and Technology, Vol. 8, No. 11, pp. 484-493, 2017.

[10] Laghari, R.A., Li, J., Laghari, A.A., Mia, M., Wang, S., Aibo, W., Poonam, K.K.: *Carbide tool life prediction and modeling in SiCp/Al turning process via artificial neural network approach*, IOP Conference Series: Materials Science and Engineering, Vol. 600, Article ID: 012022, 2019.

[11] Ojha, D.K., Dixit, U.S.: *An economic and reliable tool life estimation procedure for turning*, The International Journal of Advanced Manufacturing Technology, Vol. 26, No. 7-8, pp. 726-732, 2005.

[12] Królczyk, G., Gajek, M., Legutko, S.: *Effect of the cutting parameters impact on tool life in duplex stainless steel turning process*, Tehnički vjesnik – Technical Gazette, Vol. 20, No. 4, pp. 587-592, 2013.

[13] Gao, T., Li, Y., Huang, X., Li, H.: *Turning tool life reliability analysis based on approximate Bayesian theory*, Proceedings of the Institution of Mechanical Engineers, Part O: Journal of Risk and Reliability, Vol. 236, No. 5, pp. 696-709, 2022.

[14] Albertelli, P., Mussi, V., Monno, M.: *Development of generalized tool life model for constant and variable speed turning*, The International Journal of Advanced Manufacturing Technology, Vol. 118, No. 5-6, pp. 1885-1901, 2022.

[15] Mishra, S., Bhardwaj, P.: *Remaining useful life estimation by stochastic Markov model and Monte-Carlo simulation*, International Journal of Industrial and Systems Engineering, Vol. 39, No. 1, pp. 59-70, 2021.

[16] Hage, R.M., Hage, I., Ghnatios, C., Hamade, R.: *Statistically Validated and Optimized Tabu Search Estimation of Cutting Tool Life in Turning*, Proceedings of the ASME 2018 International Mechanical Engineering Congress and Exposition, Article ID: V002T02A038, 6 pages, Pittsburgh, ASME, New York, 2018.

[17] Karkalos, N.E., Markopoulos, A.P.: *Applicability of ANN models and Taguchi method for the determination of tool life in turning*, Proceedings of the 21st Innovative Manufacturing Engineering & Energy International Conference, Iasi, Article ID: 06005, 6 pages, EDP Sciences, Les Ulis, 2017.

[18] Walter GPS, 2024, https://www.walter-tools.com/en-gb/gps

[19] Madić, M., Radovanović, M., Manić, M., Trajanović, M.: *Optimization of ANN models using different optimization methods for improving CO_2 laser cut quality characteristics*, Journal of the Brazilian Society of Mechanical Sciences and Engineering, Vol. 36, No. 1, pp. 91-99, 2014.

[20] Weckman, G.R., Paschold, H.W., Dowler, J.D., Whiting, H.S., Young, W.A.: *Using Neural Networks with Limited Data to Estimate Manufacturing Cost*, Journal of Industrial and Systems Engineering, Vol. 3, No. 4, pp 257-274, 2010.

ACKNOWLEDGMENTS

This research was financially supported by the Ministry of Science, Technological Development and Innovation of the Republic of Serbia (Contract No. 451-03-65/2024-03/200109).

Authors:

PhD Miloš Madić, PhD Milan Trifunović, PhD Predrag Janković, University of Niš, Faculty of Mechanical Engineering in Niš, Aleksandra Medvedeva 14, 18104 Niš, Serbia, Phone: +381 18 500-626, Fax: +381 18 588-244.

E-mail: milos.madic@masfak.ni.ac.rs; milan.trifunovic@masfak.ni.ac.rs; predrag.jankovic@masfak.ni.ac.rs

MMA 2024 FLEXIBLE TECHNOLOGIES

15th INTERNATIONAL SCIENTIFIC CONFERENCE
NOVI SAD, SERBIA, SEPTEMBER 24-26, 2024

Original research paper https://doi.org/10.24867/MMA-2024-01-003

Baralić, J., Nedić, B., Jovičić, A.

MULTILAYER CUTTING WITH ABRASIVE WATER JET

Abstract: *The main goal of today's production is to produce as many parts as possible in the shortest possible time. In order to achieve this goal, when machining with an abrasive water jet, in practice the traverse speed is usually increased. Another way is to cut several layers of material at the same time. In this paper, multilayer cutting of C45 steel was analyzed. Special attention is paid to the research of the quality of the samples obtained in this way. The basic parameters for evaluating the quality of samples are the roughness of the machined surface and the kerf taper. To evaluate the roughness of the machined surface, the parameter Ra was taken, while the kerf taper was determined by the width of the cut at the entrance and exit of the AWJ from the material, that is, at the top and bottom of the sample, as well as the angle of the kerf, α. Square samples with dimensions of 40x40 mm were cut from C45 plate material, 6 mm thick. Samples I and IV were cut in the same cutting modes without and with a distance of 1.2 mm between plates. For samples II and III, samples were cut from three layers, without the distance between the plates. When cutting these samples, the traverse speed was varied.*

Key words: *abrasive water jet machining, multilayer cutting, surface roughness, kerf taper*

1. INTRODUCTION

Modern industrial production is exposed to intense pressures to increase quality, reduce product manufacturing time, reduce prices, as well as flexible changes in the production program in order to meet changing and increasingly complex customer demands. Increasing competitiveness and ensuring the required level of efficiency, effectiveness of production and quality of the obtained products, as one of the highest requirements, is directly related to the introduction of new advanced technologies and forms of production itself [1, 2]. Non-conventional machining enable the realization of various production operations, which are very difficult or almost impossible to realize with conventional machining procedures. Great technical and technological progress has led to the constant development of production and application of new modern materials. These materials have significantly better mechanical and tribological characteristics, high tensile strength and hardness, high resistance at low and high temperatures, as well as significantly higher resistance to wear and the like [3].

The abrasive water jet (AWJ) machining is an unconventional process of recent date, which is increasingly used in modern production processes. The mechanism of AWJ machining is based on erosion. AWJ is particularly suitable for machining brittle and composite materials and is superior to similar machining procedures when it comes to cutting parts with complex 2D contours. The great advantage of this machining process is that there is no significant increase in temperature in the cutting zone and the cutting forces are very small [4]. Due to the savings in the time required for the production of a part, today, AWJ is used to cut several layers of material at the same time more and more often. That is why more and more research is being done on how certain parameters of the machining process and the characteristics of the workpiece material affect the kerf taper and surface roughness [5, 6].

2. ABRASIVE WATER JET MACHINING

When machining with an abrasive water jet, a specially designed cutting head is used, Fig. 1. Water under high pressure passes through the primary (jewel) orifice and enters the mixing chamber. Abrasive powder mixed with water is dosed into the mixing chamber.

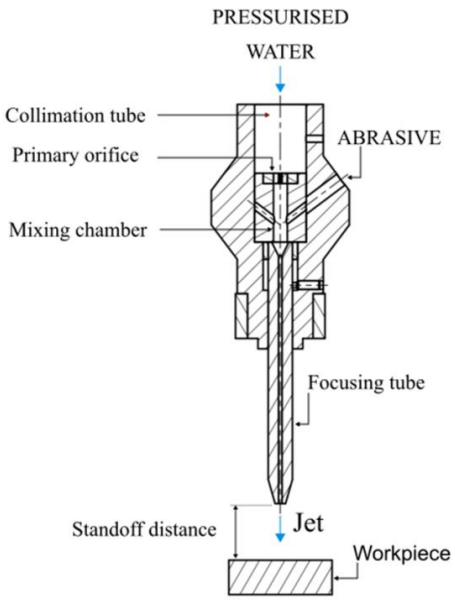


Fig. 1. Appearance of the cutting head for AWJ machining [7]

The abrasive mixture obtained in this way passes through the focusing tube, and creates a coherent abrasive water jet. The focusing tube is usually made of hard metal (tungsten carbide) with an internal diameter of 0.2 to 2 mm and a length of 50 to 100 mm, and serves to direct the abrasive water jet to a small surface.

2.1 Characteristics of the surface machined with an abrasive water jet

The basic characteristics of the surface machined with an abrasive water jet are:

- cut width W at the top of the sample and at the bottom of the sample,
- kerf taper angle α and
- roughness of the machined surface, i.e. Ra measured at the top and bottom of the sample.

The geometry and roughness of the machined surface are influenced by parameters of the abrasive water jet machining process such as: operating pressure, traverse speed, abrasive mass flow rate, nozzle diameter, stand off distance etc. [8, 9]. Fig. 2 shows the influence of some parameters of the abrasive water jet on the quality of the machined surface, where Smax represents the maximum cutting depth.

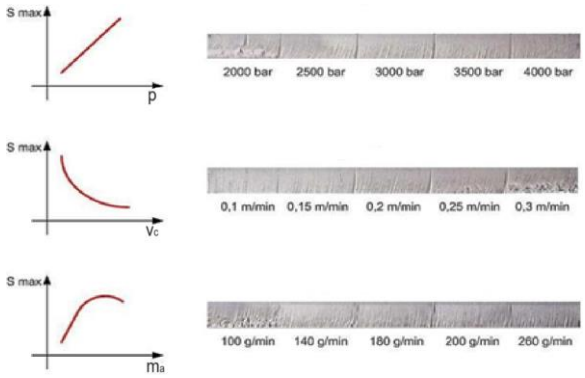


Fig. 2. The influence of AWJ machining parameters on the quality of the machined surface [8]

3. EXPERIMENTAL MEASUREMENTS

In this paper, the multilayer cutting of the same material and the influence of traverse speed and the distance between the material layers were investigated. The samples were cut on an NCT 30 abrasive water jet machine, manufactured by Water Jet Sweden.

Samples were cut from two plates of C45, the same thickness-6 mm, without a gap-sample I and with a gap 1.2 mm-sample IV, to determine whether there is an effect of the distance between the plates on the kerf width and the kerf taper, as well as on the machined surfaces roughness. All AWJ machining parameters were the same in both cases.

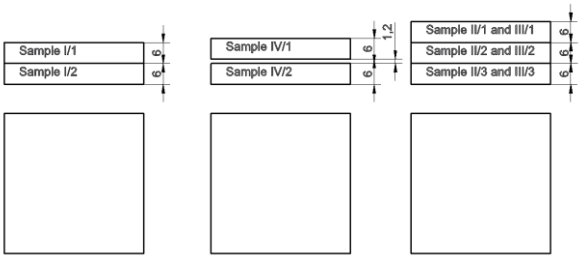


Fig. 3. The method of cutting the samples

Samples II and III were cut from three plates of C 45, each 6 mm thick, with no distance between them, with different traverse speeds. The cutting modes for all samples are given in Table 1.

Sample No	P [bar]	m_a [g/min]	Vc [mm/min]	s [mm]	Distance [mm]
I/1	4600	200	68.512	12	0
I/2	4600	200	68.512	12	0
II/1	4600	300	50.434	18	0
II/2	4600	300	50.434	18	0
II/3	4600	300	50.434	18	0
III/1	4600	300	56.494	18	0
III/2	4600	300	56.494	18	0
III/3	4600	300	56.494	18	0
IV/1	4600	200	68.512	12	1.2
IV/2	4600	200	68.512	12	1.2

Table 1. The cutting modes for samples

For all the samples, the roughness of the machined surface Ra and the kerf width on the top and the bottom of the sample were measured. Based on the measured values of the kerf width, the kerf taper angle was calculated. The results obtained in this way are shown in Table 2.

Sample No.		W [mm]	α [°]	Ra [μm]
I/1	Top	1.72	5.363	1.946
	Bottom	1.16		2.113
I/2	Top	1.18	3.442	2.543
	Bottom	0.82		4.059
II/1	Top	1.82	5.556	1.652
	Bottom	1.24		1.878
II/2	Top	1.2	2.293	1.812
	Bottom	0.96		2.295
II/3	Top	0.91	1.528	2.394
	Bottom	0.75		3.608
III/1	Top	1.67	3.538	2.351
	Bottom	1.3		3.178
III/2	Top	1.34	1.146	3.341
	Bottom	1.22		5.63
III/3	Top	1.24	1.528	5.758
	Bottom	1.08		7.868
IV/1	Top	1.62	2.963	2.533
	Bottom	1.31		3.482
IV/2	Top	1.55	1.433	7.925
	Bottom	1.4		5.09

Table 2. Kerf width, kerf taper angle and machined surface roughness

Fig. 4 shows the change in the Ra parameter for samples II and III. It can be seen from the picture that Ra is larger at the bottom than at the top of the samples. This is more pronounced in samples III, which were cut with a traverse speed that was 10% higher than the traverse speed with which samples number II were cut. Also, the parameter Ra is the smallest for samples II/1 and III/1, and the largest for samples II/3 and III/3. The difference between the values of Ra at the top and bottom of the samples is the largest in samples II/3 and III/3 and the smallest for samples II/1 and III/1.

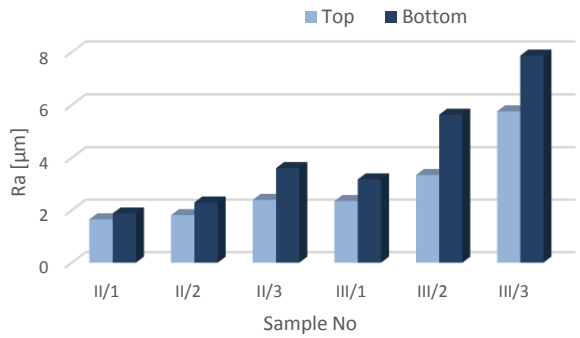


Fig. 4. Ra values for samples II and III

Fig. 5 and 6 show the value of the kerf width at the top and bottom of the samples, as well as the kerf taper angle. From the diagram, it can be seen that the kerf widths are the largest for samples II/1 and III/1 and the smallest for samples II/3 and III/3. In accordance with these results, the kerf taper angle is the highest for samples II/1 and III/1 and the lowest for samples II/3 and III/3. Also, it can be observed that the values of the kerf width are larger for samples III which were cut with a higher traverse speed.

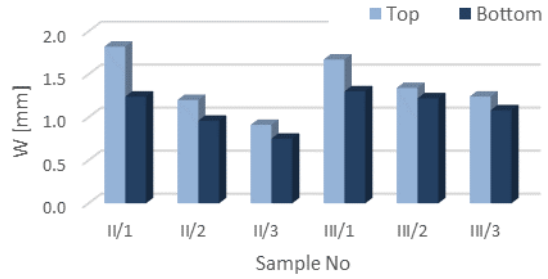


Fig. 5. Kerf width values for samples II and III

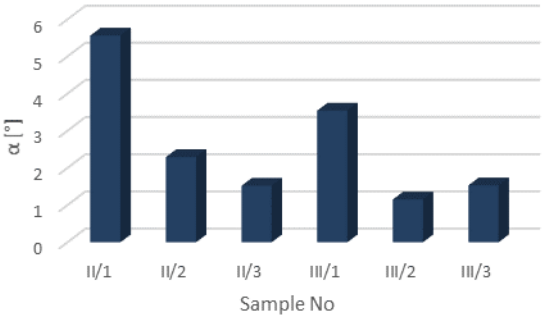


Fig. 6. Values of the kerf taper angle for samples II and III

Fig. 7 shows the values of the parameter Ra for samples I and IV. It can be concluded from the figure that Ra is higher for samples I/2 and IV/2 than in samples I/1 and IV/1. The difference in Ra values is the largest for sample IV/2, which is at a distance of 1.2 mm from sample IV/1.

Fig. 8 and 9 show the kerf width at the top and bottom of the sample, as well as the values of the kerf taper angle.

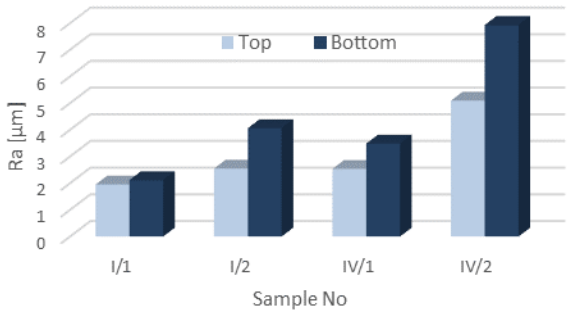


Fig. 7. Ra values for samples I and IV

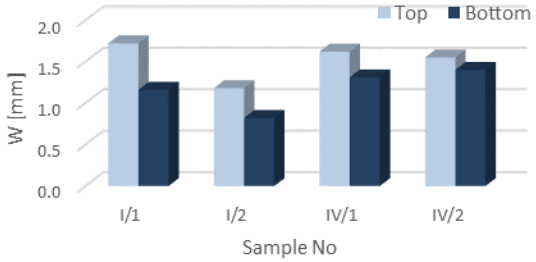


Fig. 8. Kerf width values for samples I and IV

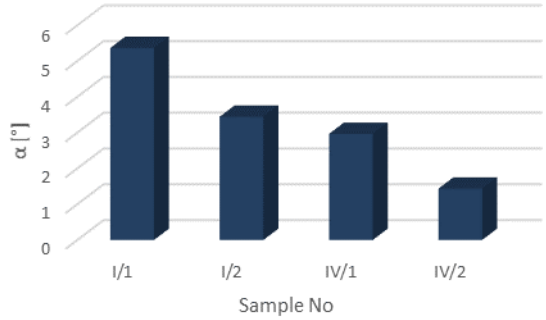


Fig. 9. Kerf taper angle values for samples I and IV

It can be noticed from the pictures that the difference in the kerf width at the top and bottom of the samples is more pronounced in samples I than in samples IV. The highest slope of the cut is in sample I/1 and the lowest in sample IV/2.

4. CONCLUSION

Based on the results obtained by measuring the samples shown in the pictures, it can be concluded that the roughness parameter of the machined surface Ra increases with the increase in the cutting depth. In all samples, the Ra parameter at the top of the sample is smaller than at the bottom of the sample. Also, the traverse speed significantly affects the roughness of the machined surface, that is, the Ra parameter. By comparing samples II/3 and III/3, it can be observed that an increase in traverse speed of 10% leads to an increase in the value of Ra at the bottom of the sample by almost 100%. The kerf width and the kerf taper angle are very important for the accuracy of machining process. By analyzing the results of measuring the kerf width and the kerf taper angle, it can be concluded that the value of the kerf taper angle decreases with the growth of traverse

speed. In the case of samples that were at the bottom during cutting, the value of the kerf taper angle is the smallest. It is particularly interesting that in the case of sample IV/2 (which was cut with a distance of 1.2 mm from the sample IV/1), the value of the kerf taper angle is the lowest of the samples that were cut with the same cutting modes.

The paper presents the results of research into the cutting of multiple layers-plates of material with an abrasive water jet. For parts that do not have high requirements in terms of accuracy and machining quality, it is quite feasible to cut them from several layers of material. In order to check how justified this multilayer machining is, it is necessary to determine how much time is needed to produce one piece from one layer and from several layers of material, because cutting with abrasive water jet from several layers of material requires lower traverse speed.

5. REFERENCES

[1] Nedić, B., Lazić, M.: Proizvodne tehnologije: obrada metala rezanjem, Skripta, Mašinski fakultet u Kragujevcu, Kragujevac, 2007.

[2] Lazić, M.: Nekonvencionalni postupci obrade, Naučna knjiga, Beograd, 1990.

[3] Milikić, D.: Nekonvencionalni postupci obrade - priručnik za studije i praksu, Fakultet tehničkih nauka, Novi Sad, 2002.

[4] Baralić, J., Nedić, B., Radovanović, M., Janković, P.: Obradivost materijala rezanjem abrazivnim vodenim mlazom, Monografija, Fakultet inženjerskih nauka Univerziteta u Kragujevcu, Kragujevac, 2015.

[5] Ng. Peter Singh, N.P., Srinivasu, D.S.,Babu, N. R.: A study on the interaction of jet with constituent layers of multilayered structure in through kerfing with abrasive waterjets, Journal of Manufacturing Processes, Vol. 60, pp. 117-133, 2020.

[6] Barabas, B., Deaconescu, A.: Study of kerf geometry of multilayers materials in abrasive water jet cutting process, MATEC Web of Conferences 94, 2017, DOI: 10.1051/matecconf/20179403001

[7] Annoni, M., Arleo, F., Viganò, F.: Micro-waterjet Technology, pp. 129–148, in Micro-Manufacturing Technologies and Their Applications, Fassi, I., Shipley, D., Eds.: Springer Tracts in Mechanical Engineering: New York, NY, USA, 2017.

[8] Glatki, T., Lacković, M., Kos, S., Lončar, J.: Obrada vodenim i abrazivnim mlazom, Tehnički glasnik, Vol. 8, No. 3, pp. 245-251, 2014.

[9] Momber, A., Kovacevic, R.: Principles of Abrasive Water Jet Machining, Springer-Verlag London Limited, London, 1998.

ACKNOWLEDGMENTS

This study was supported by the Ministry of Science, Technological Development and Innovation of the Republic of Serbia, and these results are parts of the Grant No. 451-03-66/2024-03/200132 with University of Kragujevac - Faculty of Technical Sciences Čačak.

Authors:

PhD Jelena Baralić, PhD Aleksandar Jovičić, University of Kragujevac, Faculty of Technical Sciences, Svetog Save 65, 32102 Čačak, Serbia, Phone.: +381 32 302-700/736.
E-mail: jelena.baralic@ftn.kg.ac.rs; aleksandar.jovicic@ftn.kg.ac.rs

PhD Bogdan Nedić, University of Kragujevac, Faculty of Engineering, Sestre Janjić 6, 34000 Kragujevac, Serbia, Phone.: + 381 34 335-990/637.
E-mail: nedic@kg.ac.rs

MMA 2024
FLEXIBLE TECHNOLOGIES

15th INTERNATIONAL SCIENTIFIC CONFERENCE
NOVI SAD, SERBIA, SEPTEMBER 24-26, 2024

Original research paper https://doi.org/10.24867/MMA-2024-01-004

Kovac, P., Taric, M., Rodic, D., Savkovic, B., Dudic, B., Jesic, D.

NEURO-FUZZY SYSTEMS MODELING OF HARD STEEL SURFACE ROUGHNESS PARAMETERS

Abstract: *The objective of this study is to examine the influence of machining parameters on throughnes of surface finish during turning of hard steel. A new approach in modeling surface roughness which uses design of experiments is described in this paper. Used were as well adaptive-neuro-fuzzy-inference system (ANFIS) model. The values of surface roughness predicted by different models were then compared. The results showed that the proposed systems can significantly increase the accuracy of the product profile when compared to the conventional approaches. The results indicate that the design of experiments with central composition plan modeling technique and ANFIS can be effectively used for the prediction of the surface roughness for hard steel.*
Key words: *modeling, design of experiments, turning, hard steel, neuro-fuzzy.*

1. INTRODUCTION

Based on a large number of literary sources, research in the field of processing hard-to-machine steels is carried out in the following directions: application of new types of cutting tools and determination of their stability, analysis of the influence of elements of the processing mode on the quality of processing, analysis of forces occurring during processing, as well as analysis of cutting tools from the aspect of the cutting material, its geometry and wear, as well as its influence on the processing process. In recent times, artificial neural networks (ANN models) and neuro fuzzy systems (ANFIS models) are increasingly being used to optimize the output parameters of production processes, and predict the quality of the treated surface, etc.

Hard machining has been established as a leading technology in machining technology for various machine components made of hardened steel such as gear shafts, bearings, and hydraulic components that replaces grinding [1, 2].

Most scientists and engineers consider hard machining to cover problems such as cutting mechanics, chip formation, tool wear, machined surface integrity, and machining accuracy. Energy balance during hard machining was the goal of research in works [1, 2, 3].

Based on the analysis of the treatment of hardened steel from the aspect of the quality of the treated surface with the application of mathematical modeling, Viktor et al. [4] that it is more expedient to apply scraping processing compared to grinding processing. In the research, they used tools based on ceramics and CBN, taking into account their chemical stability towards carbon. In addition, they also analyzed the impact of intermittent / continuous cutting on the cutting tool. During continuous cutting, a comparison was made between tools made of CBN and oxide-carbide ceramics, and during intermittent cutting, a comparison was made between CBN and SiC ceramics. CBN-based tools gave better results compared to ceramics in both processing methods.

The surfaces of machine parts obtained during cutting can never be perfectly smooth, they always have micro-unevennesses that arise as a result of processing. These microgeometrical irregularities of the surfaces of the machined parts are called the roughness of the machined surface.

If we look at machining by cutting, there are many influencing factors on the roughness of the machined surface. The influencing factors could be classified into several groups: factors determined by the workpiece (chemical composition, mechanical properties, surface condition,...), factors determined by the selected machine (stability, working characteristics, precision, ...), factors determined by the selected tool (type of tool material, tool geometry, state of the cutting surface,...), factors determined by the selected processing modes (cutting depth, feed and cutting speed) and factors determined by the cooling and lubricating agent (chemical composition, viscosity, method and position of cooling supply,...) [5].

The processed surfaces during cutting are not ideally smooth geometric surfaces, microscopically they represent rough surfaces. The development of advanced models allows to meet accelerated requirements in terms of productivity, product quality and reduction of production costs. Process modeling represents support for more efficient performance of the activities that make up one process. In creating a process model, it is first necessary to define the goal or goals of the process.

The main goal of process and system modeling is the definition of mathematical models and other representations, which will adequately describe the studied process/system with the appropriate degree of accuracy. Certain models with simulation are effective for adaptive management of processing processes, then reducing or eliminating errors.

The aim of this article is to present the application of neurofuzzy logic for modeling roughness parameters during processing of hard-to-machine hardened steel.

2. EXPERIMENTAL PROCEDURE AND MATERIAL

2.1 Terms of the experimental study

The experimental machine tool was a universal lathe - Prvomajska DK480, Fig 1.



Fig. 1. Turning machine

Tool: For the study was used interchangeable plates of hard metal CNMA 120404 ABC 25/F producer ATRON from Germany. Used was insert holder for external processing PCLNR 25 25 M16. The markings of the cutting tips according to DIN 4983 more closely define the geometry, as follows: the shape of the plate C → rhomb; the rake angle N → = 0°, C → = 7; tolerance class M; Type of tile → with opening A, W and G; length of cutting blade → 12.7 mm (12); cutting edge thickness → 4.76 mm (04); radius of tool tip → 0.4 mm (04). All tiles have a rake angle (γ=-6°).

Fig. 2 shows the measuring chain during the performance of this experiment. Comparative measurements of cutting forces, temperature and roughness of the treated surface were performed. The emphasis in this work is on the measured roughness values of the treated surface. The Talysurf 6 roughness measuring device is a computerized measuring system for measuring and analyzing roughness that gives the basic characteristics of the microgeometry of contact surfaces, which enables the measurement of a wide range of parameters that describe the characteristics of technical surfaces.

Variation of the experiment input factor (cutting regime) was performed in 5 levels of values. The mean value between the two adjacent levels was the geometric mean of these values. Selected levels of factors are shown in Table 1.

Factor Levels	Cutting speed v (m/min)	Cutting speed v (m/s)	Feed f (mm/rev)	Dept of cut a (mm)
Highest +1.41	180	3	0.25	0.7
High +1	160	2.66	0.2	0.5
Middle 0	120	2	0.1	0.22
Small -1	90	1.5	0.05	0.1
Smallest -1.41	80	1.33	0.045	0.07

Table 1. Selected levels of factors

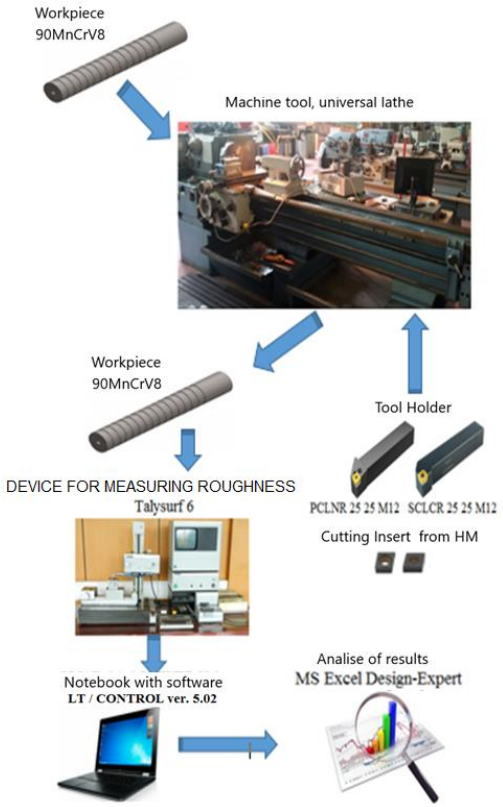


Fig. 2. Measurement of roughness surface in the process of turning with HM cutting tiles

Tables 2 show the measurement results according to the experiment plan for the HM tool material.

No.	Variable factors			Measurement results	
	v m/min	f mm/r	a mm	R_a [μm]	R_{max} [μm]
1	90	0,05	0,10	0,53	2,7
2	160	0,05	0,10	0,61	2,5
3	90	0,20	0,10	1,1	7,1
4	160	0,20	0,10	1,18	5,7
5	90	0,05	0,50	0,86	4,2
6	160	0,05	0,50	0,98	6,8
7	90	0,20	0,50	1,17	6,8
8	160	0,20	0,50	1,28	5,8
9	120	0,10	0,22	1,41	6,2
10	120	0,10	0,22	1,42	6,6
11	120	0,10	0,22	1,48	5,1
12	120	0,10	0,22	1,49	6,7
13	80	0,10	0,22	1,19	6,4
14	180	0,10	0,22	0,85	4,6
15	120	0,045	0,22	0,81	4,1
16	120	0,25	0,22	1,72	6,7
17	120	0,10	0,07	0,89	4,3
18	120	0,10	0,70	1,57	5,8
19	80	0,10	0,22	1,77	5,6
20	180	0,10	0,22	1,11	6,4
21	120	0,045	0,22	0,63	4,9
22	120	0,25	0,22	1,91	7,9
23	120	0,10	0,07	0,78	3,5
24	120	0,10	0,70	0,76	4,2

Table 2. Experimental input factor levels

Before the experimental performance, preparation of the workpiece was carried out. The workpiece is

thermally treated steel Č3840 (90MnCrV8) whose working hardness was 55 HRC, circular cross-section Ø34 mm and length 500 mm. To make it easier to perform, and for more credible measurement results, the workpiece tends to the chuck head at one end, and relies on the other end to the spike. It is necessary to remove a certain layer of material in order to avoid throwing-ovality and the results were more reliable. The length of the workpiece bar of 500 mm, it was divided into 24 fields with a length of 10 mm on which the longitudinal cutting, without the presence of cooling and lubricating agents was provided. Each field on workpiece was planned for one experimental point measurement.

2.2 Experimental results and analyze

Equations (1) and (2) for surface roughness parameters R_a and R_{max}, modeled by design of central compositional experimental plan determined by software:

$$R_a = 2{,}8264 \cdot v^{-0.04471} \cdot f^{0.59975} \cdot a^{0.00716} \quad (1)$$

$$R_{max} = 9{,}0036 \cdot v^{-0.3717} \cdot f^{0.3739} \cdot a^{-0.6148} \quad (2)$$

Equations (1) and (2) for surface roughness parameters R_a and R_{max}, modeled by design of central compositional experimental plan determined by software, Tabel 3.

Based on the experimental and calculated values given in equation 1 in Fig. 3, there is a comparison diagram of the experiment-model during turning processing with a TM CNMA cutting insert (γ=0°, α=7°, λ=- 6°) and with tool holder SCLCR 25 25 M12, for mean arithmetic roughness Ra.

Model adequacy		R_a	R_{max}
		Fa=4,33219	Fa=1,65230
Significance	F_{ro}	16.62	1372,91
	Fr1(v)	0.66 (*)	0,03*
	Fr2(f)	282.91	35,04
	Fr3(a)	23.35	16,03

Table 3. Adequacy of models and significance of parameters

Figs. 4 and 5 shows the correlation between the experimental and obtained values by factorial experimental design of surface roughness parameters (R_a, R_{max}). From the diagram can be seen that the points are near regression line and correlation is good.

As mentioned before, ANFIS modeling was used for analysis and optimization of surface roughness parameters in turning process. The obtained results of ANFIS model are given in the Table 4, side by side with the experimental results. For reduction of a model deviation, is needed to increase the number of experimental inputs trials.

Calculation of percental deviation for measured and model surface roughness parameters values was performed according next formula:

$$E = \frac{|Ri_{exp} - Ri_m|}{Ri_{exp}} \cdot 100\% \quad (3)$$

where are: Ri_{exp}- experimental value, Ri_m- model value.

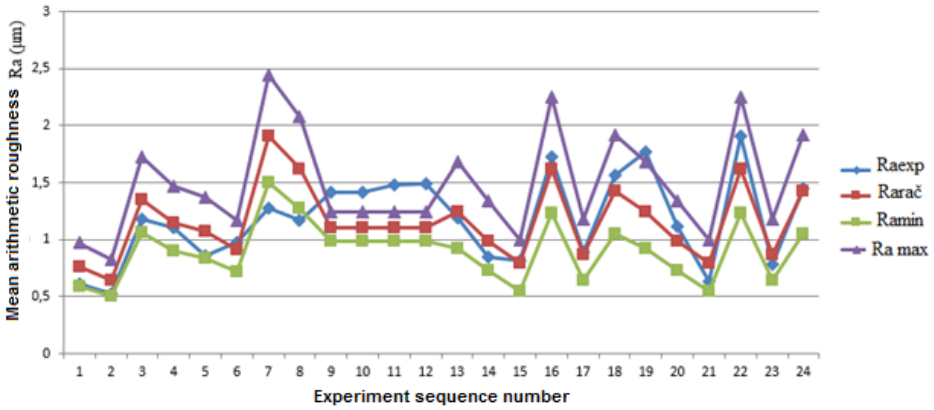


Fig. 3. Graphic representation of the obtained values for the mean arithmetic roughness

Factor			R_i - experimental roughness		R_i - modeled roughness	
v [m/s]	s [mm/rev]	a [mm]	R_a [µm]	R_{max} [µm]	R_a [µm]	R_{max} [µm]
81	0.1	0.22	0.7	3.93	0.99561	3.9245
182	0.1	0.22	0.65	3.5	0.74177	2.87921
121	0.045	0.22	0.39	2.5	0.42268	2.47317
122	0.25	0.22	1.82	8.3	1.85709	8.19655
123	0.1	0.07	1.04	2.8	0.97167	6.17389
119	0.1	0.7	1.38	6.2	0.84962	5.0787
Average deviation %					6.20950	8.8208

Table 4. Experimental values and values of surface roughness obtained with percentage deviation

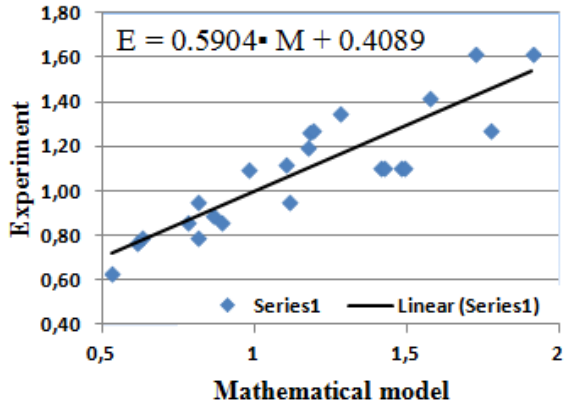


Fig. 4. Experiment-model comparison diagram when machining with a HM cutting insert for the mean arithmetic roughness Ra

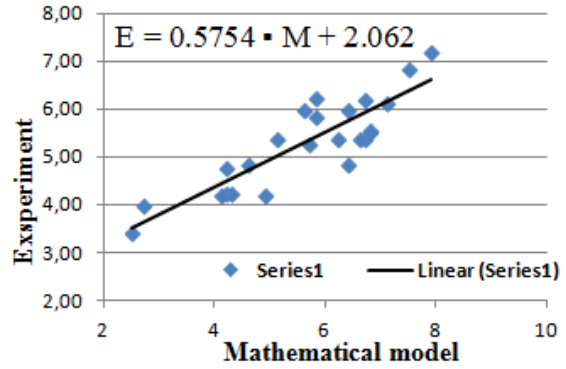


Fig. 5. Correlation between experimental and obtained values of surface roughness Rmax

Deviation of experimental and model values of surface roughness is shown on Fig 6. Deviation of 7 testing numbers of ANFIS is on Fig 7.

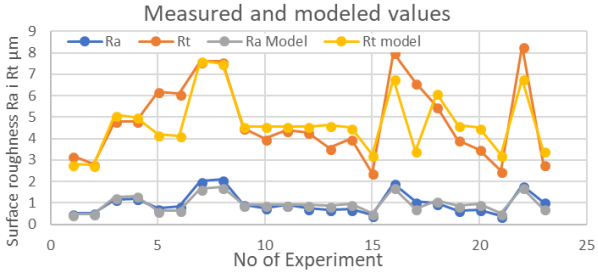


Fig. 6. Deviation of experimental and model values of surface roughness

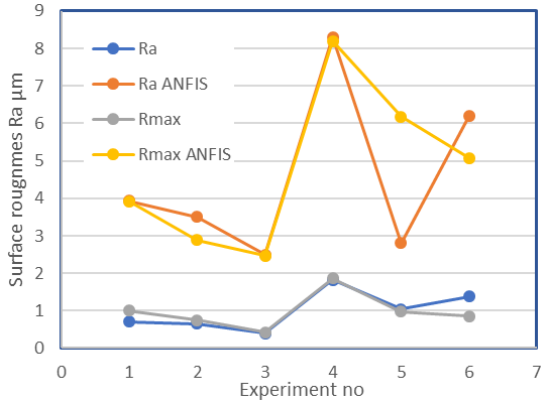


Fig. 7. Deviation of 6 testing numbers of ANFIS

3. CONCLUSION

Intelligent optimization techniques give the influence of cutting conditions on machining surface quality during turning hard material, are investigated through experimental verification. The investigation results confirm the highly consent of experimental research and intelligent techniques modeling. The intelligent optimization techniques and experimental results show some good information which could be used by future researches for optimal control of machining conditions. This paper has successfully established ANFIS model, for predicting the workpiece surface roughness parameters. Figs. 5 and 6 shows the compared predicted values obtained by experiment and estimated by ANFIS shows a good comparison with those obtained experimentally. The average deviations of models are checked and are found to be adequate. The model adequacy can be further improved by considering more variables and ranges of parameters.

4. REFERENCES

[1] Davim, J. P. (Ed.): *Machining of hard materials*. Springer Science & Business Media, 2011.

[2] Byrne, G., Dornfeld, D., & Denkena, B. J. C. A.: Advancing cutting technology. *CIRP Annals*, *52*(2), 483-507, 2003.

[3] Grzesik, W., Denkena, B., Żak, K., Grove, T., & Bergmann, B.: Energy consumption characterization in precision hard machining using CBN cutting tools. *The International Journal of Advanced Manufacturing Technology*, *85*, 2839-2845, 2016.

[4] De Godoy, V. A. A., & Diniz, A. E.: Turning of interrupted and continuous hardened steel surfaces using ceramic and CBN cutting tools. *Journal of Materials processing technology*, *211*(6), 1014-1025, 2011.

[5] Naveen, S. A., Aravindan, S., & Noorul Haq, A.: Influence of machining parameters on surface roughness of GFRP pipes. *Advances in Production Engineering & Management Journal*, *4*(1-2), 47-58, 2009.

Authors:

PhD Pavel Kovac, PhD Dragan Rodic, PhD Borislav Savkovic, University of Novi Sad, Faculty of Technical Sciences, Trg Dositeja Obradovica 6, 21000 Novi Sad, Serbia, Phone.: +381 21 485-23-29.
E-mail: pkovac@uns.ac.rs; rodicdr@uns.ac.rs; savkovic@uns.ac.rs

PhD Mirfad Taric, Srednja škola metalskih zanimanja, Sarajevo, Bosnia and Hercegovina.
E-mail: mirfad.taric@hotmail.com

PhD Branislav Dudic, Comenius University Bratislava, Faculty of Management, 820 05 Bratislava, Slovakia
E-mail: branislav.dudic@fm.uniba.sk

PhD Dusan Jesic, International Technology and Management Academy – MTMA, Novi Sad, Serbia.
E-mail: dusanjesic@hotmail.com

MMA 2024
FLEXIBLE TECHNOLOGIES

15th INTERNATIONAL SCIENTIFIC CONFERENCE
NOVI SAD, SERBIA, SEPTEMBER 24-26, 2024

Original research paper https://doi.org/10.24867/MMA-2024-01-005

Vorkapic, N., Kokotovic, B., Zivanovic, S.

COMPARATIVE ANALYSIS OF STATISTICAL FEATURES OF SIGNALS IN THE TIME DOMAIN IN INTERNAL TURNING OPERATIONS

Abstract: *This paper presents the results of research on the use of statistical features of the processed signal, recorded during the machining process, on the occurrence of chatter. The change in the value of the selected features is also their ability to indicate the occurrence of chatter during machining. The signals recorded during the internal turning of a stepped surface at certain processing modes were compared. The idea is that by changing the depth of cutting during internal turning, the values of the measured signals change. On that occasion, the stepped inner surface was machined, in such a way that the tool keeps the same diameter during processing. During machining, two signals were measured, force and acceleration along the Y direction. The obtained results show that the analyzed statistical features in stable and unstable processing modes show significantly different values and that they can be useful as indicators for the detection of chatter during the machining process.*
Key words: *chatter, detection, statistical features, internal turning*

1. INTRODUCTION

One of the crucial aspects in machining processes is the maintenance of consistent surface quality and dimensional accuracy of the produced parts, which directly impacts the overall production flow, product quality, and their market delivery. Due to the varying characteristics of machining systems, particularly in terms of rigidity and natural frequencies, which are used in manufacturing processes, certain phenomena can lead to the occurrence of chatter during machining operations. Chatter most commonly arises due to mode coupling or the regenerative effect that occurs under these conditions [1-3]. To avoid chatter, researchers are striving to develop autonomous and intelligent systems for its detection during machining processes [4].

Detecting chatter is not straightforward. Visually, it can be identified by the appearance of a very rough surface on the part being machined or by increased noise levels, but by then it is often too late. The development of systems that can detect irregularities in measured signals through time-domain, frequency-domain, and time-frequency domain analysis, based on pre-defined indicators or trained systems, is of great benefit. Significant advancements in chatter detection systems have been achieved through the use of Fast Fourier Transform (FFT) and Wavelet applications [5, 6]. The analysis of statistical parameters in the time domain is currently prominent in machine learning-based research [7]. Utilizing statistical parameters in the time domain enables reliable signal analysis, establishing a threshold that distinguishes significant signal changes from noise and chatter.

This paper includes a comprehensive literature review. The second chapter describes the experimental setup for internal turning, along with the cutting conditions. The third chapter presents the analysis of the results obtained, while the fourth chapter provides the corresponding conclusions.

2. EXPERIMENT SETUP

This chapter describes the experimental setup, which includes the preparation of the processing system and the data acquisition system. The elements of the experimental setup are shown in Fig. 1.

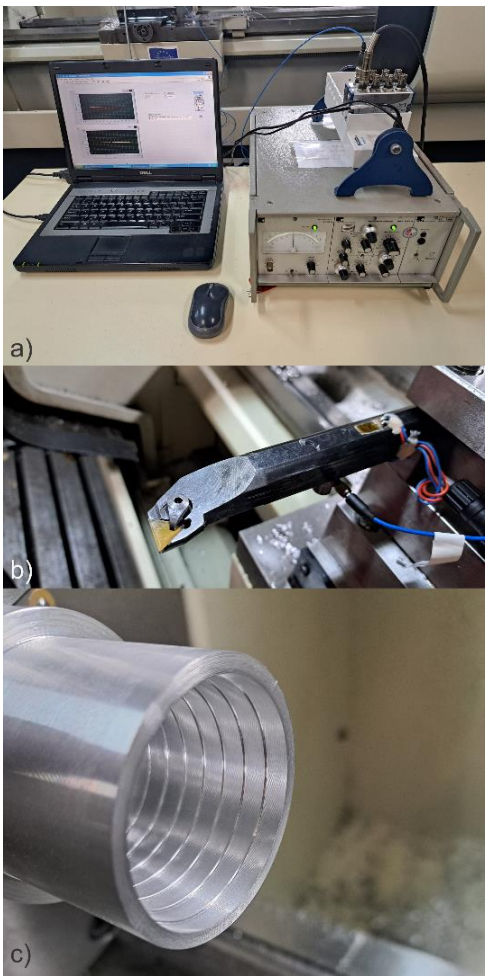


Fig. 1. Experimental setup

In Fig. 1a. the system for data acquisition is presented, which includes a computer, amplifier and cDAQ NI 9174, with S/V Input Module NI9234 and NI9215, driven by NI-LabView, were used for data acquisition. The sampling frequency was set at 6400 S/s.

During machining tests, the workpiece material was AlSi3 aluminum. Machine: Echo-Eng TCN410 - 2 axis CNC lathe. Tool: R S36.8 -25-16 with TPMR 160312 4C40 P40 TiN coated carbide insert. Cutting speed was 90m/min. Fig. 1b. shows an accelerometer, the PCB Piezotronics 352C03, was affixed to the tool shank, which we used for measuring acceleration. The two measuring tapes, resistance 120 ohms, are glued to the upper and lower sides of the tool shank, so that they form a Wheatstone half bridge to measured cutting force. Fig. 1c. shows a workpiece with a stepped inner surface. The cutting tool direction as well as the cutting area during the experiment are shown in Fig. 2.

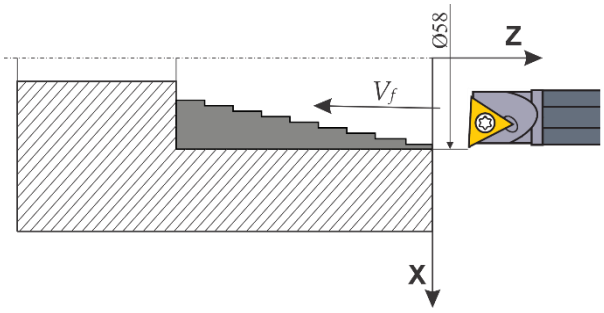


Fig. 2. Cutting area in machining test

Machining was carried out on a diameter of 58 mm, where the cutting depth increased by 0.5 mm when moving from one to another stepped surface. The length of each step was 5 mm.

3. SIGNALS ANALYSES

Within the framework of this chapter, the recorded force and acceleration signals recorded during the machining process are analyzed. In Fig. 3a. the values of the measured force are shown, while in Fig. 3b. acceleration values measured along the Y direction are shown.

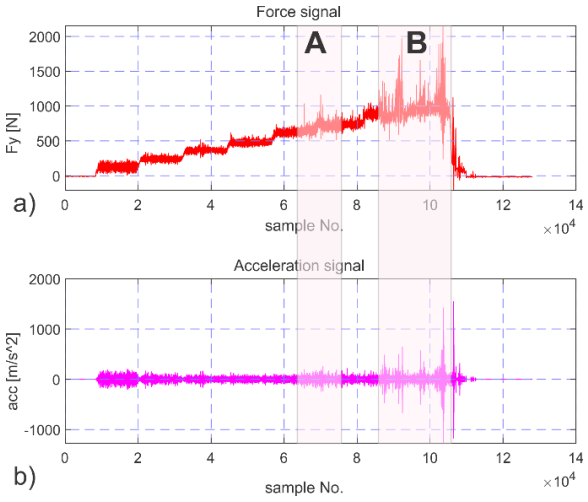


Fig. 3. Original signals: a) force signal, b) acceleration signal

The measured force diagram exhibits a linear trend as the depth gradually increases, as shown in Fig. 2. In the final few steps, there is an increase in amplitude, indicating the presence of chatter during machining, which is marked as B zone. Zone A represents the transition state and the appearance of chatter. The second diagram, displayed in Fig. 3b, shows the acceleration recorded captured during the same process. The amplitude values fluctuate around zero, as expected. However, towards the end, there is a sudden spike in amplitude, suggesting the presence of chatter.

3.1 Signal extraction and statisical features definition

First, the characteristic part of the signal is extracted for analysis. Signal processing is performed in a sliding window (here called buffers). The width of the window is 450 samples, and the overlapping factor is 0.5 (225 samples) [8]. Table 1 shows the formulations of statistical features used for signal analysis.

Formulation	Statistical featutes
$x_m = \frac{1}{n}\sum_{i=1}^{n} x_i$	Mean value
$x_{std} = \sqrt{\frac{1}{n-1}\sum_{i=1}^{n}(x_i - x_m)^2}$	Standard deviation
$x_{rms} = \sqrt{\frac{1}{n}\sum_{i=1}^{n}(x_i)^2}$	Root mean square
$x_{ske} = \frac{\sum_{i=1}^{n}(x_i - x_m)^3}{(n-1)\cdot x_{std}^{\ 3}}$	Skewness
$x_{kur} = \frac{\sum_{i=1}^{n}(x_i - x_m)^4}{(n-1)\cdot x_{std}^{\ 4}}$	Kurtosis

Table 1. Formulation of statistical features from time domen

Skewness is a statistical measure that assesses the asymmetry of a probability distribution, quantifying the degree to which the data is skewed or shifted to one side. Positive skewness indicates a longer tail on the right side of the distribution, while negative skewness indicates a longer tail on the left side. Kurtosis is a statistical parameter used to characterize a signal, providing a measure of the "peakedness" of a random signal. This feature is widely utilized in systems that monitor assemblies with rolling bearings. Signals with higher kurtosis values exhibit more peaks that exceed three standard deviations. The standard deviation measures the extent of signal distortion from the mean value. Root Mean Square (RMS) represents the square root of the mean of the squares of the values. RMS is particularly useful for measuring the magnitude of a varying signal, as it provides an effective value that represents the overall power of the signal. In the context of signal processing, RMS is often used to quantify the energy or intensity of vibrations, especially in systems with rotating components.

3.2 Analisis of force signal

In this sub-chapter, the analysis of the measured force signal was performed. Therefore, the maximum number of buffers, which is 424, was extracted from the entire signal. A certain statistical value from table 1 is calculated over each of the buffers. Fig. 4 shows the values of the statistical features of the force signal.

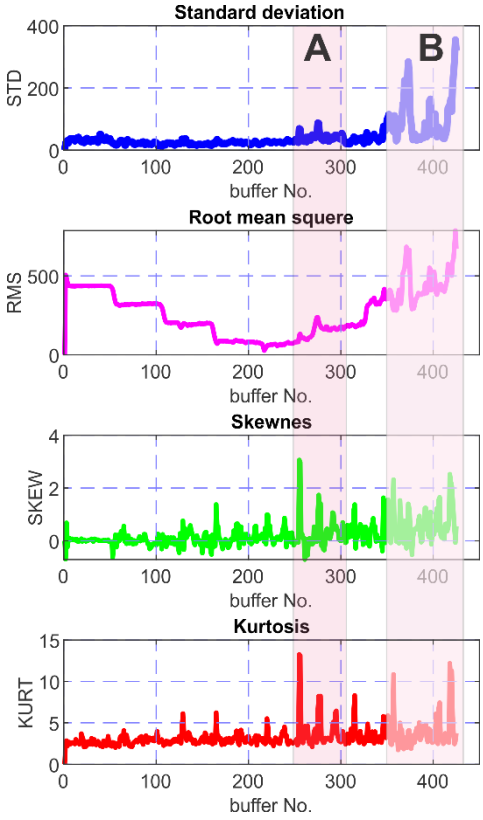


Fig. 4. Statistical features of force signal

Zones A and B are also marked in Fig. 4, representing sections of the signal shown in Fig. 3. The diagrams of statistical features in Table 1 reveal significant changes in the signal within the marked zones A and B. In these zones, the standard deviation, kurtosis, and RMS exhibit a sharp increase, while skewness shows a notable rise and a dense concentration of value changes. To further confirm the influence of statistical features on signal variation during chatter, a characteristic segment of the signal recorded during the stable operation of the manufacturing system was isolated. The results of this analysis are presented in Fig. 5. It is evident that there is a change in the statistical feature values during stable operation. However, these values are 2-8 times lower compared to those observed when chatter occurs.

During the experiment, acceleration values were also measured. Considering that both the measuring tapes and the accelerometer are glued to the tool shank, changes in statistical features on identical buffers are expected. Fig. 6 shows the values of the statistical features of the accelerometer signal.

Even though the sensors used in the experiment haven't the same measurement character, the changes in the statistical features are identical, which is shown in Figs. 4 and 6.

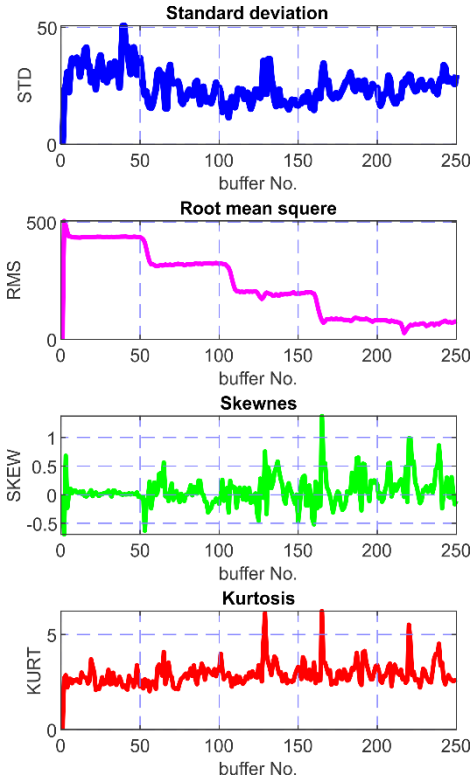


Fig. 5. Statistical features of force stabile signal

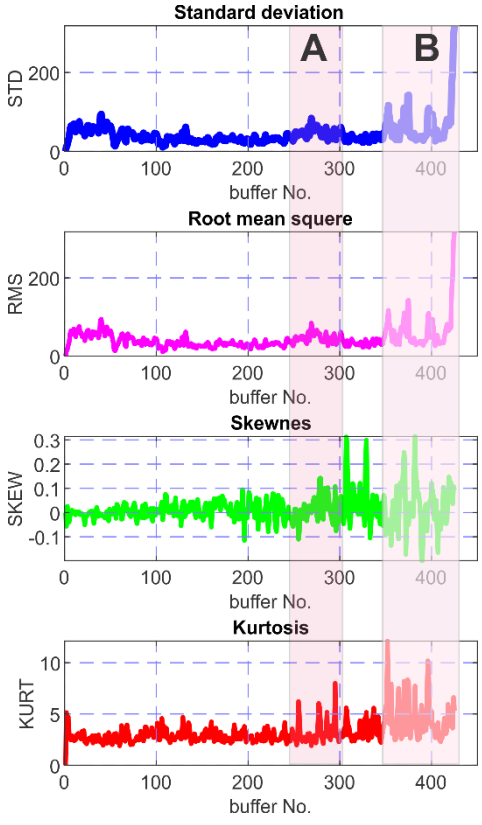


Fig. 6. Statistical features of acceleration signal

Figure 7 shows the results of the analyzed accelerometer signal, which were recorded during the stable operating mode of the manufacturing system. It can also be observed that there are no sudden changes in the statistical features, except that the values are 2-8 times less compared to the results from Fig. 6.

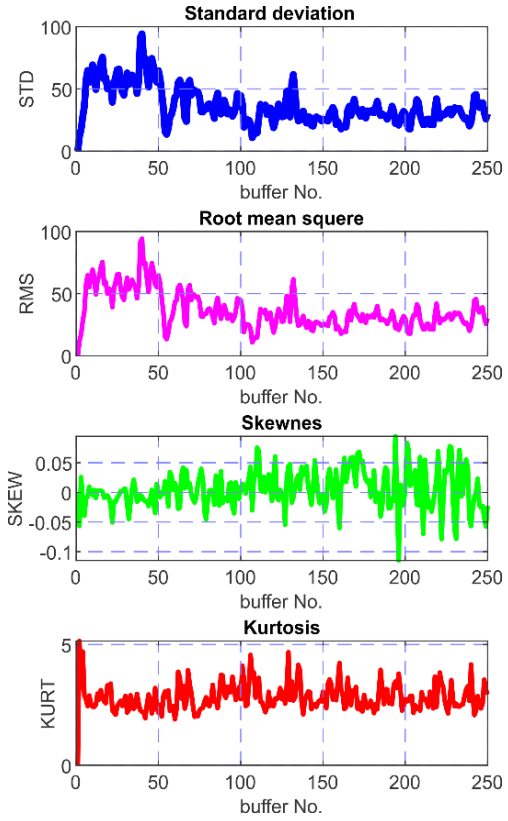


Fig. 7. Statistical features of acceleration stabile signal

4. COCNLUSION

This paper illustrates the potential of statistical characteristics of time-domain signals recorded during machining processes. While these characteristics cannot replace identification algorithms based on the Fast Fourier Transform (FFT) and Wavelet Transform, they can serve as supplementary criteria for monitoring the stability of machining processes. This limitation arises from the fact that chatter is accompanied by a significant increase in amplitude (force, acceleration), yet recognizing large amplitudes in the signal does not necessarily indicate the presence of chatter. The study demonstrates that changes in certain parameters, in this case, force, during stable operation do not affect the statistical parameters until chatter appears in the signal.

Future work will focus on formulating additional derived parameters, for which a clear threshold can be defined, aiming to more accurately identify the onset of chatter.

5. REFERENCES

[1] Altintas, Y.: *Manufacturing automation: Metal cutting mechanics, Machine tool vibrations, and CNC design*, Second Edition, University of British Columbia, 2012.

[2] Mlađenović, C., Košarac, A., Zeljković, M., Knežev, M.: *Experimental Definition of Machining Systems Stability Lobe Diagram*, Proceedings of the XIII International Scientific Conference MMA 2018 – Flexible Technologies, pp. 95-98., Novi Sad, 2018.

[3] Yuvaraju, B.A.G., Nanda, B.K., Srinivas, J.: *Investigation of stability in internal turning using a boring bar with a passive constrained layer damping*, FME Transactions, Vol. 49, No. 2, pp. 384-394, 2021.

[4] Lauro, C.H., Brandão, L.C., Baldo, D., Reis, R.A., Davim, J.P.: *Monitoring and processing signal applied in machining processes – A review*, Measurement, Vol. 58, pp.73-86, 2014.

[5] Vorkapic, N., Kokotovic, B., Zivanovic, S.: *Comparison of signal features from time and frequency domain for chatter detection*, Proceedings of the 39th International Conference on Production Engineering of Serbia, pp. 42-47, Novi Sad, 2023.

[6] Vorkapic, N., Kokotovic, B., Zivanovic, S.: *Standard deviation and spectral analisys for chatter detection using wavelet transform packet*, Proceedings of the 6th International Conference mechanical engineering in XXI century - MASING, pp. 179-183, Niš, 2023.

[7] Zheng, Q., Chen, G., Jiao, A.: *Chatter detection in milling process based on the combination of wavelet packet transform and PSO-SVM*, The International Journal of Advanced Manufacturing Technology, Vol. 120, No. 1-2, pp. 1237-1251, 2022.

[8] Vorkapic, N., Kokotovic, B., Zivanovic, S.: *Wavelet transform packet for signal analysis using standard deviation and signal spectrum*, Innovative Mechanical Engineering, ISSN 2812-9229 (First Online), 2024.

ACKNOWLEDGMENTS

The paper is a part of the research done within the projects that was supported by the Ministry of Education, Science and Technological Development of the Republic of Serbia by contract no. 451-03-65/2024-03/200105 dated 5 February 2024

Authors:
MSc Nikola Vorkapic, PhD Branko Kokotovic, PhD Sasa Zivanovic, University of Belgrade, Faculty of Mechanical Engennering, Kraljice Marije 16, 11090 Beograd, Serbia, Phone: +381 62-850-8056.
E-mail: nvorkapic@mas.bg.ac.rs; bkokotovic@mas.bg.ac.rs; szivanovic@mas.bg.ac.rs

MMA 2024 FLEXIBLE TECHNOLOGIES

15th INTERNATIONAL SCIENTIFIC CONFERENCE
NOVI SAD, SERBIA, SEPTEMBER 24-26, 2024

Original research paper https://doi.org/10.24867/MMA-2024-01-006

Aleksić, A., Rodić, D., Gostimirović, M., Sekulić, M., Savković, B., Kosanović, A.

PRELIMINARY INVESTIGATION OF THE IMPACT OF MQL ON SURFACE ROUGHNESS DURING THE TURNING ALUMINUM ALLOY 6082

Abstract: *Aluminum alloys are particularly significant in the aerospace industry due to their unique combination of properties, including strength, ductility, toughness, fatigue resistance, and oxidation resistance, all while being lightweight materials. The influence of cutting parameters on surface roughness during the turning of aluminum alloy 6082-T6 was investigated in this study. The experiments were conducted on a CNC lathe using a cemented carbide tool. The turning experiments were designed following the Taguchi L9 orthogonal array method, with cutting parameters including depth of cut, feed rate, cutting speed, and nose rate evaluated under both Dry cutting and Minimum Quantity Lubrication (MQL) conditions. The effects of these parameters on surface roughness were analyzed, and insights into improving surface quality during the machining process were provided. It was found that the surface quality is better when MQL is used compared to dry cutting.*

Key words: *Aluminium alloys, machining parameters, surface roughness, dry turning, MQL, Taguchi method*

1. INTRODUCTION

Engineering is always looking for lighter materials that are more reliable and cost-effective. Reducing the weight of products is often achieved by using lightweight materials like aluminum alloys (AA) [1]. However, there are significant differences in the machinability of various aluminum alloys. These differences are influenced by factors such as alloying elements, heat treatments, variations in the casting process, and impurities present in the material.

AA6082-T6 is a specific aluminum alloy from the Al–Mg–Si series, known for its ability to improve mechanical properties through heat treatment. This series of alloys is widely utilized in industries such as automotive, chemical, architecture, and machinery manufacturing [2]. The choice of AA6082-T6 as a focus in this study highlights its importance in applications where both strength and lightweight properties are crucial.

During the machining process, aluminum and its alloys tend to produce tangled chips that can become caught on the workpiece. These tangled chips can obstruct the cutting fluid from reaching the cutting zone and may cause surface scratches, leading to damage of the machined part. Although aluminum's low melting point does not significantly alter the properties of the cutting tool, its high thermal conductivity means that a substantial amount of heat generated during machining is absorbed by the workpiece. This absorption can lead to thermal expansion, which may cause surface imperfections and dimensional inaccuracies [3].

To mitigate these issues, lubrication and cooling (lubricooling) environments are essential. They help reduce tool wear and decrease the amount of heat absorbed by the workpiece, thereby preventing or minimizing the negative effects of thermal expansion. In this context, minimal quantity lubrication (MQL) emerges as an effective alternative to dry machining.

MQL involves using cutting fluids in very small quantities, typically three to four orders of magnitude less than those used in traditional flooded lubrication conditions. When selecting a cutting fluid for MQL, it is important to consider not only its primary characteristics, such as cutting performance, but also its secondary characteristics, including biodegradability, oxidation stability, and storage stability. Processes where friction and adhesion play a significant role generally require minimal fluid application. The MQL approach is also known as "near dry lubrication" [4]or "micro lubrication" [5]

Garcia et al. conducted a study in which they optimized the cutting parameters—cutting speed, feed rate, and depth of cut—during the finish turning of 6082-T6 aluminum alloy using an uncoated carbide tool under dry and reduced quantity lubricant (RQL) conditions. The study utilized a Box–Behnken design of experiments to combine and randomize the input variables. Surface roughness parameters Ra and Rz were measured for each combination of parameters. The optimization results showed that the best surface quality was achieved under RQL conditions, which improved chip formation, reduced the occurrence of scratches, burrs, and waviness on the machined surface, and yielded superior surface finish compared to dry machining [6].

Saravanakumar et al. investigated surface roughness and roundness in the turning of aluminum using solid carbide inserts. They employed a Full Factorial design and ANOVA to analyze the effects of feed rate, spindle speed, and depth of cut on surface quality. The study found that increasing cutting speed improved surface roughness and roundness, while higher depth of cut and feed rate worsened surface roughness. Increasing the nose radius of the insert also reduced roughness and roundness. Grey relation analysis identified the optimal parameters as a cutting speed of 1800 mm/min, feed rate of 0.1 mm/rev, depth of cut of 0.5 mm, and nose radius of 0.8 mm [7].

Palaniappan et al. conducted an experimental study

on the machining of Aluminum 6082 alloy to determine optimal CNC turning parameters, focusing on surface roughness (SR). Using an L27 orthogonal array, they performed turning experiments with fixed parameters, including spindle speed, feed rate, and depth of cut. They found that feed rate was the most significant parameter affecting surface roughness. The optimal parameters for minimizing SR were 1200 rpm spindle speed, 0.15 mm/rev feed, and 1.5 mm depth of cut, resulting in an SR of 0.63 mm at a temperature of 76°C. Another effective combination was 1600 rpm speed, 0.15 mm/rev feed, and 2 mm depth of cut, which achieved an SR of 0.76 mm at a temperature of 91°C. The temperature during machining varied from 50°C to 93.3°C [8].

2. TAGUCHI METHOD

The Robust Design method, also known as the Taguchi method and pioneered by Dr. Genichi Taguchi, enhances engineering productivity by providing a systematic approach to process optimization and high-quality system design. Based on fractional factorial design, Taguchi's parameter design minimizes process or product variation, creating robust and adaptable processes or products.

Taguchi's method is user-friendly, even for those with limited statistical knowledge, contributing to its widespread adoption in engineering and science. It reduces sensitivity to variation, leading to high-quality products at lower development and manufacturing costs. Numerous companies worldwide have saved millions by applying this method across various industries, including automotive, electronics, and telecommunications.

Taguchi outlined a standard procedure for optimizing processes, which includes determining quality characteristics, identifying noise factors, designing and conducting experiments, analyzing data, and predicting performance. The Signal-to-Noise Ratio (S/N ratio) and orthogonal arrays are key tools in robust design, helping to assess and optimize control factors. The S/N ratio, with its focus on variation, plays a crucial role in determining optimal conditions for minimizing process variation, as demonstrated in surface roughness optimization using the "smaller is better" criteria [9].

3. EXPERIMENTAL SETUP

The experimental work was carried out at the Faculty of Technical Sciences in the Conventional Machining Laboratory. The conditions for the experimental tests are given in this chapter.

The conditions apply to:

- the workpiece material,
- the machine tool,
- the cutting tool,
- the machining conditions,
- the measuring technique.

The workpiece material: The experimental tests were carried out with the aluminum alloy 6082-T6. This material is used in almost all fields, especially in aerospace, marine and automotive industries. The chemical structure is shown in Table 1. The workpiece had a length of 550 mm (cut length) and a diameter of 45 mm.

Si	**Cu**	**Fe**	**Zn**	**Mg**	**Mn**
1.08	0.01	0.25	0.03	0.75	0.51
Ni	**Pb**	**Sn**	**Ti**	**Cr**	**Ti+Zr**
0.01	0.03	<0.05	0.03	0.019	0.04

Table 1. Chemical structure of AL 6082-T6

Machine tool: Machining was performed on an Index GU -600 CNC lathe in dry condition.

Cutting tool: A turning cutter SDJCR2020K11 with cemented carbide inserts (SECO type DCGT11T302F-AL KX, DCGT11T304F-AL KX, and DCGT11T308F-AL KX) was used, corresponding to nose radii of 0.2 mm, 0.4 mm, and 0.8 mm, respectively. Table 2 illustrates the geometrical characteristics of the mentioned inserts [10].

Geometrical characteristics of DCGT11T302/4/8F-AL KX insert	**Value**
Clearance angle major	7°
Insert included angle	55°
Theoretical cutting edge length	11.60 mm
Nose rate	0.2/0.4/0.8 mm
Insert thickness	3.97 mm

Table 2. Geometrical specifications of DCGT11T302/4/8F-AL KX insert

Machining conditions: Depth of cut, feed rate, cutting speed, and nose rate were used as cutting conditions. In Table 3 lists the cutting parameters and their values depending on the workpiece material of the workpiece and the tool manufacturer's recommendations.

Simbol	**Parameters**	**Levels**		
		1	**2**	**3**
A	Depth of cut a, [mm]	0.2	1.1	2
B	Feed rate s, [mm/rev]	0.05	0.12	0.2
C	Cutting speed v, [m/min]	300	450	600
D	Nose rate r, [mm]	0.2	0.4	0.8

Table 3. Machining parameters and their levels

Measuring technique: A Mitutoyo SurfTest SJ-210 was used for the surface roughness measurements. Measurements were taken three times for each experiment, and the mean value was selected for data processing.

4. RESULTS AND DESCUSSION

The experimental tests, performed using Minimum Quantity Lubrication (MQL) and following the Taguchi orthogonal array L9 (34), were analyzed using MINITAB software. The experimental setup and measured results of average surface roughness Ra are shown in Table 4.

It can be seen from Table 4 that the use of MQL cooling and lubricating fluids results in an improvement in the quality of the machined surface in most cases. Specifically, it is evident that MQL leads to significant

improvements in surface roughness, particularly for experimental points 1, 2, and 7. At these points, the application of MQL results in a reduction in surface roughness by 50% or more compared to dry cutting conditions. This demonstrates the effectiveness of MQL in enhancing the surface finish in various machining scenarios.

Exp. no.	A	B	C	D	Dry R_a [µm]	MQL R_a [µm]	Dry/MQL Ratio (%)
1	1	1	1	1	1.144	0.778	47
2	1	2	2	2	1.407	0.863	63
3	1	3	3	3	1.863	2.347	-21
4	2	1	2	3	1.876	1.798	4
5	2	2	3	1	3.256	3.564	-9
6	2	3	1	2	3.174	3.009	6
7	3	1	3	2	1.411	0.340	315
8	3	2	1	3	1.805	1.389	30
9	3	3	2	1	6.684	6.449	4

Table 4. Setup of experiments performed using MQL and results of average surface roughness R_a.

Additionally, Fig. 1 displays the measurement results based on the Taguchi L9 plan for both conditions: dry cutting and MQL application.

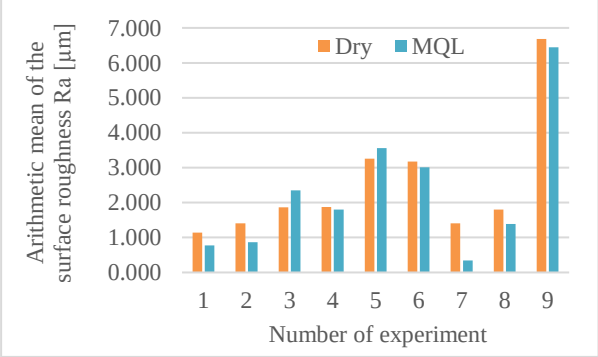


Fig. 1. Comparison of Measurement Results for Dry Cutting vs. MQL

In addition, the influence of the parameters on the output characteristic Ra was also analyzed. To determine this impact, ANOVA analysis was used. The effect of the cutting process parameters on R_a for dry cutting is presented in Fig. 2, while the corresponding effects for MQL application are shown in Fig. 3. The graphical representation of these impacts is illustrated through the slope of the line connecting different parameter levels.

From Figs. 2 and 3, it is clear that the best surface quality is achieved with minimal cutting depth, feed rate, and cutting speed. However, the lowest surface roughness is obtained with the maximum nose radius in dry cutting conditions, and with the medium nose radius when MQL is used. Additionally, the figures indicate that the greatest influence on surface roughness is exerted by the feed rate, followed by the nose rate, cutting depth, with cutting speed having the least impact.

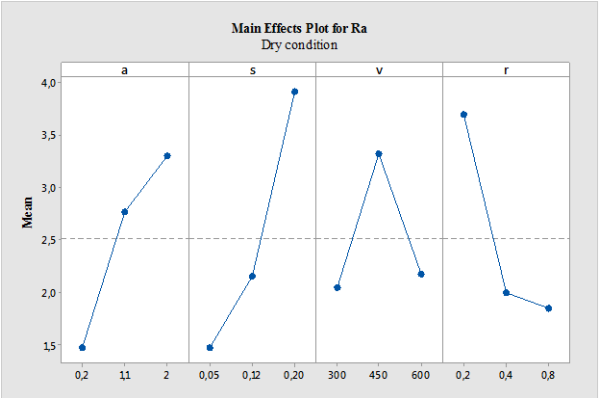


Fig. 2. ANOVA Response Graph for Average Surface Roughness (R_a) in Dry Cutting Conditions

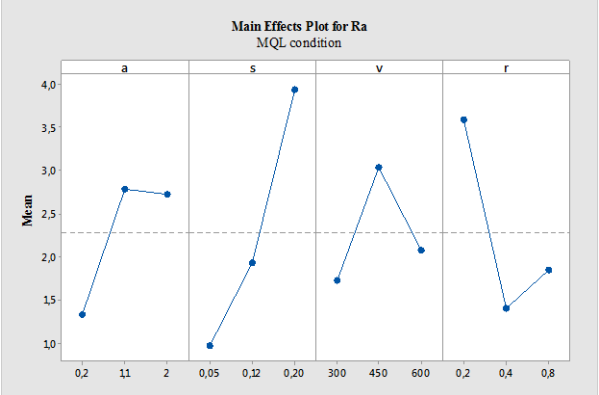


Fig. 3. ANOVA Response Graph for Average Surface Roughness (R_a) in MQL Conditions

5. CONCLUSION

This paper presents the application of the Taguchi method for analyzing surface roughness in the turning of Al 6082-T6 under both dry and MQL conditions. The analysis was conducted using Analysis of Variance (ANOVA) based on the Taguchi L9. The main findings are summarized as follows

- The application of MQL significantly improves surface roughness compared to dry cutting conditions. This suggests that MQL is an effective method for enhancing surface quality during the turning process.
- Among the cutting parameters, the feed rate has the most significant impact on the average surface roughness (Ra), followed by the nose radius, cutting depth, with cutting speed having the least influence. This indicates that careful control of the feed rate is crucial for achieving optimal surface finish.
- For dry cutting, the lowest surface roughness is achieved by setting the cutting depth, feed rate, cutting speed, and nose rate to their minimum values. This highlights the importance of minimizing these parameters to improve surface quality in dry cutting operations.
- In contrast, when using MQL, the minimum surface roughness is attained with minimal values for cutting depth, feed rate, and cutting speed, while a medium nose rate is optimal. This demonstrates that while some parameters need to be minimized, a balanced

approach to the nose rate is necessary for optimal results with MQL.

Future research will aim to expand the scope of experiments and explore advanced cooling techniques. This includes investigating the use of Vortex tubes and hybrid cooling methods that combine Vortex tubes with MQL. Additionally, future studies will focus on process modeling and the optimization of process parameters to enhance output characteristics and further improve the efficiency and quality of machining processes.

6. REFERENCES

[1] J. Jeswiet et al., "Metal forming progress since 2000," CIRP J Manuf Sci Technol, vol. 1, no. 1, pp. 2–17, 2008, doi: 10.1016/j.cirpj.2008.06.005.

[2] V. Kumar and D. Kumar, "Investigation of tensile behaviour of cryorolled and room temperature rolled 6082 Al alloy," Materials Science and Engineering: A, vol. 691, pp. 211–217, Apr. 2017, doi: 10.1016/j.msea.2017.03.051.

[3] A. Aleksić, M. Gostimirović, M. Sekulić, B. Savković, and D. Rodić, "Optimization of surface roughness in turning of Aluminum Alloy 2024-T3 using Taguchi method," 39th International Conference on Production Engineering of Serbia, Novi Sad 2023.

[4] F. Klocke and G. Eisenblätter, "Dry Cutting," CIRP Annals, vol. 46, no. 2, pp. 519–526, 1997, doi: 10.1016/S0007-8506(07)60877-4.

[5] A. Hemaid, T. Tawfeek, and A. A. Ibrahim, "Experimental Investigation on Surface Finish during Turning of Aluminum under Dry and Minimum Quantity Lubrication Machining Conditions," American Journal of Materials Engineering and Technology, vol. 4, no. 1, pp. 1–5, 2016, doi: 10.12691/materials-4-1-1.

[6] R. F. Garcia, E. C. Feix, H. T. Mendel, A. R. Gonzalez, and A. J. Souza, "Optimization of cutting parameters for finish turning of 6082-T6 aluminum alloy under dry and RQL conditions," Journal of the Brazilian Society of Mechanical Sciences and Engineering, vol. 41, no. 8, p. 317, Aug. 2019, doi: 10.1007/s40430-019-1826-4.

[7] G. S. Kumar, P. V. Reddy, and D. M. Krishnudu, "Multi-response optimisation in CNC turning of Al-6082 T6 using grey Taguchi method coupled with principal component analysis," International Journal of Computer Aided Engineering and Technology, vol. 13, no. 4, p. 508, 2020, doi: 10.1504/IJCAET.2020.110487.

[8] S. P. Palaniappan, K. Muthukumar, R. V. Sabariraj, S. Dinesh Kumar, and T. Sathish, "CNC turning process parameters optimization on Aluminium 6082 alloy by using Taguchi and ANOVA," Mater Today Proc, vol. 21, pp. 1013–1021, 2020, doi: 10.1016/j.matpr.2019.10.053.

[9] B. Ramreddy and G. Varvatte, "Optimization of Process Parameters in Cnc Turning of Aluminium Alloy 7075 By Taguchi Method Using Regression Analysis," Indian J Sci Res, vol. 12, no. 1, pp. 203–208, 2015, [Online]. Available: https://go.gale.com/ps/i.do?p=AONE&u=googlescholar&id=GALE%7CA454619925&v=2.1&it=r&sid=AONE&asid=9d22dcb9

[10] Secotools.com, "Elektronski katalog reznih alata za obradu struganjem." Accessed: Aug. 15, 2024. [Online]. Available: https://www.secotools.com

ACKNOWLEDGMENTS

This research has been supported by the Ministry of Science, Technological Development and Innovation (Contract No. 451-03-65/2024-03/200156) and the Faculty of Technical Sciences, University of Novi Sad through project "Scientific and Artistic Research Work of Researchers in Teaching and Associate Positions at the Faculty of Technical Sciences, University of Novi Sad" (No. 01-3394/1).

Authors:

MSc Anđelko Aleksić, PhD Dragan Rodić, PhD Marin Gostimirović, PhD Milenko Sekulić, PhD Borislav Savković, Aleksandra Kosanović, University of Novi Sad, Faculty of Technical Sciences, Trg Dositeja Obradovica 6, 21000 Novi Sad, Serbia, Phone.: +381 21 485-24-76.

E-mail: andjelkoa94@uns.ac.rs; rodicdr@uns.ac.rs; maring@uns.ac.rs; milenkos@uns.ac.rs; savkovic@uns.ac.rs; kosanovica@uns.ac.rs

MMA 2024
FLEXIBLE TECHNOLOGIES

15th INTERNATIONAL SCIENTIFIC CONFERENCE
NOVI SAD, SERBIA, SEPTEMBER 24-26, 2024

Original research paper https://doi.org/10.24867/MMA-2024-01-007

Savkovic, B., Rodic, D., Sekulic, M., Kovac, P., Aleksic, A., Kosanovic, A.

DEVELOPMENT OF A MEASUREMENT-ACQUISITION SYSTEM FOR MEASURING CUTTING FORCES AND TEMPERATURES USING VIRTUAL INSTRUMENTATION

Abstract: *This paper presents a model of an information system for determining cutting forces and temperatures. The developed model provides very efficient, precise, reliable and fast acquisition, monitoring and display of cutting forces and temperatures in the time domain. The presented acquisition system was developed in two interactions, the first one was independently developed for the cutting temperature, while the second one is only for the cutting forces. The multi-functional measurement acquisition system combines the measurement of both temperature and cutting force at the same time. Application of the virtual instrument developed in this way is suitable for turning or grinding processes. The paper describes the management, measurement and processing software and hardware of the developed system. The experimental results for the milling process are presented in the form of tables as well as graphical diagrams obtained on the basis of part of the data recorded by acquisition.*
Key words: *sensor, acquisition, virtual instrumentation, cutting forces, temperature.*

1. INTRODUCTION

The rapid development of computer and information technologies and the application of the concept of the Internet of Things further encourage the rapid growth of the number of generated data. Compared to traditional data sets, big data usually includes unstructured data sets that need deeper real-time analysis. With the development of computers, acquisition and measurement technologies were developed, which are based on microcomputer technology.

The term data acquisition could be defined as the activity of collecting data on the occurrence of an event or process that is monitored and analyzed in order to become familiar with it [1, 2].

The application of electronic and computer technology has led to measurement and acquisition systems of high sensitivity, low consumption, high speed of operation, high reliability, high flexibility and with the possibility of data transmission.

The concept of virtual instrumentation was set up by the National Instruments company, which is the leading company in the world in terms of measurement and acquisition systems. By virtual instrumentation we mean a combination of hardware and software elements, most often used with a PC (hence the other name - PC-based instrumentation), which realizes the function of a classic instrument. By applying this methodology, it is possible to design a multipurpose instrument, which will be able, in addition to standard signal monitoring operations, to perform more complex processing operations [3].

One of the most important areas in mechanical engineering, where the emergence of information technology has caused significant changes, is the area of material processing technology research. These changes primarily relate to the integration, optimization, measurement and management of processing systems.

Monitoring of the machining process involves computer monitoring of the output characteristics of the process (tool wear, temperature, forces, quality of the machined surface, chip shape, etc.) [4-6]. Then control of the state of the processing system (ma-chine tool, cutting tool, accessories, measuring instruments, workpiece, etc.) and information flows of the processing process (accuracy and quality of processing, productivity, economy of processing, reliability of the process, etc.).

Cutting forces (resistance) and their moments are of great importance in mechanical engineering technology and generally in the theory of metalworking. They represent the basic categories of the mechanics of the cutting process, which means that the cutting force expresses one of the basic characteristics of the condition and behavior of the cutting process.

Accordingly, the goal of this research is the development of an adequate measurement and acquisition system that will collect and record data. Specifically, the system envisaged for the realization of this task should acquire data for three orthogonal cutting forces as well as for the temperature in the contact zone at the place where the appropriate thermocouple is placed. This measurement and acquisition system should also satisfy in terms of the accuracy of the measured quantities of workability, taking into account that the signals and quantities collected from the corresponding sensors are not in units from the SI system. Consequently, it is necessary to translate these collected signals into measurement quantities from the SI system, i.e. and express them in values that are used in the investigated processing. The developed measurement acquisition chain is intended for the milling process, but by replacing the sensor it can be adapted to the grinding or turning process as well. The data collected in this way are very applicable for further processing and modeling.

2. EXPERIMENTAL SETUP

The experimental work was carried out through two

stages of creation of the measurement system. Namely, in the first part of the research, a measurement acquisition system was developed for independent measurement of cutting temperature, i.e. a system for measuring cutting forces, while in the second part, a measurement acquisition system was developed that performs comparative measurements for three components of force and one component of temperature during the processing process.

2.1. Development of a measurement-acquisition system for measuring cutting forces during milling using virtual instrumentation

Fig. 1 schematically shows the measurement-acquisition system for measuring forces during milling using virtual instrumentation.

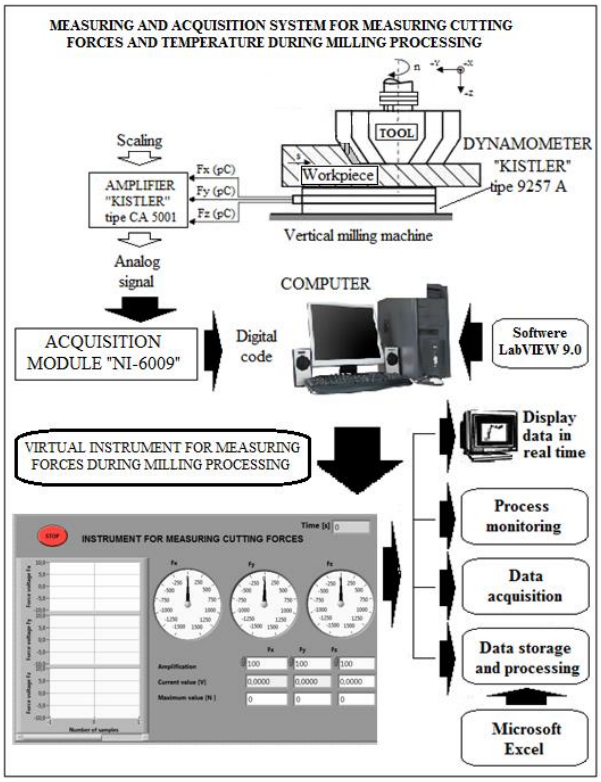


Fig. 1. Measurement scheme for face milling

The figure shows that the system consists of the following components:

- Milling machine - "Prvomajska" FSS-GVK-3,
- Dynamometer - "KISTLER"-9257A,
- Amplifier - "KISTLER" - CA 5001,
- Acquisition module – NI-6009,
- Computer.

The Universal Serial Bus (USB) acquisition module was initially designed to connect peripheral devices such as keyboards and mice to a PC. However, USB has proven useful for many applications, including measurement and automation. The USB measurement device (NI USB-6009) provides basic digital data acquisition functionality for easy application in data acquisition, portable measurements and laboratory experiments. The NI USB-6009 is a cost-effective multi-function module designed for data acquisition, test, measurement and process control and is powerful enough for more sophisticated measurement applications. The system is accompanied by diagnostic software (LabView 9) and software drivers (DAQ 9.5) that facilitate the development of applications in a Windows environment.

2.1.1. Front panel layout and user manual VI

The appearance of the front panel of the virtual instrument is shown in Fig. 2. The appearance is adapted to the user so that almost no knowledge of the concept of graphic programming in the LabVIEW programming language is required.

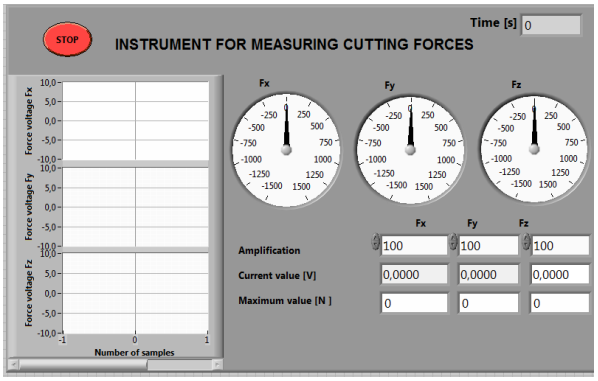


Fig. 2. View of the front panel of the virtual instrument for measuring cutting forces

When the VI starts its window changes to RUN form. During the measurement itself, the diagram shows the change in the voltage value of the forces. By pressing the STOP button the measurement is stopped, a table is generated on the front panel (with columns for time, forces as voltage quantities and forces with their physical units). A Windows-specific dialog box also opens. In this window, you need to specify the path and enter the name of the file to be generated. In addition to the file name, it is necessary to enter the extension for the corresponding file type, so the file in Excel has the extension .xls. The table generated in Excel, whose columns are identical to the columns in the table on the front panel, can be further manipulated.

Pairs of fields above the table on the front panel "max force [N]" and "elapsed time" are used to read the highest force values as well as the time that has passed from the be-ginning of the measurement to the appearance of the highest values.

After building the front panel, the code is added to the block diagram window to manage the placed objects. The code is a graphical presentation of the functions with which this management is performed. The block diagram is a window that opens simultaneously with the opening of the front panel and contains the source code of the program in graphic form. The graphic form emphasizes the flow of data and therefore the problem is placed on the level of a clear physical understanding. Problem solving itself takes on a more natural form, and information and its flow are given priority by this performance. Fig. 3 shows the layout of the block diagram used in the experimental measurement.

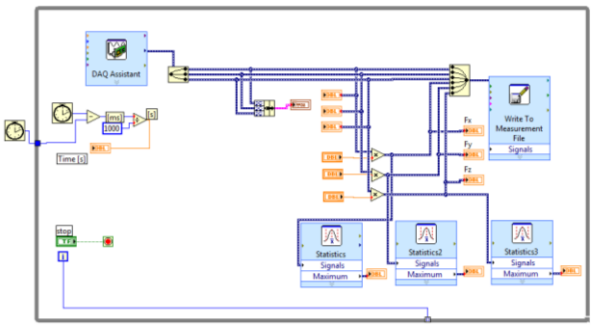


Fig. 3. Block diagram of the virtual instrument

Front panel objects are represented by corresponding terminals on the block diagram. By double-clicking the mouse on the block diagram terminal, the corresponding object on the front panel is marked separately. Terminals are input and output points where information is exchanged between the front panel and the block diagram. The data entered into the control objects on the front panel are entered into the block diagram through the corresponding control terminals. During program execution, the output data stream goes through the indicator terminals where they leave the block diagram and re-turn to the front panel. There, the data is displayed on the front panel indicator objects.

Graphical connection represents the most effective technique for the implementation of the PC-based measurement-acquisition system program. Modern programming tools based on the concept of graphic programming provide the possibility of high-quality development of programs for data acquisition, management, analysis and presentation. The basis of the virtual instrument program is represented by a block diagram. Given that the program is created using graphic symbols, the programmer is freed from the difficulties associated with finding out in detail how these symbols work, which is not the case with classic software packages. Writing user interface control code generally means creating a block diagram with already defined structures found in the LabVIEW libraries, where the structures are adapted to the needs by setting changeable parameters (configuration).

Realization of a graphic program, which is called a block diagram in the LabVIEW software package, takes place in three steps: selection of functions, connection of functions and configuration of function parameters. Functions are selected via palettes and menus. In the case of complex functions, the designer is left with the possibility of implementation using several functional blocks. Connecting the output and input of the selected functions is necessary in order to function the measurement-acquisition system, process and display data, i.e. to ensure a certain flow of information.

DAQ Assistant - an interactive guide for configuring, testing and collecting measurement data. With one click, one can even generate code based on the configuration, making it easier and faster to develop complex operations, Fig. 4. Using the DAQ as-assistant menu reduces programming errors and drastically reduces the time to set up the DAQ system when performing measurements. In the DAQ assistant menu, the number of channels, the physical value to be measured, the number of samplings per second are selected and the hardware connection method is displayed, Fig. 5.



Fig. 4. An interactive guide to configuring, testing and collecting measurement data

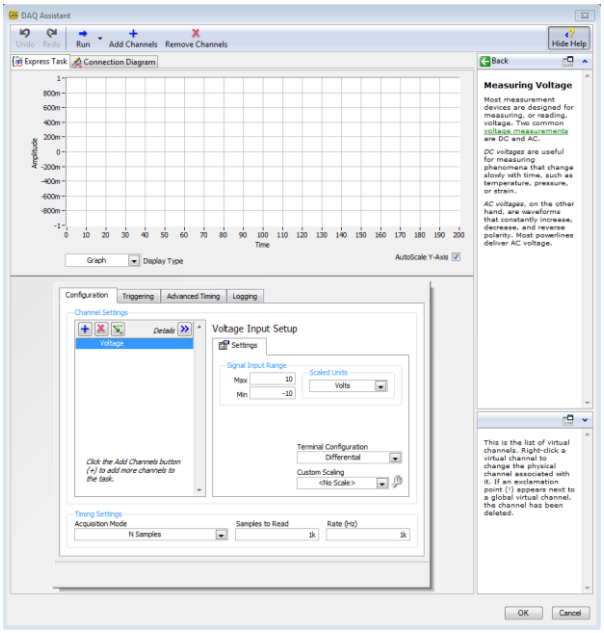


Fig. 5. Window for setting the physical signal of the input channel

There are several options for saving measurement data in LabVIEW. Write To Measurement File Express VI functions are used to save measurement data generated by virtual instruments in a text file, Fig. 6.

The Write To Measurement File function writes measurement data to a text-based file (.lvm), a binary measurement with header (.tdm), or a binary measurement without header (.tdms) file.

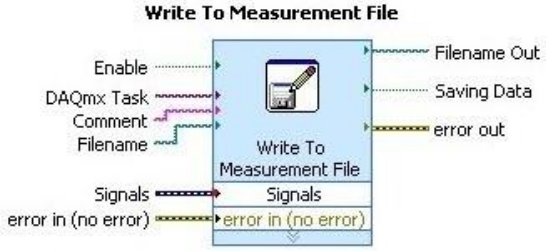


Fig. 6. Write To Measurement File Express VI - functions for saving data

2.2. Development of a measurement-acquisition system for measuring temperature cutting during milling using virtual instrumentation

In milling, in contrast to machining on a lathe, there are problems of signal trans-mission from the tool to the measuring instrument. Due to the fact that the tool performs a cycloidcircular motion during milling, it is not possible to directly lead the thermocouple wires to

the measuring instrument. The thermocouple wires are connected to copper rings which, together with graphite brushes, provide sliding contact. The copper rings are placed on the spindle of the milling machine and are isolated from each other and from the machine by pertinax and plexiglass and rotate together with the spindle. Graphite brushes are placed in the support of the special construction of Fig. 6, they are stationary in relation to the tool and are isolated from the support. Contact with the copper rings is ensured by springs. Two brushes are placed on each ring, in order to ensure the best possible contact and reduce voltage loss due to the eccentricity of the rotating rings. The thermal voltage that occurs during temperature measurement is 10 to 50 mV, so even small losses mean large measurement errors [7].

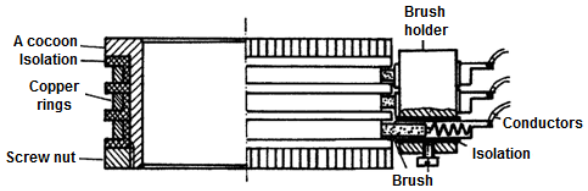


Fig. 7. Device for transferring thermal voltage to the measuring instrument

Digital multi-thermometer TR 2112 was used, which can measure temperature, DC and AC current, voltage and resistance. The temperature measurement range is from -100°C to 1600°C.

The TR2112 device has an analog output that is directly connected to the acquisition card NI 6009, through which the temperature values are digitized on a PC. In this case, the multi-thermometer serves as hardware to adjust the signal.

Fig. 8 shows the front panel of the virtual instrument for measuring temperature during cutting. On the VI, it is possible to set the appropriate gain, that is, to see the current temperature value in voltage value as well as in degrees Celsius. If it is necessary to use the instrument in laboratories where temperature measurements are expressed in Kelvin or Faraday, it is possible to make a correction in the amplification field.

Fig. 9 shows the block diagram of the previously defined front panel of the virtual temperature measuring instrument.

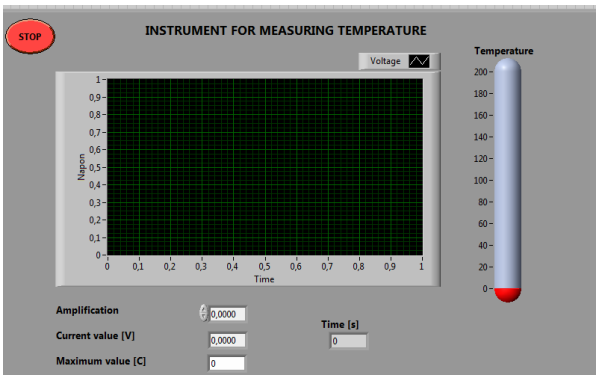


Fig. 8. View of the front panel of the virtual instrument for measuring temperature cutting

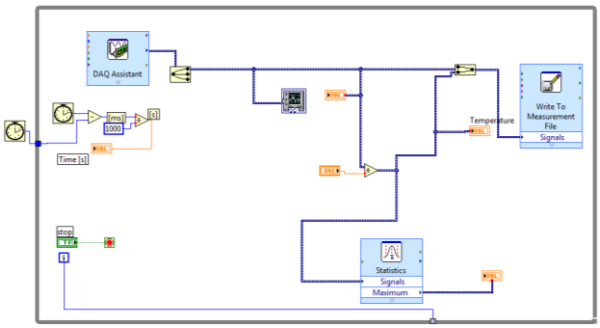


Fig. 9. Block diagram of the virtual instrument

2.3. Development of a measurement-acquisition system for measuring cutting forces and temperatures during milling using virtual instrumentation

Fig. 10 schematically shows the measurement-acquisition system for measuring cutting forces and temperatures during milling using virtual instrumentation. This measurement acquisition system combines the two previously presented systems.

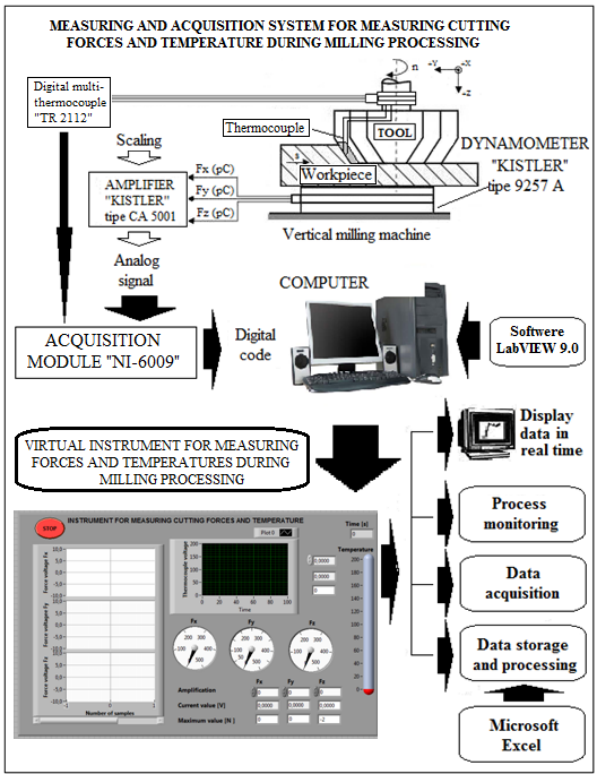


Fig. 10. Measurement scheme for face milling

Figs. 11 and 12 show the final layout of the front panel and the block diagram for the virtual instrument, which can be used to measure three components for cutting force and one component for temperature.

Apart from the simple reading of voltage values for forces from the dynamometer and temperature from the thermocouple, the virtual instrument is designed to display both the change in the force value and the change in the temperature value on the diagram, displaying the maximum and current values in certain time intervals.

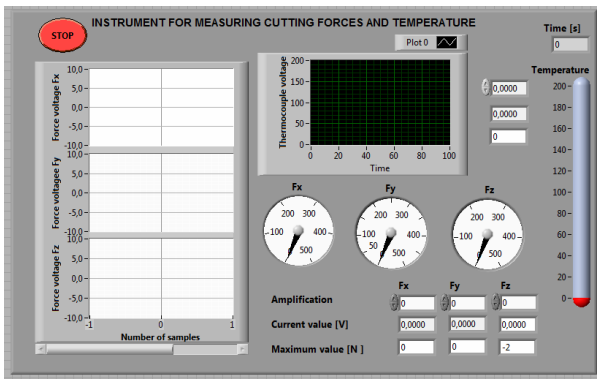


Fig. 11. View of the front panel of the virtual instrument for measuring cutting force and temperature

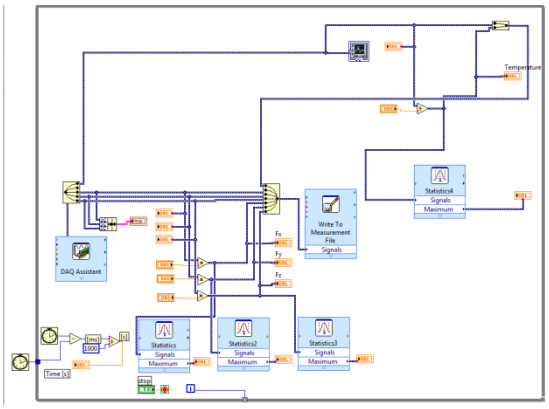


Fig. 12. Block diagram of the virtual instrument

3. EXAMPLE OF MEASUREMENT USING VI

Experimental tests were performed on aluminum alloy 7075 (Al-Zn-Mg-Cu), the width and length of all workpieces were 100 mm, and the thickness is 15 mm. During the tests, the head for face milling "JUGOALAT" G.037 ϕ100 mm was used, with mechanically attached cutting plates, with the following characteristics: number of teeth z =1, attack angle κ=75°, chest angle γ = 0°. As a cutting tool, rotating plates made of hard metal, quality K20.

Table 1 shows one experimental record of measured values, where 4 channels were used, which detected changes every 5000 samples per second. The first four channels marked with 1, 2, 3 and 4 show changes in electrical quantities in the form of records in volts, while the other four records are the sizes that were obtained after the calibration of the device itself and represent the actual sizes (1', 2', 3', 4').

Column 1 shows the temperature change value in volts obtained by the installed thermocouple, while column 1' shows the actual temperature value in [°C]. Columns 2, 3 and 4 represent the records of the change of cutting resistance in three orthogonal directions x, y and z shown in electrical quantities. The generated display of values is in volts obtained from the piezoelectric sensor. The last three columns represent the actual force change values Fx, Fy and Fz in newtons.

Channels	1	2	3	4	1'	2'	3'	4'
Samples	5000	5000	5000	5000	5000	5000	5000	5000
Date	07.9.2023	07.9.2023	07.9.2023	07.9.2023	07.9.2023	07.9.2023	07.9.2023	07.9.2023
Time	22:12.5	22:12.5	22:12.5	22:12.5	22:12.5	22:12.5	22:12.5	22:12.5
Y_Unit_Label	Volts	Volts	Volts	Volts	Celsius	Newton	Newton	Newton
X_Dimension	Q	Fx	Fy	Fz	Q	Fx	Fy	Fz
X0	0.00E+00	0.00E+00	0.00E+00	0.00E+00	0.00E+00	0.00E+00	0.00E+00	0.00E+00
Delta_X	0.0002	0.0002	0.0002	0.0002	0.0002	0.0002	0.0002	0.0002
End_of_Header								
Time [s]	Temp. [V]	Force Fx [V]	Force Fy [V]	Force Fz [V]	Temp. [°C]	Force Fx [N]	Force Fy [N]	Force Fz [N]
0	0.204773	0.09278	0.144812	-0.27499	20.47729	9.277964	14.48116	-27.4992
0.0002	0.204773	-0.07275	0.062051	-0.2075	20.47729	-7.27483	6.205108	-20.7497
0.0004	0.19968	-0.00017	0.096429	-0.00756	19.96799	-0.01707	9.642854	-0.75601
0.0006	0.204773	0.18191	0.283595	0.216573	20.47729	18.19101	28.35947	21.65731
0.0008	0.2035	0.230295	0.390547	0.201291	20.34997	23.02952	39.05469	20.12913
-	-	-	-	-	-	-	-	-
-	-	-	-	-	-	-	-	-
6.8582	0.28244	0.087686	-0.00925	-0.20368	28.24404	8.768647	-0.92503	-20.3677
6.8584	0.28244	0.153898	0.007302	-0.28773	28.24404	15.38977	0.730178	-28.7727
6.8586	0.281167	0.119519	0.008575	-0.23424	28.11672	11.95188	0.857502	-23.424
6.8588	0.277347	0.083867	0.102795	-0.00374	27.73475	8.386659	10.27947	-0.37397
-	-	-	-	-	-	-	-	-
-	-	-	-	-	-	-	-	-
17.1636	0.55364	-1.76241	-0.14167	0.798555	55.36401	-176.241	-14.1667	79.85554
17.1638	0.55364	-1.94194	-0.10729	0.751436	55.36401	-194.194	-10.729	75.14365
17.1640	0.551094	-1.81589	-0.02708	0.770539	55.10936	-181.589	-2.70757	77.05387
17.1642	0.548547	-1.55359	0.068417	0.937365	54.85472	-155.359	6.841728	93.73652
17.1644	0.544727	-1.43772	-0.0831	0.981937	54.47274	-143.772	-8.30982	98.19371
17.1646	0.546001	-1.50393	-0.35048	0.945006	54.60007	-150.393	-35.0479	94.50061

Table 1. Tabular record obtained on the basis of the developed measurement-acquisition system

Records obtained in this way are suitable for further processing and presentation in the form of graphic diagrams. One example of the processed data extracted from one segment (several rows from the previous table) of the presented data is shown in Fig. 13. The figure shows a record for four revolution of the cutting tool and the changes occurring in three orthogonal directions.

After the source record obtained in this way, with the help of a sophisticated measurement-acquisition system, it is possible to further translate orthogonal forces into components of the resulting cutting force: Fg-main cutting force, Fr-radial cutting force, Fp-penetration force and Fa-axial force, Fig. 13. This translation, i.e. decomposition of the measured cutting forces, is carried out by means of the developed equations, which are described in detail in the article [8].

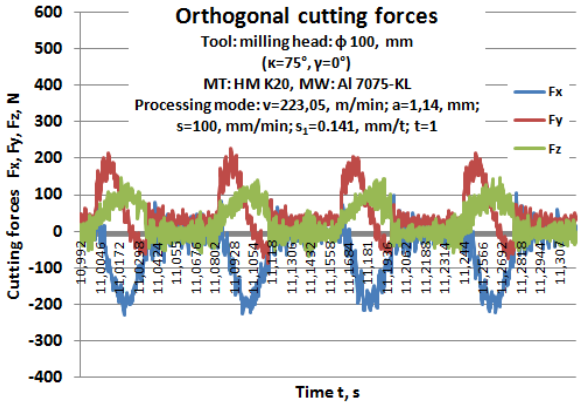


Fig. 13. Orthogonal record of cutting force components for several revolutions of the tool

4. CONCLUSIONS

Based on the developed system, conducted theoretical and experimental tests, per-formed analyzes and everything previously presented, the following conclusions can be drawn:

- The developed virtual instrument fully justified its role and proved to be a significant step forward in experimental tests, from the aspect of simplicity of measuring the cutting force in three orthogonal directions Fx, Fy and Fz, efficiency, accuracy of the obtained results, display of the obtained results in real time and comfort in work.
- The big advantage of the developed system lies in the fact that during the development of the application it is very easy to observe the flow of the program, find out where the error is and eliminate it. As mentioned earlier, LabVIEW can be used on different platforms, because according to the manufacturer, the virtual instrument does not depend on the operating system.

5. REFERENCES

[1] Popović, A., Marković, M., Panić, B., & Nikolić, M.: Sakupljanje i obrada podataka (Data acquisition and processing). *Integritet i vek konstrukcija*, *6*, 1-2, 2006.

[2] Dong, J., Hu, J., & Luo, Z.: Quality Monitoring of Resistance Spot Welding Based on a Digital Twin. *Metals*, *13*(4), 697, 2023.

[3] Bolic, M., Drndarevic, V., & Samardzic, B.: Distributed measurement and control system based on microcontrollers with automatic program generation. *Sensors and Actuators A: Physical*, *90*(3), 215-221, 2001.

[4] Lee, K., Hayasaka, T., & Shamoto, E.: Novel real-time monitoring method of depths of cut and runout for milling process utilizing FFT analysis of cutting torque. *Precision Engineering*, *81*, 36-49, 2023.

[5] Caggiano, A.: Tool wear prediction in Ti-6Al-4V machining through multiple sensor monitoring and PCA features pattern recognition. *Sensors*, *18*(3), 823, 2018.

[6] Mohamed, A., Hassan, M., M'Saoubi, R., & Attia, H.: Tool condition monitoring for high-performance machining systems - A review. *Sensors*, *22*(6), 2206, 2022.

[7] Savković, B., Rodić, D., Sekulić, M., Kovač, P., Štrbac, B., & Klančnik, S.: Implementation of a Virtual Instrument in the System for Measuring Forces and Temperatures in the Milling Process. *Processes*, *12*(7), 1344, 2024.

[8] Savković, B., Kovač, P., Stoić, A., & Dudić, B.: Optimization of machining parameters using the Taguchi and ANOVA analysis in the face milling of aluminum alloys Al7075. *Tehnički vjesnik*, *27*(4), 1221-1228, 2020.

ACKNOWLEDGMENTS

This research has been supported by the Ministry of Science, Technological Development and Innovation (Contract No. 451-03-65/2024-03/200156) and the Faculty of Technical Sciences, University of Novi Sad through the project "Scientific and Artistic ResearchWork of Researchers in Teaching and Associate Positions at the Faculty of Technical Sciences, University of Novi Sad" (No. 01-3394/1).

Authors:

PhD Borislav Savkovic, PhD Dragan Rodic, PhD Milenko Sekulic, PhD Pavel Kovac, MSc Andjelko Aleksic, MSc Aleksandra Kosanovic, University of Novi Sad, Faculty of Technical Sciences, Trg Dositeja Obradovica 6, 21000 Novi Sad, Serbia, Phone.: +381 21 485-23-29.

E-mail: savkovic@uns.ac.rs; rodicdr@uns.ac.rs; milenkos@uns.ac.rs; pkovac@uns.ac.rs; andjelkoa94@uns.ac.rs; kosanovica@uns.ac.rs

MMA 2024
FLEXIBLE TECHNOLOGIES

Section B:
MACHINE TOOLS AND AUTOMATIC FLEXIBLE TECHNOLOGICAL SYSTEMS, CAx AND CIM PROCEDURES AND SYSTEMS

MMA 2024
FLEXIBLE TECHNOLOGIES

15th INTERNATIONAL SCIENTIFIC CONFERENCE
NOVI SAD, SERBIA, SEPTEMBER 24-26, 2024

Review paper https://doi.org/10.24867/MMA-2024-02-001

Karabegović, I., Husak, E., Mahmić, M., Karabegović, E.

CHINA IS THE LEADING COUNTRY IN THE WORLD DEVELOPING AND IMPLEMENTING ROBOT TECHNOLOGY IN ALL INDUSTRY BRANCHES

Abstract: *In the past ten years, we have witnessed great changes around us brought about by the fourth industrial revolution. The basic technologies of the fourth industrial revolution are: Robotics, Sensor Technology, Internet of Things (IoT), Big Data, Cloud Computing, Virtual and Augmented Reality (AR), Digital Twins, Artificial Intelligence (AI), Advanced Security Systems, etc. (because to date Industry 4.0 has been implemented with over forty technologies). All developed and developing countries have adopted a strategy to implement Industry 4.0 (some countries are now adopting it) to prepare their companies for the global market. China has adopted a strategy called "Made in China 2025" with which it wants to become one of the most technologically developed countries in the world. Among the many technologies of Industry 4.0, China is the leading country in the development and implementation of robotic technology in the world. The paper provides an analysis of the implementation of robotic technology in the world with a comparative analysis of the implementation of robots in China and its industries and production process. Conclusions are given as to why China is the leading country in the world in the development and implementation of robotic technology.*

Key words: *Industry 4.0, robotic technology, production processes, automotive industry, electrical/electronic industry*

1. INTRODUCTION

One of the basic technologies of the fourth industrial revolution is robotic technology, without which there would be no fourth industrial revolution, i.e. Industry 4.0, which was announced in 2016 at the World Economic Forum [1,2]. In this industrial revolution, we are moving to ever more present mobility, bridging the digital and physical environment, using the fundamental technologies of Industry 4.0, in a completely new way. This leads us to wide possibilities of implementing innovations, automation, optimization with which we bring the production processes in the industry to a higher level. Industry 4.0 is a concept of production in which everything is networked. In production processes, machines and devices are connected by wireless connection and sensors, and also connected to a system that can make decisions on its own that are motivated by a large amount of data. The very concept of Industry 4.0 is in the process of implementation in our environment, but the concept of Industry 4.0 in itself is not yet widespread, and the expectations are that the implementation of this concept will improve and advance all aspects and segments of human life [3]. In reality, Industry 4.0 is a new phase in the organization and control of the industrial value chain, which primarily relies on Cyber-Physical Systems (CPS), and the corresponding service, most often implemented in the cloud (Cloud Computing). There are big changes in all branches of industry, as well as new business methods, transformation of production systems, consumption, delivery and transport. We can attribute these changes to the implementation of new technological achievements, first of which is robotic technology, followed by new technologies: Big Data, Internet of Things (IoT), Additive Technologies, Smart Sensors, Artificial Intelligence (AI), Virtual and Augmented Reality (AR), Advanced Security Systems, etc., and to date we have over forty Industry 4.0 technologies [3,4]. The paper presents an analysis of the implementation of robots in production processes in the world, as well as a comparative analysis of the implementation of robotic technology in the country of China, which is the leading country in the world in the application of robotic technology in industrial branches with leading countries that have been leaders in the adoption of robotic technology for years. At the end of the paper, an analysis was made, which conditions were key for China to be the leading country in the world in the application of robotic technology. The implementation of robotic technology leads to flexible automation, that is, by implementing the basic technologies of Industry 4.0, the company provides competitive capabilities to the global market [5,6].

2. THE TREND OF APPLICATION OF ROBOT TECHNOLOGY IN THE WORLD AND IN CHINA WITH PREDICTIONS OF IMPLEMENTATION AND APPLICATION

In the World, we will observe the real picture of the application of robotic technology through the application of industrial robots and service robots in the last five years. In order to arrive at the trend of the use of robots, an analysis was made based on statistical data taken from the International Federation of Robotics (IFR), the UN Economic Commission for Europe (UNECE) and the Organization for Economic Cooperation and Development (OECD). The trend of the implementation of industrial robots on an annual level in the world is shown in Fig. 1 [7-11].

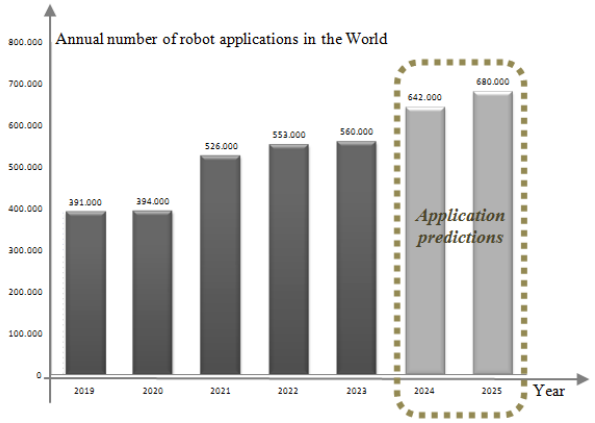


Fig. 1. Annual application of industrial robots in the last five years and prediction of application until 2025

The diagrams shown in Fig. 1 show that every year the number of applications of industrial robots in the world increases on an annual basis so that in 2023 the application was around 560,000 units of industrial robots, and such a trend will continue in the coming years. Predictions are that the use of industrial robots in 2025 will amount to around 680,000 units. Fig. 2 [8] shows on which continent industrial robots are used the most.

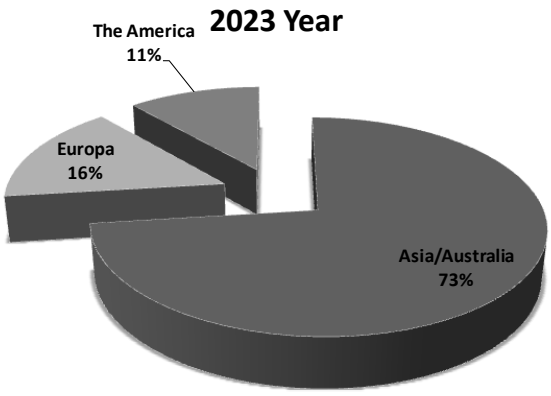


Fig. 2. Application of industrial robots by content in 2023

As Fig. 2 shows, in the year 2023, the world uses industrial robots the most on the continent of Asia/Australia, 73% of the total annual installations, then on the continent of Europe, 16%, and America, 11%. In Asia, there are the most companies from the automotive and electrical/electronic industry, where more than 50% of industrial robots are installed annually. China is in the Asia continent, which is the leading country in the development and implementation of robotic technology [7]. To confirm this fact Fig. 3 shows trend of the application of industrial robots in the world and in China in the last five years in the period 2019-2023 [8-10].

The trend of the application of industrial robots at the current level in the period 2029-2023 in the world and in China shows us that China is increasing its participation in the application of industrial robots in the world. In 2019, about 37% of the world's total use of industrial robots was used in China, while in just five years the use increased to 53% in 2023. It can be concluded that China is the leading country in the application of industrial robots in the world.

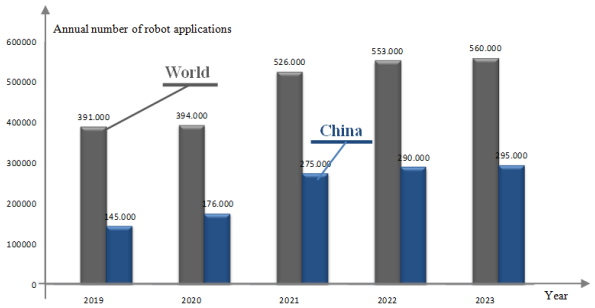
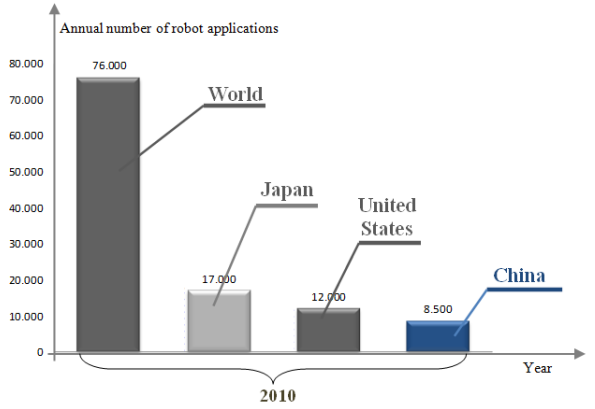
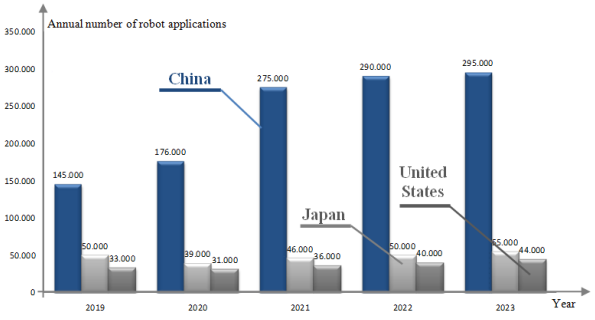


Fig. 3. Annual application of industrial robots in the last five years both in the World and in China



a) application of industrial robots in 2010



b) application of industrial robots in the period 2019-2023

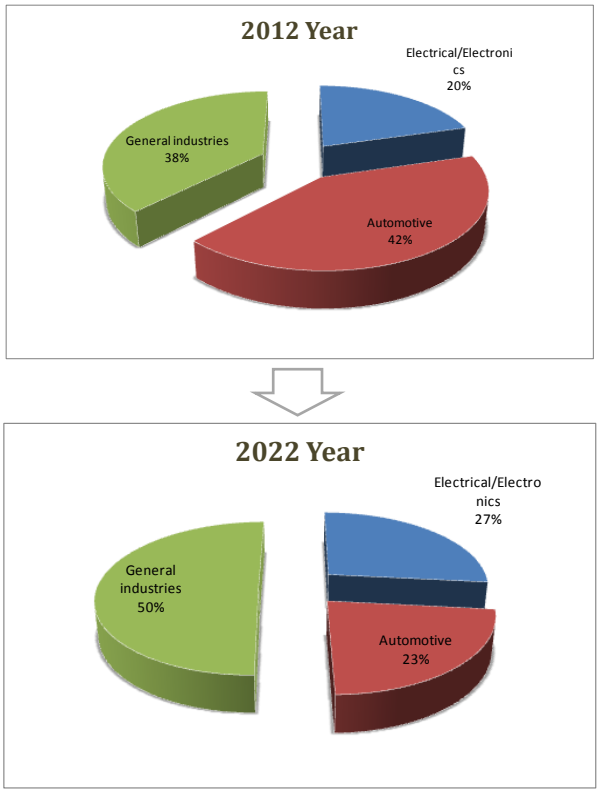
Fig. 4. Combined analysis of the use of industrial robots on an annual basis in the last five years in three leading countries: China, Japan and United States

In order to get a complete picture of the application of industrial robots in Fig. 4, we have shown the application of industrial robots in three countries: Japan, America and China, which in the last fifteen years have been the world leaders in the application of industrial robots [8]. Fig. 4.a) shows the trend in the use of industrial robots in 2010. It can be concluded that in 2010, the use of robots in China was very small, only about 11% compared to the annual use in the world, while the leading country was Japan with the use of about 22% compared to the world's use of robots. In the last five years for the period 2019-2023, Fig. 4.b), can be seen that the leading country in the world in the use of industrial robots is China and that there is a very big difference from the use of industrial robots in Japan and

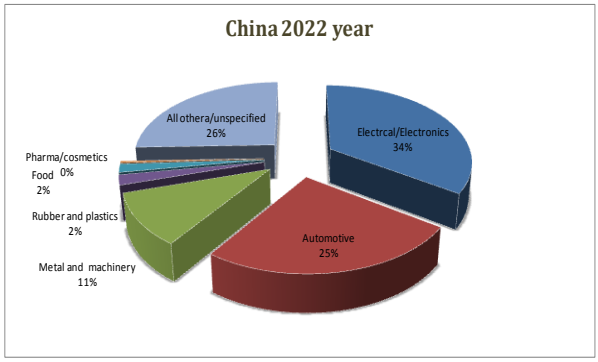
the United States, which were the leaders in 2010. in implementing industrial robots. In 2023, China implemented 4.5 times more robots than Japan, while it implemneted 6.7 times more industrial robots than the United States.

3. APPLICATION OF ROBOTS IN CHINA BY INDUSTRIAL BRANCHES

From the first installation of industrial robots until today, one of the most represented industries is the automotive industry, and it was in the first place in the world for the application of industrial robots. Fig. 5 shows a comparative analysis of the application of industrial robots by industry in the world and in China [10-12].



a) application of industrial robots in the world in: automotive, electro/electronic and other industries



b) application of industrial robots in China in all branches of industry

Fig. 5. Consolidated analysis of the use of industrial robots by industry in the world and in China

In the world, electro/electronic and automotive industries are the industries with the most installations of industrial robots in year 2012. Around 62% of applications in these two industries were implemented in the world (Fig. 5.a), while this ratio changed over the next ten years so that in the in the year 2022, these two industries implemented about 50% of industrial robots in relation to the total use of robots in that year. It can be seen that in these two industries, the use of industrial robots decreased by 12% in ten years. In China, the application in these two industries in 2022 is about 59%, almost identical application as in the world in 2012. Representation of industrial robots in industrial branches in China in 2022 is as follows: electrical/electronic industry 34%, automotive industry 25%, metal industry and machinery 11%. These three industries are the most represented by the application of robots in China. In fourth and fifth place are the rubber and plastic industry 2%, food industry 2%. Since China is investing in research, development and implementation of industrial robots in the coming years, it is expected that the use of robots in other industrial branches will increase [12-16].We come to the conclusion that China is the leading country in the world in the application of industrial robots, and there are many reasons why this is so. Let's list only the basic ones:

- China is implementing the national strategy "Made in China 2025", the goal of which is to make China the most technologically developed country in the world.
- China wants to: increase productivity, increase production speed, increase quality, safety, accuracy and agility in its production processes.
- In China, the price of labor increases every year and the price of robots decreases, so companies use robots to be competitive in the global market.
- China produces the most products in the electrical/electronic industry and vehicles in the world, where it wants to automate production processes in those industrial branches, etc.

4. CONCLUSION

Based on the analysis, we can conclude that China is the leading country in the world in implementation of industrial robots in the last ten years. Only in 2023, the application in China amounted to 53% of the total world application of industrial robots. China mostly implements industrial robots in the electrical/electronic and automotive industries; about 50% will be applied in 2023 in these two industries. China is the leader in the world in research, development and implementation of industrial robots, and there are several reasons for this, which we have listed in the last chapter of this paper. China implements Industry 4.0 in its production processes (one of the basic technologies of Industry 4.0 is robot technology), which is one of the reasons that it is the first in the world to apply industrial robots, and the reason is that companies from China are competitive on the global world market.

5. REFERENCES

[1] Karabegović, I., Majstorović, V., Industry 4.0:

Digital transformation is shaping the future, Society of Robotics in Bosnia and Herzegovina, ANU BiH, Bihać/Sarajevo 2024.
[2] Schwab, K.: The Fourth Industrial Revolution, World Economic Forum, Geneva, Switzerland, 2016.
[3] Karabegović, I., Kovačević, A., Banjanović Mehmedović, L., Dašić,P.: Integrating Industry 4.0 in Busniess and Manufacturing, IGI Global,Hershey, PA, USA, 2020.
[4] Thoben, K.D. Wiesner, S. Wuest, T.; Industrie 4.0 and smart manufacturing-a review of research issues and application examples. International Journal Automation Technology, Vol. 11, pp. 4–16. 2017.
[5] Karabegović, I., Husak, E., Karabegović, E., Mahmić M.: China is the leading country in the world in the implementation of robotic technology as the basic technology of Industry 4.0“, 12th International Conference – KOD 2024 „Machine and Industrial Desing in Mechanical Enginering, pp. 128-129, 2024.
[6] Karabegović, I., Karabegović, E., Mahmić, M., Husak E., : The Implementation of Industry 4.0 by Using Industrial and Service Robots in the Production Processes, Chapter 1. Handbook of Research on Integrating Industry 4.0 in Business and Manufacturing, IGI Global, USA, pp. 1-30, 2020.
[7] IFR, “World Robotics Report: ‘All-Time High’ with Half a Million Robots Installed in one Year,” IFR International Federation of Robotics. https://ifr.org/ifr-press-releases/news/wr-report-all-time-highwith-half-a-million-robots-installed [Accessed; June 26, 2024].
[8] Bill, M.. Müller, C., Kraus, W., and Bieller, S.,: World Robotics Report, 2023. [Online]. Available: https://ifr.org/ifr-press-releases/news/world-robotics-2023-report-asia-ahead-of-europe-and-the-americas
[9] International Federation of Robotics, “Executive Summary World Robotics 2010 Industrial Robots” 2010. [Online]. Available: https://ifr.org/img/worldrobotics/Executive_Summary_WR_Industrial_Robots_2010.pdf
[10] International Federation of Robotics, “Executive Summary World Robotics 2022 Industrial Robots” 2022. [Online]. Available: https://ifr.org/img/worldrobotics/Executive_Summary_WR_Industrial_Robots_2022.pdf
[11] Karabegović,I., Turmanidže, R., Dašić, P.: Analysis of Patent Trends from Industry 4.0 and theImplementation of Robot Technology in theCountries of China, USA, Japan, Republic of Korea and Germany, 6th International Scientific Conference on Mechanical Engineering Technologies and Applications - COMET-a, pp. 273-286., 2022.
[12] International Federation of Robotics, “Executive Summary World Robotics 2012 Industrial Robots.”2012. [Online]. Available: https://ifr.org/img/worldrobotics/Executive_Summary_WR_Industrial_Robots_2012.pdf
[13] Karabegović, I., Karabegović , E., Mahmić, M., Husak, E.: Implementation of Industry 4.0 and Industrial Robots in Production Processes In: Isak Karabegović (eds) New Technologies, Development and Application. Lecture Notes in Networks and Systems. Springer Nature Switzerland AG 76, pp. 96-102. 2020.
[14] Karabegović, I., Husak, E. Karabegović, E., Mahmić, M.: How the Core Technologies of Industry 4.0 Are Changing the Automotive Industry in the World, With a Focus on China, IX International Congress Motor Vehicles and Motors (MVM 2022) IOP Conf. Series: Materials Science and Engineering 1271 012017, pp.1-14, 2020.
[15] Chryssolouris, G., Mavrikios, D., Papakostas, N., Mourtzis, D., Michalos, G., Georgoulias, K.: Digital manufacturing: History, perspectives, and outlook, Journal of Engineering Manufacture, Proceedings of the Institution of Mechanical Engineers, Part B, pp. 451–462. 2009.
[16] Karabegović, I., Mahmić, M., Karabegović, E., Husak, E.; 2023, Comparative Analysis of the Implementation of Robot Technology as the Basic Technology of Industry 4.0 in America (USA) and China, 14th International Scientific Conference ETIKUM, pp. 33-40, 2023.

Authors:
PhD Isak Karabegović, Academy of Sciences and Arts of Bosnia and Herzegovina, Bistrik 7. 71000 Sarajevo,Bosnia and Herzegovina, Phone.: +387 61 138-856.
E-mail: isak1910@hotmail.com
PhD Ermin Husak, PhD Mehmed Mahmić, PhD Edina Karabegović,Univesity of Bihać, Technical faculty Bihać, Irfana Ljubijankića bb.77000 Bihać, Bosnia and Herzegovina.
E-mail: erminhusak@yahoo.com; mmahmić@gmail.com; edina-karabeg@hotmail.com

MMA 2024 FLEXIBLE TECHNOLOGIES

15th INTERNATIONAL SCIENTIFIC CONFERENCE
NOVI SAD, SERBIA, SEPTEMBER 24-26, 2024

Original research paper https://doi.org/10.24867/MMA-2024-02-002

Marinković, D., Živković, A., Mlađenović, C., Knežev, M., Mejić, L., Savković, B.

ANALYSIS OF THE INFLUENCE OF THE CUTTING REGIMES ON THE QUALITY OF THE MACHINING SURFACE IN TURNING PROCESS

Abstract: *This study examines the influence of cutting regimes on machining surface quality in the turning process, using the Taguchi method for experimental design. An orthogonal array was employed to systematically vary cutting speeds, feed rates, and depths of cut. Surface roughness measurements post-machining were analyzed to determine the impact of these parameters. Results indicate that higher cutting speeds improve surface finish, while increased feed rates and depths of cut deteriorate it. The Taguchi method efficient analysis and identification of optimal cutting conditions, revealing that the interaction between parameters significantly affects surface quality.*
Key words: *surface quality, turning process, Taguchi method*

1. INTRODUCTION

In modern manufacturing, the quality of the machined surface, machining precision and productivity are critical factors influencing the performance and lifetime of mechanical machines and components. By systematically varying parameters such as cutting speed, feed rate, and depth of cut, this research aims to identify optimal conditions that enhance surface quality.

Elbah and al. [1] compared the surface roughness criteria (Ra, Rz, and Rt) of wiper inserts and conventional inserts during the hard turning of AISI 4140 hardened steel (60 HRC). The experiment was designed using Taguchi's L27 orthogonal array. Statistical analysis revealed that feed rate and depth of cut significantly influence the reduction of surface roughness. Results indicated that the surface quality obtained with the wiper ceramic insert significantly improved compared to the conventional ceramic insert.

Panwar and associates [2] conducted fifteen experiments using the Box-Behnken design matrix to investigate the effects of machining parameters such as spindle speed, feed rate, and cutting depth. A mathematical framework for surface roughness was developed using response surface methods to assist a genetic algorithm in determining the optimal machining parameters. A genetic algorithm was employed to identify the optimal process parameter settings that maximize the material removal rate. The best surface roughness response value obtained from the single-objective genetic algorithm optimization was 1.19 µm.

In the following study Koyees, Eisselers and Schmauders [3] approach is combined with fuzzy multiple attribute decision-making methods to enhance surface quality in constant cutting speed face turning of EN 1.4404 austenitic, EN 1.4462 standard duplex, and EN 1.4410 super duplex stainless steels. Two multiple attribute decision-making techniques were employed simultaneously to determine multi-surface quality characteristics. Analysis of variance results indicated the predominant effect of feed rate on surface quality. Finally, the collected chips at constant cutting speed and varying feed rates and depths of cut showed that machining austenitic stainless steels yields more machine-friendly chips compared to duplex stainless steel grades.

In this study, two types of steel were used for the experiment: tool steel 90MnCrV8 and heat-treatable steel 42CrMo4. The experimental plan was established using Taguchi's L16 experimental design for both materials. After machining on an INDEX GU600 lathe, the surface roughness of the samples was measured using an appropriate device. The results were then processed using software, and the presentation and discussion of the results are provided in the following sections of the paper.

2. TAGUCHI EXPERIMENTAL DESIGN

The Taguchi method is a statistical approach developed by Japanese engineer and statistician Genichi Taguchi to improve the quality of industrial production. In recent times, it has been increasingly utilized in engineering, biotechnology, and marketing. Statisticians have embraced this model, particularly Taguchi's development of design for variation in significant experimental factors [4].

Num.	RPM	Depth	Feed
1	1100	0.5	0.15
2	1100	0.8	0.15
3	1100	1.1	0.2
4	1100	1.4	0.2
5	1700	0.5	0.15
6	1700	0.8	0.15
7	1700	1.1	0.2
8	1700	1.4	0.2
9	2100	0.5	0.2
10	2100	0.8	0.2
11	2100	1.1	0.15
12	2100	1.4	0.15
13	2700	0.5	0.2
14	2700	0.8	0.2
15	2700	1.1	0.15
16	2700	1.4	0.15

Table 1. Presentation of the experiment plan

By using orthogonal arrays, the Taguchi method systematically examines the effects of multiple variables simultaneously, reducing time and resource consumption. It employs signal-to-noise (S/N) ratios to measure variability and aims to make processes more consistent and less sensitive to variations. This method has gained widespread acceptance across various industries for its efficiency in optimizing product and process design, ultimately enhancing performance and reducing costs [4].

The experiment for both types of steel was conducted using the Taguchi L16 method (2^4 and 1^2) as shown in Table 1. The same cutting parameters (spindle speed, feed rate, and depth of cut) were used for both materials to allow for comparative analysis and discussion of the results. The spindle speeds were set to 1100, 1700, 2100, and 2700 RPM; the depths of cut were 0.5, 0.8, 1.1, and 1.4 mm; and the feed rates were 0.15 and 0.2 mm/rev.

3. EXPERIMENTAL SETUP

The experiment was conducted at the Faculty of Technical Sciences in Novi Sad, Department of Production Engineering. The experiments were carried out on an INDEX GU600 lathe machine using steel rods with a diameter of ϕ30 mm (90MnCrV8 and 42CrMo4) as workpieces. A TNMG 160404 cutting insert was used for machining the rod material as it is showed in Fig. 1. No cooling or lubrication was used during the machining process. Different cutting parameters were combined according to the Taguchi experimental design outlined in the previous section.

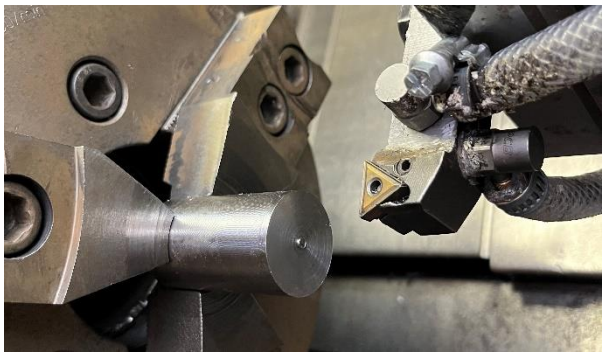


Fig. 1. Experimental setup on the INDEX GU600 lathe

Measuring the roughness of machining surfaces is a critical aspect of assessing the quality of manufactured components. After completing the machining process according to the experimental plan, the surface roughness of the machined samples was measured using a Mitutoyo SJ-210 profilometer. The output of the experiment was the arithmetic average roughness value - Ra. Roughness measurements were taken three times for each sample, and the average values were calculated. In the following sections, the measured surface roughness values were used to determine which parameter—spindle speed, feed rate, or depth of cut—had the most significant impact on the arithmetic average roughness value.

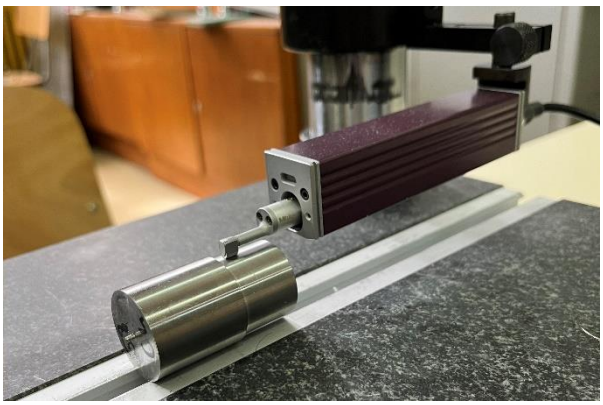


Fig 2. Display of measurement of arithmetic average roughness value (Ra) on Mitutoyo SJ-210 profilometer

The profile roughness parameters are defined in the ISO 4287:1997 standard, which is based on the "M" (mean line) system. Among the various roughness parameters available, Ra is the most commonly used, primarily due to historical reasons; early roughness meters could only measure Ra. Other commonly measured parameters include Rz, Rq, and Rsk, all of which can be assessed using the Mitutoyo SJ-210 profilometer. These parameters condense the profile information into a single value, so careful application and interpretation are essential. Small variations in filtering the raw profile data, calculating the mean line, and the measurement's physical aspects can significantly influence the calculated parameter. Modern digital equipment allows for evaluating scans to ensure no apparent glitches distort the values. The equation for the arithmetic average roughness value, Ra, is provided below:

$$Ra = \frac{1}{l_r}\int_0^{l_r} |z(x)|dx \qquad (1)$$

The results obtained from measuring surface roughness using the appropriate device shown in Fig. 2. Table 2 presents the arithmetic roughness values for the materials 90MnCrV8 and 42CrMo4. The data shows that 90MnCrV8 exhibited consistently lower Ra values under varying cutting conditions compared to 42CrMo4.

90MnCrV8	42CrMo4
Ra	
6.81	5.36
9.7	4.32
14.88	6.75
6.19	2.72
6.87	5.74
10.18	4.94
11.75	6.62
6.63	3.47
14.11	7.25
12.69	10.74
8.13	3.53
6.41	11.73
13.1	7
15.38	10.16
9.95	4.34
6.71	16.09

Table 2. The measured Ra values

4. EXPERIMENTAL ANALYSIS RESULTS

The Taguchi L16 experimental design was employed to analyze the influence of cutting regimes on the quality of the machining surface in the turning process. The experimental setup and analysis were conducted using the Minitab software, which facilitated the systematic examination of various cutting parameters [5]. The L16 orthogonal array allowed for an efficient investigation of the effects of spindle speed, feed rate, and depth of cut on the surface roughness of the machined samples. The surface roughness, characterized by the Ra value, was measured for each experimental run. Minitab's statistical tools were used to process the data, perform ANOVA, and generate response surface plots, enabling a comprehensive understanding of the main effects and interactions among the cutting parameters. The results were then interpreted to identify the optimal cutting conditions that minimize surface roughness, providing valuable insights into achieving superior machining surface quality [6].

	RPM	Depth	Feed rate
Impact on Ra [%]	19.3	51	29.7
Rank	3	1	2

Table 3. Taguchi analysis results for 90MnCrV8 steel

Table 3 presents the results of the software analysis, showing that for the 90MnCrV8 steel material, the depth of cut has the most significant influence among the cutting parameters, with an impact of 51%. This significant impact indicates that controlling the depth of cut is crucial for minimizing surface roughness in 90MnCrV8 steel. Further analysis reveals that other parameters such as spindle speed and feed rate play comparatively minor roles, emphasizing the dominant effect of cutting depth in this material's machining process.

	RPM	Depth	Feed rate
Impact on Ra [%]	65	32.3	2.7
Rank	1	2	3

Table 4. Taguchi analysis results for 42CrMo4 steel

Table 4 presents the results for the heat-treatable steel 42CrMo4. Unlike the previous case, the order of the most influential parameters differs. In this instance, the most significant parameter is the spindle speed, while the feed rate has the least impact. This suggests that optimizing spindle speed is crucial for improving surface roughness in 42CrMo4 steel, whereas adjustments to feed rate will yield minimal improvements.

The graphical representation of the influence of cutting regimes on the arithmetic mean surface roughness (Ra) is shown in Fig. 3. The steepest curve corresponds to the depth of cut, indicating that it is the most influential parameter in machining the 90MnCrV8 tool steel.

This steep curve highlights the sensitivity of surface roughness to changes in cutting depth, making precise control essential for achieving desired surface finishes. Additionally, the other curves representing spindle speed and feed rate are comparatively flatter, signifying their lesser impact on Ra for this material.

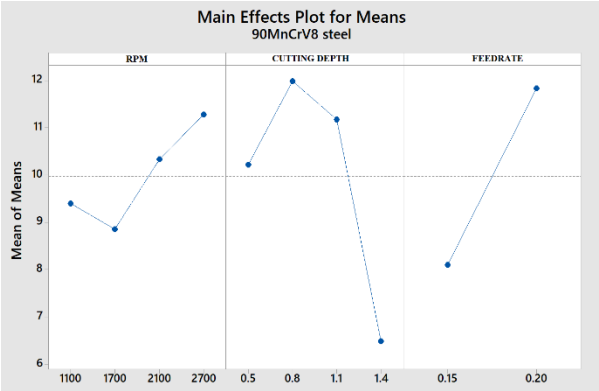


Fig 3. Main effects plot for means (90MnCrV8)

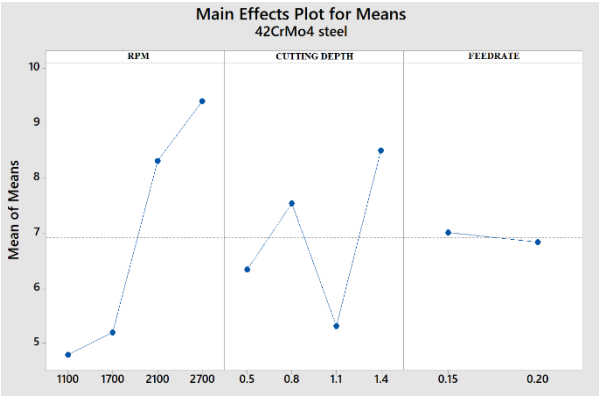


Fig 4. Main effects plot for means (42CrMo4)

On the other hand, Fig. 4 graphically presents the results for the heat-treatable steel 42CrMo4. The steepest curve is shown for the spindle speed during turning, indicating its significant influence on the arithmetic surface roughness (Ra). The flatter the curve, such as those for feed rate and depth of cut, suggests these parameters have a lesser impact on surface roughness for 42CrMo4 steel, highlighting the dominance of spindle speed in determining machining surface quality.

5. CONCLUSION

This study provides a comprehensive analysis of the influence of cutting regimes on the quality of the machining surface in the turning process, utilizing the Taguchi L16 experimental design and Minitab software for data analysis. The results indicate that the most influential parameter on the average roughness value (Ra) varies significantly between the two types of steel examined. For 90MnCrV8 tool steel, the depth of cut emerged as the most significant factor, accounting for 51% of the variation in surface roughness. This finding underscores the importance of controlling the depth of cut to achieve optimal surface finishes in hard tool steels.

In contrast, for 42CrMo4 heat-treatable steel, the spindle speed (RPM) was identified as the most critical parameter affecting surface roughness. This highlights the necessity of optimizing spindle speed to enhance surface quality in heat-treatable steels. The differences

in the most influential parameters between the two materials suggest that each material responds uniquely to different cutting conditions, emphasizing the need for material-specific machining strategies.

It is also noteworthy that the experiments were conducted without the use of lubrication. The absence of a cooling and lubrication medium likely influenced the results, as lubrication typically reduces friction and heat generation, potentially leading to different surface roughness outcomes. The lack of lubrication may have amplified the effects of certain parameters on surface roughness, and future studies could investigate how lubrication alters these relationships.

Overall, this analysis highlights the critical role of specific cutting parameters in determining surface quality and the importance of tailoring machining conditions to the material being processed. The findings provide valuable insights for manufacturing processes, suggesting that careful optimization of cutting depth for 90MnCrV8 and spindle speed for 42CrMo4 can lead to superior surface finishes. Future research could explore the inclusion of lubrication and other machining conditions to further enhance the understanding of how to achieve optimal surface quality across different materials.

6. REFERENCES

[1] Elbah, M., Yallese, M.A., Aouici, H., Mabrouki, T., Rigal, J.: *Comparative assessment of wiper conventional ceramic tools on surface roughness in hard turning AISI 4140 steel*, Measurement, Vol. 46, No. 9, pp. 3041-3056, 2013.

[2] Panwar, V., Sharma, D.K., Kumar, P.K.V., Jain, A., Thakar, C.: *Experimental investigations and optimization of surface roughness in turning of en 36 alloy steel using response surface methodology and genetic algorithm*, Materials Today: Proceedings, pp. 6474-6481, 2021.

[3] Koyee, R.D., Eisseler, R., Schmauder, S.: *Application of Taguchi coupled Fuzzy Multi Attribute Decision Making (FMADM) for optimizing surface quality in turning austenitic and duplex stainless steel*, Measurement, Vol. 58, pp. 375-386, 2014.

[4] Kovač, P.: *Methods of planning and processing experiments*, Textbook, University of Novi Sad, Faculty of Technical Sciences Novi Sad, 2015.

[5] Marinković, D.: *Application of artificial neuron networks in modeling the uniformity of the machine tools sliders movement*, Bachelor thesis, University of Novi Sad, Faculty of Technical Sciences, Novi Sad, Serbia, 2022.

[6] Shyam, K. K., Rajeshwar, S.: *An Overview of Taguchi Method*, International Journal of Engineering and Mathematical Sciences, Vol. 1, pp 11-18, 2012.

ACKNOWLEDGMENTS

This research has been supported by the Ministry of Science, Technological Development and Innovation (Contract No. 451-03-65/2024-03/200156) and the Faculty of Technical Sciences, University of Novi Sad through project "Scientific and Artistic Research Work of Researchers in Teaching and Associate Positions at the Faculty of Technical Sciences, University of Novi Sad" (No. 01-3394/1). Special thanks to the company FKL from Temerin, Serbia. The mentioned company provided the material for making the experiment described in this scientific paper.

Authors:

MSc Dejan Marinković, PhD Aleksandar Živković, PhD Cvijetin Mlađenović, PhD Miloš Knežev, PhD Luka Mejić, PhD Borislav Savković, University of Novi Sad, Faculty of Technical Sciences, Trg Dositeja Obradovica 6, 21000 Novi Sad, Serbia, Phone.: +381 21 485-24-76.

E-mail: dejan.marinkovic@uns.ac.rs; acoz@uns.ac.rs; mladja@uns.ac.rs; knezev@uns.ac.rs ; luka.mejic@uns.ac.rs ; savkovic@uns.ac.rs

MMA 2024 FLEXIBLE TECHNOLOGIES

15th INTERNATIONAL SCIENTIFIC CONFERENCE
NOVI SAD, SERBIA, SEPTEMBER 24-26, 2024

Original research paper https://doi.org/10.24867/MMA-2024-02-003

Devic, A., Vidakovic, J., Zivkovic, N., Stepanovic, A.

ADVANCEMENT OF THE INDUSTRIAL ROBOT PROGRAMMING LANGUAGE L-IRL USING AUGMENTED REALITY

Abstract: *Augmented reality is one of the most promising technologies in the development of a new generation of human-machine interfaces. In this paper, the advancement of Lola Industrial Robot programming language (L-IRL) using Augmented Reality is presented. A developed tool for programming linear path segments of Tool Centre Point (TCP) in an AR environment representing an upgraded online Walk-Through robot programming method is described. Development has been performed in Unity IDE. A path planner adapted for variable and unpredictable Unity frame rates has been used. A post-processor for generating L-IRL code has been presented. Verification is performed for the 6DoF industrial robot with revolute joints RL-15.*

Key words: *industrial robot, offline robot programming, augmented reality.*

1. INTRODUCTION

Industrial robots are important equipment for automatisation in the modern manufacturing industry, integrating advanced multi-disciplinary technology, such as machinery, electronics, control, computers, sensors, artificial intelligence, etc [1]. A robot application program is a set of instructions that cause the robot system to move the robot's end-effector, i.e. Tool Center Point (TCP) in order to perform the desired robot task correctly [2]. Conventional industrial robot programming methods are time-consuming, and often require specialized expertise [3]. Over the years, tremendous efforts have been undertaken by the international robotics community to achieve user-friendly and, at the same time, powerful programming methods [4-5].

Recently, Augmented Reality (AR) has been used to advance the programming process of industrial robots [4-6]. Augmented Reality is used to enhance the perception of the real world by integrating virtual objects into an image sequence acquired from various camera technologies [7]. Numerous AR applications in robotics in industrial settings have been developed in recent years [7-8].

In this paper, the advancement of Lola Industrial Robot programming language (L-IRL) [9-10] using Augmented Reality technology is presented. A developed tool for programming of linear path segments of Tool Centre Point (TCP) in an AR environment which can be regarded as an upgraded online Walk-Through robot programming method [4] is described.

The paper is divided as follows. In section 2, system specifications and requirements have been presented. Integration methodology has been given in Section 3. Verification of the proposed AR-supported robot programming tool is presented in Section 4. Discussion and concluding remarks are given in sections 5 and 6.

2. SYSTEM SPECIFICATIONS AND REQUIREMENTS

2.1 L-IRL language

A series of LOLA robot controllers, were developed and are being constantly upgraded in Lola Institute [11]. A new system for robot control, programming, and remote monitoring is software-oriented, open architecture, modular, and reconfigurable [11-12].

L-IRL is a procedural robot programming language that belongs to the class of higher programming languages and is developed at the Lola Institute according to the standard DIN 66312 - Industrial Robot Language (IRL), for the purposes of programming industrial robots [9-11]. An integral part of the L-IRL trajectory planner is the trajectory interpolator, whose outputs are the positions, velocities, and accelerations of the manipulator's joints, which are sent to the servo controllers at discrete time intervals, which are constant [9]. Programs written in the L-IRL language are compiled and then executed on the real-time robot controller [13], Fig. 1. L-IRL contains all general structures such as data processing, expressions, program flow control, procedures and operations, as well as robot specific structures, geometric data types, and expressions, motion statements, etc.

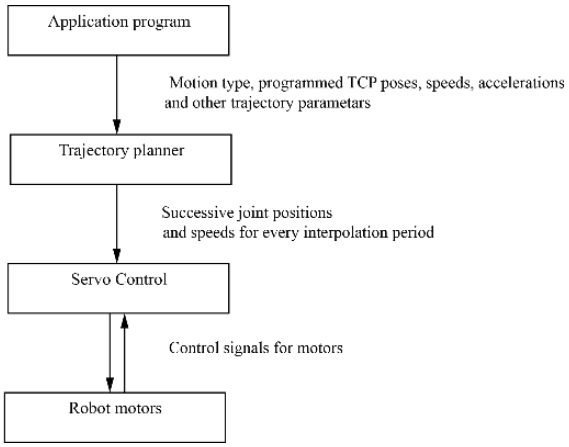


Fig. 1. Information flow in robot control system [9]

The motion instructions (so-called MOVE instructions) within the L-IRL language allow standard movements in industrial robotics, such as Point to Point (PTP) motions or Continuous Path (CP) movements of the robot's end-effector. In CP motion [12], a user defines a path to be followed by a TCP, such as linear, circle, etc. MOVE instructions are implemented through functions and procedures within the trajectory planner.

2.2 AR-supported upgraded Walk-Through robot programming tool

Industrial robot programming is usually performed using offline or online programming methods [2]. Conventional online programming methods, such as the Lead-Through method [4], i.e., robot programming using teaching pendant, is time-consuming, require downtime, and often require specialized expertise. Offline programming methods require high-fidelity 3D modeling of the robot and its workspace and are time-consuming [3]. The Walk-Through robot programming method [4] is an intuitive programming method where the human operator interacts directly with the robot by physically guiding it to the desired configuration. However, this method has two shortcomings. The first one is that it is an online method, which implies downtime, and the second one is that it is limited, as only a few lightweight robots offer the necessary zero-torque control [4].

In this research, we propose an upgraded AR-supported Walk-Through robot programming method, where offline programming of linear segments of TCP paths is enabled in an Augmented Reality environment in an online mode, and integrated with online Walk-Through programming for the definition of starting and ending TCP poses for linear path segments of a TCP.

3. INTEGRATION PROCESS

3.1 System integration

Unity [14], one of the most popular game engines, is a leading platform for the development of XR applications with high-quality 3D rendering, which can be deployed across a variety of platforms and can integrate different XR SDKs. In this study, Unity has been used as IDE. Coding is done in C#. In marker-based AR, scanning a marker triggers an augmented experience. In this paper, a smartphone/tablet was chosen as a tool for experiencing Augmented Reality. Vuforia [15], an AR Software Development Kit for mobile devices that provides essential tools for the creation of Augmented Reality applications, is used for generating AR robot image in a real laboratory environment

Development in Unity includes the following [16]:

- Development of a robot model for robot's motion simulation in Unity, based on the robot's CAD model, utilizing Unity's built-in physics engine, Nvidia PhysX, and setting up motion controllers [17]. The complete procedure is described in [16].
- Development of AR-supported upgraded offline Walk-Through robot programming functionality, including:
  - integration of solution of inverse kinematics problem;
  - integration of trajectory planner;
  - developing of functionalities for robot programming in AR;
  - development of GUI, including touchscreen interaction.
- Development of L-IRL post-processor.

In Fig. 2, a render of the 6DoF robot RL15 in the laboratory environment based on the developed 3D robot model is presented. The system architecture for the proposed AR-supported robot programming framework is presented in Fig. 3.



Fig. 2. Render of the 6DoF robot RL15 in the laboratory environment

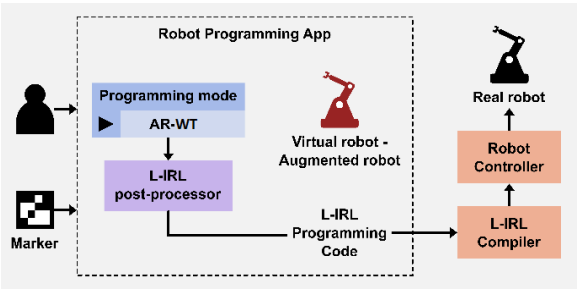


Fig. 3. System architecture for the designed AR-supported robot programming system

3.2 Trajectory planner development

Given that a standalone application has been considered herein, a trajectory planner had to be integrated. In this research, for the purposes of system verification, a separated simple trajectory planner enabling the programming of CP motion along linear paths in Unity has been used, previously developed in [16]. The planer integrates the solution for the inverse kinematics problem for the specific robot, in this case RL15, which was previously developed and presented in [9]. The planner operates by calculating the current poses using normalized time and coordinates, integrating inverse kinematics (IK) algorithms for real-time execution, and checking joint positions and speeds against predefined limits. Given that the Unity frame rate is variable and not predictable, in this research, a trajectory planner calculates joint positions for the current frame using analytical expressions and Unity built-in functions for time measurement in real-time systems. The trajectory generation relies on a cubic polynomial to smooth the path between selected poses [16]. The real-time calculation ensures that joint positions and speeds are continuously monitored and

remain within predefined limits, thereby maintaining the accuracy and safety of the robot's movements.

4. VERIFICATION OF THE NOVEL L-IRL AR-SUPPORTED TOOL FOR OFFLINE UPGRADED WALK-THROUGH PROGRAMMING OF LINEAR TCP MOTIONS

Verification of the novel L-IRL AR-supported tool for offline upgraded Walk-Through programming in an AR environment is performed using 6DoF robot RL15 previously produced in Lola Institute [9]. Fig. 4 depicts the developed GUI for the designed AR-supported Android robot programming app, with the designed various buttons and a vertical stack of numerical values of the real-time TCP position and orientation of the augmented robot in Cartesian space, and the joint angles of augmented robot.



Fig. 4. Depiction of GUI for AR-supported robot programming system in the laboratory settings. [15]

Fig. 5 shows the programming of robot RL15 using the designed Android smartphone application. Scanning a marker triggers an augmented experience, i.e. loading and initialization of the robot's RL15 3D model in Augmented Reality. The augmented robot is scaled down for demonstration purposes.



Fig. 5. GUI for AR-supported advanced Walk-Through robot programming

Advanced AR-supported Walk-through robot programming allows the user to select start and end points between linear paths of the robot's TCP in a very simple way. A user manually "drags" the TCP frame in an AR environment by using a phone as an emulated robot handle. In other words, the robot's TCP frame follows the movement of the user's hand holding the smartphone until the user decides to select and save a point in Cartesian space that marks the position of the TCP, while the orientation is defined by the orientation of the phone. This is achieved by the TCP coordinate frame becoming a child of the AR camera frame.

When the user selects several poses of the TCP in the Cartesian space, which is done by a user pressing the button as presented in Fig 5., they can simulate the programmed trajectory of the robot in Augmented Reality, which herein implies a linear TCP path between the selected waypoints. The TCP linear trajectory is achieved by robot joint motions calculated by the trajectory planner.

A user can inspect the programmed trajectory from multiple angles during different time instances/robot configurations using the slider. This is depicted in Fig.6.



Fig. 6. Simulation of the programmed movements in AR

If the user is satisfied with the programmed trajectory, they can decide to save it. The TCP poses are then sent to the developed post-processor for L-IRL language, and saved to a .txt file as L-IRL code, Fig. 7.



Fig. 7. L-IRL code generated by developed post-processor

5. DISCUSSION

The presented AR-supported CP robot programming tool represents the integration of conventional Walk-Through online programming method with offline continuous-path programming, levering advantages of both methods, namely the absence of downtime for offline programming, and the intuitive programming approach characteristic for the Walk-Through online programming method.

In robot programming, AR and, in general, XR technologies are primarily utilized to enhance visualization which benefits the robot programming

process. XR (Extended Reality) offers substantial benefits by immersing programmers in a virtual environment where they can intuitively visualize the robot's end-effector (TCP) movements within the real world. This immersion aids in identifying and understanding the robot's operational constraints in its real-world view.

Presented AR-supported industrial robot CP programming tool can be standalone, as presented in [16], or it can be created using integration of Unity with ROS [18] (ROS–Unity suite), offline/online programming environments like RoboDK [19] and other similar robot frameworks. Advantages and disadvantages are presented in [16].

6. FINAL REMARKS

In this paper, the improvement of the Lola Industrial Robot programming language using Augmented Reality technology is presented. A software tool for intuitive programming of continuous paths (linear path segments of TCP) in offline mode using Augmented Reality technology is presented. Development has been performed in Unity IDE. A post-processor for generating L-IRL code has been developed. Verification is performed for 6DoF industrial robot RL-15.

7. REFERENCES

[1] Li, Z., Li, S., Luo, X.: An overview of calibration technology of industrial robots, IEEE/CAA Journal of Automatica Sinica, Vol. 8, No 1, pp. 23-36, 2021.

[2] Biggs, G., MacDonald, B., A survey of robot programming systems, Proceedings of the Australasian conference on robotics and automation. Vol. 1, pp. 1-3, 2003.

[3] Ong, S.K., Yew, A.W.W., Thanigaivel, N.K., Nee, A.Y.C.: Augmented Reality-Assisted Robot Programming System for Industrial Applications, Robotics and Computer-Integrated Manufacturing, Vol. 61, 101820, 2020.

[4] Gaschler, A., Springer, M., Rickert, M., Knoll, A.: Intuitive Robot Tasks with Augmented Reality and Virtual Obstacles, Proceedings of the 2014 IEEE International Conference on Robotics and Automation (ICRA), pp. 6026-6031, Hong Kong, China, IEEE, 2014.

[5] Hägele, M., Nilsson, K., Pires, J. N., Bischoff, R.: Industrial robotics, in Springer Handbook of Robotics, Springer, Cham, 2016.

[6] Fang, H.C., Ong, S.K., Nee, A.Y.C. Interactive Robot Trajectory Planning and Simulation Using Augmented Reality, Robotics and Computer-Integrated Manufacturing, Vol. 28, No. 2, pp. 227–237, 2012.

[7] Makhataeva, Z., Varol, H.A.: Augmented reality for robotics: A review, Robotics Vol. 9, No. 2, 21, 2020.

[8] Wang, X., Ong, S.K., Nee, A.Y.: A comprehensive survey of augmented reality assembly research, Advances in Manufacturing, Vol. 4, pp. 1-22, 2016.

[9] Kvrgic, V.: Development of Intelligent System for Control and Programming of Industrial Robots, Ph.D. Dissertation, Faculty of Mechanical Engineering, University of Belgrade, Belgrade, Serbia, 1998.

[10] Ferenc, G., Dimić, Z., Lutovac, M., Vidaković, J., Kvrgić, V.: Open architecture platforms for the control of robotic systems and a proposed reference architecture model, Transactions of FAMENA, Vol. 37, No. 1, pp. 89-100, 2013.

[11] Dimić, Z.: An open architecture control system for reconfigurable robotic machining cells, Ph.D. Dissertation, Faculty of Mechanical Engineering, University of Belgrade, Belgrade, Serbia, 2016.

[12] Chettibi, T.: Smooth point-to-point trajectory planning for robot manipulators by using radial basis functions, Robotica Vol. 37, pp. 539–559, 2019.

[13] Ferenc, G., Dimić, Z., Lutovac, M., Vidaković, J., Kvrgić, V.: Distributed robot control system implemented on the client and server PCs based on the CORBA protocol, Proceedings of the Mediterranean Conference on Embedded Computing (MECO), pp. 158-161, Budva, Montenegro, IEEE, 2012.

[14] Unity, Unity Real Time Development Platform | 3D, 2D, VR & AR Engine, Available online: https://unity.com/ (accessed on 22 July 2024).

[15] Vuforia, Getting Started|Vuforia Library, Available online: https://developer.vuforia.com/library/ (accessed on 18 July 2024).

[16] Devic, A., Vidakovic, J., Zivkovic, N.: Development of Standalone Extended-Reality-Supported Interactive Industrial Robot Programming System, Machines, Vol. 12, No. 7, 480, 2024.

[17] Articulations - NVIDIA PhysX SDK 3.3.4 Documentation, Available online: https://docs.nvidia.com/gameworks/content/gameworkslibrary/physx/guide/3.3.4/Manual/Articulations.html?highlight=articulation (accessed on 18 July 2024).

[18] ROS, ROS: Home (v.humble). Available online: https://www.ros.org/ (accessed on 20 July 2024).

[19] RoboDK, Simulator for Industrial Robots and Offline Programming-RoboDK (v4.0.0.), Available online: https://robodk.com/ (accessed on 29 June 2024).

ACKNOWLEDGMENTS

This research was funded by the Serbian Ministry of Science, Technological Development and Innovations, grant number 451-03-66/2024-03/ 200066.

Authors:

MSc Andrija Devic, PhD Jelena Vidakovic, MSc Nikola Zivkovic, MSc Aleksandar Stepanovic, Lola Institute, Kneza Viseslava 70a, 11030 Belgrade, Serbia, Phone.: +381 11 357-29-96.

E-mail: andrija.devic@li.rs; jelena.vidakovic@li.rs; nikola.zivkovic@li.rs; aleksandar.stepanovic@li.rs

MMA 2024
FLEXIBLE TECHNOLOGIES

15th INTERNATIONAL SCIENTIFIC CONFERENCE
NOVI SAD, SERBIA, SEPTEMBER 24-26, 2024

Original research paper https://doi.org/10.24867/MMA-2024-02-004

Matin, I., Strbac, B., Ranisavljev, M., Hadzistevic, M., Vukelic, D.

RESEARCH OF THE DEVIATION BETWEEN NUMERICAL SIMULATION AND EXPERIMENTS IN PLASTIC INJECTION MOLDING

Abstract: *Various studies have already compared the results of numerical simulation with data measured during the experiments. Many injection molding technologies are used as integrated and collaborative components for Industry 4.0. However, a lot of existing injection molding machines are not ready for full automation yet. Before automatic manufacturing, how to retain good quality is one of the crucial factors in injection molding. In this research, the authors have proposed a CAD/CAE system to conduct the deviation difference between numerical simulation and experiment. Results showed that shrinkage change is almost the same for both numerical simulation and experiment study. The deviation difference between numerical simulation and experiment is reduced after injection molding parameters regulation.*

Key words: *injection molding, deviation, numerical simulation, CAD, CAE*

1. INTRODUCTION

Injection molding (IM) is a cyclic manufacturing process of plastic part manufacturing into a desired shape by forcing material under pressure into a mold cavity. The shaping is achieved by cooling (thermoplastics) or a chemical reaction (thermosets). It is one of the most common and versatile operations for mass manufacturing parts with good dimensional tolerance. By weight, approximately 32% of all plastics processed go through IM machines [1, 2]. Historically, the invention of various new alternative CAE processes, such as application of numerical simulation to the design and manufacture of plastics parts, are the major milestones of IM.

Recently, many automation technologies and equipment are expected to be installed and applied for new manufacturing systems in various sectors to applied automation for Industry 4.0. Injection molding is one of the popular ways to achieve automatic production. However, high numbers of the existed injection molding machines are not ready for full automation yet. Indeed, before automatic manufacturing, how to retain good quality is one of the main factors in injection molding. To ensure product quality and mass production of more than 10000 products, various parameters (factors) must be considered in the part design and IM process due to their complexity.

However, there are many parameters that lead to defective products, such as warpage, shrinkage, sink marks, air traps, etc. For instance, the warpage defect will cause more problems on the size accuracy. To improve the quality of parts, there are a few strategies that have been proposed from researchers. Matin et al. [2] discussed about how the gate geometry and holding parameters (holding time, filling time, holding pressure) influence the dimensional accuracy of the part. In addition, they also mentioned that the simple elastic deformation of the cavity would influence the prediction of quality. Lee et al. [3] used the idea of varying part wall thickness within dimensional tolerances to minimize the warpage and optimized the wall thickness for given IM process conditions. Zhai et al. [4] modified runner sizes to achieve flow balanced multi-cavity mold. Othman et al. [5] investigated the effect of mold design on material consumption, warpage, and shrinkage of injected plastic part. Besides optimization of part and mold design, materials selection is also related to part quality. Kovacs et al. [6] examined the warpage and shrinkage properties of injection molded part, and concluded that the flow directional shrinkages can be affected by diameter. Knoll et al. [7] have studied potential causes like the material data, IM parameters, and the machine-specific behaviors were analyzed to assess which of these causes may be decisive for a deviation between simulation and experiment. Jahan et al. [8] proposed a modeling procedure for designing optimized layouts of conformal cooling systems in injection molding. They applied the design of experiments methodology to analyze the influence of the main design dimensions, as well as the cross-section topologies.

CAE has been widely applied to various injection molding prediction, such as in general IM optimization, conformal cooling processing, fiber orientation prediction, air trap forming mechanism prediction [9-13], and so on. Furthermore, to control the quality many researchers have extensively studied on optimization on IM processing and development Melt temperature, mold temperature, injection pressure, injection time, holding pressure, holding time, and cooling time are all selected as critical IM process parameters. As a matter of fact, using CAE systems in IM design and development becomes one of the common procedures. However, the deviation between CAE simulation and experiments, and its internal mechanism are not fully understood yet.

In this study, the authors focused on the critical IM parameters which cause the difference between CAE simulation and real experiment by measuring the deviation. Specifically, we proposed a method to conduct the deviation difference between numerical simulation and experiment.

2. NUMERICAL SIMULATION THEORY OF THE IM PROCESS

It is well known that there are three 2-Domain Tait p-V-T models used in advanced simulation software.

The polymer melt can be assumed as General Newtonian Fluid. During the injection molding process, the non-isothermal 3D flow motion can be mathematically described by the following equations [2, 11]:

$$\frac{\partial \rho}{\partial t} + \nabla \cdot \rho u = 0 \quad (1)$$

$$\frac{\partial}{\partial t}(\rho u) + \nabla(\rho uu - \sigma) = \rho g \quad (2)$$

$$\sigma = -pI + \eta(\nabla u + \nabla u^T) \quad (3)$$

$$\rho C_p \left(\frac{\partial T}{\partial t} + u\nabla T\right) = \nabla \cdot (k\nabla T) + \eta\,\dot{\gamma} \quad (4)$$

where u is the velocity vector, T is the temperature, t is the time, p is the pressure, σ is the total stress tensor, ρ is the density, η is the viscosity, k is the thermal conductivity, C_p is the specific heat and $\dot{\gamma}$ is the generalized shear rate.

The modified p-V-T model describe the viscosity of polymer melt according to following equations [2, 7, 11]:

$$\eta(T, \dot{\gamma}) = \frac{\eta_0(T)}{1 + [\eta_0 \dot{\gamma}/\tau^*]^{1-n}} \quad (5)$$

with

$$\eta_0(T) = B\mathrm{Exp}\left(\frac{T_b}{T}\right) \quad (6)$$

where η is the viscosity, η_0 is the zero shear viscosity, n is the power law index, B is called the consistency index, and τ* is the parameter that describes the transition region between zero shear rate and the power law region of the viscosity curve.

A volume fraction function, *f*, is introduced to track the advance of the melt front. Here, $f = 0$ is defined as the air phase and, $f = 1$ as the polymer melt phase. Hence, the melt front is located within cells with $0 < f < 1$. The advancement of *f* over time can be expressed as the following equation (7):

$$\frac{df}{dt} = \nabla(uf) = 0 \quad (7)$$

The Modified Cross Williams-Landel-Ferry (W-L-F) viscosity model is used for injection molding numerical simulation of selected pure amorphous material is shown in equations (5, 6, 7).

Linear shrinkage is driven by volumetric shrinkage, but there is not a one-to-one relationship. If the plastic were free to shrink in all directions isotopically, the linear shrinkage Sl would be approximately one third of the volumetric shrinkage Sv. In fact, the exact relationship is defined by the following equation (8):

$$S_l = 1 - (1 - S_v)1/3 \quad (8)$$

Volumetric shrinkage for a given pressure, temperature and level of crystallinity will always be the same. However, the way volumetric shrinkage is divided into the three linear shrinkage components (thickness, parallel to flow, and perpendicular to flow) will vary.

3. RESULTS AND DISCUSION

3.1 Simulation model design and IM parameters

The authors applied both numerical simulation and experimental studies. The numerical method was adopted for injection molding processes by Moldex 3D/Solid – Pack R12 software. The simulation model of the part and its dimensions are shown in Fig. 1.

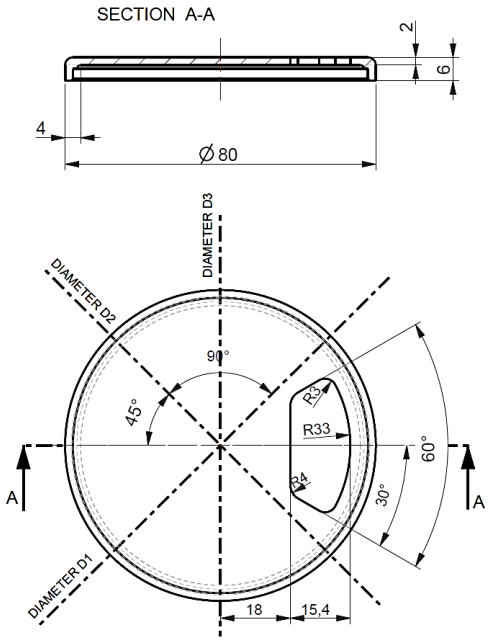


Fig.1. 2D drawing of the part

The authors defined three measuring diameters (D_1, D_2, D_3) needed for determining the deviation, as indicated in Fig. 1.

The authors can improve the dimensional stability of a product by considering:

- Material selection
- Cooling channel layout.
- Gate position and runner dimensions
- Injection molding parameters

The selected plastic material used is ABS 720 by Kumho manufacturer according to MoldFlow data-base. This material has an amorphous structure. The material properties which include temperature, dependent viscosity, and the specific volume against pressure-temperature (p-V-T) are presented in Fig. 2.

The P-V-T data for selected polymer usually is displayed as a projection onto the plane formed by the specific volume and temperature axes. This diagram shows that normal injection molding pressures will only reduce volumetric shrinkage by around half. To see this, consider the points A, B, and C on Fig. 2. Point A indicates the specific volume at room temperature and pressure, point B indicates the specific volume at a typical molding temperature, and point C indicates the specific volume at a typical molding and holding pressure. The line going through point D is an extrapolated pressure line showing the pressure required to give zero shrinkage from the melt to the solid phase as shown in Fig. 2.

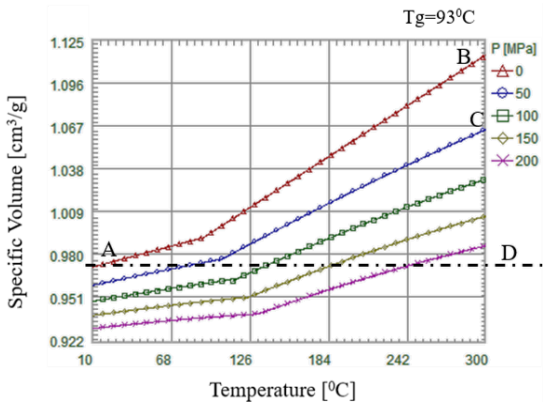


Fig. 2. P-V-T diagram for ABS 720

Such pressure would be well more than that available on an IM machine and clearly shows the impracticality of trying to eliminate shrinkage by the simple application of pressure alone. From the previous literature, the most important factors i.e. IM critical parameters on a certain model and system are not always the same. Hence, we have performed the single factor effect testing theoretically by considering six major parameters, such as injection time, melt temperature, mold temperature, holding time, holding pressure, and cooling time, as shown in Table 1. The critical IM parameters are the same for both numerical simulation and experiments, and they are shown in Table 1.

The parameters		Values
Critical IM parameters	Normal melt temperature (°C)	230
	Maximum melt temperature (°C)	260
	Mold temperature (°C)	40
	Holding time (s)	8
	Holding pressure (MPa)	238
	Ejection temperature (°C)	95
	Cooling time (s)	24.5
	Maximal injection pressure (MPa)	200
	Injection time (s)	0.9
Temperature of coolant liquid (°C)		20
Cooling channel diameter (mm)		9
Transition temperature (°C)		112
MeltFlow index MFI = (200, 5) (g/min)		1.5/10
Poisson Ratio		0.392
Drying Temperature (°C)		85
Flexural Modulus (MPa)		2.45
Tensile strength (MPa)		47
Clamping Force (kg)		200
Volumetric shrinkage on diameter D1		0.262%
Volumetric shrinkage on diameter D2		0.262%
Volumetric shrinkage on diameter D3		0.262%
Maximum shear stress (MPa)		0.295
Sink marks (mm)		0.012

Table 1. The IM process parameters

It is well known that shrinkage and consequently warpage is affected by processing conditions and clamping force. The clamping force is an important parameter for selecting and/or checking a clamping unit. The value is the required clamping force during the molding process instead of the force that injection molding machine outputs. The goal of this diagram is to identify the flash problem. If the calculated clamping force is larger than 70% of the machine maximum clamping force, there is a chance of plastic melt being squeezed outside the cavity and causing flash. Diagram of the clamping force plot versus the filling time is presented in Fig. 3. The clamping force reaches its highest value of 7787 N (804 kg) at the end of filling process and IM machine can easily provide it.

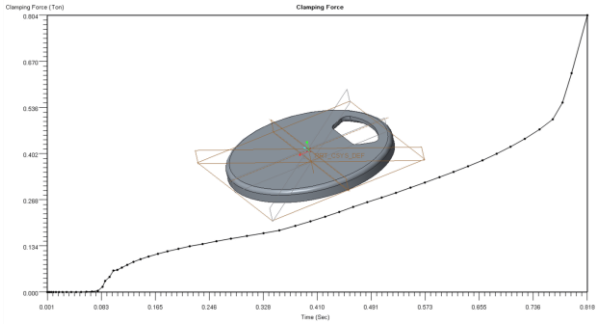


Fig. 3. Clamping force distribution

The magnitude of pressure and the time for which pressure is applied greatly affects the shrinkage of material in the cavity. The actual pressure to which the material is subjected is determined not only by machine settings, but also by the viscosity of the material and the geometry of the cavity. Areas near the gate are easier to pressurize (and depressurize) than areas at the end of flow and generally the relationship between pressure, time and shrinkage is simple. High holding pressure gives lower shrinkages as long as the pressure is kept on until the gate has frozen. In this case the shrinkage around the gate will generally be lower than that at the end of flow. If the holding pressure is not held on until the gate or runner system has frozen, then the pressure in the cavity will cause plastic to reverse flow back into the runner subsystem. This can result in a higher deviation around the gate area than in the rest of the mold cavity.

3.2 Define the deviation from the design target

To evaluate the quality factor of the injected parts, we have examined the shrinkage behavior all over the injection part. Specifically, the circumference of the injected part has been divided into six equal portions using three diameters (D_1, D_2, D_3) as shown in Fig. 1. Those three diameters have been measured individually, then add them up, and make the average, as defined by Equation (9).

$$D_{avg} = (D_1 + D_2 + D_3)/3 \quad (9)$$

The diameters of the injection product are measured one by one for both numerical prediction and real experimental testing. The average diameter of the product in simulation prediction is 79.99 mm, and the experimental result is 79.99 mm, as indicated in Table 2.

Method	Diameter measured at various position (mm)			Average (mm)
	D_1	D_2	D_3	Davg
Simulation Dsim	79.99	79.99	79.99	79.99
Experiment Dexp	79.98	79.99	79.99	79.99

Table 2. The diameters of injected molded product

Moreover, the deviation from the target value (80 mm) is defined as the difference between the injected diameter and the design diameter as in Equation (10).

$$\text{Deviation (mm)} = D_{design} - D_{avg} \quad (10)$$

Clearly the deviation difference between simulation prediction and real experiment is about 0.01 mm as indicated in Table 3. In the rest of this paper, the "deviation" quality factor will be applied as the standard for evaluating the difference between the simulation and experiment. The dimensional precision of the diameter of the injection part will be used as the criteria to evaluate of quality for this study.

	Diameter (mm)	Deviation (mm)
Original design	80	----
Simulation result	79.99	0.01
Experimental result	79.99	0.01

Table 3. Deviation of the injected part

4. CONCLUSION

In this study, the authors have proposed a procedure to determine the deviation difference between numerical simulation and experiment. We obtained that shrinkage is almost the same for both numerical simulation and experiment. From the observation, there is no significant difference between numerical simulation and experiment. The negligible gap to introduce the deviation difference is due to the response lag of the injection speed in the real experiment. After correcting the critical IM parameters the deviation difference between numerical simulation and experiment was reduced. These studies demonstrate that the similarity between simulation and experiment depends on the operating point (IM parameters) and the production scenario. Finally, there is still some difference which exists, and future research will be carried out. The authors measured only three diameters on the part, and that is the smallest satisfactory number for correct circle measurement.

In future research, the number of measurements and accuracy of measurements will be increased using CMM.

5. REFERENCES

[1] Matin, I., Štrbac, B., Ranisavljev, M., Hadžistević, M., Lanc, Z.: Numerical and experimental research of shrinkage and sink marks on injection molded plastic parts, Proceedings of the 39th International conference on production engineering of Serbia - ICPES 2023, pp. 134-139, Novi Sad, Serbia, 2023.

[2] Matin, I., Štrbac, B., Ranisavljev, M., Hadžistević, M., Lanc, Z.: Numerical simulation and verification of sink marks on the manufactured plastic parts, International Conference Industrial Engineering and Environmental Protection - IIZS 11, pp. 174-179, Zrenjanin, Serbia, 2021.

[3] Lee, B.H., Kim, B.H.: Optimization of part wall thicknesses to reduce warpage of injection-molded parts based on the modified complex method, Polymer Plastics Technology and Engineering, Vol. 34, No. 5, pp. 793-811, 1995.

[4] Zhai, M., Lam, Y.C., Au, C.K.: Runner sizing in multiple cavity injection mould by non-dominated sorting genetic algorithm, Engineering with Computers, Vol. 25, No. 3, pp. 237-245, 2009.

[5] Othman, M.H., Hassan, S., Ibrahim, M.Z., Li, L.: The Effects of Mould Design on Shrinkage and Warpage of Polypropylene Integral Hinges, 3rd International Conference on Trends in Mechanical and Industrial Engineering, pp. 270-273, Kuala Lumpur, Malaysia, 2013.

[6] Kovacs, J.G., Solymossy, B.: Effect of glass bead content and diameter on shrinkage and warpage of injection-molded PA 6, Polymer Engineering and Science, Vol. 49, No. 11, pp. 2218-2224, 2009.

[7] Knoll, J., Heim, H.P.: *Analysis of the similarity between injection Molding simulation and experiment*, Polymers, Vol. 16, No. 9, pp. 112-148, 2024.

[8] Jahan, S.; El-Mounayri, H.: A thermomechanical analysis of conformal cooling channels in 3D printed plastic injection molds, Applied Sciences, Vol. 8, pp. 2567-2585, 2018.

[9] Huang, C.T., Hsu, Y.H., Chen, B.S.: Investigation on the internal mechanism of the deviation between numerical simulation and experiments in injection molding product development, Polymer Testing, Vol. 75, pp. 327-336, 2019.

[10] Bela, Z., Szabo, F., Hatos, I., Suplicz, A., Kovacs, N.K., Hargitai, H., Tabi, T., Kovacs, J.G.: Enhanced Injection Molding Simulation of Advanced Injection Molds, Polymers, Vol. 9, pp. 77-88, 2017.

[11] Mao, H., Wang, Y., Yang, D.: Study of injection molding process simulation and mold design of automotive back door panel, Journal of Mechanical Science and Technology, Vol. 36, No. 5, pp. 2331-2344, 2022.

[12] Mehdi, M., Kazem, A., Marian, R.: Gate design and filling process analysis of the cavity in injection molding process, Advances in Manufacturing, Vol. 4, pp. 123-133, 2016.

[13] Mercado-Colmenero, J.M., Rubio-Paramio, M.A., Karlinger, P., Martin-Donate, C.: A new procedure for calculating cycle time in injection molding based on plastic part geometry recognition, The International Journal of Advanced Manufacturing Technology, Vol. 98, pp. 441-447, 2018.

Authors:

PhD Ivan Matin, PhD Branko Strbac, MSc Milos Ranisavljev, PhD Miodrag Hadzistević, PhD Djordje Vukelic, University of Novi Sad, Faculty of Technical Sciences, Department of Production Engineering, Trg Dositeja Obradovica 6, 21000 Novi Sad, Serbia, Phone: +381 21 485-23-32.

E-mail: matini@uns.ac.rs; strbacb@uns.ac.rs; ranisavljev@uns.ac.rs; miodrags@uns.ac.rs; vukelic@uns.ac.rs

MMA 2024
FLEXIBLE TECHNOLOGIES

15th INTERNATIONAL SCIENTIFIC CONFERENCE
NOVI SAD, SERBIA, SEPTEMBER 24-26, 2024

Original research paper https://doi.org/10.24867/MMA-2024-02-005

Anišić, Z., Peić Tukuljac, E.

DEVELOPMENT OF AN ELECTRONIC TOOL (ESAL – ELECTRONIC SHAFT ADJUSTER AND LOCKER) FOR DIRECT INJECTION PUMPS

Abstract: *In order to achieve the good properties of pumps with direct fuel injection (increasing the efficiency of the engine with reduced emission of harmful gases), a good synchronization of the operation of all parts is required. The adjustment and locking of the pump drive shaft must be coordinated with the feedback signals from the fuel injection sensor. The configuration of the pipe distribution of fuel from the pump to the injector, as well as the working pressures affect the dynamics of fuel dosing into the cylinders. ESAL - Electonic Shaft Adjuster and Locker. The electronic device for detecting the moment of fuel injection, along with the identification of the position of the drive shaft and the recommendation of the equipment manufacturer, enables good adjustment of the pump and maximum efficiency of the diesel engine. The operation of the device is designed to amplify the return signal from the pressure sensor on the injector and identify the current position of the drive shaft while defining the recommended manufacturing offset.*
Keywords: *high pressure pumps, electronic shaft adjuster and locker, engine efficiency*

1. INTRODUCTION

In a fuel injection system, the fuel injector pulse refers to the way in which the fuel injector delivers fuel into the combustion chamber of an engine. The system of direct injection of high-pressure diesel fuel implies the generation of high-pressure fuel in a short time interval.



Fig. 1. Signal from the injector

What are the important parameters that we want to monitor during the fuel injection process:

- Timing

The fuel injector pulse is timed to deliver fuel into the combustion chamber at the right moment in the engine's cycle. With electronic system, an electronic control unit (ECU) or engine control module (ECM) determines when to open and close the fuel injector based on various inputs such as engine speed, throttle position, engine load, and other sensor data. In a direct injection system, the position of the pump drive shaft must be adjusted so that the injection is performed following the position of the piston in the cylinder and the working pressure required for combustion. This is a simple but very effective combustion control system for diesel engines.

- Duration

The duration of the fuel injector pulse, also known as the pulse width, determines how long the fuel injector stays open to allow fuel to be sprayed into the combustion chamber. The quality of the pump, distribution system and injector determine the duration and structure of the injection pulse.

- Injection Pressure

The fuel injector pulse also controls the pressure at which fuel is injected into the combustion chamber. Modern fuel injection systems use high-pressure fuel injectors to atomize the fuel into a fine mist for better combustion efficiency.

Overall, the fuel injector pulse plays a crucial role in the fuel injection system by delivering the right amount of fuel at the right time to achieve efficient combustion and optimal engine performance. With ESAL we adjust the fuel injector pulses to ensure that the engine operates smoothly under various driving conditions.

2. HIGH PRESSURE PUMP DRIVE SHAFT POSITION MONITORING

With a direct fuel injection system, one of the most important things is to synchronize the operation of the high pressure pump with the other parts of the combustion sequence. Setting up the correct pump usually involves detecting the position of the pump drive shaft when the injection pulse is generated.

We monitor the position of the pump at every moment with a precise incremental encoder with a resolution of 3600 imp/rev. The encoder is coupled to the pump shaft drive mechanism via an elastic coupling. We use high-speed counters to detect pulses from a two-channel incremental encoder. Fine-tuning requires this resolution because a maximum deviation of 0.3 degrees is desired.

The dynamics of detecting signals from the encoder can also be used to determine the speed of rotation of the pump shaft. This information is very important because

the manufacturer declared that the pump adjustment is performed when the shaft rotates at a speed of 1150 rpm [3]. High-pressure pumps for diesel fuel injection are made as left-handed and right-handed pumps, that's why we use bidirectional encoders.

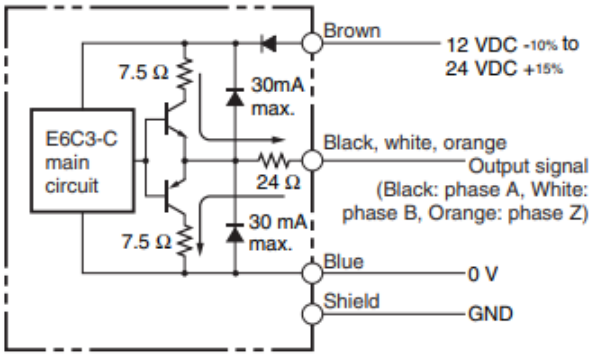


Fig. 2. Two channel incremental encoder [5]

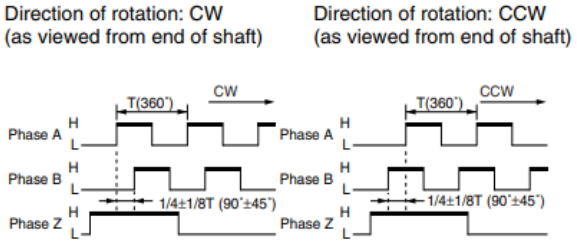


Fig. 3. Signals from the encoder – change the direction of rotation

An encoder was used that enables connection with high-speed counters on the PLC, so a variant with a 24VDC power supply was used.

3. INJECTOR WITH NEEDLE LIFT SENSOR AND MEASURING TRANSDUCER

Injector commonly refers to the nozzle holder and nozzle assembly [4]. The primary purposes of the diesel fuel injection system are graphically represented in Fig. 4.

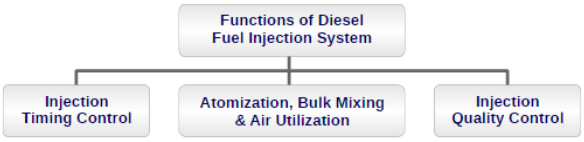


Fig. 4. Main functions of diesel fuel injection system

Our device is preliminary used for injection timing control. Start of injection (SOI) or injection timing is the time at which injection of fuel into the combustion chamber begins. It is usually expressed in crank angle degrees (CAD) relative to TDC of the compression stroke. In some cases, it is important to differentiate between the indicated SOI and actual SOI. SOI is often indicated by an easily measured parameter such as the time that an electronic trigger is sent to the injector or a signal from a needle lift sensor that indicates when the injector needle valve starts to open. The point in the cycle where this occurs is the indicated SOI. Due to the mechanical response of the injector, there can be a delay between the indicated SOI and the actual SOI when fuel exits the injector nozzle into the combustion chamber. The difference between the actual SOI and indicated SOI is the injector lag.

Start of delivery. In some fuel systems, fuel injection is coordinated with the generation of high pressure. In such systems, the start of delivery is the time when the high pressure pump starts to deliver fuel to the injector. The difference between start of delivery and SOI is affected by the length of time it takes for a pressure wave to travel between the pump and injector and is influenced by the length of line between the high pressure pump and the injector and by the speed of sound in the fuel. The difference between the start of delivery and SOI can be referred to as injection delay.

Each manufacturer defines injector log and injector delay for the entire range of their devices.

Between the injector, which contains the needle lift sensor, and the high-speed counter that receives the pulses, there is a measuring transducer. The signal (impulse) generated from the sensor has an amplitude of 1.2V and a duration of 150us, so in order to connect it to the monitoring system, it is necessary to amplify the received signal and detect the rising edge, that is, the beginning of fuel injection.

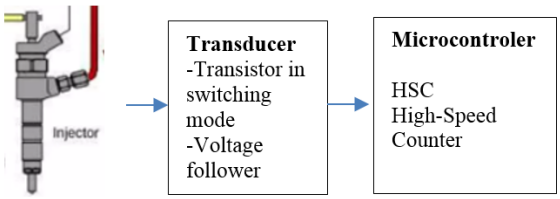


Fig. 5. Acceptance of the signal from the injector

4. MICROCONTROLLER MONITORING UNIT

The control unit has the function of receiving pulses from the incremental encoder in order to detect the position of the pump shaft, and at the same time receiving the signal from the sensor located on the injector. Due to the high resolution of the incremental encoder and the required high speed of the pump during testing, it is necessary to use high-speed counters. Realistically simple PLC devices have the possibility of fast signal processing, and they also have fast counters that can meet the necessary speed of receiving and processing signals.

As part of the project, we used WECON PLC, which has several inputs with high-speed counters with the possibility of additional configuration as a bidirectional counter, which is necessary for the final adjustment of the pump, but also when adjusting the left-hand and right-hand pumps.

The convenience of using the mentioned WECON LX3V PLC is not only reflected in the existence of a high-speed counter, but also in the power supply unit that can provide all the sensors and at the same time power the HMI. By reducing the number of necessary components, the price of the entire device is also reduced.



Fig. 6. WECON LX3V PLC with High Speed Counters (HSC) [1]

Available counter types; a) 1 phase with user start/reset: C235 to C240 b) 1 phase with assigned start/reset: C241 to C245 c) 2 phase bi-directional: C246 to C250 d) A/B phase type: C251 to C255.

Input	1 phase 1 directional										2 phase bi-directional					A/B phase				
	C235	C236	C237	C238	C239	C240	C241	C242	C243	C244	C245	C246	C247	C248	C249	C250	C251	C252	C253	C244	C255
X0	U/D						U/D			U/D		U	U		U		A	A		A	
X1		U/D					R			R		D	D		D		B	B		B	
X2			U/D					U/D			U/D		R		R			R		R	
X3				U/D				R			R			U		U			A		A
X4					U/D				U/D					D		D			B		B
X5						U/D			R					R		R			R		R
X6										S					S					S	
X7											S					S					S

U: up counter input D: down counter input R: reset counter (input) S: start counter (input) A: A phase counter input B: B phase counter input

Table 1. Structure of different counters and their connection

5. DATA VISUALIZATION AND ADJUSTMENT

In addition to processing the measurement signals, it is necessary to perform the necessary setup for the selected pump and data visualization for the final adjustment. WECON HMI 4.3 inch Levi 2043 was used to set the parameters and display the measured values. It is a monitor that allows displaying the values of all parameters in color, and is compatible with the PLC because they are from the same manufacturer.

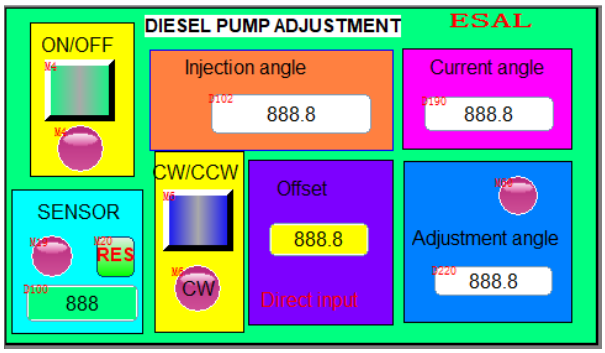


Fig. 7. HMI – Diesel pump adjustment screen [2]

The device is started by turning on the power and activating the button on the screen (ON/OFF). Before starting the device, it is necessary to connect the pump to the work table, which has the possibility of regulating the rotation speed and has a low pressure diesel fuel pump, as well as the necessary fuel distribution.

When the system is started and the pump starts to rotate, in the lower left corner of the screen, the detection of pulses coming from the sensor on the injector can be seen. Instead of counting pulses, the current speed of the pump can be displayed in the same field. In our test system, there is also a detection of the speed of rotation of the pump on the random table.

To perform a correct reading of the characteristic positions, it is necessary to check the recommended direction of rotation of the pump and select the correct direction (CW/CCW) with the switch. A new key press toggles between the two possible options. It is important to set the parameters correctly in order to obtain an adequate range of values required for setting the pump.

Parameters observed on the screen:

- Injection angle – The position of the pump shaft in relation to the reference one, at the moment of receiving the return signal from the injector sensor,
- Current angle – Reading the current position of the pump shaft
- Offset – It is necessary to rotate the shaft before locking, and based on the manufacturer's recommendation of the selected pump (173.50 - for the selected Delphi DP210 pump)
- Adjustment angle – The position that the pump shaft should take before locking. When the required position is reached, the desired lamp lights up.

6. CONCLUSION

The device shown and the adjustment procedure cannot be performed without a test table, which usually has a hydraulic motor and an automatic system for adjusting the desired pump speed. Since high-pressure diesel pumps are lubricated by the flow of fuel through them, it is necessary to connect them with a low-pressure pump and a manifold that enables proper fuel distribution.

In the created device, the WECON PLC was used as a microcontroller circuit, which proved to be a very reliable component, but the same device can be realized using other microcontroller components, only then it is necessary to adjust the signal level to the monitoring device. If a PLC is used, then the basic input signal level is 24VDC, and if development boards with microcontrollers are used, then a 5VDC power supply is sufficient.

The use of professional assemblies: encoders, converters, PLCs, HMIs speeds up the production of devices, and reduces the risks of mismatching components and signals. The resolution of the signals obtained from the available components enables receiving the signal at the necessary speed as well as adjusting the position of the locking pump with a precision of 0.3°.

When reading the characteristic position, more data was used and statistical processing (averaging the values) was performed before displaying the adjustment values. The corrective value is entered via a special keyboard, based on the manufacturer's recommendation. The pump we adjusted with the created device is DELPHI DP210.



Fig. 8. DELPHI pump on which adjustment was made

The development of the system for the accumulation of electricity and electric drives, as well as the system for the use of hydrogen, raises the question of the future of diesel machines. A recent feat achieved by Chinese engineers by achieving a thermal efficiency of 53% puts diesel engines on a whole new plane. It is evident that diesel-powered vehicles will continue to be used for some time to power large vehicles and ships.

7. REFERENCES

[1] WECON LX3V PLC Editor and Manual, www.we-con.com.cn, QQ Group, 2016.
[2] LeviStudio Programming Manual for WECON HMI 4.3inch, 2013.
[3] Delphi DP210 Workshop Manual – Delphi Diesel Systems LTD, 2008.
[4] Payri R., Salvador F.J., Gimeno J., Zapata D.L.: Diesel nozzle geometry influence on spray liquid-phase fuel penetration in evaporative conditions, Fuel, Vol. 87, No. 7, pp. 1165–1176, 2008.
[5] E6C3 Incremental Encoder - OMRON Corporation, www.ia.omron.com, 2023.

Authors:
PhD Zoran Anišić, University of Novi Sad, Faculty of Technical Sciences, Trg Dositeja Obradovica 6, 21000 Novi Sad, Serbia, Phone.: +381 21 485-24-76.
E-mail: zoran.anisic@uns.ac.rs
MSc Emil Peić Tukuljac, Subotica Tech – College of Applied Sciences, Marka Oreškovića 16, 24111 Subotica, Serbia, Phone: +381 24 655-201
E-mail: peic.emil@vts.su.ac.rs

MMA 2024
FLEXIBLE TECHNOLOGIES

15th INTERNATIONAL SCIENTIFIC CONFERENCE
NOVI SAD, SERBIA, SEPTEMBER 24-26, 2024

Original research paper https://doi.org/10.24867/MMA-2024-02-006

Devedzic, G., Kocovic, V., Djordjevic, A., Jovanovic Pesic, Z., Dzunic, D., Vukelic, D., Petrovic Savic, S.

RECONSTRUCTION AND OPTIMIZATION OF COMPLEX GEOMETRIC PARTS THROUGH REVERSE ENGINEERING

Abstract: *This paper presents a case study on the repair of oldtimer parts, with a particular focus on the damaged air duct that connects the heating and cooling system to the car's cabin. The replacement of such parts is challenging due to the cessation of production, making reverse engineering a feasible solution. Using the high-resolution and high-accuracy Artec SPIDER 3D scanner, the damaged part was digitized, followed by shape reconstruction and 3D CAD modeling processes. Furthermore, the model was modified to meet modern requirements and improve its functionality. The specification and modeling of freeform features were investigated, employing constraint-based parameterization methods and prototype-driven constraint solving. These approaches enable intuitive parameterization and precise reconstruction of complex geometric shapes. The results demonstrate that the application of modern reverse engineering technologies, along with necessary modifications, can effectively address the challenges of oldtimer restoration, ensuring the preservation of the original parts' functionality and aesthetics, thereby contributing to the maintenance of cultural heritage and the technical value of these cars.*
Key words: *Reverse Engineering, CAD, Geometric Shape, Freeform feature*

1. INTRODUCTION

Automotive companies secure their survival and expand into new markets through competitive products that offer greater functionality and higher quality, achieved by implementing high levels of innovation. The backbone of the modern automotive industry is Industry 4.0, which leverages advanced digital technologies to meet contemporary demands, such as those related to mobile services [1,2].

Digital technologies are essential for reducing the need for large inventories, cutting costs associated with unsold products, and facilitating the repair and reprocessing of defective, worn-out, or damaged components [3]. These technologies enable rapid design iteration and prototyping, the production of functional end-use parts, customized components and tools, as well as the decentralized manufacturing of spare parts. In particular, digital technologies and reverse engineering are vital for the restoration and maintenance of vintage automobiles [4]. They allow owners and restorers to accurately recreate rare or discontinued parts. Vintage cars, with their unique historical significance and aesthetic appeal, often require specific components that are hard to find on the market.

Reverse engineering allows for the precise capture of surface data from existing components using scanning or measuring devices, followed by the creation of digital models and their integration into manufacturing processes. This process involves using advanced scanning and modeling technologies to reconstruct existing parts. It starts with scanning the physical object with a 3D scanner to obtain accurate digital data on the part's shape and dimensions. Then, CAD software is used to create a digital model, which can be utilized for manufacturing a new part using CNC machines or 3D printing [1,3].

The reconstruction of digital models in CAD systems uses parametric or surface methods. After reverse engineering, where physical objects are scanned and turned into digital models, the next step often involves freeform modeling. This technique offers greater flexibility and precision for designing complex geometries that are difficult to achieve with traditional methods. Freeform modeling is essential for creating parts with intricate shapes, particularly in the automotive sector for components that need high aesthetic and functional value, such as delicate artifacts and car bodies [5,6].

The aim of this paper is to apply a method for reconstructing deformed parts of vintage cars using advanced 3D scanning and modeling techniques. The focus of the paper is on the application of freeform modeling for the repair and correction of a damaged air duct. This method includes parametric modeling based on constraints and the resolution of prototype-driven constraints, enabling precise reconstruction and restoration of parts with complex geometries. By using 3D technologies, the goal is to achieve high precision and authenticity in reconstruction, allowing for long-lasting and reliable restoration of these classic cars.

2. MATERIALS AND METHODS

In this study, the reconstruction of a damaged air duct (Fig. 1) was performed. This duct connects the heating and cooling system hoses to the car's cabin. It is crucial for maintaining optimal conditions inside the vehicle cabin, and its proper functionality directly affects the comfort and safety of the driver and passengers.

The reconstruction algorithm is shown in Fig. 2. This algorithm includes three key segments in the reconstruction process: sample preparation, 3D

scanning, and point cloud processing (reconstruction, modeling).



Fig. 1. Position of the air duct within the system assembly [7]

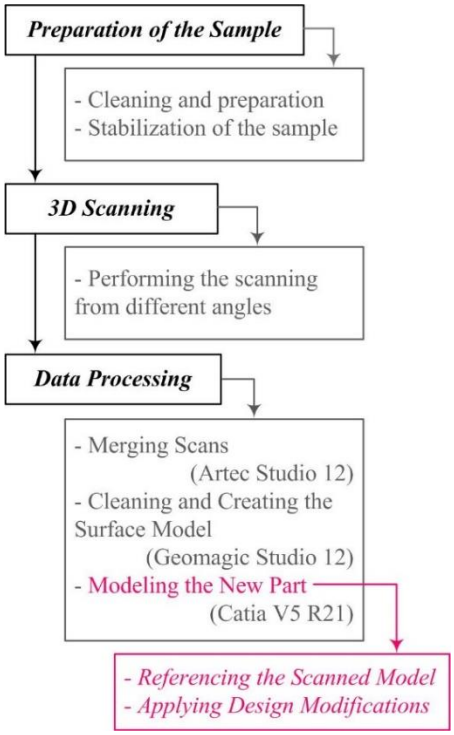


Fig. 2. Reconstruction algorithm for the air duct

2.1 Preparation of the Sample and 3D Scanning

Given that the subject of this study is a part that had already been in use, it was necessary to clean it of dirt and place it on a stable surface to eliminate possible movement during scanning. Mild detergent, soft cloths and sponges, as well as soft-bristle brushes for hard-to-reach areas, were used for surface cleaning. Compressed air was used to remove dust from cracks and openings.

The Artec SPIDER 3D scanner (https://www.artec3d.com/portable-3d-scanners/artec-spider) (Fig. 3) was used for product digitalization. This scanner can capture up to 1 million points per second with an accuracy of 0.05 mm and a resolution of 0.1 mm. These characteristics make it suitable for scanning objects with sharp edges, complex geometry, and fine details.

During the scanning process, the scanner was not fixed in place. In other words, the scanning was performed manually to capture all the complex surfaces that characterize this part.



Fig. 3. Artec SPIDER 3D scanner [8]

2.2 Data Processing

After the scanning was completed, the scans were merged and initially processed in Artec Studio software. This involved aligning the individual scans, removing any unnecessary data, and creating the initial 3D model. The alignment of the scans (Fig. 4) was achieved using point registration algorithms that minimize the differences between overlapping points. This process can be mathematically described as minimizing the error function E [9]:

$$E(R,t) = \sum_{i=1}^{N} \|Rp_i + t - q_i\|^2 \qquad (1)$$

where p_i, and q_i are corresponding points from two different scans, R is the rotation matrix, and t is the translation vector.

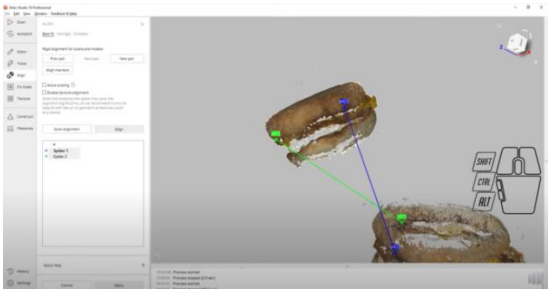


Fig. 4. Alignment of scans [10]

Further processing and reconstruction of the model were performed in Geomagic Studio 12 software. In this software, the polygonal model obtained from Artec Studio was further cleaned of irregularities and noise while maintaining its structural integrity and accuracy. The process includes [11] (Fig.5):

- Repairing polygons such as decimation (optimization that minimizes the number of polygons while preserving the geometric details of the model),
- Removing outliers and other artifacts (filtering and removing undesirable elements such as noise and irregularities), and
- Creating a smooth surface.

Once the model is prepared in this way, it is converted into a surface model in Geomagic software, which is crucial for further analysis and application in CAD software. Although the model was successfully reconstructed and imported into CATIA V5 R21, the need for re-modeling arose. Specifically, the air duct had lost its circularity in the cylindrical section (Fig. 6), and any attempt to correct the scanned model resulted in the distortion of the remaining geometry.

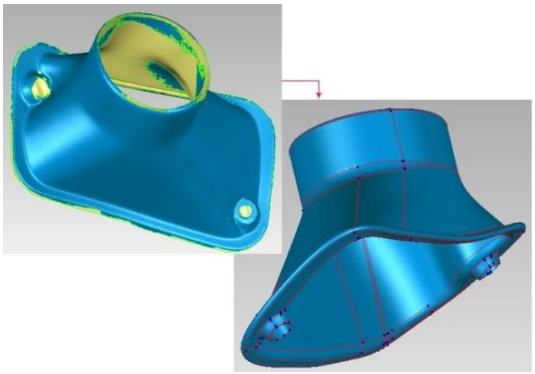


Fig. 5. Imported model from Artec Studio and adjusted model

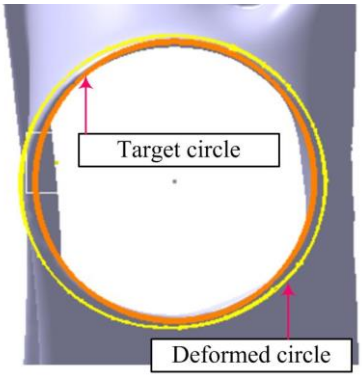


Fig. 6. Circularity deformation and desired circularity

To achieve full control over the model and its features, freeform modeling must be applied. This approach allows for the accurate creation of complex geometric shapes that are crucial for the product's functionality and integrity throughout its life cycle stages [5,6].

Freeform geometry is inherently complex and intricate. Therefore, it is essential that the shape of features can be interactively modeled during the specification of freeform classes. Furthermore, the method should allow for intuitive parametric definition of shapes and the inclusion of functional information within the class [5].

The specification of freeform shapes commenced with the creation of prototype shapes, referred to as freeform definition points (Fig. 7). These points, located in 3D space, are utilized to construct the model by connecting them with curves to establish the initial shape of the features. Mathematically, each point Pi on the model's surface is defined by its coordinates (x_i,y_i,z_i) in three-dimensional space. The points are strategically positioned on the imported model to delineate key geometric characteristics. Subsequently, these points serve as reference markers for the generation of more complex shapes [12]. Splines are then used to interpolate these points, ensuring the desired spatial configuration.

The main directions along which the geometry of the model develops define the axes that pass through the three holes on the model itself (Fig.8).

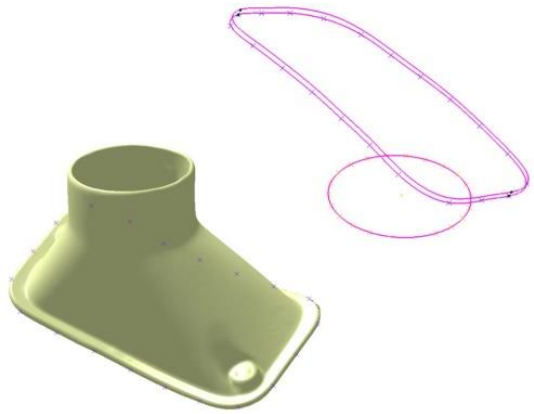


Fig. 7. Freeform definition points

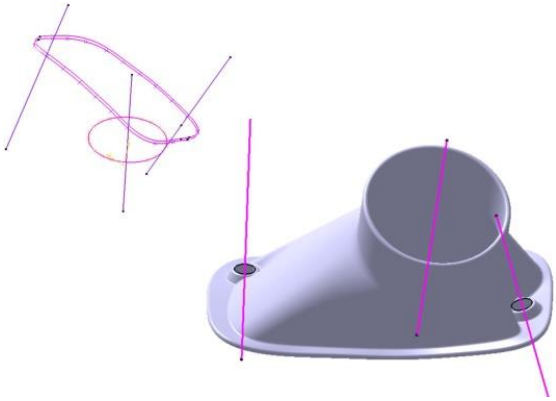


Fig. 8. Axis directions on the model

Following the definition of the basic geometry using splines and points, the next step involves the creation of surface shapes. These shapes impart either additive or subtractive characteristics to the model [5,6,12]. This process enables the formation of smooth and continuous surfaces, which are integrated into a unified model to ensure proper connectivity and continuity (Fig. 9).

All defined features are parametrically linked through geometric and dimensional constraints, with validation conditions precisely determining the relationships between model instances. The introduction of parameters and the establishment of validation conditions for the position and orientation of individual surfaces, as well as their directional extensions, facilitate the accurate positioning of the model within the assembly (Fig. 8 and 9) [5].

3. RESULTS

The application of this methodological approach results in efficient model management, facilitating not only the creation of technical drawings but also the preparation of the model for 3D printing and other essential manufacturing processes (Fig. 10). This approach ensures high precision and functionality of the model, enabling its successful integration into various stages of the production process.

This method optimizes all aspects of modeling, from initial design to final production, significantly enhancing the efficiency and quality of the final product.

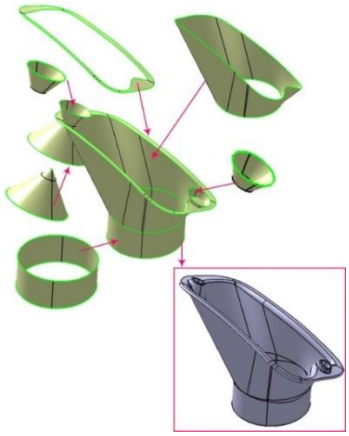


Fig. 9. Surface creation

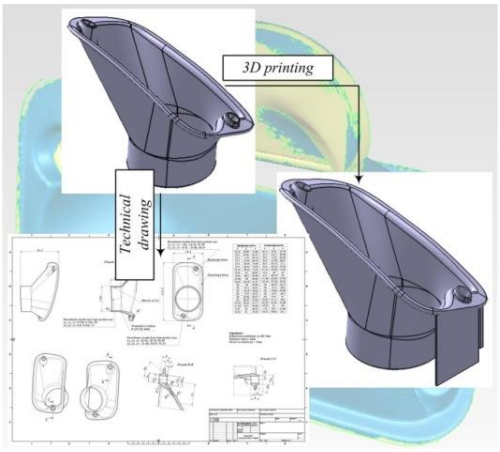


Fig. 10. Technical drawing and model for 3D printing

4. CONCLUSION

The results of this study demonstrate the successful integration of advanced 3D scanning, freeform modeling, and constraint-based parametric modeling techniques in reconstructing deformed vintage automobile parts. This modern reverse engineering approach preserves the functionality and aesthetics of original parts while enabling precise replacement and restoration. Consequently, the study aids in preserving the cultural and technical value of these historical vehicles, underscoring the importance of innovative restoration methods.

Future research should refine freeform modeling techniques to enhance reconstruction accuracy and efficiency. Additionally, integrating artificial intelligence and machine learning into reverse engineering could improve precision and automation. Expanding these methods to other vintage automobile components and fields requiring precise restoration also warrants exploration.

5. REFERENCES

[1] Dalpadulo, E., Petruccioli, A., Gherardini, F., Leali F.: *A review of automotive spare-part reconstruction based on additive manufacturing*, Journal of Manufacturing and Material Processing, Vol. 6, No. 6, pp. 133, 2022.

[2] Kyaw, A.C., Nagengast, N., Usma-Mansfield, C., Fuss, F.K.: *A combined reverse engineering and multi-criteria decision-making approach for remanufacturing a classic car part*, Procedia CIRP, Vol.119, pp. 222-228, 2023.

[3] Copani, G., Shafinejad, P., Hipke, T., Haase, R., Paizs, T.: *New metals remanufacturing business models in automotive industry*, Procedia CIRP, Vol. 112, pp. 436-441, 2022.

[4] Kanun, E., Oğuz, G.M., Zakar, M.: *3D modeling of car parts by photogrammetric methods: Example of brake discs*, Mersin Photogrammetry Journal, Vol. 4, pp. 7-13, 2022.

[5] Kunjin, H., Zongxing, Z., Weizhong, G., Zhengming, C., Zing, Z.: *Parametric representation and implementation of freeform surface feature based on layered parameters*, Journal of Computer-Aided Design & Computer Graphics, Vol. 26, pp. 826-834, 2014.

[6] Van den Berg, E., Bronsvoort, W.F.: *Validity maintenance for freeform feature modeling*, Journal of Computing and Information Science in Engineering, Vol. 10, pp. 011006, 2010.

[7] https://www.pegasusautoracing.com/productselection.asp?Product=3623, Accessed on: June 30th, 2024.

[8] https://www.aniwaa.com/product/3d-scanners/artec-spider/, Accessed on: June 30th, 2024.

[9] Zhang, Y., Gui, J., Cong, X., Gong, X., & Tao, W.: *A comprehensive survey and taxonomy on point cloud registration based on deep learning*. ArXiv. /abs/2404.13830, 2024.

[10] https://www.javelin-tech.com/blog/2022/05/3d-scanning-with-the-artec-space-spider-from-start-to-finish/, Accessed on: June 30th, 2024.

[11] Maiorova, K., Kapinus, O., Skyba, O.: *Study of the features of permanent and usual reverse-engineering methods of details of complex shapes*, Mechanical engineering technology, Vol.1, pp. 19-25, 2024.

[12] He, K., Chen, Z., Zhao, L.: *A new method for classification and parametric representation of freeform surface feature*, International Journal of Advanced Manufacturing Technology, Vol. 57, pp. 271-283, 2011.

Authors:

PhD Goran Devedzic, PhD Vladimir Kocovic, PhD Aleksandar Djordjevic, MSc Zivana Jovanovic Pesic, PhD Dragan Dzunic, PhD Suzana Petrovic Savic, University of Kragujevac, Faculty of Engineering, Sestre Janjic 6, 34000 Kragujevac, Serbia.
E-mail: devedzic@kg.ac.rs, vladimir.kocovic@kg.ac.rs, adjordjevic@kg.ac.rs, zixi90@gmail.com, dzuna@kg.ac.rs, petrovic.suzana@gmail.com

PhD Djordje Vukelic, University of Novi Sad, Faculty of Technical Sciences, Trg Dositeja Obradovica 6, 21000 Novi Sad, Serbia.
E-mail: vukelic@uns.ac.rs

MMA 2024
FLEXIBLE TECHNOLOGIES

15th INTERNATIONAL SCIENTIFIC CONFERENCE
NOVI SAD, SERBIA, SEPTEMBER 24-26, 2024

Original research paper https://doi.org/10.24867/MMA-2024-02-007

Živković, N., Pavlović, D., Ponjavić, M., Krošnjar, A., Stepanović, A.

DESIGN OF COOLING SYSTEM FOR TWO POWER TRANSISTOR MODULES

Abstract: *In high-power applications, where a significant amount of heat is generated, heat sinks are essential to prevent thermal runaway and potential damage to the electronic components by efficiently transferring the heat away. Heat sinks are typically made of materials with high thermal conductivity, such as aluminum, with proper fin structures to increase the surface area for better heat dissipation. Adding fans increases the airflow over the heat sink, improving the heat dissipation rate. Manufacturers of heat sinks often provide recommendations or even bundled fan options specifically designed for their heat sinks. However, there are many more practical applications than the manufacturer's design notes cover, so additional engineering is often required to adapt the cooling system to the actual needs. A cooling system was designed and modeled using CAD software for heat removal in a power converter. The cooling system comprises two heat sinks, an axial fan, and a duct. The two transistor modules are mounted on each heat sink as a source of power dissipation. A prototype is manufactured according to the designed CAD model. The cooling system performance was first estimated through numerical simulation. An infrared camera was used to compare the simulation results with the results of the experimental measurements. The experimental results showed reasonable compliance with the simulation model.*

Key words: *Thermal management, Electronics cooling, CAD modeling, Air-cooling, Power converter.*

1. INTRODUCTION

Semiconductor reliability and longevity are strongly influenced by operating temperatures; higher temperatures result in shorter lifespans. Therefore, effective thermal management plays a crucial role in enhancing the durability and reliability of electronic devices. This is particularly critical in high-power electronic converters, which generate substantial heat. Thermal management typically involves transferring this heat to the surrounding environment using various techniques, with the application of well-designed heat sinks being the most common approach.

Heat sinks, typically made of materials with high thermal conductivity like aluminum, are commonly used to draw heat away from high-power converters and dissipate it to the environment. Various heat sink configurations are available on the market. Still, it's important to note that these solutions may not always perfectly match the real needs, underscoring the task's complexity and challenge. Therefore, additional engineering is often necessary to adapt the heat sink to the specific requirements of the high-power converter.

Heat sinks absorb heat from high-power devices through conduction and release it into the surrounding environment through natural convection. However, relying solely on heat sinks often proves insufficient for adequately cooling high-power electronic devices. Forced convection is employed, utilizing air movers to accelerate heat transfer from the heat sinks to the environment.

Electronic circuits' growing complexity and power density have underscored the importance of simulation testing in prototyping. Initially, the electronic cooling system is meticulously designed and modeled using CAD software. Subsequently, the system's performance is simulated within a multi-physics software environment under predefined conditions. If the simulation generates viable and promising outcomes, the practical construction of the device commences. A prototype is then fabricated based on the model, enabling further real-world testing and evaluation.

This paper presents the design, simulation, and experimental testing of a cooling system for two power transistor modules. The SOLIDWORKS 2023 CAD (Computer-aided Design) software [1] was used to model the cooling system and the SOLIDWORKS Flow Simulation package for CFD (Computational Fluid Dynamics) and thermal simulation. The simulation enables the determination of pressure drops, the influence of fluid pressure, flow rate, heat exchange, heating and cooling, forces due to fluid action, and many other parameters. Application of the SOLIDWORKS Flow Simulation module and simulation is beneficial for evaluating proposed design concepts, thoroughly developing products, solving emerging problems, and quickly realizing devices.

The paper is divided into following sections: Section 2 - the design of the cooling system is presented; Section 3 - simulation results are presented and discussed; Section 4 - experimental testing results are discussed and compared with the simulation results. In the conclusion, the key takeaways of the cooling system design were given.

2. COOLING SYSTEM DESIGN

Power transistors are crucial components employed in various applications, including power processing, DC and AC motor control, and uninterruptible power supplies. These devices generate substantial heat during operation, and if not effectively managed, elevated temperatures can result in device failure. The primary function of the cooling system is to efficiently dissipate

the generated heat, maintaining the temperature of the power transistors within safe operational limits.

2.1 Initial analysis

The cooling system design for two power transistor modules intended for an uninterruptible power supply is presented in this section. The power devices used in this study are FUJI 1DI200ZA-100, triple Darlington configuration transistors in the form of power transistor modules [2]. The most important parameter when conducting thermal analysis of any semiconductor device is the core junction temperature. Therefore, the core junction temperature is the indicator of a device's cooling system performance.

The project requirements for the operating current and voltage of the single power transistor module are I_C = 37.5A and V_{CE} = 10V, respectively. Maintaining core junction temperature under a certain value while subjected to desired current I_C and voltage V_{CE} means that the cooling system should be capable of dissipating the total of P_{DT} = 750W of heat (P_{DT} = 2×375W). The core junction temperatures of the modules are to be kept under 130°C, allowing the safety margin of ~20°C. The rest of the system design requirements that are to be obeyed:

- The designed system is to be exclusively air-cooled;
- Dimensions of the system not to exceed 900x200x150mm and mass of 6kg;
- Axial DC fans 24V are to be used.

Based on the dissipated power of a single transistor module P_D = 375W, maximal junction temperature T_{jmax} = 130°C, ambient temperature T_a = 30°C and internal thermal resistance of the power transistor module R_{jc} = 0.089°C/W [2], the desired maximal thermal resistance of the single heat sink can be estimated [3]:

$$R_{hs} = \left(T_{jmax} - T_a\right)/P_D - R_{jc} = 0.178\,\square/\mathrm{W} \qquad (1)$$

Considering previously stated dimension restrictions and estimated thermal resistance from Equation (1), two MULTICOMP PRO MP008476 [4] heat sinks are chosen, each for one of the two power transistor modules. The MP008476 heat sinks have thermal resistance R_{hs} = 0.09°C/W at the 5m/s of forced air-cooling. The fans chosen based on the forced air speed requirement (5m/s) and dimensions restriction are SUNON MEC0382V1-000U-A99 [5].

The initial system design analysis based on the requirements gave a rough idea of the possible cooling system performance. To gain more information, the cooling system performance has to be tested, first through simulation, followed by prototype construction and empirical testing if simulation testing gives feasible results. Also, the additional copper rail components, installed between power modules to ensure the proper functioning of the system, are adding to the complexity of the thermal analysis, and simple analysis done so far isn't sufficient to draw any definitive conclusions.

2.2 CAD modeling

Simulation testing of the fairly complex model presented so far requires an appropriate CAD model. In Table 1, the characteristics of the materials used in the construction of the cooling system CAD model are given, and they are also used in the simulation.

Material	Density (kg/m^3)	Thermal Conductivity (W/m-K)
Silicon	2330	124
PLCC	900	0.2
Al Alloy 6061	2700	200
Copper	8900	390

Table 1. Properties of the materials used for cooling system simulation. The aluminum used in the prototype is not anodized (eloxated)

As shown in Fig. 1 and 2, the prototype contains two heat sinks positioned facing each other top planes, two axial fans, an air duct to funnel the air from fans to heat sinks fins, and one fan that reduces the temperature of the copper rails connecting two power devices and heat sink surfaces.

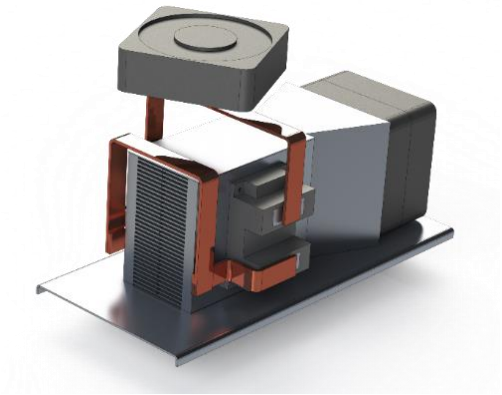


Fig. 1. Assembly model of the designed cooling system

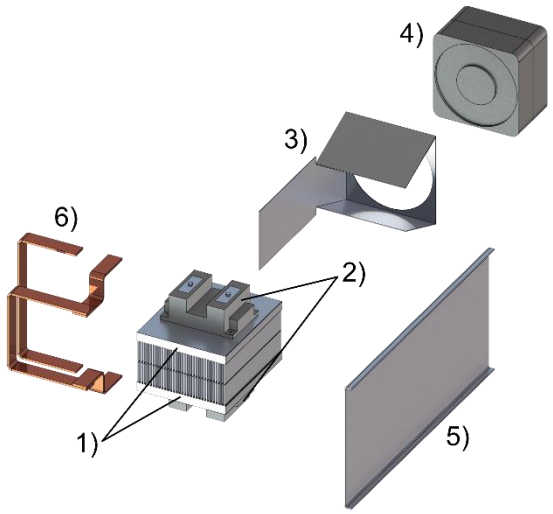


Fig. 2. Exploded view of the designed cooling system model: 1) heat sinks; 2) power modules; 3) air duct; 4) double fan configuration; 5) mounting plate; 6) copper rails.

3. SIMULATION RESULTS

Before committing to prototype manufacturing, the designed system was tested through simulation. The discretization of the reference equations was performed using a finite volume method and solved using an academic edition of the SOLIDWORKS Flow Simulation 2023. The ambient temperature condition is set to a room reference temperature of 27 °C. The amount of heat that one power transistor module releases while working is P_D = 530W (I_C= 53A, V_{CE} = 10V. The computational mesh consists of 970,911 cells (fluid cells = 494,591; solid cells = 476,320). The coupled system of equations is solved iteratively. The dissipated power rating used in simulation and experimental tests is increased significantly, which pushes power modules into overload. This is done for the sake of experimentation, and it is not intended to be a working regime.

In Fig. 3, it is possible to observe the performed analysis and thermal simulation with two transistor modules and how the heat is distributed across the entire cooling system. The highest temperature of 85°C occurs in the vicinity of a heat sink and power transistor module contact, which can be assumed as a transistor case temperature (see also Table 2). The estimated junction temperature is, therefore, T_j = 85°C+530W×0.089°C/W = 132.7°C for each power transistor module, according to Equation (1).

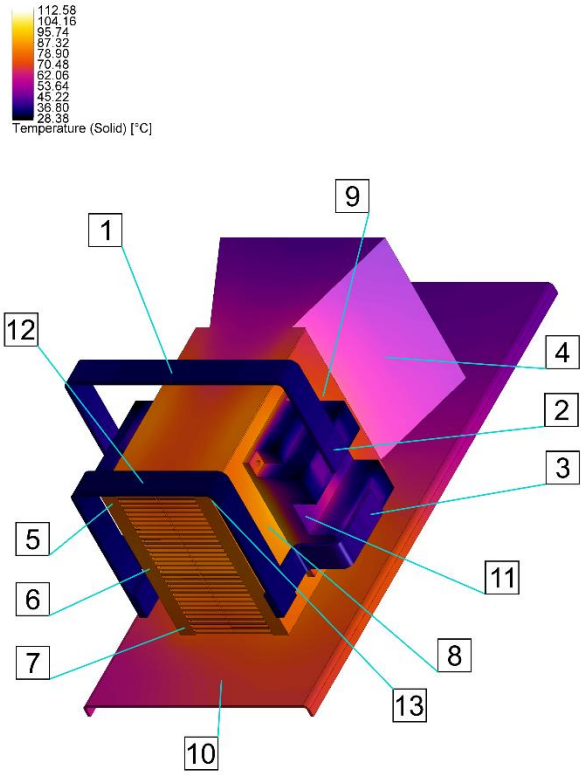


Fig. 3. Surface temperature of the cooling system components with numbered points of interest (see Table 2)

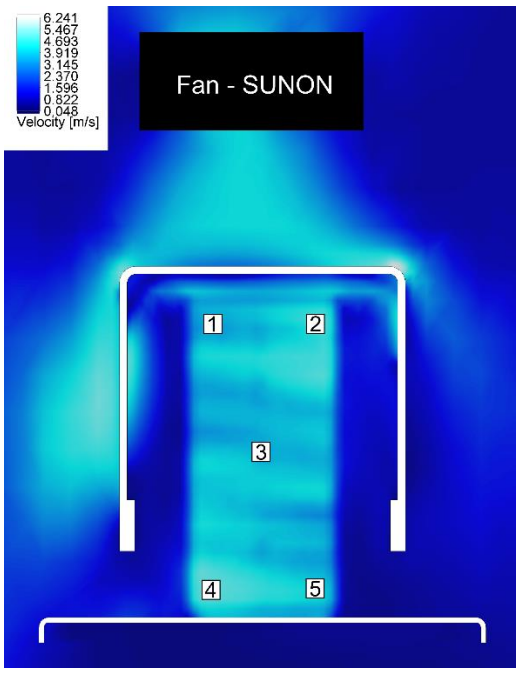


Fig. 4. Simulation result of velocity distribution at the cooling system outlet plane with numbered points of interest (see Table 3). Black rectangle at the top represents fan

4. EXPERIMENTAL TESTING

After the prototype was designed and simulated in the software, parts were purchased, and the heat sink was assembled according to the conceptual solution. The experimental setup of the cooling system prototype is shown in Fig. 5. The temperature distribution on the outer surfaces of the heat sinks and transistors was measured with a FLUKE DC300A camera (Fig. 6 and 7), and a K-type thermo-probe. The temperature distribution obtained from the simulation is in agreement with the experimental results (Table 2). There is a certain difference between simulation and experimental temperatures, which could be due to various reasons (neglected radiation effects, simplified fan model, omitted certain electrical elements from the simulation, like shunt resistors). The airflow at the cooling system outlet is close to the experimental results.



Fig. 5. Experimental setup of the designed cooling system

	Temperature (Simulation) [°C]	Temperature (Experiment) [°C]
1	31.93	36.5
2	37.26	35.8
3	39.75	33.8
4	49.05	34.2
5	74.87	67.0
6	79.44	64.0
7	73.85	65.8
8	85.26	81.3
9	75.04	68.0
10	67.92	54.5
11	44.89	46
12	30.42	39.2
13	75.61	66

Table 2. Simulation and experiment results comparison for heat sink surface temperatures.

	Airflow (Simulation) [m/s]	Airflow (Experiment) [m/s]
1	4.4	5.3
2	4.8	5.5
3	3.6	3.3
4	5.1	6.2
5	4.3	5.0

Table 3. Simulation and experiment results comparison for heat sink airflow.

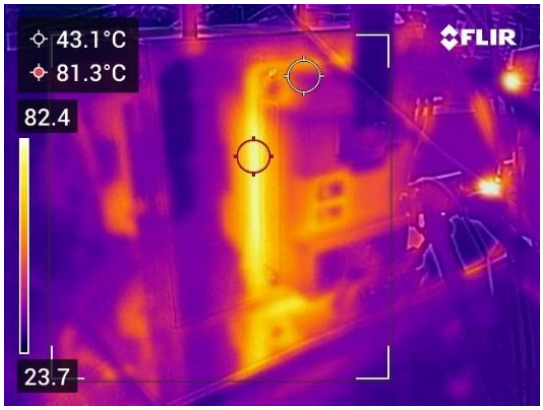


Fig. 6. Thermal imaging at the connection between a transistor power module and a heat sink. Temperature reading at the red crosshair is 81.3 ℃. This point roughly corresponds to the point 8 in Fig. 3



Fig. 7. Shunt resistors dissipate large amount of heat, hence the elevated temperature (134 ℃) is visible on the thermal image

5. CONCLUSION

An initial analysis of the power electronics cooling system's performance can be done based on specifications given by heat sinks and fan manufacturers. Considering the complexity and specific nature of each application, further testing is required. Contemporary CAD software facilitates the experimental testing of complex electromechanical systems in the virtual environment with results very close to the empirical testing. Computational fluid dynamics (CFD) and Computer-aided design (CAD) are good tools for product cooling systems development with low cost and reasonable accuracy. In this paper, simulation and experimental verification of a concrete cooling system are presented. Both simulation and experimental results show the performance of the designed cooling system with power modules working at 140% of the nominal power load. Even when power devices are overloaded, the designed cooling system offers reasonable performance within design constraints.

6. REFERENCES

[1] https://www.solidworks.com
[2] FUJI ELECTRIC, “Power transistor module,” 1DI200ZA-100 datasheet.
[3] *Thermal Management: The Complete Guide*, CUI DEVICES. [E-book] Available: CUI DEVICES Resource Library.
[4] Multicomp PRO, “Heat sink” MP008476 datasheet, Nov. 2021.
[5] SUNON, “DC Brushless Fan & Blower”, MEC0382V1-000U-A99 datasheet, July 2016.

ACKNOWLEDGMENTS
The authors gratefully acknowledge the financial support of the Ministry of Science, Technological Development and Innovation of the Republic of Serbia (Grant No. 451-03-66/2024-03/ 200066).

Authors:
MSc Nikola Živković, **PhD Dragan Pavlović**, **MSc Aleksa Krošnjar**, **MSc Aleksandar Stepanović**
Research and Development Institute Lola L.T.D., 70A Kneza Viseslava Street, 11030 Belgrade, Serbia, Phone.: +381 (11) 25 46 423.
E-mail: nikola.zivkovic@li.rs; dragan.pavlovic@li.rs; aleksa.krosnjar@li.rs; aleksandar.stepanovic@li.rs
Full professor PhD Milan Ponjavić, School of Electrical Engineering, Bulevar Kralja Aleksandra, 73, 11000 Belgrade, Serbia, Phone.: +381 (11) 32 18 301.
E-mail: ponjavic@etf.bg.ac.rs

MMA 2024 FLEXIBLE TECHNOLOGIES

15th INTERNATIONAL SCIENTIFIC CONFERENCE
NOVI SAD, SERBIA, SEPTEMBER 24-26, 2024

Original research paper https://doi.org/10.24867/MMA-2024-02-008

Šulc, J., Reljić, V., Dakić, N., Jurošević, V.

INTEGRATION OF ONE PNEUMATIC SOLUTION WITH A CNC DEVICE FOR THE REALIZATION OF THE PERFORATION PROCESS

Abstract: *This paper describes one pneumatic solution integrated with classic 3 axis CNC milling device. This new device is intended for realization of perforation process and the axis that carries the tool has been replaced by a pneumatic solution. The tool holder is developed and connected with cylinder piston rod. From the aspect of pneumatic control, it is used solution with corresponding control software. With this solution position of the tool in Z axis is detected by mechanical sensor. Signal from mechanical sensor is used to activate pneumatic cylinder that punch material. In that way hole into workpiece is formed. The depth of the hole is defined with position of the mechanical sensor. Initially, the tool offset is defined by the length of the pneumatic cylinder stroke. For the experimental purpose different types of workpieces were carried out and results are shown.*
Key words: *pneumatic, cylinder, CNC, perforation, workpiece*

1. INTRODUCTION

The perforation process is an important operation in various manufacturing industries, by which holes of a specific size and depth are made in workpieces [1, 2]. Traditional CNC milling machines, although versatile, often face limitations in efficiently and accurately performing perforation tasks due to limitations in their mechanical design and control systems [3].

To address these challenges, this study investigates the possibilities for integration of a pneumatic solution with a classic 3-axis CNC milling device. Pneumatic systems are characterized by their simplicity, speed and force control capabilities. For this reasons they provide a promising alternative to traditional mechanical methods in milling devices. By using pneumatic technology, the aim is to improve the precision and efficiency of the perforation process [4].

The main objective of this research is to develop and evaluate a novel device in which the traditional tool axis is replaced by a pneumatic system. This system includes a specially designed tool holder connected to a cylinder piston rod and uses a mechanical sensor for position detection of the Z axis. The integration of the corresponding control software helps to achieve smooth operation, with the sensor, which activates the extension of the cylinder piston rod. Extraction of the cylinder piston rod and contact between the tool and workpiece forms holes of the desired depth.

The significance of this study lies in its potential to enhance the perforation process, providing improved accuracy and operational efficiency. The findings could benefit various industries, from aerospace to automotive, where precise perforation is critical.

The rest of this paper is organized as follows: Section 2 describes the work methodology and system design in detail, Section 3 presents the experimental results and discussion, and Section 4 concludes the study with the main findings and future research directions.

2. WORK METHODOLOGY AND SYSTEM DESIGN

The basic device used in this research is a Proxxon Milling machine FF 500/BL-CNC-ready. The CNC milling machine consists of recirculating ball, spindles and powerful step motors in all 3 axes [5].

Pneumatic cylinder integrated with this CNC milling machine is AZ Pneumatics M21M20160025, double acting mini cylinder. The diameter of the cylinder piston is 16 mm, while the working stroke of the connecting rod is 25 mm [6].

The dimension of workpiece that is used for initial perforation is 50 mm x 50 mm and 20 mm thicknes. It is made from Styrodur, an extruded polystyrene foam (XPS). This material, with a temperature resistance from -50 °C to +75 °C and thermal conductivity of 0.033 W/mK, is very good for testing due to its uniform density, ease of machining, dimensional stability, and durability. Additionally, Styrodur low thermal conductivity and cost-effectiveness support its choice, ensuring consistent and reliable test results and providing a credible benchmark for evaluating the proposed perforation system. [7]. In addition to Styrodor, wood and plastic were also used for testing purposes.

For tool, it is used 4 mm diameter needle, which was sharpened at the tip. In order to attach the needle to the piston rod of the cylinder, a suitable holder was made. The tool holder is shown in Fig. 1.

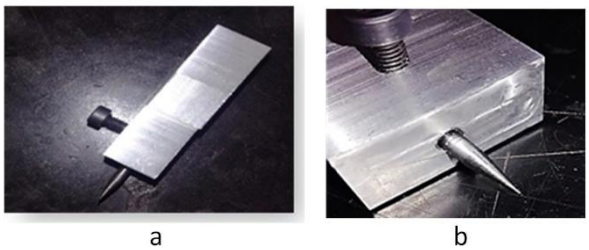


Fig. 1. Tool holder with mounted tool

Fig. 1a and 1b show the tool from different angle attached to the holder with a screw. In addition to fastening, the screw also has the role of determining the desired length of the tool. On the opposite side of the holder where the tool is attached, a thread is cut so that the holder can be attached to the top of the cylinder piston rod. The attachment of the holder to the top of the cylinder rod is given in Fig. 2.

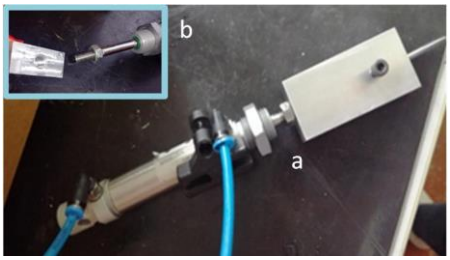


Fig. 2. Connection of the cylinder with tool holder

Fig. 2 main part labeled as "a" shows the rigid connection of the cylinder and the tool holder, while the detail labeled as "b", shows the constituent elements from the main part of Fig. 2, before connecting them. In order to connect and implement the cylinder with Z-axis milling machine, a special holder was designed. For the experimental purpose it is made using 3D printer. The detail on Fig. 3a, show the custom developed cylinder holder that is 3D printed. This is one of the of the custom holder model, since several samples were made during testing in order to demonstrate the processing of the workpiece.

2.1 Experimental setup

The prerequisite for mounting the cylinder on the milling machine is that the existing tool has previously been removed. The custom developed holder can fit into the spindle of the Proxxon milling machine. The cylinder holder should fasten firmly the pneumatic cylinder.

It should be provided that the holder has a compatible interface with the spindle's existing collet system or drawbar mechanism [8]. The existing tool is removed by loosen the drawbar or nut, securing the current milling tool and collet. In doing so, the milling tool and collet from the spindle are removed. Mount of the custom holder is done by inserting the custom holder into the spindle. Tightening the drawbar or nut, the holder is secured in place, ensuring it is firmly and safely mounted.

Attaching the pneumatic cylinder that carries the tool is achieved by connect the cylinder to the custom holder. It is necessary that the cylinder is properly aligned and securely fastened. While doing so, the stability should also be checked to ensure there is no twisting or deflection in the mounted cylinder.

After attaching the cylinder with a milling cutter machine, it is necessary to connect pneumatic lines and controls. This connection is made on the basis of the pneumatic scheme that is given in the Fig. 4. What should be taken into account when connecting, is to firmly insert pneumatic lines to the pneumatics components. Also, ensuring that the connections are secure and leak-free. Finally, integrating the pneumatic control system with the CNC control software and ensuring the mechanical sensor and pneumatic cylinder are properly synchronized. After attaching the components and connecting the control lines, the modified Z axis of the milling machine is obtained, which is shown in main part of Fig. 3, which is labeled as "a".

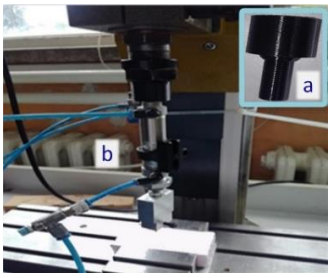


Fig. 3. Perforation machine with a developed tool

Fig. 3. also shows that the workpiece is clamped and ready for processing.

2.2 Control scheme of the pneumatic perforation solution

The connection of the components of the pneumatic system was made on the basis of the created pneumatic scheme.

The initial testing of the system was carried out for cylinder piston extraction and without one-way flow control valve. This case led to the cracking of the custom holder that connects the milling machine and the cylinder. For this reason, one-way flow control valve was added to slow down the extraction of the cylinder piston rod. The scheme of connecting the pneumatic components of the system is given in Fig. 4.

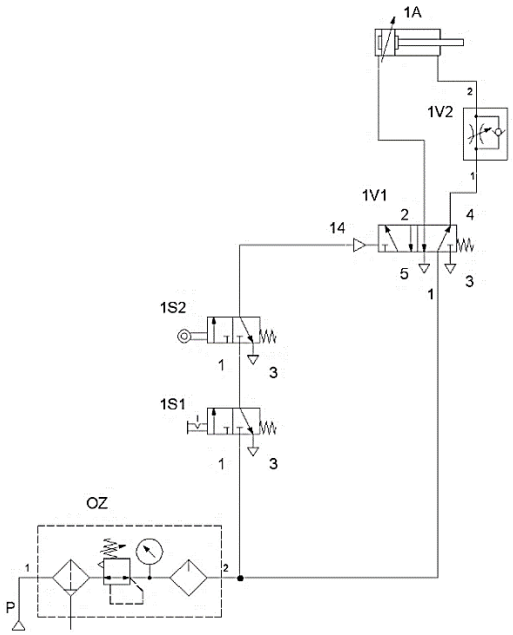


Fig. 4. Pneumatic control scheme

The pneumatic control scheme from Fig. 4 corresponds to the task of this work, which is perforation process of workpiece.

A mechanically actuated, monostable, 3/2 directional control valve was used to detect the appropriate height of the z axis assembly of the milling machine, Fig. 4 (1S2). This valve has the function of a limit switch and when it is active, there is a control signal (Fig. 4, 14) which change position of command valve 1V1 and extract the piston rod of the cylinder. When the Z-axis assembly reached appropriate height in relation to the workpiece, then the limit switch is activated.

The final appearance of the perforation machine shown for this task is given in Fig. 5.



Fig 5. Final appearance of the perforation machine

The newly acquired Z axis is further adjusted by software settings.

2.3 Software Setup and Process starting

In this experiment, Aspire 8.5 and NCAD 8 were used to prepare and execute CNC milling operations with the Proxxon FF 500/BL-CNC-ready milling machine.

The idea of the experiment is to use perforation to create holes in the material, which will be called dots. Those dots should form 2D objects, specifically letters. Letters were designed as dots by generating tool paths for precise positioning of each dot. This tool paths were exported as G-code, compatible with the Proxxon milling machine. The G-code from Aspire 8.5 was imported into NCAD 8.

After that, the starting position of the tool was set as the zero point in NCAD 8. The milling machine was moved to this starting position for perforation process. In addition to the zero position, the Z-axis was calibrated for accurate vertical movement. Following the calibration, a preliminary run test was conducted to verify settings on a sample workpiece. By previous settings the perforation process was initiated, with the milling machine guided by the G-code. The process itself was monitored, and real-time adjustments were made to ensure accuracy.

3. RESULTS AND DISCUSSION

Based on the settings for running the software simulation, the G-code is generated and uploaded to the milling machine. The task is performed on the CNC milling machine with a pneumatic cylinder attached to the Z-axis, which carries the tool, yielding the results shown in Fig. 6. The tested materials of workpiece are: Styrodyr, Fig. 6a, wood, Fig. 6b and plastic, Fig. 6c.

Styrodur is chosen for its uniform density, ease for machining, and dimensional stability, served as the primary material for initial tests. Its consistent properties ensured reliable and repeatable perforation results. Wood was used to evaluate the performance of the pneumatic tool in natural and composite materials, providing a diverse testing ground due to its varying grain structure and hardness. PVC plastic, selected for its distinct mechanical properties, offered insights into the tool's performance in materials with varying hardness and flexibility.

The perforation experiments provided insights into the behavior of different materials under the same processing conditions. In Styrodur, the letters "T" and "M" were recognizable, but some points forming the letter "M" overlapped, and the holes were not of uniform diameter, especially for the letter "M." In wood, the perforation points were clearly visible, with only a few openings joining due to proximity. In plastic, the points that make up the letters "T" and "M" were clearly expressed.

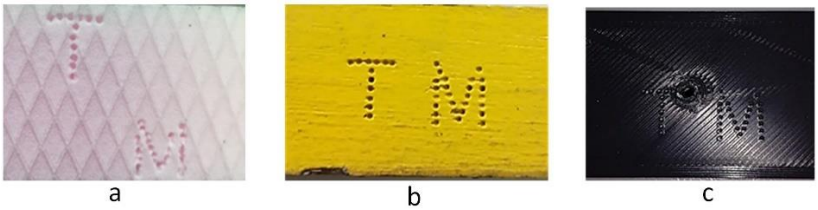


Fig. 6. Perforation results on Styrodur, wood and plastic

The overlapping points and non-uniform hole diameters in Styrodur can be attributed to its material properties, such as varying density and potential deformation under pressure, indicating a need for precise calibration and consistent compressed air pressure. Wood exhibited better clarity in perforation points due to its natural grain structure and hardness, but slight merging of holes indicated a need for careful spacing in toolpath design. The performance of the pneumatic tool in plastic was superior, with uniform hardness and stability allowing for precise and clean perforations, making it the most suitable material among the three, for high-quality perforations.

A comparative analysis of Styrodur, wood and plastic that emphasizes their different behavior during the perforation process can also be found in other works:

Material properties: each material's inherent properties impact perforation quality. Styrodur's

softness and variability challenge maintaining uniform hole diameters. Wood's grain structure provides stability but requires careful spacing to avoid overlaps. Plastic's uniformity allows for precise, clean perforations, as it is noted in studies [9].

Tool Performance: The pneumatic tool's effectiveness varies with material hardness and density. Consistent compressed air pressure and accurate calibration are crucial, especially for softer materials like Styrodur. Various techniques can modify machining procedures and CNC machine structures to improve performance [10].

Design and Execution: The toolpath design and spacing between points in the G-code generated by Aspire 8.5 are critical. Inadequate dot spacing and alignment can cause issues like overlapping holes, particularly in materials with complex grain structures or different densities. Effective tool path planning and collision avoidance control are essential for achieving desired outcomes [11].

4. CONCLUSION

Within this work, a pneumatic perforation solution using a CNC milling machine was presented, tested and implemented. This pneumatic perforation solution has been tested on three materials: Styrodur, wood and plastic.

The analysis of perforation results across these materials underscores the importance of material selection and toolpath design in CNC perforation processes. Plastic emerged as the most suitable material for achieving high-quality perforations, while wood and Styrodur require specific adjustments perforation process parameters to optimize results.

Based on the above, future work should focus on:

- Optimization of toolpath: refining the G-code to ensure precise spacing and alignment of perforation dots, particularly for complex shapes.
- Specific material adjustments: developing tailored settings and calibration procedures for different materials to enhance the consistency and quality of perforations.
- Tool maintenance: regular maintenance and inspection of the pneumatic tool to ensure consistent performance and minimize wear-related variations in hole size and shape.

By addressing these factors, the reliability and versatility of the pneumatic solution for CNC perforation processes can be further enhanced, enabling high-quality results across a wider range of materials.

5. REFERENCES

[1] Poiana, D. I., Ionel. I.: *Study of modern perforation processes specific to the automotive industry*, IOP Conference Series: Materials Science and Engineering. Vol. 898. No. 1. IOP Publishing, 2020.

[2] Mironovs, V., Kuzmina, J., Serdjuks, D., Usherenko, Y., Lisicins, M.: *Sustainable Lifecycle of Perforated Metal Materials*, Materials, 16(8), 3012, 2023.

[3] Joshi, V., Harit R., Keyur D.: *A review article on machining of closed contour profile on CNC milling machine*, AIP Conference Proceedings. Vol. 2821. No. 1. AIP Publishing, 2023.

[4] Quynh, N. X., Tung T., T.: *Design and Fabrication of a Prototype Pneumatic Cylinder*, Industrial Engineering 13(3), 1-6, 2023.

[5] Web page: https://www.proxxon.com/en/micromot/24364.php

[6] Web page: https://www.tinyurl.com/4k9wx6y3

[7] Web page: https://styrodur.com/portal/load/fid1360663/Styrodur_Technical_Data_May%202022.pdf

[8] Xu, M., Li, C., Yao, G., Zhang, Y., Gao, Y. *Load-dependent stiffness model and experimental validation of four-station rotary tool holder*, Mechanical Systems and Signal Processing, 171, 108868, 2022.

[9] Đekić, P., Milutinović, B., Ristić, M.: *Assessment of the Optimal Manufacturing Technology of the Brake Triangle Sleeve Casting Model Prototype using multi-criteria Analysis*, 21st International Symposium INFOTEH-JAHORINA. 2022.

[10] Soori, M., Arezoo B.: *Modification of CNC machine tool operations and structures using finite element methods, A review*, Jordan Journal of Mechanical and Industrial Engineering, 2023.

[11] Bacciaglia, A., Ceruti A.: *Efficient toolpath planning for collaborative material extrusion machines*, Rapid Prototyping Journal, 29(9):1814-1828, 2023.

ACKNOWLEDGMENTS

This research has been supported by the Ministry of Science, Technological Development and Innovation (Contract No. 451-03-65/2024-03/200156) and the Faculty of Technical Sciences, University of Novi Sad through the project "Scientific and Artistic Research Work of Researchers in Teaching and Associate Positions at the Faculty of Technical Sciences, University of Novi Sad" (No. 01-3394/1).

Authors:

PhD Jovan Šulc, PhD Vule Reljić, MSc Nikolina Dakić, MSc Vladimir Jurošević, University of Novi Sad, Faculty of Technical Sciences, Institute for Mechatronics, Robotics, Automation and Integrated Systems, Trg Dositeja Obradovica 6, 21000 Novi Sad, Serbia.

E-mail: sulc@uns.ac.rs; vuketa90@uns.ac.rs; nikolinadakic@uns.ac.rs; vladimirjurosevicvl@uns.ac.rs

MMA 2024 FLEXIBLE TECHNOLOGIES

15th INTERNATIONAL SCIENTIFIC CONFERENCE
NOVI SAD, SERBIA, SEPTEMBER 24-26, 2024

Original research paper https://doi.org/10.24867/MMA-2024-02-009

Budimir Buda, A., Tabaković, S., Zeljković, M., Živanović, S., Dimić, Z.

STRAIGHTNESS ANALYSIS OF MACHINE TOOL WITH NON-LINEAR KINEMATICS

Abstract: *Straightness of the machine tool affects the accuracy of the workpiece to a great extent. Using well-established technics the straightness of linear axis of the machine tools can be determined with a high accuracy. Machine tools with non-linear kinematics are much different in relation to the machine tools with serial mechanisms. It is necessaryto be sure that the existing procedures are appropriate for determining the straightness of machine tools with non-linear kinematics. For that purpose the straightness accuracy of linear axis of a machine tool with so-called O-X glide parallel mechanism, which has non-linear kinematic characteristics, is determined through laser displacement measurements.*

Key words:*Straightness, machine tool, non-linear kinematics, O-X glide*

1. INTRODUCTION

The quality of the workpiece is affected by the accuracy of the machine tool (MT) to a great extent. The accuracy of the MT depends on a big variety of factors and so the MT errors can be classified in main groups. These groups according to [1] are geometric and kinematic errors, thermal errors, cutting force induced errors, fixturing errors and controller errors. The geometric and kinematic errors have a big impacton the production process and on the workpiece quality, thus it is necessary to be aware with the momentary status of the MT.

Through MT validation the effect of these errors can be reduced. Geometric validation tests measure the MT accuracy and repeatability with series of simple positioning tests, generally operating under no-load conditions. The results of these tests are positioning accuracy, straightness, squareness and parallelism of the linear axes, the concentricity of the rotary axes, etc. [2].

One of the main characteristics of MT is the workspace and the analysis of the workspace is one of the basic elements used for machine development. The workspace of conventional mechanisms with serial orlinear kinematics differs greatly from parallel kinematic structure mechanisms with non-linear kinematics [3]. By applying parallel mechanisms in the construction of the mechanical structure of machine tools, a workspace with a complex geometric shape and reduced volume is obtained compared to conventional machine tools. This initiated the realization of a large number of researches in the field of workspace analysis [4–6], with the aim of determining the applicability of parallel mechanisms in machine tools from this point of view. As a result of those researches, in order to overcome certain shortcomings of parallel mechanisms, a larger group of mechanisms with combined, series-parallel, or hybrid kinematics appeared [7–9].

The non-linearity of the MT can also be described by the resolution of the MT. The resolution of the MT mechanism can be seen as the possible displacement of the platform of the mechanism. In MT with serial kinematics, the resolution is equal to the minimum change of internal coordinates Δp and it is valid for every point of the working space $\Delta p=\Delta x=\Delta y=\Delta z$, while in mechanisms with parallel kinematics, this is not valid due to their constructions, geometry and methods work. By changing one of the internal coordinates of the parallel mechanism, the platform will not move in the direction of the internal coordinate change, and the displacement values are different $\Delta p\neq\Delta x\neq\Delta y\neq\Delta z$ [10] .

Due to the existence of this type of nonlinear property of MT with a parallel mechanism, they are also called machine tools with nonlinear kinematics (MTNK) [11].

In the work the straightness of three linear axis X, Y and Z is measured in all perpendicular directions with a laser straightness interferometer measuring system.

2. STRAIGHTNESS MEASUREMENT OF MACHINE TOOLS

The definition of straightness error of the linear axis according to ISO 230-1 [12], is the value of the largest positive straightness deviation added to the absolute value of the largest negative straightness deviation with respect to any previously defined reference straight line. There are three types of defining the reference line:

- Mean minimum zone reference straight line;
- Least square reference straight line;
- End-point reference straight line.

Fig. 1. shows the end-point reference straight line. It is the most common method to express the straightness error of a linear axis. In the figure *a* and *b* are the end points, *1* is the straight reference line, *2* is the biggest positive deviation of the reference straight line, *3* is the biggest negative deviation of the reference straight line and *4* is the measured deviation of the straightness.

Straightness measurements can be performed using various methods: straightedge and linear displacement sensor, microscope and taut wire, alignment telescope, alignment laser, and laser straightness interferometry.

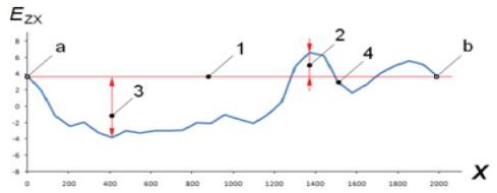


Fig. 1. End-point reference straight line for an imaginary Z-axis in direction of X-axis [12]

The development of a system, by which the 2D motion errors of the linear axes of the MT can be measured at the same time using the direction regulation of the laser interferometer, is performed by [13]. According to this procedure, the positioning accuracy, straightness and flatness of individual linear axes can be checked at the same time.

Fig. 2 shows the principles of the laser straightness interferometry. Laser beam goes through the interferometer, also referred to as a Wollaston prism, the laser beam splits in two parts due to the two initial frequencies (double frequency laser beam f_1, f_2) by a small angle θ. The two laser beams arrives to the reflector, and reflects back to the interferometer. Inside the interferometer the recombination of the beams creates a new beam which heads back to the sensor of the laser head. Relative displacement of the axis (Δx) of the prism causes changes in the recombination of the reflected laser beams, thus using this principle the deviation from the initial straight line can be measured.

The orientation of the reflector defines if the measurement of the displacement is performed in the horizontal or vertical plane.

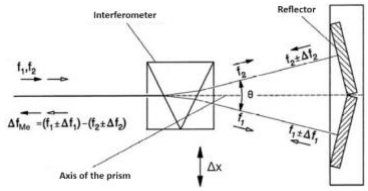


Fig. 2. Principles of the laser straightness interferometry [14]

3. EXPERIMENTAL SETUP

Straightness measurements are performed on a MT with hybrid (serial-parallel) mechanism, which has non-linear kinematics. The movement in X-Z plane is realized with so-called O-X glide mechanism [15,16] and the movement in the Y axis with a serial mechanism. In Fig. 3 the O-X glide mechanism is shown and in Fig. 4 the experimental setup for measuring the straightness error of linear axes of the machine tool is shown.

The movements along the Y-axis are performed using the serial mechanism and it has a purely linear kinematic characteristic. Movements along the Z-axis are performed using the parallel mechanism and it has a non-linear kinematic characteristic. On the other hand, the movements along the X-axis are performed using the parallel mechanism, but it has a linear kinematic characteristic, which is variable along the Z axis. It is the reason why the X-axis has quasi-linear kinematic characteristics.

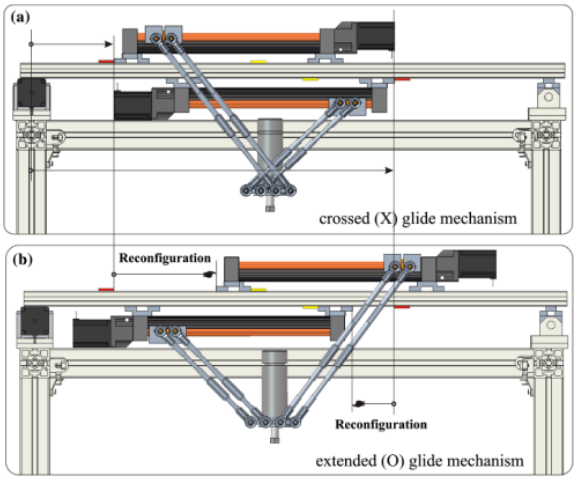


Fig. 3. The O-X glide mechanism [16]

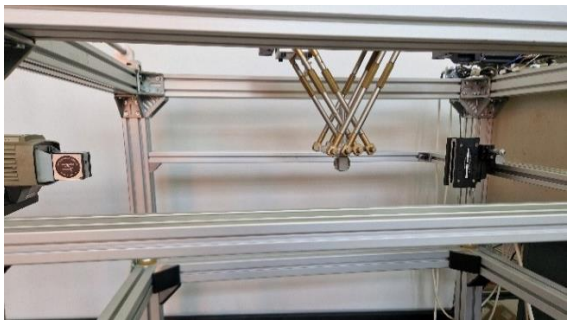


Fig. 4. The experimental setup on the O-X glide for measuring the X-axis in perpendicular Z-axis

The straightness measurements are conducted in bi-directional way, which refers to a series of measurements in which the approach to a target position is always made in either directions along the axis [17]. The two directions are called positive and negative. Positive movement direction means movement along an axis in positive, increasing coordinates and negative is the opposite.

4. RESULTS OF THE STRAIGHTNESS MEASUREMENTS

After conducting the measurements for all threelinear axes (X, Y and Z) in two perpendicular planes (X-Y, X-Z, Y-X, Y-Z, Z-X and Z-Y) the data of straightness of the linear axis is obtained. In Fig. 5-10 the results of measurements in two normal planes for each axis are graphically illustrated. The end-point reference straight line method is used to show the acquired values.

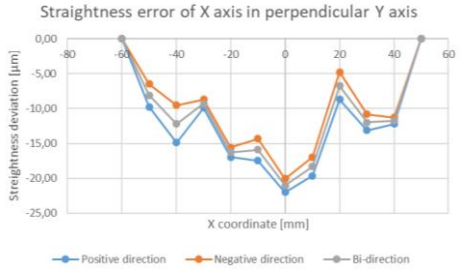


Fig. 5. Straightness error of X-axis in Y direction

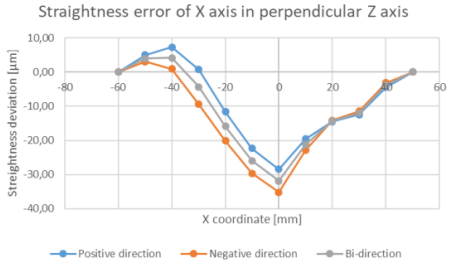


Fig. 6. Straightness error of X-axis in Z direction

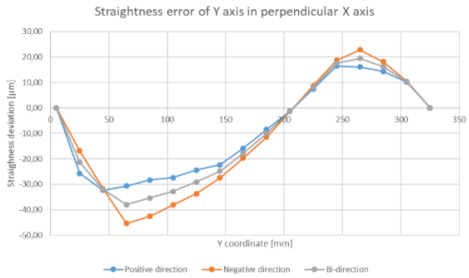


Fig. 7. Straightness error of Y-axis in X direction

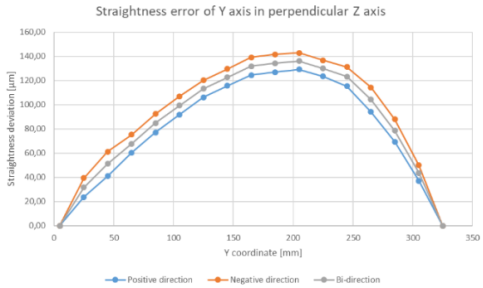


Fig. 8. Straightness error of Y-axis in Z direction

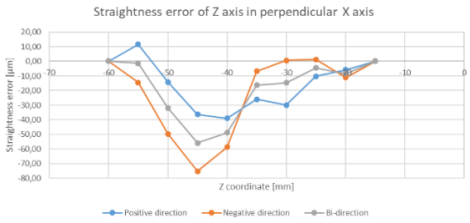


Fig. 9. Straightness error of Z-axis in X direction

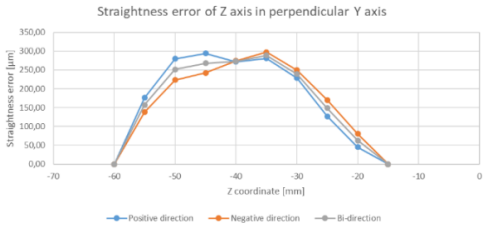


Fig. 10. Straightness error of Z-axis in Y direction

Table 1 shows the maximum positive and maximum negative values of the measured straightness's for every axis from both positive and negative movement directions. Values obtained for X axis are in optimal range, the absolut values under 50 µm according to [17]. Values obtained for Y-axis in perpendicular X-axis are also under 50 µm, thus acceptable. On the other hand the Z-axis in both perpendicular X and Y axis and also Y-axis in perpendicular Z-axis are over the acceptable limit.

Main axis	Perpend. axis	Straightness displacement [µm]	
		Max. positive	Max. negative
X	Y	0	-21,97
	Z	7,36	-28,45
Y	X	22,79	-45,29
	Z	142,96	0
Z	X	11,63	-75,22
	Y	297,23	0

Table 1. Straightness errors of the axis

5. DISCUSSION

After analyzing the obtained values about the straightness error of all three axis, the next conclusions can be drawn:

- The quasi-linear X-axis has the best straightness characteristics of all axis.
- The linear Y axis is worse than the X axis but better then the Z axis.
- The Z-axis, which has non-linear characteristics is the worst. In both X and Y perpendicular directions the values of straightness deviation are above the acceptable 50 µm limit.

The parallel mechanism is constructed from rods with changeable length. The rods are put together from 3 (the shorter rods) and from 4 (the longer rods) separate subparts with threads on them. Length of the rods can be changed tightening or loosening up the previously mentioned threads. During the construction of the MT the length of these rods are fixed, calibrated and precisely measured, because it plays an important role in the definition ofmachine tool internal kinematics.

The straightness error of Y axis in positive movement direction is greater, then the straightness error in negative movement direction.

The straightness error of X axis in perpendicular Y direction is greater in the negative movement direction then in positive, but the straightness error of X axis in perpendicular Z direction is greater in the positive movement direction then in negative in major part of the movement path of the linear axis.

The straightness error of the Z axis can be divided in two parts:

- The part within coordinates from -60 to -40 mm – lower subpart of the movement path.
- The part within coordinates from -40 to -15 mm– upper subpart of the movement path.

The -40mm coordinate is a transition point, where the significance of the positive movement direction decreases and the negative movement direction increases, or vica versa. For the perpendicular X direction the straightness error of Z axis is greater in positive movement direction at the upper subpart, but in the lower subpart the negative movement direction has a greater significance.

On the other hand, for the perpendicular Y direction the straightness error of Z axis is greater in positive movement direction in the lower subpart of the movement path, but in the upper subpart the negative movement direction has a greater significance.

Bi-directional straightness error of all three linear

axis follows the trend of the straightness errors of both unidirectional movement directions.

6. CONCLUSION

The straightness measurements of all three linear axis's were conducted using the laser straightness interferometry method, to obtain the necessary straightness deviation values. They provide good insight in the current condition of the machine tool with O-X glide parallel mechanism. The X-axis has not to big issues, but the Y and mainly the Z axis is in very poor condition. Further investigation for finding the reasons of this state of the axis are necessary. However, the Y and Z axes have significantly larger straightness deviations. The main reason for this is that the testing was done on a prototype primarily intended to check kinematic characteristics and control algorithms. A possible reason for deviations could be the characteristics of the joints and errors in the internal kinematic equations. Because the control of the MT is out of sync with the real position of the platform.

7. REFERENCES

[1] Mekid S.: Introduction to precision machine design and error assessment, *CRC Press;* 2008.

[2] de Lacalle N.:, Mentxaka A.: Machine tools for high performance machining, *Springer Science & Business Media;* 2008.

[3] Tabaković S.: Razvoj programskog sistema za automatizovano projektovanje mašina alatki na bazi paralelnih mehanizama i optimalni izbor njihovih komponenti doktorska disertacija, *Univerzitet u Novom Sadu, Fakultet tehničkih nauka,*. 2008.

[4] Kanaan D., Wenger P., Chablat D.: Kinematic analysis of a serial–parallel machine tool: The VERNE machine, *Mech Mach Theory,*.44:2, 2009**.**

[5] Chablat D., Wenger P., Majou F., Merlet JP.: An interval analysis based study for the design and the comparison of three-degrees-of-freedom parallel kinematic machines, *Int J Rob Res,*.23:6, 615–24. 2004.

[6] Harib K., Moustafa K., Ullah A., Zenieh S.: Parallel, serial and hybrid machine tools and robotics structures: comparative study on optimum kinematic designs, *Ser Parallel Robot Manip Dyn Control Optim Dr Serdar Kucuk,*. 2012.

[7] Harib K., Moustafa K., Ullah A., Zenieh S.: Parallel, serial and hybrid machine tools and robotics structures: comparative study on optimum kinematic designs, *Ser Parallel Robot Manip Dyn Control Optim Dr Serdar Kucuk,*. 2012.

[8] Zhang H., Fang H., Fang Y., Jiang B.: Workspace analysis of a hybrid kinematic machine tool with high rotational applications, *Math Probl Eng,*.2018.

[9] Tang T., Zhang J.: Conceptual design and kinetostatic analysis of a modular parallel kinematic machine-based hybrid machine tool for large aeronautic components, *Robot Comput Integr Manuf,*.57, 1–16, 2019.

[10] Vasilić G.: Koncepcijsko projektovanje jedne klase kompleksnih mašina alatki, *Univerzitet u Beogradu, Mašinski fakultet*, 2023.

[11] Budimir A., Tabaković S., Živanović S., Zeljković M., Dimić Z.: Kinematic analysis of machine tool with non-linear kinematics for calibration purposes, *The 6th International Conference "Mechanical Engineering In XXI Century."Niš;* 2023.

[12] ISO 230–1: 2012: Test Code for Machine Tools—Part 1: Geometric Accuracy of Machines Operating under No-Load or Quasi-Static Conditions, *ISO Office Geneva;* 2012.

[13] Ibaraki S., Hiruya M.: A novel scheme to measure 2D error motions of linear axes by regulating the direction of a laser interferometer, *Precis Eng,*.67, 152–159, 2021.

[14] Weck M., Brecher C.: Messtechnische Untersuchung und Beurteilung, dynamische Stabilität, *Springer Vieweg;* 2013.

[15] Tabaković S., Živanović S., Zeljković M., Dimić Z.: Konfigurisanje nove edukacione mašine alatke na bazi mehanizma sa hibridnom kinematikom, *Tehnika,*.76:5, 603–612, 2021.

[16] Živanovic S., Tabakovic S., Zeljkovic M., Dimic Z., Modelling and analysis of machine tool with parallel–serial kinematics based on OX glide mechanism, *J Brazilian Soc Mech Sci Eng,*.43, 1–15, 2021.

[17] ISO 230-2:2014: Test code for machine tools-Part 2: Determination of accuracy and repeatability of positioning of numerically controlled axes, *Berlin: Beuth,*. 2014.

ACKNOWLEDGMENTS

This research has been supported by the Ministry of Science, Technological Development and Innovation through projects "Scientific and Artistic Research Work of Researchers in Teaching and Associate Positions at the Faculty of Technical Sciences, University of Novi Sad", grant number 451-03-65/2024-03/200156, "Integrated research in macro, micro, and nano mechanical engineering", grant number 451-03-65/2024-03/200105 and "Research project of the Institute Lola Ltd.", grant number 451-03-66/2024-03/200066.

Authors:

MSc Alexander Budimir Buda, PhD Slobodan Tabaković, PhD Milan Zeljković, University of Novi Sad, Faculty of Technical Sciences, Trg Dositeja Obradovica 6, 21000 Novi Sad, Serbia, Phone.: +381-63/114-6954.

E-mail: buda.karate@gmail.com; tabak@uns.ac.rs; milanz@uns.ac.rs

PhD Saša Živanović, University of Belgrade, Faculty of Mechanical Engineering, Kraljice Marije 16, 11120 Belgrade, Serbia.

E-mail: szivanovic@mas.bg.ac.rs

PhD Zoran Dimić, LOLA Institute, Belgrade, Republic of Serbia, Kneza Višeslava 70a, 173580 Belgrade, Serbia.

E-mail: zoran.dimic@li.rs

MMA 2024 FLEXIBLE TECHNOLOGIES

15th INTERNATIONAL SCIENTIFIC CONFERENCE
NOVI SAD, SERBIA, SEPTEMBER 24-26, 2024

Original research paper https://doi.org/10.24867/MMA-2024-02-010

Tabaković, S., Zeljković, M., Živanović, S.

METHODS OF MONITORING AND APPLYING ENERGY BALANCE PARAMETERS IN THE EXPLOITATION OF MODERN MACHINE TOOLS

Abstract: *The digitization procedures of machine tools, which are the basis of modern industry development strategies, are to the greatest extent based on the application of information collected during the operation of the machines. In this way, it is possible to monitor and manage production processes by applying different criteria. The paper describes the procedure for monitoring and applying energy balance parameters in drive motors of machine tools in real time and the possibility of their application in production conditions.*
Key words: *Energy balance, Machine Tool, Digitalization, Monitoring*

1. INTRODUCTION

Numerically controlled machine tools have been the basic production element of modern industry for the last 50 years. In that period, they went through various stages of improvement and integration with other machines, manipulation, and transport systems to form a flexible, computer-integrated production.

This trend continues with expectations that the market for machine tools and their subsystems will continue to grow. Market analyses indicate a growth trend in the global market for numerically controlled machine tools from 84 billion dollars in 2021 to 141 billion in 2029. Their share has increased in recent years most in the production areas that include material processing in medium-sized series as well as in smaller series in branches industry that contains workpieces with complex geometry and high accuracy. These are also the areas where the optimization of the use of production resources gives the most significant results.

That is why research conducted to improve production as well as planned strategies for the development of industry in regional and global frameworks [1] devote a significant role to the energy balance of production systems and also machine tools as their basic production components (their building units) [2]. It is very significant from the point of view of:

- minimization of the use of energy resources of the machine tool as a whole and optimization of the consumption of energy resources on individual subsystems of the machine tool as well as
- monitoring and analysis of energy parameters to detect changes in machines, tools, and other elements of the production system.

The paper presents the possibilities of monitoring and recording energy parameters of drive motors of machine tools during their operation, as well as the possibilities of applying that information in the processing process.

2. DIGITALIZATION OF PRODUCTION AND ENERGY BALANCE OF MACHINE TOOLS

Modern industrial development strategies as a continuation of improvement imply interconnection of machines and systems involved in production to the extent that enables the use of data that thus becomes available to the wider business environment [3] (Fig. 1).

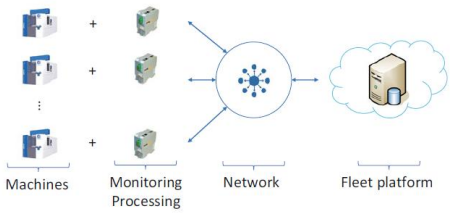


Fig. 1. Schematic view of connecting machines and systems

Previous research in this field, carried out in the last 10 years, has ensured the development of the necessary infrastructure based on open architecture control systems, sensors with appropriate characteristics, as well as communication protocols that enable the parallel use of data.

In this way, the foundations for the development of the so-called Intelligent machine tools [4] which, in addition to increasing the amount of information available to users in their daily work, also enable an increase in machine autonomy according to several criteria. Such an approach to machine tool development is recognized in industry development strategies such as "Industry 4.0", "FutureFactory", "Made in China 2025".

Among the information that has the greatest potential in the process of improving machine tools are the energy resources management parameters of the machine that are used in machine monitoring, preventive maintenance, but also overload prediction, processing process optimization, etc. By monitoring the parameters of electricity (current voltage and current), engine temperature, electricity consumption as well as the achieved torque, it is possible to monitor the current state of the processing process: the state of the engine elements (shafts, bearings, motor windings), the

efficiency of the cooling process, systematic and random friction changes in mechanical elements. In an indirect way, information is also obtained about processes that affect the state of the machine itself and are the result of the previous one (vibrations, wear of mechanical elements, etc.). In addition, the monitoring of this information enables the creation of multiple control feedback loops on the desired subsystems, which, by analyzing the available information, activate preventive activities that maintain the accuracy and productivity of the machine tool.

Modern research considers the application of energy parameters of machine tools as suitable for application at multiple levels [5]. Those are:

- The machine level, which is used to improve the functioning of certain subsystems of the machine tool;
- A process level that enables a more efficient realization of the machining processes covered by the machine tool;
- Production level that enables control and management of flexible technological systems; and
- Factory level which manages the complete production within the factory

According to the need and planned application, information can be collected, stored and used in different ways.

3. PROCEDURES OF MONITORING AND COLLECTION OF OPERATING PARAMETERS OF MACHINE TOOLS

Digitization of production systems and improvement of control systems of machine tools as a result, has provided more opportunities to collect and process information that arises in the process of exploitation of machine tools.

Depending on the amount generated during machine operation and the needs of their application, information can be stored:

- locally, on the management system;
- locally, on a special computer system that is an extension of the machine's control system;
- on remote computer systems that are part of the factory's information system or independent of it (cloud).

Local storage of information on the control system generated during the operation of machine tools can be:

- in the form of discrete values placed in system variables of the control system and used for feedback during machine operation (Fig. 2),
- in the form of documents (files) suitable for later analysis directly on the machine or on remote computer systems.

This type of information storage is limited in size due to the memory capacity of control systems and the potential impact on the speed of their operation. Therefore, they are most often used as a basis for defining subroutines and functions that are managed during the execution of the control program on the machine (interrupted, directed to alternative subroutines, etc.). This is achieved by comparing the values obtained from the sensors or from the process on the machine (temperature, vibrations, humidity, current number of processed parts, values of dimensions measured in the processing process, etc.) with the limit defined by the control program.

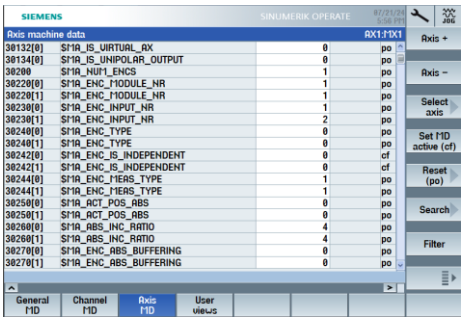


Fig. 2. System variables of the machine tool control system

In addition, locally stored files are used for insight into the machine operation process (error reports, measurements of geometric dimensions on parts in serial production) which is used for further analysis of machine operation or for managing manipulation and transport systems within flexible technological systems.

Information stored on special computer systems is used for analytical processing of information in real time using special software solutions. The information obtained in this way is used in the processes:

- management during operation of the machine tool or
- distribution of information received in the process of machine operation.

The information processed in this way belongs to one of the basic directions of digitalization development in the industry called Edge computing and forms the basis of modularly designed machine tools adaptable to specific tasks. Machine tools conceived in this way are often called machine tools 4.0 in the literature. Figure 3 shows the schematic structure of the application of this concept of improving machine tools [6]

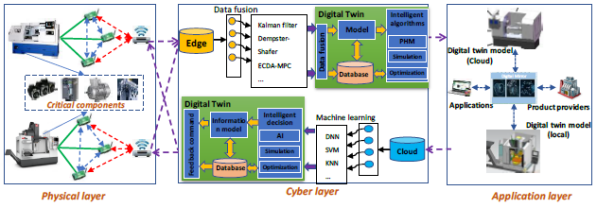


Fig. 3. Schematic structure of edge computing machine tool improvement

The last type of storage of information created in the processes of machine tools involves the use of dedicated computer systems within the factory or rented (cloud) memory space accessed via the Internet. The data stored in this way are processed as necessary by dedicated applications and/or software systems and their results are distributed to the services that use them. This enables the detection of individual events but also the processing

of a large amount of generated data that can be processed using an artificial intelligence system. This ensures the entire area of application of expert knowledge that is integrated into appropriate software available to users as a service.

Such services are most often useful for specialized services of the factory, such as services for production capacity planning, procurement (tools, materials), maintenance, management structures, etc.

The application of this concept enables the communication of machine tools as the carrier of industrial production with other types of computer devices with defined access rules and the amount of information that can be accessed without affecting immediate production.

4. REALISED RESEARCH

In order to analyze the usability of information collection and analysis procedures, an appropriate experiment was conducted. It was realized during research aimed at determining the impact of changes in the components of the mechanical structure of machines on their accuracy. Changes in the parameters of the energy balance (engaged power and achieved torque of the drive motors) were taken as a measure of influence. The test covers the movement of individual axis slides in accordance with the ISO 230-2 standard. This activates the drive and transmission elements of the system for the feedrate movement of one axis, which is suitable for determining deficiencies in the mechanical and energy segment of this subsystem and gathering information necessary for the formation of the appropriate knowledge base.

The research was carried out on a milling machining center with three numerically controlled axes and a control system Sinumerik 840d sl. with activated information collection functions in the process of machine operation and appropriate authorizations for their access.

The measurement was carried out in the diagnostic mode of the machine tool (Fig. 5), during which the following parameters were collected:

- current slider positions of a specific axis in the machine's coordinate system,
- programmed slider positions of a specific axis,
- acceleration values achieved during slider movement,
- the torque of the drive of the feedrate movement of a specific axis,
- the activated power of the drive of the feedrate movement of the specific axis.

The parameter collection was realized automatically, during the operation of the machine, by integrating a system variable that activates the recording of parameters into the driver program that controls the movement in accordance with the mentioned standard during the positioning accuracy test. The values were recorded on the memory disk of the control system with a frequency of 0.008s. The data were archived in xls format for further processing for research purposes on another computer. For the purposes of checking the correctness of the measurements on the machine, a diagram of the values in real time was displayed during the test (Fig. 6).

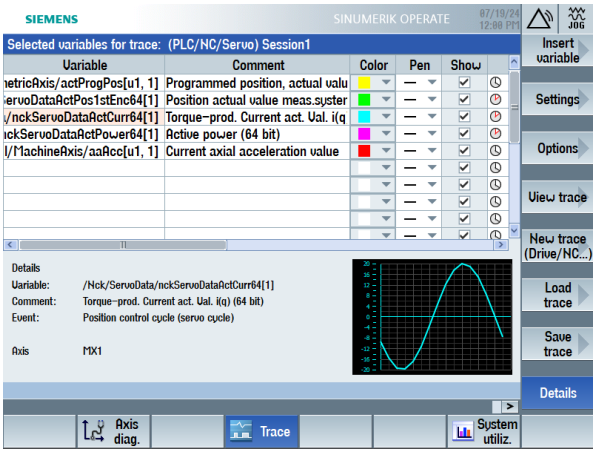


Fig. 5. Display of management system settings for local parameter storage

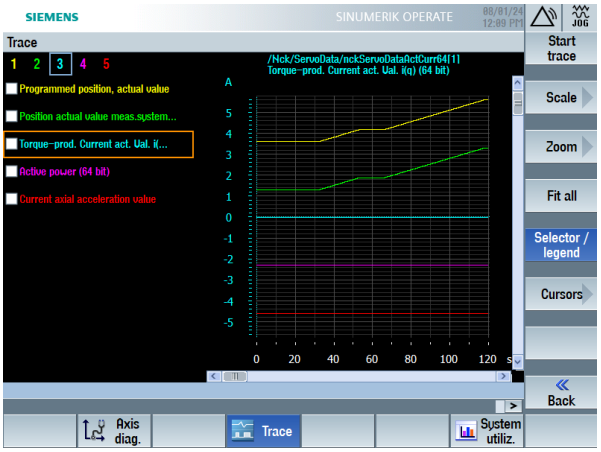


Fig. 6 Diagram of test parameters change

5. RESULTS

On the basis of the realised tests, which were repeated three times (for different slider movement speeds) on all three numerically controlled axes of the machining center for milling, a large amount of data was obtained. Specifically, when collecting the information mentioned in the previous chapter for the X-axis in the movement range -150÷200 mm in the machine coordinate system (350 measuring mm) with an auxiliary movement speed of 500 mm/min, a matrix of 11780 data sets containing the collected parameters was obtained. The movement was carried out continuously from the starting point to the end point of the axis in order to detect changes in absolute values as well as changes in values observed in a unit of time. Fig. 7 and 8 show diagrams of the engine torque value and its changes over time.

The obtained results have greater research significance when viewed in a smaller domain, ranging from 0 to 20 mm for the X axis (Fig. 9 and 10).

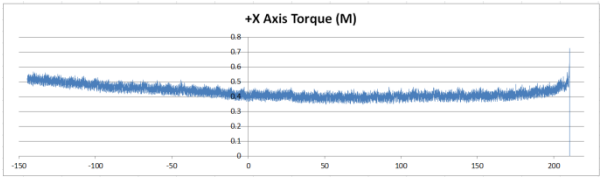


Fig. 7. Absolute values of the torque

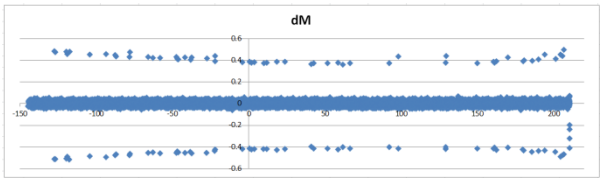


Fig. 8. Values of the change in torque

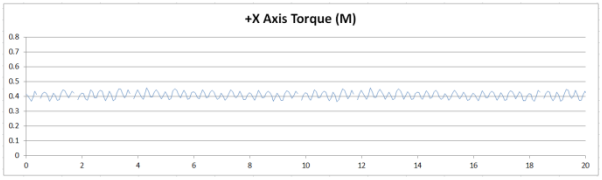


Fig. 9. Values of X-axis drive torque change

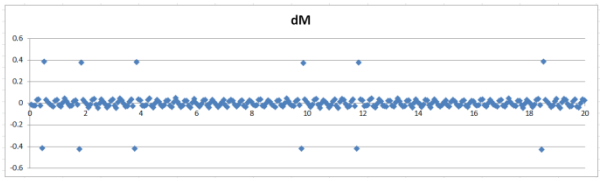


Fig. 10. Values of X-axis drive torque change

Based on the analysis of the last two diagrams, changes in engine torque can be observed on the observed segment x axis can be observed at six positions (coordinates x: 0.448, 1.781, 3.780, 9.771, ...). The obtained results coincide with the errors on the observed axis obtained by testing the machine according to the ISO 230-2 standard. This confirms the hypothesis that by forming a method of analysis of changes in the energy balance of the drives of individual axes, it is possible to determine changes in the mechanical structure of machines (wear, appearance of deposits, etc.).

6. DISCUSSION AND CONCLUSIONS

The application of the existing interface of the Sinumerik 840d sl control system for the purpose of collecting energy balance parameters of subsystem elements for auxiliary movement of machine tools enables the collection and local storage of relevant information for further research and potentially commercial use. In the work, the PCU segment of the control system was used as a computer system that implemented the data collection process, which greatly limited the number of parameters that are collected, as well as the size of the documents that are obtained. The structure of the control system enables the use of dedicated computers intended for these activities, which completely eliminates the potential impact on the processes that are carried out on the machine tools.

Creation of foundations for further digitization in industry and improvement of computer systems and appropriate methods for its implementation on machines, tools and other elements of production systems, efforts to further improve the application of computer systems in the integration of all activities in industrial production continue.

7. REFERENCES

[1] Mirani, A.A.; Velasco-Hernandez, G.; Awasthi, A.; Walsh, J. Key Challenges and Emerging Technologies in Industrial IoT Architectures: A Review. *Sensors*, *22*, 5836, 2022.

[2] Grigor'ev, S.N., Kuznetsov, A.P., Volosova, M.A. *et al.* Classification of metal-cutting machines by energy efficiency. *Russ. Engin. Res.* **34**, 136–141 2014.

[3] Youssef Abdelmajied F. Industry 4.0 and Its Implications: Concept, Opportunities, and Future Directions [Internet]. Supply Chain - Recent Advances and New Perspectives in the Industry 4.0 Era. IntechOpen; 2022.

[4] Lou, P., Liu, Sh., Hu, J., Li, R., Xiao, Z., Yan, J.: Intelligent Machine Tool Based on Edge-Cloud Collaboration. IEEE Access. 8. 2020..

[5] Andrei M, Thollander P, Sannö A. Knowledge demands for energy management in manufacturing industry - A systematic literature review. Renewable & sustainable energy reviews [Internet]. Elsevier; 2022.

[6] Jian Z., Changyi D., Pai Z., Xun X., Zhentao M.:Development of an edge computing-based cyber-physical machine tool,Robotics and Computer-Integrated Manufacturing,Volume 67, 2021.

ACKNOWLEDGMENTS

This research has been supported by the Ministry of Science, Technological Development and Innovation through projects "Scientific and Artistic ResearchWork of Researchers in Teaching and Associate Positions at the Faculty of Technical Sciences, University of Novi Sad", grant number 451-03-65/2024-03/200156, "Integrated research in macro, micro, and nano mechanical engineering", grant number 451-03-65/2024-03/200105

Authors:

PhD Slobodan Tabaković, PhD Milan Zeljković University of Novi Sad, Faculty of Technical Sciences, Trg Dositeja Obradovica 6, 21000 Novi Sad, Serbia, Phone.: +381-63/114-6954.E-mail: tabak@uns.ac.rs; milanz@uns.ac.rs

PhD Saša Živanović, University of Belgrade, Faculty of Mechanical Engineering, Kraljice Marije 16, 11120 Belgrade, Serbia, E-mail: szivanovic@mas.bg.ac.rs

MMA 2024 FLEXIBLE TECHNOLOGIES

15th INTERNATIONAL SCIENTIFIC CONFERENCE
NOVI SAD, SERBIA, SEPTEMBER 24-26, 2024

Original research paper https://doi.org/10.24867/MMA-2024-02-011

Jokić, A., Jevtić, Đ., Brenjo, K., Petrović, M., Miljković, Z.

DEEP LEARNING-BASED VISUAL SERVOING ALGORITHM FOR WHEELED MOBILE ROBOT CONTROL

Abstract: Production-oriented companies that aspire to the concept of Industry 4.0 primarily focus on the increasing flexibility and reconfigurability of the entire manufacturing system. By integrating a robotic material transport/handling system that features a high level of efficiency, flexibility, and intelligence, the entire manufacturing system reaps the benefits. With that in mind, the authors propose a deep learning-based visual servoing algorithm for the intelligent control of a wheeled mobile robot. By utilizing a visual servoing algorithm, mobile robotic systems can flexibly and efficiently adapt their trajectories to real-world conditions. Moreover, deep learning algorithms allow mobile robots to learn robust visual features that make visual servoing even more applicable. The authors utilize state-of-the-art deep learning models to train the mobile robot to perform visual servoing even without distinct features that are necessary for such a system to function properly. Experimental evaluation with the own developed mobile robot RAICO – Robot with Artificial Intelligence based COgnition has shown the benefits of the proposed visual control algorithm.

Key words: *Deep learning, Visual servoing, Mobile robot, Intelligent control, Industry 4.0*

1. INTRODUCTION

The manufacturing environment interested in the benefits of the Industry 4.0 concept must achieve higher levels of autonomy, flexibility, and efficiency [1]. One of the ways these characteristics can be achieved is through the implementation of industrial mobile robots for material transport and handling operations [2]. For mobile robots to be able to accomplish these tasks in unstructured and stochastic manufacturing environments, their perception system needs to be highly accurate, efficient, and provide valuable data for decision-making, localization, and obstacle avoidance [3]. Moreover, to correctly position the workpiece within the machine tool, their final position must be highly accurate. One of the standard algorithms that can provide such accuracy is visual servoing.

Visual servoing represents a control algorithm that relies solely on visual information for the positioning of the dynamic robotic system. There exist four visual servoing categories [4], namely (i) Image-based Visual Servoing (IBVS), (ii) Position-based Visual Servoing (PBVS), (iii) Hybrid Visual Servoing (HVS), and (iv) Direct Visual Servoing (DVS). IBVS utilizes image features such as points, lines, or contours to generate velocities the robot needs to achieve. Within PBVS, the 3D pose of an object in the scene is generated and utilized to deduce the velocities. The HVS represents the combination of IBVS and PBVS, while the DVS uses entire images or some of their representations to generate velocities. Since the mobile robots most commonly used in the industry utilize standard wheels and therefore have a nonholonomic nature and constraints, the most useful algorithm is PBVS. The usefulness of the PBVS arises from the fact that the velocities are generated according to the 3D data and therefore can be directly utilized to plan the set of maneuvers necessary to forgo the nonholonomic constraints and ensure the mobile robot reaches the desired position. However, the PBVS algorithm has a non-trivial requirement regarding the estimation of the pose of the object in the scene.

Therefore, in this paper, we explore the possibility of training a deep learning model, to estimate the velocities generated by a PBVS algorithm, and therefore forgo the aforementioned requirement.

2. LITERATURE REVIEW

There are numerous scientific attempts at integrating deep learning models within visual servoing algorithms. The authors of [5] developed an intelligent IBVS algorithm by training two CNN models. The inputs to the dual AlexNet architecture are the current and the desired images, while the single output of the dual networks is the position difference, as well as the difference in the orientation regarding the Z axis. The experimental evaluation with an industrial robot shows that the desired pose is achieved with the proposed CNN-based visual servoing controller. In the paper [6], the authors propose a CNN model based on ResNet152 architecture with two additional fully connected layers at the end of the network, to predict the desired pose. The CNN model is trained by using an image generated in a simulation environment, and two loss functions are proposed – one for the pose difference and one for the image similarity difference. The experimental results show the high accuracy of the proposed visual servoing model both in simulation and on a real-world industrial robot. In reference [7], the authors analyzed the usage of a framework based on the CNN model for 3D detection of the objects in the image, which is later used for PBVS visual servoing. CNN is used to generate 2D belief maps that are used within the greedy Perspective-n-Point algorithm for the estimation of the object's 3D pose. The encoder of the CNN network is based on pretrained

VGG16 model. The PBVS servoing is performed based on the error between the estimated pose of the object in both the current and desired image. The experimental evaluation of the proposed method on a industrial robot shows that the final pose is achieved with high accuracy.

Since deep learning models have a reputation for being high in demand for computing power, which mobile robots usually do not have, the following analysis will consider light-weight efficient deep learning models utilized within mobile robotic applications. The authors [8] develop a deep learning model based on transformer architecture for depth estimation. The architecture consists of the convolution, the semantic, the transformer, and the decoder modules. Semantic information module is utilized to increase the accuracy by leveraging semantic segmentation knowledge. The proposed deep learning model achieves state-of-the-art accuracy and a processing speed of 59 FPS on the Nvidia Jetson Nano. The utilization of transformer-based architecture within mobile robot exploration farmwork is considered in [9]. The pyramid transformer encoder is used within the mapping module for the occupancy grid estimation. The estimated occupancy grid is utilized both in path planning and in state estimation. The proposed framework is tested on the mobile robot with Nvidia Jetson Nano, achieving around 0.75 FPS. The transformer architecture utilized in the visual tracking task on edge devices is described in [10]. The modified ResNet18 backbone is utilized as a feature extractor, while the acquired features are then combined within the cross-attention transformer module. The proposed network achieves state-of-the-art accuracy with a high processing speed of 55 FPS on the Jetson AGX Xavier board.

Compared to the analyzed approaches, the network proposed in this work includes an output head specially designed for the regression, and the entire model is implemented in real time on the Nivida Jetson Nano.

3. VISUAL SERVOING METHOD

In this paper, the utilized visual servoing method is based on PBVS since it is the most useful for nonholonomic mobile robot control. The method estimates the mobile robot pose based on the plain that is defined with four spheres (Fig. 1). Since the spheres are blue, their center can be distinguished with a color thresholding algorithm.

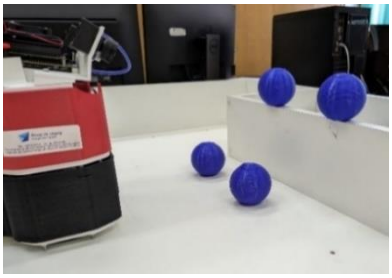


Fig. 1. The spheres used as features for the PBVS algorithm

After the homogeneous centers of spheres are detected on both current $\mathbf{p} \in \mathbb{R}^3$ and desired image ($\mathbf{p}^*$), they can be linked by estimating the homography matrix $\mathbf{H}$ (1):

$$\mathbf{p}^* = \mathbf{H}\,\mathbf{p}. \tag{1}$$

The decomposition of homography matrix (2) provides the difference between mobile robot poses (defined with translation vector $\mathbf{t}$ and rotation matrix $\mathbf{R}$) in the current and desired pose:

$$\mathbf{H} = \gamma\mathbf{K}(\mathbf{R}+\mathbf{t}\mathbf{n}^T)\mathbf{H}^{-1}, \tag{2}$$

where $\mathbf{n}$ defines the normal unit vector of the plane defined with blue spheres, $\mathbf{K}$ is the calibration matrix, and γ is the scale factor. More details regarding the decomposition and estimation methods for the homography matrix can be found in [11]. The utilized decomposed pose difference between poses is utilized in three-phase controllers to make a mobile robot move to the desired pose (Fig. 2).

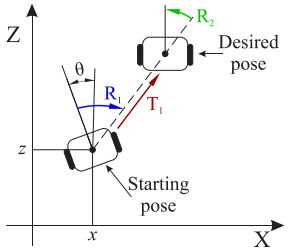


Fig. 2. The three phase algorithm for mobile robot control

The mobile robot rotates to the desired position (R_1), translates to the desired position (T_2), and achieves the desired pose by rotating (R_2). The controllers for these three phases are given in (3), (4), and (5):

$$\text{Phase \#1}: v = 0,\ \omega = k_{\omega 1} e_1, \tag{3}$$

$$\text{Phase \#2}: v = -k_v e_2,\ \omega = 0, \tag{4}$$

$$\text{Phase \#3}: v = 0,\ \omega = k_{\omega 3} e_3. \tag{5}$$

where $k_{\omega 1}$, k_v, and $k_{\omega 3}$ are control gains. The error in phase #1 (6) is defined based on the difference between orientation in the starting and desired pose, and the angle between the starting and desired position:

$$e_1 = \theta + \text{atan2}(t_x, t_z). \tag{6}$$

The error in the second phase (e_2) is defined (7) with the distance between the starting and desired pose, projected on the Z axis of the plane since the camera is inclined to a defined angle (see Fig. 1):

$$e_2 = t_z n_z. \tag{7}$$

Finally, the error in the third phase (e_3) is defined as the pure difference between the desired and current orientation (8):

$$e_3 = \theta. \tag{8}$$

3.1 PBVS based on CNN

Since the detection of features (centers of spheres), as well as the estimation of homography, can be prone to noise, resulting in errors of the difference in the pose, this process is performed with a convolutional neural network. The input of the network is the current image, while the output represents the 3×3 homography matrix ($\mathbf{H}$). The backbone of the network is ResNet18, which

transforms the input image of 800×600×3 pixels to 19×25×9 features that are flattened, and connected to a fully connected layer to produce 9 output values. The entire architecture is presented in Fig. 3. The details regarding the layers and blocks of the architecture can be found in [12].

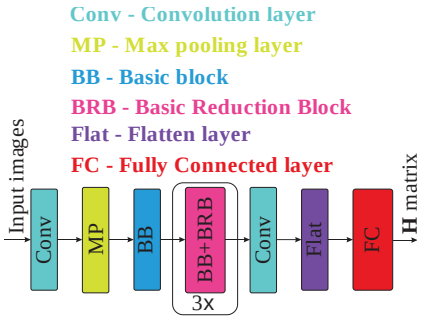


Fig. 3. Architecture of the utilized CNN network

The mean square error loss function is utilized, with a stochastic gradient descent algorithm, the learning rate of $5 \cdot 10^{-5}$, and a batch size of 16. The training was performed for 150 epochs without pretraining, by utilizing PyTorch 1.6.0. The dataset is created by utilizing the mobile robot RAICO in the laboratory model of the manufacturing environment by executing the previously explained PBVS visual servoing algorithm. Every image generated during the visual servoing control is saved with corresponding values of the homography matrix. The overall dataset contains 606 images utilized for training. After the training is completed, the CNN is converted to ONNX and TensorRT so that it can be utilized in real-time on Nvidia Jetson Nano. The convergence curve of the loss function during the training process can be seen in Fig. 4.

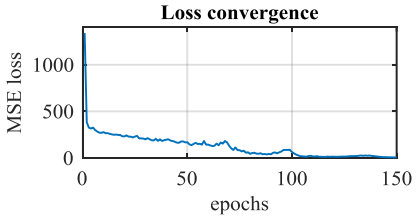


Fig. 4. Convergence curve of the MSE loss value

4. EXPERIMENTAL RESULTS

The experimental evaluation is performed in the laboratory model of the manufacturing environment, by using the mobile robot RAICO. The same desired image (Fig 5.) is utilized as the one from the dataset for training the neural network, the while mobile robot is set to an initial pose (23cm, -6.5cm, -10°).

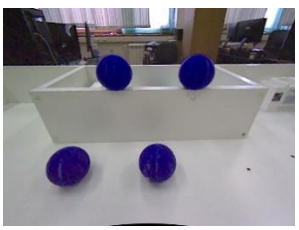


Fig. 5. Desired image utilized for CNN-based PBVS

Afterwards, the visual servoing control based on CNN is utilized to achieve the desired pose. Initial image, as well as images generated at the end of each phase of the visual servoing process, are shown in Fig. 6.

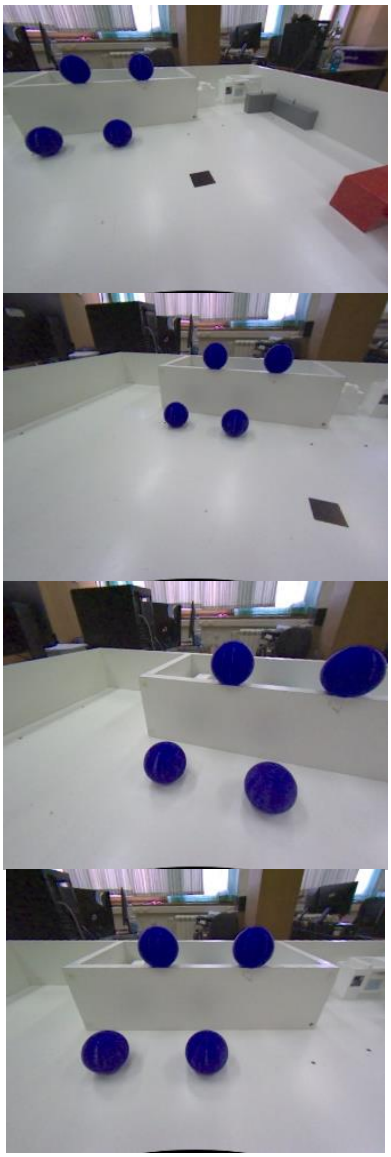


Fig. 6. Images generated during CNN-based PBVS

As can be seen, the mobile robot translates towards the target pose and achieves it with an error of (3cm, -0.8cm, -2°). The achieved error is comparable with the error in the standard PBVS controller, which indicates that the CNN model learned visual features well, and can approximate the process of estimating the homography matrix. The convergence curves of each phase of the algorithm are shown in Fig. 7. As can be seen, all the curves have a trend similar to linear, which is expected for this type of PBVS controller. The difference in scale between phases concerns the fact that the error in phases #1 and #3 are defined in [°], whereas the error in phase #2 is in [m]. All phases have different numbers of iterations, depending on the distance the mobile robot needs to travel in that phase. The inference time of the CNN model is around 15 FPS, which is fast enough for the visual servoing controller.

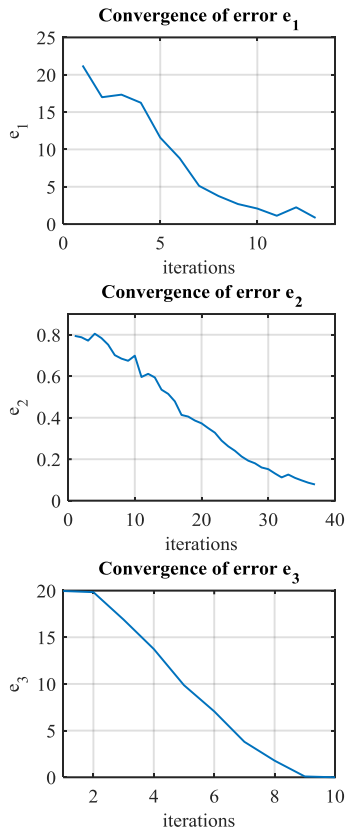


Fig. 7. Convergence curves for all phases of the CNN-based PBVS algorithm

5. CONCLUSION

In this paper, the authors presented the novel visual servoing controller based on deep learning approach. The PBVS controller based on three phases is implemented on the mobile robot RAICO, and images are generated during the several runs of the algorithm for the training of neural networks. The homography matrix utilized to estimate the difference in the desired and current pose is generated based on the Convolutional Neural Network. Trained CNN is then utilized directly in the visual servoing controller, eliminating the need for the feature extraction and homography estimation process. The experimental evaluation is performed on the real-world mobile robot RAICO, and the results show the validity of the CNN-based visual servoing controller. Future research includes the training of the CNN model independent of the desired image.

6. REFERENCES

[1] Ghobakhloo, M.: Industry 4.0, digitization, and opportunities for sustainability, Journal of cleaner production, Vol. 252, p. 119869, 2020.

[2] Fragapane, G., Ivanov, D., Peron, M., Sgarbossa, F., Strandhagen, J. O.: Increasing flexibility and productivity in Industry 4.0 production networks with autonomous mobile robots and smart intralogistics, Annals of operations research, Vol. 308, No. 1, pp. 125–143, 2022.

[3] Ghodsian, N., Benfriha, K., Olabi, A., Gopinath, V., Arnou, A.: Mobile manipulators in Industry 4.0: A review of developments for industrial applications, Sensors, Vol. 23, No. 19, p. 8026, 2023.

[4] Jokić, A., Petrović, M., Miljković, Z.: Methods for visual servoing of robotic systems: A state of the art survey (In Serbian), Tehnika, Vol. 73, No. 6, pp. 801–816, 2018.

[5] Liu, J., Li, Y.: An image based visual servo approach with deep learning for robotic manipulation, arXiv:1909.07727, 2019.

[6] He, Y., Gao, J., Chen, Y.: Deep learning-based pose prediction for visual servoing of robotic manipulators using image similarity, Neurocomputing, Vol. 491, pp. 343–352, 2022.

[7] Al-Shanoon, A., Lang, H.: Robotic manipulation based on 3-D visual servoing and deep neural networks, Robotics and Autonomous Systems, Vol. 152, p. 104041, 2022.

[8] Liu, X., Wei, W., Liu, C., Peng, Y., Huang, J., Li, J.: Real-time monocular depth estimation merging vision transformers on edge devices for aiot, IEEE Transactions on Instrumentation and Measurement, Vol. 72, pp. 1–9, 2023.

[9] Zhang, T., Hu, X., Xiao, J., Zhang, G.: Tvenet: Transformer-based visual exploration network for mobile robot in unseen environment, IEEE Access, Vol. 10, pp. 62056–62072, 2022.

[10] Chen, X., Kang, B., Wang, D., Li, D., Lu, H.: Efficient visual tracking via hierarchical cross-attention transformer, in European Conference on Computer Vision, 2022, pp. 461–477.

[11] Jokic, A., Khazraei, A., Petrovic, M., Jakovljevic, Z., Pajic, M.: Cyber-Attacks on Wheeled Mobile Robotic Systems with Visual Servoing Control, in IEEE/RSJ International Conference on Intelligent Robots and Systems (IROS), 2023, pp. 6342–6348.

[12] Petrović, M., Miljković, Z., Jokić, A.: Efficient Machine Learning of Mobile Robotic Systems based on Convolutional Neural Networks, In: Azar, A.T., Koubaa, A. (eds), Artificial intelligence for Robotics and Autonomous Systems, Studies in Computational Intelligence, Vol. 1093, Springer, Charm, 2023.

ACKNOWLEDGMENTS

This research has been financially supported by the Ministry of Science, Technological Development, and Innovation of the Serbian Government, through the project "Integrated research in macro, micro, and nano mechanical engineering – Deep learning and cyber security of cyber-physical systems within Industry 4.0" (contract No. 451-03-65/2024-03/200105, 05/02/2024).

Authors:

MSc Aleksandar Jokić, MSc Đorđe Jevtić, MSc Katarina Brenjo, PhD Milica Petrović, PhD Zoran Miljković, University of Belgrade, Faculty of Mechanical Engineering, Production Engineering Department, Kraljice Marije 16, 11120 Belgrade, Serbia.

E-mail: ajokic@mas.bg.ac.rs; drjevtic@mas.bg.ac.rs; kbrenjo@mas.bg.ac.rs; mmpetrovic@mas.bg.ac.rs; zmiljkovic@mas.bg.ac.rs

MMA 2024 FLEXIBLE TECHNOLOGIES

15th INTERNATIONAL SCIENTIFIC CONFERENCE
NOVI SAD, SERBIA, SEPTEMBER 24-26, 2024

Original research paper https://doi.org/10.24867/MMA-2024-02-012

Knežev, M., Mlađenović, C., Marinković, D., Calin, A., Živković, A.

FINITE ELEMENT ANALYSIS OF TURNING CUTTING TOOL

Abstract: *Machining is a complex process involving multiple factors that affect the accuracy and quality of the machining. The occurrence of tool vibrations is one of the most influential parameters that negatively impacts the lifespan of cutting tools, the quality of machined parts, and machining accuracy. This recognizable phenomenon occurs in many machining operations, including turning, milling, drilling, etc. The aim of this paper is to examine the static and dynamic behavior of the turning tool, as well as to compare the obtained computational and theoretical results. The workpiece material used in the experiments is tool steel 100MNCrW4, and the cutting tool material is tungsten carbide (DNMG 150608 MGS).*

Key words: *Deflection, Finite elements, Cutting tools, Modal Analysis*

1. INTRODUCTION

The modern machining industry is focused on achieving high machining quality, high accuracy of workpieces, high productivity, and cost-effectiveness. During turning operations, vibrations frequently occur, leading to a decrease in the quality and accuracy of the machined surface, damage to the cutting tool, and irritating noise. Under certain tool loads, the amplitude of vibrations continuously increases, leading to the occurrence of self-excited vibrations. The practice to avoid self-excited vibrations is reduced to using optimal machining regimes and the length of the tool holder overhang during turning [1].

In metal cutting tool faces, including the rake face, major flank face and minor flank face are subjected to both shear and normal loads due to the pressure between the chip and the machined surfaces, friction between the tool face, chip, and the machined surface [2] as shown in Fig. 1.

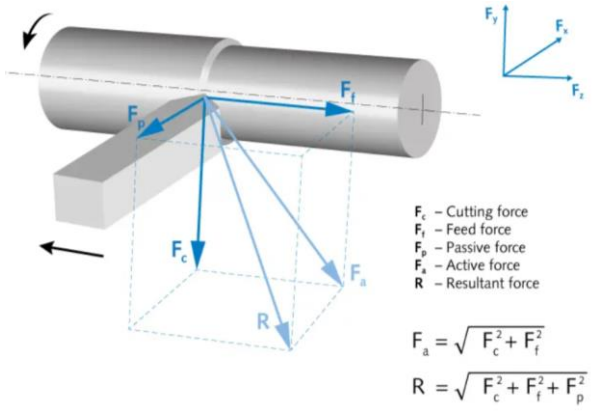


Fig. 1. The graphic displays of cutting forces [3]

The cutting force in turning refers to the main cutting force F_c which is tangential and often the largest force (except hard turning). As displayed in Fig. 1, in turning, F_c is the main cutting force acting tangentially to the rotational direction. While F_c, the feed force F_f and the passive force F_p can be measured directly during turning, the active Force F_a and the resultant force R are calculated. The active force is the vectorial sum of the main cutting force F_c and feed force F_f. It is sometimes used to compare different process settings. The resultant force is the vectorial sum of the main cutting force Fc, feed force F_f, and the passive force F_p and applied to compare different process settings as well [3].

Previous investigations [4, 5] have showed that in about 50% of all cases tool life of carbide tools expires just because of the tool fracture. It has been reported that about 15% of tool breakage is the result of the wrong choice of cutting data [6]. Generally, when induced stress in a cutting tool reaches a critical value, tool failure will occur. The critical load or critical stress for a certain type of cutting tool is dependent on the tool material and will not be changed according to cutting parameters. Therefore, the state of stress in a cutting tool would be the best criterion for predicting premature tool failure [6]

Chiou and colleagues [7] presented a new dynamic model of the cutting process to investigate the mechanism of self-excited vibrations. vibrations that occur alongside wear on the tool's flank surface. The model shows the impact of cutting force on tool wear occurrence. Laplace domain analysis provides an analytical solution for stability limits regarding the main characteristics of the machine and cutting regimes.

2. FINITE ELEMENT ANALYSES OF THE CUTTING TOOL

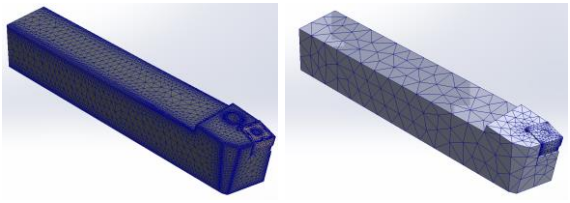
2.1 Static analysis

The assumptions made for the static finite element analysis are as follows:

- The orthogonal machining process is steady state.
- The tool is a rigid body.
- The workpiece material is elastic.

Static analysis calculates the effects of static loading conditions on the structure, neglecting inertia and damping effects, such as those caused by time-varying loads. In static analysis, the stiffness matrix for each element is calculated according to the given specifications.

Generating model geometry is one of the most difficult aspects of FEA. A common mistake among FEA users is assuming that a computer-aided design (CAD) model created as part of the product design process can be plugged directly into an FEA study. CAD models typically include tremendous detail, which would take hours or days of processing to incorporate into a simulation analysis. However, much of this detail is often unnecessary in FEA. Worse, the inclusion of unnecessary details in an FEA model can result in poor quality meshes, inefficient simulations run times and inaccurate results. Perhaps the most common details that can be immediately removed from most CAD models are the fillets, rounds, carvings, etc.



a) b)

Fig. 2. Mode complexity a) before b) after removing unnecessary object features

The number of finite elements to be selected for model discretization is related to the desired accuracy. Figure 2 shows significant reduction in the number of finite elements, without affecting accuracy. Before reduction number was 92173, after is 6709, it significantly reduces calculation time.

The mechanical properties of the insert and tool holder are given in Table 1, cutting conditions, and cutting forces are calculated and given in Table 2.

	Material properties	
	Tool holder	Insert
Density [kg/m^3]	7850	15700
Poisson's ration	0.3	0.28
Yield strength [MPa]	620	2683
Young's modulus	207000	683000

Table 1. Mechanical properties of the insert and tool holder.

Cutting conditions	Cutting forces
v=180 m/min	F_c=603 N
f=0.19 mm/o	F_p=298 N
a=0.6 mm	F_f=149 N

Table 2. Mechanical properties of the insert and tool holder.

During the analyses, cutting forces are assumed to be uniformly distributed loads that act onto the nose of insert. Fig. 3 shows the insert and the components of the resultant force in three axes and Fig. 4 shows the finite element model with applied forces and boundary conditions.

Static analysis helps to identify regions where stress (Fig. 5) and displacement (Fig. 6) values reach their maximum. These regions are highlighted to determine the most critical zones, which will be used in the dynamic analysis.

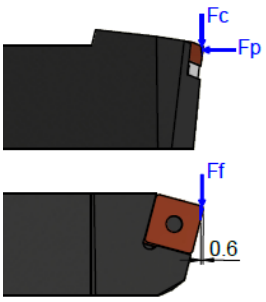


Fig. 3. Schematic model of the insert and the components of the resultant force

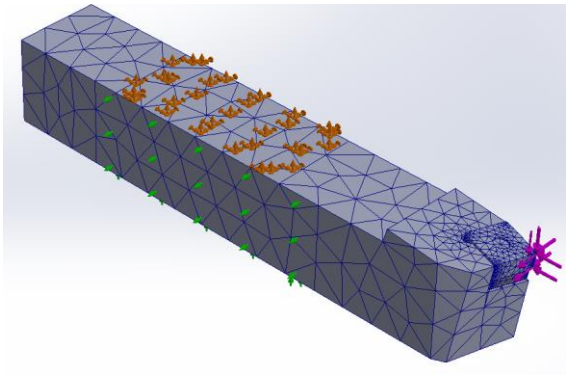


Fig. 4. Finite element model of the insert and the components of the resultant force

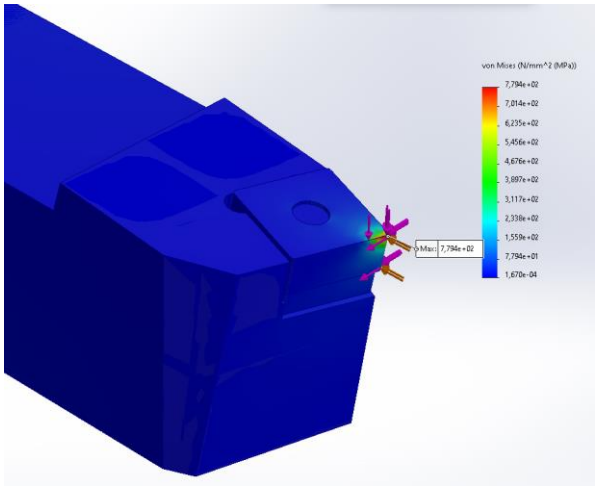


Fig. 5. Finite element model results Stress

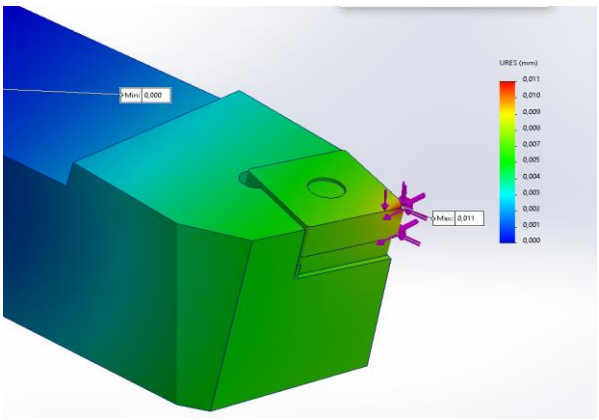


Fig. 6. Finite element model results Deflection

2.3 Modal analysis

Modal analysis represents the study of the dynamic properties of the observed system in the frequency domain. The application of modal analysis in appropriate finite element method-based software allows for the testing, optimization, and validation of various systems [8, 9]. It is widely used in the automotive industry, aerospace, construction, mechanical engineering, and even in the musical instrument manufacturing industry, among others. In this study, modal analysis was performed, and the maximum frequency obtained at a certain overhang value (Table 3).

Set	Frequency [Hz]
1.	6102
2.	6229
3.	11665
4.	12029
5.	14728

Table 3. Modal analysis

Natural frequencies and mode shapes are important parameters for dynamic loading conditions. Stresses obtained from modal analysis do not represent the actual stresses in the cutting tool but provide an indication of the relative stress distributions for each mode. Amplitude values are normalized relative to the stiffness matrix in modal analysis. The natural frequencies and mode shapes are shown in Fig. 7 and Fig. 8.

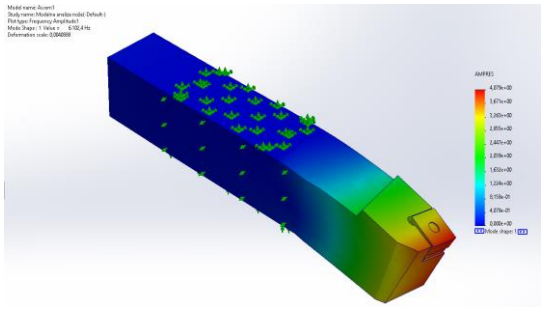


Fig. 7. Natural frequencies and mode shapes for modal analysis Mode 1 *f*=6102 Hz

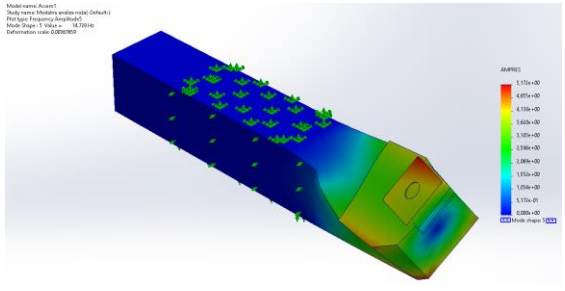


Fig. 8. Natural frequencies and mode shapes for modal analysis Mode 5 *f*=14728 Hz

Harmonic response analysis is done by including the cutting forces that act on insert (Table 2) into the model at this natural frequency. In Fig. 9 Von Misses Stress of the cutting edge in harmonic response analysis are shown. In Fig. 10 displacements in y axes, and Fig. 11 total displacement are shown.

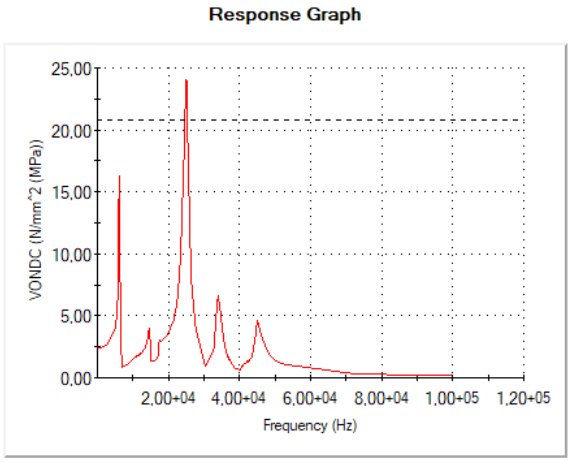


Fig. 9. Von Misses Stress of the cutting edge in harmonic response analysis

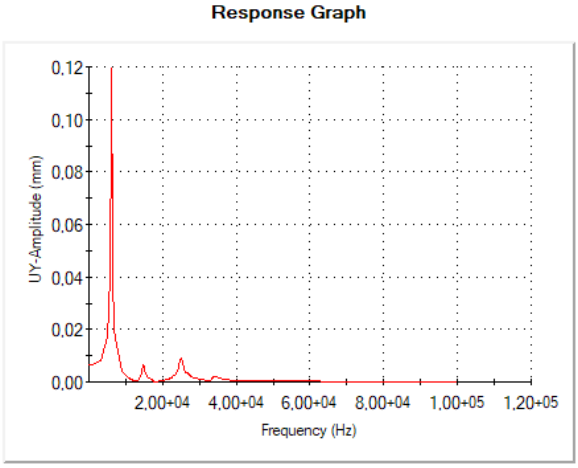


Fig. 10. Displacements of the cutting edge in harmonic response analysis in Y axis

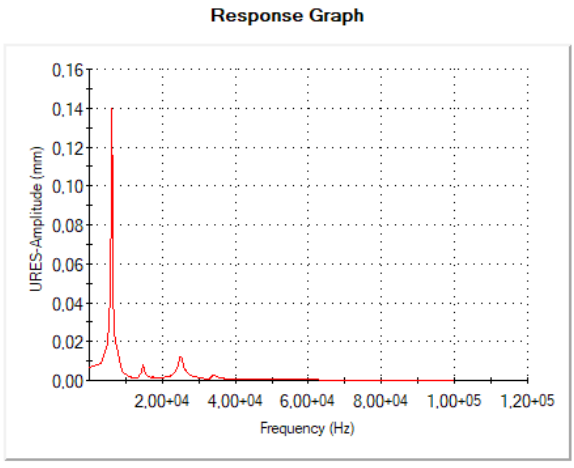


Fig. 11. Total Displacements of the cutting edge in harmonic response analysis.

The displacements and the stresses obtained from the harmonic response analysis are then evaluated and material stress is calculated. This calculated stress is compared with the material yield strength of the insert material and the tool fracture is determined.

3. FINAL REMARKS

To improve the construction of tools, number of authors deal with the problem of static and dynamic behavior of tools in exploitation. Already in the tool design itself, it is especially important to systematically predict the interconnected effects of static and dynamic characteristics for different exploitation conditions. The effects of the static and dynamic behavior of the tool must be predicted with great certainty at the design stage. To achieve the most favorable construction, the defined static and dynamic model must consider a number of parameters that influence the behavior of the corresponding bearing.

Summarizing the research presented in this paper, it can be concluded that a mathematical model based on the finite element method has been developed to predict the static and dynamic behavior of the tool holder. The advantage of such models is the ability to predict the behavior of the tool holder during operation, at the design stage.

Static analysis has shown that the maximum stresses occurring on the cutting edge are 779 MPa, which is well below the Yield Stress of insert 2686 MPa, meaning the safety factor is approximately 3.5. This implies that there is no danger of tool failure.

Modal analysis has shown that the first natural frequency is 6102 Hz, this frequency exceeds the technical capabilities of the machine tool.

Harmonic response analysis is done by including the cutting forces into the model at this natural frequency.

4. REFERENCES

[1] Sam Paul, P., Lawrence, G., Yadav, R.K., Mohankrishnan, N.V., Nair, N., Vasanth, X.A. Analysis of dynamic characteristics of boring tool holder, International Conference on Advances in Manufacturing and Materials Engineering, AMME, pp. 2283-2292, 2014.

[2] Cemal Cakir, M., Yahya, I.: Finite element analysis of cutting tools prior to fracture in hard turning operations, Material and Design, Vol. 26, No. 2, pp. 105-112, 2005.

[3] https://www.kistler.com/GB/en/cutting-forces-in-turning-operations/C00000103 June 10th, 2024.

[4] Kals, H.J.J.: Definition and measurement of strength and toughness behavior of carbides, Proceedings of the international conference on hard material tool technology, pp. 260-274, Pittsburg USA, Eindhoven, 22-24 Jun, 1976.

[5] Tlusty, J., Masood, Z.: Chipping and breakage of carbide tools, Journal of Manufacturing Science and Engineering, Vol 100, No. 4, pp. 403-412, 1978.

[6] Zhou, J., M., Anderson, M., Stahl J.,E.: Cutting tool fracture and strength evaluation by stress identification, part I, stress modal. Int Mach Tools Manufact, Vol 12, pp. 101–1714, 1997.

[7] Chiou, Y., S., Chung, E., S., Liang, S., Y.: Analysis of tool wear effect on chatter stability in turning, International Journal of Mechanical Sciences, Vol. 37 No. 4, pp. 391-404, 1995.

[8] Knežev, M., Živković, A., Mlađenović, C., Marinković, D., Ilić, V., Moravec, M.: Finite element and experimental modal analysis of high-speed spindle, 16th International Conference on Accomplish in Mechanical and Industrial Engineering Demi, Banja Luka, pp. 60-63, 2023.

[9] Knežev, M., Živković, A., Marinković, D., Mlađenović, C., Calin, A., Ilić, V.: Modal analysis of motorized spindle using finite element method, Journal of Production Engineering, Vol. 26 No. 1, pp. 9-12, 2023.

ACKNOWLEDGMENTS

The paper presents a part of the research results of the project "Management of machining process parameters using artificial intelligence tools in production" No. 000827481 2024 09418 003 000 000 001 01 001, supported by the Provincial Secretariat for Higher Education and Scientific Research of the Autonomous Province of Vojvodina.

Authors:

PhD Miloš Knežev, PhD Cvijetin Mlađenović, MSc Dejan Marinković, PhD Aleksandar Živković, University of Novi Sad, Faculty of Technical Sciences, Trg Dositeja Obradovica 6, 21000 Novi Sad, Serbia, Phone.: +381 21 485-24-76.

E-mail: knezev@uns.ac.rs; mladja@uns.ac.rs; dejan.marinkovic@uns.ac.rs; acoz@uns.ac.rs

PhD Andrei Calin, University Politehnica of Bucharest, Faculty of Mechanical Engineering and Mechatronics, Splaiul Independenceei 313, 060042 Bucharest, Romania, Phone.: +40-21402 91 00.

E-mail: andrei.calin@upb.ro

MMA 2024
FLEXIBLE TECHNOLOGIES

15th INTERNATIONAL SCIENTIFIC CONFERENCE
NOVI SAD, SERBIA, SEPTEMBER 24-26, 2024

Original research paper https://doi.org/10.24867/MMA-2024-02-013

Nešovanović, Lj., Živanović, S., Konjević, P.

INACCURACY ANALYSIS OF CHEBYSHEV'S MECHANISM

Abstract: *Converting rotary motion into rectilinear motion can be very useful in mechanical applications. This type of conversion is mostly achieved using specific types of joints. However, it can be convenient to use mechanisms that can convert rotary motion into rectilinear motion for a specific engineering purpose. The mechanisms with this possibility are called Straight-line generators. The mechanism described in this paper is part of this group, and it is called Chebyshev's mechanism. Chebyshev's mechanism consists of four connected links with proportional dimensions. It is important to point out that this mechanism and most mechanisms from the Straight-line generators group do not generate the perfect straight line. The generated line is an approximate straight line with a changeable deviation from the perfect straight line. This paper shows how the parameters of the mechanism impact the deviation, how the generated line can be described, and what the generated line specifics are.*
Key words: *Straight-line generators, Chebyshev's mechanism, proportional, approximate.*

1. INTRODUCTION

This paper analyzes Chebyshev's mechanism, which represents the straight-line generator group. The mechanisms from this group have the ability to transform the rotary motion of linkages into the rectilinear motion of the desired element or point [1, 2]. Three main types of Straight-Line generators are elliptical, lemniscoidal, and conchoidal [3]. This paper focuses on Chebushev's mechanism, which is a lemniscoidal Straight-Line generator. The lemniscoidal mechanisms got the name by lemniscates, which is Complex line consisting of points of a connecting rod of a four-hinge mechanism [3].

One of the first representatives of lemniscoidal mechanisms is the Watts parallelogram. Two known types of Watts parallelogram are reduced Fig. 1 a) and full Fig. 1 b). The deviation from a straight line of Watts parallelogram was close to 2mm [3].

The mechanism, which is an improved version of Watts parallelogram, is Chebyshev's mechanism. The similarity between those two mechanisms is that both generate approximately straight line. This means that additional improvement is needed to achieve a perfect straight line, which is achieved with the Peaucelliers mechanism, Fig. 1 c).

Chebyshev's mechanism, an upgraded version of Watt's linkage, is directly used as a steam-engine machine [3]. However, the considered mechanism is mostly used in complex machines as a subassembly. Some of the applications of this mechanism in the vehicle industry are shown in [4, 5]. Chebyshev's mechanism can be used as a passive translation rotary joint as part of a novel parallel mechanism, as shown in [6, 7].

Compared to other Straight-Line generators, Chebyshev's mechanism provides a quality balance between mechanism simplicity and accuracy. With this in mind, this paper analyzes Chebyshev's mechanism further, explaining how the mechanism works, with a special emphasis on the inaccuracy analysis of the considered mechanism.

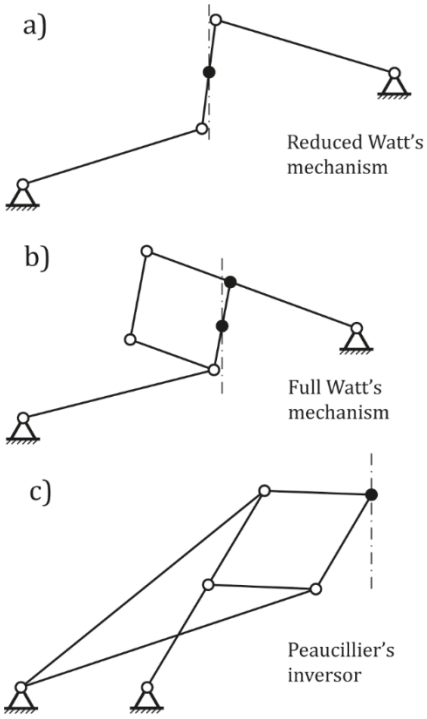


Fig. 1. Straight-line Generators [3]

2. APPROXIMATELY STRAIGHT-LINE GENERATION USING THE CHEBYSHEV'S MECHANISM

This chapter will explain how Chebyshev's mechanism works and the mechanism's characteristics. As previously mentioned, generating a perfectly straight line using Chebyshev's mechanism is impossible. The line generated using this mechanism is a line that deviations from a straight line.

Chebyshev's mechanism consists of four links connected with the rotary joints, shown in Fig. 2. Each rotary joint allows 1 degree of freedom (DOF). Three out of four links are movable (links AD, BC, and CD). The

last link is fixed and does not move (link AB). The links AD and BC have the same dimensions and are partially movable. The link CD is the one with the smallest size and is completely movable.

The rotary joints A and B are not movable and present the centres of two circles described with rotary joints D and C, respectively. The radius of these two circles has the value c, one of the parameters of Chebyshev's mechanism. As mentioned, the shortest link connects the rotary joints C and D.

With this in mind, it can be concluded that the shortest link describes the most complex motion similar to lemniscates. For Chebyshev's mechanism to work properly, it is of great importance to have the right proportion between mechanism parameters. The parameters of the mechanism are the lengths of its linkages. The parameter *b* describes the length between rotary joints A and B, parameter *a* describes the dimension between rotary joints C and D, and the last parameter describes the length between rotary joints C and B, as well as A and D. Proportion between these three mechanism parameters, is strictly defined and shown below.

$$a : b : c = 2 : 4 : 5 \quad (1)$$

The most important point of Chebyshev's mechanism is located exactly on the half of the link CD. This point is shown in Fig. 2 and signed as point P. Moving the links of the considered mechanism makes it possible to generate the approximately straight line with the characteristic point P on the mechanism. Approximately line generation is only possible to achieve if the previously shown proportion is implemented in the dimensions of the mechanism.

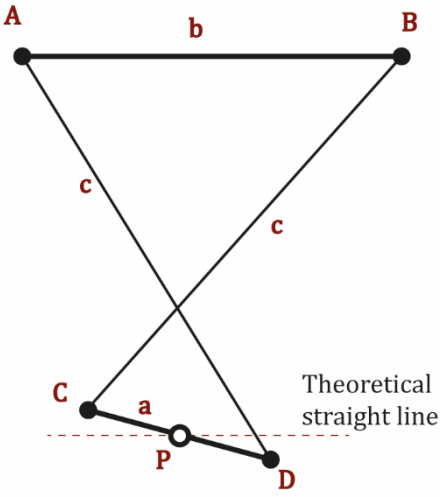


Fig. 2. Chebyshev's mechanism

Chebyshev's mechanism generates an approximately straight line by rotating link BC around point B and consequently rotating link AD around point A. With these two rotations, the link CD describes the lemniscates, and point P generates the approximately straight line. The considered mechanism with described movements is shown in Fig. 3

3. STRAIGHT LINE DEVIATION ACHIEVED USING THE CHEBYSHEV'S MECHANISM

As mentioned in previous chapters, Chebyshev's mechanism is an approximate straight-line generator, which means that while generating the straight line, this mechanism shows specific deviation from the straight line. This chapter explains the deviation profile and generated curve specific.

The approximate straight line and zone of interest are created by moving the shortest link from one vertical position to another. The first vertical position of the considered mechanism's shortest link (CD) is achieved when point C is closest to link AB and points A, C, and D are aligned and connected, forming the vertical line, shown in Fig. 4 a). The second vertical position is achieved when point D is closest to link AB and points B, D, and C are aligned and connected, forming the vertical line, shown in Fig. 4 b). These two positions present the starting and ending positions between which the movement of the point P creates an approximately straight line.

The line generated using the previously explained procedure is shown in Fig. 5. While analyzing the generated complex line, it is easy to conclude that it has sinusoidal characteristics. It is shown that the complex line achieves the minimum distance from link AB in three points. These three points would be part of the theoretical perfect straight line. All other points generated using Chebyshev's mechanism deviate from this theoretical straight line.

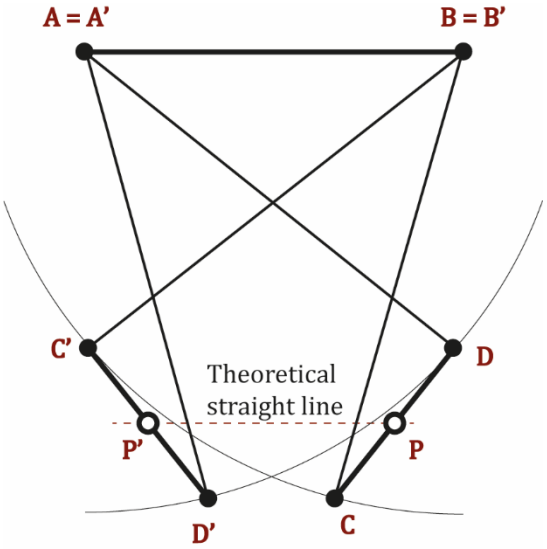


Fig. 3. Movements of Chebyshev's mechanism

The previously mentioned starting and ending positions are two out of three positions, achieving the minimum distance from link AB to point P. The third position of the minimum distance between point P and link AB is achieved when the distance between point C and link AB is equal to the distance between point D and link AB, as shown in Fig. 4 c).

Symmetry is one of the most important characteristics of the complex line generated using Chebyshev's mechanism. This characteristic simplifies the problem of how to approximate the deviation

between the generated line and the perfect straight line, which will be the topic of future research.

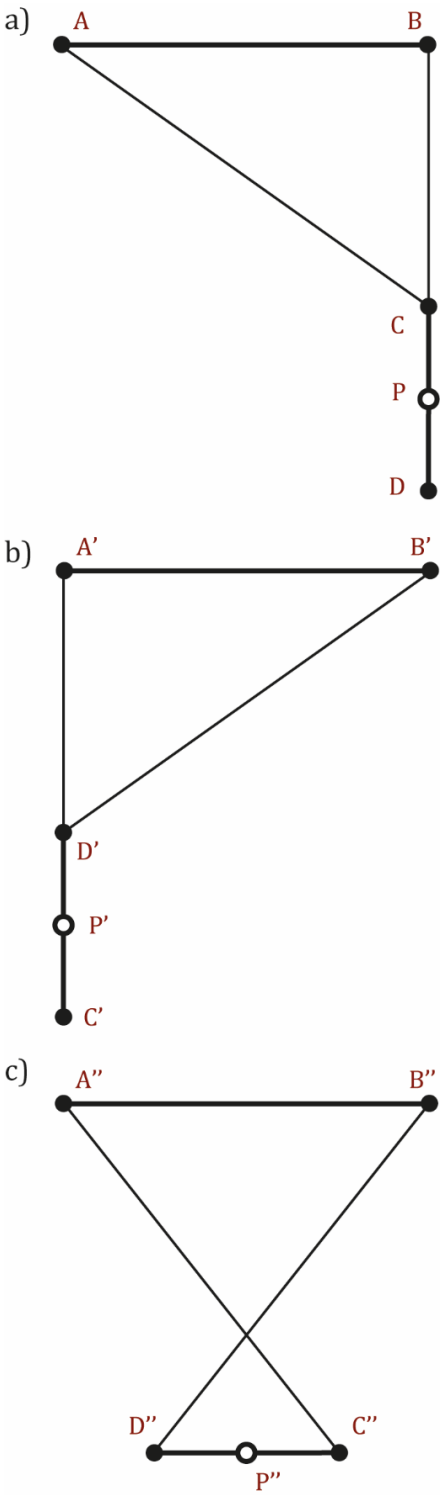


Fig. 4. The Chebyshev's mechanism positions with minimum distance between point P and link AB

Fig. 5 shows that the line created using the considered mechanism has two maximum deviations from the theoretically straight line. This means that in two positions, the mechanism while generating the approximate straight line, describes the highest inaccuracy. The maximum deviation is one of the most important parameters. As previously mentioned, the generated curve has a sinusoidal curve, so considering this information, it is concluded that the maximum deviation value equals the curve amplitude.

Considering the previously explained mechanism parameters, the proportion can be simplified, and parameters *a*, *b*, and *c* can be presented as one parameter h multiplied with specific constant values. With this considered, Chebyshev's mechanism proportion has a new shape, as shown below.

$$a : b : c = h : 2 * h : 2.5 * h \qquad (2)$$

The mechanism dimensions are now connected to the parameter *h*. The next important topic is to show the connection between parameter *h* and the amplitude of the generated curve. This connection is shown in Fig. 6, where it can be seen that the amplitude follows the parameter *h*.

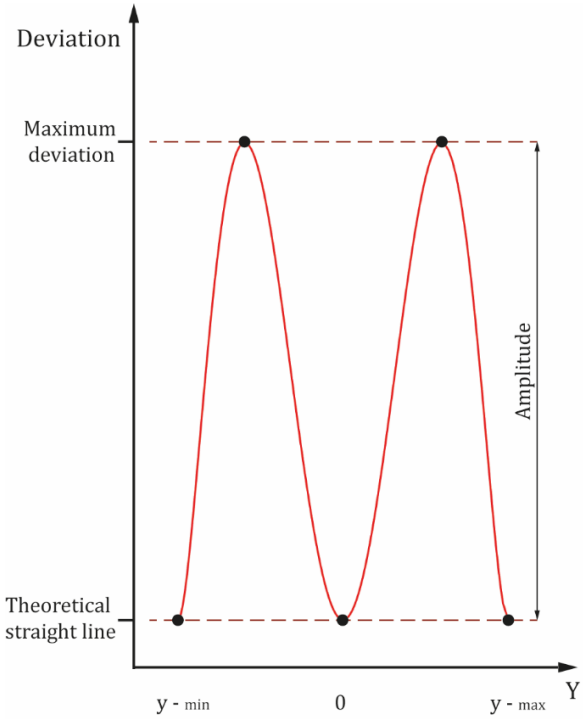


Fig. 5. The line created using the Chebyshev's mechanism

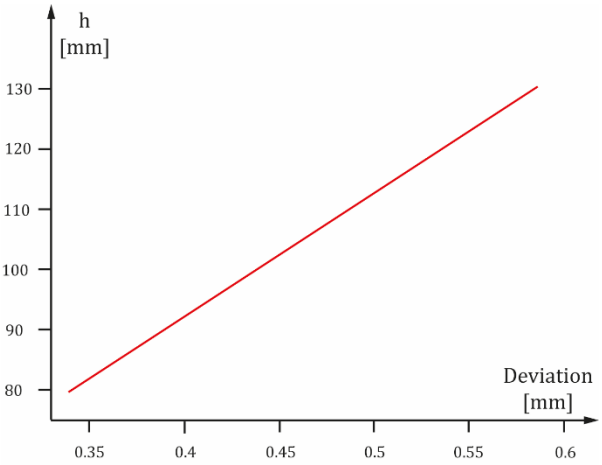


Fig. 6. The connection between parameter *h* and deviations amplitude

Considering the connection between parameter *h* and the generated line amplitude, it can be concluded that the amplitude is linearly connected to the mechanism parameter *h*. A linear increase of amplitude follows the linear increase of parameter *h's* value.

5. CONCLUSION

This paper, in detail, shows the functionality and characteristics of Chebyshev's mechanism. It explains the most important parameters of the considered mechanism and how they are connected. The proportional connection between mechanism parameters allows the considered mechanism to become an approximate straight-line generator.

The main topic of this paper is to show and analyze the inaccuracy that the considered mechanism generates while describing a straight line. It is confirmed that the line described using Chebyshev's mechanism has sinusoidal characteristics. The mechanism does not derivate from the straight line in three positions, and in two positions, the inaccuracy is highest. One of the most important conclusions of this paper is that mechanisms parameter h and generated curve amplitude are linearly connected.

The research presented in this paper confers the base for future research, which will include the design of a parallel mechanism based on Chebyshev's mechanism. The initial papers about this topic have already been published, presenting how Chebyshev's mechanism will be used. One future research study will focus on solving the inverse geometry problem of the parallel mechanism based on Chebyshev's mechanism. The important thing to point out is that the presented results about deviation from the straight-line using Chebyshev's mechanism will have an impact on the solution to the inverse geometry problem. The presented results can be used in the control of the parallel mechanism based on Chebyshev's mechanism to cancel mechanisms' inaccuracy.

6. REFERENCES

[1] Shigley, J.E., Uicker J. J., Pennock, G.R., *Theory of Machines and Mechanisms*, Oxford University Press 198 Madison Avenue, New York, 1980.

[2] Klyukin, D., Shchedrin, M., Tarabarin, V., *Straight-Line Mechanisms in the Collection of Bauman Moscow State Technical University*, The 13th World Congress in Mechanism and Machine Science, A21_451, Member Organization Mexico of IFToMM, Guanajuato, 2011.

[3] Glavonjić, M., Milutinović, D., Živanović, S., *Troosni paralelni mehanizmi sa specifičnim rešenjima pasivnog translatornog zgloba.* (In Serbian) Proceeding of 32th Jupiter Conference, ppt. 3.1-3.4, Zlatibor, University of Belgrade, Faculty of Mechanical Engineering, 2006.

[4] Manickavelan, K., Balkeshwar, S., Sellappan, N., *Design, Fabrication and Analysis of Four Bar Walking Machine Based on Chebyshev's Parallel Motion Mechanism*, European International Journal of Science and Technology, Vol. 3 No. 8., 2014.

[5] Nayak, A., Gupte, V., Singru, P., *Recent Advances in Machines and Mechanisms*, Springer, 2022.

[6] Nešovanović, Lj., Živanović, S., *Conceptual design of a novel mechanism with parallel kinematics based on Chebyshev's linkage*, Proceedings DEMI 2023, pp. 35–40, Banja Luka, Full Prof. Aleksandar Milašinović, PhD, 2023.

[7] Nešovanović, Lj., Živanović, S**.,** *Verification of kinematic joints on a physical prototype of a novel parallel mechanism based on Chebyshev's linkage*, Proceedings of 39th International Conference on Production Engineering of Serbia, pp. 246-251, Novi Sad, University of Novi Sad, Faculty of technical science, 2023.

ACKNOWLEDGMENTS

The presented research was supported by the Ministry of Education, Science and Technological Development of the Republic of Serbia by contract no. 451-03-65/2024-03/200105 dated 2024 and by contract 451-03-66/2024-03/ 200066 dated 2024.

Authors:

MSc Ljubomir Nešovanović, MSc Predrag Konjević, LOLA Institute, Kneza Višeslava 70A, 11030, Belgrade, Serbia, Phone.: +381 65 838-94-14.
E-mail: ljubomir.nesovanovic@li.rs; predrag.konjevic@li.rs

PhD Saša Živanović, University of Belgrade, Faculty of Mechanical Engineering, Kraljice Marije 16, 11000 Beograd, Serbia, Phone.: +381 11 3302-423.
E-mail: szivanovic@mas.bg.ac.rs

MMA 2024 FLEXIBLE TECHNOLOGIES

15th INTERNATIONAL SCIENTIFIC CONFERENCE
NOVI SAD, SERBIA, SEPTEMBER 24-26, 2024

Original research paper https://doi.org/10.24867/MMA-2024-02-014

Suvajac, Z., Nedeljkovic, D., Jakovljevic, Z.

OBJECT POSITION AND ORIENTATION DETECTION IN ASSEMBLY TASKS – AN APPROACH BASED ON YOLOV8 ALGORITHM

Abstract: *Automated assembly plays a crucial role in today's manufacturing, facilitating high precision, increased efficiency, and reduced production costs. Tasks such as manipulation and mating often require the information about position and orientation of parts. In computer vision-based systems, this information is obtained through image processing and analysis which can be based on different techniques. Deep learning offers significant advantages over traditional image processing methods, particularly in systems where images are the main source of information. These advantages include enhanced feature extraction capabilities, higher accuracy in recognizing complex patterns, and the ability to learn and improve through the analysis of large datasets. In this work, YOLOv8 model, primarily based on convolutional layers, is employed to identify the position and orientation of objects in the scene. Real-world images were used to fine-tune YOLOv8 model. The performance evaluation was carried out by comparing the ground truth and estimated position and orientation. The application of YOLOv8 model proved to be effective, achieving high position and orientation accuracy.*

Key words: *Automatic assembly, Vision systems, Object position and orientation detection, Deep learning, YOLOv8*

1. INTRODUCTION

Automated assembly has become indispensable in modern manufacturing, ensuring high precision, enhanced efficiency, and substantial cost savings. The ability to automate complex tasks that traditionally required human intervention has led to significant improvements in manufacturing processes across various industries. The applications that include manipulation and mating tasks often depend on information about parts' position and orientation. In computer vision-based systems this information can be obtained using different techniques for image processing and analysis.

Traditional image analysis techniques have been widely used to address these challenges. Various methods utilizing Hough transform [1] have been employed to detect object position and orientation [2, 3]. A template matching technique based on the proposed edge detector and a threshold that defines the number of object edges has also been used for this task [4].

However, these techniques have shown drawbacks in dealing with complex patterns, varied environments, illumination changes, etc. In such conditions, Deep Learning (DL) techniques prove to be effective, providing significant advantages over traditional methods. With advanced feature extraction capabilities and capacity to learn from large datasets, DL techniques provide higher accuracy and robustness in recognizing and processing visual information. Since images are the main carriers of information in computer vision tasks, most DL techniques designed for these purposes rely on Convolutional Neural Networks (CNN).

In object detection, DL methods are classified into one-stage and two-stage detectors, each with distinct trade-offs in terms of speed and accuracy [5]. One-stage detectors directly predict object classes and bounding boxes from the entire image in a single pass through the network. YOLO (You Only Look Once) [6] and SSD (Single Shot MultiBox Detector) [7] are examples of one-stage detectors widely applied in various industrial tasks, such as surface defect detection [8] and quality control and inspection [9].

On the other hand, two-stage detectors first generate regions of interest and then classify and refine the bounding boxes of these regions in the second step. In addition to other two-stage models, R-CNN (Regions with CNN features) [10] and its upgraded version, faster R-CNN [11], are extensively used in different manufacturing tasks [12].

In some approaches traditional and DL techniques are combined. For example, in [13] CNN, deep and reverse Hough transform were combined to detect meaningful line structures from images.

In this paper, we explore the performance of YOLOv8 in detecting the position and orientation of a selected part. The dataset created within this research was used to fine-tune YOLOv8 model. The performance was evaluated by comparing the real and predicted positions and orientations.

The remainder of the paper is structured as follows. In Section 2 we give a brief overview of YOLOv8 algorithm, whereas Section 3 refers to the experimental setup used for dataset acquisition. The performance of YOLOv8 in object position and orientation detection is presented in Section 4. Finally, in Section 5 we provide conclusions and future work guidelines.

2. YOLOv8

YOLO represents a real-time object detection DL model introduced in 2015 [6]. It detects objects straight from the image and provides object's bounding box coordinates and class probabilities as output. The core idea behind YOLO is its single-stage detection process, which processes the entire image in one pass. It divides

the image into a grid, and for each grid cell, it predicts a fixed number of bounding boxes, confidence scores for those boxes, and class probabilities for each object class. This method significantly speeds up the detection process and enhances generalization ability.

There are several YOLO model versions and the core of each of them is a CNN, although its architecture evolves significantly with each new version. In this work, we employed YOLOv8, which offers multiple improvements over previous versions, including the ability to detect the orientation of bounding boxes. The architecture of YOLOv8 algorithm consists of three main blocks: Backbone, Neck, and Head [14].

Backbone is a block that uses architecture called CSPDarknet53 [14], which represents a CNN composed of a series of convolutional modules (convolutional layer, batch normalization, and activation), CSP (Cross Stage Partial) Layers, and SPPF (Spatial Pyramid Pooling Fast) modules. In this block, low-order and high-order features of the input image are extracted. Neck consists of a series of convolution modules and CSPLayer, and its main goal is to connect the Backbone and Head blocks. This block integrates extracted features to find the objects of different dimensions. Besides, it enables a better understanding of the global context of the scene in which the objects are detected. Finally, the Head is responsible for generating output from the network. In this block, bounding boxes are created, i.e., the position and orientation of objects in the scene are detected. The Head block consists of a series of convolutional modules and convolutional layers.

3. EXPERIMENTAL SETUP

The experimental setup used for dataset acquisition is shown in Fig. 1. The key part of the vision system is Cognex In-Sight 2000-120 monochrome camera that has the resolution of 640×480 pixels and the maximum speed of 75 frames per second. The connection between computer and camera is achieved via Ethernet/IP protocol. Camera triggering, i.e., image acquisition, was performed using In-Sight Explorer software.

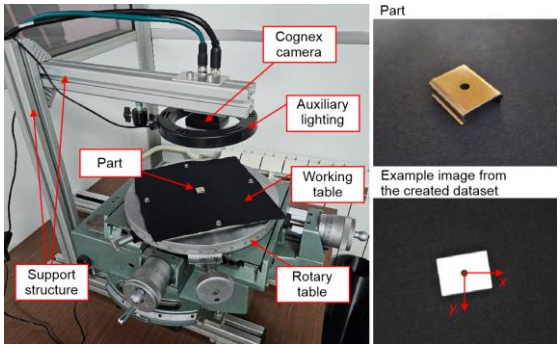


Fig. 1. Experimental setup, part, and example image from the dataset

Camera is calibrated using Camera Calibrator module within MATLAB R2023b Image Processing Toolbox. During calibration a set of images of calibration template containing 5×8 black and white fields with dimension of 10×10 mm was acquired in different positions and orientations. After calibration the coefficients of radial and tangential distortion and the image matrix composed of the values of focal length and coordinates of the principal point are obtained. Furthermore, it was established that 1 mm represents 7.8 pixels in the acquired image.

The experimental part (Fig. 1) was mechanically positioned in the center of the worktable on the manually driven mechanism with two translatory (x and y) and one rotary axis (C). A black pad was used during image acquisition and different positions and orientations of part were achieved by worktable shifting and rotating. Created dataset contains a total of 1,800 images.

4. YOLOv8 IMPLEMENTATION AND EXPERIMENTAL RESULTS

Since YOLOv8 provides five different models that vary in complexity and performance, it is necessary to choose the appropriate one. For this study, YOLOv8 nano model was chosen since it is the most appropriate for application in computationally restricted resources in assembly automation tasks. It is the smallest (3.1 million parameters) and fastest model, although with a slightly lower accuracy. YOLOv8 nano was implemented in Python using Ultralytics library, which is designed for computer vision, in particular object detection tasks. The dataset for model fine-tuning contains two types of data:

- images with objects that need to be detected,
- text files that include the class of object in the image and the normalized coordinates of four vertices of its bounding box in the following format:

$$class\ index, x_1, y_1, x_2, y_2, x_3, y_3, x_4, y_4 \qquad (1)$$

where x_i and y_i, $i \in \{1,...4\}$ represent normalized coordinates of bounding box vertices listed in order that follows the continuity of the polygon.

YOLOv8 model is fine-tuned using 1,500 generated images of the selected part in different positions and orientations within the scene. To obtain the coordinates of the bounding box vertices and create the text files, an algorithm based on Hough transform [1] was created. In the process of model fine-tuning, the values of two parameters were varied: number of epochs $\in$ {50, 100, 150, 200} and batch size $\in$ {2, 4, 8, 16, 32}. According to the loss and validation loss values, the best-performing models were obtained using 100 epochs for fine-tuning. Therefore, the performance of five models differing in batch size was tested. The workstation used for YOLOv8 fine-tuning has triple Nvidia Quadro RTX6000 GPUs, double Intel Xeon Silver 4208 CPUs, and 192GB DDR4 RAM.

A set of images for testing the developed models was obtained by moving the worktable along x and y axes and its rotation by an angle α. Only one parameter (x, y, or α) was varied between acquisition of two consecutive images. The linear movement of the worktable along x and y axes was performed for the values x, $y \in$ {-10, -5, 0, 5, 10 mm}, whereas the angle α was varied in the range $\alpha \in \{0,15,...165°\}$, resulting in a total of n=300 images in the test set. All these values are defined relative to the initial position x, y, α = [0, 0, 0] in which the part is in the center, and its external edges are parallel to the edges of the acquired image.

Fine-tuned models were tested using the following statistical characteristics: minimum error (*min*), maximum error (*max*), mean error (μ), and standard deviation (σ) of the error between ground truth (defined by moving/rotating the worktable) and the estimated value of parts' pose coordinates. Thus, in the case of *x* axis, these characteristics are calculated as follows:

$$\begin{aligned} min_x &= \min(|x_i - \hat{x}_i|) \\ max_x &= \max(|x_i - \hat{x}_i|) \\ \mu_x &= \frac{\sum_i^n (|x_i - \hat{x}_i|)}{n} \\ \sigma_x &= \sqrt{\frac{\sum_i^n (|x_i - \hat{x}_i| - \mu_x)^2}{n}} \end{aligned} \quad (2)$$

where x_i and $\hat{x}_i$ are the ground truth and estimated value of *x* coordinate of the part center, whereas $i \in \{1,2,...n\}$ represents current image from the test set. The values of statistical characteristics for *y* and α are calculated using the same procedure as in (2).

The results (in mm for *x* and *y*, in ° for α) of three fine-tuned models that performed the best in detecting position and orientation are shown in Table 1. The obtained mean error values for the position parameters *x* and *y*, as well as for the α that defines part orientation, meet the requirements of different industrial applications, such as robotic grasping and manipulation tasks. The maximum values are significantly higher than the mean values, but considering the standard deviation, it can be concluded that the maximum values represent individual cases and cannot be used as a main metrics to define the model's accuracy. The best results (the lowest values) for each parameter are in bold.

Statistical charact.		batch=4	batch=8	batch=16
min error	min_x	0.0004	0.0009	0.0026
	min_y	0.0010	0.0003	0.0004
	min_α	0.0030	0.0043	0.0061
max error	max_x	0.8459	0.9111	0.8249
	max_y	0.5961	0.5279	0.5580
	max_α	2.0216	1.7728	2.1451
mean error	μ_x	0.2507	0.2827	0.2399
	μ_y	0.1750	0.1678	0.1736
	μ_α	0.6595	0.5406	0.6814
standard deviation	σ_x	0.1834	0.1960	0.1615
	σ_y	0.1260	0.1170	0.1314
	σ_α	0.4428	0.3979	0.4700

Table 1. Performances of three best models in position and orientation detection

It should be noted that the model fine-tuned with a batch size of 8 achieved the best performance for 7 out of 12 considered parameters. The model created with a batch of 4 provided the best results in only two parameters (min_x and min_α), whereas the third model achieved the remaining three best results. Therefore, the model with the best performance (batch=8) was chosen for further analysis.

To analyze the impact of the change in α on the model accuracy, three positions defined by coordinates *x* and *y* were chosen (Fig. 2). The selected positions include the center (0, 0), the position furthest from the center (10, -10), and one arbitrary position (5, 10).

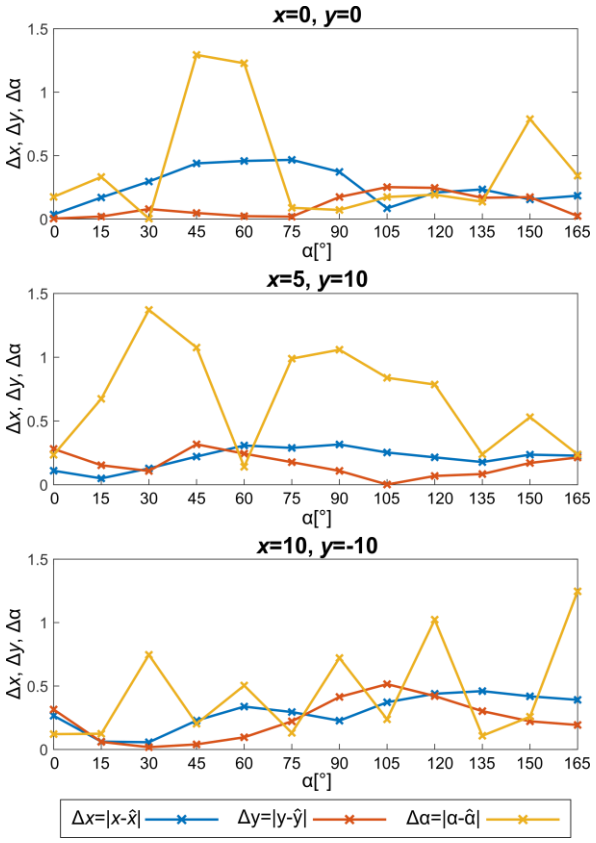


Fig. 2. Effect of α variation on model detection accuracy

If we exclude certain values, this analysis shows that the model prediction error concerning *x* and *y* is relatively uniform (in the range 0-0.5 mm). However, the error between real and detected α varies significantly in all selected positions (in the range 0-1.45°).

The model's prediction error was not uniformly distributed along *x* and *y* axes, as presented in the 3D diagrams in Fig. 3. In the case of the *x* axis, Δ*x* has the minimum value for *x*=5, whereas increasing or decreasing *x* leads to a rise of the Δ*x* (Fig. 3a). The change of *y* had no significant impact on Δ*x*. On the other hand, changing the *y* values caused a change in the Δ*y* error, which reaches its minimum at *y*=0. Increasing or decreasing the *y* resulted in higher Δ*y*, whereas different *x* values did not cause notable effects. In the case of Δα, there are no strong dependencies as for Δ*x* and Δ*y* (Fig. 3c). The orientation error Δα reached its highest values in the region around coordinate (-5, 10).

5. CONCLUSION

This paper explored the performance of YOLOv8 nano model in detecting the position and orientation of a part in the scene. This model was fine-tuned and tested using a dataset of 1,800 real-world images generated within this research. An evaluation of the model's performance was carried out on 300 images with different positions (*x*, *y*) and orientations (α) of the part. The min, max, and mean error values of the fine-tuned model, as well as the standard deviation, were obtained by comparing the ground truth and estimated values of the parameters *x*, *y*, and α.

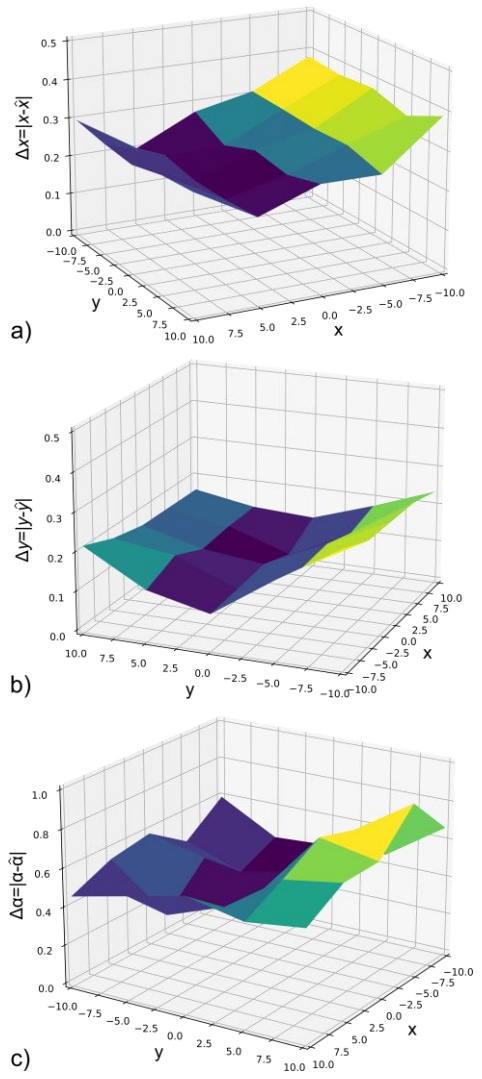


Fig. 3. Effect of x and y variation on the model detection accuracy: a) Δx, b) Δy, c) $\Delta \alpha$

The obtained results show that YOLOv8 nano model can detect position and orientation with an accuracy that meets the requirements of different industrial applications, such as robotic grasping. However, the number of model parameters requires significant computational resources for real-time application in industrial setting. Further research will focus on the position and orientation detection of multiple objects with more complex geometry, as well as on the application of the obtained results in automatic assembly tasks.

6. REFERENCES

[1] Hough, P.V.: *Method and means for recognizing complex patterns*, U.S. Patent, No. 3,069,654, 1962.

[2] Ulrich, M., Steger, C., Baumgartner, A.: *Real-time object recognition using a modified generalized Hough transform*, Pattern Recognition, Vol. 36, No. 11, pp. 2557-2570, 2003.

[3] Chen, H., Gao, T., Qian, G., Chen, W., Zhang, Y.: *Tensored generalized Hough transform for object detection in remote sensing images*, IEEE J of Selected Topics in Applied Earth Observations and Remote Sensing, Vol. 13, pp. 3503-3520, 2020.

[4] Jiao, J., Wang, X., Deng, Z., Cao, J., Tang, W.: *A fast template matching algorithm based on principal orientation difference*, Int J of Adv Robotic Systems, Vol. 15, No. 3, article 1729881418778223, 2018.

[5] Han, J., Ding, J., Li, J., Xia, G.S.: *Align deep features for oriented object detection*, IEEE Trans on Geosci and Remote Sensing, Vol. 60, pp. 1-11, 2021.

[6] Ultralytics, YOLO (2015), [Online], Available: https://docs.ultralytics.com/models/, Accessed on: August, 2024.

[7] Liu, W., Anguelov, D., Erhan, D., Szegedy, C., Reed, S., Fu, C.Y., Berg, A.C.: *SSD: Single shot multibox detector*, Proceedings of the 14th European Conf on Computer Vision (ECCV), pp. 21-37, Amsterdam, Netherlands, Springer, 2016.

[8] Zuo, Y., Wang, J., Song, J.: *Application of YOLO object detection network in weld surface defect detection*, 11th IEEE Annual Int Conf on Cyber Technology in Automation, Control, and Intelligent Systems, pp. 704-710, Jiaxing, China, 2021.

[9] Yao, K., Ortiz, A., Bonnin-Pascual, F.: *A DCNN-based arbitrarily-oriented object detector with application to quality control and inspection*, Comput. Ind., Vol. 142, article 103737, 2022.

[10] Girshick, R., Donahue, J., Darrell, T., Malik, J.: *Rich feature hierarchies for accurate object detection and semantic segmentation*, Proceedings of the IEEE Conf on Computer Vision and Pattern Recognition, pp. 580-587, IEEE, USA, 2014.

[11] Ren, S., He, K., Girshick, R., Sun, J.: *Faster R-CNN: Towards real-time object detection with region proposal networks*, IEEE Trans Pattern Anal Mach Intell, Vol. 39, No. 6, pp. 1137-1149, 2016.

[12] Mouzenidis, P., Louros, A., Konstantinidis, D., Dimitropoulos, K., Daras, P., Mastos, T.: *Multi-modal variational faster r-cnn for improved visual object detection in manufacturing*, Proceedings of the IEEE/CVF Int Conf on Computer Vision, pp. 2587-2594, IEEE/CVF, Montrael, Canada, 2021.

[13] Zhao, K., Han, Q., Zhang, C.B., Xu, J.: Cheng, M.M., *Deep hough transform for semantic line detection*, IEEE Trans Pattern Anal Mach Intell, Vol. 44, No. 9, pp. 4793-4806, 2021.

[14] Terven, J., Córdova-Esparza, D.M., Romero-González, J.A.: *A comprehensive review of YOLO architectures in computer vision: From YOLOv1 to YOLOv8 and YOLO-NAS*, Mach Learn Knowl Extr, Vol. 5, No. 4, pp. 1680-1716, 2023.

ACKNOWLEDGMENTS

This research was supported by the Ministry of Science, Technological Development and Innovations of the Serbian Government under the contract No. 451-03-65/2024-03/200105.

Authors:

MSc student Zivojin Suvajac, Assist. Prof. Dr. Dusan Nedeljkovic, Prof. Dr. Zivana Jakovljevic, University of Belgrade, Faculty of Mechanical Engineering, Kraljice Marije 16, 11120 Belgrade, Serbia, Phone: +381 11 330-22-00.

E-mail: 1004.2022mfbg@gmail.com; dnedeljkovic@mas.bg.ac.rs; zjakovljevic@mas.bg.ac.rs

MMA 2024
FLEXIBLE TECHNOLOGIES

15th INTERNATIONAL SCIENTIFIC CONFERENCE
NOVI SAD, SERBIA, SEPTEMBER 24-26, 2024

Original research paper https://doi.org/10.24867/MMA-2024-02-015

Maletić J., Vorkapic, N., Živanović S.

PROGRAMMING AND VERIFICATION OF THE MACHINING PROGRAM FOR A TEST WORKPIECE FOR A MACHINE WITH A HORIZONTAL ROTARY AXIS

Abstract: *This paper presents the testing of the working accuracy of a 3-axis CNC mill. The machine has two translational axes and a horizontal rotary axis, with the structure A'OXZ. For this machine, a postprocessor was developed utilizing the kinematic equations. In this study, a specialized test piece was designed and machined to verify the accuracy and reliability of both the postprocessor and the machine. The test piece was designed with specific geometric features intended to evaluate the performance of the machining system and the postprocessing program under various operational scenarios. PTC Creo Parametric software was used for part design and toolpath generation processes. The generated toolpath was tested in a virtual machining environment on a virtual machine using Vericut software. The final test piece will be machined on the machine, ensuring an evaluation of the machining system's performance.*

Key words: *verification, CAD/CAM, virtual machining*

1. INTRODUCTION

The subject of this paper is a 3-axis milling machine used for rapid prototyping. The development of this machine is shown in [1]. In the case of this rapid prototyping machine, one of the translational axes found in a typical 3-axis milling machine was replaced with a rotary axis. This machine has one horizontal rotary axis A, and two translational axes, X and Z. The resulting kinematic structure is A'OXZ, as the tool's motion is defined by the two translational axes, X and Z, and the workpiece is based on the rotary axis A, Fig.1.

There has been much research regarding the accuracy of machining with a rotary axis, mainly in the form of testing multi-axis machines, such as in [2]. Ibaraki et al. proposed a method of estimating kinematic errors based on a kinematic model of a five-axis machine. This method was tested on a commercial five-axis machining center, and the estimates are compared to those estimated based on ball bar measurements. There are numerous ways to estimate the accuracy of machining systems. Su and Wang, in [4], make a categorization of testing of multi-axis machines, which can be expanded on general machining systems. These categories are (i) kinematic error measurement and compensation based on special measuring devices, (ii) machining performance detection based on machining tests and (iii) machining accuracy estimation of specified parts based on measured geometric errors. Given this classification, the machining of the test piece described in this paper can be placed in the third category, as it represents a simple test piece that can be easily machined and created to test specific situations in the machining process. This approach to evaluating a machining system is intuitive and cost-effective.

The programming of the test workpiece for this machine was done using the software PTC Creo and a custom-made postprocessor. The CAD/CAM software is used to define the toolpath for machining the workpiece, resulting in a CL (Cutter Location) file. A CL file is a general machining program containing the tool's position and orientation regarding the workpiece coordinate system. The data in a CL file cannot be used directly in a machining process, as it has no information about the layout of the machine's axes. A postprocessor is a program designed specifically for a certain machine that translates the CL file into a G-code suited for running on said machine.

Normally, programming of 3-axis machine tools is straightforward, as the desired tool motions are directly translated into the displacements of the machine's axes. However, given that the considered machine has a rotary axis, certain kinematic transformations are required during the postprocessing stage of machining programming in order to develop an appropriate machining program.

The postprocessor for this machine was developed based on the postprocessing software developed in [5]. The specialized postprocessor was used to translate the CL file information, which outlines the precise toolpath required for the machining process of the test part, into the G-code program.

The postprocessor was utilized to ensure that the toolpath was described in a way that ensured the correct communication with the machine, ensuring that it was able to perform the necessary actions needed to perform the machining of the test piece.

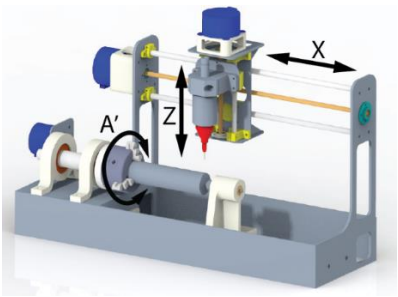


Fig. 1. The model of the 3-axis machine with two translation and one rotary axes

In this paper, the intent behind the design of the test workpiece is shown in the second chapter, followed by the description of the postprocessing procedure in the third chapter. Next, the verification of the experiment in a virtual environment is described in the fourth chapter, followed by the results from the experiment on the real-life machine in the fifth chapter.

2. DESIGNING AND PROGRAMMING THE TEST WORKPIECE FOR MACHINING VERIFICATION

The test workpiece was designed with a specific geometry to verify particular situations during machining that may lead to issues or complications. The test workpiece was designed using the CAD/CAM software PTC Creo Parametric, which is later used to program the CL file of the machining process.

2.1 Description of the Geometry of the Test Piece for the Rotational Axis

A machining test workpiece with a specific geometry was formed to verify the working accuracy of the machine's rotary axis. As shown in Fig. 2, the test workpiece is cylindrical, with specific grooves and surfaces used to test the machining capability. The first element (1) of the test piece is a spiral groove designated to test the accuracy of interpolation of the translatory and rotary axis as well as test the rotary axis's full range of motion, with the rotary axis moving clockwise, completing two full circles. Next, a rectangular groove (2) was designed to test the changing directions of the machine's axis on a continuous tool path. The third element of the test workpiece is another spiral groove (3) obtained with the rotary axis moving in a counterclockwise direction. This element is used to check the machine rotary axis moving in the opposite direction, and it is required for the axis to a full circle.

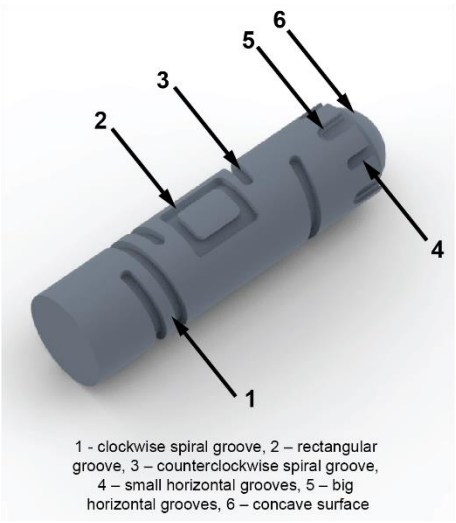


Fig. 2. The design of the test workpiece

The next element of the rotary axis test piece is eight horizontal grooves placed at 45-degree intervals, used for testing indexed machining on this machine.

These grooves are accompanied by four wider grooves spaced 90 degrees apart. The wider grooves are used to test the machine's repeating accuracy. The last element for the rotary axis test piece is a concave surface that tests the ability to generate a curved surface. The intent behind this workpiece design is to test the machine's ability to execute the machining process and the conversion of the coordinates for the postprocessing part of the manufacturing definition.

3. POSTPROCESSOR IMPLEMENTATION

As mentioned before, the 3-axis milling machine presented in this paper has one rotary axis, consequently needing kinematic transformations during the postprocessing stage of machining programming to develop an appropriate machining program. The postprocessing software developed in [5] is used to postprocess the toolpath contained in the CL file. This postprocessor is instrumental in translating the CL file, which contains the toolpath for the machining process of the test part, into a G-code program that the machine can execute. The developed postprocessor was modified using the kinematic equations for the stated machine. The postprocessing software was adapted using the kinematic equations specified for this machine. The kinematic transformation is the equivalent of converting spatial movement from Cartesian to polar cylindrical coordinates. This transformation of machine tools coordinates is given in Eq. 1-3.

$$X = Q_X \tag{1}$$

$$A = atan2(Q_Z, Q_Y) - {}^{\pi}/_{2} \tag{2}$$

$$Z = \sqrt{Q_Z^2 + Q_Y^2} \tag{3}$$

Given the origin of the trigonometric function, the resulting angle has a boundary in the form of A=[-2π, 0]. To prevent errors during machining, an addition to the postprocessing software was made. The addition ensures that the angle of the rotary axes changes continuously by adding either π or -π when the angle value approaches the range's boundary angle. This added condition in the postprocessing software ensures the continual change of the value of the angle A without jumping to the boundaries of the range.

4. PROGRAMMING THE MACHINING PROCESS AND VIRTUAL ENVIRONMENT SETUP

The programming of the toolpath was done using the PTC Creo Parametric software, resulting in the CL file of the machining process. The toolpath was verified using a material removal simulation in the PTC Creo software, shown in Fig. 3. The resulting simulation verified that the desired toolpath was generated and that it could be done on the three-axis machine with one rotational and two translational axes. However, this simulation is based on the CL file, not the actual G-code that will be executed on the machine. Consequently, another form of verification on a virtual machine was needed. Testing the machining process using the G-code program was done using the Vericut software.

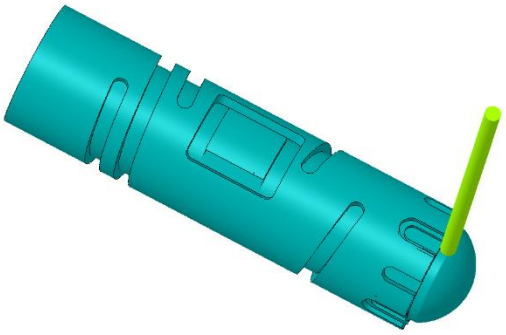


Fig 3. Material removal simulation in the PTC Creo software

First, a machine model was built in the virtual machining environment, shown in Fig. 4. As mentioned before, the machine consists of two translational axes and one rotary axis. The machine's components were defined, respecting the machine's kinematic structure (A'OXZ).

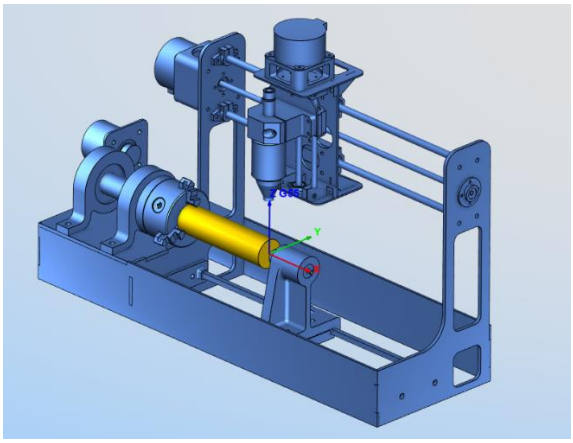


Fig 4. Virtual machine in the Vericut software

The Vericut virtual machining software enables an intuitive way to define the structure of the machine, ensuring the correct movements of the machine's axes. Foremost, the base of the machine is defined as a non-moving component of the machine. The axes of the machine are then defined in terms of type and order according to the structural formula of the machine. Considering the machine's structural formula, two branches of the machine kinematics are defined after the machine base. The first branch, referred to as the workpiece branch, carries the rotational axis A, onto which the workpiece is subsequently mounted. The second branch, known as the tool branch, starts with defining the X-axis, to which the Z-axis is added. The machine's tool is positioned at the end of the Z-axis.

Aside from the structure of the machine, to simulate the machining process, it is necessary to define the tools, the spindle of the machine, the referent coordinate system, and the workpiece that would be virtually manufactured.

In the Vericut software, the material removal simulation is conducted using only the G-code program, so the machined virtual test workpiece mirrors the physical workpiece after machining. The virtual model machine is assembled with components corresponding to the real-life machine components. As such, this machining process simulation can be classified as virtual machining.

5. VIRTUAL MACHINING

After designing the workpiece model, programming the machining process, and setting up a virtual machining environment, the verification in the form of virtual machining needs to be concluded. The steps and the process of virtual machining correspond to the process of real-life machining, which is why it is used for the final testing of the machining program.

The starting workpiece is cylindrical, with a diameter and length that matches the desired test piece. Given that the first five elements of the test piece are in the form of grooves, the machining does not require any roughing steps. The clockwise and counterclockwise grooves, as well as the rectangular groove, are obtained with the continual motions of axes A' and X, while the Z axis has a constant value. The horizontal grooves are used to test the repeating positioning of the axis A. The horizontal grooves are machined in the form of indexed machining, meaning that the rotary axis A is not moving continuously but only when positioning the workpiece for the machining of the next groove. These operations of the machining process were conducted using end mills of different diameters. The concave calotte element of the workpiece requires a large tool depth for material removal and, as such, requires a roughing machining process that precedes the finishing. For the concave calotte element, the roughing was conducted using an end mill, and the finishing process was executed using a small ball mill.

The G-code for the test workpiece was executed on the virtual three-axis mill-turn machine. The result of this virtual machining is a virtual workpiece in the form of an STL file, corresponding to the workpiece's model that was defined during the modelling stage. The resulting virtual workpiece is shown in Fig. 5. The virtual machining process was conducted on the virtual machine corresponding to the real-life machine using the computed G-code program. This simulation confirmed that during the virtual machining process, no collision occurred between the machine's moving parts. The machining process during specific segments during the virtual machining process is shown in Fig. 6.

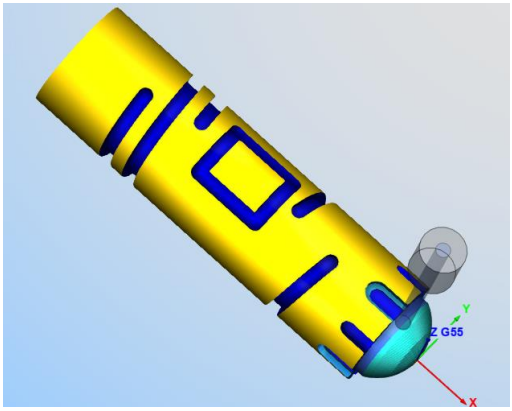


Fig 5. STL of the workpiece after virtual machining

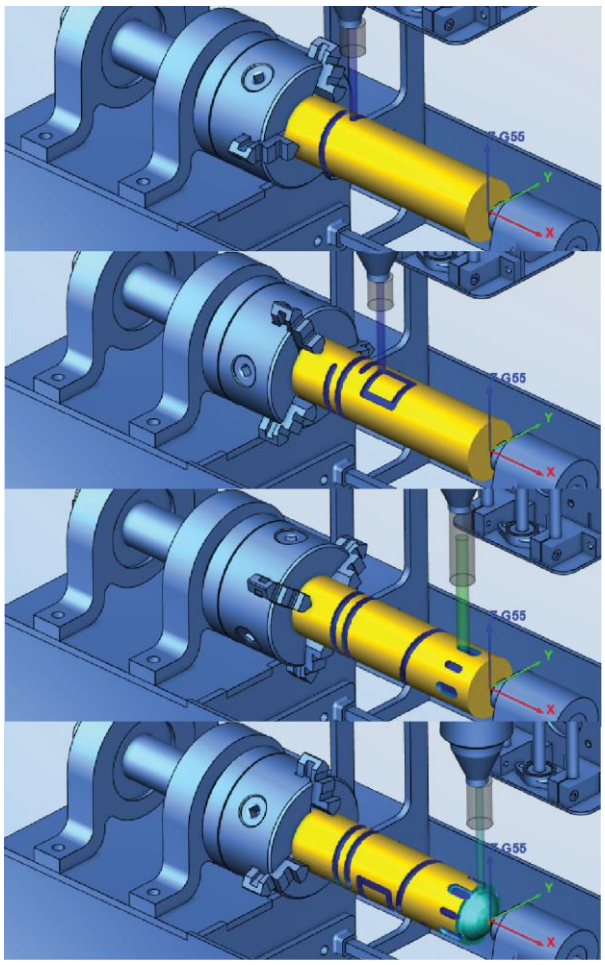


Fig 6. Virtual machining of the test workpiece

The test will also be conducted on a real machine, as a preparation for the later testing of the prototype machine with a similar configuration (LOLA VMC4) [6].

6. CONCLUSION

This paper presents the development of a verification environment for machine tools with rotary axes. The research shown describes the forming of the geometry of the test workpiece mode. The geometry of the workpiece was determined to assess the machine's working capability in various geometric positions. The programming of the machining process was executed using the CAD/CAM software PTC Creo and a custom-made postprocessor. The specific geometry of the workpiece was utilized to test the capability of the developed postprocessor to calculate the desired toolpath correctly.

The G-code program was tested in a virtual environment using Vericut software. A virtual machine is also configured for the purposes of simulation and program verification. The simulation's result was a virtual workpiece model that corresponded with the assigned geometry. The considered tests will be realized on real machines, on the desktop variant and on the industrial prototype.

This dual approach of using both simulations and physical tests offers a dependable system for verifying the operational capability of the machining system. The insights gained from this study can be used to enhance the performance of both the machine and the postprocessor, ultimately leading to more reliable and precise manufacturing processes. The current phase serves as both the preparation and verification of the environment necessary for thorough testing and investigation of an industrial prototype for a full-scale machine. The process shown in this paper is used to set the groundwork for more extensive studies and practical applications by establishing a solid foundation in this initial stage.

7. REFERENCES

[1] Vorkapić, N., Živanović, S., Dimić, Z.: *Razvoj edukacione 3-osne CNC mašine alatke za brzu izradu prototipova sa dve translatorne i jednom obrtnom osom*, Tehnika,Vol.69, pp. 725-732, 2020. DOI: 10.5937/tehnika2006725V

[2] Ibaraki, S., Sawada, M., Matsubara, A., Matsushita, T.: *Machining tests to identify kinematic errors on five-axis machine tools*, Precision Engineering, Vol. 34, No 3, pp. 387-398, 2010. DOI: 10.1016/j.precisioneng.2009.09.007

[3] ISO 10791–7. Test conditions for machining centres, Part 7. Accuracy of a finished test piece, ISO (International Organization for Standardization); 1998.

[4] Su, Z., Wang, L.: *Latest development of a new standard for the testing of five-axis machine tools using an S-shaped test piece*, Proceedings of the Institution of Mechanical Engineers, Part B: Journal of Engineering Manufacture, Vol. 229, No. 7, pp.1221-1228, 2015.

[5] Maletić, J., Živanović, S.: *Verification of inverse kinematic equations for a five-axis machine tool with a spindle tilting configuration*, Advanced Technologies & Materials, Vol. 47, No. 1, pp. 33-38, 2021. DOI: 10.24867/ATM-2022-1-006

[6] Lola Vertical Machining Center 4- LOLA VMC4, https://www.li.rs/o-institutu/vesti/629-velika-nagrada-korak-u-buducnost-lola-institut-u, 2024.

ACKNOWLEDGMENTS

The presented research was supported by the Ministry of Education, Science and Technological Development of the Republic of Serbia by contract no. 451-03-65/2024-03/200105 dated 2024 and by contract 451-03-66/2024-03/ 200066 dated 2024.

Authors:

MSc Julija Maletić, Lola Institut, Kneza Višeslava 70a, 11030 Belgrade, Serbia, Phone: +381645411114.
E-mail: julija.maletic@li.rs

MSc Nikola Vorkapić, PhD Saša Živanović, University of Belgrade, Faculty of Mechanical Engineering**,** Kraljice Marije 16 11120, Belgrade, Serbia, Phone: +381 11 3302-423.
E-mail: nvorkapic@mas.bg.ac.rs, szivanovic@mas.bg.ac.rs

MMA 2024
FLEXIBLE TECHNOLOGIES

Section C:
METROLOGY, QUALITY, FIXTURES, CUTTING TOOLS AND TRIBOLOGY

MMA 2024 FLEXIBLE TECHNOLOGIES

15th INTERNATIONAL SCIENTIFIC CONFERENCE
NOVI SAD, SERBIA, SEPTEMBER 24-26, 2024

Original research paper https://doi.org/10.24867/MMA-2024-03-001

Tanasić, Z., Vuković, M., Panić, M., Janjić, G.

IMPROVEMENT ASSEMBLY PROCESS USING LEAN MANUFACTURING METHODS AND TOOLS

Abstract: *Nowadays, the market is constantly changing and becoming increasingly demanding. Securing a leadership position is the most challenging task in the business world. For survival in the market, companies need to achieve the highest possible profit with the lowest possible production cost. One way to maintain a competitive edge in the market is the implementation of the lean concept with recognizable methods and tools for designing, implementing, and improving business systems and processes. The aim of this paper is to improve the stator assembly process for industrial machines in the company "XY" by applying the methods of VSM – Value Stream Mapping, work standardization, and JIT – Just in Time, which are some of the fundamental methods and tools of lean manufacturing. It has been proven that by using these lean manufacturing methods and with minimal investment, time standards can be reduced, and the movement of workers, materials, and tools can be optimized.*

Key words: *implementation, lean, VSM, JIT*

1. INTRODUCTION

The goal of every enterprise is to thrive and succeed, which entails ensuring customer satisfaction through both the quality and quantity of products or services, with minimal costs and maximum profit. This means achieving fast, cost-effective, and secure operations. Continuous improvements and refinements across the entire production system, employing modern quality tools and techniques, are necessary to achieve these objectives.

One of the most commonly used concepts in advanced manufacturing is lean production. The goal of lean methodology is to implement its tools, methods, and philosophy with all employees to optimize production as effectively as possible and reduce unnecessary losses. Successfully implementing lean methodology not only helps us surpass the competition but also surpass ourselves. [1].

2. LEAN MANUFACTURING

2.1 Lean principles

The lean concept is a developed model of production management in the context of quality improvement and engineering processes, where the reorganization process is carried out through the identification of five principles (Womack and Jones, 1996):

- defining the value of the product for the customer,
- determining value streams,
- creating value streams,
- introducing the principle of "pull",
- striving for perfection [2].

Nowadays, companies strive to include these principles in their work processes, but they are usually implemented only in certain functions and very rarely in all of them. These five principles lead to an understanding of the lean approach in companies, because only their joint application in all functions of the production system can significantly enhance and improve production.

2.2 Lean Wastes

The goal of lean manufacturing is to identify all losses and deficiencies in the production process and ultimately eliminate them. The original Toyota production process identified seven key areas for reducing and eliminating losses (wastes) (Fig. 1) [3].



Fig. 1. Seven types of waste

Recently, an eighth type of waste has been added – the underutilization of human potential. These losses in modern organized business systems amount to about 60%, which means they are still not sufficiently researched, nor are there clearly defined systems for their elimination, and they represent a measure of the success of lean implementation [4].

3. LEAN METHODS AND TOOLS

3.1 Work Standardization

Standardization of work is one of the fundamental concepts of lean thinking. Standardization involves performing individual tasks with no activities that do not add value, and they are executed in a specified sequence. The framework for achieving effective

standardization includes the following [5]:

- Standards – rules or examples that provide clear explanations;
- Standard work – a set of work procedures establishing the current best and reliable methods and sequence of steps for each process and each employee;
- Standardization – the practice of establishing effective communication for monitoring and improving standards and standardized work.

3.2 Value Stream Mapping – VSM

Value Stream Mapping is a tool in the lean concept that allows organizations to visually depict all steps in work processes, discover waste spots in processes, and identify their causes [6].

The value stream is everything we do to convert raw materials into a finished product that creates value. Value is everything the customer is willing to pay for. Adopting the value stream perspective means working on the bigger picture, not just individual processes. The goal is to improve the whole, rather than just optimizing parts of the process.

A Value Stream Map is a visual representation of material and information flows within a specific value stream. It consists of three main components [7]:

- material flow,
- information flow, and
- timeline.

In the application of the VSM tool, the following steps are proposed:

- selecting a team leader and forming a functional lean team,
- choosing a product for mapping,
- collecting data and generating the current state map,
- analyzing the current state and creating the desired future state, and
- developing improvement plans and implementing them.

3.3 Just in time – JIT

Just-in-Time (JIT) is a modern production principle whose principles provide a good example of how to survive in the market, i.e., what we should focus on to remain competitive. JIT is an economic concept that represents a strategy to reduce costs in production, achieved by minimizing the storage time of parts and materials or even avoiding storage altogether, and integrating them into the production process as quickly as possible. Some basics of this production are increasing product quality, boosting productivity, minimizing inventory to the lowest possible level, eliminating warehouses, reducing costs, and reducing defects.

The primary objectives of implementing the JIT concept are [8]:

- Zero lead time,
- Zero failures,
- Flexible manufacture,
- Zero inventory,
- Eliminate waste,
- Flow process.

The JIT method is based on four key elements (tools) that support this unique approach at every level of the process:

- Heijunka,
- Elimination of waste,
- Takt Time,
- Kanban.

In his JIT implementation handbook, H. Hiroyuki emphasized: "Through the JIT approach, we declare comprehensive war on defects and call upon ourselves to find ways to completely prevent their recurrence." Therefore, JIT requires improvement in three steps from detecting defects to reducing shortcomings and ultimately preventing defects from occurring [9].

4. CASE STUDY: PROCESS IMPROVEMENT FOR STATOR ASSEMBLY

Using a practical example (stator assembly process), we will demonstrate the application of lean methods and tools, specifically how implementing standardized work, VSM, and JIT methods can reduce waste in production, as well as movements of workers, materials, and tools.

4.1 Production program at company "XY"

The production program RUT is a part of the production schedule at company "XY" that pertains to manufacturing stators for starters and electric motors of various shapes and dimensions. Machines involved in this production program are predominantly specialized or utilize modular tooling designed specifically for these operations, often for a single type or dimension of product.

Before implementing lean tools and methods, an analysis of the technical documentation and real-time monitoring of stator assembly in the company were conducted. Based on this, a Value Stream Mapping was performed for the assembly line in question (Fig. 2). Value Stream Mapping is a way to visualize all activities, processes, and flows of materials and information in one place, demonstrating the interconnectedness from raw materials through processes to the customer.

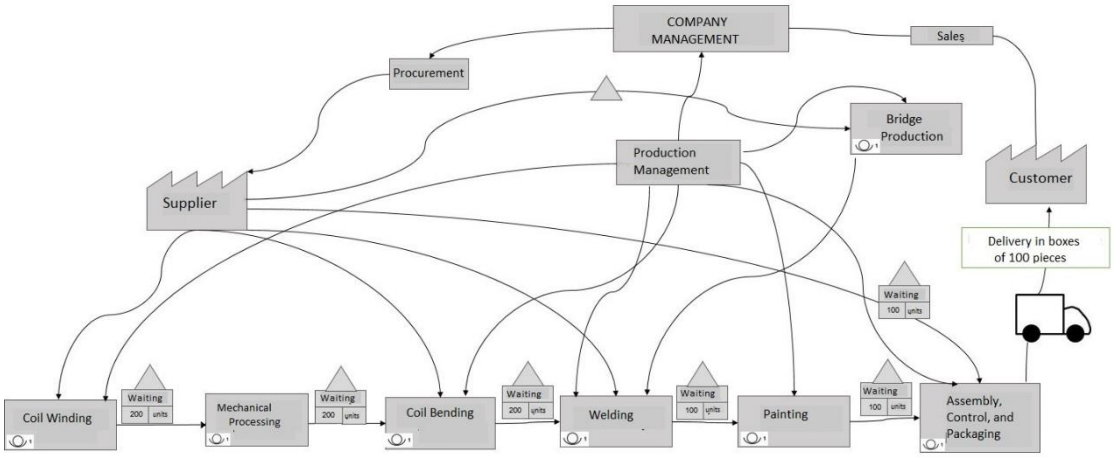


Fig. 2. Application of VSM Method for Production Program RUT

4.2 Analysis of the current state of the stator assembly line (AZE)

The assembly process of stator AZE consists of five operations:

- Winding insertion into the core (2893),
- Bolt tightening (2679),
- Calibration and tightening to specified torque (2680),
- Internal diameter and penetration inspection (2685),
- Brush holder, plug, spring, and packing installation (1339).

There are five workstations planned, with their layout shown in Fig. 3.

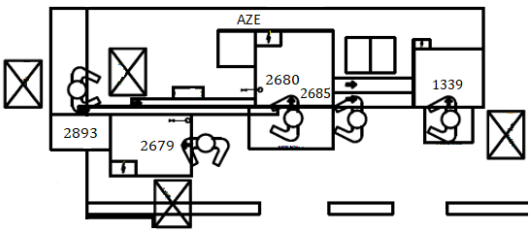


Fig. 3. The layout of workstations and operations on the assembly line AZE

The workstation layout is structured based on a subject principle, as the products are of the same type, differing only in dimensions or certain aesthetic surfaces. Product interaction with the surroundings is unregulated, leading to instances where the effective capacity of the assembly line is significantly lower than time standards at one moment, while at other times, time standards drop to zero due to order suspensions. According to the production plan for 100 units, the manufacturing time is Ti = 41.4 minutes, and the preparatory finishing time Tpz = 15 minutes.

Tracking the movement of products, workers, and raw materials is depicted using a Spaghetti diagram shown in Figure 4. The diagram highlights excessive worker movements, primarily due to the distance between the workstation and the raw materials, requiring workers to fetch materials themselves. Unnecessary worker movement represents a production loss, adding to the time and cost of transporting materials without adding value to the product. Consequently, workers often fail to meet production quotas, leading to delays in customer deliveries. Additionally, the need for extra work contributes to unnecessary worker fatigue and process delays.

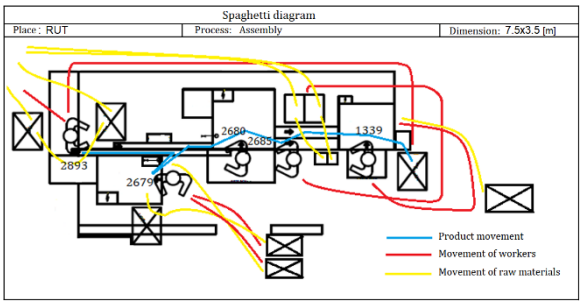


Fig. 4. Spaghetti diagram

4.3 Improvement proposal - U the cell for the assembly line AZE

Through the analysis of the current state of the assembly line, it was concluded that there are many inefficiencies present. Following the basic principles of lean manufacturing, which aim to eliminate waste and improve worker efficiency, a proposed layout for the assembly line is shown in Fig. 5.

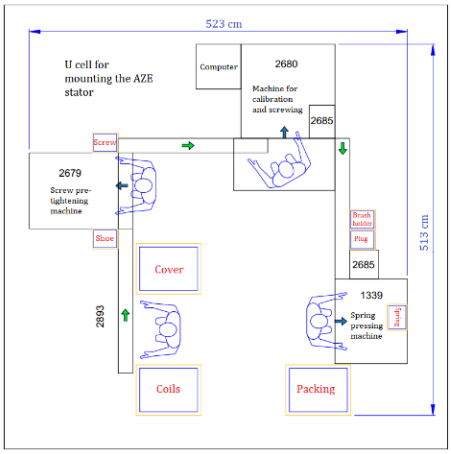


Fig. 5. Proposed workstation layout - U the cell

By implementing the proposed layout, several advantages are achieved:

- reduction in the number of workstations, hence fewer workers,
- shorter assembly time,
- leveling of time/takt (evening out operations - see Figures 6 and 7), and
- reduction in the footprint of the assembly line.

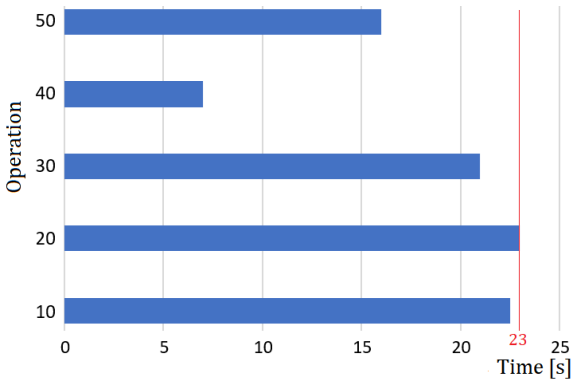


Fig. 6. Duration of operations according to the current state

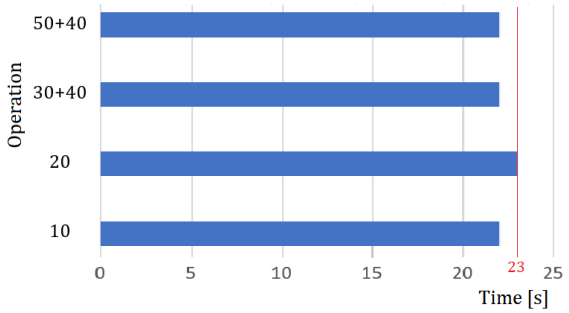


Fig. 7. Duration of operations after implementation of the proposed layout

5. CONCLUSION

In today's competitive and fast-paced market environment, every loss in production can significantly impact the entire company's operations. Customer trust is easily lost, and competing firms are eager to seize any opportunities that arise.

Lean manufacturing is a beneficial concept in production that helps companies remain competitive. By implementing lean principles, the focus is on eliminating waste, organizing workspaces effectively, boosting morale and satisfaction among employees, fostering good relationships with suppliers and customers, and more.

Through analysis of the current state of the assembly line, it was identified that there were numerous inefficiencies causing production delays, product delivery issues, employee dissatisfaction, reduced product quality, and increased scrap rates. Additionally, disorganized movement of workers and materials resulted in operations taking longer than prescribed times.

Reorganizing the workstation layout, specifically by adopting the U-shaped arrangement for machines, would effectively address many of these issues. It would eliminate major problems, reduce losses, decrease the required number of workers (from 5 to 4), cut down workspace requirements by approximately 15%, and improve overall morale and employee satisfaction.

Importantly, these improvements can be achieved with minimal financial investment, which is typical in lean manufacturing implementations. It is crucial to raise awareness among employees about the benefits of lean concepts and gain support from senior management within the company to successfully implement lean practices.

6. REFERENCES

[1] Tanasić, Z., Janjić, G., Soković, M..: *Napredni koncepti proizvodnje*, Mašinski fakultet, Univerzitet u Banjoj Luci, Banja Luka, 2022.

[2] Womack, J.P., Jones, D.T.:*Lean Thinking*, Simon & Schuster, New York, 1996.

[3] Plumlogix, *Waste in Lean Manufacturing: Where to To Look and How to Reduce It*, From: https://plumlogix.com/waste-in-lean-manufacturing-where-to-to-look-and-how-to-reduce-it/, accessed on: June 5., 2024.

[4] Marić, B., Božičković, R.: *Održavanje tehničkih sistema i lean koncept*, Mašinski fakultet, Istočno Sarajevo, 2014.

[5] Panić, M.: *Unapređenje procesa montaže statora za industrijske mašine*, diplomski rad, Banja Luka, 2023.

[6] Hermold, M.: *Lean Management and Kaizen: Fundamentals from Cases and Examples in Operations and Supply Chain Management*, Springer, 2002.

[7] King, P.: *Lean for the Process Industries: Dealing with Complexity*, Taylor & Francis Group, 2019.

[8] Monden, Y.: *Toyota Production System an Integrated Approach to Just-In-Time*, Second Edition, CRC Press Taylor & Francis Group, 2012.

[9] Hirano, H.: *JIT Implementation Manual The Complete Guide to Just-In-Time Manufacturing*, 2nd ed., CRC Press Taylor & Francis Group, 2009.

Authors:

PhD Zorana Tanasić, MSc Maja Vuković, BSc Mićo Panić, PhD Goran Janjić, University of Banja Luka, Faculty of Mechanical Engineering, Vojvode Stepe Stepanovića 71, 78 000 Banja Luka, Bosnia and Herzegovina, Phone.: +387 51 433-000.

E-mail: zorana.tanasic@mf.unibl.org; maja.vukovic@ mf.unibl.org; mico.panic@student.mf.unibl.org; goran.janjic@mf.unibl.org

MMA 2024
FLEXIBLE TECHNOLOGIES

15th INTERNATIONAL SCIENTIFIC CONFERENCE
NOVI SAD, SERBIA, SEPTEMBER 24-26, 2024

Original research paper https://doi.org/10.24867/MMA-2024-03-002

Milosevic, A., Kocovic, V., Santosi, Z., Sokac, M., Simunovic, G., Tadic, B., Vukelic, D.

MODELLING THE BORING PROCESS ON THE BASIS OF CENTRIFUGAL FORCE USING A SPECIALLY DESIGNED TOOL HOLDER

Abstract: *The study investigated the boring of C45 steel with a specially designed tool holder. The input parameters that were varied were the number of revolutions, the feed rate and the number of passes. The experimental investigations were carried out according to a custom experimental design using the D-optimal criterion. The initial parameters measured were the hole diameter before and after boring, while the diameter deviation was calculated. A detailed analysis and evaluation of the effects of the input parameters on the output parameters was performed. The model was diagnosed. An appropriate regression equation was established. The obtained model was verified by confirmation experiments.*

Key words: *boring, centrifugal force, tool holder*

1. INTRODUCTION

Boring is a machining process for enlarging a hole in order to achieve a better surface finish and dimensional and geometric tolerances. The research problem of accurate modelling has always been a hot topic in machining. In the past, the boring process was modeled according to various aspects. Sortino et al. [1] presented a dynamic model of the tooling system based on finite element analysis and empirical models. The model was based on physical and geometrical assumptions and was refined by experimental observations obtained from modal tests of boring bars with different geometries. Wang et al. [2] created a model to predict the dynamic cutting force components in radial, tangential and feed directions. The stiffness, chip deformation and plowing interference affecting the cutting force were considered using the principles of cutting mechanics and the Oxley's orthogonal cutting model. Chen et al. [3] developed four finite element models, namely the advection model, the surface heat model, the heat transfer model and the ring heat model, to predict the workpiece temperature in cylinder boring. Venkata Rao and Murthy [4] developed models to study the effects of nose radius, cutting speed and feed rate on surface roughness and root mean square of workpiece vibration during boring. Response surface methodology, artificial neural network and support vector machine were used to predict the surface roughness and root mean square of workpiece vibration. Li et al. [5] presented a nonlinear model to investigate the dynamic properties of boring. A damping implementation of the dynamic vibration absorbers was performed. Du et al. [6] presented an analytical model to predict the dynamic cutting force during boring considering the tool path and chip breakage. The dynamic cutting force model was validated using a planned boring experiment and a classical cutting force model.

In contrast to the previous work, the aim of this research is to model the boring process with a specially designed tool holder. The input parameters considered are the number of revolutions, the feed rate and the number of passes, and the output parameter is the diameter deviation. The specially designed tool holder is based on the generation of centrifugal forces that occur during rotation. The material is removed by controlling the centrifugal force and not by adjusting the depth of cut.

2. MATERIALS AND METHODS

The experimental investigations were carried out on a workpiece with an initial diameter of $120^{\pm 0.1}$ mm made of C45 steel.

The boring process (Fig. 1) is carried out with a specially designed tool holder (Fig. 2), the operating principle of which is explained in detail in [7]. The material removal is achieved by applying a centrifugal force (F). The centrifugal force is generated by a specially designed movable unit consisting of tool and tool holder. Boring is performed on conventional machine tools with conventional cutting inserts. The design of the tool and tool holder unit enables the intensity of the penetration force to be regulated, i.e. the depth of cut. The regulation is achieved by the number of revolutions (n) of the moving unit.



Fig. 1. Boring process

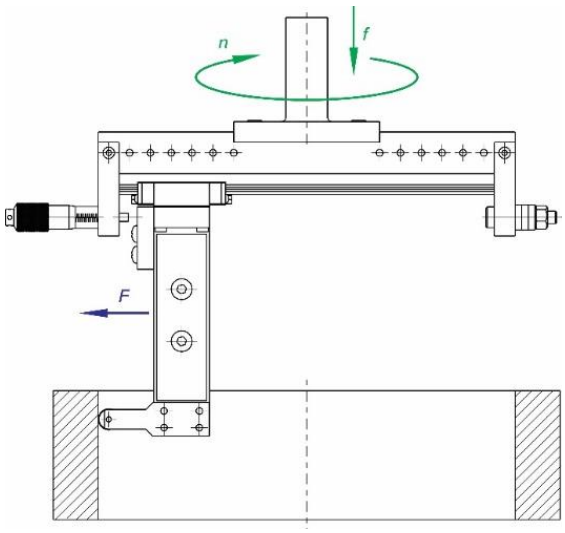


Fig. 2. Tool holder [7]

The hole was machined on a CNC milling machine with an cutting insert with the following properties: substrate: HW, insert shape: round, insert thickness: 4 mm, fixing hole diameter: 4.4 mm, inscribed circle diameter: 10 mm, corner radius: 5 mm, face land width: 0.1 mmm, face land angle: 15°, and clearance angle major: 7°.

Three input parameters were varied during the experimental research: number of revolutions (*n*), feed rate (*f*) and number of passes (*i*). The ranges of input parameters are: *n*= 120-200 (rev/min), *f* = 0.1-0.5 (mm/rev), mm and *i*=1-16. The input and output parameters were treated as continuous factors.

The dimensions were measured under controlled microclimatic conditions on a Carl Zeiss Contura G2 coordinate measuring machine. The ball diameter was 5 mm. The measurement strategy used is point by point. The diameter was measured before and after boring. The diameter deviation (ΔD) was calculated as the difference between these two values.

3. RESULTS

The experimental research was conducted using a custom design of experiment. The experimental design was determined on the basis of predefined input and output parameters. An a priori model with main effects, their squares and two-factor interactions was created. D-optimal criteria for optimality were used in the experimental design, focusing on the precise estimation of the model coefficients. The number of experimental points was chosen depending on the complexity of the model and the desire for accurate estimation effects. The evaluation of the planned experiment showed that 25 test points have sufficient statistical power to determine actual effects. To exclude possible systematic bias, the data were randomized. Table 1 shows the randomized experimental design with the measurement results.

The statistical analysis was carried out using JMP software. A model was created that includes main effects, their squares and two-factor interactions. Such a model enables the analysis of complex relationships between input parameters and output. Due to the non-normal distribution of the data, a logarithmic transformation of the dimensional deviation was performed to improve the interpretation of the statistical method.

No.	*n* (rev/min)	*f* (mm/rev)	*i*	Δ*D* (mm)
1.	120	0.1	1	0.406
2.	200	0.2	1	0.009
3.	180	0.4	8	0.006
4.	120	0.5	16	0.002
5.	180	0.5	1	0.004
6.	200	0.1	16	0.003
7.	180	0.1	1	0.024
8.	120	0.5	16	0.023
9.	200	0.5	1	0.123
10.	120	0.5	4	0.406
11.	140	0.2	8	0.064
12.	200	0.1	1	0.011
13.	120	0.1	16	0.003
14.	120	0.1	16	0.008
15.	180	0.2	16	0.024
16.	200	0.5	16	0.003
17.	120	0.4	1	0.037
18.	200	0.5	16	0.005
19.	120	0.2	1	0.033
20.	200	0.1	16	0.015
21.	200	0.4	4	0.175
22.	140	0.5	1	0.033
23.	140	0.4	16	0.009
24.	140	0.1	4	0.006
25.	200	0.1	8	0.003

Table 1. Results of experimental research

Table 2 shows the summary of the fit, which provides information about the quality of the regression model. The predictions of the coefficient of determination (RSquare, Rsquare Adj) are close to 1, which indicates a very good fit of the model to the data. The RSquare value shows that 97 % of the variability of the dimensional deviation is explained by the spindle speed, the feed rate and the number of passes. The low value of the Root Mean Square Error (RMSE) indicates minimal variability between the actual and predicted values and reflects the high precision of the model.

RSquare	0.97341
RSquare Adj	0.968092
Root Mean Square Error	0.275156
Mean of Response	-4.12812

Table 2. Summary of Fit

Table 3 shows the analysis of variance for the selected regression model. The high F-value of the model, 183.0431 for the dimensional deviation, shows that the model effects are statistically significant. The low p-value (<.0001) shows that there is at least one statistically significant effect in the model.

Source	DF	Sum of Squares	Mean Square	F Ratio	Prob > F
Model	4	55.433542	13.8584	183.0431	<.0001*
Error	20	1.514221	0.0757		
C. Total	24	56.947763			

Table 3. Analysis of Variance

Fig. 3 shows a visual assessment of the model's quality of fit through a representation of actual and predicted plot. The resulting plots show that the points follow the line, indicating a good fit of the model, i.e. that the predicted values are close to the actual values. The range of the confidence interval is narrow, indicating that the predicted values are precise.

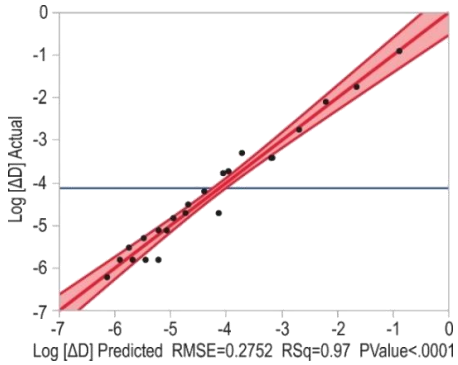


Fig. 3. Actual by Predicted Plot

The estimated input parameters of the model, sorted by statistical significance, are shown in Fig. 4. As can be seen, the main effect of the number of passes and the number of rotations, the quadratic effect of the number of rotations and the two-factor interactions between the number of rotations and the number of passes have a statistically significant influence on the dimensional deviations.

Source	LogWorth	PValue
i(1,16)	14.967	0.00000
n(120,200)	10.793	0.00000
i*i	5.761	0.00000
n*i	5.174	0.00001

Fig. 4. Effect Summary

Fig. 5 shows the the residuals by row plot. Plotting the residuals by row allows systematic irregularities and to check the appropriateness of the model. The residuals are randomly distributed along the horizontal axis, which indicates that there are no systematic irregularities.

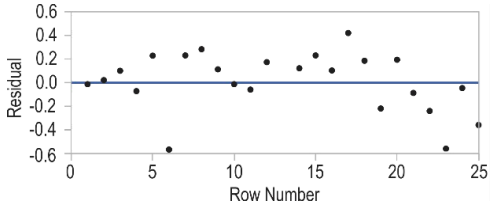


Fig. 5. Residual by Row Plot

Fig. 6 shows the assessment of the normality of the residuals in the model. The points on the diagram follow the diagonal line and remain within the confidence bands, which indicates that the residuals are normally distributed.

Fig. 7 shows how spindle speed and number of passes influence the dimensional deviation. It can be seen from the figure that the smallest dimensional deviation is achieved when the spindle speed and the number of passes are at their lowest. Increasing the spindle speed and the number of passes leads to an increase in the dimensional deviation.

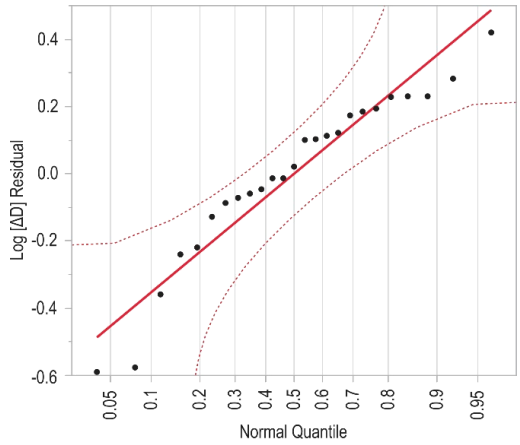


Fig. 6. Residual Normal Quantile Plot

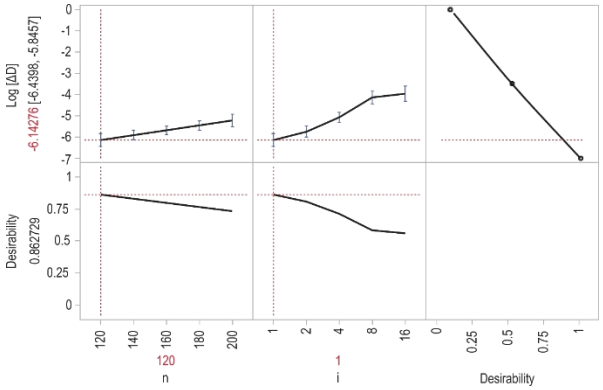


Fig. 7. Prediction Profiler

Fig. 8 shows a statistically significant interaction between the spindle speed and the number of passes. The strongest effect is observed when both input parameters reach their maximum values, while the smallest effect is observed at the minimum values of both parameters.

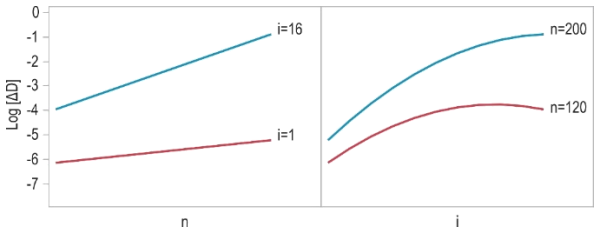


Fig. 8. Interaction Profiles

The statistical analysis of the selected regression model results in the following regression equation for the dimensional deviation:

$$\text{Log } \Delta D = -7.74106 + 0.23122 \times i + 0.00975 \times n - 0.01768 \times i^2 + 0.00179 \times i \times n \quad (1)$$

The regression models were confirmed by 5 additional experiments. The confirmation experiments were carried out with combinations of input parameters for which the processing model had not originally been developed. The results obtained and the calculated absolute and percentage errors are shown in Table 4.

No.	n (rev/min)	f (mm/rev)	i	ΔD		Error	
				Measured (mm)	Calculated (mm)	Absolute (mm)	Percentage (%)
1	120	0.2	1	0.002	0.002	0.0000	0.00
2	140	0.1	4	0.009	0.0088	0.0002	2.22
3	160	0.5	4	0.015	0.013	0.0020	13.33
4	180	0.2	2	0.008	0.007	0.0010	12.50
5	200	0.3	8	0.123	0.111	0.0120	9.76

Table 4. Results of confirmation experiments

4. CONCLUSION

In the study, the modelling of the machining parameters was performed from the point of view of changing the diameter deviation of the hole for the boring process performed with a specially designed tool holder.

The results of the experimental research and statistical processing of the measured results have shown that there is a mutual functional dependence between the number of revolutions and the number of passes on the one hand and the diameter deviation on the other. The diameter deviation increases with an increase in the number of revolutions and the number of passes. Changing the feed rate had no effect on the diameter deviation. With a suitable combination of input machining parameters, output parameter values in a wide range can be achieved, namely: ΔD= 0.002-0.406 mm. This is very important for practical applications when it comes to achieving the required diameter deviation.

The results of the prediction and confirmation show that it is possible to model the change in diameter as a function of the number of revolutions and the number of passes. The percentage modelling errors range from 0 to 13.33 %. The absolute errors are between 0 and 0.012 mm and correspond to these percentage errors. The values of the errors obtained are low and indicate the possibility of practical implementation of the methodology presented in a real production environment.

The study carried out also has certain limitations. The results obtained can be applied to the range of input parameters with which the experiments were performed. In order to achieve greater universality of the developed model, experimental studies are planned on workpieces with different properties and with cutting inserts with different geometric and technological characteristics. In addition, future research will focus on modelling a larger number of variables, i.e. including a larger number of input and output parameters in the model.

5. REFERENCES

[1] Sortino, M., Totis, G., Prosperi, F.: Modeling the dynamic properties of conventional and high-damping boring bars, Mechanical Systems and Signal Processing, Vol. 34, No. 1-2, pp. 340–352, 2013.

[2] Wang, G., Dong, H., Guo, Y., Ke, Y.: Dynamic cutting force modeling and experimental study of industrial robotic boring, International Journal of Advanced Manufacturing Technology, Vol. 86, No. 1-4, pp. 179–190, 2016.

[3] Chen, L., Tai, B.L., Yang, J.A., Shih, A.J.: Experimental Study and Finite Element Modeling of Workpiece Temperature in Finish Cylinder Boring, Journal of Manufacturing Science and Engineering, Transactions of the ASME, Vol. 139, No. 11, 111003, 2017.

[4] Venkata Rao, K., Murthy, P.B.G.S.N.: Modeling and optimization of tool vibration and surface roughness in boring of steel using RSM, ANN and SVM, Journal of Intelligent Manufacturing, Vol. 29, No. 7, pp. 1533–1543, 2018.

[5] Li, L., Sun, B., Hua, H.: Nonlinear system modeling and damping implementation of a boring bar, International Journal of Advanced Manufacturing Technology, Vol. 104, No. 1-4, pp. 921–930, 2019.

[6] Du, W., Wang, L., Peng, D., Shao, Y., Mechefske, C.K.: A new dynamic boring force calculation method using the analytical model of time-varying toolpath and chip fracture, Journal of Materials Processing Technology, Vol. 306, 117642, 2022.

[7] Kocovic, V., Vukelic, D., Kostic, S., Bijelic, I., Prica, M., Tadic, B.: Micro-cutting of holes by centrifugal force, International Journal of Advanced Manufacturing Technology, Vol. 124, pp. 1437–1455, 2023.

ACKNOWLEDGMENTS

This research has been supported by the Ministry of Science, Technological Development and Innovation (Contract No. 451-03-65/2024-03/200156) and the Faculty of Technical Sciences, University of Novi Sad through project “Scientific and Artistic Research Work of Researchers in Teaching and Associate Positions at the Faculty of Technical Sciences, University of Novi Sad” (No. 01-3394/1).

Authors:

MSc Aleksandar Milosevic, PhD Zeljko Santosi, PhD Mario Sokac, PhD Djordje Vukelic, University of Novi Sad, Faculty of Technical Sciences, Trg Dositeja Obradovica 6, 21000 Novi Sad, Serbia.
E-mail: aleksandar.milosevic@uns.ac.rs; zeljkos@uns.ac.rs; marios@uns.ac.rs; vukelic@uns.ac.rs

PhD Vladimir Kocovic, PhD Branko Tadic, University of Kragujevac, Faculty of Engineering, Sestre Janjic 6, 34000 Kragujevac, Serbia.
E-mail: vladimir.kocovic@kg.ac.rs; btadic@kg.ac.rs

PhD Goran Simunovic, University of Slavonski Brod, Mechanical Engineering Faculty, Trg Ivane Brlic Mazuranic 2, 35000 Slavonski Brod, Croatia.
E-mail: gsimunovic@unisb.hr

MMA 2024
FLEXIBLE TECHNOLOGIES

15th INTERNATIONAL SCIENTIFIC CONFERENCE
NOVI SAD, SERBIA, SEPTEMBER 24-26, 2024

Original research paper https://doi.org/10.24867/MMA-2024-03-003

Vidakovic, I., Simunovic, K., Pacarek, G., Barac, Z., Rozing, G.

APPLICATION OF NiCrBSi AND NiCrBSi-WC COATINGS AS WEAR PROTECTION FOR PARTS OF AGRICULTURAL TECHNIQUE

Abstract: *This paper presents the results of a study investigating the abrasion wear of NiCrBSi and NiCrBSi-WC coatings deposited by flame spraying with simultaneous fusing on previously quenched and tempered steel (42CrMo4+QT). A wear resistance test was conducted by moving the specimen in the abrasive mass (quartz sand) at a speed of 1.70 m/s and impact angles of the abrasive particles of 45° and 90°. This was accompanied by metallographic analysis of the coating and the coating/substrate interface. The objective of this study was to compare the wear resistance of the coatings tested with each other and with the uncoated base material as a function of impact angle and to investigate the possibility of using the coatings as wear protection for agricultural machinery parts. The tests demonstrated that a greater mass loss occurred at a smaller impact angle for all samples tested, with the NiCrBSi-WC coating exhibiting the lowest mass loss. Both coatings tested exhibited significantly lower mass loss than the uncoated base material.*

Key words: *NiCrBSi, NiCrBSi-WC, flame spraying with simultaneous fusing, abrasion wear, wear protection*

1. INTRODUCTION

During exploitation, the working parts of many technical systems are subject to various forms of wear and tear, resulting in damage and the need for earlier replacement of worn parts, which ultimately leads to an increase in overall maintenance costs. A special form of wear occurs during the movement of the working parts of the tool in the abrasive mass to which the working parts of many agricultural, construction or mining machines are most frequently exposed [1]. Soil cultivation is one of the most important parts of agricultural production, because without good soil cultivation there can be no good yields. All agricultural machines used in tillage (plows, subsoilers, disk harrows, harrows, cultivators, etc.) are exposed to various forms of wear caused mainly by the movement of their working parts through the mass of the soil [2]. A tribological system is very complex and represents the interaction between tillage tools and the soil itself and as such represents a complicated tribological problem [2,3]. During the movement of the tool through the soil, which usually has a different chemical composition, the most important form of wear is abrasive wear, which is caused by hard abrasive particles in the soil, usually quartz.

Various methods are used to protect against wear, which relate to a change in the material structure or a change in the type of material of the working surface of the tool [4]. One of the ways to change the type of material of the working surface is spraying with a flame spraying with simultaneous fusing, which was used in this research. With this procedure, it is possible to apply coatings at the point of exploitation, as well as to apply coatings to uneven or rotating parts. Various alloys can be used as coating materials. Nickel-based alloys (NiCrBSi, NiCrBSi-WC, etc.) were frequently used in research and were also used in this study. The alloys mentioned are used where protection of the materials against wear, oxidation and corrosion is required at elevated working temperatures and difficult working conditions [5].

A review of previous research found a smaller number of papers investigating the wear resistance of nickel-based alloys in the mass of abrasives [6,7]. This work involved a study of the wear resistance of the aforementioned alloys by movement in the abrasive mass at a constant speed of movement of the samples and different impact angles of the abrasive particles and the worn surface in order to determine the applicability of NiCrBSi and NiCrBSi-WC alloys as possible protection against wear of working parts of agricultural machinery.

2. MATERIALS AND METHODS

The research includes testing the wear resistance of coatings made of NiCrBSi and NiCrBSi-WC alloys and the base material without coatings, as well as justifying the use of said alloys as wear protection for working parts of agricultural machinery. The test was carried out on an apparatus for wear by the movement of samples in the mass of abrasives, and the measure of wear resistance was the loss of mass of the samples after the entire wear path.

2.1 Base material

A previously quenched and tempered chromium-molybdenum steel (42CrMo4+QT) was selected as the base material. The specified steel belongs to the group of high-strength, low-alloy steels and is used for the manufacture of highly stressed machine parts [8]. Fig. 1 shows the microstructure of the base material, taken with an optical microscope. The image shows the martensitic (needle-shaped) microstructure of the base material.

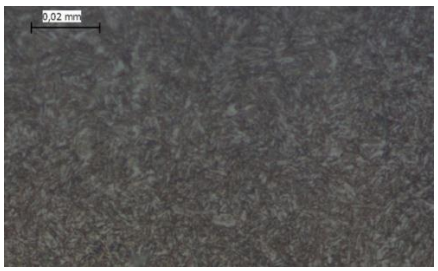


Fig. 1. Microstructure of the base material, etched in nital 3%, magnification 1000x

The steel 42CrMo4+QT is used for the production of parts of agricultural machinery parts, and in practice it is very often necessary to apply of the mentioned coatings to a substrate that has been previously heat-treated, especially when replacing worn parts, which was precisely the main reason for choosing this steel as the base material.

2.2 Coating material

The coating material used was the powder of two nickel-based alloys NiCrBSi (Castolin Eutalloy 10009, BoroTec) and NiCrBSi-WC (Castolin Eutalloy 10112, TungTec) with a ratio of NiCrBSi matrix and tungsten carbide particles of 40% matrix and 60% tungsten carbide. The chemical composition of the powders used to produce the coatings: NiCrBSi powder (wt, %): C 0,7%, Cr 15%, Fe 3,5%, B 3,2%, Si 4,4%, Ni - balanced, NiCrBSi-WC powder (wt, %): C max. 0,1%, Cr 7%, Fe 5,8%, B 3%, Si 4,5%, Ni – balanced [9].

The coating was applied by gas flame spraying with simultaneous fusing (trade name SuperJet Eutalloy - Castolin) in order to achieve a metallurgical bond between the coating and the base material and to reduce porosity. Flame spraying is classified as a low-speed spraying process according to the criterion of the speed of the molten particles, as the spraying speed is less than 100 m/s [10].

2.3 Wear test

The wear test was carried out on a device for the wear of the abrasive mass under certain kinematic parameters. During the test, the test specimens placed on a three-armed specimen carrier move in a circular motion inside the container with the abrasive, simulating real conditions similar to those in exploitation. The device for the wear in the abrasive mass is shown in Fig. 2.


Fig. 2. Device for wear in the mass of abrasives

2.4 Abrasive used in the test

During cultivation, the working parts of agricultural machinery are exposed to the abrasive effect of soil particles. Since the composition of the soil contains a certain percentage of quartz, which is the most important abrasive, quartz sand of the brand KEMA "FB150S" with a grain size of 0.5 - 1.5 mm was chosen as the abrasive in this study. The chemical composition of the abrasive used in the test - quartz sand is it (wt, %): SiO_2 > 99%, Fe_2O_3 0,297%, Al_2O_3 0,658%, TiO_2 0,032%, CaO 0,041%, MgO 0,027%, P_2O_5 0,009%, K_20 0,104% [11].

2.5 Performance parameters of the experiment

The determination of the wear resistance of NiCrBSi and NiCrBSi-WC coatings in the mass of the abrasives was carried out at a constant movement speed of the samples of 1.70 m/s. In order to determine the wear resistance of the aforementioned coatings as a function of the collision angle between the abrasive particles and the worn surface, the tests were carried out at impact angles of 45° and 90°. Based on literature data [8] and the assumption about the abrasiveness of the quartz sand used, the tests were carried out at an angle with a total wear distance of 20000 meters.

2.6 Equipment for determining the mass loss

The mass loss of the samples after the entire wear path was determined as a measure of wear resistance. The indicated loss was determined based on the difference in mass of the samples before and after the abrasion test. The samples were weighed on an analytical balance Kern & Sonh GmbH ALJ 160-4A, with an accuracy of 10-4 g and a measuring interval of 0 to 160 g.

3. METALLOGRAPHIC ANALYSIS OF THE SAMPLES

A metallographic analysis of the samples was carried out to determine the microstructural properties of the coating and the interface between the coating and the substrate, as well as the effects of the spraying process on the substrate. For the analysis, the samples were imaged using a scanning microscope SEM. Prior to metallographic analysis, the samples were prepared. This included casting the samples in a three-component acrylic resin, grinding and polishing the samples, etching the samples in Nital (2%), rinsing and drying the samples.

Fig. 3 shows the cross-sectional microstructure of the sample with NiCrBSi coating.

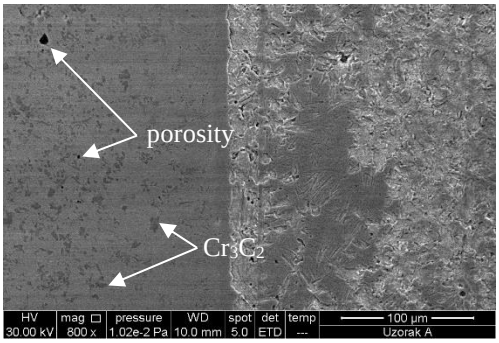


Fig. 3. SEM image of the NiCrBSi coating/substrate interface

It can be seen from the image that the coating is compact, without damage and cracks, with a clearly defined boundary between the coating and the substrate and a small amount of porosity. The image shows that there are many small, dark gray areas inside the coating, which are probably chromium carbide (Cr3C2) particles. Fig. 3 also shows that the structure of the substrate corresponds to the structure of martensite. This means that there was no significant change in the microstructure due to the spraying process, which proves that the input of thermal energy during the spraying process using a gas flame had no significant effect on the material of the substrate.

Fig. 4 shows the microstructure of the sample with NiCrBSi-WC coating in cross-section. It can be seen that the coating is compact, without damage or cracks and has a clearly visible boundary between the coating material and the substrate.

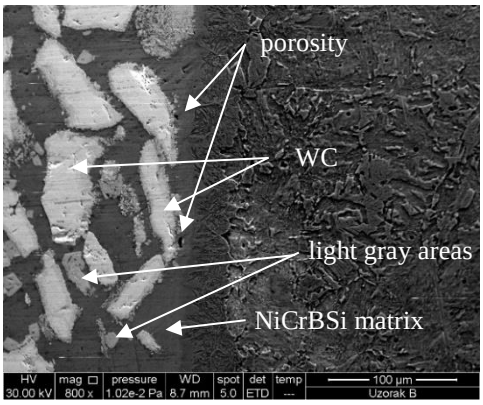


Fig. 4. SEM image of the NiCrBSi-WC coating/substrate interface

The Fig. 4 shows that the coating consists of three different phases. In the dark gray NiCrBSi matrix there are large areas of irregular shape, which are probably tungsten carbide particles. Around these areas, light gray, irregularly shaped areas can be seen, which are evenly distributed over the cross-section of the coating and which are probably nickel, chromium and silicon carbides. In studies [12,13], similar microstructures were observed in NiCrBSi-WC coatings. Fig. 4 also shows that the microstructure of the substrate corresponds to the microstructure of the martensite, which means that in this case, too, the injection process did not cause any significant change in the microstructure.

4. RESULTS AND DISCUSSION

In order to be able to perform a qualitative analysis of the research results, the wear test of the examined coatings and the base material without coatings was performed in two repetitions for each angle of impact of the abrasive and the worn surface (45° and 90°). The repetition was performed in such a way that after the total wear distance of 20 000 meters and the measurement of mass loss, the test was performed on the same sample, which in reality is not a repetition but a continuation of the test under the same conditions. For this reason, the wear was determined as the average mass loss after the first and second repetition. The results of the test are shown in Table 1.

Analyzing the mass loss results listed in Table 1, it can be seen that almost all samples show a greater mass loss after the first repetition. Similarly, the authors [12] found in their investigations that the specimens wear more heavily at the beginning of the test until the so-called uniform wear, i.e. until the unevenness on the wear surface has been removed, after which a lower mass loss occurs.

Sample	Impact angle, [°]	Mass, [g]		
		Mass loss after the 1st repetition	Mass loss after the 2nd repetition	Average mass loss
NiCrBSi	45	0.0182	0.0139	0.0161
NiCrBSi	90	0.0151	0.0094	0.0123
NiCrBSi-WC	45	0.0125	0.0092	0.0109
NiCrBSi-WC	90	0.0029	0.0124	0.0077
Base material	45	0.0512	0.0480	0.0496
Base material	90	0.0338	0.0294	0.0316

Table 1. The results of the analysis of the mass loss of the tested samples

Fig. 5 shows a comparative diagram of the mass loss of the tested samples. It can be seen from the diagram that both coatings tested and the base material without coating exhibit a greater mass loss at a smaller impact angle (45°). Looking at the single contact of an abrasive particle with a worn surface, a larger mass loss at a smaller impact angle is the result of a longer contact between the abrasive particles and the worn surface, where the particles continue to slide on the worn surface after hitting the worn surface, while at a larger impact angle the abrasive particles are repelled more strongly from the surface, so that the contact between the abrasive particles and the worn surface is shorter.

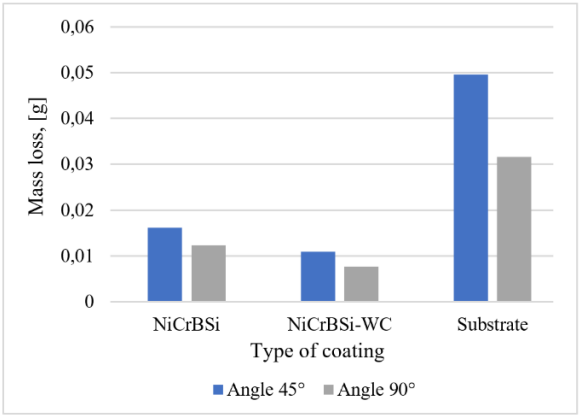


Fig. 5. Comparative diagrammatic presentation of the mass loss of the tested samples

It can be seen from the diagram that the NiCrBSi-WC coating has a lower mass loss compared to the

NiCrBSi coating at both impact angles. This result is a consequence of the presence of tungsten carbide in the composition of the NiCrBSi-WC coating.

The image also shows that both coatings examined exhibit a significantly lower mass loss at both impact angles compared to the base material without coating. Such a result is a consequence of the significantly lower surface hardness of the base material (37 HRC) compared to the surface hardness of the NiCrBSi coating (63 HRC) and the NiCrBSi-WC coating (64 HRC). These results prove the justification of the application of the tested coatings as protection against wear of the working parts of agricultural machinery, which are exposed to severe abrasive wear during operation due to the impact of soil particles.

5. CONCLUSION

Based on the tests carried out, it was found that the NiCrBSi-WC coating has a lower mass loss compared to the NiCrBSi coating at both collision angles (45° and 90°), which is a consequence of the presence of tungsten carbide in the composition of the NiCrBSi-WC coating, which has an impact on increasing the resistance to wear.

Both coatings examined (NiCrBSi and NiCrBSi-WC) had a significantly lower mass loss at both impact angles compared to the base material without coating (42CrMo4+QT). This result is a consequence of the significantly higher surface hardness of the tested coatings compared to the base material without coating. The results of the tests carried out show that the use of the coatings investigated as wear protection for working parts of agricultural machinery is justified.

When comparing the mass loss of the tested samples, it was found that all test samples showed a greater mass loss at a smaller impact angle (45°) than at a larger impact angle (90°). The reason for this result is the longer contact time between the abrasive particles and the worn surface at a smaller impact angle, as the abrasive particles continue to slide on the surface after contact with the worn surface at a smaller impact angle, whereas they bounce off the surface at a larger impact angle.

Based on the obtained research results, the need to continue this research was observed depending on the speed of the sample (the future test was carried out at the same speed), as well as depending on the different granulation of the abrasive.

6. REFERENCES

[1] Ivušić, V.: *Tribologija*, Fakultet strojarstva i brodogradnje, Sveučilište u Zagrebu, Zagreb, 1998.

[2] Vidaković, I., Heffer, G., Grilec, K., Samardžić, I.: *Resistance of modified material surfaces for Agricultural tillage tools to wear by soil particles*, Metalurgija, Vol. 61, No. 2, pp. 355-358, 2022.

[3] Kostencki, P., Stawicki, T., Królicka, A., Sędłak, P.: *Wear of cultivator coulters reinforced with cemented-carbide plates and hardfacing*, Wear, pp. 438-439, 2016.

[4] Vidaković, I., Heffer, G., Šimunović, K., Rozing, G.: Application of heat treatment in wear protection for working parts of agricultural machinery, Proceedings of 10th International Conference of Mechanical Technologies and Structural Materials, Split, Hrvatsko društvo za strojarske tehnologije (HDST), Split, 2021.

[5] Huang, S., Zhou, J., Sun, K., Yang, H., Cai, W., Liu, Y., Zhou, P., Wu, S., Li, H.: *Microstructural Charactistics of Plasma Sprayed NiCrBSi Coatings and Their Wear and Corrosion Behaviours*, Coatings, Vol. 11, No.170, pp. 1-13, 2021.

[6] Heffer, G., Samardžić, I., Schauperl, Z., Vidaković, I.: *Wear of Induction Cladded Coating in the Abrasive Mass at Various Speeds and Impact Angels*, Tehnički vjesnik – Technical Gazette, Vol. 25, No. 6, pp. 1776-1782, 2018.

[7] Brezinová, J., Landová, M., Guzanová, A., Dulebová, L., Draganovská, D., *Microstructure, Wear Behaviour and Corrosion Resistance of WC-FeCrAl and WC-WB-Co Coatings*, Metals, Vol. 8, No.6, pp. 399, 2018.

[8] Dizdar, S., Skoglund, P., Bengtsson, S.: *Process, quality and properties of high-density P/M gears*, Höganäs AB, Resarch and Development, Höganäs, Sweden, pp. 10, 2015.

[9] Priručnik Castolin: *Metall – und Keramikpulver zum thermischen Spritzen, Produkt- und Anwendungsinformation*, Castolin GmbH, Kriftel.

[10] Fauchais, P.L., Heberlein, J.V.R., Boulos, M.I.: *Thermal Spray Fundamentals, From powder to Parts*, Springer, New York, Heidelberg, Dordrecht, London, pp. 1566, 2014.

[11] KEMA tehnički list za pijesak FUGA SAND, Baumit Crna Gora d.o.o., Podgorica, 2015.

[12] Rachidi, R., El Kihel, B., Delauonis, F.: *Microstructure and mechanical characterization of NiCrBSi alloy and NiCrBSi-WC composite coatings produced by flame spraying*, Materials Science and Engineering B, Vol. 241, pp. 13-21, 2019.

[13] Simunovic, K., Slokar, Lj., Havrlisan, S.: SEM/EDS investigation of one-step flame sprayed and fused Ni-based self-fluxing alloy coatings on steel substrates, Philosophical Magazine, Vol. 97, No. 4, pp. 248-268, 2017.

Authors:

PhD Ivan Vidaković, M.Sc.Mech.Eng. Goran Pačarek, PhD Željko Barač, Josip Juraj Strossmayer University of Osijek, Faculty of Agrobiotechnical Sciences Osijek, Vladimira Preloga 1, 31000 Osijek, Croatia, Phone.: +385 31 554 978.
E-mail: ividakovic@fazos.hr; gpacarek@fazos.hr; zbarac@fazos.hr

PhD Katica Šimunović, University of Slavonski Brod, Faculty of Mechanical Engineering, Trg Ivane Brlić Mažuranić 2, 35000 Slavonski Brod, Croatia, Phone.: +385 35 493 430.
E-mail: ksimunovic@unisb.hr

PhD Goran Rozing, Josip Juraj Strossmayer University of Osijek, Faculty of Electrical Engineering, Computer Science and Information Technology Osijek, Kneza Trpimira 2b 1, 31000 Osijek, Croatia, Phone.: +385 31 224 600.
E-mail: goran.rozing@ferit.hr

MMA 2024
FLEXIBLE TECHNOLOGIES

15th INTERNATIONAL SCIENTIFIC CONFERENCE
NOVI SAD, SERBIA, SEPTEMBER 24-26, 2024

Original research paper https://doi.org/10.24867/MMA-2024-03-004

Jotic, G., Strbac, B., Sokac, M., Tanasic, Z., Runje, B., Acko, B., Hadzistevic, M.

OPTIMIZATION OF THE MEASUREMENT PROCESS USING A 3D LASER SCANNER

Abstract: *The application of optical coordinate measurement systems (OMS) in industry has become more frequent. Advantages in the application of these measurement systems include simple scanning procedures and high data density (sampled points). In addition, optical measurement systems are integrated in the processes of dimensional and geometric analysis of products, reverse engineering, additive technologies, etc. However, the accuracy of OMS is significantly lower compared to the accuracy that can be realized using a coordinate measuring machine (CMM). The characteristic of OMS metrology is a large number of factors that affect the accuracy of measurement results. In this work, an overview of influencing factors on the accuracy of a 3D laser scanner was performed. On the basis of previous researches, dominant influential factors were singled out. The experiment includes an analysis of the significance of influencing parameters on measurement results using the Design of Experiment (DOE) technique. The experiment was conducted according to the Taguchi L8 orthogonal array. The results indicate that the selection of appropriate values of the influential parameters contributes to the reduction of measurement error.*
Key words: *Coordinate metrology, Accuracy, Optical measurement systems.*

1. INTRODUCTION

Increasing the productivity and flexibility of the production process can be achieved through a combination of intelligent production systems and advanced technologies, among which coordinate measuring systems play a significant role. CMMs with contact measuring sensors are one of the most common measuring systems in the industry. Compared to other types of measuring systems, coordinate measuring machines offer significant advantages in terms of accuracy and precision. However, CMMs are not the best solution in production systems that require rapid inspection. In this way, optical measurement sensors overcome certain limitations related to CMMs, offering advantages in terms of the way and time of digitizing workpieces [1]. The workpiece scanning process the involves the collection of sampled points data on the surface of the object and their conversion into digital form [2]. The result of the digitization process is a spatial set of points, the so-called cloud of points, where the position of each point is defined by coordinates (x, y, z). Based on the point cloud, it is possible to define a virtual three-dimensional model of the scanned object that can be used in various applications such as GD&T inspection, reverse engineering modeling, CAD inspection, additive technologies, etc. [3]. Considering the possibility of three-dimensional data acquisition, optical measurement systems are often considered as an alternative to contact measurement systems. However, the accuracy of measurement results obtained using optical measuring systems are still significantly lower compared to CMM. One of the reasons for this is a lack of research in the field of interaction of influencing parameters on the accuracy of optical measurement results.

The quality of the measurement results of optical measuring systems, specifically triangulation 3D laser scanners, depends on a large number of influential factors [4]. One of the key problems when evaluating the performance of a certain measuring system is to provide an adequate reference standard. Carmignato et al. [5] emphasize the key role of standards in the process of establishing measurement traceability. The paper analyzes the main characteristics of certain reference standards and their availability. The authors of paper [6] analyze procedures for the verification of measurement systems from a statistical point of view. Barbero and Ureta in paper [7] present a comparative analysis of five different optical measuring systems. The analysis includes triangulation scanners based on laser and structured white light and a CT scanner. For the purposes of GD&T analysis, three calibrated and two uncalibrated objects of complex geometry were used. The 3D scanner based on structured light stands out in terms of dimensional accuracy, while the CT has the largest deviations from calibrated values. The author of paper [8] provides a systematic approach to the analysis of the accuracy of Atos 3D scanners in accordance with VDI/VDE 2634-part 3. The paper deals with the practical implementation of the acceptance test of ATOS non-contact 3D scanners by measuring a calibrated workpiece developed by the manufacturer of the measuring system. In paper [9], Mendricky investigates the influence of various parameters on the accuracy of a 3D scanner based on the principle of structured light. Among other things, the influence of calibration, exposure, number of images, scanning angle and quality of reference points was analyzed. The experiment proved that the quality of the reference points has the greatest influence on the accuracy of the measurement results.

In this paper, the optimization of the measurement process of the test workpiece was performed using a laser 3D scanner. The research includes a dimensional and geometric analysis of a calibrated workpiece with a

complex geometric shape. L8 Taguchi orthogonal array was used to conduct the experiment. The goal of the experiment is to define the optimal values of the parameters of the measurement process that will result in a minimum value of the measurement error.

2. MATERIALS AND METHODS

For the purpose of experimental research, a dimensional and geometric inspection of the calibrated test workpiece was performed (Fig. 1). The material of the test workpiece was AlCu4Mg1 (T351). Geometry of the test workpiece was defined with the aim of testing the possibility of realizing various measuring tasks using a laser 3D scanner. The accuracy of the laser scanner was analyzed in relation to the calibrated (reference) values of test part parameters. The calibrated value was obtained using a CMM with a contact sensor. Deviations, defined as the difference between a measured and calibrated values, were observed as output parameters (Table 1).

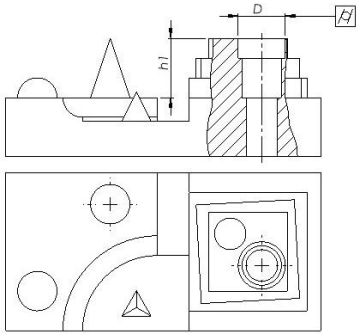


Fig. 1. The test workpiece

Parameter	Values/mm
Hole diameter D	16.1318
Cylindricity C	0.0167

Table 1. Calibrated values of test workpiece parameters

Scanning of the test workpiece was performed using a 3D laser scanner MMDx100 integrated into the Nikon MCAx 2.0+ measuring arm (Fig. 2). Technical specifications of the optical measurement system are shown in Table 2. 3D point cloud processing was performed using the Focus 10 software. GD&T analysis of the test workpiece was performed using GOM Inspect software.

Realization of the object scanning process implies the selection of optimal values of the scanning parameters in order to obtain high-quality of part mesh. Compared to CMM, the accuracy of optical measuring systems is characterized by a significantly larger number of influencing factors. For the purpose of an efficient measurement process, it is necessary to investigate the influence of a certain number of influential factors on the accuracy of the measurement system. The classification of influential factors includes certain factors classified by groups: measurement system, workpiece, environment, measurement strategy, operator and software. In accordance with the methodology of the measurement process, the dominant influencing factors are proposed as follows: the distance between the points, the exposure time and the intensity of the laser beam source.

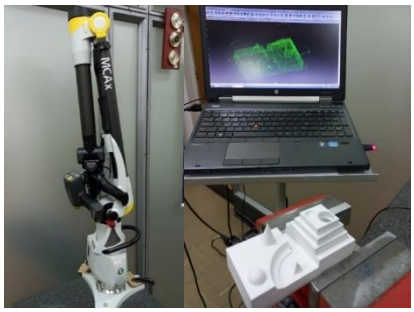


Fig. 2. The 3D laser scanner

Technical specification	Parameters value
Line width	100 mm
Object distance	95 mm
Accuracy	10 µm
Accuracy in combination with measuring arm	48 µm
Sampling frequency	max 150 Hz
Points per line	1000
Laser power	class 2
Weight	400 g

Table 2. Specifications of the 3D laser scanner

The Taguchi design of experiment was used to suggest parameters that contribute to the generation of optimal measurement values. The experiment was performed using three factors at two levels, Table 3.

Parameter	Symbol	Level 1	Level 2
Points distance /mm	A	0.2	0.8
Time of exposure/ms	Bw	1	5
Laser power in relation to the maximum power/%	C	35	98

Table 3. Scanning process parameters

3. RESULT AND DATA ANALYSIS

The Minitab 20 statistical software was used for statistical data processing and defining the sequence of experiments. Full factorial design is not practical for application because it requires a large number of experiments, which results in high costs and long-term research. Given that the optical measurement process is time-consuming, the Taguchi L8 orthogonal array was selected. Taguchi's experimental design is based on the calculation of the *S/N* (signal-to-noise) ratio and calculates the *S/N* ratio for each treatment. The *S/N* ratio is defined as the ratio between the magnitudes of the input signals and the signals affected by noise [10]. Therefore, the value that maximizes the *S/N* ratio of each controlled factor becomes robust to noise. In this case, the deviation of dimensional and geometric parameters of the test part were analyzed, for this reason the *S/N* ratio "the smaller the better" was used.

$$S/N = -10log\left(\frac{1}{n}\sum_{i=1}^{n} y_i^2\right) \quad (1)$$

here y_i is the response value of the specific treatment at i repetition, and i is the number of repetitions.

Table 4 shows the Taguchi design and deviation responses for a certain combination of input parameters. Also, Table 4 shows the values of the S/N ratio for each iteration of the experiment. Tables 5 and 6 show the values f the S/N ratio for each input parameter of the process, distance parameter and the cylindricity tolerance C.

Exp. no.	Parameters			Results			
	Points distance l/mm	Time of exposure t/ms	Laser power q/%	Distance h_1/mm	S/N ratio /dB	Cylindricity C/mm	S/N ratio /dB
1	0.2	5	35	0.0161	34.5771	0.0662	21.2858
2	0.2	5	98	0.0119	47.8939	0.0457	23.0165
3	0.2	1	35	0.0175	24.0022	0.0974	20.2270
4	0.2	1	98	0.0089	25.7672	0.0923	20.6978
5	0.8	5	35	0.0632	21.5829	0.1203	18.3932
6	0.8	5	98	0.0120	23.8723	0.0997	20.0261
7	0.8	1	35	0.0747	20.1005	0.1268	17.9376
8	0.8	1	98	0.0251	22.3177	0.1066	19.4473

Table 4. Experimental design and calculated results

Level	Points distance/mm	Time of exposure/ms	Laser power/%
1	33.06	23.05	25.07
2	21.97	31.98	29.96
Delta	11.09	8.93	4.9
Rank	1	2	3

Table 5. The S/N response table for the distance parameter

Level	Points distance/mm	Time of exposure/ms	Laser power/%
1	21.31	19.58	19.46
2	18.95	20.68	20.8
Delta	2.36	1.1	1.34
Rank	1	3	2

Table 6. The S/N response table for cylindricity tolerance

A graphic illustration of the influence of three input factors on the value of the measurement error of the analyzed parameters is shown in Fig. 3 and 4.

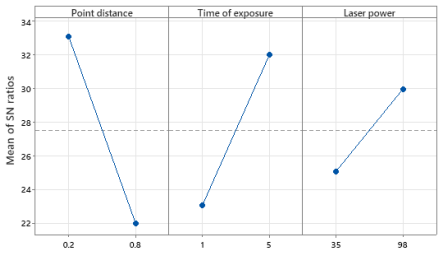


Fig. 3. *S/N* response for the distance parameter

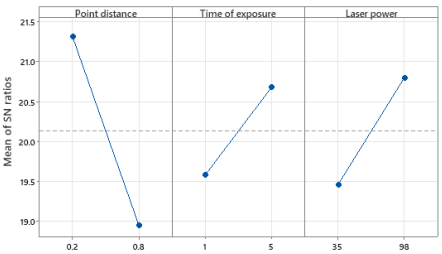


Fig. 4. The S/N response for cylindricity tolerance

Based on the analytical and graphical representation of the results of the Taguchi experiment, it follows that the factor distance between points has the greatest influence on the value of the distance parameter, followed by the exposure time and finally the laser power parameter. When inspecting the cylindricity tolerance, the largest contribution to the process response is made by the distance points factor, and the smallest contribution is made by the exposure time factor. As mentioned, the optimal combination of selected factors is for higher values of the S/N ratio. Namely, the optimal values of the controlled factors when measuring the distance parameter and cylindricity tolerance are the distance between the points 0.2 mm, the exposure time 5 ms and the intensity of the laser beam 98 % (Figures 3 and Figure 4). The specified values of the measurement process parameters result in the minimum value of the systematic measurement error of the analyzed parameters of the workpiece.

Analysis of variance (ANOVA) was performed to determine the statistical significance of input parameters on the response of the measurement process. Thus, the ANOVA test is used to estimate the percentage response magnitude of each factor in an orthogonal experiment (Table 7 and 8). The test was conducted with a confidence level of 95 %, i.e., a significance level of 5 %. Given that the level of significance is defined at a value of 5 %, it follows that factors with p value less than 0.05 are statistically significant at the response of the measurement process.

Source	DF	Adj SS	Adj MS	F-value	p-value	%
Points distance	1	0.004303	0.004303	31.72	0.005	59.6
Time of exposure	1	0.001798	0.001798	13.25	0.022	24.9
Laser power	1	0.000575	0.000575	4.24	0.109	8
Error	4	0.000543	0.000136			7.5
Total	7	0.007218				100

Table 7. Results of the ANOVA test for the distance parameter

Based on the comparison of the probability values of the controlled factors (p), it follows that the two factors, namely distance between points and exposure time are statistically significant for the distance measurement

error value. On the contrary, the laser power factor is not statistically significant in terms of distance measurement error (Table 7). The results of the ANOVA test indicate that all three input factors have a statistically significant impact on cylindricity tolerance (Table 8).

Source	DF	Adj SS	Adj MS	F-value	p-value	%
Points distance	1	0.001426	0.001426	45.53	0.003	62.4
Time of exposure	1	0.000266	0.000266	8.5	0.043	11.6
Laser power	1	0.000474	0.000474	15.14	0.018	20.7
Error	4	0.000125	0.000031			5.3
Total	7	0.002291				100

Table 8. Results of the ANOVA test for cylindricity tolerance

4. CONCLUSIONS

The use of optical measuring systems in the industry has increased significantly in the last few years. However, the quality of the obtained data is affected by a large number of measurement process parameters. Given the variety of optical measurement systems available on the market, procedures for determining accuracy are under development. Certain procedures for determining accuracy are available in the series of standards ISO 10360 and VDI/VDE 2634. The implementation of existing procedures implies strictly controlled conditions and precisely defined values of variables. However, in most cases such conditions cannot be provided in usual practice. For this reason, the influence of the parameters of the measurement process on the accuracy of the laser 3D scanner was examined.

In this paper, the influence of point distance, time exposure and laser power on the accuracy of OMS measurement results was analyzed.

The accuracy of the tested measuring system is expressed through the value of the systematic measurement error of dimensional and geometric characteristics of the calibrated workpiece. The Taguchi technique was used for the purpose of optimizing the measurement process (reducing measurement error). Based on the S/N ratio, it can be concluded that the optimal combination of input parameter levels that result in the smallest systematic measurement error of the test part analyzed parameters are: 0.2 mm distance between points in cloud, 5 ms time of exposure and 98 % laser power. The results of the ANOVA analysis show that the distance measurement error value is primarily influenced by the distance between point's factor with 59.6 % contribution, then the exposure time factor with 24.9 % contribution and, finally, the laser beam intensity factor with 8 %. The contributions of influential factors to the error of cylindricity measurement are as follows: distance between points with 62.4 %, laser power 20.7 % and exposure time 11.6 %.

Considering the wide application of optical measuring systems in the field of digitization of complex geometry objects, research in the field of procedures for determining the accuracy of OMS is of great importance.

5. REFERENCES

[1] Brajlih, T., Tasic, T., Drstvensek, I., Valentan I.: Possibilities of Using Three-Dimensional Optical Scanning in Complex Geometrical Inspection, Strojniški vijesnik, Vol. 57, pp. 826-833, 2011.

[2] Budak, I., Hodolič, J., Bešić, I., Vukelić, Đ., Osanna, P.H., Durakbasa, N.: Koordinatne merne mašine i CAD inspekcija, Fakultet tehničkih nauka Novi Sad, 2009.

[3] Carmignato, S.: Experimental study on performance verification tests for coordinate measuring systems with optical distance sensors, Three – Dimensional Imaging Metrology, Vol. 7239, pp. 153–162, 2009.

[4] Van Gestel, N., Cuypers, S., Bleys, P., Kruth, J. P.: A performance evaluation test for laser line scanners on CMMs, Optics and Lasers in Engineering, Vol. 47, pp. 336–342, 2009.

[5] Carmignato, S., De Chiffre, L., Bosse, H., Leach, R. K., Balsamo, A., Estler, W. T.: Dimensional artefacts to achieve metrological traceability in advanced manufacturing, CIRP Annals, Vol. 69, Issue 2, pp. 693–716, 2020.

[6] Petrò, S., Moroni, G.: A statistical point of view on the ISO 10360 series of standards for coordinate measuring systems verification, Measurement, Vol.172, Issue 2, 2021.

[7] Barbero, B. R., Ureta, E. S.: Comparative study of different digitization techniques and their accuracy, Computer – Aided Design, Vol. 43, Issue 2, pp. 188–206, 2011.

[8] Mendricky, R.: Determination of measurement accuracy of optical 3D scanners, MM Science Journal, Issue 6. pp. 1565–1572, 2016.

[9] Mendricky, R.: Aspects affecting accuracy of optical 3d digitization, MM Science Journal, Vol. 1, pp. 2267–2275, 2018.

[10] Owczarek, D., Ostrowska, K., Sładek, J. A.: Examination of optical coordinate measurement systems in the conditions of their operation, Journal of Machine Construction and Maintenance, Vol. 4, pp. 7–19, 2017.

Authors:

MSc Goran Jotic, PhD Zorana Tanasic, University of Banja Luka, Faculty of Mechanical Engineering, Stepe Stepanović 71, 78000 Banja Luka, BiH.
E-mail: goran.jotic@mf.unibl.org; zorana.tanasic@mf.unibl.org

PhD Branko Strbac, PhD Mario Sokac, PhD Miodrag Hadzistevic, University of Novi Sad, Faculty of Technical Sciences, Trg Dositeja Obradovica 6, 21000 Novi Sad, Serbia.
E-mail: strbac.br@gmail.com; marios@uns.ac.rs; miodrags@uns.ac.rs.

PhD Biserka Runje, Faculty of Mechanical Engineering and Naval Architecture, Ivana Lučića 5, 10002 Zagreb, Croatia.
E-mail: biserka.runje@fsb.hr

PhD Bojan Acko, Faculty of Mechanical Engineering, Smetanova 17, 2000 Maribor, Slovenia.
E-mail: bojan.acko@um.si

MMA 2024 FLEXIBLE TECHNOLOGIES

15th INTERNATIONAL SCIENTIFIC CONFERENCE
NOVI SAD, SERBIA, SEPTEMBER 24-26, 2024

Original research paper https://doi.org/10.24867/MMA-2024-03-005

Ognjenčić, K., Šimunović, G.

MEASUREMENT TECHNIQUES FOR REDUCING WATER LOSS IN SUPPLY SYSTEMS: FLOW, PRESSURE, AND NOISE ASSESSMENT

Abstract: *A significant challenge in water supply systems is the loss of water, which denotes the discrepancy between the volume of water extracted and the volume billed. This paper delves into measurement techniques that aid in mitigating these losses, with a focus on flow, pressure, and noise assessments. It will elucidate the working principles of ultrasonic, electromagnetic, and turbine flow meters. Additionally, the paper will cover the usage of manometers, piezoelectric sensors, and membrane sensors for pressure measurement in water supply systems. The application of geophones and correlators for noise detection will also be discussed, providing a detailed method for precise leak localization. The objective of this study is to present a comprehensive overview of fault detection and localization techniques within water supply networks.*

Key words: *Water supply, water loss, flow measurement, pressure measurement.*

1. INTRODUCTION

The activity of public water supply involves the extraction of groundwater and surface water for human consumption and its conditioning, as well as delivery to the end user. There are rare cases when water can be delivered to users without pumping or treatment. The quality of the water that is extracted is often not suitable for human use and requires treatment. All these procedures increase transportation costs. The transportation network itself ages irreversibly and is prone to failures, such as ruptures. The difference between the extracted water, which has passed through the meters at the extraction points or surface catchments, and the revenue-generating water, i.e., the water that has passed through the users' meters, represents a direct loss. According to the State Bureau of Statistics for 2021, in the Republic of Croatia, water loss amounts to around 40% of the extracted water [1]. Every non-revenue water that is extracted represents a direct cost to the public water supply and reduces revenues. Fighting losses is a vicious circle; no matter how much effort is put into reducing them, due to the aging of the network, their increase is inevitable.

2. FLOW MEASUREMENT

Flow measurement monitors the movement of water in a certain area in real-time, allowing the optimization of water resource distribution. Continuous flow monitoring enables the rapid detection of unexpected changes, whether an increase or decrease in consumption.

2.1 Ultrasonic Flow Measurement

Ultrasonic flow meters measure flow based on the interaction of ultrasonic waves passing through the fluid flow. The measurement results are not affected by the temperature, pressure, or density of the fluid being measured, and even tolerate the presence of foreign particles in the fluid. Two measurement methods based on the Doppler effect and the transit time of ultrasonic waves through the fluid are used in practice. These methods are used because of their ease of installation, mobility, and measurement accuracy.

2.1.1 Doppler Effect Method

In ultrasonic flow measurement using the Doppler method, an ultrasonic signal of high (constant) frequency is emitted from one probe (transmitter, T), which reflects off gases or solid particles in the water and is registered in the receiver (R), as shown in Fig 1. [2].

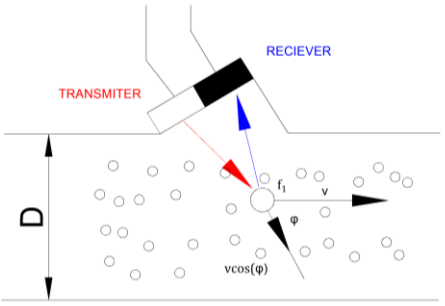


Fig 1. Ultrasonic Flow Meter Using the Doppler Effect

$$q_v = A \cdot v = \frac{D^2}{4} \cdot \frac{c}{2 \cdot f_0 \cdot cos\varphi} \cdot \Delta f \qquad (1)$$

Upon reflection, a frequency shift (Doppler effect) occurs, from which the velocity of the water itself, i.e., the flow through the cross-section of the pipeline, is calculated.

2.1.2. Transit Time Method

This method is based on measuring the time required for an ultrasonic signal to travel between two sensors placed along the pipe through which the water flows. The sensors can be positioned diagonally from opposite sides of the pipe or on the same side of the pipe, at a certain distance. Both probes simultaneously send and receive ultrasonic signals.

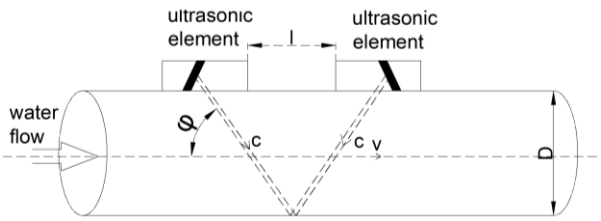


Fig 2. Ultrasonic Flow Meter Using Transit Time Method

$$q_v = A \cdot v = \frac{D^2 \cdot \pi \cdot c^2}{8 \cdot l \cdot cos\varphi} \cdot \Delta t \qquad (2)$$

Due to the positioning of the probes, one probe sends an ultrasonic signal in the direction of the water flow, while the other probe sends the ultrasonic signal in the opposite direction of the fluid movement. The difference in the transit times of these two ultrasonic signals is directly proportional to the fluid velocity [3], as shown in Fig 2. The transit time in the direction of the fluid is shorter due to the flow velocity, while the transit time in the opposite direction is longer, analogous to the movement of a boat downstream and upstream of a river. This method does not require the presence of particles in the fluid, making it suitable for measuring clean fluids. Before measurement, the sensors must be calibrated by entering data about the type of pipe, wall thickness, diameter, type of fluid, pressure, and temperature, as each parameter affects the speed of the ultrasonic signal through the fluid.

2.2 Electromagnetic Flow Measurement

Electromagnetic flow meters utilize Faraday's law of induction, which states that moving a conductor through a magnetic field induces a voltage proportional to the velocity of movement. Such meters have magnetic poles on opposite sides of the pipe, with probes placed perpendicularly to them, as shown in Figure 3. A magnetic field is created between the magnets through which the water passes, generating a voltage that is read by the probes. To avoid measurement errors caused by signal noise, changing polarity electromagnets are used. The magnetic field periodically changes as the poles switch, while the noise remains mostly constant. As the polarity changes, the sign of the induced voltage also changes, while the noise remains constant [4].

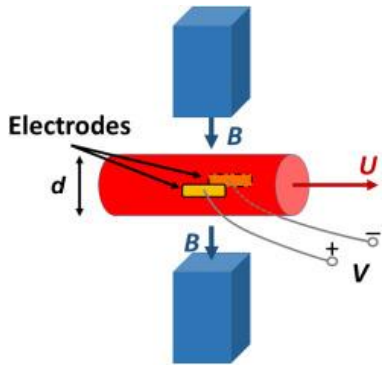


Fig 3. Schematic of an electromagnetic flowmeter [5]

$$E_+ = B \cdot v \cdot L + N \qquad (3)$$

$$E_- = -B \cdot v \cdot L + N \qquad (4)$$

$$q_v = k \cdot \Delta E \qquad (5)$$

The difference between the positive and negative induced voltages on the probes eliminates the error. The flow velocity is proportional to the induced voltage on the probes after noise removal [6].

2.3 Turbine Flow Meters

This type of meter operates on the principle of measuring flow velocity using a rotor with blades. The fluid moves tangentially, as shown in Fig 4, to the rotor and strikes the blades, rotating the rotor at a certain speed. The rotation is transmitted via gear sets to mechanical or electronic counters that display the amount that has flowed through the meter [7]. These devices need to be calibrated to determine how much water passes through the device for one rotation of the rotor. They are suitable for measuring different flow velocities, at various temperatures, and pressures in the system. They are very often used as installed water meters for end users.

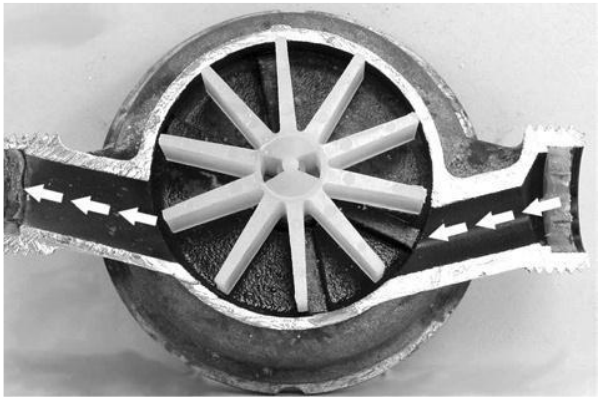


Fig 4. Flow Meter with Rotor and Blades

3. PRESSURE MEASUREMENT

Measuring pressures in the water supply system ensures timely response to changes in the system. In case of pipeline rupture or increased consumption, the system pressure drops, while during blockages, the system pressure rises. Monitoring pressure ensures system optimization.

3.1 Manometer

A manometer is a device used to measure fluid pressure, and there are several types. The most commonly used are tube manometers and Bourdon tube manometers. A tube manometer contains a tube filled with liquid, usually water or mercury. The pressure difference between the two ends of the tube causes the liquid to move, resulting in a proportional height difference between the two columns of liquid.

$$\Delta P = \rho \cdot g \cdot \Delta h \qquad (6)\ [8]$$

A Bourdon tube, shown in Fig. 5, is a curved vacuum or liquid-filled tube that straightens under external pressure, causing its free end to move. The movement of the free end of the tube is transmitted via a lever or gears

to the pointers. The deflection of the pointer is calibrated, and a calibrated scale is placed behind it [9].

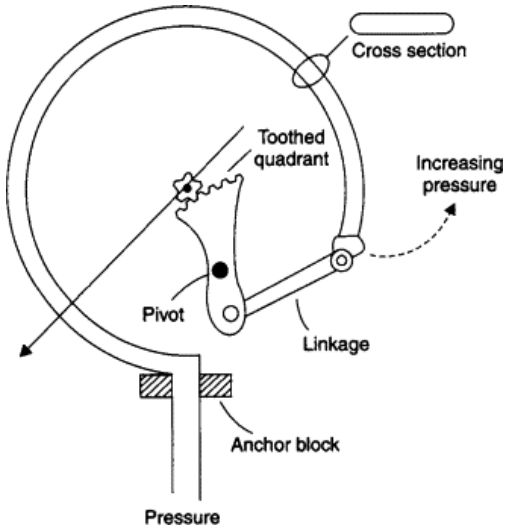


Fig 5. Bourdon Tube

3.2 Piezoelectric sensors

Piezoelectric sensors utilize the property of certain crystals to generate an electric charge proportional to the applied force when subjected to mechanical stress. Fluid pressure creates mechanical deformation on the piezoelectric material, shown in Fig. 6, placed between two electrodes, generating an electric charge that can be measured as an electrical signal. The advantage of such pressure meters is their very quick response to pressure changes, durability, and ability to detect very small pressure changes.

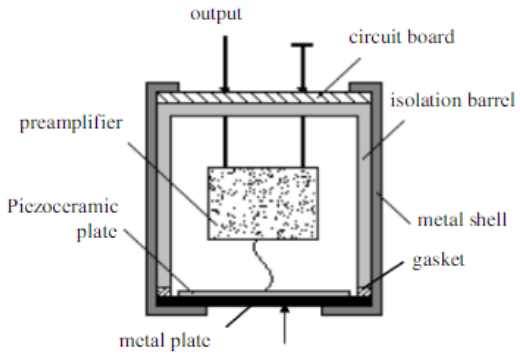


Fig 6. The structure of the piezoelectric sensor [10]

3.3 Membrane Sensor

A membrane pressure sensor consists of a housing with a flexible membrane that divides two chambers. One side is exposed to the pressure being measured, while the other side is exposed to a reference pressure or vacuum. When pressure acts on the membrane, it deforms proportionally to the applied pressure, as shown in Fig 7. The deformation is measured by piezoresistive, capacitive, inductive, or optical sensors. Equation (11) shows the proportionality of membrane deformation under pressure, with other values such as membrane thickness, Poisson's ratio of the membrane material, and membrane radius being constant.

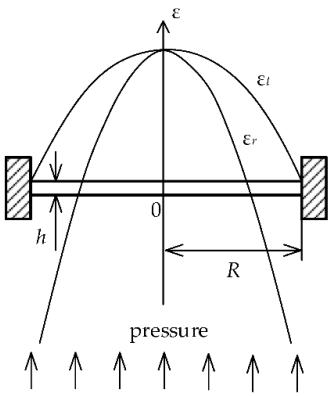


Fig 7. Circular membrane with indication of radial and tangential components of deformation caused by pressure

$$\epsilon_c = \frac{3 \cdot p \cdot R^2 \cdot (1-\mu^2)}{8 \cdot E \cdot h^2} \qquad (7)\ [11]$$

4. NOISE DETECTION

Devices for detecting noise created by water leaking through a crack are used for precise leak location in water supply systems. Hydrophones and correlators are most commonly used.

4.1 Geophones

Geophones are microphones that detect the sound of water noise leaking through a crack. They consist of a bell containing piezoelectric material, shown in Fig. 8, that converts noise into electrical signals. Signals are transmitted via cable or wireless transmission to data processing devices. The signal strength is increased, and unwanted frequencies and noises are removed. Traffic, footsteps, and other ambient sounds sometimes dominate, so using geophones can sometimes only be performed at night. Not all pipe materials transmit sound equally well. A rupture in iron pipes can be detected from a distance of several hundred meters, while in PVC or PEHD pipes, the noise is often barely detectable from few meters away.

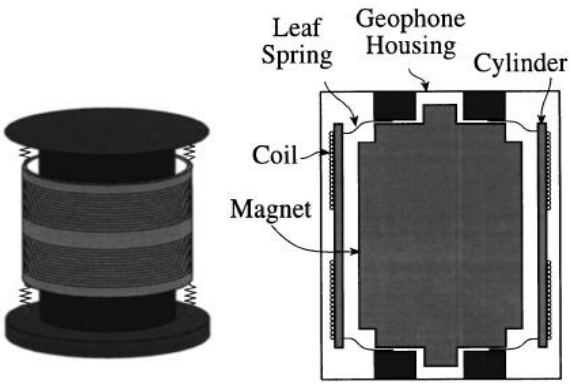


Fig 8. Schematic drawing and cross-sectional view of a geophone [12]

4.2 Correlators

Correlators are sophisticated devices used for precisely locating leaks in water supply systems. They use geophone sensors placed at various points along the

pipeline, as shown in Fig. 9, to detect and analyze sound signals produced by leaking water. Using algorithms, the correlator compares the arrival time of these signals at each geophone, enabling accurate leak location. This method provides high precision and efficiency, reducing the time and costs required for repairs, and ensuring non-invasive detection of infrastructure issues.

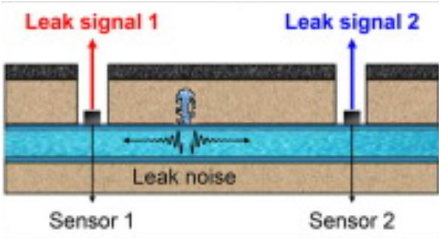


Fig 9. Buried water pipe with leak [13]

5. CONCLUSIONS

This paper provides insight into measurement methods used in water supply systems for locating leaks. The process of finding leak locations moves from a global to a local approach. Electromagnetic flow meters and manometers are positioned at fixed measurement points to monitor the system in real-time, while turbine flow meters are placed at system exits, i.e., towards users. When discrepancies or unaccounted water are detected, further localization is performed using ultrasonic flow meters and mobile manometers. The final step involves using correlators and geophones to pinpoint the leak to a very short pipeline section with high accuracy.

6. REFERENCES

[1] Sakupljanje, pročišćavanje i distribucija vode u 2023. https://podaci.dzs.hr/2024/hr/77328 (accessed July 30, 2024)

[2] Matić, F.: Metode i principi mjerenja ultrazvukom, 2021.

[3] Pantelar Županić, M.: Usporedba mjerenja protoka ultrazvučnim i elektromagnetskim protokomjerom, Manuela Pantelar Županić, 2017.

[4] Wyatt, D. G.: Noise in electromagnetic flowmeters, Medical and biological engineering, Vol. 4, pp. 333-334, 1996.

[5] Ostadfar, A.: Chater 8 Real Time Measurement Techniques of Biofluids, Bioflud Mechanics Principles and Applications, pp. 295-322, 2016.

[6] Rasales, C., Sanderson, M. L.: Streaming current noise generation in electromagnetic flowmeters measuring conducting fluids, Flow Measurement and Instrumentation, Vol. 14, No. 3, pp. 97-108, 2003.

[7] Užar, J.: Water Losses in Water Supply System, Technical journal, Vol. 6, No. 2, pp. 213-218, 2012.

[8] Grace, D. R.: Chapter 2 – classic pressure control procedures while drilling, Blowout and Well Control Handbook, pp. 39-89, 2003.

[9] Marris, S. A., Langari, R.: Chapter 15 – Pressure Measurement, Measurement and Instrumentation (Second Edition), pp. 463-491, 2016.

[10] Wang, L., Lei, Q., Li, L.: Piezoelectric dynamic pressure sensor, The 2010 IEEE International Conference on Information and Automation, 2010.

[11] Fajkus, M., Nedoma, J., Martinek, R., Fridrich, M., Bednar, E., Zabka, S., Zmij, Z.: Pressure Membrane FBG Sensor Realized by 3D Technology, Sensors, 2021.

[12] Barzilai, A., Van Zandt T., Kenny, T.: Technique for measurement of the noise of a sensor in the presence of large background signal, The Review of scientific instruments, Vol. 69, No. 7, pp. 2767-2772, 1998.

[13] Iwanaga, M. K., Brennan, M. J., Alemida, F. C. L, Scussel, O., Cezar, S. O.: A laboratory-based leak noise simulator for buried water pipes, Applied Acoustics, Vol. 185, 2022

Authors:

Krešimir Ognjenčić mag. ing. mech, PhD Goran Šimunović, University of Slavonski Brod, Faculty of Mechanical Engineering, Trg Ivane Brlić Mažuranić 2, 35000 Slavonski Brod, Croatia.

E-mail: kresimir.ognjencic@gmail.com; gsimunovic@unisb.hr

MMA 2024
FLEXIBLE TECHNOLOGIES

15th INTERNATIONAL SCIENTIFIC CONFERENCE
NOVI SAD, SERBIA, SEPTEMBER 24-26, 2024

Original research paper https://doi.org/10.24867/MMA-2024-03-006

Bozic, D., Runje, B., Razumic, A., Lisjak, D., Strbac, B.

RISK ASSESSMENT FOR NON-CENTERED MODELS IN METROLOGY

Abstract: *Product quality assessment focuses on evaluating whether a product meets specified requirements. The assessment is performed by measuring the characteristic property of the item of interest. A measurement may be accepted even if it doesn't meet the specifications. This poses a risk to the consumer. Measurements that are not in compliance with specifications pose a risk to the producer. In this study, the percentage change in the risk of producers and consumers is evaluated if the best estimate of the measured value is not located at the center of the tolerance interval. The risk assessment was conducted for manufacturing a vernier calliper, for the model of minimization of consumers' risk, model of minimization of producer's risk and shared risk model. It was measured the thickness of the lines on the main scale. By shifting the value of the thickness of the line away from the center of the tolerance interval, the risk values increase. Using the confusion matrix metrics, significant differences were found in the behaviour of recall and precision metrics between models.*

Key words: *Consumer's risk, producer's risk, non-centered model, confusion matrix*

1. INTRODUCTION

Risk assessment is carried out by assessing the conformity of some measured quantity with specified requirements. An item of interest is considered to comply with a specified requirement if the measured value of one of its properties falls within the designated tolerance interval. Should this criterion not be met, the measurement is considered non-compliant with the specifications. Measurement uncertainty, which arises during the measurement process, can result in scenarios where the measured value resides within the prescribed tolerance interval, yet the associated measurement uncertainty surpasses the limits of the tolerance interval [1]. In such instances, erroneous decisions may be made, resulting in the acceptance of non-compliant products or the rejection of products that confirm to specifications. To mitigate the risk of such erroneous decisions, the risk assessment process incorporates an acceptance interval in addition to the tolerance interval.

The tolerance interval and acceptance interval can be in various interrelationships [2,3]. This study focuses on three specific positional relationships between the tolerance interval and the acceptance interval. If the acceptance interval is within the tolerance interval, it pertains to reducing the probability of falsely accepting a non-conforming item. This model is also known as the model of minimization of global consumer's risk. For simplicity, this model is designated as M1. If the tolerance interval is within the acceptance interval, it pertains to reducing the probability of falsely rejecting a conforming item. This is the model of minimization of the global producer's risk [4]. This model is designated as M3. In both cases, the tolerance interval and the acceptance interval are separated by a guard band [5]. When the tolerance and acceptance interval coincide, it represents the shared risk model. This model is designated as M2. In all the models mentioned above, the tolerance interval and the acceptance interval are closed intervals.

The best estimate y_0 of a measured value is typically located at the center of the tolerance interval. However, this is not always the case. This study conducts a risk assessment for non-centered models, implying that the value y_0 varies along the entire acceptance interval or tolerance interval, depending on the model. Additionally, the percentage change in the global risk of the producers and consumers for the non-centered model is monitored compared to the centered model. These calculations were performed during the production process of a vernier calliper for all three positional relationships between the tolerance interval and the acceptance interval.

The risk assessment procedure is based on Bayes' theorem [6]. This theorem combines two types of information. Information about the possible distribution of parameters that describe the true value of the measured data is modelled using a prior distribution denoted as $g_0(\eta)$, where η represents the values that the prior can take. The decision regarding the possible parameters of the prior is made based on the measurer's experience, previous measurements and research, manuals, historical data, and similar sources [7]. According to the principle of maximum entropy, the prior distribution can be a non-parametric, single-parameter, or two-parameter distribution. If the information about the best estimate of the measured quantity y_0 and its associated measurement uncertainty u_0 are known, then a two-parameter distribution is taken as the prior.

Measurement data are modelled using a likelihood function for a normal distribution, denoted as $h(\eta_m|\eta)$. Here, η_m represents the values that the likelihood takes under the condition that the true value of the measurement is η. The expression for likelihood includes the measurement uncertainty u_m associated with the measurements carried out in the process of quality control of the product. The product of the prior distribution and the likelihood function is the integrand of the double integral for calculating the global risk of

producers and consumers. This double integral can be simplified and reduced to a single integral [8]. After simplifying, the integral was solved numerically using pre-built functions from the R programming language package [9].

2. METHODS

2.1 Measurement description

The risk calculation was conducted for data obtained from measuring the line thicknesses on a vernier calliper scale. In the production process of vernier callipers with a measurement range from 0 to 150 mm and a resolution of 0.02 mm, control of the line thicknesses on the primary millimetre scale was carried out. The line thickness control was performed using a universal microscope on a sample of 120 lines. According to the producer's specifications, the lower limit of the tolerance interval for line thicknesses is T_L=80 μm, and the upper limit of the tolerance interval is T_U=130 μm. The best estimate of the line thickness is located at the midpoint of the tolerance interval and is y_0=105 μm. The measurement uncertainty associated with the best estimate of line thickness is u_0=14 μm. These two quantities are input data for the prior $g_0(\eta)$. The measurement uncertainty of the product quality control procedure is u_m=5 μm.

2.2 Risk calculation

The basic procedure for assessing global risk of the producer and the consumer is provided in *Evaluation of measurement data – The role of measurement uncertainty in conformity assessment* 106:2012 [6]. With the simplification described in [8] and the assumption that the prior is a normal distribution, the probability that the measured value of an item of interest is within the acceptance interval while the true value is outside the tolerance interval, i.e., the global consumer's risk R_C, can be calculated from the equation:

$$R_C = \int_{-\infty}^{\frac{T_L - y_0}{u_0}} \varphi_0(z)F(z)dz + \int_{\frac{T_U - y_0}{u_0}}^{\infty} \varphi_0(z)F(z)dz \qquad (1)$$

The probability that the measured value is outside the acceptance interval while the true value is within the tolerance interval, i.e., the global producer's risk R_P, is calculated from the equation:

$$R_P = \int_{\frac{T_L - y_0}{u_0}}^{\frac{T_U - y_0}{u_0}} \varphi_0(z)\big(1-F(z)\big)dz \qquad (2)$$

These formulas are valid when both the tolerance interval and the acceptance interval are closed intervals. In equations (1–2), φ_0 denotes the standard normal distribution, and the expression F(z) is given by the equation:

$$F(z) = \phi\left(\frac{A_U - y_0 - zu_0}{u_m}\right) - \phi\left(\frac{A_L - y_0 - zu_0}{u_m}\right) \qquad (3)$$

where A_L is the lower bound of the acceptance interval and A_U is the upper bound of the acceptance interval and ϕ denotes cumulative distribution function for the standard normal distribution. The values R_P and R_C represents the global risk of producer's and consumer's, respectively, calculated when y_0 is located at the center of the tolerance interval.

The percentage change in the global risk of producer's p_{RP} and the percentage change in the global risk of consumer's p_{RC} of the non-centered model relative to the centered model are given by the expressions:

$$p_{RP} = \frac{100(R_{PN} - R_P)}{R_P} \qquad (4)$$

$$p_{RC} = \frac{100(R_{CN} - R_C)}{R_C} \qquad (5)$$

where R_{PN} and R_{CN} are the global producer's and consumer's risk of the non-centered models. These risks are obtained under the assumption that the tolerance interval and the acceptance interval have fixed values, and that y_0 can take on any value along the entire tolerance interval or acceptance interval, depending on the model being considered. Additionally, it is assumed that for each chosen best estimate value y_0, the associated measurement uncertainty is always the same and equals u_0=14 μm.

For the given tolerance interval T_i=[80, 130] μm, the study examined the model of minimization of global consumer's and producer's risk and the shared risk model. The list of acceptance intervals A_i for the observed models and the risk values when y_0 is exactly at the center of the tolerance interval are provided in Table 1.

Model	A_i / μm	R_C / %	R_P / %
M1	[85, 125]	0.37	10.80
M2	[80, 130]	1.58	3.43
M3	[75, 135]	3.70	0.65

Table 1. The range of acceptance intervals for the selected models and the values of the global producer's and consumer's risk for the centered models

To minimize the global producer's risk, the acceptance interval is chosen such that the tolerance interval occupies 80% of the acceptance interval. In the model of minimizing the global consumer's risk, the acceptance interval is set at 80% of the length of the tolerance interval.

2.3 Models evaluation

The models were evaluated using metrics related to the confusion matrix. Since the global producer's risk represents the probability of a false rejection (FR) and the global consumer's risk represents the probability of a false acceptance (FA), it is possible to construct a confusion matrix by determining the probability of a true positive measurement (TP) and the probability of a true negative measurement (TN). A measurement belongs to the TP category if the actual value of the measured quantity of the item of interest lies within the tolerance interval, and the measured value lies within the acceptance interval. Similarly, a measurement belongs to the TN category if the measured value lies outside the acceptance interval, and the actual value of the measured quantity lies outside the tolerance interval [8,10]. The probability that a measurement is in the TP category is obtained from the TP = $p_C - R_P$. The probability that a measurement belongs to the TN category is obtained

from the TN =1 – p_C – R_P The quantity p_C is called the conformance probability and represents the probability that the true value of an item of interest lies within the tolerance interval [6]. It is calculated from the equation:

$$p_C = \int_{T_L}^{T_U} g_0(\eta)d\eta \qquad (6)$$

Given that in the centered model, the values y_0 and u_0 are fixed, as well as the range of the tolerance interval, the conformance probability is the same for all centered models and equals p_C = 92.59%.

3. RESULTS AND DISCUSSION

Upon the deviation of y_0 from the center of the tolerance interval, the values of the global producer's risk R_{PN} increase towards the edges of the tolerance interval or acceptance interval, reaching a maximum point, and then decreasing. Similarly, if the best estimate y_0 for the width of the lines of a vernier calliper shifts left or right from the center of the tolerance interval, the global consumer's risk R_{CN}, increases towards the edges of the tolerance interval or acceptance interval, as shown in Figure 1.

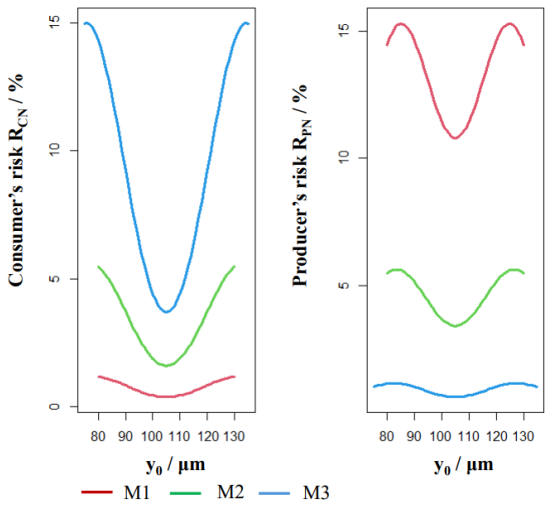


Fig. 1. Changes in the values for the global consumer's risk R_{CN} and global producers' risk R_{PN} with change in best estimate value y_0

However, the maxima of the risk curves in this case were observed only for model M1. The maxima of the other models are located at the edges of the tolerance interval. The line width values y0 at which the maximum risks are achieved, as well as the values of these risks, are presented in Table 2.

Risk type	Model	Maximum (µm, %)
R_{CN}	M1	(80, 1.61), (130, 1.61)
R_{CN}	M2	(80, 5.46), (130, 5.46)
R_{CN}	M3	(75.7, 15.00), (134.3, 15.00)
R_{PN}	M1	(85.1, 15.28), (124.9, 15.28)
R_{PN}	M2	(83.5, 5.64), (126.5, 5.64)
R_{PN}	M3	(82.5, 1.18, 127.5, 1.18)

Table 2. The points of maxima for the risk curves R_{CN} and R_{PN}

As seen in Table 2, all models have maxima of the global consumer's risk curves when y_0 is both within the tolerance interval and within the acceptance interval, regardless of the observed model. The maximum of the global consumer's risk curve for model M3 is within the acceptance interval and outside the tolerance interval. The risk curves shown in Figure 1 all have a minimum value on the *x*-axis at the point y_0 = 105 µm. The corresponding minimum values on the *y*-axis are presented in Table 1.

The curves describing the percentage change in the global producer's risk p_{RP} and the percentage change in the global consumer's risk p_{RC} of the non-centered models relative to the centered models, in both cases, follow the order of the global consumer's risk curves shown in Figure 1. The highest percentage change in p_{RP} and p_{RC} is observed in the model M3, followed by model M2, with the smallest percentage change in model M1, as shown in Figure 2.

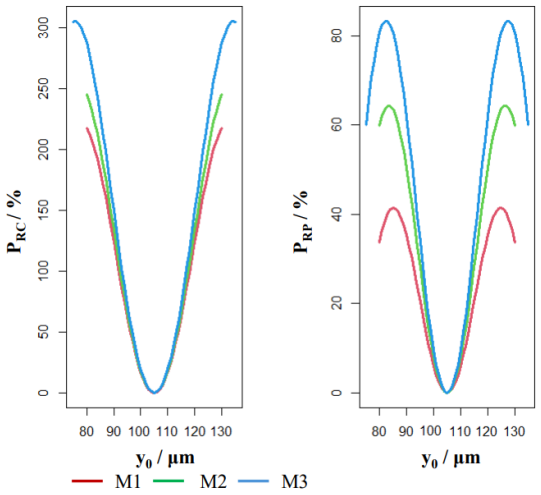


Fig. 2. The percentage change in the global consumer's risk p_{RC} and global producer's risk p_{RP} of non-centered models versus centered models

The percentage changes in the global consumer's risk for all models increase significantly faster compared to the percentage changes in the global producer's risk. In both cases, model M1 exhibits the smallest percentage change with the shift of the best estimate y_0 to the left or right of the center of the tolerance interval. The values of the maximum percentage changes are provided in Table 3.

Percentage	Model	Maximum (µm, %)
p_{RC}	M1	(80, 217.22), (130, 217.22)
p_{RC}	M2	(80, 244.94), (130, 244.94)
p_{RC}	M3	(75.7, 305.38), (134.3, 305.38)
p_{RP}	M1	(85.1, 41.42), (124.9, 41.42)
p_{RP}	M2	(83.5, 64.36), (126.5, 64.36)
p_{RP}	M3	(82.5, 83.34, 127.5, 83.34)

Table 3. The points of maxima for the percentage changes in the global producer's risk p_{RP} and global consumer's risk p_{RC}

Among the many metrics associated with confusion matrices, the most significant differences in model

behaviour are observed in the metrics of precision and recall. According to [8,10], the precision metric gives the probability that a measured value is true positive and lies within the acceptance interval, and it can be calculated from the equation:

$$\text{precision}=\frac{p_C-R_P}{p_C-R_P+R_C} \qquad (7)$$

The recall metric represents the probability that the true value of the measured quantity belongs to the true positive category TP and lies within the tolerance interval, and it can be calculated from the equation:

$$\text{recall}=1-\frac{R_P}{p_C} \qquad (8)$$

For models M1 and M2, the values of the precision metric are higher than the values of the recall metric. For model M3, the situation is reversed. The values of the recall metric are higher than those of the precision metric, as depicted in Figure 3, left-hand side. The difference between the precision and recall metrics is shown on the right side of Figure 3. For model M3, this difference is always less than zero, whereas for models M1 and M2, it is always greater than zero. For the M2 model, that difference is close to zero. Given that the models M1, M2 and M3 have different behaviour for the difference in precision and recall metrics, this difference can be applied to classify the belonging of the data to one of the models.

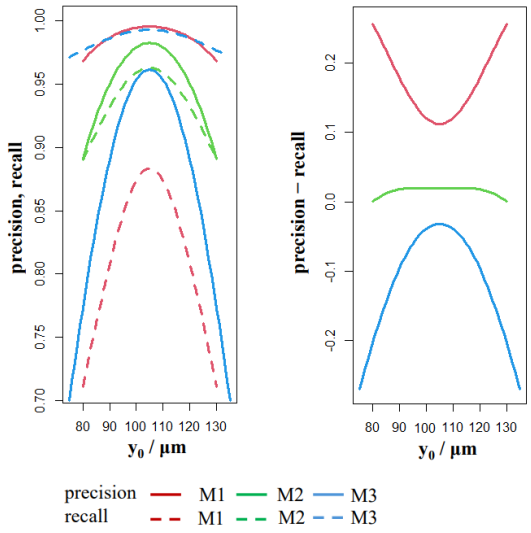


Fig. 3. Relationship between precision and recall metrics (left side), difference between precision and recall metrics (right side)

4. CONCLUSION

Although the best estimate of the measured value y_0 is usually positioned at the center of the prescribed tolerance interval and the selected acceptance interval, it should be noted that this is not always the case. Shifting the best estimate of the property of the interest to the left or right of the center of the tolerance interval and acceptance interval, while keeping the measurement uncertainty u_0 fixed, results in an increase in both the global producer's and consumer's risk. This shift has significant effect on the global consumer's risk.

5. REFERENCES

[1] Dias, F.R.S., Lourenço, F.R.: Measurement uncertainty evaluation and risk of false conformity assessment for microbial enumeration tests, Journal of Microbiological Methods, Vol. 189, 106312, 2021.

[2] Hibbert, D.B., Korte, E., Örnemark, U.: Metrological and quality concepts in analytical chemistry (IUPAC Recommendations 2021), Pure and Applied Chemistry, Vol. 93, No. 9, pp. 997-1048, 2021.

[3] ILAC-G8:09/2019.: Guidelines on Decision Rules and Statements of Conformity. ILAC, 2019.

[4] Runje, B., Horvatić Novak, A., Razumić, A., Piljek, P., Štrbac, B., Orošnjak, M.: Evaluation of Consumer and Producer Risk in Conformity Assessment Decision, 30th DAAAM International Symposium, pp.0054-0058, Zadar, DAAAM International, Vienna, 2019.

[5] Pereira, W.D.P., Carvalheira, L., Lopes, M. J. et al.: Data reconciliation connected to guard bands to set specification limits related to risk assessment for radiopharmaceutical activity, Heliyon, Vol. 9, No.12, e22992, 2023.

[6] BIPM; IEC; IFCC; ILAC; ISO; IUPAC; IUPAP; OIML.: Evaluation of Measurement Data—The Role of Measurement Uncertainty in Conformity Assessment, JCGM 106:2012, BIPM, 2012.

[7] Separovic, L., de Godoy Bertanha, M.L., Saviano, A.M., Lourenço, F.R.: Conformity Decisions Based on Measurement Uncertainty—A Case Study Applied to Agar Diffusion Microbiological Assay, Journal of Pharmaceutical Innovation, Vol.15, pp. 110–115, 2020.

[8] Božić, D., Runje, B., Lisjak, D., Kolar, D.: Metrics Related to Confusion Matrix as Tools for Conformity Assessment Decisions, Applied Sciences, Vol. 13, No. 14, 8187, 2023.

[9] Borchers, H.W.: Pracma: Practical Numerical Math Functions, R Package Version 2.4.2/r532, 2011.

[10] Božić, D., Runje, B.: Selection of an Appropriate Prior Distribution in Risk Assessment, 33rd International DAAAM Virtual Symposium, Vienna, DAAAM International, pp.0471-0479, Vienna, 2022.

Authors:

Dubravka Bozic, mag. math., PhD Biserka Runje, PhD Andrej Razumic, PhD Dragutin Lisjak, University of Zagreb, Faculty of Mechanical Engineering and Naval Architecture, Ivana Lucica 5, 10000 Zagreb, Croatia, Phone.: +385 1 6168 486.
E-mail: dubravka.bozic@fsb.unizg.hr;
biserka.runje@fsb.unizg.hr;
andrej.razumic@fsb.unizg.hr;
dragutin.lisjak@fsb.unizg.hr

PhD Branko Strbac, University of Novi Sad, Faculty of Technical Sciences, Trg Dositeja Obradovica 6, 21000 Novi Sad, Serbia, Phone.: +381 21 485 2316.
E-mail: strbacb@uns.ac.rs

MMA 2024
FLEXIBLE TECHNOLOGIES

15th INTERNATIONAL SCIENTIFIC CONFERENCE
NOVI SAD, SERBIA, SEPTEMBER 24-26, 2024

Original research paper https://doi.org/10.24867/MMA-2024-03-007

Rodinger, T., Lukšić, H., Ćorić, D., Rede, V.

THE INFLUENCE OF ARTIFICIAL AGING PARAMETERS ON THE ABRASIVE WEAR RESISTANCE OF AN Al-Zn-Mg ALLOY

Abstract: *In this study, the influence of artificial aging parameters on the abrasive wear resistance of an aluminum alloy was investigated. The heat treatment of an Al-Zn-Mg alloy consisted of solution annealing at 490 °C for 1 h and artificial aging at 130, 160, and 190 °C for 1, 5, and 9 h. The hardness (HV1) of all samples was measured, together with their abrasive wear resistance. Wear resistance tests were performed on a Taber abrader device with a sandpaper with Al_2O_3 abrasive particles. The highest hardness was measured for the samples artificially aged at 130 °C/5 h, 227 HV1. These samples were also characterized with the highest wear resistance. The lowest hardness was measured for the samples aged at 190 °C/9 h, and these samples, together with those samples aged at 190 °C/5 h, showed the lowest wear resistance.*

Key words: *aluminum alloy, precipitation hardening, abrasive wear, hardness*

1. INTRODUCTION

Aluminum alloys play an important role in numerous technical applications, but in the initial state, their mechanical properties are relatively limited. Different hardening methods have been developed to improve them. Depending on their chemical composition, aluminum alloys can be hardened either by cold working or by heat treatment at elevated temperatures. The development of hardening processes for aluminum alloys is particularly important in the field of light-weight construction engineering, especially in the aeronautical [1,2] and automotive industries [3,4]. By implementing hardened aluminum alloys, the mass of a given part can be reduced by up to 60%, while maintaining the required mechanical properties [5,6]. This can lead to significant fuel savings for vehicles with the internal combustion engines and lower environmental pollution or increased range for electric battery-powered vehicles.

For heat-treatable aluminum alloys, heat treatment consists of solution treatment at temperatures usually above 450 °C, quenching in water, and aging at room temperature (natural aging) or elevated temperatures (artificial aging) [7]. The solution treatment is carried out with the aim of dissolving the alloying elements in the aluminum matrix, while quenching to room temperature results in a supersaturated solid solution α-Al matrix. The solution treatment must be carried out at a temperature above solvus temperature for certain alloy in order to achieve the single phase α-Al, but also below the solidus temperature to avoid the formation of the molten phase. The improvement of mechanical properties is the result of the precipitate formation from a supersaturated α-Al matrix during the aging process [8]. Al-Zn-Mg alloys are generally characterized by a particularly high yield strength and ultimate tensile strength (UTS) after artificial aging [9].

The costs caused by abrasive wear in the industry are considerable, as the energy required to overcome friction increases and also causes production stoppages because worn or damaged parts have to be replaced. According to some sources [10], the costs caused by abrasive wear are estimated to account for up to 1–4% of the gross national product of industrialized countries. For this reason, a great deal of research is focusing precisely on the processes that can be used to increase the wear resistance and extend the service life of parts. The wear of the 7xxx group of aluminum alloys was investigated by Reis et al. [11]. They confirmed that wear decreases with increasing hardness and UTS. Pruthvi and Shenoy [12] investigated the influence of different contents of Mg and Zn in Al-Zn-Mg alloys. With different parameters of retrogression re-aging heat treatment, they concluded that the material is more resistant to wear if it has a higher Zn content and if the retrogression re-aging time is prolonged.

This study aimed to determine the optimal parameters for artificial aging of the tested aluminum alloy to achieve the highest hardness and the lowest wear rate. The samples were solution treated at 490 °C for 1 h and artificially aged at different temperatures and times (130, 160 and 190 °C; 1, 5 and 9 h). The hardness was measured using the standard Vickers method (HV1), while the abrasive wear tests were performed on a Taber abrader device using the Al_2O_3 sandpaper with an average abrasive grain size of 25.8 μm.

2. MATERIALS AND METHODS

An Al-alloy with the chemical composition shown in Table 1 was used. The composition was analyzed using a GDS 850A (Leco, Saint Joseph, MI, USA) optical emission spectrometer. The alloying elements indicate that this is an Al-Zn-Mg alloy which is suitable for hardening by solution treatment and artificial aging process.

After analyzing the chemical composition, the density of the material was measured to calculate the volume loss (ΔV) and wear rate ($\dot{\omega}$) based on the mass loss (Δm) after the abrasion tests. The density was measured by the Archimedes principle using an

analytical balance, type JP703C (Mettler Toledo, Zürich, Switzerland). The average density value of the three measurements was ρ = 2.7857 g/cm^3.

Element	wt. %
Zn	7.68
Mg	3.54
Fe	0.222
Mn	0.206
Si	0.151
Zr	0.109
Cu	0.044
Sb	0.042
Ti	0.039
Cr	0.013
Al	bal.

Table 1. Chemical composition of the tested Al-alloy

For the heat treatment, a total of 20 samples with the dimensions of ⌀20 mm × 10 mm were cut from the cylindrical aluminum rod, Fig. 1.

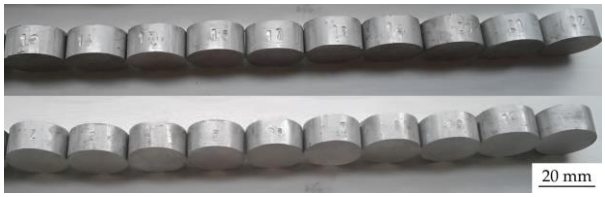


Fig. 1. Samples prepared for heat treatment

All samples were first solution treated at 490 °C for 1 h in an electric furnace (Over, Sveta Nedelja, Croatia) with subsequent quenching in water. The temperature for solution treatment was determined using the ternary Al-Zn-Mg diagram, Fig. 2. A slightly lower temperature than the solidus temperature (≈550 °C) was used for this treatment.

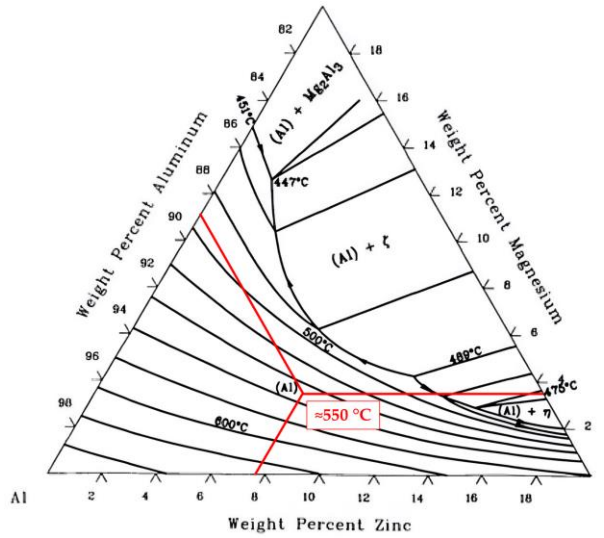


Fig. 2. Al-Zn-Mg solidus projection with the indicated solidus temperature of the alloy used [13]

Two samples (ST-Q) were left in this state (without aging) while the others were artificially aged on the temperatures and times given in Table 2. For each experimental state, two samples were treated. Artificial aging was also performed in the same electric furnace. After artificial aging, the samples were cooled to the room temperature in still air.

State	Artificial aging temperature, °C	Artificial aging time, h
ST-Q	-/-	-/-
130/1	130	1
130/5	130	5
130/9	130	9
160/1	160	1
160/5	160	5
160/9	160	9
190/1	190	1
190/5	190	5
190/9	190	9

Table 2. Artificial aging temperatures and times

The samples' hardness was measured by the Indentec hardness tester (Zwick Roell, Ulm, Germany), using the Vickers method and an indentation load of 9.81 N (HV1). Ten hardness measurements were performed on each sample, and the mean values were calculated. Prior to the hardness measurements, the samples were metallographically prepared, which included mounting, grinding and polishing. Grinding was carried out with four different grades of sandpapers: from P600 to P4000. The grinding plate rotated at a speed of 300 rpm and was cooled with water to prevent heating of the samples and possible microstructural changes. This was followed by polishing in two steps. In the first step, diamond paste with an average diameter of abrasive particles of 3 µm was used, while in the second step, the average size was 0.03 µm. During polishing, the plate rotated at a speed of 150 rpm.

The wear resistance of the samples was tested using the Taber abrader device (Taber Industries, North Tonawanda, NY, USA) with a rotating abrasive paper with a diameter of 125 mm. The measurement method is presented in Fig. 3.

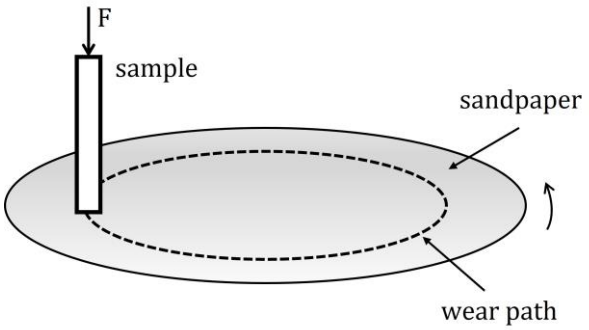


Fig. 3. Measurement method on the Taber abrader device

The samples with the dimensions of approximately 5 mm × 5 mm × 10 mm were cut from the heat treated samples. The samples were pressed with a constant force of 4.91 N against the sandpaper which rotated at the speed of 0.251 m/s. The Al_2O_3 sandpaper with abrasive particles with an average grain size of 25.8 µm was used. Each test lasted for 100 s, resulting in an approximate

wear length of 25 m. Before each test, the exact dimensions of the contact surface and the sample mass were measured. The masses were also measured after the tests to determine the mass loss, which was converted into volume loss and wear rate. For weighing, a precision balance with a resolution of 0.0001 g, type B5C 1000 (Mettler Toledo, Zürich, Switzerland) was used.

3. RESULTS AND DISCUSSION

The results of the hardness measurements for different heat treatment samples are presented in Fig. 4.

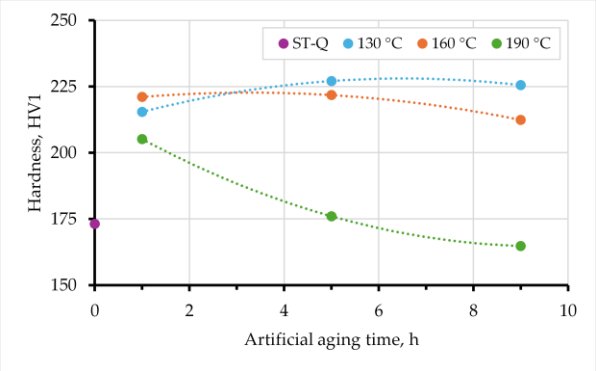


Fig. 4. Hardness vs. aging time and temperature

All heat treatment cycles resulted in higher hardness compared to the initial hardness, which was 135 ± 1.09 HV1. In addition, all samples, except those aged for 5 and 9 h at 190 °C, achieved significantly higher hardness values than the samples that were only solution treated (173 ± 6.21 HV1). In the case of artificial aging at 130 and 160 °C, the hardness values slowly increase or decrease during aging. Opposite, treatment at 190 °C leads to a sudden drop in hardness with longer aging times and the highest hardness was reached already after only 1 h of aging (205 ± 5.31 HV1). The optimal hardness can probably be achieved with a shorter aging than 1 h.

For aging at 130 °C, the highest hardness was achieved after 5 h (227 ± 9.57 HV1), which is also the highest hardness overall. Slightly lower values were achieved at the same temperature, but after 9 h (225 ± 5.64 HV1) and for aging at 160 °C for 1 h (221 ± 5.46 HV1) and 5 h (222 ± 4.61 HV1).

State	Mass loss (Δm), g	Volume loss (ΔV), mm^3
ST-Q	0.0017 ± 0.0005	0.6103 ± 0.1795
130/1	0.0008 ± 0.0002	0.2872 ± 0.0718
130/5	0.0007 ± 0.0001	0.2692 ± 0.0179
130/9	0.0011 ± 0.0001	0.4128 ± 0.0179
160/1	0.0011 ± 0.0003	0.3949 ± 0.1077
160/5	0.0012 ± 0.0002	0.4308 ± 0.0718
160/9	0.0008 ± 0.0002	0.2872 ± 0.0718
190/1	0.0011 ± 0.0001	0.3949 ± 0.0359
190/5	0.0020 ± 0.0008	0.7180 ± 0.2872
190/9	0.0018 ± 0.0000	0.6462 ± 0.0000

Table 3. Mass and volume losses of samples after abrasion tests

The measured mass losses after the wear tests are presented together with the calculated volume losses in Table 3, while the wear rate as a function of hardness for different heat treatment cycles is shown in Fig. 5.

Based on the wear tests, the volume loss (ΔV) was calculated as the ratio of mass loss (Δm) and sample density (ρ = 2.7857 g/cm^3), while the wear rate ($\acute{w}$) was determined as the ratio of volume loss and the contact sample surface.

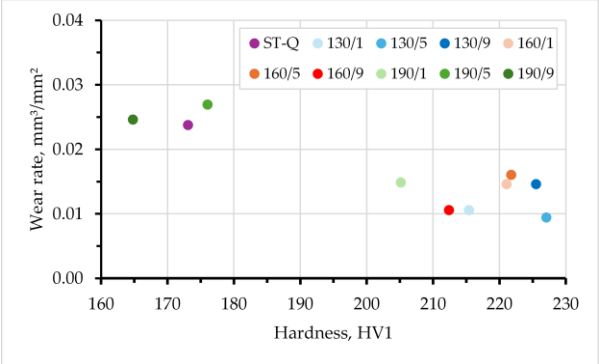


Fig. 5. Wear rate vs. hardness for different heat-treatment cycles

Fig. 5 shows that the lowest wear rates are observed for samples aged at 130 °C for 5 h (0.0101 ± 0.0007 mm^3/mm^2) and 1 h (0.0106 ± 0.0027 mm^3/mm^2), but also for the samples aged at 160 °C for 9 h (0.0106 ± 0.0027 mm^3/mm^2). The wear rate decreases as the hardness value increases, i.e. the material will have longer lifetime if higher hardness is achieved. The highest wear rates are observed for samples that were only solution treated (0.0237 ± 0.0068 mm^3/mm^2), but also for samples that were aged at 190 °C for 5 h (0.0266 ± 0.0100 mm^3/mm^2) and 9 h (0.0246 ± 0.0003 mm^3/mm^2).

4. CONCLUSIONS

In this paper, the influence of the artificial aging parameters of the Al-Zn-Mg alloy on its hardness and abrasion wear resistance was analyzed. All samples were first solution treated at 490 °C for 1 hour and then quenched in water. Two samples were tested in this state, while the others were artificially aged at different temperatures (130, 160 and 190 °C) for different time periods (1, 5 and 9 h). Based on the measured hardnesses and the tested wear rates, the following conclusions can be drawn:

- Compared to the hardness of initial state (135 ± 1.09 HV1), the heat treatment increased the hardness of all tested samples. All samples artificially aged at 130 and 160 °C, and those aged at 190 °C for 1 h reached a hardness above 200 HV1, while the samples that were only solution treated and those artificially aged for 5 and 9 h at 190 °C had a significantly lower hardness, but still higher than the initial state.
- The heat treatment parameters have a significant influence on the hardness values. The highest hardness was achieved in samples artificially aged at 130 °C for 5 h (227 ± 9.57 HV1), while the lowest

hardness values were measured in samples artificially aged for 9 h at 190 °C (165 ± 9.48 HV1). These values are lower than the hardness of the solution treated sample, without subsequent artificial aging (173 ± 6.21 HV1).

- In the samples aged at 190 °C, the hardness decreases significantly with increasing aging time, indicating that the highest hardness can probably be achieved at an aging time of less than 1 h.
- The parameters of artificial aging (time and temperature) have a major influence on the abrasion behavior. Considering the wear rates, the most favorable values of artificial aging parameters for this alloy are also aging at 130 °C for 5 h. With these parameters, the samples had the lowest wear rates (0.0101 ± 0.0007 mm3/mm2), i.e. the highest abrasion resistance.

5. REFERENCES

[1] Zhou, B., Liu, B., Zhang, S.: *The Advancement of 7XXX Series Aluminum Alloys for Aircraft Structures: A Review*, Metals, 11, 718, 2021. doi:10.3390/met11050718.

[2] Dursun, T., Soutis, C.: *Recent Developments in Advanced Aircraft Aluminium Alloys*, Mater. Des., 56, pp. 862-871, 2014. doi:10.1016/j.matdes.2013.12.002.

[3] Ma, P., Liu, C., Chen, Q., Wang, Q., Zhan, L., Li, J.: *Natural-Ageing-Enhanced Precipitation Near Grain Boundaries in High-Strength Aluminum Alloy*, J. Mater. Sci. Technol., 46, pp. 107-113, 2020. doi:10.1016/j.jmst.2019.11.035.

[4] Yang, Z., Zheng, X., Liang, Z., Banhart, J.: *Refreshing Industrially Processed 6xxx Series Aluminum Alloys After Prolonged Natural Aging*, Adv. Eng. Mater., 25, 2301102, 2023. doi:10.1002/adem.202301102.

[5] Hirsch, J.: *Recent Development in Aluminium for Automotive Applications*, Trans. Nonferrous Met. Soc. China, 24(7), pp. 1995-2002, 2014. doi:10.1016/S1003-6326(14)63305-7.

[6] Luo, A.A.: *Recent Advances in Light Metals and Manufacturing for Automotive Applications*, CIM J., 12(3), pp. 79-87, 2021. doi:10.1080/19236026.2021.1947088.

[7] Sha, G., Marceau, R.K.W., Ringer, S.P.: *Precipitation and Solute Clustering in Aluminium: Advanced Characterisation Techniques*, in: Fundamentals of Aluminium Metallurgy: Production, Processing and Applications, Woodhead Publishing, Cambridge, UK, pp. 345-366, 2011.

[8] Lendvai, J.: *Precipitation and Strengthening in Aluminium Alloys*, Mater. Sci. Forum, 217-222, pp. 43-56, 1996. doi:10.4028/www.scientific.net/MSF.217-222.43.

[9] Kenesei, P., Horváth, G., Bernstorff, S., Ungár, T., Lendvai, J.: *Early Stages of Nucleation and Growth of Guinier-Preston Zones in Al-Zn-Mg and Al-Zn-Mg-Cu Alloys*, Int. J. Mater. Res., 97(3), pp. 315-320, 2006. doi:10.1515/ijmr-2006-0050.

[10] Swain, B., Bhuyan, S., Behera, R., Sanjeeb Mohapatra, S., Behera, A.: *Wear: A Serious Problem in Industry*, in: Tribology in Materials and Manufacturing – Wear, Friction and Lubrication, IntechOpen, Rijeka, Croatia, pp. 1-20, 2021.

[11] Reis, B.P., Lopes, M.M., Garcia, A., dos Santos, C.A.: *The Correlation of Microstructure Features, Dry Sliding Wear Behavior, Hardness and Tensile Properties of Al-2wt%Mg-Zn Alloys*, J. Alloys Compd., 764, pp. 267–278, 2018. doi:10.1016/j.jallcom.2018.06.075.

[12] Pruthvi, H.M., Ghanashyam Shenoy, H.: *Effect of Wear Parameter on Al-Zn Alloy on Wear Rate by Using Taguchi's Technique*, International Journal of Mater. Today Proc., 59(1), pp. 79-84, 2022. doi: 10.1016/j.matpr.2021.10.204.

[13] Raghavan, V.: *Al-Mg-Zn (Aluminum-Magnesium-Zinc)*, J. Phase Equilibria Diffus., 28(2), pp. 203-208, 2007. doi:10.1007/s11669-007-9029-6.

Authors:

Assist. Tomislav Rodinger, Assist. Helena Lukšić, Full Prof. Danko Ćorić, Full Prof. Vera Rede, University of Zagreb, Faculty of Mechanical Engineering and Naval Architecture, Ivana Lučića 5, 10 000 Zagreb, Croatia, Phone.: +385 1 6168 222, Fax: +385 1 6156 940.

E-mail: tomislav.rodinger@fsb.unizg.hr; helena.luksic@fsb.unizg.hr; danko.coric@fsb.unizg.hr; vera.rede@fsb.unizg.hr

MMA 2024
FLEXIBLE TECHNOLOGIES

15th INTERNATIONAL SCIENTIFIC CONFERENCE
NOVI SAD, SERBIA, SEPTEMBER 24-26, 2024

Original research paper https://doi.org/10.24867/MMA-2024-03-008

Kasalica, V., Zivanovic, S., Stojadinovic, S.

SIMULATION OF MEASUREMENT ON CMM BY IMPLEMENTING A DIGITAL TWIN MODEL

Abstract: *The purpose of this paper is to improve the quality of measurement inspection process, reduce and complete eliminate collisions, and quantitatively increase productivity by minimizing the time required for measurement. Digital twin models are becoming more significant in industrial environments as they enable monitoring, control, and simulation of measurements, while also offering the possibility of inspecting objects or processes in a digital environment. In this study, a digital twin model for the quality control of a prismatic part was created. To define and display a realistic simulation in the digital space, the following were modeled: a coordinate measuring machine (Mitutoyo CRYSTA Apex), workpiece, and auxiliary equipment. The workpiece underwent an analysis of metrology for defined form and location tolerance, while for the virtual measuring machine, it was necessary to establish kinematic links between all subsystems of the machine. For the digital twin of the measuring machine to have consistent movement, it was necessary to define the connections between the coordinate systems of the workpiece and the measuring probe, as well as between the workpiece and the measuring machine. The advantage of this digital twin model is that, in addition to off-line mode, it can be directly integrated (on-line mode) into complex technological systems.*

Key words: *Digital twin, Simulation, CMM, Modelling, Inspection planning*

1. INTRODUCTION

With the increase in global production and the demands for ever more precise manufacturing of parts, including narrower tolerance fields and higher accuracy, there is an escalating need for high-quality inspection of manufactured components.

The entire quality control and quality management of production are based on the use of measurement systems and the direct utilization of measurement results, regardless of the technological phase (manufacturing, assembly, maintenance, etc.). Without the development and application of modern measurement systems, the advancement of the most sophisticated programmed and adaptively controlled machining systems and machining centers would not be possible.

Today's manufacturing systems have the flexibility to fabricate a large variety of parts with high complexity, low volume, and with restricted tolerances. In order to accommodate these requirements, intelligent process control is needed not only to assist in providing the flexibility and accuracy, but also to be implemented in real-time and inprocess controlling procedures [1].

These definitions imply and demonstrate the significance of measuring machines in quality control. This trend and the demand for a universal, flexible, and precise inspection device that could provide full capability for integration into the vision of Computer Integrated Manufacturing (CIM) have accelerated the goal oriented development process of Coordinate Measuring Machines (CMM) in the past [2].

The main idea of this paper is to create a simulation of measurement inspection on a CMM using a digital twin model. Virtual inspection allows for the visualization and optimization of the process, identification, elimination of collision avoidance between components involved in the process, and reduction of quality control costs.

In the following chapters, the concept of the digital twin and the effects of its implementation in the production system will be described in detail. Subsequently, the modeling of a complex measuring system and the simulation of measurement inspection will be discussed.

2. DIGITAL TWIN

Digital Twins are getting attention because they integrate artificial intelligence (AI), Internet of things (IoT), and machine learning (ML) to bring data, algorithms, and context together, which makes DT a key part of the Industry 4.0 agenda [3].

Typically described as consisting of a physical entity, a virtual counterpart, and the data connections in between, the Digital Twin is increasingly being explored as a means of improving the performance of physical entities through leveraging computational techniques, themselves enabled through the virtual counterpart [4].

In the work [5], a detailed literature review on DT can be found, highlighting both their initial applications and future prospects. Here we mention that this concept dates back to the NASA Apollo program, during which two identical spacecraft were built to mirror the conditions of the spacecraft during the mission.

One of the key aspects of the functioning and application of the digital twin is the real-time data flow between the digital and physical systems. There are two approaches, or bidirectional information flows. In the first working principle, it is based on continuous data collection from the real system through various types of sensors and their application to the virtual one. While in the second approach, data from the digital simulation of

the process is implemented into the physical system [6].



Fig. 1. 3D CAD model (Virtual Twin) of the CMM Mitutoyo CRYSTA Apex

In this paper, the DT concept is based on the CMM machine Mitutoyo CRYSTA Apex. The goal is to simulate virtual measurement system and inspection using the measuring machine, as well as verification by generating the output .ncl (dmis) code. The software package PTC Creo Parametric was used for modeling, simulation, and inspection. Fig. 1 shows the mentioned measuring machine created in the software, with all its subsystems and elements. The dimensions of the virtual model are perfectly aligned with the real model, which is the essence of the entire DT concept, to fully implement the real system into the computer model.

3. MODELING AND SIMULATION THE MEASURING SYSTEM

In this chapter, the essence of this paper will be presented and described, focusing on the modeling, simulation, and verification of measurement inspection.

3.1 Modeling the measuring system

As previously mentioned, modeling is a crucial aspect of the DT concept. The model must be detailed, concise, accurate, and visually identical, representing a true image of the real object in the virtual environment. For the purposes of this paper, the complete Mitutoyo CRYSTA Apex measuring machine (Fig. 1), the workpiece, and auxiliary clamping tools were modeled. In addition to these components, it was necessary to modify the existing measuring probe within the PTC Creo Parametric software package and define its configurations to meet the required task.

When creating the model of the workpiece, Fig. 2, in addition to dimensionally defining it based on the technical drawing, all tolerances (flatness, cylindricity, parallelism, location, etc.) were also defined on the model. Additionally, measurement bases were created on the model itself.

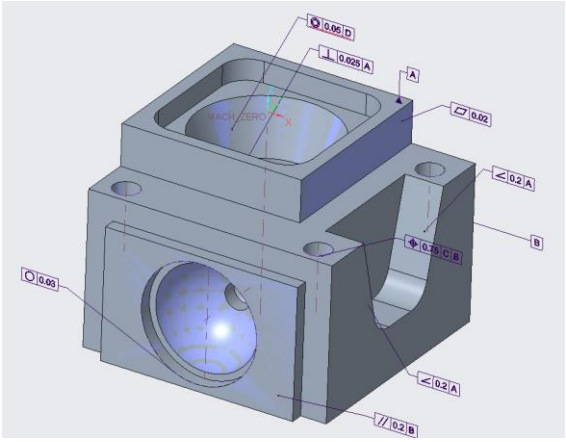


Fig. 2. 3D CAD model of the workpiece

After the workpiece, it is necessary to create the model of the clamping tool, Fig. 3. Stability and accessibility during measurement inspection are vital factors that affect the accuracy of the obtained results. Additionally, it is important to optimize number of clampings as possible (ideally, one clamping of the workpiece during inspection). Each new clamping and change in position introduces time spent and measurement errors that impact the overall control report. Also, the human factor plays a significant role in the positioning process. One adequate and precise clamping reduces the quality control time, which ultimately brings significant benefits to the production process.

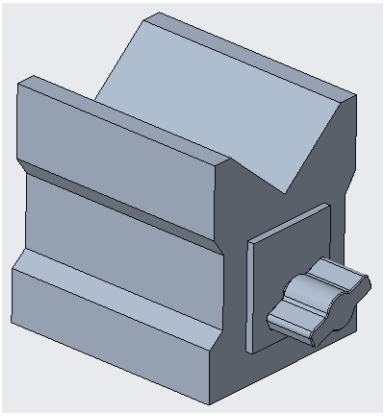


Fig. 3. 3D CAD model of the auxiliary clamping tool

3.2 Defining kinematic connections

The next step in defining an accurate virtual twin (digital measuring machine) is establishing the kinematic links between the main components of this machine. Building on the previous chapter and Fig. 1, we define the three main components of the measuring machine:

1. Machine base—provides stability and support to other components;
2. Measuring bridge—allows the measuring probe to move along 3 directions and take the necessary positions during the inspection;
3. Z-axis that contains the rotating head, the control unit (the brain of the CMM), as well as the probe itself on its top [7].

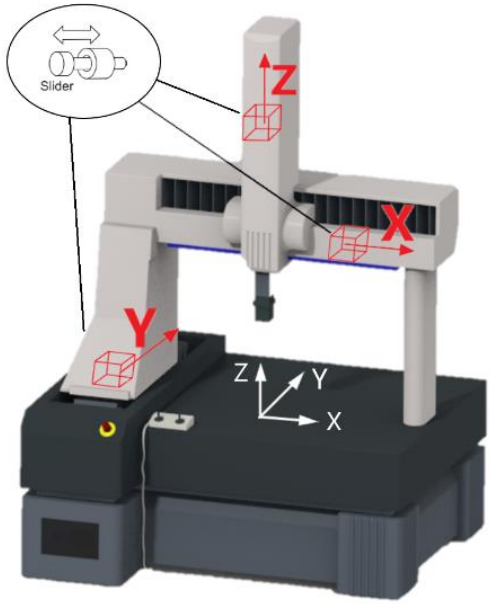


Fig. 4. Overview of kinematic links on the CMM model

The kinematic structure of the virtual CMM is defined to replicate the movements of the real physical system. For this specific measuring machine, three translational movements along the X, Y, and Z axes need to be defined. In the PTC Creo Parametric software package, achieving linear movement along the desired machine axis is accomplished using "slider" constraints, as shown in Fig. 4. In addition to creating these constraints and establishing their relationships, it is also necessary to define the limits within the movements along the intended axes of the measuring machine.

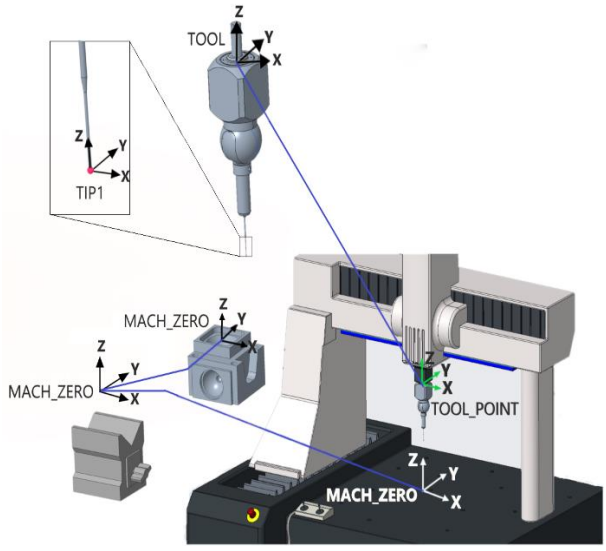


Fig. 5. Connections between the coordinate systems

After modeling the measuring machine, the workpiece, the auxiliary clamping tools, the measuring probe and its configurations, and establishing the kinematic links between the translational axes of the movable components of the measuring machine, the final step in creating the virtual twin of the CMM follows.

The final step before simulation and verification involves defining the coordinate systems of the workpiece, the measuring probe, and the measuring machine, Fig. 5. The goal of defining the mentioned coordinate systems, in addition to ensuring proper alignment and precise movement of the virtual machine, is to facilitate the interaction between components that affect the measurement inspection itself (accuracy of control and collision avoidance).

It is necessary to define coordinate systems on:

- working table, market as MACH_ZERO,
- workpiece, market also as MACH_ZERO,
- head of sensor, market as TOOL_POINT, which axis is defined with same direction and orientation as the axis of coordinate system on workpiece, and
- probe, market as TOOL, if it is necessary to create own probe, [8].

As seen in Fig. 5, the coordinate systems MACH_ZERO defined on the workpiece, the clamping fixture, and the measuring machine serve as alignment, allowing for the placement of the clamping fixture on the virtual machine's worktable and then clamping the workpiece onto the fixture. The same procedure applies to TOOL and TOOL_POINT, which are used for positioning the measuring probe on the sensor head. While the coordinate system TIP1 represents the center of the spherical end of the measuring probe.

3.3 Simulation of the virtual CMM

As previously mentioned, some of the advantages of simulation include the elimination of the need to design and manufacture expensive prototypes, significant time savings, and real-time visualization and monitoring of the measurement process. Additionally, simulation enables the detection and avoidance of collisions in the actual system. Integrating these advantages results in substantial cost savings.

As well, simulation plays a key role in verifying the functionality, reliability, and performance of the design before conducting the actual inspection.

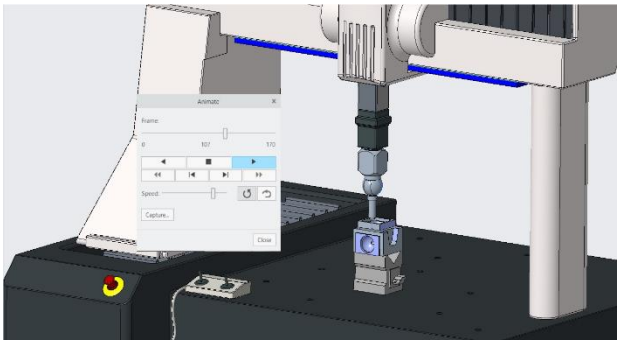


Fig. 6. Display of the complete measurement system during virtual inspection

Fig. 6 shows a visual representation of the complete measurement system during the simulation of measurement inspection within the digital environment of the PTC Creo Parametric software.

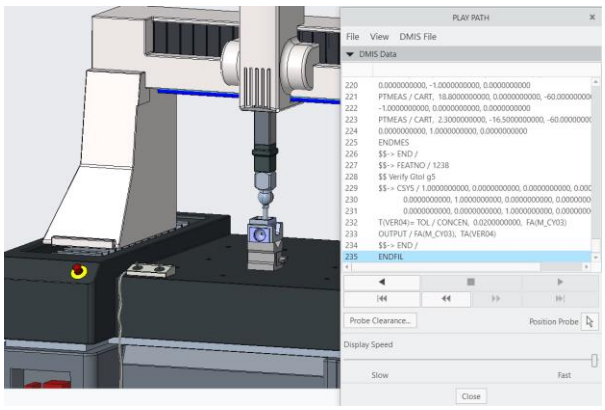


Fig. 7. Measuring path simulation on virtual CMM

A crucial aspect of the simulation and the entire concept of the digital twin is the verification of the quality control process of the workpiece. Verification is reflected in the output code generated by PTC Creo. This output code is developed after the successful completion of the simulation and validation of the measuring path. The obtained code describes the generated path of the probe (the center of the spherical tip of the measuring probe) and is saved in a CL (Cutter Location) file. The CL file contains the DMIS program, which serves as a set of instructions for the actual CMM during the measurement process.

The display of the generated DMIS (.dms) code after the execution of the measurement inspection operation in the virtual measurement system is shown in Fig. 7.

4. CONCLUSION

In the realm of production metrology, the role of the digital twin is to oversee the measurement process, and quality of products, as well as improve dimensional accuracy. This, in turn, leads to a reduction measurement time and production costs.

The contribution of this paper lies in the detailed modeling of the measuring machine and all the components necessary to create a dimensionally, geometrically, and functionally fully defined replica of the real measurement inspection process. Additionally, kinematic links and the necessary coordinate systems have been established on the machine model, all with the aim of generating a complete simulation in the digital world. In this way, the concept of the digital twin has once again been confirmed and applied in the field of mechanical engineering, specifically in the quality control of a workpiece on a CMM.

Future research will focus on the direct implementation of the obtained data (DMIS file) on the real measuring machine. As previously stated in the paper, there is a bidirectional data flow within the concept of the digital twin. Our goal is to turn to the second approach, which involves implementing the data obtained from the simulation of the virtual system directly into the real system and the control process.

5. REFERENCES

[1] Gohari, H.; Berry, C.; Barari, A. A Digital Twin for Integrated Inspection System in Digital Manufacturing. IFAC Pap., 52,182–187. 2019.

[2] Mantel, Matthew. “Coordinate measuring machines: a modern inspection tool in manufacturing.” (1993).

[3] Stojadinovic, S., Majstorovic, V., Zivkovic, S., Kasalica, V., Stanic, D.: An Approach of Development Digital Twin Based on CMM as Support Industry 4.0. Industry 4.0, 7(2), 50-53., 2022.

[4] David Jones, Chris Snider, Aydin Nassehi, Jason Yon, Ben Hicks, Characterising the Digital Twin: A systematic literature review, CIRP Journal of Manufacturing Science and Technology, Volume 29, Part A, Pages 36-52, ISSN 1755-5817, 2020.

[5] Concetta Semeraro, Mario Lezoche, Hervé Panetto, Michele Dassisti, Digital twin paradigm: A systematic literature review, Computers in Industry, Volume 130, 103469, SSN 0166-3615, 2021.

[6] Stojadinovic, S., Majstorovic, V., Zivkovic, S., Kasalica, V., Stanic, D.: An Approach of Development Digital Twin Based on CMM as Support Industry 4.0. Industry 4.0, 7(2), 50-53., 2022.

[7] Kasalica, Vidoje, Stojadinović, Slavenko, "Data interoperability in communication between real and digital measuring twin." in Proceedings of the 39th International Conference on production Engineering of Serbia – ICPES 2023:48-54, 2023.

[8] Marjanovic, Miladin A., Slavenko M. Stojadinovic, and Sasa T. Zivanovic. "Modelling and Simulating the Digital Measuring Twin Based on CMM" Modelling 4, no. 3: 382-393, 2023.

[9] Stojadinovic, Slavenko, Zivanovic, Sasa & Slavković, Nikola. Verification of the CMM Measuring Path Based on the Modified Hammersly’s Algorithm. 10.1007/978-3-030-18177-2_3., 2019.

Authors:
MSc Vidoje Kasalica, PhD Sasa Zivanovic, PhD Slavenko Stojadinovic, University of Belgrade, Faculty of Mechanical Engineering, Kraljice Marije 16, 11120 Belgrade, Serbia, Phone.: (+381 11) 3302-200.
E-mail: vidoje.kasalica@gmail.com; szivanovic@mas.bg.ac.rs ; sstojadinovic@gmail.com

MMA 2024 FLEXIBLE TECHNOLOGIES

15th INTERNATIONAL SCIENTIFIC CONFERENCE
NOVI SAD, SERBIA, SEPTEMBER 24-26, 2024

Original research paper https://doi.org/10.24867/MMA-2024-03-009

Santosi, Z., Sokac, M., Milosevic, A., Ivanov, V., Vukelic, D.

3D RECONSTRUCTION OF MACHINE VISE BY APPLICATION OF PHOTOGRAMMETRY AND REVERSE ENGINEERING

Abstract: *Photogrammetric 3D digitization is a robust method for creating precise 3D models of physical objects. This approach offers significant advantages in flexibility and non-contact operation, achieving high accuracy through meticulous planning. The mechanical vise is essential in machining and manufacturing for securely clamping workpieces. Specialized equipment, including an automated turntable, and RealityCapture photogrammetry software were used to create a polygonal model of the vise body and sliding jaw. These polygonal 3D models served as the basis for reconstructing CAD models using SolidWorks CAD software. Validation via Computer Aided Inspection (CAI) showed minimal deviations, highlighting photogrammetry's reliability and effectiveness in industrial applications for quality assurance and design optimization.*

Key words: *Reverse engineering, photogrammetry, mechanical vise*

1. INTRODUCTION

Digitalization in mechanical engineering is paramount for enhancing productivity and production performance. Reverse engineering (RE) initially emerged as a solution for replacing broken or worn-out parts lacking technical data, often due to imported parts without drawings or misplaced originals [1]. RE aims not to replicate an identical twin of the original part (technically impossible), but to recreate a part with equivalent form, fit, and function through engineering analysis [2]. This is crucial in scenarios like replacing spiral bevel gears where design data is missing, necessitating the determination of the necessary specifications and machine-tool settings for replacement or improvement [3].

Three-dimensional (3D) digitization methods encompass various technologies to digitally capture the shape, size, and texture of physical objects. Devices used for this, commonly known as 3D scanners, are integral to the reverse engineering process. These scanners operate primarily on two principles: non-contact scanners using reflected light detected by cameras, and contact scanners employing probing methods across object surfaces. Contact scanners utilize pressure-sensitive probes typically mounted on Coordinate Measuring Machines (CMMs), either on articulated arms or integrated into robotic systems for industrial automation.

Currently, non-contact 3D scanners predominantly employ optoelectronic technology, utilizing light properties for information capture, transfer, and presentation [4]. 3D digitizing methods include Photogrammetry, Laser Scanning (LiDAR), Structured Light Scanning, Contact Scanning (Touch Probe CMMs), and X-ray Computed Tomography (CT), each chosen based on factors like object size, material properties, detail requirements, and intended use of the 3D model. In the context of reverse engineering, which often involves redesigning or modifying existing products, CMM is utilized to capture data. This physical data was converted into an electronic format compatible with CAD software, resulting in the creation of a new design model, the production of a master mold, or the fabrication of a prototype [5]. CMMs are also used to validate non-contact 3D digitization methods such as photogrammetry [6], or in the entire reconstruction process [7]. Industrial automation's high level of task automation enables efficient large-scale production. Digitalization, an evolution of industrial automation, aims to further reduce costs and lead times [8].

This paper presents the 3D reconstruction of a machine vise using photogrammetry and reverse engineering to create a digital replica. This digital replica will be used in simulation tasks during offline CMM programming for various measuring and inspection tasks, optimizing and reducing measurement times.

2. PHOTOGRAMMETRIC 3D DIGITIZATION

Photogrammetric 3D digitization is a technique used to create accurate 3D models of physical objects using photographs taken from various angles. It is a powerful method for creating 3D models from photographs, with advantages in versatility and non-contact operation [9]. However, it requires careful planning, processing time, and attention to detail to achieve high accuracy and quality models. As object for 3D reconstruction machine vise was used. The main parts of vise are body with stationary jaw and base, sliding jaw, jaw plates, screw and handle showed in Fig. 1.



Fig. 1. Mechanical vise

It is commonly used in machining and manufacturing processes to securely hold work pieces of various shapes and sizes. It provides flexibility in positioning and clamping, making it suitable for both manual and automated operations in workshops and production facilities. The vise ensures precision and stability during tasks such as milling, drilling, grinding, and inspection, thereby enhancing productivity and accuracy in industrial applications. It is adjustable features and robust design cater to diverse machining needs, making it a versatile tool in modern manufacturing environments.

2.1 Photo acquisition

To achieve complete 3D digitization of the mechanical vise, it is essential to disassemble it into smaller sub-assemblies and parts. Two main components were digitized using photogrammetry: the first sub-assembly includes the body with base, stationary jaw, and jaw plate, while the second sub-assembly consists of the sliding jaw with jaw plate. The following section focuses specifically on the photo acquisition process for the first sub-assembly. The whole setup for photo acquisition is shown in Fig. 2. The Vise body is placed on an automated turn table specially designed for photogrammetry 3D digitization. The turntable was constructed from Plexiglas, with a plate diameter of 400 mm. The Digital Single Lens Reflex DSLR camera CANON 1200d and turn table are connected through a USB connection to the laptop.

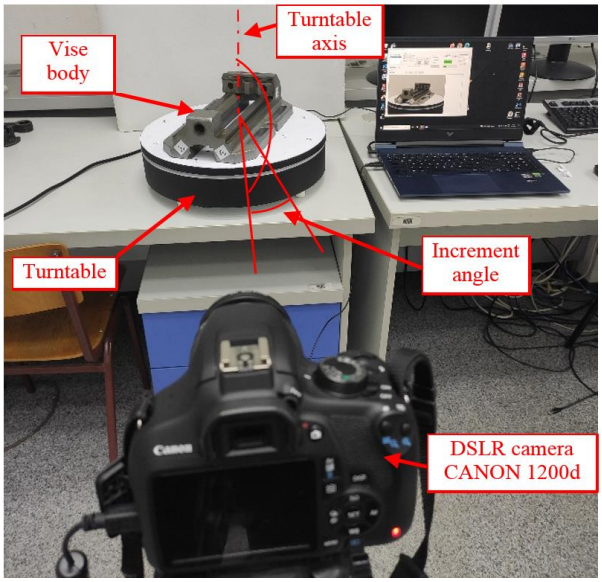


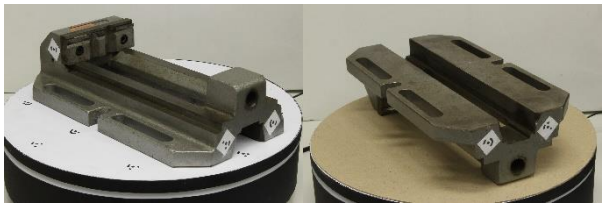
Fig. 2. Photo acquisition setup

The camera and turntable are controlled by a specialized software named "Photogrammetric Turntable 1.0", developed at the Department for Production Engineering, Faculty of Technical Sciences in Novi Sad. The software facilitates synchronized movement of the turntable and captures photos simultaneously. The camera is placed approximately 1.3 meters away from the rotation axis of the turntable. With the lens focal length set to 55mm, the entire object is within the camera field of view. The remaining camera settings can be found in Table 1. Depth of Field (DoF) is calculated based on parameters from Table 1, is 0.37 m, and ensures that the entire object is within the calculated DoF.

Photo resolution (pix)	5184x3456
Aperture (F-number)	18
Shutter speed (sec)	3/5
ISO	400
File format	JPEG
White balance	custom

Table 1. Camera settings parameters

Printed coded markers were placed at known distances on the turntable plate to determine the proper scale of the reconstructed model. However, coded markers were also attached directly to the vise body to ensure visibility even when the body is turned upside down, as the goal is the 3D digitization of the entire geometry (Fig. 3a and Fig. 3b).



a) b)

Fig. 3. Representative captured photographs in two different positions a) initial b) upside down

Table 2 presents an overview of photo distribution and acquisition statistics.

Initial position			
No. of ring	Camera angle relative to turntable axis (°)	Increment angle (°)	Number of photographs
1	80	10	36
2	60	15	24
3	45	20	18
4	30	20	18
Upside down position			
1	80	10	36
2	60	15	24
3	45	15	24

Table 2. Overview of photo distribution

A total of 180 photographs were captured: 96 from the initial side and 84 from the upside-down perspective.

2.2 RealityCapture photos post-processing

RealityCapture photogrammetry software [10] stands out for its exceptional accuracy in scan results and remarkable processing speed. Unlike from other software, it swiftly handles large datasets without causing significant delays. Moreover, it is lighter on RAM usage compared to its counterparts. Post-processing photographs in photogrammetry refers to the series of computational steps taken after capturing a set of overlapping images of a subject or area. These steps are crucial to transforming these 2D images into a 3D model. The first step is to ensure that all images are

correctly aligned. This involves identifying common points or features across multiple images and using them to align the images accurately. Once the images are aligned, the software extracts key features from each image. Features such as corners, edges, and other distinctive points can be identified across multiple images, and these features are used to establish correspondences between them. Using the correspondences established in the previous step, the software calculates the 3D coordinates of these features, generating a sparse point cloud. This point cloud represents the approximate 3D structure of the scene or object. The sparse point cloud is then used as a reference to generate a dense point cloud. This step involves calculating the 3D position of points in every image pixel, resulting in a cloud of points densely covering the surface of the object or scene. Next from the dense point cloud, a mesh (or series of polygons) is generated to create a surface representation of the object or scene. This mesh defines the geometry of the 3D model. To give the 3D model a realistic appearance, textures from the original images are mapped onto the mesh. This process involves aligning the images onto the mesh surface accurately, so the textures wrap around the geometry seamlessly (Fig. 4.).

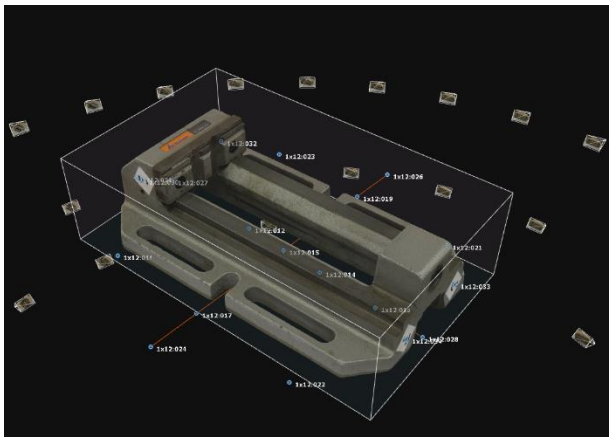


Fig. 4. 3D model of mechanical vise with texture

In photogrammetry, defining scale in the resulting 3D model is crucial for ensuring accurate measurements and realistic representation of the object or scene. RealityCapture can automatically detect and precisely locate coded markers in images, reducing manual effort and potential human error in identifying reference points. During post-processing, photogrammetry software analyzes the images, identifies the coded markers, and calculates their 3D coordinates based on the known marker distances. Finally, the processed 3D model is exported in .stl format and it is ready for defining of coordinate system in external software. Using Zeiss Inspect software [11], a 3D polygonal model can be oriented to x, y, and z planes, because of easier manipulation in CAD software.

3. REVERSE ENGINEERING APPROACH

The reverse engineering approach begins by importing a polygonal 3D model obtained through photogrammetry 3D digitization. This polygonal model serves as the reference for CAD modeling, using SolidWorks (SW) 2022 as the primary tool. Key tools for solid modeling in SolidWorks include extrude, cut extrude, draft, chamfer, and fillet options. The modeling process starts with defining a base sketch on the top plane, which is subsequently extruded to the specified dimensions measured on the polygonal mesh. The resulting model is depicted in Fig. 5. To achieve the desired shape, a combination of extrusions and cut extrusions is employed. Draft angles are added using the draft tool to accommodate the casting process used for manufacturing the vise body.

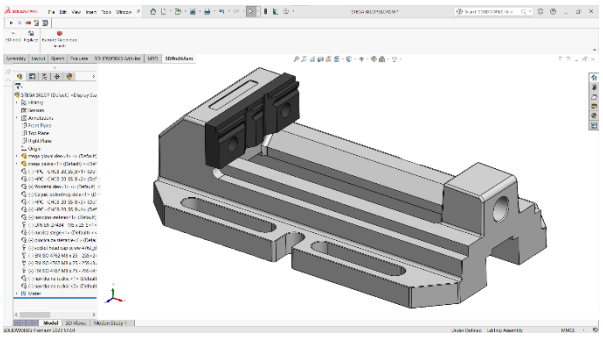


Fig. 5. CAD model of vise body with jaw plate

Further refinement involves adding chamfers, fillets, and holes to complete the final geometry. Similarly, the sliding jaw and jaw plate are reconstructed using the same methodology. Additional components such as screws and handles are modeled based on precise measurements obtained using a caliper.

Standard components like bolts are sourced using the 3Dfindit search engine, seamlessly integrated as a plug-in within SolidWorks. It is the next-dimension visual search engine that crawls billions of 3D CAD & BIM models from hundreds of manufacturer catalogs worldwide [12]. The assembly of mechanical vise is illustrated in Fig. 6.

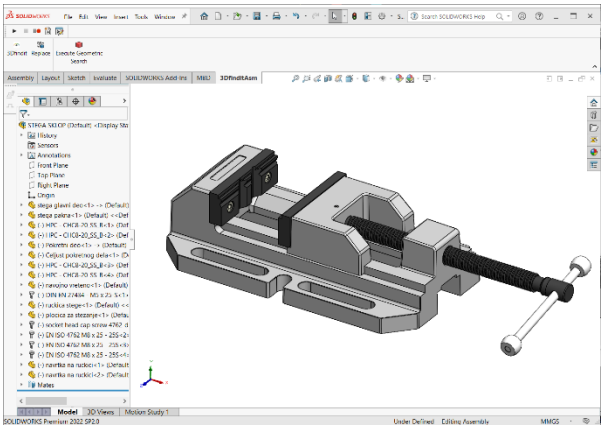


Fig. 6. Complete CAD model of mechanical vise

This comprehensive approach ensures that each component of the vise is accurately modeled and integrated, leveraging advanced CAD tools and precise measurements to achieve the desired functionality and product design.

4. VALIDATION OF RESULTS

To validate the results, Computer Aided Inspection (CAI) was conducted by comparing the 3D model of the vise body with its scanned counterpart obtained through photogrammetry. CAI is a process that uses computer software and technology to assess and verify the accuracy, quality, and conformity of manufactured parts or products against their design specifications. Results are represented as a color map, also known as a deviation map or color contour map. It is a visual representation used to display deviations between a digital CAD model or nominal data and actual measured data of a physical object. Fig. 7. is presented the CAI report.

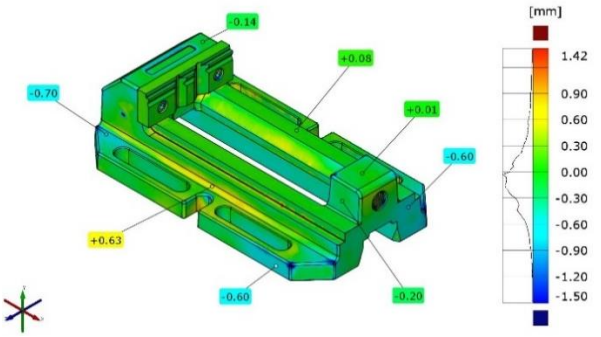


Fig. 7. CAI comparison results of CAD model and 3D polygonal model reconstructed by photogrammetry

The minimum and maximum deviations range from -1.5 mm to 1.42 mm, with a standard deviation of 0.49 mm, indicating an average deviation of approximately half a millimeter. The accuracy of photogrammetry depends on several factors, such as the number, resolution, and quality of photos, the percentage of overlapping photos, the accuracy of printed markers, and the precision of the determined scale.

4. CONCLUSONS

This paper outlines the process of photogrammetric 3D digitization and its application in reverse engineering a mechanical vise. Photogrammetry demonstrated its effectiveness in generating precise 3D models of the vise from photographs, leveraging its versatility and non-contact capabilities. This technology significantly enhances quality assurance, facilitates design optimization, and improves manufacturing efficiency across various industrial sectors.

5. REFERENCES

[1] A. Kumar, P. K. Jain, P. M. Pathak: Reverse Engineering in Product Manufacturing: An Overview, pp. 665–678, 2013.

[2] W. Wang, Engineering Reverse of Reinvention Technology. 2011.

[3] I. Gonzalez-Perez, A. Fuentes-Aznar: Reverse engineering of spiral bevel gear drives reconstructed from point clouds, Mechanism and Machine Theory, vol. 170, no. 2021, p. 104694, 2022.

[4] D. Palka, M. Sobota, P. Buchwald: 3D Object Digitization Devices in Manufacturing Engineering Applications and Services Multidisciplinary Aspects of Production Engineering, vol. 3, no. 1, pp. 450–463, 2020.

[5] P. W. Anggoro, B. Bawono, I. Sujatmiko: Reverse Engineering Technology in Redesign Process Ceramics: Application for CNN Plate, Procedia Manufacturing, vol. 4, no. 1 pp. 521–527, 2015.

[6] M. Faizin, P. Paryanto, N. Cahyo, R. Rusnaldy: Investigating the accuracy of boat propeller blade components with reverse engineering approach using photogrammetry method, Results in Engineering, vol. 22, no. 4, p. 102293, 2024.

[7] B. Vijaya Ramnath et al., Implementation of Reverse Engineering for Crankshaft Manufacturing Industry, Materials Today: Proceedings, vol. 5, no. 1, pp. 994–999, 2018.

[8] M. Thurner, P. Glauner, Digitalization in Mechanical Engineering, no. 4, pp. 107–117, 2020.

[9] Ž. Santoši, I. Budak, M. Šokac, T. Puškar, Đ. Vukelić, and B. Trifković, 3D digitization of featureless dental models using close range photogrammetry aided by noise based patterns, Facta Universitatis, Series: Mechanical Engineering, vol. 16, no. 3, p. 297, 2018.

[10] RealityCapture - 3D Models from Photos and/or Laser Scans. https://www.capturingreality.com/ (accessed Jul. 14, 2024).

[11] ZEISS INSPECT: Your standard in digital industrial inspection. https://www.zeiss.com/metrology/en/software/zeiss-inspect.html (accessed Jul. 15, 2024).

[12] CAD content platform for engineers, architects, purchasers. https://www.3dfindit.com/en/ (accessed Jul. 15, 2024).

ACKNOWLEDGMENTS

This research has been supported by the Ministry of Science, Technological Development and Innovation (Contract No. 451-03-65/2024-03/200156) and the Faculty of Technical Sciences, University of Novi Sad through project "Scientific and Artistic Research Work of Researchers in Teaching and Associate Positions at the Faculty of Technical Sciences, University of Novi Sad" (No. 01-3394/1).

Authors:

PhD Zeljko Santosi, PhD Mario Sokac, MSc Aleksandar Milosevic, PhD Djordje Vukelic
University of Novi Sad, Faculty of Technical Sciences, Trg Dositeja Obradovica 6, 21000 Novi Sad, Serbia, Phone: +381 21 485-24-76.
E-mail: zeljkos@uns.ac.rs; marios@uns.ac.rs; aleksandar.milosevic@uns.ac.rs; vukelic@uns.ac.rs

PhD Vitalii Ivanov, Sumy State University, Faculty of Technical Systems and Energy Efficient Technologies, Department of Manufacturing Engineering, Machines and Tools, 116, Kharkivska St., Sumy, 40007, Ukraine, Phone:+380-542-331-024.
E-mail: ivanov@tmvi.sumdu.edu.ua

MMA 2024 FLEXIBLE TECHNOLOGIES

15th INTERNATIONAL SCIENTIFIC CONFERENCE
NOVI SAD, SERBIA, SEPTEMBER 24-26, 2024

Original research paper https://doi.org/10.24867/MMA-2024-03-010

Bozic, D., Runje, B., Razumic, A., Lisjak, D., Strbac, B.

RISK ASSESSMENT FOR LINEAR REGRESSION MODELS IN METROLOGY: HYPOTHETICAL CASES

Abstract: *The risk assessment is carried out to ensure the quality of the measurements and the compliance of the measurements with specified requirements. Accepting a non-compliant measurement as a compliant or rejecting a compliant measurement represents a risk for the consumer and producer, respectively. The regression line, as a result of calibration, most often intersects the line y=x. Although rare, it can hypothetically happen that the regression line will be equal to or parallel to the y=x line. In this research, the risk was assessed for such regression lines. The risk assessment was based on simulated data. Simulated were the data for the calibration of the roundness measuring device. The risk was estimated for the model with linearized tolerance intervals. The producer's risk increases, and the consumer's risk decreases along the guard band axis. In models where the regression line and the y=x line intersect, the risk curves along the moderate scale are parabolas. However, here they are straight lines parallel to the moderate scale.*

Key words: *Consumer's risk, producer's risk, regression, metrology*

1. INTRODUCTION

The most prevalent and arguably the most useful statistical method applied in metrology is regression analysis. Regression aims to establish a relationship between an independent, given variable and one or more dependent variables, i.e., measured quantities [1]. As with all measurements, measurement uncertainty arises here, significantly affecting the measurement results. Therefore, the evaluation of the quality of regression models can include risk assessment. Risk assessment refers to the procedure of evaluating the conformity of a measured value with given specifications. This implies that the measured value, in this case, the dependent variable, must lie within a specified tolerance interval. Accepting a non-compliant measurement as conforming to specifications poses a risk to the consumer. Conversely, rejecting a compliant measurement as non-compliant poses a risk to the manufacturer.

To mitigate the possibility of making incorrect decisions during the risk assessment procedure, in addition to the tolerance interval, an acceptance interval is introduced [2]. The acceptance interval can be within the tolerance interval. This model is denoted as M1 and represents the model of minimizing the global consumer risk. The model where the boundaries of the acceptance interval and the tolerance interval coincide is called the share risk model, denoted as M2. The model that focuses on minimizing the global producer risk is denoted as M3. In this model, the tolerance interval is within the acceptance interval [3].

Risk assessment in regression models represents a natural two-dimensional and three-dimensional extension of the standard risk assessment procedure given in *Evaluation of measurement data – The role of measurement uncertainty in conformity assessment 106:2012* [4]. If this method is applied to risk calculation in calibration, then the risk is calculated not only for a single point but for all points on the moderate scale, i.e., for functionally connected data. This procedure involves the application of Bayes' theorem. The prior $g_0(\eta)$ is usually a normal distribution with parameters y_0 and u_0, where y_0 is the best estimate of the measured quantity, and u_0 is the measurement uncertainty associated with the best estimate y_0. In the two-dimensional and three-dimensional extensions of the standard risk assessment method, it is assumed that the best estimate of the measured quantity is actually the fitted regression line $y_{fi}=\alpha+\beta x_i$, where x_i, $i=1,\ldots,$ n are the values of the moderate scale, α and β are the parameters of the regression model, and y_{fi} are the values of the regression line $y_f=\alpha+\beta x$ evaluated at the points of the moderate scale x_i. The prior transformation in Bayes' theorem ensures the continuity of the risk curves, i.e. the smoothness of the surfaces, which are the result of the extension of the standard method for risk assessment. In addition to the prior, the likelihood function is also included in the risk calculation according to Bayes' theorem. The likelihood function $h(\eta_m|\eta)$ is modeled as a normal distribution. The expression for the likelihood function incorporates the measurement uncertainty u_m of a future inspection process in the evaluation of the measurement's quality. In this study, $u_m=u_0/2$. However, u_m may possess any other value that is either greater or lesser than u_0.

The regression line, as a result of calibration, most often intersects the line y=x. The line y=x describes a perfect measurement. This implies the ideal measurement without measurement uncertainty. In the risk assessment model for regression, the tolerance interval and acceptance interval are established for every point on the moderate scale. The results are tolerance and acceptance lines that are parallel to the line y=x [5]. This linearized model for risk assessment in regression is shown in Fig. 1. For model M1, it holds that $[A_{L+}, A_{U-}] \subset [T_L, T_U]$, and for model M3, it holds that $[T_L, T_U] \subset [A_{L-}, A_{U+}]$. In models where the regression line intersects the line y=x, the behavior of the model

along the moderate scale is described by parabolas with a minimum at the intersection of the regression line and the line y=x, as shown in Fig. 1.

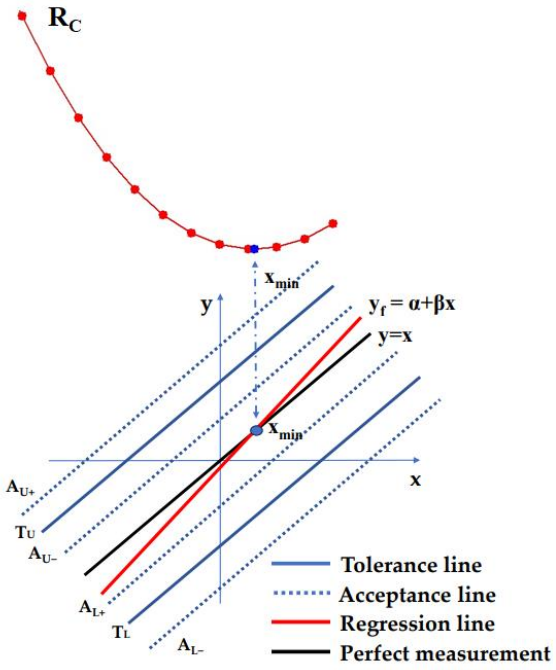


Fig. 1. Linearized model of tolerance and acceptance intervals, and risk curve

Although it is rare in practice, it is hypothetically possible for measurements to be such that the fitted regression line coincides with or is parallel to the line y=x. In this work, we are interested in the risk assessment specifically for such regression lines.

2. METHODS

2.1 Sample generation

Since calibration data rarely yield regression lines that coincide with or are parallel to the line y=x, such data have been generated artificially. The data are generated to simulate the originally conducted measurements in the procedure of calibrating the roundness measurement device, Mahr MMQ3. The data were generated for the process of calibrating the inductive contact probe on a moderate scale from −30 µm to 30 µm. The original measurements were carried out in the Laboratory for Precise Measurement of Length of the Faculty of Mechanical Engineering and Naval Architecture, University of Zagreb. The measurement procedure is described in [6]. As with the original measurement, three samples $\mathbf{y}_j=(y_{j,1}, y_{j,2}, \ldots, y_{j,n})$, j=1,2,3 was generated for each reference value $\mathbf{x}=(x_1, x_2, \ldots, x_n)$ on the moderate scale, where n=13.

The parameters of the regression line α and β for the simulated data, where the regression line $y_f=\alpha+\beta x$ coincides with the line y=x, must satisfy the following conditions [7]:

$$\beta=\frac{S_{XY}}{S_{XX}}=1, \qquad (1)$$

$$\alpha=\bar{y}-\beta\bar{x}=0, \qquad (2)$$

where is:

$$S_{XY}=\sum_{i=1}^{n} x_i y_{j,i}-n\bar{x}\bar{y}, \qquad (3)$$

$$S_{XX}=\sum_{i=1}^{n} x_i^2-n\bar{x}^2. \qquad (4)$$

Given that the measurement simulations were conducted on an equidistant scale symmetrical around zero for the points of the moderate scale holds that $\bar{x}=0$. Consequently, the arithmetic mean of each generated sample is $\bar{y}=0$. Based on the equations (1) and (3-4) it can be inferred that the generated sample must satisfy the subsequent equation:

$$\sum_{i=1}^{n} x_i y_{j,i}=\sum_{i=1}^{n} x_i^2, \; i=1,2,\ldots,n, \; j=1,2,3 \qquad (5)$$

The regression line y=x is obtained using the method of least squares; therefore, the entire sample composed of all three simulated samples must pass the normality test and satisfy the Gauss-Markov conditions. In addition to meeting conditions (1-2) and (5), the generated samples passed the Shapiro-Wilk test, the Breusch-Pagan test, and the Durbin-Watson test. Also, the samples are generated such that they do not contain outliers.

For data where the regression line is parallel to the line y=x, in addition to equation (5), it holds that the arithmetic mean of the generated sample is $\bar{y}=\alpha$, where the parameter α is predetermined.

2.2 Determination of measurement uncertainty

The combined standard measurement uncertainty $u_c(L_P)$ of the simulated measurement is determined from the equation:

$$u_c(L_P)=\sqrt{u^2(L_{ULM})+u^2(L_{LE\,1})+u^2(L_{LE\,2})+u^2(L_N)}, \qquad (6)$$

where the term $u(L_{ULM})$ represents the standard uncertainty due to the influence of the accuracy of the ULM device. The mark $u(L_N)$ indicates standard uncertainty due to the influence of the resolution of the measuring device. The mark $u(L_{LE\,1})$ stands for the standard uncertainty of the linear error due to the error of the probe tilt angle, while $u(L_{LE\,2})$ stands for the standard uncertainty of the linear error due to the error of the probe position [5,6]. Regardless of the generated sample, the measurement uncertainty of the sample depends only on the value $u(L_N)$, as the calculation of this value encompasses sample noise. For all generated samples, the values of the other quantities from equation (6) remain the same [6].

The first generated sample $y_{0j,i}$, which, when fitted with the least squares method, produces the line $p_0 \ldots y=x$, has a measurement uncertainty of $u_0=0.121$ µm. Once a sample is generated that results in a regression line p_0, it is easy to generate samples that produce lines y=α+x parallel to the line y=x for a predetermined α. Moreover, it is possible to generate these lines so that they have the same measurement uncertainty as the line p_0. This is achieved by selecting a sample for which the following condition holds:

$$y_{\alpha j,i}=x_i+\alpha+\left(x_i-y_{0j,i}\right), \qquad (7)$$

where i=1,2, …, n and j=1, 2, 3. Here, $y_{0j,i}$, j=1,2,3 is a sample generated to obtain the regression line y=x, while

$y_{\alpha j,i}$ is a sample generated to obtain the line y=α+x for a given α. Note that the expression x_i-$y_{0j,i}$ represents the deviation of the sample used to obtain the regression line p_0 from the reference values of the moderate scale.

2.3 Tolerance and acceptance intervals

According to the producer's specifications, the tolerance interval range for the inductive contact probe over the calibration range of ±30 µm is 0.6 µm. The tolerance lines, or the limits of the tolerance interval for each point on the moderate scale x_i, are therefore given by $[T_{Li}, T_{Ui}]=[x_i-0.3, x_i+0.3]$, i=1,…,n. The acceptance interval limits are determined by introducing a multiplicative factor r∈[−1,1] and establishing the maximum range of the guard band between the acceptance interval and the tolerance interval:

$$w_{max\,i}=0.2(T_{Ui}-T_{Li}),\ i=1,\ldots,\ n. \qquad (8)$$

The lower and upper limits of the acceptance interval are determined by previous subdivision of the interval [−1,1] with a subdivision rate of 0.1. The nodes of this subdivision are calculated from the equation $r_k=-1+0.1\cdot k$, where k=0,1,…,m, and m=20. The limits of the acceptance interval are then calculated using the equations [5]:

$$A_{L_{i,k}}=T_{L_i}+\frac{r_k\cdot w_{max\,i}}{2},\ i=1,\ldots,n,\ k=0,1,\ldots,\ m, \qquad (9)$$

$$A_{U_{i,k}}=T_{U_i}-\frac{r_k\cdot w_{max\,i}}{2},\ i=1,\ldots,n,\ k=0,1,\ldots,\ m, \qquad (10)$$

When $r_k\in[-1,0\rangle$, it is about model M3. For $r_k=0$, it is shared risk model M2, while for $r_k\in\langle 0,1]$ it refers to model M1. For $r_k=-1$, the acceptance interval has the form $[A_{L-}, A_{U+}]$. For $r_k=0$, the acceptance interval coincides with the tolerance interval $[T_L, T_U]$. For the $r_k=1$, the acceptance interval takes the form $[A_{L+}, A_{U-}]$, as shown in Fig. 1.

In addition to the sample for the line p_0, seven more samples were generated to obtain hypothetical regression lines p_α…y=α+x parallel to the line y=x. Thus, there are a total of eight samples for which the intercept α∈S, and S={0, 0.21, 0.24, 0.27, 0.30, 0.33, 0.36, 039}. The illustrations of the initial positions of these lines related to the point x_n=30 µm on the moderate scale are depicted in Fig. 2.

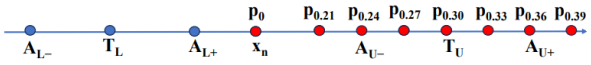


Fig. 2. The mutual positions of the generated lines p_α, tolerance intervals, and acceptance intervals related to the point of the moderate scale x_{13}

The lines p_α shown in Fig. 2 occupy all possible positions relative to the acceptance intervals $[A_{L-}, A_{U+}]$ and $[A_{L+}, A_{U-}]$ and the tolerance interval $[T_L, T_U]$.

It can be shown that the risks for lines $p_{-\alpha}$…y=−α+x, which are axisymmetric to the lines p_α with respect to the line y=x, have the same risk values as the lines p_α. Furthermore, samples for the lines $p_{-\alpha}$ can be generated such that they have the same measurement uncertainty u_0=0.121 µm as the lines p_α.

2.4 Risk calculation

The global consumer's risk R_C and the global producer's risk R_P are calculated for fixed limits of the tolerance interval and each value of the acceptance interval $[A_{Li,k}, A_{Ui,k}]$, i=1,…,n, k=0,1,…,m. The risks are computed for the regression lines p_α, α∈S. According to [4,5], the global consumer's risk, i.e. the probability of falsely accepting a non-conforming item, can be calculated from the equation:

$$R_{C_{i,k}}=\int_{-\infty}^{\frac{T_{L_i}-y_f(x_i)}{u_0}}\varphi_0(z)F(z)_{i,k}dz+\int_{\frac{T_{U_i}-y_f(x_i)}{u_0}}^{\infty}\varphi_0(z)F(z)_{i,k}dz, \qquad (11)$$

i=1,…,n, k=0,1,…,m. The global consumer's risk, i.e. the probability of falsely rejecting a conforming item, is calculated from the equation:

$$R_{P_{i,k}}=\int_{\frac{T_{L_i}-y_f(x_i)}{u_0}}^{\frac{T_{U_i}-y_f(x_i)}{u_0}}\varphi_0(z)\left(1-F(z)_{i,k}\right)dz, \qquad (12)$$

i=1,…,n, k=0,1,…,m. In equations (11-12) φ_0 denotes the standard normal distribution. Expression F(z) is given by:

$$F(z)_{i,k}=\phi\left(\frac{A_{U_{i,k}}-y_f(x_i)-zu_0}{u_m}\right)-\phi\left(\frac{A_{L_{i,k}}-y_f(x_i)-zu_0}{u_m}\right), \qquad (13)$$

i=1,…,n, k=0,1,…,m.

In addition to the global risk of producers and consumers, as a measure of model quality conformance probability p_c was calculated:

$$p_{C_i}=\frac{1}{u_0\sqrt{2\pi}}\int_{T_{L_i}}^{T_{U_i}}\exp\left[-\frac{1}{2}\left(\frac{z-y_f(x_i)}{u_0}\right)^2\right]dz,\ i=1,\ldots,n \qquad (14)$$

Conformance probability refers to the probability that the true value of an item of interest is within the tolerance interval.

3. RESULTS AND DISCUSIONS

Risk surfaces on a two-dimensional domain bounded by the interval $[A_{L-}, A_{U+}]$ on the guard band axis *w* and the interval [−30, 30] on the moderate scale axis *x* are shown in Fig. 3.

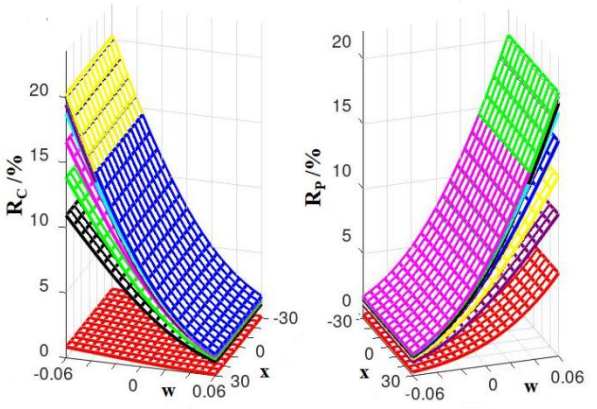


Fig. 3. The surfaces of global consumer's risk (left side) and global producer's risk (right side) for lines p_α, α∈S

Along the guard band axis *w*, the values for the global consumer's risk decrease, while the values for the

global producer's risk increase. Unlike the case where the risk curves are parabolas with a minimum at the point of intersection of the y=x line and the regression line, as in Figure 1, when the regression line coincides with the y=x line or is parallel to it, the risk is the same for all points of the moderate scale Fig. 3. For global consumer risk, these straight lines take the form p…y=$R_{Ci,k}$, and for global producer risk these straight lines have the form p…y=$R_{Pi,k}$, i=1,…,n, k=0,1,…,20. The values of $R_{Pi,k}$ and $R_{Ci,k}$, i=1,…, n, k=20, for α∈S and for the values of the multiplicative factor r=1 are listed in Table 1.

α	color	$R_{Ci,k}$ /%	$R_{Pi,k}$ /%
0		0.0963	6.3852
0.21		1.0563	19.4743
0.24		1.2921	20.3117
0.27		1.4892	20.0629
0.30		1.6174	18.7410
0.33		1.6553	16.5722
0.36		1.5969	13.8437
0.39		1.4522	10.9262

Table 1. Risk lines y=$R_{Ci,k}$ and y=$R_{Pi,k}$, i=1,…, n, k=20 along the moderate scale *x*

The order of the global consumer's risk surfaces is not the same as the order of the global producer's risk surfaces Fig. 3. The order of the surfaces for the global consumer's risk follows the order of the values of parameters α∈S, with the exception that the risk surfaces for α=0.30 and α=0.39, as well as the risk surfaces for α=0.33 and α=0.36, intersect each other for r≈−0.605. The surfaces of the global producer's risk for α=0.30 and α=0.21 intersect each other for r≈0.5905, and the surfaces for α=0.27 and α=0.24 intersect each other for r≈0.5906. Based on the values for global consumer risk listed in Table 1, one could conclude that the model for α=0.39 is a better model for the consumer than the model for α=0.27 due to the lower risk. A similar conclusion can be drawn for the global producer's risk values. However, it should be kept in mind conformance probability Fig. 4.

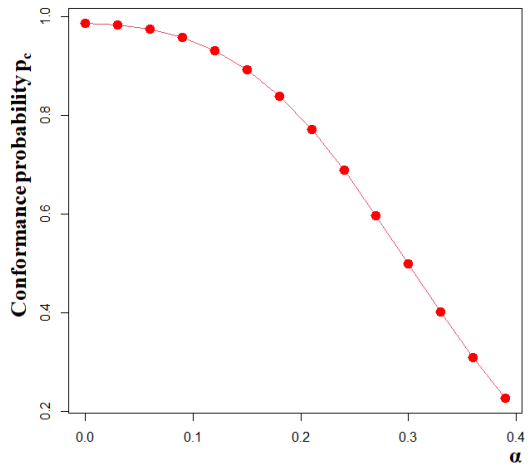


Fig. 4. Conformance probability p_c

Not only the risk value determines the quality of the model. Rather, it depends on the initial position of the line p_α. The further away the line p_α is from the line y=x, the lower the conformance probability is, and the quality of the model is worse for the consumer.

4. CONCLUSION

If the regression line and the y=x line intersect, then the behavior of the global risk of producers and consumers along the moderate scale axis in the linearized regression risk assessment model is described by parabolas. If the regression line is parallel to the y=x line or coincides with it, the risk is described by straight lines parallel to the moderate scale axis. It is noteworthy that the described procedure for evaluating the global risk of producers and consumers in regression models because of the linearization of the tolerance interval is also applicable for determining the risk of calibration.

5. REFERENCES

[1] Chatterjee, S., Simonoff J.S.: *Handbook of regression analysis*, John Wiley & Sons, Inc., Hoboken, New Jersey, 2013.

[2] Runje, B., Horvatić Novak, A., Razumić, A., Piljek, P., Štrbac, B., Orošnjak, M.: *Evaluation of Consumer and Producer Risk in Conformity Assessment Decision*, 30th DAAAM International Symposium, pp.0054-0058, Zadar, DAAAM International, Vienna, 2019.

[3] Božić, D., Runje, B., Lisjak, D., Kolar, D.: *Metrics Related to Confusion Matrix as Tools for Conformity Assessment Decisions*, Applied Sciences, Vol. 13, No. 14, 8187, 2023.

[4] BIPM; IEC; IFCC; ILAC; ISO; IUPAC; IUPAP; OIML.: *Evaluation of Measurement Data—The Role of Measurement Uncertainty in Conformity Assessment, JCGM 106:2012*, BIPM, 2012.

[5] Božić, D., Runje, B., Razumić, A.: *Risk Assessment for Linear Regression Models in Metrology*, Applied Sciences, Vol. 14, No. 6, 2605, 2024.

[6] Bednjanec, F.: *Umjeravanje uređaja za mjerenje kružnosti*, Diplomski rad, Fakultet strojarstva i brodogradnje, Sveučilište u Zagrebu, 2016.

[7] Huzak, M.: *Vjerojatnost i Matematička Statistika, Predavanja*, PMF-Matematički Odjel, Zagreb, 2006.

Authors:

Dubravka Bozic, mag. math., PhD Biserka Runje, PhD Andrej Razumic, PhD Dragutin Lisjak, University of Zagreb, Faculty of Mechanical Engineering and Naval Architecture, Ivana Lucica 5, 10000 Zagreb, Croatia, Phone.: +385 1 6168 486.
E-mail: dubravka.bozic@fsb.unizg.hr; biserka.runje@fsb.unizg.hr; andrej.razumic@fsb.unizg.hr; dragutin.lisjak@fsb.unizg.hr

PhD Branko Strbac, University of Novi Sad, Faculty of Technical Sciences, Trg Dositeja Obradovica 6, 21000 Novi Sad, Serbia, Phone.: +381 21 485 2316.
E-mail: strbacb@uns.ac.rs

MMA 2024
FLEXIBLE TECHNOLOGIES

Section D:
PROCESS PLANNING, OPTIMIZATION, LOGISTICS AND INTERNET TECHNOLOGIES IN PRODUCTION ENGINEERING

MMA 2024 FLEXIBLE TECHNOLOGIES

15th INTERNATIONAL SCIENTIFIC CONFERENCE
NOVI SAD, SERBIA, SEPTEMBER 24-26, 2024

Original research paper https://doi.org/10.24867/MMA-2024-04-001

Makovec, I.

GENERATIVE ARTIFICIAL INTELLIGENCE IN COLABORATIVE MANUFACTURING

Abstract: *As in almost all fields, Generative Artificial Intelligence (GenAI) also has considerable potential in the area of collaborative manufacturing. GenAI capabilities can be used to improve the efficiency and profitability of collaborative manufacturing in particular but not exclusively in: supply chain management, process optimization, product design, quality control, predictive maintenance, human-supervised autonomous robots and administration. The research highlights how GenAI enhances a company's operational efficiency, cost savings, customer satisfaction, and sustainability. The critical issues of GenAI hallucination, bias and ethics are addressed as well. In addition to reviewing the potential areas for GenAI implementation, the aim of the paper is in understanding the role of GenAI in collaborative manufacturing and to propose a new concept of Cognitive Cyber-Physical Production System (C-CPPS).*

Key words: *generative artificial intelligence (GenAI), collaborative manufacturing, Cognitive Cyber-Physical Production System (C-CPPS)*

1. INTRODUCTION

Generative artificial intelligence (GenAI) has the potential to transform entire industries. There are several reasons for this: multi-domain, multi-modality and the generation of new content by reusing training data to solve new problems. The comprehensive networking of systems has enabled accessibility and new ways of using data relevant to business-to-business interactions. At the same time, customer service and personalization of products have increased dramatically. The availability of data has enabled the use of artificial intelligence (AI). The development of multi-modal and multi-domain GenAI has encouraged its use in all areas of business.

The purpose of this research paper lies in identifying potential opportunities for GenAI in collaborative manufacturing.

The methodology section outlines the methodology used in the research. This is followed by a research chapter in which we first review the definitions of collaborative manufacturing. What follows is the definitions of GenAI and the review of the identified potential applications in the field of collaborative manufacturing. The article also addresses the issues of hallucinations and ethical problems caused by technology. A new revised C-CPPS concept is also proposed. The limitations of the research are stated and some suggestions for future research directions are made.

2. METHODOLOGY

The current state of the field under investigation was analyzed by employing a qualitative descriptive methodology. To collect and combine the findings of international scientific research, a compilation approach was utilized. The desktop research technique was used for the systematic collection and analysis of secondary sources. Relevant selected sources that comprehensively cover the field are cited. The recommendations for the application of GenAI in the domain of collaborative production were presented using an inductive method.

3. RESEARCH

3.1 Definition of collaborative production

From a taxonomy perspective, collaborative production can be defined from a broad view to a detailed one. However, Anders et al. [1] dealt with a data model in a collaborative environment comprising replenishment, production and delivery plans. It is clear from the paper that collaborative manufacturing is understood as multiple entities working together to optimize the production processes and improve its efficiency. This collaboration involves different stakeholders such as manufacturers, suppliers and customers sharing information and integrating their processes to achieve common goals.

Colombo et al. [2] presented a 3D view of collaborative manufacturing (Fig. 1). The X axis represents the value chain along the supply chain from suppliers to customers, the Y axis represents the product life cycle from design to support, and the Z axis is the domain within the company from administrative to technical or IT infrastructure.

Considering the different contextual aspects of collaborative manufacturing, they include:

- Collaboration in the supply chain, which aims at transparency, reduction of lead times and optimisation with increased profitability.
- Distributed manufacturing, which involves decentralising the production processes across multiple sites.
- Smart manufacturing with data-driven decision-making processes, the Internet of Things, the artificial intelligence and flexible and self-optimizing production.
- Cyber-Physical Systems (CPS) with integrated

computational, network and physical processes with the aim of improving data exchange and control mechanisms.

- Human-robot collaboration using collaborative robots (cobots), where humans and robots perform tasks together in real time.

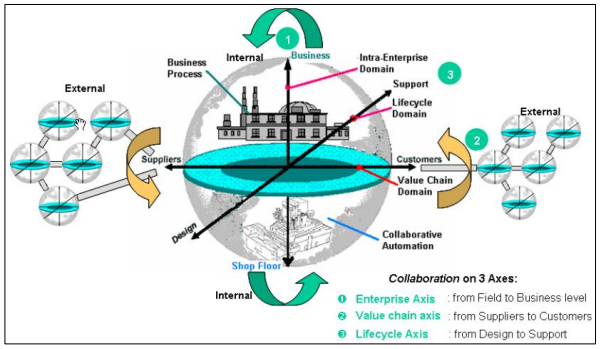


Fig. 1. Collaboration on 3 axes [2]

3.2 Definition of generative AI

GenAI is just a part of the broader field of artificial intelligence. According to Nadeem [3], the beginning of GenAI can be marked by the introduction of Generative Adversarial Networks (GANs) in year 2014. A GAN consists of two neural networks. First, the generator learns to create realistic data samples, while the discriminator evaluates and provides feedback. This learning process enables GANs to produce highly convincing and original results, such as realistic images, texts, and music.

However, the true breakthrough occurred with the simultaneous emergence of four key factors:

- The availability of vast amounts of digitized content, from texts to images. Among the largest repositories are Common Crawl, Wikipedia, and GitHub. Common Crawl is the largest repository, containing over 250 billion web pages [4], and today it serves as a fundamental corpus for training large language models, including ChatGPT.
- The availability of powerful hardware, essential for training deep neural networks on which GenAI is based. Examples include Nvidia A100 graphics cards, which have 6912 CUDA processing cores, enabling parallel computation of neural network parameters.
- In 2017, the Google Brain research team [5] introduced the concept of the neural network Transformer. This neural network encodes not only words but also their meaning (context) in sentences, which is crucial since the meaning of words often depends on the meaning of other words in the sentence. According to Zewe [6], the transformer encodes each word in a corpus of text as a token and then generates an attention map, which captures each token's relationships with all other tokens. This attention map helps the transformer understand the context when it generates new text. The transformer learns from a large amount of data and can be fine-tuned for different purposes using significantly smaller amounts of labelled task-specific data.
- The increased demands for digitalization within the framework of Industry 4.0 created the conditions for critical development in the areas stated above.

The definitions of GenAI vary slightly. According to Pinaya et al. [7], Generative *"AI refers to a set of artificial intelligence techniques and models designed to learn the underlying patterns and structure of a dataset and generate new data points that plausibly could be part of the original dataset."* Martineau [8] provides a somewhat broader definition, stating that Generative *"AI refers to deep-learning models that can generate high-quality text, images, and other content based on the data they were trained on."* They explain that it is not limited to language. GenAI can learn programming, image generation, and processing various complex types of data. A short definitions is given by Zewe [6]: *"Generative AI can be thought of as a machine-learning model that is trained to create new data, rather than making a prediction about a specific dataset."*

NVIDIA [9], one of the leading AI technology companies, has summarised the potential basic applications of GenUI in Fig 2.

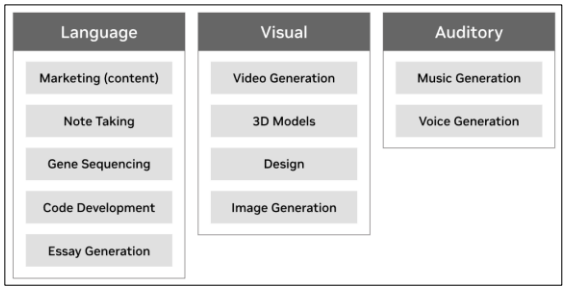


Fig. 2. GenAI use cases [9]

3.3 Generative AI opportunities in collaborative production

Some areas of the application of GenAI in collaborative production have already been identified. Using d discover new ones. Identified GenAI opportunities:

- Supply chain management involves numerous activities with many management decisions. Fosso Wamba et al. [10] surveys current projects and perceptions of these technologies in US and UK supply chains. Their key findings state that GenAI is being used in different projects from proof of concept to implementation in variety applications, including inventory management, demand forecasting, process efficiencies, and customer service. A number of benefits have been shown:
  - Operational efficiency particulary through task automation and process optimization;
  - Cost savings through optimized inventory levels and improved procurement processes.
  - Customer satisfaction with quick and accurate response and enhanced engagement.
  - Better decision-making with analyzing data and predicting.
  - Better sustainability through better resource management.

GenAI can also help by correspondence between the suppliers, manufacturers and buyers involved. GenAI can greatly speed up the work of the administration here.

- Process optimization involves analyzing and improving production processes to increase efficiency, reduce waste, and boost profitability. Typically, resources, production times, and quality are optimized. Hieu [11] explains that GenAI enhances decision-making in product development and manufacturing by simulating and evaluating scenarios. AI algorithms provide extensive insights and data-based recommendations, helping managers by making informed choices.
- Product design and customization. Classical development is still time-consuming and expensive. According to Rane [12] GenAI can help engineers and designers to co-design and innovate by generating creative concepts and providing instant feedback. By Hieu [11] the capacity for rapid prototyping is particularly valuable in industries where design innovation is crucial, such as automotive, aerospace, and consumer electronics
- Quality control. AI in quality control with image recognition has long been used. Hieu [11] sees the opportunities for GenAI in the ability of learning to inspect products with high accuracy, identifying defects and inconsistencies with a level of precision and consistency far beyond human capabilities. Next comes the ability to predict potential failures before they occur.
- Predictive maintenance. Regular maintenance of equipment can be too early, on time or even too late. In the first and third cases, this leads to unnecessary costs and downtime. According Rane [12] GenAI can predict equipment failures from a mass of historical data and enable proactive maintenance.
- Human-Supervised Autonomous Robots. Gregory & Gupta [13] identified opportunities and stated that GenAI could significantly accelerate the deployment and enhance the capabilities of autonomous robots by improving interaction, task planning, motion generation, perception, scenario generation, testing, failure recovery, and design automation.

Hozdić & Makovec [14] discuss the structure of a Cognitive Cyber-Physical Production System (C-CPPS): *"The basis for the construction of the C-CPPS model is the concept of the three-level architecture of the multi-agent model for the distributed control of manufacturing systems"*.

In the era of GenAI and with the new AI processors, this concept can be further enhanced. It will no longer be necessary to have many agents at the business level, corporate level, and operational level; only one GenAI agent will substitute for them. The prerequisite for this will be the new powerful AI processors, which will bring GenAI to the local level. As a modification of the C-CPPS model, a new concept with only one local GenAI agent per system is proposed. (Fig. 3).

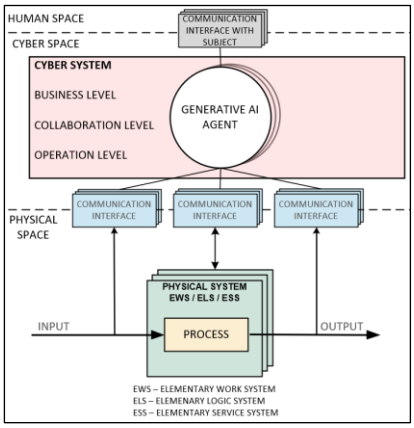


Fig. 3. C-CPPS with GenAI – modified from [14]

3.4. Hallucinations, privacy concern and ethical considerations

The primary feature of GenAI models is their ability to generate text based on the stored probability of word sequences, without understanding the actual content. This often results in what is known as "hallucination," where the model produces text that appears plausible but is factually incorrect. Essentially, the model creates content that does not exist, leading to misinformation.

It is important to be aware of this limitation and to check GenAI responses. OpenAI [15] published in the GPT-4 Technical Report tests of factual accuracy against various publicly available academic and professional texts.

Fig. 4 illustrates the differences and progress among various GPT models. Here, an accuracy of 100% indicates that the model's answers are entirely consistent with the ideal human responses for all evaluated questions. The accuracy of GPT models varies across different domains, with some already achieving over 80% accuracy.

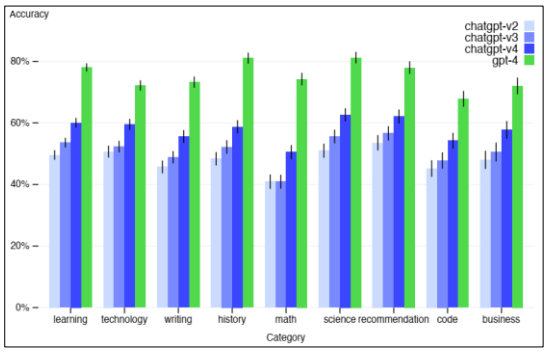


Fig. 4. Factual accuracy of GPT models [15]

But hallucinating is not the only source of incorrect answers. The Transformer Network also does not (yet) think and cannot understand the real meaning behind the words generated.

Since GenAI is mostly not on-premises and privacy cannot be guaranteed by private data storage and access control alone, Bouchard [16] has made some suggestions to ensure privacy:

- Private endpoints (such as the Azure OpenAI service) with a privacy guarantee from the cloud

service provider.
- Use of public APIs with anonymized data.
- Using own model for the highest level of control and data security. Higher costs and expertise required.
- Rethinking + alternatives. In many cases, the traditional AI solutions are sufficient.

There are two key issues that need to be raised with regard to the ethical issues concerning the use of GenAI. The first one is the issue of bias over which users have no control. Because GenAI learns from a large number of sages on the internet, the bias depends on the training set, which is defined in the learning phase. The second issue concerns the authorship of the generated content. GenAI generated content cannot be used as our own work because we did not create it ourselves and at the same time, we cannot cite the GenAI model as the source (author) since the content was not generated by the GenAI model itself but is based on our prompts.

4. CONCLUSION

In this article, the potential of GenAI in collaborative manufacturing has been explored. Key opportunities identified include supply chain management, process optimization, product design and customization, quality control, predictive maintenance, and autonomous robots. Additionally, the article addresses GenAI hallucinations and its ethical and privacy challenges, which require careful consideration to maintain trust and ensure responsible GenAI applications.

The research has the limitation of being focused on relevant sources; only one of the sources was a survey.

The use of GenAI is growing. Due to its involvement in virtually all areas of work, future research should focus on specific areas, e.g. those mentioned in section 3.3.

To sum up GenAI has become an important factor in our lives. It is a new tool which can increase the efficiency of work in many areas including collaborative manufacturing, where new opportunities are being discovered.

5. REFERENCES

[1] Andres, B., Poler, R., & Sanchis, R. *A data model for collaborative manufacturing environments*. Computers in Industry, 126, 103398, 2021

[2] Colombo, A. W., Bangemann, T., & Karnouskos, S. *IMC-AESOP outcomes: Paving the way to collaborative manufacturing systems*. 12th IEEE International Conference on Industrial Informatics (INDIN), pp. 255-260. IEEE, 2014

[3] Nadeem, A.: *The Evolution of Generative AI and Generative Machine learning*. 2023. https://www.linkedin.com/pulse/evolution-generative-ai-machine-learning-nadeem-amin/

[4] Common crawl.: *Common Crawl maintains a free, open repository of web crawl data that can be used by anyone*. 2023. https://commoncrawl.org/

[5] Vaswani, A., Shazeer, N., Parmar, N., Uszkoreit, J., Jones, L., Gomez, A. N., Kaiser, L. & Polosukhin, I.: *Attention is all you need*. Advances in neural information processing systems 30. 2017

[6] Zewe, A.: *Explained: Generative AI*. MIT News, 2023. https://news.mit.edu/2023/explained-generative-ai-1109

[7] Pinaya, W. H., Graham, M. S., Kerfoot, E., Tudosiu, P. D., Dafflon, J., Fernandez, V., ... & Cardoso, M. J.: *Generative ai for medical imaging: extending the monai framework*. 2023. https://doi.org/10.48550/arXiv.2307.15208

[8] Martineau, K.: *What is generative AI.* 2023. https://research.ibm.com/blog/what-is-generative-AI

[9] *What is Generative AI?* Nvidia. https://www.nvidia.com/en-us/glossary/generative-ai/

[10] Fosso Wamba, S., Guthrie, C., Queiroz, M. M., & Minner, S.: *ChatGPT and generative artificial intelligence: an exploratory study of key benefits and challenges in operations and supply chain management*. International Journal of Production Research Vol. 62, No. 16, pp. 1–21, 2024. https://doi.org/10.1080/00207543.2023.2294116

[11] Hieu, D. V.: *Incorporating Generative AI into Quality Management Systems Enhancing Process Optimization and Product Development.* International Journal of Applied Machine Learning and Computational Intelligence, Vol. 13, No. 11, pp. 1–8, 2023. https://neuralslate.com/index.php/Machine-Learning-Computational-I/article/view/65

[12] Rane, N.: *ChatGPT and Similar Generative Artificial Intelligence (AI) for Smart Industry: role, challenges and opportunities for industry 4.0, industry 5.0 and society 5.0*. Innovations in business and strategic management. Vol. 2, No. 1, pp. 10-17, 2024. https://doi.org/R10.61577/ibsm.2024.100002

[13] Gregory, J. M., & Gupta, S. K.: *Opportunities for Generative Artificial Intelligence to accelerate deployment of human-supervised autonomous robots.* In Proceedings of the AAAI Symposium Series (Vol. 2, No. 1, pp. 177-181), 2023

[14] Hozdić, E., & Makovec, I.: *Evolution of the human role in manufacturing systems: On the route from digitalization and cybernation to cognitization.* Applied System Innovation, Vol. 6, No. 2, 2023. https://doi.org/10.3390/asi6020049

[15] *GPT-4 Technical Report.* OpenaAI, 2023. https://doi.org/10.48550/arXiv.2303.08774

[16] Bouchard, L. F.: *The Concern of Privacy with LLMs*. Medium, 2024. https://pub.towardsai.net/the-concern-of-privacy-with-llms-2630828dda67

Author:

M.Sc. Igor Makovec, University of Novo mesto, Faculty of economics and informatics, Na Loko 2, 8000 Novo mesto, Slovenia, Phone.: +386 31- 605-734.
E-mail: igor.makovec@uni-nm.si

MMA 2024 FLEXIBLE TECHNOLOGIES

15th INTERNATIONAL SCIENTIFIC CONFERENCE
NOVI SAD, SERBIA, SEPTEMBER 24-26, 2024

Original research paper https://doi.org/10.24867/MMA-2024-04-002

Bozic, D., Lukic, D., Milosevic, M., Spaic, O., Marinovic, B., Radovanovic, M.

OPTIMIZATION OF MACHINING PROCESS PLANNING – CASE STUDY OF A PRISMATIC PART

Abstract: *Modern manufacturing companies are unimaginable without the use of CNC machines, which enable high product quality. CNC milling machines are a crucial segment in this context, and their programming using CAM (Computer Aided Manufacturing) software is essential for optimal results. This paper focuses on the optimization of machining technology using SolidCAM software, integrated into the SolidWorks CAD platform. The study presents a case study analyzing different machining variants of the most complex milling operation, followed by an analysis of the sequencing variants of all operations. The results demonstrated that the optimized machining variant can reduce machining time by 35 minutes. Subsequently, the sequencing of all operations was optimized, with the results showing a potential additional savings of two minutes per piece. These results are of great significance from the standpoint of serial and mass production, where even the smallest time savings can have a significant impact on the overall efficiency of the production process.*

Key words: *Machining process planning, Optimization, CAD/CAM, SolidCAM, iMachining*

1. INTRODUCTION

A modern company engaged in manufacturing activities cannot be imagined without CNC machines. Observing this trend, it is easy to conclude that companies have recognized this development and are equipping themselves with modern machines that ensure the required quality of their products. CNC milling machines represent just one segment of this development, but it is necessary to pay attention to every segment to achieve satisfactory end results for all. Programming CNC milling machines is an interesting job that is currently performed using software known as CAM (Computer Aided Manufacturing). This paper focuses on optimizing machining technology with the help of a CAM software. The software used for machining simulation and obtaining machining times is SolidCAM. SolidCAM is a CAM module that can be integrated into various CAD software. In this paper, the version of SolidCAM integrated into SolidWorks CAD software was used. In the section of the paper that discusses the case study, the first part presents variants of machining the most complex operation in milling, with results expressed in time units. Following this, variants of operations for machining the entire part are presented, using the optimal operation from the first part of the case study and varying the other operations by machining order. The optimal machining variant is graphically presented at the very end of the paper.

2. LITERATURE REVIEW

The wide range of applications and research in the field of CAD/CAM modules is shown by many scientific papers demonstrating the advantages of using software in the field of manufacturing automation. Some advantages of the SolidCAM software, particularly the part about the iMachining module, are described in the work of author Vetrivel et al. [1] This paper explores various methods for reducing production and cycle time in CNC workshops, emphasizing the reduction of cycle times through the application of CAM software, high-speed CNC machines with rapid tool change and arrangement. SolidCAM, with its iMachining module, claims it can save 70% or more in cycle time, increase tool life five times or more [2]. The analysis of the iMachining module in SolidCAM for machining process control is described in the work of author Petrakov et al [3]. It is detailed how geometric criteria are used for designing the tool path, but also how the cutting process is not stabilized. To influence the cutting process, a method based on the simulation of the material removal rate (MRR) is proposed. A comparison of the accuracy between two CNC machine programming systems is conducted in the work of author Varga et al. [4]. The comparison was made between the SolidCAM system and the Heidenhain TNC 426 system, with the greatest impact on accuracy being the tool overlap in the reference plane. The total production time of samples was longer in SolidCAM compared to Heidenhain TNC 426, with the main reason being that SolidCAM generates the tool path based on the entire model, while Heidenhain TNC 426 uses specific cycle types to define the strategy. The need for optimization of manufacturing processes requires innovative machining methods. Increasing efficiency, ensuring high surface quality, and dimensional accuracy suggest that new methods, as well as the development of materials and tool geometry, are necessary. For these reasons, in the work of author Zaleski et al. [5], The results of the impact of machining strategy on cutting torque, material removal rate (MRR), surface topography, and chip shape during the machining of aluminum alloys can be found, comparing the classical strategy with the iMachining strategy. In the work of Ardelean [6] it is described how CAM software such as SolidCAM or MasterCAM can offer advantages in mold making compared to EDM methods. These software tools accelerate programming, reduce

engineering errors, and enable process visualization. Stable cutting operations with constant cutting force are prioritized, as discussed by Hnatik et al. [7], Cutting force was measured during machining to compare the efficiency of iMachining against traditional strategies. A Kistler 9123C rotary dynamometer was used for precise measurements. The results show that iMachining maintains constant tool load, while traditional strategies show variable load. Description and evaluation of tool path generation strategies for star-shaped pocket machining, comparing self-developed algorithms with various CAM software strategies, are presented in the work of Jacso [8]. In the paper by Lukić et al. [9] the possibility of improving the design and optimization of manufacturing processes is analyzed using modern techniques based on feature technologies and simulations. During the cutting process, we need to watch numerous parameters. Modern solutions include cloud-based systems, as exemplified in the work of Milošević et al. [10] the system for predictive monitoring of cutting tool wear uses sensor data and cloud-based machine learning to estimate wear, enabling intelligent services in smart manufacturing. The paper [11] explores the significance of internet technologies in process planning and modern production preparation. It emphasizes the role of the e-CAPP system in facilitating global collaboration among geographically dispersed development teams, enhancing process planning efficiency, knowledge sharing, and expert knowledge acquisition, as part of the broader e-Manufacturing concept.

3. CASE STUDIES

The input data used for selecting the optimal variant, the workpiece material, was aluminum with dimensions of 300x200x25. The aluminum plate is initially cut to size using a saw, and then the final shape of the part is achieved through milling, as shown in Fig. 1 below.

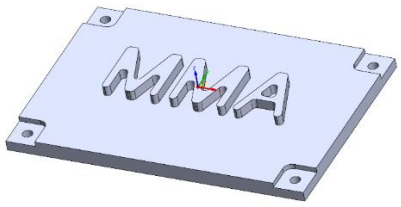


Fig. 1. 3D model of the workpiece

SolidCAM, as a powerful CAM programming tool, provides optimization capabilities across various criteria, leading to innovative solutions and results that can be highly beneficial in the industry. The Hermle_5A machine, listed in the SolidCAM database, was used for machining operations within the software.

3.1 Selection of the Optimal Machining Variant for the Most Complex Operation – Objective Function: Machining time

Process planning can be simplified if standard shapes align with machining templates. In pursuit of this goal, Fig. 2 illustrates standard shapes on the model, while Table 1 defines these standard shapes as configured within the CAD software.

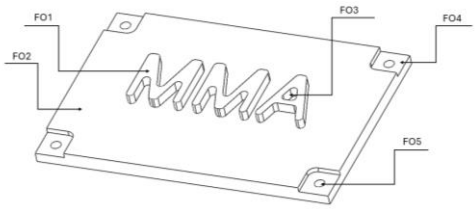


Fig. 2. 3D model with the defined manufacturing features

Feature	Operation Name	Operation ID	Tool ID	Tool Name
FO1	Face milling	Z1	T1	Face mill
FO2	Milling open pocket	Z2	T2	End mill
FO3	Milling pocket	Z3	T3	End mill
FO4	Milling open pocket	Z4	T4	End mill
FO5	Spot drilling Drilling	Z5 Z6	T5 T6	Spot drill Drill

Table 1. Machining operations for the specific features with cutting tools for the milling process

To find the optimal machining sequence based on standard shapes, the most complex operation will first be optimized. Subsequently, by optimizing the machining sequence, the optimal variant will be determined. Machining time serves as our optimization function, allowing us to conclude that geometric feature (feature) FO2, with the largest machining allowance to be removed, represents this most complex operation. Therefore, four machining variants for this operation have been set using the classical SolidCAM method (2 variants) and iMachining as a modern tool for SolidCAM (2 variants):

- Variant 1 (Classical SolidCAM method) – Machining is performed in multiple passes per depth, where the tool descends to a specific depth and performs machining at one level, then continues machining at each next level. Machining is initially done with a larger diameter tool, followed by a smaller diameter tool to achieve the required contour.
- Variant 2 (Classical SolidCAM method) – Machining is performed in multiple passes per depth, where the tool descends to a specific depth and performs machining at one level, then continues machining at each next level. Machining is done with a smaller diameter tool to achieve the required contour using only one tool.
- Variant 3 (iMachining) – Machining is performed by at once descending the tool to the required depth. Machining is initially done with a larger diameter tool, followed by a smaller diameter tool to achieve the required contour.

- Variant 4 (iMachining) – Machining is performed by at once descending the tool to the required depth. Machining is done with a smaller diameter tool to achieve the required contour using only one tool.

The most time-consuming operation during machining is the operation for machining geometric feature (feature) FO2, as clearly shown in Fig. 3. Operations for each feature are depicted in terms of the required number of seconds for machining each feature across processing variants. Operation FO2 is the most complex. The superior use of iMachining strategy in rough cutting can be seen, where Variant III and Variant IV yield the best results, with Variant III proving to be the best among them. Specifically for feature FO2, the use of iMachining strategy justifies a time difference of over seventeen minutes compared to Variant I, and over thirty-five minutes compared to Variant II. Further optimization strategy for processing the required workpiece will be explored through iMachining strategy variants, focusing on machining feature FO2 using Variant III.

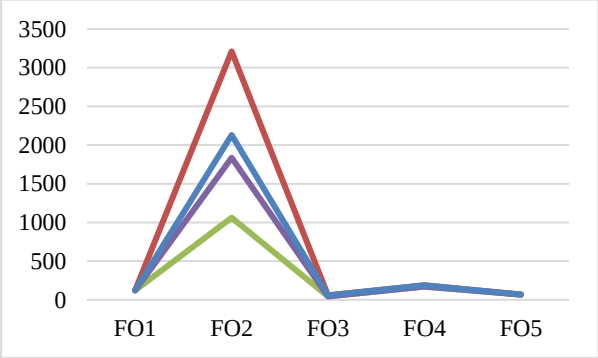


Fig. 3. The most complex operation based on machining time

3.2 Selection of the Optimal Machining Variant – Objective Function: Machining Time

The necessary machining operations required to produce the desired product are explained below with their respective labels:

- A – Milling of the upper surface, through this operation the workpiece achieves its final height – FO1.
- B – Operation that provides nearly complete representation of letters on the workpiece – FO2.
- C – Milling of the pocket to obtain fully defined letters on the workpiece – FO3.
- D – Milling of ends in preparation for drilling – FO4.
- E – Countersinking and drilling of holes – FO5.

In Fig. 4, machining operations from the SolidCAM software simulation are depicted, clearly showing the tool and workpiece. Table 2 presents the machining variants along with the respective machining times for each variant.

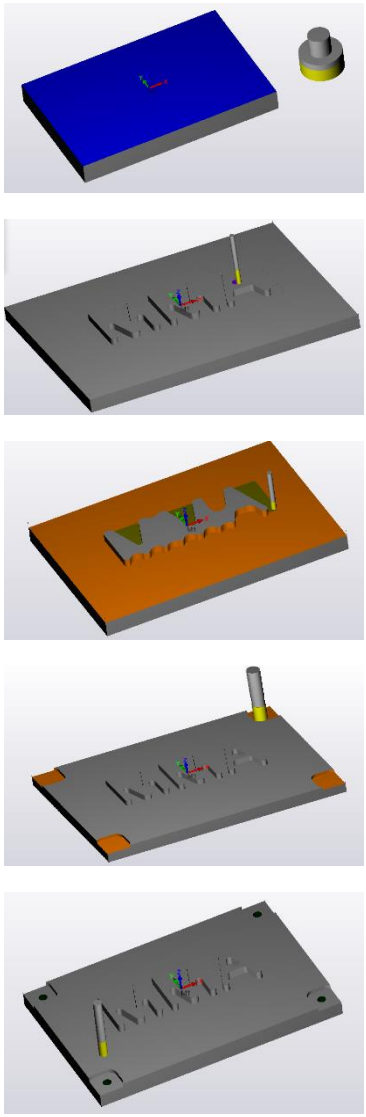


Fig. 4. Output from the simulation of milling operations for the part

Variant 1	Variant 2	Variant 3	Variant 4
A	B	D	A
B	A	B	D
C	C	C	B
D	D	A	E
E	E	E	C
Time: 0:23:41	Time: 0:22:18	Time: 0:21:08	Time: 0:22:31

Table 2. Set variants of operation sequences with given machining times obtained from simulation

Based on the results obtained, it can be concluded that Variant 3 is the best as it has the shortest machining time compared to all other variants. The largest difference is between Variant 3 and Variant 1, with a time difference of over two minutes, which is significant especially in high-volume production where it makes a significant difference in deciding the sequence of operations. Fig. 5 shows the sequence of machining steps for the optimal variant, Variant 3.

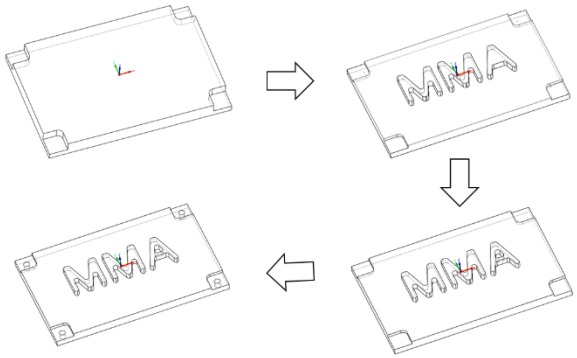


Fig. 5. Sequence of machining operations for the milling process

4. CONCLUSION

This paper examines the possibility of optimizing machining technology by applying the modern CAM module SolidCAM, which was used for the milling process. The first part of the paper provides a literature review, presenting examples of SolidCAM usage and the results of various machining optimization variants. The optimization of the longest-lasting operation in the entire process was analyzed through four variants, where the results showed that the best variant for that operation achieved a time saving difference of thirty-five minutes. After defining the optimal variant of the most complex machining operation, the order of all operations for machining the part was optimized by varying the sequence of operations. The results of the four variants showed that by optimizing the order of operations, a time difference of more than two minutes per piece could be achieved. This result is extremely important, especially in serial or mass production, as saving more than two minutes per piece can lead to a significant time difference in the total quantity of required products.

5. REFERENCES

[1] Vetrivel, A., Arun, A., Thahir, A. S. A., Gokulakrishnan, N.: *Manufacturing Time and Cycle Time Reduction in CNC Machine Shop*, IJRESM, Vol. 1, No. 4, 2018.

[2] „Revolutionizing CNC Machining Efficiency with iMachining“. Accessed: 24. Jun 2024. [On the internet]. Available at: https://www.solidcam.com/imachining/imachining-overview

[3] Petrakov, Y. V. and Myhovych, A.V.: *IMachining technology analysis for contour milling*, Mechanics and Advanced Technologies, Vol. 89, No. 2, 2020, doi: 10.20535/2521-1943.2020.89.202065.

[4] Varga J., Toth, T., Frankovsky, P., Dulebova, L., Spisak, E., Zajacko, I., Zivcak J.: *The Influence of Automated Machining Strategy on Geometric Deviations of Machined Surfaces*, Applied Sciences, Vol. 11, No. 5, pp. 2353, 2021, doi: 10.3390/app11052353.

[5] Zaleski, K., Matuszak, J., Zyśko, A.: *Highly Efficient Milling on the Example of Selected Machining Strategies*, Adv. Sci. Technol. Res. J., Vol. 14, No. 1, pp. 167–177, 2020, doi: 10.12913/22998624/116356.

[6] Ardelean, A.: *About a mould cavity manufacturing using SolidCAM, auo fmte*, Vol. 1, No. 19, 2010, doi: 10.15660/AUOFMTE.2010-1.1774.

[7] Hnatik, J., Kutlwaser, J., Sklenicka, J.: *IMachining Cutting Force Measurement*, DAAAM Proceedings, Vol. 1., No. 1, pp. 0955–0959, 2016 doi: 10.2507/26th.daaam.proceedings.134.

[8] Jacsó, A.: *Tool path generation for pocket machining with uniform tool load*, 2021, doi: 10.13140/RG.2.2.14780.56960.

[9] Lukić, D., Milošević, M., Vukman, J., Đurđev, M., Borojević, S., Antić, A.: *Analyzing possibilities of improving machining process planning and optimization by applying feature technologies and simulation technique*, VII International Conference Industrial Engineering and Environmental Protection (IIZS 2017), Zrenjanin, pp. 1-9, 2017.

[10] Milošević, M., Lukić, D., Ostojić, G., Lazarević, M., Antić, A.: *Application of cloud-based machine learning in cutting tool condition monitoring*, *J. Prod. Eng.*, Vol. 25, No. 1, pp. 20–24, 2022, doi: 10.24867/JPE-2022-01-020.

[11] Milosevic, M., Lukic, D., Antic, A., Lalic, B., Ficko, M., Simunovic, G.: *e-CAPP: A distributed collaborative system for internet-based process planning*, Journal of Manufacturing Systems, Vol. 42, pp. 210–223, 2017, doi: 10.1016/j.jmsy.2016.12.010.

ACKNOWLEDGMENTS

This research has been supported by the Provincial Secretariat for Higher Education and Scientific Research of the AP Vojvodina through the project “Trends of development and application of the Industry 4.0 model in SMEs” (No. 000435212 2024 09418 003 000 000 001) as well as supported by the Ministry of Science, Technological Development and Innovation (Contract No. 451-03-65/2024-03/200156) and the Faculty of Technical Sciences, University of Novi Sad through project “Scientific and Artistic Research Work of Researchers in Teaching and Associate Positions at the FTS, University of Novi Sad” (No. 01-3394/1).

Authors:

Dejan Bozic, PhD Dejan Lukic, PhD Mijodrag Milosevic, University of Novi Sad, Faculty of Technical Sciences, Trg Dositeja Obradovica 6, 21000 Novi Sad, Serbia, Phone: +381 21 485-24-76.
E-mail: bozic997dejan@uns.ac.rs; lukicd@uns.ac.rs; mido@uns.ac.rs

PhD Obrad Spaic, PhD Budimirka Marinovic, Milica Radovanovic, University of East Sarajevo, Faculty of Production and Management, Stepe Stepanovica bb, 89101 Trebinje, Republic of Srpska, Bosnia and Herzegovina, Phone: +387 59 240-654.
E-mail: obrad.spaic@fpm.ues.rs.ba; budimirka.koprivica@fpm.ues.rs.ba; milica.radovanovic@fpm.ues.rs.ba

MMA 2024
FLEXIBLE TECHNOLOGIES

15th INTERNATIONAL SCIENTIFIC CONFERENCE
NOVI SAD, SERBIA, SEPTEMBER 24-26, 2024

Original research paper https://doi.org/10.24867/MMA-2024-04-003

Trstenjak, M., Opetuk, T., Cajner, H., Đukić, G., Mustapić, M.

METHODS AND TOOLS FOR ERGONOMIC ASSESSMENT IN MODERN INDUSTRIAL ENVIRONMENT

Abstract: *Ergonomic analysis in most cases of industrial applications is focused on physical ergonomics. In the modern workplace, which is characterized by constant changes, novel and complex technologies, and the great possibility of information overload, for the worker to remain at an optimal level of productivity, the adaptation of the workplace according to the principles of physical ergonomics is no longer sufficient and needs to be upgraded. Physical injuries and fatigue are usually associated with risky and demanding work positions and activities, but there are many examples of how fatigue associated with cognitive overload can lead to physical injuries and stress that leads to a decrease in worker productivity and motivation. Therefore, this paper gives a literature review of the methods and tools used to assess both physical and cognitive condition of the worker for well-being assessment. Based on the results from the literature review, the general framework of the universally applicable assessment will be suggested and discussed.*

Key words: *human factors and ergonomics, cognitive ergonomics, workplace optimization, wellbeing*

1. INTRODUCTION

In most industrial applications, ergonomic analysis primarily focuses on physical ergonomics. However, in the modern workplace-characterized by constant changes, novel and complex technologies, and a significant potential for information overload-adapting the workplace solely based on physical ergonomics is no longer sufficient for maintaining optimal productivity [1].

Physical ergonomics is a discipline focused on the mechanical properties of the human body and their improvements in order to avoid injuries at work [2]. Many methods are available to measure body position and movement resulting in a value for the level of risk of physical injury. It deals with the quality of human work where the health and safety of workers enable greater productivity.

Cognitive ergonomics describes how human cognition affects work and how work affects it. The quality of work therefore also depends on the workers' understanding of the activities, their goals and limitations. Challenges arise when the human capacity to process a large amount of information becomes insufficient to meet the technological demands of the workplace [3]. According to the principles of cognitive ergonomics, it is necessary to develop methods that can produce a comprehensive qualitative analysis of risk situations, in order to ensure the well-being of workers and a sustainable workplace.

While physical injuries and fatigue are commonly linked to demanding and hazardous work conditions, there are numerous instances where cognitive overload-induced fatigue results in physical injuries and stress, subsequently diminishing worker productivity and motivation [4]. The dynamism and changeability of the work environment is another segment that workers must deal with, so the principles of cognitive ergonomics become very important in this case. There are many examples of improving the workplace using tools and principles of physical ergonomics, but only a few of them refer to the principles of cognitive ergonomics, while there is a significant gap in the literature regarding the joint application of both physical and cognitive ergonomics to ensure the well-being of workers [1,5].

2. METHODOLOGY

The Web of Science, as the most relevant scientific database, was browsed by the following strings: “Ergonomics 4.0”, “Ergonomics 5.0”, “Human factors and ergonomics” AND “Industry 5.0”, “Operator 5.0”, “Human Centered” AND “Ergonomics”, “Human Centered” AND “Human factors”, “Wellbeing” for the papers published field of engineering (mechanical, industrial, multidisciplinary to acknowledge the current findings of the use of models and tools for ergonomic assessment in the modern industrial environment.

3. RESULTS

To understand the most commonly used methods and tools, the findings from the literature were divided into following groups: (1) empirical, (2) analytical and (3) combined approach in ergonomic assessment.

3.1. Empirical approach

The empirical approach is prone to human subjectivity because it is based on self-assessment with questionnaires. The most common questionnaire is the NASA-TLX [6], a subjective, multidimensional tool that assesses perceived workload to assess the demandingness of activities, system or team effectiveness, or other aspects of performance. The total workload is divided into six subjective subscales that are presented on one page: mental demand, physical demand, time demand, performance, effort and frustration. Each subscale is scored within a 100-point

range with 5-point increments. These ratings are then combined with an activity load index. Another method is the workload profile technique, a subjective, multidimensional tool for assessing mental workload (MWL). It is used to determine the level of difficulty imposed by the activity through eight dimensions: perceptual or central processing of the activity, response selection and execution, spatial processing of the activity, verbal processing of the activity, visual processing of the activity, auditory processing of the activity, manual output and speech output. The rating is on a scale from 0 to 1, where 0 indicates no need for mental strain, and 1 indicates a maximum need for mental strain [7]. In industrial settings, NASA-TLX was shown to be more sensitive to experience, while MLW showed greater sensitivity to task differentiation. While both techniques had a similar degree of intrusiveness, NASA-TLX gained greater acceptance [8,9]. NASA-TLX was also used to investigate differences in the mental workload of local and remote operators [10], but also for work in a multitasking environment [11]. In addition to the assessment of cognitive load, it was also used to assess the operator's processing speed [12]. By upgrading the NASA-TLX method, the performance of self-assessment can be improved, but still one of the main limitations remains the impossibility of objective verification of factor assessments with physiological measurements of cognitive load [13]. Fatigue predictors (sleep duration, work shift and production levels) and subjective assessments of workload (NASA-TLX) were used in a study to assess workload in complex manual assembly activities [14], which can later be extended with neurophysiological tools available only at the theoretical level [15].

3.2. Analytical methods

Analytical methods refer to the direct analysis of data on human behaviour and vital signs such as heart rate, heart rate variability, gaze tracking, pupil dilation, EEG, skin conductance, etc. Physiological measurements can be more insightful while minimizing biased parameters and results [16]. The combination of pupillometry and heart rate variability indicated that future research should focus on the influence of additional personal characteristics of workers on variations in cognitive load in manufacturing environments [17]. Another study found that eye tracking and heart activity could be used to measure technology acceptance among older workers. Their performance was shown to include an increased number of errors and a longer duration of performance during multiple tasks, while eye behaviour partially reflected increased cognitive load [18]. On the other hand, the results of pupil size analyses suggest that current laboratory procedures may still not be suitable for the application of mobile pupillometry in an industrial setting [19,20]. Detection of human movement patterns directly from stereo camera input images, especially head position estimation and skeleton tracking that can predict unanticipated movements can also be used in industrial settings to measure cognitive load, in addition to physical state assessment itself [21]. Wearable sensors that measure heart rate, breathing rate, geospatial data (GPS coordinates) of worker movements, speed and acceleration placed in a short-sleeved shirt or bra and sent to a processing unit have proven to be effective in measuring the level of stress caused by new IoT technologies [22,23].

3.3. A combined approach

By combining analytical and empirical methods, it was shown that cognitive monitoring feedback can improve learning performance [24], as well as the use of virtual reality (VR) technologies alone in combination with cognitive state feedback (self-assessment method, performance evaluation and assessment of parameters such as heart rate, heart rate variations, electrodermal data and pupil diameter) [25,26]. In human-machine interaction, it is very important to understand cognitive load, but there is little evidence of the effect of cognitive workload on task performance and muscle activity. Muscle activity can be recorded as a combination of integrated electromyography (EMG) and self-report (NASA-TLX) [27]. When combining NASA-TLX and heart rate variability measurement, certain challenges may arise - heart rate is characterized by a signal that is easily affected by noise due to frequent body movements, while NASA-TLX requires an interruption of activities, so that the operator can perform a self-assessment [28]. Electroencephalography (EEG) and NASA-TLX were combined to investigate the possibilities of a multimodal human-machine interface combining speech and gesture control for automated guided vehicles (AGVs). EEG-based outcomes such as alertness and relaxation significantly affect performance. This research showed significant improvements in human performance [29]. The user's level of technology acceptance and trust towards the technology can predict the perceived level of stress affecting cognitive load which was measured by questionnaires and gaze tracking [30]. The attitude of workers towards different interfaces of the Manufacturing Execution System (MES) was analyzed by measuring body temperature, heart rate, skin conductance and self-assessment (NASA TLX) [31]. Multi-criteria decision-making methods, such as PROMETHEE [32] and Analytic Hierarchy Process (AHP) can also be used [33]. To ensure accurate categorization of workload intensity induced by multitasking situations, statistical waves corresponding to brain frequencies act as features for categorization tasks. A multi-criteria decision-making approach was adopted to rank the algorithms for selecting the best one, in which the weights of the parameters of physical condition during work, mental load, lighting and thermal stress at the workplace are defined

4. DISCUSSION AND CONCLUSION

The framework of the ergonomic assessment in the modern industrial environment based on the Industry 5.0 principles requires the modification of the traditional approaches in the sense of incorporation of principles of cognitive ergonomics and well-being. Here, well-being is not related to organizational challenges such as work-life balance, but to the intrinsic and extrinsic factors that influence human motivation and satisfaction level,

therefore also human productivity. The literature shows that the analytical methods that measure human vital signs can give a good insight into the level of stress and fatigue, as well as cognitive load. In this field, research works are mostly limited to laboratory settings and not to continuous real-time data exchange as well as a way to provide feedback to employees and management. Also, there is no comparative study of vital sign analysis and related measurement tools that could be implemented and used in different industrial settings. On the other hand, the empirical approach can give direct feedback from workers which is needed to assess the cognitive load, but NASA-TLX and similar methods are very subjective and do not provide any specific details about human work.

Even with the combined approach, no comparative study of these cognitive load assessment methods was found, which is recognized as a significant scientific gap. Another gap is related to the combination of cognitive and physical ergonomic analysis, which should also be taken into consideration.

The novel assessment method should be able to be implemented and sustainably monitored in the existing business system. This requires defining associated key performance indicators (KPIs) that signal information about worker well-being, productivity, and efficiency. The collection and monitoring of data on people in real-time brings certain social and ethical challenges that need to be taken into account, just like the legislative framework of an individual country, which is why a multidisciplinary approach is needed to ensure the definition of an optimal strategy for the industrial implementation of the model, mostly related to the adoption of technology and monitoring capabilities, which enables the sustainability of the model as an important part of the work environment.

5. REFERENCES

[1] M. Trstenjak, M. Hegedić, H. Cajner, T. Opetuk, and N. Tošanović, "Cognitive Ergonomics in Industry 5.0," in Flexible Automation and Intelligent Manufacturing: Establishing Bridges for More Sustainable Manufacturing Systems, F. J. G. Silva, L. P. Ferreira, J. C. Sá, M. T. Pereira, and C. M. A. Pinto, Eds., in Lecture Notes in Mechanical Engineering. Cham: Springer Nature Switzerland, pp. 763–77, 2024.

[2] L. Gualtieri, I. Palomba, F. A. Merati, E. Rauch, and R. Vidoni, "Design of Human-Centered Collaborative Assembly Workstations for the Improvement of Operators' Physical Ergonomics and Production Efficiency: A Case Study," Sustainability, vol. 12, no. 9, 2020.

[3] N. Dadashi, G. Lawson, M. Marshall, G. Stokes, "Cognitive and metabolic workload assessment techniques: A review in automotive manufacturing context", Human Factors and Ergonomics in Manufacturing, vol. 32, no. 2, 2021.

[4] S. O. Johnsen, S. S. Kilskar, and K. R. Fossum, "Missing focus on Human Factors – organizational and cognitive ergonomics – in the safety management for the petroleum industry," Proceedings of the Institution of Mechanical Engineers, Part O: Journal of Risk and Reliability, vol. 231, no. 4, pp. 400–410, 2017.

[5] Briken K, Moore J, Scholarios D, Rose E, Sherlock A. Industry 5 and the Human in Human-Centric Manufacturing. Sensors, vol. 23, no. 14, 2023.

[6] "NASA Task Load Index | Digital Healthcare Research." Accessed: Apr. 22, 2024. [Online]. Available: https://digital.ahrq.gov/health-it-tools-and-resources/evaluation-resources/workflow-assessment-health-it-toolkit/all-workflow-tools/nasa-task-load-index

[7] P. S. Tsang and V. L. Velazquez, "Diagnosticity and multidimensional subjective workload ratings," Ergonomics, vol. 39, no. 3, pp. 358–381, 1996.

[8] M. A. Barajas-Bustillos, A. A. Maldonado-Macías, M. A. Serrano-Rosa, J. L. Hernandez-Arellano, L. Llamas-Alonso, and O. Balderrama-Armendariz, "Impact of experience on the sensitivity, acceptability, and intrusive of two subjective mental workload techniques: The NASA TLX and workload profile," Work, vol. 75, no. 4, pp. 1265–1275, 2023.

[9] L.-O. Bligård and A.-L. Osvalder, "CCPE: Methodology for a Combined Evaluation of Cognitive and Physical Ergonomics in the Interaction between Human and Machine," Human Factors and Ergonomics in Manufacturing & Service Industries, vol. 24, no. 6, pp. 685–711, 2014.

[10] M. Zimmer, A Al-Yacoub, P. Ferreira, E-M Hubbard, N Lohse, "Experimental study to investigate mental workload of local vs remote operator in human-machine interaction", Production and Management Research, vol 10, no. 1, 2022.

[11] M. Putri, X. Yang, and J. H. Kim, "Sensitivity, Bias, and Mental Workload in a Multitasking Environment," in Engineering Psychology and Cognitive Ergonomics, D. Harris, Ed., Cham: Springer International Publishing, pp. 10–18, 2016.

[12] Daniela Cavallo, Salvatore Digiesi, Francesco Facchini, Giovanni Mummolo, "An analytical framework for assessing cognitive capacity and processing speed of operators in industry 4.0", Procedia Computer Science, vol 180, pp. 318-327, 2021.

[13] P. Thorvald, J. Lindblom, and R. Andreasson, "On the development of a method for cognitive load assessment in manufacturing," Robotics and Computer-Integrated Manufacturing, vol. 59, pp. 252–266, 2019.

[14] Y. Torres, S. Nadeau, and K. Landau, "Evaluation of Fatigue and Workload among Workers Conducting Complex Manual Assembly in Manufacturing," IISE Transactions on Occupational Ergonomics and Human Factors, vol. 9, no. 1, pp. 49–63, 2021.

[15] J. Wolfartsberger and R. Riedl, "Smart Production and Manufacturing: A Research Field with High Potential for the Application of

Neurophysiological Tools," in Information Systems and Neuroscience, F. D. Davis, R. Riedl, J. vom Brocke, P.-M. Léger, A. B. Randolph, and G. R. Müller-Putz, Eds., Cham: Springer International Publishing, pp. 211–218, 2022.
[16] Z. Zakeri, A. Arif, A. Omurtag, P. Breedon, and A. Khalid, "Multimodal Assessment of Cognitive Workload Using Neural, Subjective and Behavioural Measures in Smart Factory Settings," Sensors, vol. 23, no. 21, p. 8926, 2023.
[17] X. Ma, R. Monfared, R. Grant, and Y. M. Goh, "Determining Cognitive Workload Using Physiological Measurements: Pupillometry and Heart-Rate Variability," Sensors, vol. 24, no. 6, p. 2010, 2024.
[18] P. Pluchino et al., "Advanced workstations and collaborative robots: exploiting eye-tracking and cardiac activity indices to unveil senior workers' mental workload in assembly tasks," Front. Robot. AI, vol. 10, 2023.
[19] B. B. Van Acker et al., "Mobile pupillometry in manual assembly: A pilot study exploring the wearability and external validity of a renowned mental workload lab measure," International Journal of Industrial Ergonomics, vol. 75, p. 102891, 2020.
[20] F. N. Biondi, B. Saberi, F. Graf, J. Cort, P. Pillai, and B. Balasingam, "Distracted worker: Using pupil size and blink rate to detect cognitive load during manufacturing tasks," Applied Ergonomics, vol. 106, p. 103867, 2023.
[21] M. Lagomarsino, M. Lorenzini, E. De Momi, and A. Ajoudani, "An Online Framework for Cognitive Load Assessment in Industrial Tasks," Robotics and Computer-Integrated Manufacturing, vol. 78, p. 102380, 2022.
[22] A. Kajmakovic, S. Manfredi, M. Brillinger, and D. Leder, "Poster: IOT as enabler of workers' stress detection in manufacturing systems of the future," in Proceedings of the 11th International Conference on the Internet of Things, in IoT '21. New York, NY, USA: Association for Computing Machinery, pp. 196–199, 2022.
[23] Elizabeth M. Argyle, Adrian Marinescu, Max L. Wilson, Glyn Lawson, Sarah Sharples, Physiological indicators of task demand, fatigue, and cognition in future digital manufacturing environments, International Journal of Human-Computer Studies, vol. 145, 2021.
[24] J. H. Kim, "The Impact of Metacognitive Monitoring Feedback on Mental Workload and Situational Awareness," in Engineering Psychology and Cognitive Ergonomics, D. Harris, Ed., Cham: Springer International Publishing, pp. 32–41, 2018.
[25] A. Brunzini, F. Grandi, M. Peruzzini, and M. Pellicciari, "An integrated methodology for the assessment of stress and mental workload applied on virtual training," International Journal of Computer Integrated Manufacturing, pp. 1–19, 2023.
[26] A. Brunzini, F. Grandi, M. Peruzzini, and M. Pellicciari, "Virtual training for assembly tasks: a framework for the analysis of the cognitive impact on operators," Procedia Manufacturing, vol. 55, pp. 527–534, 2021.
[27] F. N. Biondi, A. Cacanindin, C. Douglas, and J. Cort, "Overloaded and at Work: Investigating the Effect of Cognitive Workload on Assembly Task Performance," Hum Factors, vol. 63, no. 5, pp. 813–820, 2021.
[28] E. Klose, V. Manghisi, S. Digiesi, F. Facchini, M. Foglia, and C. Mummolo, "Heart rate variability based assessment of cognitive workload in smart operators," Management and Production Engineering Review, vol. 11, pp. 56–64, 2020.
[29] L. Overmeyer, F. Podszus, and L. Dohrmann, "Multimodal speech and gesture control of AGVs, including EEG-based measurements of cognitive workload," CIRP Annals, vol. 65, no. 1, pp. 425–428, 2016.
[30] T. Panchetti, L. Pietrantoni, G. Puzzo, L. Gualtieri, and F. Fraboni, "Assessing the Relationship between Cognitive Workload, Workstation Design, User Acceptance and Trust in Collaborative Robots," Applied Sciences, vol. 13, no. 3, art. no. 3, 2023.
[31] Dörner, A.; Bures, M.; Simon, M.; Pirkl, G. „Making Cognitive Ergonomics in the Human–Computer Interaction of Manufacturing Execution Systems Assessable": Experimental and Validation Approaches to Closing Research Gaps, Machines, vol. 12, no. 3, 2024.
[32] S. Mohdiwale, M. Sahu, G. R. Sinha, and V. Bajaj, "Automated Cognitive Workload Assessment Using Logical Teaching Learning-Based Optimization and PROMETHEE Multi-Criteria Decision Making Approach," IEEE Sensors Journal, vol. 20, no. 22, pp. 13629–13637, 2020.
[33] M. Rezvanizadeh, M. Mohammad-Ghasemi, A. Soltanzadeh, and M. Sadeghi-Yarandi, "Development of a novel ergonomic index assessment in the workplace based on physical, cognitive, and environmental components," Work, vol. 75, no. 3, pp. 1071–1086, 2023

Authors:
PhD Maja Trstenjak, PhD Tihomir Opetuk, PhD Hrvoje Cajner, PhD Goran Đukić, University of Zagreb, Faculty of Mechanical Engineering and Naval Architecture, Ivana Lucica 5, 10 000 Zagreb, Croatia.
E-mail: maja.trstenjak@fsb.unizg.hr; tihomir.opetuk@fsb.unizg.hr; hrvoje.cajner@fsb.unizg.hr; goran.dukic@fsb.hr
PhD Miljenko Mustapic, University North, Trg dr. Žarka Dolinara 1, 48 000 Koprivnica, Croatia.
E-mail: mmustapic@unin.hr

MMA 2024
FLEXIBLE TECHNOLOGIES

15th INTERNATIONAL SCIENTIFIC CONFERENCE
NOVI SAD, SERBIA, SEPTEMBER 24-26, 2024

Original research paper https://doi.org/10.24867/MMA-2024-04-004

Vukelic, Z., Cajner, H., Trstenjak, M.

THE ASPECT OF TECHNOLOGICAL HUMANISM IN THE IMPLEMENTATION OF ROBOTIC SYSTEMS (RS) AND ARTIFICIAL INTELLIGENCE (AI) IN INDUSTRY 5.0

Abstract: *Manufacturing companies are increasingly exposed to highly volatile market conditions and multiple pressures for business improvement. While the inclusion of robots in production has been a company practice for some time, artificial intelligence (AI) is a new area of information technology development with very high potential to increase performance, but also with challenges. The impact on workers in both these areas is very significant and therefore there is a need for its deeper research and understanding. The new concept of Industry 5.0 solves the problems identified earlier and includes the consideration of technological humanism. Researching its degree in digital transformation is a demanding area that has not been sufficiently studied so far. In accordance with the research model of technological humanism, the conducted case study provides insight into the implementation of robotic systems (RS) and AI that companies should think about in order to enable successful man and machine collaboration.*

Key words: *Robotic systems, Artificial intelligence, Technological humanism, Transformation towards Industry 5.0*

1. INTRODUCTION

Manufacturing companies are today facing conditions of business uncertainty and high volatility and are facing increasing pressures to improve its agility and flexibility. The implementation of the smart factory concept and the management of digital production has become imperative for manufacturing companies, which brings the need for multiple organizational changes. The implementation of new technologies and digital transformation affect the entire company, increase its performance and enable the acquisition of a competitive advantage [1]. Since the history of the implementation of smart production under the concept of Industry 4.0 has shown that the biggest challenge is not technology but people [2], the focus should be placed on the overall organization as a socio-technical system [1]. This is incorporated within the new concept Industry 5.0, as an update to Industry 4.0. It has a human-centred approach and is focused on values considering technical aspects and human needs together.

The inclusion of robots in production has been a company practice for some time. As part of Industry 5.0, robotic systems (RS) are increasingly being incorporated into manufacturing operations to ensure non-stop work and improve productivity, and more recently to provide a solution to labour shortages. Modern robots are completely different from the automation machines of the past and involve the use of advanced technologies, machine learning and artificial intelligence (AI), enabling more complex and deeper interactions with people. AI itself also represents an important part of Industry 5.0. The industry faces critical questions to ensure the responsible and effective integration of RS [3] and AI use in the workplace creates opportunities, but also many challenges [4]. Therefore, there is a need for deeper research and understanding of the involvement of RS and AI in the operations and business system of manufacturing companies.

2. ADVANCED ROBOTIC SYSTEMS AND ARTIFICIAL INTELLIGENCE

Current automation technologies are the result of many years of research and development that have led to numerous advances with benefits for companies [5]. Advanced robotics allows improving the ability of robots to engage in more complex interactions with humans and other automated systems [3], and creating autonomous production systems. AI, machine learning (ML) and deep learning (DL) are transforming the field of advanced robotics, making robots more intelligent, efficient and adaptable to complex tasks and environments [6]. Since manufacturing companies have begun to invest significantly in workspaces with close interaction between humans and robots [7], they must successfully establish a functional cooperative organization that will benefit both the company and its workers. Collaborative robots play an increasingly important role in manufacturing [8] and are one of the newest applications in the field of AI. As technology continues to advance it is necessary for industries to analyse its new capabilities, along with its responsible use [3]. AI is increasingly being adopted in production, which leads to dynamic changes in work design and corresponding responsibilities [9]. It can increase the productivity of the company, but its involvement in complex socio-technical environments significantly changes the situation of the human operator [4]. As AI has extremely fast development, any noticeable problems need to be solved quickly in order to avoid their repetition and multiplication in the future. In order to avoid limiting the effectiveness of the application of RS and AI in the production processes of manufacturing companies, the goal is to enable successful cooperation between man and machine, with technology at the service of man and his development, well-being and fulfilment. This is contained in the concept of technological humanism.

3. INDUSTRY 5.0 AND TECHNOLOGICAL HUMANISM

Industry 5.0 took technological settings and solutions from Industry 4.0, but after noticing the neglect of the human factor in the previous framework, it included this important component. This new framework is designed to complement the digital development of industrial systems with purposeful and efficient cooperation between humans, machines and systems in a digital environment [10]. It helps people and machines work together to improve the efficacy of industrial production and represents a tool for enabling sustainable and resilient industry [10].

Technological humanism represents a new concept that enables man-machine synergy, it is one of the most important new trends in the labour world [11], and the Industry 5.0 framework implements it in business and production processes and relationships [12]. It can fulfil that the technology has a purpose and goal of promoting social integration and human development, with shared values with company goals [13]. As RS and AI increasingly becomes a standard component of production processes [14], adequate management of technological humanism in manufacturing companies is very important in their transformation towards Industry 5.0.

4. A CASE STUDY OF RESEARCHING ASPECT OF ROBOTIC SYSTEMS AND ARTIFICIAL INTELLIGENCE IN MEASURING THE DEGREE OF TECHNOLOGICAL HUMANISM

With the aim of gaining insight into the technological-humanistic aspect of using RS and AI in production, organization and management depending on the employee's work position in the company, a case study was conducted. It was based on a model designed to examine the degree of technological humanism within manufacturing companies in their transformation towards Industry 5.0 which contains the following components [12]:

- Information and Knowledge Management – accessibility and distribution of new information and knowledge.
- Workplace Organisation Management – how positions are organised and processes aligned with the identified elements of change.
- Workplace Ergonomics Management – ergonomics in work positions is aligned with the necessary changes in workplace organisation.
- Workforce Wellbeing Management – achieving worker satisfaction in changing working conditions.
- Long-Term Work Quality Management – ensuring lasting work quality by retaining existing and attracting new high-quality workers.

In accordance with the model, a case study was conducted on a sample of employees in two Croatian manufacturing companies to identify the degree of employee knowledge and awareness of using RS and AI in production, organization and management as the component of Industry 5.0 implementation, and its influences on the company and on them personally. The research covered the five components of Industry 5.0 relating to the role of technological humanism in line with the model. Both surveyed companies are small companies with annual revenues in the range of EUR 2–7 million. An additional goal was to determine whether there is a statistically significant difference in employee perceptions in relation to their work positions, and further to obtain their opinion on how the company could better organise the necessary educational and training processes.

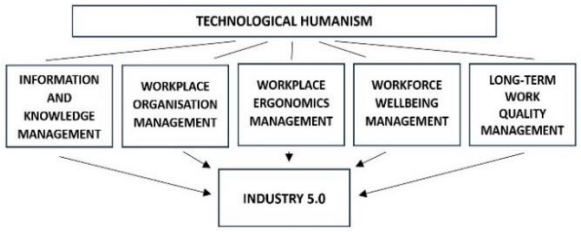


Fig. 1. Graphic representation of the model [12]

The case study included all company employees, and their work positions were considered in six categories:

- Auxiliary staff,
- Operational non-production worker,
- Operational production worker,
- Non-production department head,
- Production department head,
- Top management.

The survey questions 1-5 are presented below, and they followed the model components (1-5):

1. To what extent are you familiar with the potential that new technologies can offer the company you work in?
2. In your opinion, to what extent can the application of new technologies affect your work position?
3. In your opinion, to what extent can the application of new technologies affect or could affect the improvement of the ergonomics of your workplace?
4. In your opinion, to what extent can new technologies affect or could affect improvement of your satisfaction at work?
5. In your opinion, to what extent can new technologies affect or could affect your decision to be a long-term employee in your company?

For each question, nine areas addressing the technological aspects of Industry 5.0 were listed, and for the purpose of this research, the one that read “Application of autonomous robotics” and the one that read "Use of artificial intelligence in production, organization and management" were analysed in detail. Employees were asked to give answers to the questions based on a five-point Likert scale. Statistical analysis of results was performed to identify possible correlations between factors that influence significant differences. In total, 60 properly-filled out responses were obtained, with 77% of the total number of employees in the first company and 82% of the total number in the second. Responses from both companies were pooled into a

single sample and examined on the basis of work position categories.

In order to obtain information about possible differences in respondents' answers depending on their workplace, the Kruskal Wallis statistical test was performed. The analysis of data related to the application of autonomous robotics showed that there is no significant difference in the perception of respondents of different work position categories in questions related to the model components 1 to 5. The analysis of data related to the use of AI in production, organization and management showed that there is no significant difference in the perception of respondents of different work position categories in questions related to the model components 1, 2, 3 and 5. In the case of the question about work satisfaction, which concerns the model component 4, a trend is visible that indicates that category 6 employees could have a different perception than the others. The Kruskal Wallis test with a significance level of 5% showed that there is no statistically significant difference. In both cases, it is important to take into account that the sample of the case study was very small. This indicates that the results are not completely valid and research on a larger sample is recommended. Fig. 2 illustrates the results for the identified differences in the model component 4 related to the aspect of using AI in production, organization and management depending on the employee's work position in the company.

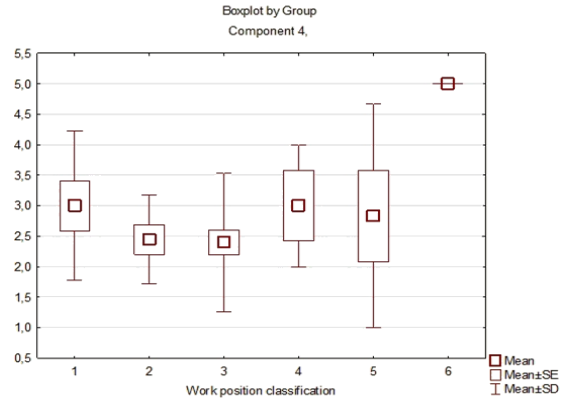


Fig. 2. Graphic display of results for the component 4

The case study results did not indicate significant differences between work positions within the aspects of the application of autonomous robotics, and using AI in production, organization and management in the processes surrounding the transformation of production companies towards Industry 5.0 within the aspect of technological humanism. The visible trend that category 6 employees might have a different perception than others in the case of the AI use is important because work category 6 represents top management that is responsible for decision-making, managing the company's transformation, and creating processes related to the implementation of AI and transformation towards Industry 5.0.

One of the most common obstacles preventing the transition to smart manufacturing is the lack of knowledge about digital principles and awareness of the future benefits of new technology [15]. The results of descriptive statistics show that in the case of robotics as well as AI, the lowest mean data values are in the component 1 of the research model of technological humanism, which corresponds to the company information and knowledge management. Tables 1 and 2 give an overview of the descriptive statistics results pertaining to the relationship of the classification determinants relating the type of the components of the research model (1-5).

Variable	All Groups Descriptive Statistics (RS)							
	Mean	Median	Mode	Freq	Min	Max	Std.Dev.	Skewnes
Component 1	**2,18**	2,00	1,00	20	1,00	5,00	1,10	0,66
Component 2	2,50	2,00	2,00	17	1,00	5,00	1,27	0,46
Component 3	2,67	3,00	3,00	18	1,00	5,00	1,19	0,31
Component 4	3,03	3,00	3,00	30	1,00	5,00	1,01	0,14
Component 5	2,93	3,00	3,00	22	1,00	5,00	1,07	0,14

Table 1. Statistical data for the use of RS

Variable	All Groups Descriptive Statistics (AI)							
	Mean	Median	Mode	Freq	Min	Max	Std.Dev.	Skewnes
Component 1	**2,12**	2,00	1,00	23	1,00	5,00	1,14	0,84
Component 2	2,55	3,00	3,00	21	1,00	5,00	1,21	0,35
Component 3	2,43	2,00	1,00	18	1,00	5,00	1,29	0,64
Component 4	2,70	3,00	3,00	19	1,00	5,00	1,25	0,44
Component 5	2,53	2,00	2,00	21	1,00	5,00	1,29	0,60

Table 2. Statistical data for the use of AI

The literature points to numerous challenges during the transition of companies towards Industry 5.0, including those related to intelligent RS and AI implementation [5, 6], and that these challenges can be overcome with successful knowledge management [15]. Although the case study research sample is small, its results point to the need for future research on knowledge management in the organization during its transition to Industry 5.0 with the aim of investigating the relationship between employees' related knowledge and their relationship to the implementation of new technologies. The results can bring information that can be used to overcome the problem that employees, due to lack of adequate knowledge, have unrealistic perceptions and expectations about the company's technological transition, which can significantly harm its success.

5. CONCLUSION

Advances in the field of automation have made it possible to create robots that have been used in manufacturing companies for some time. With the further development of technology, advanced and intelligent RS were created and their autonomous functioning in the plant was enabled. AI is a technology that has already been implemented in various areas, and is increasingly being used in the creation of advanced RS. The implementation of RS and AI technology has a significant impact on the organization and on the workplaces of employed people. For reasons of ensuring smooth transformation processes of companies when adopting new technologies and the concept of Industry 5.0, these technological means require understanding and clear interpretation.

In order to achieve long-term benefits of the RS and AI use in manufacturing companies, and to ensure that

this technology is at the service of humans and their development, technological humanism is an important component in the transformation towards Industry 5.0. This paper presents the results of the examination of the degree of technological humanism on a sample of manufacturing companies in the transformation towards Industry 5.0, which focus on the aspect of using RS and AI in production, organization and management. The conducted case study did not show statistically significant different perceptions of the examined categories of employees within the components of technological humanism from the aspect of using RS and AI. On the other hand, there is a visible trend that indicates a possible difference in the perception of AI technology use by top management compared to other categories of employees. This is very important because in manufacturing companies there is a wide range of employees in different positions and with different education, and top management is at the decision-making level and leads the company. In its transition towards Industry 5.0, the company should respect all categories of employees, applying an approach according to employee work duties and abilities.

The case study also revealed a relative low level of knowledge of the respondents about the potential that new technologies can offer to the company, while at the same time they gave answers about the impact of the same technologies on technological humanism. In order to prevent the problem that employees, due to lack of adequate knowledge, have unrealistic perceptions and expectations about the company's technological transition with RS and AI use which can significantly harm its success, new research on a larger sample is needed. This research with a focus on knowledge management and its consequent relationships during the transition towards Industry 5.0 can help manufacturing companies to successfully implement the necessary processes, in accordance with the principles of technological humanism, ensuring joint business and social progress.

6. REFERENCES

[1] Koldewey, C., Hobscheidt, D., Pierenkemper, C., Kühn, A. and Dumitrescu, R.: Increasing firm performance through industry 4.0-a method to define and reach meaningful goals, Sci, Vol. 4, No. 4, pp. 39, 2022.

[2] Ejsmont, K.: The impact of industry 4.0 on employees-insights from Australia, Sustainability, Vol. 13, No. 6, pp. 3095, 2021.

[3] Licardo, J.T., Domjan, M. and Orehovački, T.: Intelligent Robotics-A Systematic Review of Emerging Technologies and Trends, Electronics, Vol. 13, No. 3, pp. 542, 2024.

[4] Passalacqua, M., Cabour, G., Pellerin, R., Léger, P.M. and Doyon-Poulin, P.: Human-centered AI for industry 5.0 (HUMAI5. 0): Design framework and case studies, Human-centered AI, pp. 260-274, 2024.

[5] Chamola, V., Hassija, V., Sulthana, A.R., Ghosh, D., Dhingra, D. and Sikdar, B.: A review of trustworthy and explainable artificial intelligence (xai), IEEE Access, 2023.

[6] Soori, M., Arezoo, B. and Dastres, R.: Artificial intelligence, machine learning and deep learning in advanced robotics, a review, Cognitive Robotics, 2023.

[7] Simões, A.C., Pinto, A., Santos, J., Pinheiro, S. and Romero, D.: Designing human-robot collaboration (HRC) workspaces in industrial settings: A systematic literature review, Journal of Manufacturing Systems, No. 62, pp. 28-43, 2022.

[8] Liu, L., Zou, Z. and Greene, R.L.: The effects of type and form of collaborative robots in manufacturing on trustworthiness, risk perceived, and acceptance, International Journal of Human–Computer Interaction, Vol. 40, No. 10, pp. 2697-2710, 2024.

[9] Rožanec, J.M., Novalija, I., Zajec, P., Kenda, K., Tavakoli Ghinani, H., Suh, S., Veliou, E., Papamartzivanos, D., Giannetsos, T., Menesidou, S.A. and Alonso, R.: Human-centric artificial intelligence architecture for Industry 5.0 applications, International journal of production research, Vol. 61, No. 20, pp. 6847-6872, 2023.

[10] Babkin, A., Shkarupeta, E., Kabasheva, I., Rudaleva, I. and Vicentiy, A.: A framework for digital development of industrial systems in the strategic drift to Industry 5.0, International Journal of Technology, Vol. 13, No. 7, 2022.

[11] ESADE: Humanismo Tecnológico o cómo hacer al ser humano el centro de la automatización global, Conclusiones del Foro de Humanismo Tecnológico, Madrid, 2020.

[12] Vukelić, Ž., Cajner, H. and Barić, G.: Research model of the degree of technological humanism in manufacturing companies in the transformation towards Industry 5.0, Technical Journal, in press, 2024.

[13] Hernando, A.: Humanismo digital: la tecnología al servicio de las personas y del propósito de las empresas, Institute for Social Innovation, Barcelona, 2022.

[14] Dmitrieva, E., Balmiki, V., Lakhanpal, S., Lavanya, G. and Bhandari, P.: AI evolution in Industry 4.0 and Industry 5.0: an experimental comparative assessment, BIO Web of Conferences, EDP Sciences, Vol. 86, p. 01069, 2024.

[15] Kandasamy, J., Venkat, V. and Mani, R.S.; Barriers to the adoption of digital technologies in a functional circular economy network, Operations Management Research, Vol. 16, No. 3, pp. 1541-1561, 2023.

Authors:

PhD Zeljko Vukelic, Marius d.o.o., Vocarska cesta 44, 10000 Zagreb, Croatia, Phone.: +385 1 463-54-54.
E-mail: zeljko.vukelic@marius.hr

PhD Hrvoje Cajner, PhD Maja Trstenjak, University of Zagreb, Faculty of Mechanical Engineering and Naval Architecture, Ul. Ivana Lucica 5, 10000, Zagreb, Croatia, Phone.: +385 1 616-82-22.
E-mail: hrvoje.cajner@fsb.unizg.hr; maja.trstenjak@fsb.unizg.hr

MMA 2024 FLEXIBLE TECHNOLOGIES

15th INTERNATIONAL SCIENTIFIC CONFERENCE
NOVI SAD, SERBIA, SEPTEMBER 24-26, 2024

Original research paper https://doi.org/10.24867/MMA-2024-04-005

Štrbac, G., Štrbac, B., Milošević, M., Ranisavljev, M., Hadžistević, M.

IMPORTANCE OF 3D CAD SEARCH ENGINES IN GEAR MAINTENANCE

Abstract: *This paper explores the utilization of CAD models in advanced web-based search methods for engineering applications. CAD models contain comprehensive parametric data crucial for manufacturing, encompassing geometry, tolerances, materials, and more. Recent advancements leverage web search engines to facilitate efficient retrieval of similar parts or counterparts based on diverse criteria detailed herein. This research presents a method utilizing a specialized search engine for reverse engineering mechanical parts like gears. Integrated with CAD software and accessible online, it facilitates finding specific components with high similarity matches based on geometric features. Users can assess and interact with search results to support informed decision-making. Upon identification, engineers can seamlessly initiate procurement via integrated ERP systems, pivotal in modern manufacturing for optimizing operations, enhancing collaboration, ensuring data integrity, and boosting productivity. This study underscores the transformative role of CAD models and web technologies in streamlining production processes.*

Key words: *CAD models, 3D search enginees, gears*

1. INTRODUCTION

3D solid models are widely used across various fields such as architecture, graphics, engineering, and manufacturing. Efficient storage, retrieval, and reuse of the knowledge embedded in these models is a significant contemporary challenge. To address this, 3D solid digital libraries have been developed to extract, retrieve, and browse key engineering 3D solid models and related information, including tolerance, design/manufacturing features, and assembly relationships. Retrieving information from a 3D solid model involves searching for a model or assembly with a similar graph structure [1].

Regarding 3D CAD search engines, these tools are crucial for retrieving design and engineering information by structurally indexing 3D models, enhancing data searchability and accessibility [2,3].

Traditional text-based document search methods are ineffective for classifying, searching, and reusing 3D data. Numerous research efforts focus on content-based retrieval, utilizing methods that measure shape similarity between 3D models. Context-based retrieval currently relies on textual annotations (e.g., keywords), which are typically added manually and represent only a small fraction of the stored information. As the number and popularity of 3D objects continue to grow, the academic community has shifted its focus to search systems. One notable example is the VICTORY project (2006), which aims to develop a distributed 3D search engine for searching, accessing, and retrieving 3D and other digital content in a distributed object repository via peer-to-peer networks. The 3D search engine on the project's website uses five different global descriptors as search alternatives. However, it does not support combining, weighting, or other forms of user interaction with the search engine. Currently, very few commercial 3D search engines are available. Siemens PLM software represents the state-of-the-art in commercial search engines for Product Lifecycle Management (PLM), though geometry-based retrieval is just one of the challenges that need addressing. The domain's unique characteristics add complexity to the problem. Knowledge is not only contained in digital media but also in the methods used to acquire and transform them, with each context adding another semantic layer of information to shape resources. Current 3D media repositories focus primarily on the geometric aspects of models, rather than the knowledge they represent. While there are numerous approaches to geometric or structural representation of resources, very little work has been done at the semantic level until now [2].

Using generic keyword-based search engines like Google does not produce relevant results for 3D models, as these engines index websites based on text content and citation frequency. Extensive research has been conducted on search algorithms involving 3D model surface meshes, mainly to retrieve similarly shaped parts from databases. The primary methods for shape search can be categorized into several major approaches: manufacturing feature recognition (feature relationship graphs), global feature descriptors, local feature descriptors, graph-based methodologies, and histogram-based techniques [4].

Keyword-based search engines work well when there is a need to find parts such as screws, bolts, and fixtures, but more complex parts, such as gears, and assemblies that require scheduled maintenance months ahead of time are more difficult to find. Especially when there is no information about existing part geometry and tolerances, from an older machine or assembly.

In this paper, we present the importance of search engines that utilize search based on the nominal CAD model, for important groups of parts for power transmission, such as gears. Gear parameters and digital representation were unavailable for this particular case. A CAD model of the gear was reconstructed based on flank, lead, and pitch measurements with the help of a

coordinate measurement machine (CMM) and then inserted in a search engine called 3Dfindit. This search engine includes various smart search methods, such as geometric similarity search, text, color, or sketch search.

2. EXPERIMENTAL SET-UP

In order to showcase how CAD search engines operate, spur gear with 23 teeth was reconstructed based on measurement results acquired from Mitutoyo Crysta-Apex S9106 CMM. This CMM has a maximum permissible error of $MPE_E = (1.7 + 3L/1000)$, where L is in mm. Every tooth was measured, at the temperature of 20℃, according to an algorithm embedded into MCOSMOS CMM software. This gear algorithm or sub-program has the ability to make paths on gear teeth based on simple inputs of information such as the number of teeth. This measuring sub-program is useful when the rotational table is not available on the CMM but the indexible measuring head is. Reconstruction of gear geometry was carried out in SolidWorks 2022. The physical part (see Fig. 1.) is from the Pfauter hobbing machine. A section of the output report with a graphical representation of the deviation for gear teeth is shown in Fig. 2. Since this machine can produce a plethora of different gears, the accuracy of manufacturing for a particular gear is expected to be high.

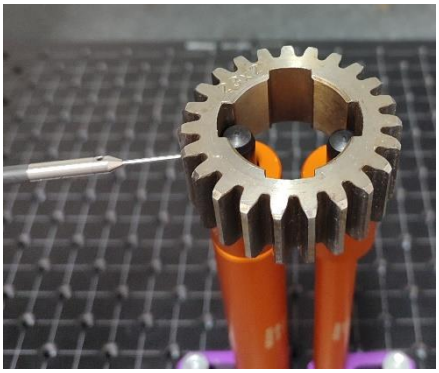


Fig. 1. Gear from the Pfauter hobbing machine

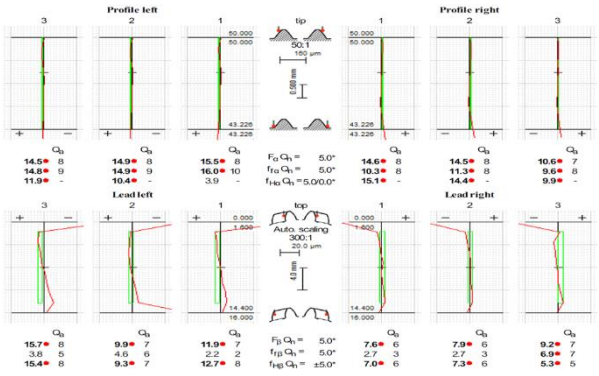


Fig. 2. Measurement results for profile and lead of the workpiece

The train of thought for most users, when they need to find a specific part or assembly, is to look up the manufacturer portfolio, which, hopefully, has new parts in the stock, but when there is little to no information, the only solution is to reverse engineer it. Engineered parts can be used as a reference to make a new part in the machine shop, or they can be used as input to a particular search engine. The algorithm that displays decision-making is shown in Fig. 3.

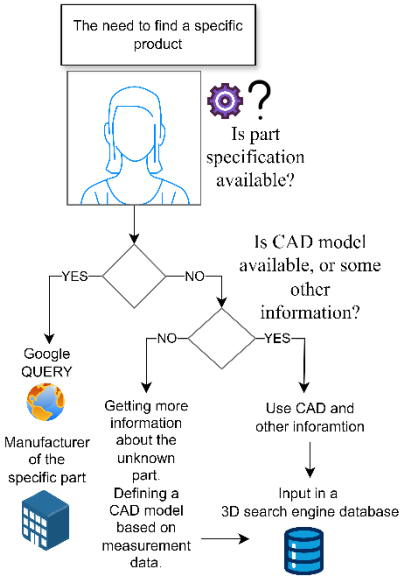


Fig. 3. Decision-making algorithm for part search

3. RESULTS AND DISCUSSION

3.1 3D Search engine showcase: 3Dfindit

This search engine is freely available with a database for CAD models, like GrabCAD, and can be fully integrated into the existing CAD software, for example, SolidWorks, as a plug-in. However, 3Dfindit primarily functions as a web application. With the "Enterprise" subscription, the user can choose between different industry types depending on several factors. The most influential factor should be users' judgment on where is the highest probability of finding a specific part or assembly. For a gear, "Product Design Aircraft", "Product Design Automotive" or "Tooling" should be considered. The choice of different industry types and Enterprise User Interface (UI) is shown in Fig. 4.

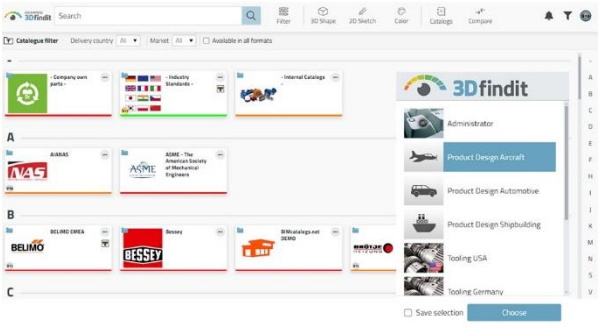


Fig. 4. Enterprise 3Dfindit search engine UI

For the purpose of this work, PD - Automotive was selected. Navigating through UI is enabled with the help of additional filters. Users have a choice to select filter search across all catalogs and apply search across all formats of files. Primary search is conducted through options that are available in the top bar, such as 3D shape, 2D sketch, and Color. The mechanical part such as any type of part included in the transmission of energy

and motion (gear) certainly can not be described with only color. Even a 2D sketch isn't enough in this case, so the only other option is to upload a CAD model and conduct a search. The uploaded file of the gear, in .stp format, is shown in Fig. 5.

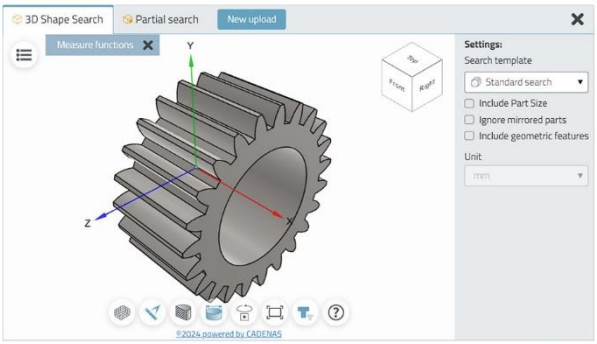


Fig. 5. Available options upon upload of CAD model

In option 3D shape search, there are additional options that provide the search engine algorithm with information about parts geometry, inclusion of geometric features, size, etc. In the Partial search option, the user can define custom settings such as part similarity, units of measurement, and a significant option called "find a counterpart". Find a counterpart is an option that searches for the mating part in most cases. An example of that would be to find ball bearings for the shaft or another gear with the same modul but different diameter. Since gears with the same modul can be paired, there is no need to use the "find a counterpart" option. Search results are shown in Fig. 6.

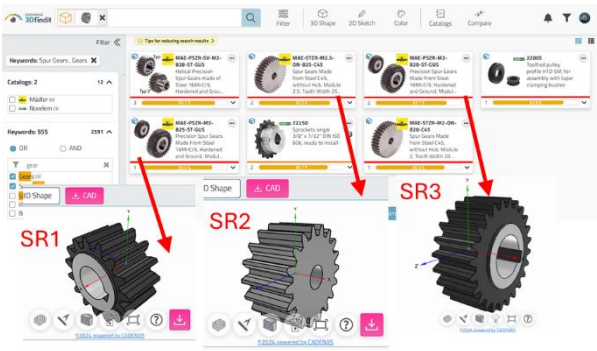


Fig. 6. Search results based on geometric features' similarity

One can evaluate search results based on the similarity percentage. Similarity percentage is calculated based on different factors (size and shape of geometrical features). For particular results displayed, the similarity percentage is greater than 80, which suggests a good match between the reference CAD model (uploaded by the user) and search results. However, this parameter can be misleading because the reference model and search result (SR) model, shown in Fig. 5. can have one or two exact features, and the software will return a large similarity percentage, but physical parts can be diametrically different. For example, in Fig. 7. search results are displayed without additional filters. The search engine algorithm found parts with a similarity percentage larger than 90 percent, but in practical terms, founded parts have no common use in gear maintenance.

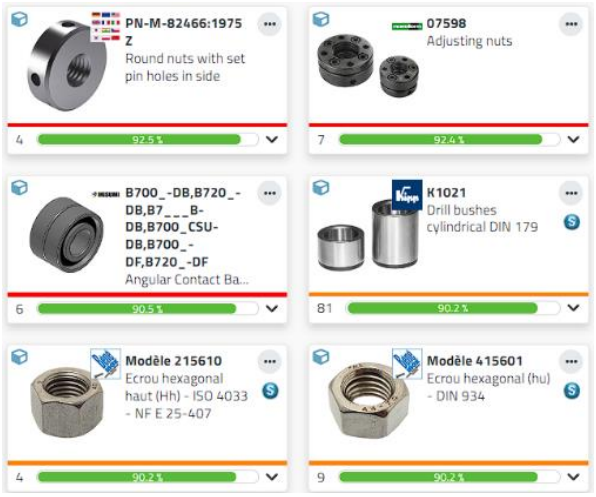


Fig. 7. Mechanical parts that have a high similarity percentage but are considerably different form gears

When the desired search results are found, one can proceed to investigate how much these results reflect the reference CAD part. By choosing one of the options displayed, additional information with an interactive window appears. A closer look is shown in Fig. 8. It is possible to compare search results by directly choosing multiple gears, as depicted in Fig. 9.

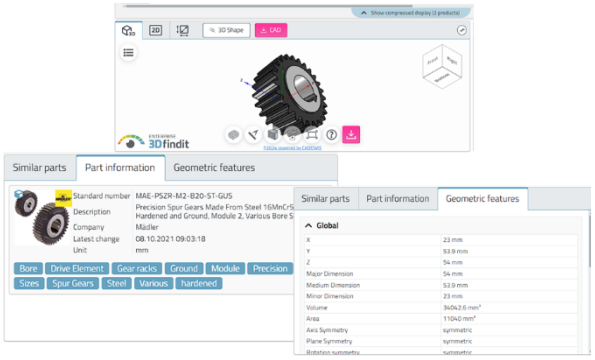


Fig. 8. Search results for the spur gear

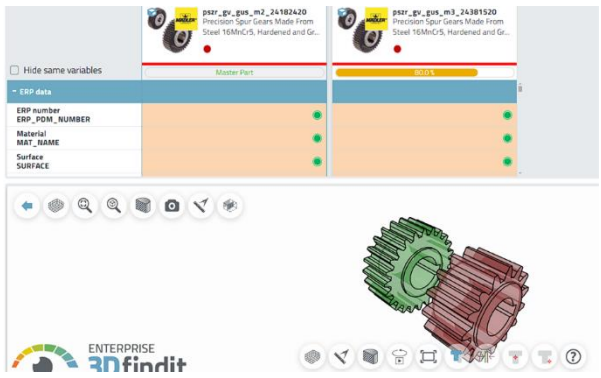


Fig. 9. Compare option for similar parts

From the interactive window, where the CAD model is depicted, the user can rotate, move, create a section,

or check the basic dimensions of the part.

For the subsequent changes in the part model, the download option is available. Information necessary for decision-making and logistics is depicted in Table 1.

Product No. ARTNR	24182520	L ±0.05 L [mm]	23
Modul M	2	B - H6 BH6 [mm]	20
Number of teeth Z	25	Weight GEW [g]	269
Material MAT	Stahl 16MnCr5, Einsatzgehärtet HRC 58± 2 und geschliffen	ND ND [mm]	35
b B [mm]	20	NL NL [mm]	1,5/1,5
da -0.1 DA [mm]	54	d D [mm]	50

Table 1. Information about spur gear

When the appropriate part or assembly is found, the user can choose the option "Request and EPR number". ERP stands for Enterprise Resource Planning, and it's vital for any organization. This option enables the user to directly contact the manufacturer of the specific part, requesting a purchase. In the ERP dialog window, all the information about the part is filled in, and the chance of ordering a part with the wrong specification is minimal.

4. CONCLUSION

In today's ever-increasing competitiveness in production engineering, finding quick and reliable solutions is of the highest priority. CAD models of various parts and assemblies are carriers of important information and can be used in a number of different ways. Inside the CAD model, there is parametric information about parts' geometry, tolerances, surfaces, material, density, and other valuable information needed for successful manufacturing processes. Recently, CAD models of complex geometry shapes such as gears have been used in advanced search methods via web search engines. These web applications utilize provided information about uploaded parts and try to find similar parts or counterparts based on a number of different factors described in this paperwork. After the part is found, the engineer working in the production facility or maintenance can easily request parts through an embedded ERP system. ERP systems are indispensable in modern production because these systems streamline operations, enhance collaboration, ensure data accuracy, and drive productivity, making them essential tools for optimizing manufacturing processes and achieving operational excellence.

Future research should explore the integration of CAD systems with cloud computing technologies. As illustrated in [5], this integration offers significant benefits, including cost-effectiveness, scalability, and enhanced collaboration for maintenance tasks. Cloud computing services provide a robust platform for storing and accessing CAD data, thereby enabling seamless collaboration among engineers engaged in gear maintenance activities.

5. REFERENCES

[1] Shui-hua, H., Zheng-ding, L., & Chuan-bo, C. *Structural indexing for 3D solid digital library.* Wuhan University Journal of Natural Sciences, 6, pp. 438-442, 2001.

[2] Pitikakis, M., Vavalis, M., & Houstis, C. *Semantically interoperable three-dimensional scientific objects.* The Knowledge Engineering Review, 27(1), pp. 33-55, 2012.

[3] Jadeja, Y., & Modi, K. *Cloud computing-concepts, architecture and challenges.* In 2012 international conference on computing, electronics and electrical technologies (ICCEET) pp. 877-880, IEEE, 2012.

[4] Angrish, A., Craver, B., & Starly, B. *"FabSearch": A 3D CAD model-based search engine for sourcing manufacturing services.* Journal of Computing and Information Science in Engineering, 19(4), 041006, 2019.

[5] Wang, J., Zhang, L., Duan, L., & Gao, R. X. *A new paradigm of cloud-based predictive maintenance for intelligent manufacturing.* Journal of Intelligent Manufacturing, 28, 1125-1137, 2017.

ACKNOWLEDGMENTS

The authors thank Enterprise 3D Find It for their invaluable support through their service. Their comprehensive resources significantly enhanced the depth and quality of this scientific work.
https://www.3dfindit.com/en/

Authors:

MSc Goran Strbac, PhD Branko Strbac, PhD Mijodrag Milosevic, MSc Milos Ranisavljev, PhD Miodrag Hadžistević, University of Novi Sad, Faculty of Technical Sciences, Trg Dositeja Obradovica 6, 21000 Novi Sad, Serbia, Phone.: +381 21 485-24-76.
E-mail: goranm.strbac@gmail.com; strbacb@uns.ac.rs mido@uns.ac.rs; mranisavljev97@uns.ac.rs, miodrags@uns.ac.rs

MMA 2024
FLEXIBLE TECHNOLOGIES

15th INTERNATIONAL SCIENTIFIC CONFERENCE
NOVI SAD, SERBIA, SEPTEMBER 24-26, 2024

Original research paper https://doi.org/10.24867/MMA-2024-04-006

Vukman, J., Milošević, M., Borojević, S., Ungureanu. N., Božić, D., Lukić, D.

OPTIMIZATION OF THE MACHINING PARAMETERS OF ALUMINUM PARTS AS A FUNCTION OF THE PERPENDICULARITY DEVIATION OF THIN-WALLED SURFACES

Abstract: *Thin-walled aluminum structures are mostly used as construction parts in the aerospace, automotive and military industry due to their homogeneity and excellent ratio relationship between load capacity and weight. Manufacturing of these parts occurs by removing a large volume of material, which can amount up to 95% of the initial mass of raw material. The manufacturing process of these structures is time-consuming and very demanding. During the fact that is necessary to remove large volume of material to achieve high manufacturability while satisfying the accuracy and surface quality. On the other hand, achieving high manufacturability limits the lack of rigidity of thin-walled parts, which leads to the occurrence of errors in the machining process. Within this paper, the accuracy of machining process from the aspect of achieving the perpendicularity of thin-walled line structures is discussed. Based on realized Taguchi L27 experimental plan, it is performed ANOVA analysis, regression analysis and finally optimization of the parameters of high-speed machining process of thin-walled linear parts of aluminum alloy from the aspect of perpendicularity machining surface.*
Key words: *Taguchi, ANOVA, thin wall, AL*

1. INTRODUCTION

Parallel with the increasing market demands for machining thin-walled structures (parts) made of different alloys, research is being conducted aimed at optimizing the design to reduce weight, deformations, vibrations, and increase load capacity and strength, as well as optimizing the technological processes of manufacturing these components to reduce processing time and costs while simultaneously increasing processing quality [1]. Due to its homogeneity, corrosion resistance, and excellent strength-to-weight ratio, thin-walled aluminum components are increasingly used as structural parts in the aerospace, automotive, military industry, etc. [2].

Manufacturing of thin-walled structures is mainly performed by removing material from solid blanks, up to 95% of their mass. Due to such a large volume of material removal, it is necessary to achieve high productivity while ensuring the required accuracy and quality [3]. The process of manufacturing these parts is very complex [4].

The main subject and objective of the research in this paper is the optimization of parameters for high-speed machining of linear thin-walled structures made of aluminum alloy in terms of perpendicularity of the thin-walled surfaces as a goal function.

2. RESERARCH METODOLOGY

2.1 Working methodology description

By increasing market demands for machining thin-walled structures, research is being conducted to optimize the design and manufacturing processes of these components. The design optimization aims to reduce weight, deformations, vibrations, and increase load capacity and strength, while the optimization of technological processes aims to reduce machine time and costs, increase accuracy and surface quality etc. [5]. To analyze the impact of parameters of thin-walled parts on perpendicularity of machining surfaces, it was necessary to set up and conduct experimental research, and then analyze the results and define certain conclusions.

Taguchi's method of experimental design is a unique and powerful technique for experimental analysis and optimization of products, processes, etc. In order to eliminate the drawbacks of classical experimental design, which are reflected in a too complex and time-consuming execution of a large number of experiments, an alternative has been found in *Taguchi's* method based on the application of special, partial factorial designs obtained from orthogonal designs that cover the entire experimental space [6]. *Taguchi* proposed an aggregate statistical measure that combines information about means and variances into a single measure of performance, known as the signal-to-noise ratio (*Signal-to-Noise* (*S/N*) *ratio*). For a detailed examination of the importance of the main factors and their interactions on the response, analysis of variance (*ANOVA*) can be used. There are three categories of S/N relationships, the *smaller the better*, *the larger the better*, and *nominally the best* [7]. The procedure for planning experiments is based on a statistical approach and involves several activities: (a) identifying and formulating the problem, (b) selecting output variables, (c) selecting input variables, (d) choosing an experimental design, (e) conducting the experiments, (f) statistical processing and analysis of experimental data, (h) conclusions and recommendations.

3. EXPERIMENTAL RESEARCH

The main optimization task is to define the influence

of input parameters: wall thickness (*a*), number of revolutions (*n*), feed ratio (*f*), depth of cut (*δ*) and tool path strategies (*TPS*), on the perpendicularity of machining surface (Δd), Fig. 1. The material of thin-walled parts is aluminum *alloy Al7075* (*AlZnMgCu1.5*). For the machining process, a tool manufactured by YG, No. *E5909080* was chosen [8]. The diameter of end mill is 8 mm and consist of two cutting edges. The machine is a high-speed five-axis CNC machining center for milling - *DIGMA HSC 850*.

Assuming that the mathematical relations between input parameters and process performance are complex and nonlinear, three levels of variation were selected for each of the five input parameters: wall thickness (*a*), number of revolution (*n*), feed (*f*), depth of cut (*δ*), and *TPS*, Table 1. Based on selected variable process factors and corresponding levels of variation, an experimental matrix plan was created in accordance with the standard Taguchi orthogonal sequence L27, performed ANOVA analysis, regression analysis and finally optimization of parameters of the high-speed machining process for thin-walled linear parts made of aluminum alloy.

Measurement result for surface perpendicularity Δ*d* was performed by coordinate measurement machine Mitutoyo Strato – APEX 9166. For each parameter, multiple measurements were performed, and then their average values were calculated as the final output parameters. Perpendicularity deviation (Δ*d*), Table 2. It is measured for the left and right side of the wall, so that we have:

- Δd_{LV} – perpendicularity deviation of left vertical wall side,
- Δd_{DV} – perpendicularity deviation of right vertical wall side.

4. OPTIMIZATION OF MACHINING PARAMETERS IN THE FUNCTION OF SURFACE PERPENIDCULARITY

In this analysis, the following factors wall thickness (A), number of revolution (B), feed ratio (C), depth of cut (D) and tool path strategy (E) are observed on surface perpendicularity - Δ*d*. Since the goal for surface perpendicularity is **s**maller is better was chosen. The S/N values for each factor are shown in Table 3. The mean S/N response for each influential factor is shown in Table 4. Fig. 2 shows the *S/N* response for the surface perpendicularity by influence factors, while Figure 3, shows the response of the medium arithmetic surface perpendicularity of influence factors.

Level	A	B	C	D	E
1	18.147	14.324	16.315	16.083	16.580
2	18.127	15.896	13.652	13.525	14.002
3	9.236	15.289	15.543	15.902	14.928
Difference	8.911	1.572	2.663	2.557	2.578
Rank	1	5	2	4	3

Table 3. S /N response for surface perpendicularity for function smaller is better

Level	A	B	C	D	E
1	0.1391	0.2263	0.1733	0.1837	0.1723
2	0.1261	0.1921	0.2478	0.2519	0.2431
3	0.3538	0.2006	0.1979	0.1834	0.2036
Difference	0.2277	0.0342	0.0745	2.557	0.0707
Rank	1	5	2	4	3

Table 4. Response of surface perpendicularity by influencing factors

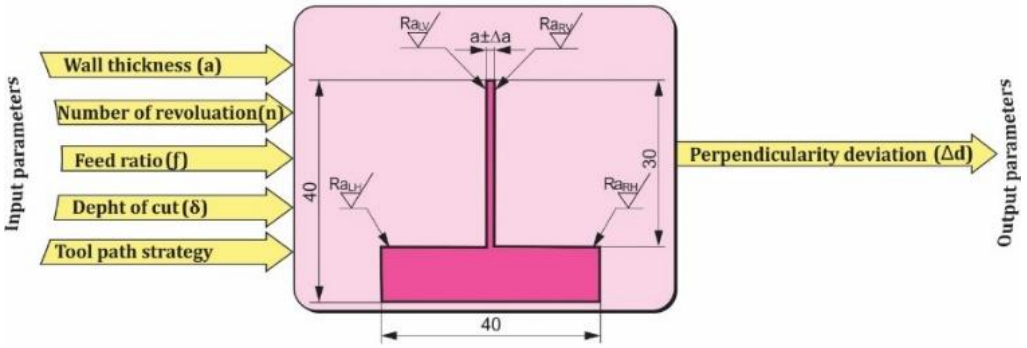


Fig. 1 Model of experimental research [1]

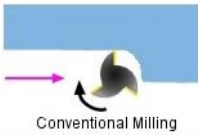
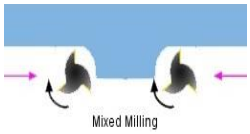
Parameter and label	Units	Level		
Wall thickness (a)	mm	0.5	1.0	1.5
Number of revolutions (n)	o/min	6000	12000	24000
Feed ratio (f)	mm/min	600	1200	2400
Depth of cut (δ)	mm	1	2	3
Tool Path Strategy (TPS) - Cimatron	-	Path 1-climb 	Path 2-convecional 	Path 3 - mixed 

Table 1. Input parameters and levels of variations [1]

Exp. No	A	B	C	D	E	Δd_{DV}	Δd_{LV}	$\Delta dsr=(\Delta d_{DV}+\Delta d_{LV})/2$
1	0.5	6000	600	1	1	0.086	0.082	0.084
2	0.5	6000	1200	2	2	0.388	0.378	0.383
3	0.5	6000	2400	3	3	0.131	0.113	0.122
4	0.5	12000	600	2	3	0.132	0.100	0.116
5	0.5	12000	1200	3	1	0.097	0.088	0.093
6	0.5	12000	2400	1	2	0.096	0.107	0.102
7	0.5	24000	600	3	2	0.160	0.107	0.134
8	0.5	24000	1200	1	3	0.114	0.125	0.120
9	0.5	24000	2400	2	1	0.092	0.108	0.100
10	1.0	6000	600	2	2	0.134	0.116	0.125
11	1.0	6000	1200	3	3	0.177	0.169	0.173
12	1.0	6000	2400	1	1	0.118	0.116	0.117
13	1.0	12000	600	3	1	0.088	0.100	0.094
14	1.0	12000	1200	1	2	0.117	0.101	0.109
15	1.0	12000	2400	2	3	0.168	0.134	0.151
16	1.0	24000	600	1	3	0.106	0.133	0.120
17	1.0	24000	1200	2	1	0.133	0.148	0.141
18	1.0	24000	2400	3	2	0.103	0.109	0.106
19	1.5	6000	600	3	3	0.339	0.126	0.233
20	1.5	6000	1200	1	1	0.567	0.091	0.329
21	1.5	6000	2400	2	2	0.745	0.198	0.472
22	1.5	12000	600	1	2	0.521	0.146	0.334
23	1.5	12000	1200	2	3	0.717	0.201	0.459
24	1.5	12000	2400	3	1	0.523	0.022	0.273
25	1.5	24000	600	2	1	0.573	0.070	0.322
26	1.5	24000	1200	3	2	0.668	0.181	0.425
27	1.5	24000	2400	1	3	0.532	0.148	0.340

Table 2. Analysis of results for perpendicularity deviation (Δd)

Based on the analysis of the results, which are shown in Table 3, as well as based on Fig. 2, it can be concluded that the greatest influence on surface perpendicularity is wall thickness. Also, the speed has the least impact on the deviation of wall thickness.

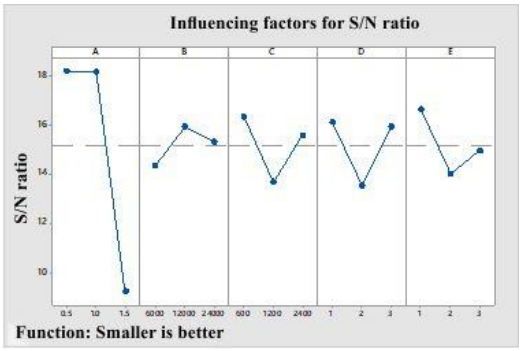


Fig. 2. S /N response for surface perpendicularity

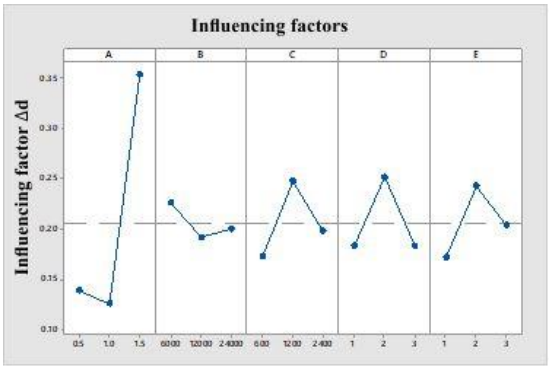


Fig. 3. Response of surface perpendicularity by influencing factors

Based on table 4 and figure 3, we can determine the optimal cutting conditions within the provided levels of factors, based on the goal function "Smaller is better ".

The optimal combination of selected factors is: wall thickness on level 2, number of revolution on level 2, feed rate on level 1, depth of cut on level 3 and tool path strategies on level 1. The results of the *ANOVA* analysis show that of the five inputs, *F-values* of input factors are lower than critical value of *Fcr* (*Fcr* =3.63, for a value of confidence level of 95%) only for factor related to number of revolutions, this implies that this factor is not significant. For all other input factors, we obtained *F-values* greater than the critical value. The results of the analysis of variance for the deviation of surface perpendicularity are shown below. The deviation of the surface perpendicularity, factor wall thickness is influenced by 69.81%, the number of revolutions by 1.36%, the feed rate by 6.15%, the depth of cut by 6.66%, and tool path strategies by 5.36%. The experiment error accounts for 10.66%, or the influence of other factors that were not considered in this experiment.

Through regression analysis, was obtained an equation of dependence of input factors in this experiment on the output function of surface perpendicularity deviation.

$$\Delta d = -0.0317 + 0.2147\,A - 0.000001\,B + 0.000006\,C - 0.0001\,D + 0.0156\,E \quad (1)$$

After defining the optimal input parameters, the predicted optimal responses were obtained using the Taguchi and ANOVA methods. The prediction of the

optimum input parameters to achieve the smallest deviation of surface perpendicularity using the Taguchi method was found at the level: *A1-B2-C1-D3-E1*. In Figure 4, Taguchi's prediction results for optimized input parameters using MiniTab software are shown. After finding the optimal input parameters and obtaining the S/N response, the dependence of the input factors on the deviation of surface perpendicularity Δd was determined using equation 1. Table 5 shows the optimal processing regimes and significant factors.

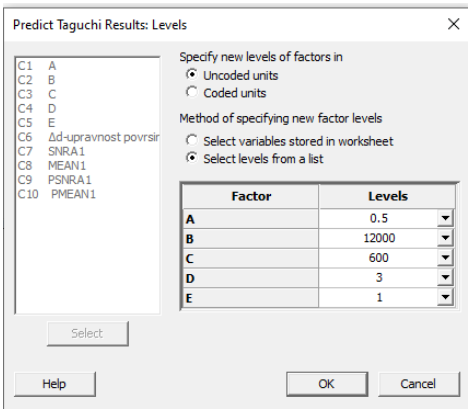


Fig. 4. Taguchi predictive results for optimal input parameters using MiniTab software

Response	Optimal input parameters	Significant parameters	Prediction of optimal response	
			S/N Response	Value
Δd	A1-B2-C1-D3-E1	A-C-D-E	22.1600	0.0825

Table 5. Optimal input parameters and significant parameters

5. CONCLUSION

In the paper, implemented experimental research is presented, which was conducted to optimize the parameters of high-speed machining of linear thin-walled parts made of aluminum alloy. The observed study segment focused on the optimization of these parameters in terms of deviations surface perpendicularity as the objective function.

Based on the obtained results of the experiments, an ANOVA analysis, regression analysis, and finally optimization of the process parameters was performed: wall thickness, number of revolutions, feed ratio, depth of cut, and tool path strategies. As the output result, a function of the dependence of the surface perpendicularity deviation on the input parameters was obtained. Wall thickness have greatest influence on the surface perpendicularity deviation, while the number of revolutions, and has the least influence. Optimum input parameters in order to achieve the smallest surface perpendicularity deviation, a result was obtained at the level: *A1-B2-C1-D3-E1*.

6. REFERENCES

[1] Vukman, J.: Optimization technological process of machining thin-walled aluminum structures (In Serbian), (PhD thesis). Faculty of Technical Sciences, University of Novi Sad, 2022.

[2] Vukman, J., Milosevic, M., Antic, A., Bozic, D., Todic, V., Lukic, D.: Optimization of high-speed machining parameters of thin-walled aluminum structures in the function of surface roughness, 1. International Conference on Accomplishments in Mechanical and Industrial Engineering – DEMI, Banja Luka: Faculty of Mechanical Engineering, University of Banja Luka, 1-2 June, 2023, pp. 104-109, ISBN 978-99976-11-04-8, 2023.

[3] Hirsch, J., Al-Samman, T.: Superior light metals by texture engineering: Optimized aluminum and magnesium alloys for automotive applications, Acta Materialia, Vol. 61, No. 3, pp. 818-843. 2013.

[4] Borojevic, S.; Lukic, D.; Miloševic, M.; Vukman, J.; Kramar, D.: Optimization of Process Parameters for Machining of Al 7075 Thin-Walled Structure, Adv. Prod. Manag., Vol. 13, pp. 125–135. 2018.

[5] Pandian, P., Prabhu, R., Sakthimurugan, K.: Surface error compensation in HSM of thin wall structures, International Journal of Engineering Science Invention, Vol. 2, No. 2, pp. 1-11. 2013.

[6] Taguchi, G., Chowdhury, S., Wu, Y.: Taguchi's Quality Engineering Handbook, John Wiley & Sons, Inc., 2005.

[7] Montgomery, D.C.: Design and Analysis of Experiments, John Wiley & Sons, Inc., 2001.

[8] ALU-pow (140513) (yg-1.pl)

ACKNOWLEDGMENTS

This research has been supported by the Provincial Secretariat for Higher Education and Scientific Research of the AP Vojvodina through the project "Trends of development and application of the Industry 4.0 model in SMEs" (No. 000435212 2024 09418 003 000 000 001) as well as project "Collaborative systems in the digital industrial environment" (No. 142-451-3178/2022-01/01).

Authors:

PhD Jovan Vukman, Robert Bosch, Serbia, Phone: +381 22 313 843
E-mail**:**jovan.vukman@yandex.com

Phd Mijodrag Milosevic, Phd Dejan Lukic, MSc Dejan Božić, University of Novi Sad, Faculty of Technical Sciences, Trg Dositeja Obradovica 6, 21000 Novi Sad, Serbia, Phone.: +381 21 485-2476.
E-mail: mido@uns.ac.rs; bozic997dejan@uns.ac.rs; lukicd@uns.ac.rs

PhD Stevo Borojević, University of Banja Luka, Faculty of Mechanical Engineering, Vojvode Stepe Stepanovica 71, 78000, Banja Luka, Bosnia and Herzegovina, Phone: +387 51/433-066
E-mail: stevoborojevic@hotmail.com

PhD Nicolae Ungureanu, Faculty of Engineering in Baia Mare, Technical University of Cluj Napoca, Dr. Victor BABES 62A, Baia Mare, Maramures 430083, Romania, Phone: 0264-202-975
E-mail: nicolae.ungureanu@imtech.utcluj.ro

MMA 2024
FLEXIBLE TECHNOLOGIES

15th INTERNATIONAL SCIENTIFIC CONFERENCE
NOVI SAD, SERBIA, SEPTEMBER 24-26, 2024

Original research paper https://doi.org/10.24867/MMA-2024-04-007

Ćurčić, S., Milovančević, M., Savković, B.

IMPROVING THE SAFETY OF THE TRANSPORT ZONE USING THE MAKIGAMI METHODOLOGY

Abstract: *Efficient management of logistics processes, resources and risks is becoming imperative for achieving competitive advantage of production systems. One approach that is increasingly recognized as crucial in optimizing logistics processes is the World Class Manufacturing (WCM) methodology. This approach involves continuous improvement and integration of all production processes, with a focus on eliminating losses and increasing efficiency. Losses are not just financial losses, as losses can be different (organizational, security and others). This paper presents practical applications of WCM methodology in solving logistics problems within the production system. The application of wcm methodology should be of particular interest, due to the necessity of improving safety standards. Also, this paper aims to provide insight into the practical application of WCM methodology in solving logistical challenges, emphasizing the importance of continuous improvement and proactive approach in logistics process management.*

Key words: *logistics processes, rational management, world class manufacturing*

1. INTRODUCTION

World Class Manufacturing (WCM) is a comprehensive approach to optimizing production processes, with the main goal of achieving high standards of quality, efficiency and continuous improvement. This methodology stems from the Japanese business model, especially known through the practices of Japanese companies (Toyota), and was later adopted globally for its efficiency. Companies engaged in WCM have a strategy of focusing on improving operations, eliminating losses and developing production that relies on the above, resulting in a high level of production in terms of quality, safety and cost reduction. The WCM system is based on the systematic reduction of all types of costs and losses through the contribution of all employees and with the precise use of methods, standards and tools that production of the world vote requires. The World Class Manufacturing methodology incorporates key principles from Kaizen, Lean and Six Sigma to create a holistic approach to manufacturing process management. WCM methodology is based on the principles of continuous improvement (Kaizen), employee engagement, process visualization (through a tool such as Makigami) and a system approach. Kaizen involves constantly looking for small improvements, while employee engagement is encouraged to allow active participation in identifying and solving problems. Visualizing processes through tools like Makigami helps identify potential losses and unnecessary steps. [1]

A key element of WCM methodology is Kaizen. The Kaizen concept is based on: constantly seeking, implementing and improving small, gradual changes in processes, products or services to achieve efficiency, reduce losses and improve quality. Kaizen does not strive for revolutionary, but evolutionary changes that come from the initiatives and engagements of all members of the organization. This concept encourages proactivity, teamwork, innovation and a versatile commitment to continuous improvement, thus creating an organizational culture that supports continuous improvement in all aspects of work. [2]

Makigami it is a powerful tool for visualizing and analyzing processes in an organization. Inspired by Japan's philosophy of continuous improvement, this tool uses large papers or billboards placed on the wall to create process diagrams. In modern times, visualization is achieved using software. Makigami's goal is to provide transparent insights into the workflow, identify key steps and resources, and make it easier for teams to identify areas of optimization. Teams use this tool to map all stages of work, identify unnecessary steps, and show interactions between different parts of the process. Visual representation allows organizations to more easily understand the complexity of their operations. [2].

2. ANALYSIS OF LOGISTICS PROCESSES THROUGH MAKIGAMI

Makigami is a process visualization and analysis tool that is often used within the World Class Manufacturing (WCM) methodology. The key purpose of Makigami is to enable organizations to clearly see and understand workflows, identify unnecessary steps and optimize processes. The basic steps in applying Makigami are: Process identification, Team formation; Gathering information and visualizing workflows; Identification of losses and unnecessary steps; Analysis of the possibilities of improvement; Understanding anomalies and implementing improvements; and Standardization, training and continuous monitoring. This cycle of continuous monitoring and improvement is the essence of the Makigami methodology. [4]

2.1 Process identification

As part of this paper, we will show how the company TETRAPAK from Gornji Milanovac recognized the

need to improve security in the zone between the production hall and the raw material warehouse. The series of near misses in this area has become a key trigger for the formation of the WCM team, whose main task was to minimize safety risks.

Near miss Indicates a situation where a dangerous situation or incident occurs, but without direct consequences for people or property.

Near miss analysis has the value of learning and contributes to improving safety by identifying weaknesses in processes and applying improvements to reduce the risks of future incidents. In the Fig. 1 display of Near miss from security cameras is shown part of the footage from the security cameras and shows one of the near misses who initiated the launch of the team. From figure 1, you can see the car that the factory visitors strayed into the unloading zone of the truck. While the driver was looking for a way to get to the administration building between the trucks that were in the process of unloading, a forklift flew out. The forklift, although he did not expect anyone in this zone, managed to stop the forklift and thus not injure the passengers in the car. After long-term analysis and monitoring of near misses, the concentration of such situations was observed in the zone between the production hall and the warehouse of raw materials. A depiction of the zone where Near misses occurred is shown in Fig. 2. A series of close encounters with potential hazards in this zone marked the need for a proactive approach in addressing security challenges. Although fortunately none of the near misses resulted in serious injuries, the seriousness of the situation was recognized. The company's risk assessment decided to form a team to fight this security loss.



Fig. 1 View Near miss from security cameras



Fig 2. Display of the zone where Near misses took place

2.2 Formation of the team

Tetrapak's management decided to form a WCM team to systematically eliminate these security risks. The nine-member team consisted not only of logistics engineers, but also representatives of other sectors, including forklifts, electrical engineers, operators and managers. This approach reflects the diversity of perspectives and skills needed to solve problems from multiple angles. In WCM teams, the participation of representatives of different sectors plays a key role. Team diversity ensures a complete picture of the problem, allowing for a better understanding of the complexity of the situation. They have the roles of leader and tutor of the team. Team Leader it plays a key role in leading team activities. His responsibilities include directing discussions, setting goals, as well as motivating and supporting team members. In the case of this team, the team leader is an experienced colleague from the logistics sector. Tutors in the WCM team have the role of experts who help and mentor team members in applying WCM principles. Their role is to transfer knowledge, guide the team through continuous improvement processes, and provide guidance to achieve optimal results.

2.3 Collecting information and visualizing flows

The data collection phase in the Makigami process is an essential step towards creating an in-depth insight into the current workflow. The goal of this phase is to gain a deep understanding of the current state of the process - to identify each step, resource, execution time and interconnections between them. Our intention is to capture all relevant data that will help us visualize the process in a way that allows us to identify potential losses, unnecessary steps and effective points for improvement.

Process visualization is a key component of the Makigami methodology, undergoing significant changes over time, especially with technological advances. Various tools, such as digital boards, specific diagramming software, or even applications such as MS Excel, allow teams to create, edit and share visualizations electronically. However, regardless of technological changes, the essence of visualization remains the same: providing a clear insight into workflows and identifying points for improvement. Digital visualization now allows for greater flexibility and faster collaboration, while the traditional paper-based method has retained its value in direct engagement of teams. At TETRAPAK, the team started the process of optimizing part of the factory circuit by analyzing the existing zone, where the existing parking spaces for unloading trucks, waste vehicles, delivery vehicles and repairers' vehicles were drawn. In the Fig. 3 shown a depiction of the zone with the routes of movement of vehicles and unloading places is given a depiction of the zone and the places where the vehicles are positioned are drawn. In the zone around the vehicle, forklifts are constantly moving. Table 1 shown the description of parking positions shows the layout and purpose of parking positions.

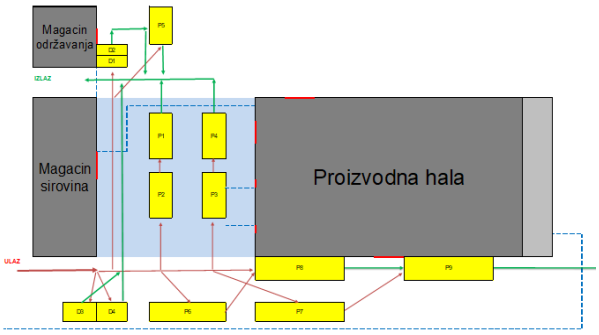


Fig 3. Display of zones with vehicle routes and unloading points

Parking pos.	The purpose of the position
P1	Unloading position for trucks
P2	Unloading position for trucks
P4	Unloading position for trucks
P4	Unloading position for trucks
P5	Waste loading position
P6	Parking position for waiting for unloading
P7	Parking position for waiting for unloading
P8	Unloading position for tanks
P9	Unloading position for tanks
D1	Position for couriers and mail
D2	Position for couriers and mail
D3	Position for repairers and contractors
D4	Position for repairers and contractors

Table 1. Description of parking positions

After the team has sketched the zone for each of the parking positions, a Makigami process map is made. The Makigami process map is a visual way to analyze and map processes within an organization. The visual representation of a map uses symbols and colors to clearly show the complexity of the process, and detailed analysis includes aspects such as execution time, resources and interdependencies. In Fig. 4, the Makigami process map is shown an estimate of the maps for one of the parking positions. On the left side of the process map are the so-called Stakeholders. They represent the owners of certain stages within the framework of an activity. From the example given in Figure 5. The Makigami process map is seen to be Stakeholders: Planning, Logistic Planner, Autoprevoznik and others in a vertical column and are rounded by a red line. The blue line in Fig. 5 indicates the phases, that is, the actions carried out by the Stakeholders. In this way, you can see the general sequence of each common process.

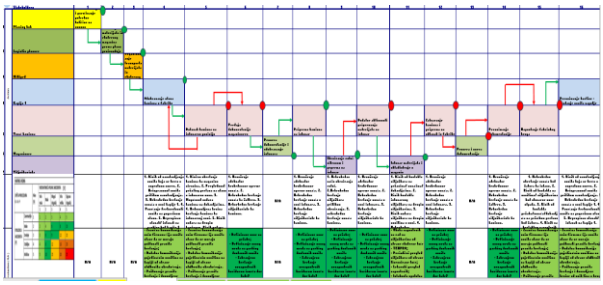


Fig. 4. Makigami process map

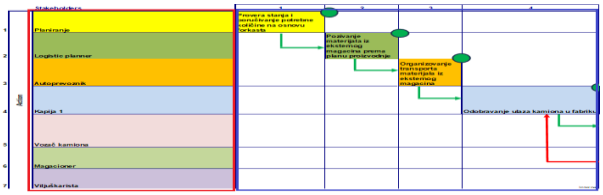


Fig. 5. Makigami process map

The green arrow from a particular action implies that the information for the next action is complete and reached the next Stakeholder in time. A representative example may be the first action: "Checking the balance and ordering the required quantity based on forecast". This information goes from Planning to Logistic Planner and cannot be incomplete. The information is complete and on time.

The red arrow from a particular action implies that the information for the next action is incomplete or did not reach the next Stakeholder in time. A representative example of this is the action when Gate 1. approves the entry of the Autocarrier, but does not give it enough precise information that the Auto prevoznik could reach the unloading place without error and thus does not jeopardize the safety of other participants. Red arrows can go forward and backward. When the arrow is pointed backwards, it means that the Stakeholder must return to a certain step to supplement the incomplete information. Obviously, in actions where we have red arrows, irregular conditions can occur, and therefore security risks. With this approach, it can be noted which parts of the process are not defined and where situations that are not foreseen in advance may occur. Such situations bring instability into the system, which in our case is a security system.

The next thing you can see on stocks are the green and red circles in the corner of the action. We can divide them into two groups:

- VA (Value Added) – Activities that add value (security is the size to which the value is added in this Maximami analysis). Value-added activities are all activities whose performance contributes to security. An example of this would be the action "Approval of the entry of trucks into the factory" announced by Stakeholder Gate 1. During this action, Gate 1. will contribute to safety by giving the driver detailed instructions on movement within the factory circle, on the parking position and all other parameters that will make his stay in the factory safer. So Gate 1 contributes to security.
- NVA (Non Value Added) - Activities that do not add value. Activities that do not add value are all activities whose execution does not contribute to safety or reduces security. An example that can be given for NVA activity is getting drivers out of trucks and going to logistics to hand over documentation. At first glance, activity looks like an activity that is safe, but if we analyze the broader picture of the action, we come to the conclusion that the activity can be very risky. One of the risks is internal transport vehicles (forklifts) that move through the circuit very quickly and from the cargo carried by forklifts do not have full visibility. A driver who goes to the office can put these vehicles in an unsafe situation. In addition to these risks to the driver, there are risks of other trucks in the factory circuit as well as numerous

other potential hazards in the zone of the warehouse itself. Within the Maxigami methodology, the team strives to eliminate all NVA actions because they have no contribution. As far as the case is concerned, this action can be eliminated. A truck driver does not necessarily have to go to the logistics office to submit documentation. Instead of that action, the logistics operator, who knows all the risks of the factory circuit, can reach out to the driver and take documentation. In this case, the hazard is reduced to a lower level because the logistics operator knows the dangers and is trained in how to move safest, but the risk still exists. The next step would be to send the freight forwarding documentation by e-mail to logistics and to have this NVA procedure completely expelled. In this case, the driver would not have the need to leave the cab of the truck and thus expose himself to danger. Then we would eliminate such a risk completely, which is one of the goals of the team. If we take into account the number of trucks that are unloaded or loaded in this factory per day, which is about 40 per day, we will come to the conclusion that this risk is not negligible. Such an action, no matter how small it may seem, would be of great importance to security.

For each of the actions performed by Stakeholders at the bottom of the table, a risk assessment was made. Risk assessment is the systematic process of identifying, analyzing and evaluating potential adverse events that may affect the achievement of an organization's objectives. This methodology enables the identification and understanding of potential threats in order to take appropriate preventive or corrective measures. It includes identifying potential hazards, assessing the likelihood and severity of damage, and making informed decisions regarding risk management. Risk assessment is a key component of effective business process management and ensures the achievement of organizational goals while minimizing unintended consequences. This process often involves periodic updates to respond to dynamic changes in the business environment. Fig. 6 shows the fields from the Maxigami table in which the risk assessment is entered some fields from the table are shown where the risks that the team has observed for certain actions are listed. Due to the confidentiality of this type of data, only some fields from the table are displayed.

1. Risk of stopping the vehicle. 2. Malfunction of the vehicle when stopping. 3. Unsafe driver movement in the gate area. 4. Increasing the frequency of vehicles at the wrong entrance. 5. Irregular entry/exit to the parking lot.	1. Risky turning of the truck towards the warehouse of raw materials. 2. Visibility of the pedestrian crossing at the entrance to the unloading zone. 3. Possibility of truck collision with suppliers. 4. Illegal acceleration speed of the truck at the unloading zone. 5. Risk of truck collision with another vehicle. 6. Risk of truck collision with pedestrians.	1. Not wearing adequate safety equipment. 2. Unsafe movement of the driver towards the counter. 3. Unsafe movement of the forklift towards the truck.

Fig. 6. Fields from the Maxigami table in which the risk assessment is entered

2.4 Risk Matrix

After all the risks have been listed, the team performs a risk assessment for each of the potential risks so that they can see where the concentration of risk is greatest. In order to quantitatively assess a risk, the so-called Risk Matrix is used. One such matrix is shown in Fig. 7. the risk matrix is shown. With the help of this matrix, any risk can be expressed quantitatively. The matrix was filled out by each member of the team separately so that the final assessment was objective. If all, or most, of the team members, assess an activity as risky (marked yellow, orange or red), then this is a sufficient indicator that addressing that risk must be addressed.

MATRICA RIZIKA							
OPŠTA PROCEDURA R = V · P		Nivo (V)	VEROVATNOĆA POJAVE AKCIDENTA (V)				
			Vrlo mala	Mala	Moguć događaj	Vrlo velika	Siguran događaj
			1	2	3	4	5
POSLEDICA AKCIDENTA (P)	Zanemarljiv	1	1	2	3	4	5
	Malo	2	2	4	6	8	10
	Srednje	3	3	6	9	12	15
	Ozbiljno	4	4	8	12	16	20
	Kritično	5	5	10	15	20	25

Fig. 7. Risk Matrix

2.5 Identification of losses and unnecessary steps

During the process of visualizing workflows, the team carefully analyzed each step, identifying potential challenges and losses in the process. Identification of losses and unnecessary steps is a key stage that allows the team to develop strategies to improve safety and efficiency in the process analyzed. By optimizing or eliminating a particular step in the process, we achieve significant benefits. By eliminating unnecessary steps, we rationalize resource management, thus achieving financial efficiency. We also reduce the risk because redundant steps often create additional points that can cause irregularities or errors. One such mistake could be a security breach. Focusing on key activities contributes to reducing potential problems and increasing process security.

2.6 Analysis of opportunities for improvement

This stage in the Makigami methodology involves a thorough analysis of the collected data, consideration of potential risks and discussion within the team in order to draw informed conclusions. During the analysis, the focus is on quantifying the impact of losses on process efficiency and safety. Identified problems and risks are studied in detail to determine their real meaning for the organization. The key to this stage is the collection of all proposals and the late filtering of them. After analysis and discussion, the team is ready for the next step in the Makigami methodology - the implementation of improvements.

2.7 Understanding anomalies and implementing improvements

This step requires the development of a detailed action plan, which precisely defines the tasks, responsible persons, deadlines and resources necessary to implement the changes. Implementing improvements is a key stage that requires careful guidance in order to achieve the desired results and ensure long-term success.

Below are some of the changes identified by this team as potential solutions for the biggest risks in this zone, which are:

- The team's first and main action is to relieve and redistribute parking spaces for trucks that are unloading. By eliminating one parking space, the zone would be relieved and visibility would become better. Mesh fences provide a physical separation of forklifts that move in different directions, and in addition, visibility is retained. In Figure 8. The simplified appearance of the zone before the implementation of the actions is shown the appearance of the zone before the promotion actions. After the actions carried out, this zone got the appearance shown in Fig. 9. The green arrows show the forklift movement trajectories.

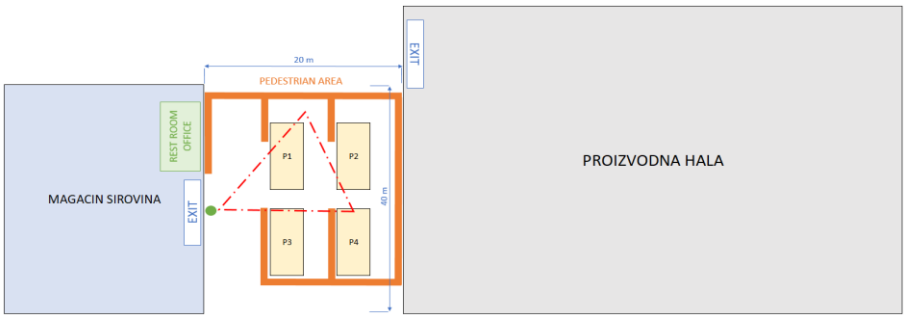


Fig. 8. Simplified appearance of the zone before carrying out actions

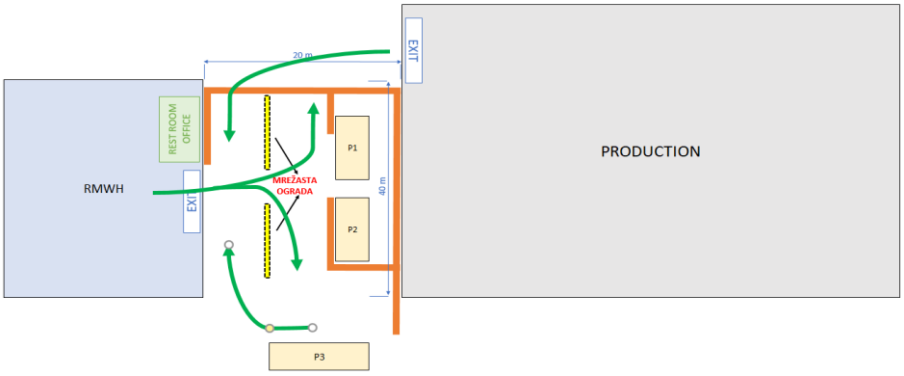


Fig. 9. Simplified appearance of the zone after the implementation of actions

- After these changes, the marking of parking spaces in this zone has been improved. The marking involves adding vertical and horizontal signaling so that there can be no misunderstanding between the logistics operator and the truck driver. Truck drivers will not receive a card marked with a parking space marking where they will be unloaded. This avoids misunderstanding between the driver and the security guard at the gate about the unloading site. This eliminates the incomplete information factor and the driver with complete information goes to the unloading point.

- The process team analyzed the frequency of entry of vehicles to the gates determined that not all gates were equally loaded. The team did a detailed analysis of the frequency of the vehicle in certain zones of the factory circuit and determined which suppliers could be diverted to other gates. The action includes notifying suppliers, their "hosts" and gatekeepers about new actions.

- In order to ensure that the truck driver cannot enter one-way streets at the beginning of one-way sections, one-way ramps have been added. With this type of ramps, it will not be possible for a truck to enter the one-way section, because the ramp will only be raised if the truck comes from the right side of the ramp. This type of action completely eliminates the potential danger of a vehicle moving in the opposite direction, because it is physically prevented from the vehicle being able to do so.

- Spherical mirrors are added in places where visibility is limited to improve safety in the analyzed area. These improvements bring several key advantages: Visibility increases in vast places, thereby reducing the risk of collisions or accidents. Mirrors allow for better real-time tracking of vehicles or other objects, giving drivers extra time to respond to potential hazards. Reducing "blind spots" contributes to reducing the risk of accidents, especially in areas where vehicles often move backwards or where there is interference with different types of traffic.

Given the challenges of vastness in certain places, a decision was made to remove certain plants and trees that restricted visibility. Instead, these plants are transplanted to other areas where they do not represent an obstacle to visibility. This intervention aims to improve overall insight and reduce the potential risks of accidents. In addition, preserved plants continue to contribute to the aesthetics of the environment in the new places where they are planted, thus achieving a balance between safety and preservation of the natural environment.

- In order to improve security, a decision was made to move parking spaces for guests to locations that provide a higher level of security. Establishing parking spaces in safer places contributes to reducing the risk of potential accidents or safety incidents, providing guests with a safer parking environment. Changing the position of

parking spaces also contributes to improving visibility in given places, which is crucial for reducing potential points of reduced visibility and increasing overall safety. - "As part of the initiatives to improve safety, a large billboard was installed in the open space at the entrance to the factory circle. In the Fig. 10 dat the appearance of the billboard for the promotion of safety is shown the appearance of the billboard that promotes respect for security standards.



Fig. 10. The appearance of the billboard for the promotion of security

2.8 Standardization, training and continuous monitoring

This phase is crucial because it ensures the long-term sustainability and success of the implemented improvements. Standardization involves setting clear and measurable standards arising from new procedures. These standards serve as guidelines for employees and ensure the consistent application of new approaches. At the same time, trainings are conducted to ensure that the team and employees fully understand and effectively implement new processes. This is key to preserving the quality of work and eliminating any resistance to change. Through continuous monitoring, the team analyzes the results of implemented changes and monitors key performance indicators. A focus on standardization, training and continuous monitoring ensures that the organization maintains high standards in performance and safety over time, making this methodology crucial for achieving and maintaining excellence in business.

3. CONCLUSION

By applying the Makigami methodology in the fitma TETRAPAK and from Gornji Milanovac, not only potential hazards were identified, but also implemented changes that directly contributed to increasing safety in the workplace. This methodology, which relies on the principles of continuous improvement, has enabled the team to systematically solve problems and optimize processes. Standardization, training and continuous monitoring, as key stages after the implementation of changes, are the basis for maintaining the achieved results. The commitment to long-term success is reflected in continuous monitoring and adjustment, which indicates the company's maturity in using the Makigami methodology. Maturity in the use of some of the methodologies indicates the maturity of the organization and how to solve problems. Through all phases, TETRAPAK demonstrated its commitment to continuous improvement and safety, setting high standards and building a culture of responsibility. The application of the Makigami methodology not only solved specific logistical challenges, but also laid the foundation for lasting change and agility of the organization in dealing with future challenges. Despite their modest appearance, the measures taken have a significant impact on improving safety. Each of these measures stems from thorough analyses spanning different expert domains and perspectives. The very core of WCM is not radical change, but a methodology based on long-term but small improvements. The decisive actions, resulting from an accurate risk assessment, have managed to effectively mitigate the greatest security threats. With this approach, although seemingly small, we are achieving significant steps towards a safer working environment.

4. REFERENCES

[1] World Class Manufacturing model in production management - K. Pałucha, Management and Administration Institute, Organization and Management Faculty, Silesian University of Technology, Poland
[2] The Toyota Way - J.K. Liker, 14 management principles from the world's greatest manufacturer, Mc Graw-Hill 2004.
[3] Gemba Kaizen A commonsense, low-cost approach to management, The Mc Graw Hill Companies - M. Imai, 1997.
[4] https://jipmglobal.com/service/learning - The official website of the Jimp Institute in Japan, which developed the WCM methodology – Dec 2023.

ACKNOWLEDGMENTS

This study was supported by the Ministry of Science, Technological Development and Innovation of the Republic of Serbia, and these results are parts of the Grant No. 451-03-66 / 2024-03 / 200132 with University of Kragujevac - Faculty of Technical Sciences Čačak. Grant No. 451-03-65/2024-03/ 200122, Faculty of Science, University of Kragujevac.

Authors:
PhD Srećko Ćurčić, University of Kragujevac, Faculty of Technical Sciences, Svetog Save 65 32000 Čačak, Serbia, Phone: +381 32 302737.
E-mail: srecko.curcic@ftn.kg.ac.rs
PhD Miloš Milovančević, University of Niš, Faculty of Mechanical Engineering, Aleksandra Medvedeva 14, Niš, Serbia, Phone: +381 64 1138300.
E-mail: milos.milovancevic@gmail.com
Bogdan Savković, TETRAPAK, Takovska 2, Gornji Milanocvac, Phone: +381 60 3659060.
Email: bogdansavkovic1@gmail.com

MMA 2024
FLEXIBLE TECHNOLOGIES

Section E:
MATERIALS, METAL FORMING, CASTING AND WELDING

MMA 2024
FLEXIBLE TECHNOLOGIES

15th INTERNATIONAL SCIENTIFIC CONFERENCE
NOVI SAD, SERBIA, SEPTEMBER 24-26, 2024

Review paper https://doi.org/10.24867/MMA-2024-05-001

Lukšić, H., Rede, V.

EFFECT OF LASER WELDING PARAMETERS ON THE WELDED JOINT IN BATTERY SYSTEMS OF ELECTRIC VEHICLES: A REVIEW

Abstract: *Electric vehicle battery systems consist of hundreds of individuals, interconnected lithium-ion battery cells. Battery cells are connected in parallel and/or series connection, thus forming battery modules, and by connecting several modules, a battery pack is obtained. The parts of the battery system that are joined are very thin and often made of dissimilar materials, which makes the joining process difficult. There are several methods for joining parts of battery systems, but one of the most effective methods is laser welding. This paper presents a review of published manuscripts on the topic of effect of laser welding parameters on the welded joint of aluminum and steel in the battery systems of electric vehicles. Fundamental metallurgical difficulties in laser welding of aluminum and steel were discussed, and the latest findings in the optimization of process parameters of laser welding were especially mentioned.*

Key words: *laser welding parameters, battery system of electric vehicle, microstructure, properties*

1. INTRODUCTION

More frequent extreme weather conditions are the result of climate change and intense global warming. The primary cause of this problem is the emission of harmful greenhouse gases, and the transport sector contributes significantly to these emissions. In order to mitigate the effects of climate change, and as an alternative to conventional internal combustion vehicles, hybrid electric vehicles and electric vehicles have been increasingly developed in recent decades [1,2]. An integral part of a hybrid electric vehicle and an electric vehicle is the battery system, and the most used batteries in electric vehicles are lithium-ion batteries due to their numerous advantages. These include a long-life cycle, high energy density, and low self-discharge rate [3,4]. A conventional electric vehicle battery system consists of several hundred individual lithium-ion batteries interconnected in series and/or parallel connections to ensure a sufficient supply of electricity. The configuration of the battery pack of electric vehicles is usually a battery-module-cell structure. Battery cells are connected in a battery module, and by connecting several battery modules, a battery pack is obtained. According to the geometry, the types of battery cells used in automotive battery applications are divided into cylindrical cells, prismatic cells, and pouch cells [5]. Fig. 1 shows two battery packs composed of a) prismatic and b) cylindrical cells [6].

The most used type of battery cells are 18650 lithium-ion cylindrical battery cells, which are preferred due to the built-in safety features [7]. The casing of the battery cell is most often made of steel, nickel-plated steel, and aluminum [6]. Cell tabs are typically made of aluminum, copper, or nickel and are connected in parallel or series configurations using steel, aluminum, or copper busbars [8]. Due to all the above, when joining components of battery systems, dissimilar materials are often joined.

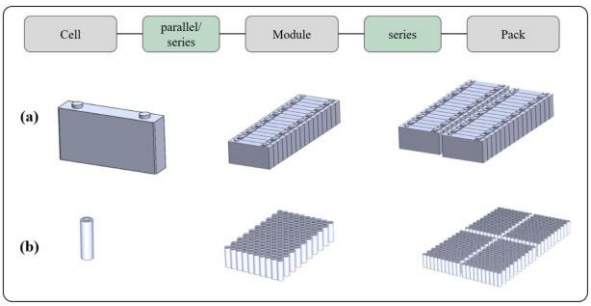


Fig. 1. Battery packs composed of a) prismatic and b) cylindrical cells

Several techniques can be used to join the components of battery systems, including laser welding, ultrasonic welding, resistance spot welding, wire bonding, mechanical assembly, soldering, and brazing. The applicability of each method depends on the geometry and material of the component being joined [6]. Of the mentioned methods, laser welding is considered one of the most effective methods of connecting parts of battery systems. With laser welding, it is possible to join dissimilar materials with a narrow heat affected zone and with high welding speed and high precision [9].

Welding dissimilar materials represents a significant technical challenge due to possible differences in their physical, chemical, and thermal properties. Such differences can result in the formation of brittle and hard intermetallic compounds, as well as the appearance of pores and cracks. Furthermore, the welding of components in battery systems presents a significant challenge, given the small thickness of the material (typically between 0.3 mm and 1 mm) [10]. In the production of battery systems for electric vehicles, aluminum and steel parts are often joined.

This paper provides a review of published manuscripts on the effect of laser welding parameters on the welded joint of aluminum and steel in battery systems of electric vehicles. Basic metallurgical issues

and challenges associated with this process are discussed, as well as the latest developments in welding technique optimization.

2. METALLURGICAL CHALLENGES IN LASER WELDING OF ALUMINUM AND STEEL

Welding of aluminum and steel is quite common when joining components of electric vehicle battery systems. However, welding Al-alloys and Fe-alloys is very challenging due to the great difference in their thermophysical properties. The melting temperatures of aluminum and iron are significantly different, and there is a big difference between their thermal conductivities, as well as thermal expansion coefficients, Table 1 [11,12].

	Melting point, °C	Boiling point, °C	Thermal conductivity, W/m K	Thermal expansion coefficient, 10^{-6}/K
Al	660	2467	247.0	22.8
Fe	1538	2750	80.4	11.7

Table 1. Thermophysical properties of aluminum and iron [12,13]

Furthermore, the mutual solubility of aluminum and iron is very low (almost zero). Due to all of the above, laser welding of aluminum and steel is very demanding, and it is difficult to achieve a quality metallurgical joint [14]. Moreover, because of the metallurgical incompatibility of Al and Fe during welding, hard and brittle intermetallic compounds are intensively formed. Fig. 2 shows the Fe-Al binary diagram [10].

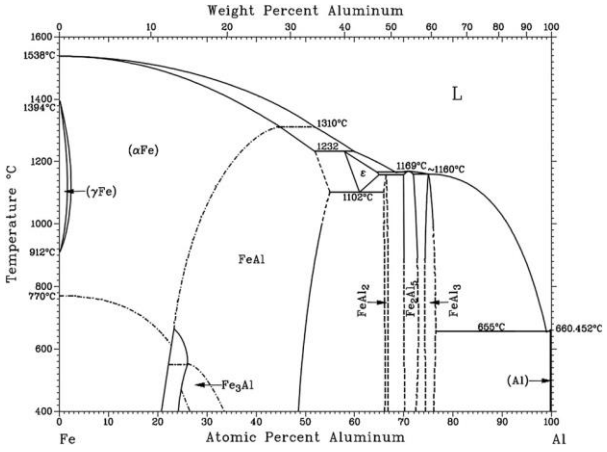


Fig. 2. Fe-Al phase diagram [10]

The formed intermetallic compounds based on iron and aluminum have different chemical compositions, crystal structures, hardness (Table 2), and different Gibbs free energy values (Table 3) [1]. Intermetallic compounds FeAl and Fe_3Al are rich in iron, while Fe_2Al_5, Fe_4Al_{13}, and $FeAl_2$ are rich in aluminum [14]. Additionally, aluminum-rich intermetallic phases have higher hardness than iron-rich intermetallic phases. The formation and growth of Fe-Al intermetallic compounds primarily depends on the Gibbs free energy. For example, Fe_2Al_5 has a low Gibbs free energy and is thermodynamically more stable, so it forms first followed by Fe_4Al_{13}, $FeAl_2$, FeAl, and $FeAl_3$ [14]. In addition to the mentioned differences, different intermetallic compounds also have different coefficient of thermal expansion, which during cooling of the weld can lead to the initiation and propagation of cracks in the weld metal [1,15].

Phases	Al, at. %	Hardness, HV	Crystal structure
Fe_2Al_5	70.0 – 73.0	1000 – 1100	orthorhombic
Fe_4Al_{13} $FeAl_3$	74.5 – 76.6	820 – 980	BC monoclinic
$FeAl_2$	66.0 – 66.9	1000 – 1050	triclinic
FeAl	23.0 – 55.0	400 – 520	simple cubic (B2 type)
Fe_3Al	23.0 – 34.0	250 – 350	BCC

Table 2. Properties of the different FexAly intermetallic compounds [1]

Phases	ΔG, KJ mol^{-1}
Fe_2Al_5	−19.64
Fe_4Al_{13} $FeAl_3$	−22.87
$FeAl_2$	−17.00
FeAl	−11.09
Fe_3Al	−4.83

Table 3. Gibbs free energy of the different Fe_xAl_y intermetallic compounds [1]

3. EFFECT OF LASER WELDING PARAMETERS ON THE FORMATION OF INTERMETALLIC COMPOUNDS

The morphology of Fe-Al intermetallic compounds that are formed during laser welding of steel and aluminum has a significant influence on the mechanical and electrical properties of the resulting welded joint. Therefore, the formation and growth of intermetallic phases in the weld metal should be controlled as much as possible during the welding process. In the majority of cases, the improvement in the electrical and mechanical properties of the welded joint is achieved through the variation of key laser welding parameters, including power, beam diameter, welding speed and laser beam focus. Torkamany et al. [15] investigated the influence of laser welding parameters on the welded joint of Al-alloy 5754 (2 mm thick) and low carbon steel (0.8 mm thick) using a pulsed Nd:YAG laser. The objective of this study was to analyze the impact of three key process parameters - peak power (PP), pulse duration (D) and overlap factor (Of). The researchers concluded that increasing the laser power resulted in a negative impact, leading to the formation of more spatter and intermetallic compounds. As a consequence of the formation of these intermetallic phases, the propagation of cracks in the weld metal, at the fusion line and the heat-affected zone in the direction of the Al-base metal, was observed, Fig. 3. A similar trend, as in the increase in power, resulted in an increase in the duration of the pulse. However, reducing the pulse duration below the critical level, as well as high welding speeds resulted in insufficient fusion and reduced strength of the welded

joint. Finally, it was concluded that with a peak power of 1430 W, a pulse duration of 5 ms and a welding speed of 4 mm/s, it is possible to achieve welded joints without obvious macroscopic defects, with very good surface quality, and with a low proportion of formed intermetallic compounds, which favorably affects the strength of the welded joint [15].

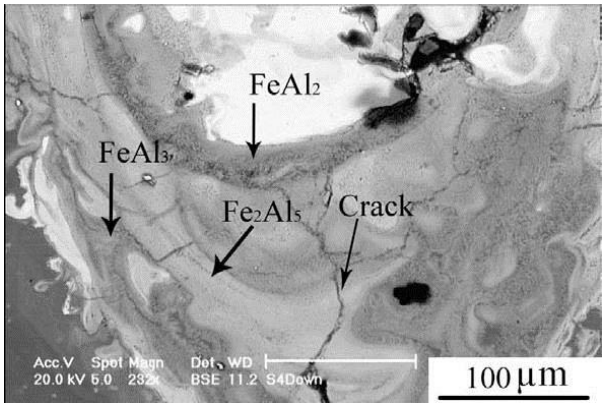


Fig. 3. Microstructure of the welded joint of Al-alloy and low carbon steel [15]

In a study conducted by Trinh et al. [16], the impact of laser power on the microstructure and mechanical properties of the welded joint of pure aluminum and a steel casing of a battery cell was investigated. The experiment was conducted using a nanosecond-pulsed fiber laser with varying laser powers (ranging from 10 to 20 W). The results indicated that the laser power had a significant impact on the morphologic characteristics of the welded joint, while the presence of pores influenced the strength of the welded joint [16]. However, in some scientific research, it was concluded that power, in combination with other process parameters, is not the main factor. Guan et al. [17] studied the influence of laser welding process parameters on the tensile strength and geometry of the welded joint of low carbon steel DC04 (1 mm thick) and Al-alloy AA6061 (1 mm thick). The weld was performed with a fiber laser. They concluded that the primary factor affecting the properties of the welded joint is the welding speed, while the laser power and focus of the laser beam are secondary factors. As the welding speed increases, the reaction time of aluminum and iron decreases, which ultimately leads to the formation of a smaller volume of intermetallic compounds. Furthermore, they reported optimum laser welding values that include a laser power of 1400 W, a welding speed of 40 mm/s, a laser beam focus of 0 mm, and a gas flow of 35 L/min [17]. The influence of different welding speeds and different laser beam focuses on the welded joint of aluminum alloy 5083 and Q235 steel was studied by Cui et al [18]. The weld was performed with an autogenous fiber laser in a keyhole mode. It was concluded that with an increase in the welding speed and focus of the laser beam, there is a significant decrease in the amount of formed intermetallic compounds Fe_2Al_5 and Fe_4Al_{13}. That has a positive effect on the mechanical properties [18]. Optimal welding process parameters, to obtain favorable mechanical properties and microstructure, were also studied by Pereira et al. [19]. In their research, the welded joint DP1000 steel and aluminum alloy AA1050 was performed with a pulsed Nd:YAG laser in an overlap configuration. They concluded that at low laser power, which is low enough to prevent complete penetration of the aluminum, a quality weld is achieved with a tensile strength approximately equal to that of AA1050 aluminum alloy [19]. The effect of penetration depth on mechanical properties was also studied by Yang et al. [20]. In their research, a laser-welded joint of stainless steel SS316L and pure aluminum was performed in the overlap configuration with the steel on the top. The results showed that when welding with higher penetration depths, aluminum-rich intermetallic compounds are formed. At smaller penetration depths, aluminum-rich intermetallic compounds are formed, and the weld macrostructure is without visible defects, which favorably affects the mechanical properties of the welded joint [20].

The formation and growth of intermetallic compounds can be controlled using different coatings and interlayers when welding aluminum and steel [10,21]. An example of this can be seen in the manufacturing of electric vehicle batteries, where the surface of the battery cell casing is plated with nickel to improve electrical conductivity and weld strength [22].

Chen et al. [23] investigated the influence of Ni-interlayer on laser welding of 201 stainless steel and 5052 aluminum alloy. The results showed that the welded joint with Ni-interlayer has better tensile strength and toughness than the welded joint without Ni-interlayer. Additionally, when welding with a Ni-interlayer, the metallurgical bond between iron and aluminum improved, which led to the formation of a new intermetallic compound $Al_{0.9}Ni_{1.1}$ [23].

4. CONCLUSION

In this review, the latest studies on laser welding of aluminum and steel in battery systems of electric vehicles are summarized, and it can be concluded that great technical progress has been achieved. Significant progress has been made in the welding technique. This includes the optimization of welding parameters as well as the use of coatings and interlayers to improve the metallurgical bond. However, the challenges associated with controlling the formation and growth of intermetallic compounds, that significantly affect the mechanical and electrical properties of the welded joint, are still unsolved. Further research aimed at controlling the formation of intermetallic compounds will lead to a wider application of laser welding of aluminum and steel in battery systems of electric vehicles.

5. REFERENCES

[1] Feng, J.; Zhang, P.; Yan, H.; Shi, H.; Lu, Q.; Liu, Z.; Wu, D.; Sun, T.; Li, R.; Wang, Q. Application of Laser Welding in Electric Vehicle Battery Manufacturing: A Review. Coatings 2023, 13.

[2] Li, Z.; Khajepour, A.; Song, J. A Comprehensive Review of the Key Technologies for Pure Electric Vehicles. Energy 2019, 182, 824–839.

[3] Zeng, X.; Li, M.; Abd El-Hady, D.; Alshitari, W.;

Al-Bogami, A.S.; Lu, J.; Amine, K. Commercialization of Lithium Battery Technologies for Electric Vehicles. Advanced Energy Materials 2019, 9, doi:10.1002/aenm.201900161.
[4] Zubi, G.; Dufo-López, R.; Carvalho, M.; Pasaoglu, G. The Lithium-Ion Battery: State of the Art and Future Perspectives. Renewable and Sustainable Energy Reviews 2018, 89, 292–308, doi:10.1016/j.rser.2018.03.002.
[5] Baazouzi, S.; Feistel, N.; Wanner, J.; Landwehr, I.; Fill, A.; Birke, K.P. Design, Properties, and Manufacturing of Cylindrical Li-Ion Battery Cells—A Generic Overview. Batteries 2023, 9, 309, doi:10.3390/batteries9060309.
[6] Zwicker, M.F.R.; Moghadam, M.; Zhang, W.; Nielsen, C. V. Automotive Battery Pack Manufacturing – a Review of Battery to Tab Joining. Journal of Advanced Joining Processes 2020, 1, doi:10.1016/j.jajp.2020.100017.
[7] Bieliszczuk, K.; Zyskowska, M. Selected Properties of Single-Sided Resistance Spot Welded Joints on 18650 Battery Tab. Welding Technology Review 2024, 96, 4–15, doi:10.26628/simp.wtr.v96.1176.4-15.
[8] Kumar, N.; Masters, I.; Das, A. In-Depth Evaluation of Laser-Welded Similar and Dissimilar Material Tab-to-Busbar Electrical Interconnects for Electric Vehicle Battery Pack. Journal of Manufacturing Processes 2021, 70, 78–96, doi:10.1016/j.jmapro.2021.08.025.
[9] Brand, M.J.; Schmidt, P.A.; Zaeh, M.F.; Jossen, A. Welding Techniques for Battery Cells and Resulting Electrical Contact Resistances. Journal of Energy Storage 2015, 1, 7–14, doi:10.1016/j.est.2015.04.001.
[10] Sadeghian, A.; Iqbal, N. A Review on Dissimilar Laser Welding of Steel-Copper, Steel-Aluminum, Aluminum-Copper, and Steel-Nickel for Electric Vehicle Battery Manufacturing. Optics and Laser Technology 2022, 146, doi:10.1016/j.optlastec.2021.107595.
[11] Shah, L.H.; Ishak, M. Review of Research Progress on Aluminum-Steel Dissimilar Welding. Materials and Manufacturing Processes 2014, 29, 928–933, doi:10.1080/10426914.2014.880461.
[12] Wallerstein, D.; Salminen, A.; Lusquiños, F.; Comesaña, R.; García, J.D.V.; Rodríguez, A.R.; Badaoui, A.; Pou, J. Recent Developments in Laser Welding of Aluminum Alloys to Steel. Metals (Basel) 2021, 11.
[13] Bunaziv, I.; Akselsen, O.M.; Ren, X.; Nyhus, B.; Eriksson, M.; Gulbrandsen-Dahl, S. A Review on Laser-Assisted Joining of Aluminium Alloys to Other Metals. Metals (Basel) 2021, 11, 1680, doi:10.3390/met11111680.
[14] He, H.; Gou, W.; Wang, S.; Hou, Y.; Ma, C.; Mendez, P.F. Kinetics of Intermetallic Compound Layers during Initial Period of Reaction between Mild Steel and Molten Aluminum. International Journal of Materials Research 2019, 110, 194–201, doi:10.3139/146.111735.
[15] Torkamany, M.J.; Tahamtan, S.; Sabbaghzadeh, J. Dissimilar Welding of Carbon Steel to 5754 Aluminum Alloy by Nd:YAG Pulsed Laser. Materials and Design 2010, 31, 458–465, doi:10.1016/j.matdes.2009.05.046.
[16] Trinh, L.N.; Lee, D. The Characteristics of Laser Welding of a Thin Aluminum Tab and Steel Battery Case for Lithium-Ion Battery. Metals (Basel) 2020, 10, 1–15, doi:10.3390/met10060842.
[17] Guan, Q.; Long, J.; Yu, P.; Jiang, S.; Huang, W.; Zhou, J. Effect of Steel to Aluminum Laser Welding Parameters on Mechanical Properties of Weld Beads. Optics and Laser Technology 2019, 111, 387–394, doi:10.1016/j.optlastec.2018.09.060.
[18] Cui, L.; Chen, B.; Qian, W.; He, D.; Chen, L. Microstructures and Mechanical Properties of Dissimilar Al/Steel Butt Joints Produced by Autogenous Laser Keyhole Welding. Metals (Basel) 2017, 7, doi:10.3390/met7110492.
[19] Pereira, A.; Cabrinha, A.; Rocha, F.; Marques, P.; Fernandes, F.; Alves de Sousa, R. Dissimilar Metals Laser Welding between DP1000 Steel and Aluminum Alloy 1050. Metals (Basel) 2019, 9, 102, doi:10.3390/met9010102.
[20] Yang, J.; Li, Y.L.; Zhang, H. Microstructure and Mechanical Properties of Pulsed Laser Welded Al/Steel Dissimilar Joint. Transactions of Nonferrous Metals Society of China (English Edition) 2016, 26, 994–1002, doi:10.1016/S1003-6326(16)64196-1.
[21] Yang, J.; Yu, Z.; Li, Y.; Zhang, H.; Guo, W.; Zhou, N. Influence of Alloy Elements on Microstructure and Mechanical Properties of Al/Steel Dissimilar Joint by Laser Welding/Brazing. Welding in the World 2018, 62, 427–433, doi:10.1007/s40194-017-0540-z.
[22] Schmitz, P. Comparative Study on Pulsed Laser Welding Strategies for Contacting Lithium-Ion Batteries. Advanced Materials Research2016, 1140, 312–319, doi:10.4028/www.scientific.net/amr.1140.312.
[23] Chen, S.; Huang, J.; Ma, K.; Zhang, H.; Zhao, X. Influence of a Ni-Foil Interlayer on Fe/Al Dissimilar Joint by Laser Penetration Welding. Materials Letters 2012, 79, 296–299, doi:10.1016/j.matlet.2012.03.073.

Authors:
Assist. Helena Lukšić, Full. Prof. Vera Rede, University of Zagreb, Faculty of Mechanical Engineering and Naval Architecture, Ivana Lučića 5, 10000 Zagreb, Croatia, Phone.: +385 1 6168 222, Fax: +385 1 6156 940.
E-mail: helena.luksic@fsb.unizg.hr; vera.rede@fsb.unizg.hr

MMA 2024 FLEXIBLE TECHNOLOGIES

15th INTERNATIONAL SCIENTIFIC CONFERENCE
NOVI SAD, SERBIA, SEPTEMBER 24-26, 2024

Original research paper https://doi.org/10.24867/MMA-2024-05-002

Terek, V., Kovačević, L., Škorić, B., Drnovšek, A., Čekada, M., Bobić, Z., Zagoričnik, M., Terek, P.

TRIBOLOGICAL TESTING OF MULTILAYER TiAlSiN COATING AT HIGH TEMPERATURES

Abstract: *In this study, multilayer TiAlSiN coating was magnetron sputtered on X15CrNiSi25-22 and IN-100. The tribological behavior of the coating was tested at room temperature (RT), 500, 600, 700 and 800 °C, using a high temperature (HT) tribometer. Al_2O_3 was used as a counterbody. Wear tracks were evaluated using stylus profilometry, confocal microscopy and scanning electron microscopy. At RT coefficient of friction (COF) values were similar and stable. However, at HT the COF curves exhibited instability across all samples, but the values of COF were comparable among the different substrates. The wear rate was similar at RT, while at HT the IN-100 substrate demonstrated a significantly lower wear rate. Abrasive and adhesive wear mechanisms were predominant. SEM analysis revealed the presence of small protrusions on the surface of the coating deposited on IN-100, where material accumulates during tribo-tests. These protrusions are suggested to have a significant impact on the coating's behavior, particularly regarding wear.*

Key words: *TiAlSiN, High-temperature tribology, PVD hard coatings, Wear rate, COF*

1. INTRODUCTION

TiAlN/TiSiN is a contemporary coating, and in recent years it has been widely investigated and used on industrial level. It can exhibit high hardness, oxidation resistance and thermal stability [1]. It is usually used to protect cutting tools made of WC-Co cemented carbide, such as cutting inserts, drills or end mills. Additionally, it can be used on tools in hot-extrusion, high pressure die casting or forging tools, which are usually made of hot-working tools steel [2].

Both hot-work tool steel and cemented carbide (WC-Co) have a problem with oxidation at high temperatures [3]. This makes tribo-tests at temperatures higher than 600 °C for hot-work tool steel and 700 °C for cemented carbide quite problematic when they are used as substrate materials. The main problem in that case is wear rate assessment, because the wear track fills up with oxide from substrate which results in a lower wear rate than it is. Therefore, in this paper heat resistant steel EN X15CrNiSi25-22 and IN 100 were chosen as substrate materials that do not oxidize at temperatures over 1000 °C.

2. MATERIAL AND METHODS

The substrate materials used in this study were heat resistant steel (EN X15CrNiSi25-22) and superalloy (IN-100). The samples were ground and polished, and then cleaned in ultrasonic bath before the deposition process. Multilayer TiAlSiN coating was deposited using an industrial DC magnetron sputtering unit (CC800/9, CemeCon). For the deposition of the coating two TiAl and two TiSi targets were used. The coating consists of three different layers. The first is TiAlN (2.4) when just the two TiAl targets are used, the second is TiSiN (3.8) deposited using two TiSi targets, and the third top layer is nanolayered TiAlN/TiSiN (0.6) deposited using all four targets.

The thickness of the coating was 6.8 μm and it was measured using a ball cratering method. Mechanical properties of the coating were determined on IN-100 substrate using nanoindentation (H100C, Fischerscope). The 50 mN load was used to keep penetration depth below 10% of coating thickness to minimize the influence of the substrate. Hardness of the substrates on as-deposited samples was determined using the standard HRC test and Vickers hardness tester using a load of 2 and 5 kg (HV2, HV5).

The coating was tribologically tested using a high-temperature pin-on-disk tribometer (THT, Anton Paar). Tribological tests were performed in ambient air at room temperature (RT), 500 °C, 600 °C, 700 °C, and 800 °C. Alumina (Al_2O_3) ball with a diameter of 6 mm was used as a counterbody. The tests were conducted using a dead load of 1N, linear velocity of 5 cm/s and the number of cycles was 2000.

The resulting wear tracks were characterized after the tribo-tests using confocal microscope (CFM) Axio CSM700 (Zeiss), 2D tactile profilometer Talysurf (Taylor Hobson), and scanning electron microscope (SEM) Quanta 650 ESEM (FEI) equipped with energy dispersive spectroscopy (EDS) technique used for chemical analysis. Six profilometry scans along the wear tracks were obtained and used to calculate the worn volume of the coating. The wear rate was calculated using the following equation: $K = V / (w \cdot s)$, where V is the worn volume (mm^3), w is the normal load (N), and s is the sliding distance (m).

3. RESULTS AND DISCUSSION

Mechanical properties of the substrates and the coating are presented in Table 1. The substrates were measured in the initial state, in as deposited, and in annealed at 700 °C. The hardness of the substrate

measured in HRC is converted to Vickers for easier comparison. Initial hardness of heat resistant steel was ~100 HV higher than of IN 100. However, when exposed to 450 during the deposition, hardness of heat resistant steel reduced for about 100 HV while hardness of IN 100 remained the same. Additionally, samples were annealed at 700 °C to simulate the effect of heat on the substrates during the tribological tests. Heat resistant steel softened for ~60 HV and retained nearly half of the original hardness, while the hardness of IN 100 was only 10% lower than in the initial state and ended up being higher than that of X15CrNiSi25-22 substrate. An additional problem is the hardness directly at high temperatures (hot hardness), however that was not measured in this investigation.

Substrate	Initial	As deposited	Annealed at 700 °C
X15CrNiSi25-22	412 HV5	310 HV2	250 HV5
IN-100	323 HV*	323 HV*	303 HV*
Coating	HV0.005 (GPa)	E	H^3/E^2
TiAlN/TiSiN	3288 (32.2)	365.7 GPa	0.25

* Converted from HRC

Table 1. Hardness of the substrate and the coating

3.1 CFM analysis

CFM images of the wear tracks after tribo-tests at RT, 500 °C, 600 °C, 700 °C, and 800 °C are, for coating on both substrates, presented in Fig. 1.

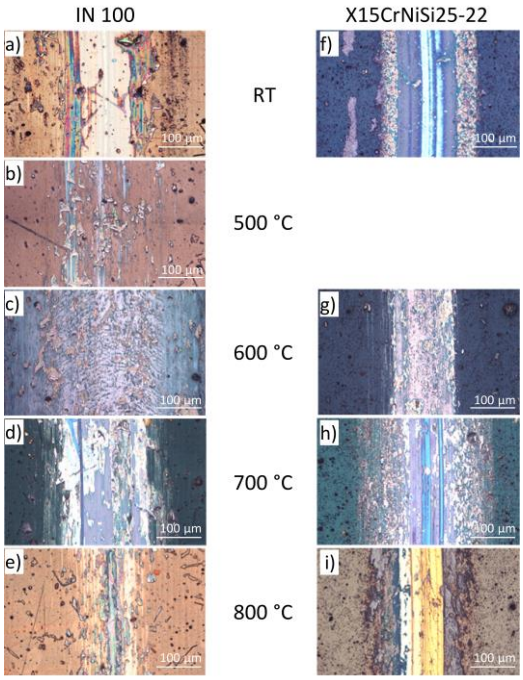


Fig. 1. CFM images of the wear tracks after tribo-tests at different temperatures

The wear tracks for coating on X15CrNiSi25-22 substrate are slightly wider than on IN 100, except for tribo-tests at 600 °C which showed a completely opposite behavior. All wear tracks are characterized by smooth regions but also have adhered material sporadically scattered throughout the wear tracks. This indicates that more than one wear mechanism is present, mainly abrasive and adhesive, while on high temperatures oxidation is also expected.

The surface of the coating deposited on IN 100 substrate is covered with thin randomly scattered protrusions, while the coating on X15CrNiSi25-22 substrate appears significantly smoother. In all tribo-tests with IN 100 as a substrate, the worn material accumulates on these protrusions. To analyze this accumulated material, SEM and EDS were employed.

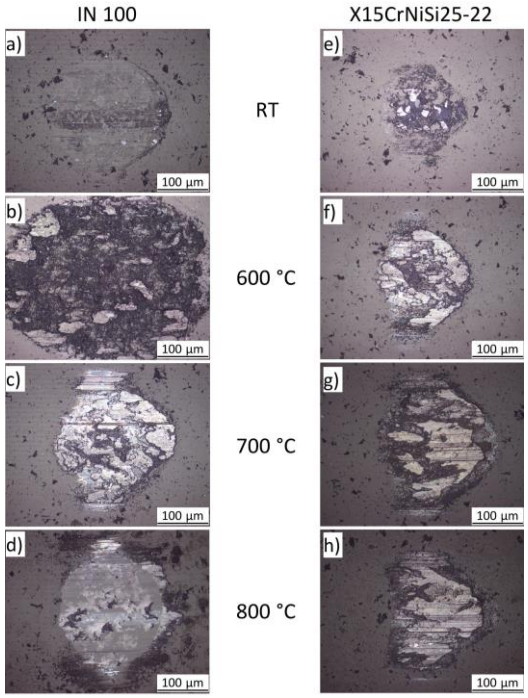


Fig. 2. CFM images of counterballs after tribo-tests

Fig. 2 displays CFM images of the alumina counterballs. CFM image of counterball after 500 °C is not shown because at that temperature there is only a test on IN 100 sample. When IN 100 was used as a substrate material, the counterballs appeared slightly more worn than for X15CrNiSi25-22 samples. Additionally, only a small amount of adhered material is present on the counterballs. On the other hand, when the substrate was X15CrNiSi25-22, the marks on the counterballs were smaller and significantly more adhered material is present on their surface than in the case of IN 100.

3.2 SEM and EDS analysis

SEM images with marked locations of EDS analysis for coating deposited on IN100 are shown in Fig. 3. Randomly scattered needle-like protrusions are present inside of both wear tracks and on the surface outside the wear tracks (Fig. 3a, c). A more detailed analysis inside of the wear track showed that these protrusions are more durable than the rest of the coating and do not wear out so easily. Additionally, worn material accumulates on these protrusions during the tribo-tests. EDS analysis (Table 2) showed that the coating is oxidized both inside and outside the wear track. According to our previous paper, oxides that can be found for this type of coating are mostly Al-O and Ti-O [3]. However, EDS on

location 3 showed a significant increase in Al and O signals which suggests that mostly Al-O is present. This agrees with the counterballs being highly worn during the tribo-tests on coated IN100, which resulted in the transfer of the counterball material to the coating's surface.

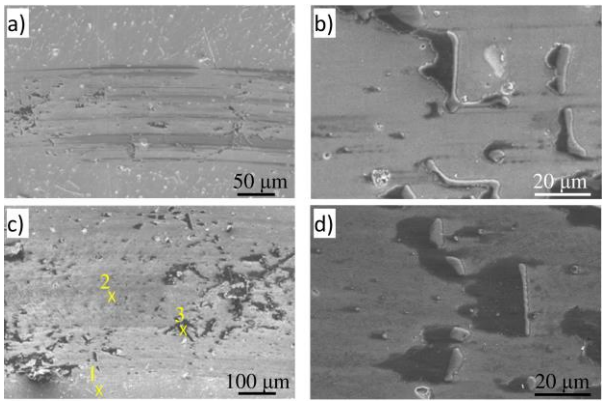


Fig. 3. SEM images of coating deposited on IN100: a, b) 500 °C; c, d) 600 °C

Fig. 4 displays SEM images and EDS locations for coating deposited on X15CrNiSi25-22. In this case, there are no protrusions on the coating's surface, and the wear track is rather smooth with only a small amount of adhered material in the wear track. EDS analysis at 600 °C outside and inside the wear tracks showed a similar ratio of elements as in the case of IN100 substrate, which is expected. However, EDS analysis of coating on this substrate at 800 °C showed that both wear products and wear track contain significantly lower amount of Al. Wear products and oxides inside the wear tracks are mostly Ti-O. This is again in agreement with counterballs wear, which are less worn and have more adhered material on them when tested against coated X15CrNiSi25-22 samples. This suggests that a very low amount of material was transferred from a counterball to the surface. Additional EDS analysis of counterball surface is needed to confirm this postulation. The surface of the coating after tribo-test at 800 °C shows signs of oxidation and delamination of these oxides (Fig. 4d). This confirms that oxidative wear mechanism is also present at high temperatures.

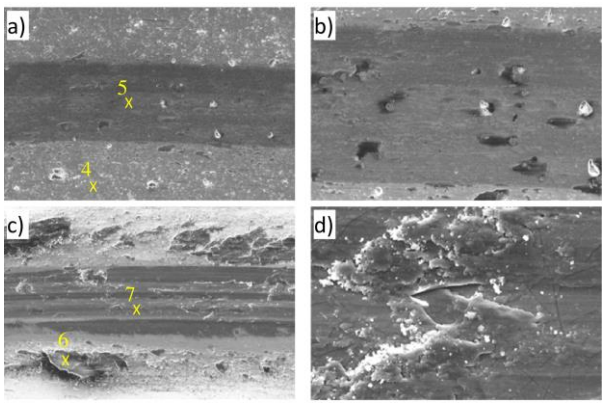


Fig. 4. SEM images of coating deposited on heat resistant steel: a, b) 600 °C; c, d) 800 °C

Chemical composition [at %]					
Location	Ti	Al	Si	N	O
1	30.6	5.6	4.5	41.1	18.1
2	34.5	5.5	5.0	41.3	13.7
3	7.7	29.0	1.1	-	62.2
4	33.1	5.7	4.8	39.1	17.3
5	36.1	5.4	5.4	43.5	10.1
6	25.1	2.0	3.9	-	69.1
7	30.2	0.1	5.1	29.0	35.6

Table 2. EDS analysis performed on locations from Figs. 3 and 4

3.3 Tribological behavior

Coefficient of friction (COF) curves for performed tribo-tests are presented in Fig. 5. At room temperature COF curves were steady for coating on both substrates. The higher value of COF for coating on X15CrNiSi25-22 is suggested to be due to a more pronounced adhesive wear and slightly wider wear track. At 600 °C the COF for coating on IN100 significantly increased which agrees with the high increase of wear track width, while for X15CrNiSi25-22 COF remained the same. The constant increase of COF at 700 and 800 °C for coating on IN100 is suggested to be due to sliding of alumina counterball against itself that is caused by material accumulation on protrusions in the wear track [4]. On the other hand, COF at these temperatures for the coating on X15CrNiSi25-22 decreased with higher number of cycles. This is due to the formation of Ti-O that was found to be predominant in these wear tracks, and which is known to reduce the COF especially at these temperatures [5].

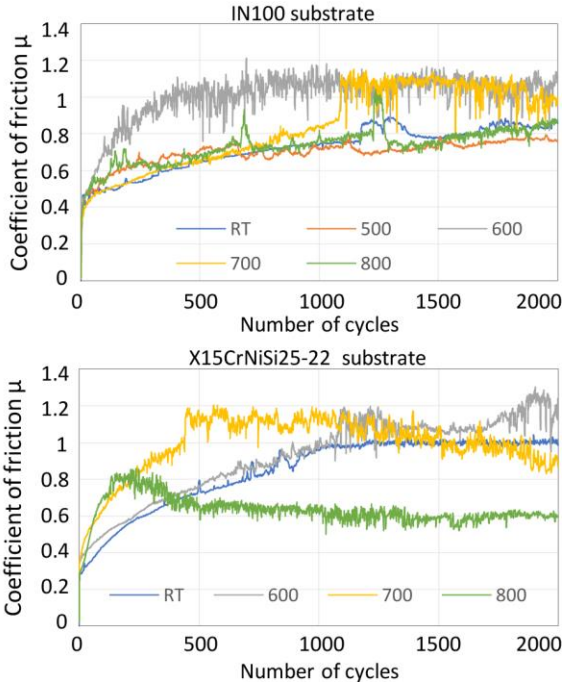


Fig. 5. COF curves of coating tested at different temperatures, on both substrates

Fig. 6 displays the wear rate of the coating at different testing conditions. Even though the coating is the same, significant differences can be observed for different substrates. The wear rate of the coating deposited on X15CrNiSi25-22 is higher than on IN100,

for both RT and high temperature tests. Except for tribo-test at 600 °C, for which additional investigations are required to confirm that behavior. The main difference between the coatings on these two substrates is the protrusions which are present on the coating deposited on IN100. It was observed that these protrusions are less prone to wear. Additionally, the counterball wear is considerably higher on the coating deposited on IN100. Therefore, it is suggested that, because of these protrusions, the counterball wears significantly more than the coating which results in coating being less worn. These protrusions are carbides of the substrate that were less ion etched than the rest of the surface. The coating usually grows epitaxially on these carbides which results in coating having extraordinary properties on these locations [6].

The coating on X15CrNiSi25-22, which has no protrusions of these kinds, there is nothing to slow down the coating wear, which is confirmed with lower wear of counterballs and higher wear of the coating. Additionally, the constant increase of wear rate with increase in temperature is linked to the significant decrease in hardness of the X15CrNiSi25-22 substrate. While the hardness of the IN100 substrate remains almost the same. According to profilometry scans, the coating was not worn out in either of the tribo-tests.

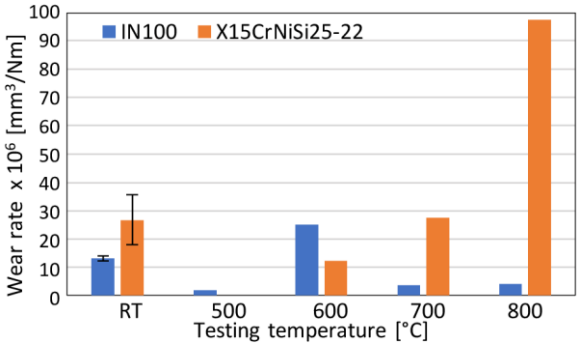


Fig. 6. Wear rate of TiAlN/TiSiN deposited on two substrates tested in different conditions

4. CONCLUSIONS

From the presented results, several conclusions can be drawn:

- After annealing at 700 °C, hardness of the IN100 substrate decreased only about 10%, while hardness of the heat resistant steel reduced significantly (~50%).
- Wear mechanisms and the surface morphology inside the wear tracks are similar for coating on both substrates. Abrasive and adhesive wear mechanisms are present in all tribo-tests, while at high temperatures oxidative wear mechanism is also observed.
- Random protrusions were present on the surface of the coating deposited on IN100. They were more durable and less prone to wear than the rest of the coating, which is attributed to epitaxial growth of the coating on these locations.
- The wear rate of the coating was significantly lower on IN100 than on X15CrNiSi25-22. This was due to counterball sliding on the protrusions which resulted in high counterball wear, while the coating on heat resistant steel had no protrusions and consequently low counterball wear.

5. REFERENCES

[1] Z.W. Xie, L.P. Wang, X.F. Wang, L. Huang, Y. Lu, J.C. Yan, Influence of oxidation on the structural and mechanical properties of TiAlSiN coatings synthesized by multi-plasma immersion ion implantation and deposition, Nucl. Instruments Methods Phys. Res. Sect. B Beam Interact with Mater. Atoms. 271, 1–5, 2012.

[2] B. Navinšek, P. Panjan, I. Urankar, P. Cvahte, F. Gorenjak, Improvement of hot-working processes with PVD coatings and duplex treatment, Surf. Coatings Technol. 142–144, 1148–1154, 2001.

[3] V. Terek, L. Kovačević, A. Drnovšek, P. Panjan, B. Škorić, J. Kovač, Z. Bobić, P. Terek, High-temperature tribological behavior of nanolayered TiAlN/TiSiN coating deposited on WC-Co cemented carbide, Surf. Coatings Technol. 477, 2024.

[4] X. Dong, S. Jahanmir, S.M. Hsu, Tribological Characteristics of α- Alumina at Elevated Temperatures, J. Am. Ceram. Soc. 74, 1036–1044, 1991.

[5] N. He, H. Li, L. Ji, X. Liu, H. Zhou, J. Chen, High temperature tribological properties of TiAlSiN coatings produced by hybrid PVD technology, Tribol. Int. 98, 133–143, 2016.

[6] A. Miletić, Design of nanolayered and nanocomposite metal-nitride coatings, University of Novi Sad, Novi Sad, Serbia, 2015.

ACKNOWLEDGEMENTS

This research has been supported by the Ministry of Science, Technological Development, and Innovation through project no. 451-03-47/2023-01/200156 "Innovative scientific and artistic research from the FTS (activity) domain". This work was also funded by the Slovenian Research Agency (program P2-0082) and European Regional Development Funds (CENN Nanocenter, OP13.1.1.2.02.006).

Authors:

MSc Vladimir Terek, PhD Lazar Kovačević, PhD Branko Škorić, MSc Zoran Bobić, MSc Marko Zagoričnik, PhD Pal Terek, University of Novi Sad, Faculty of Technical Sciences, Trg Dositeja Obradovića 6, 21000 Novi Sad, Serbia, Phone.: +381 21 450 810.
E-mail: vladimirterek@uns.ac.rs; lazarkov@uns.ac.rs; skoricb@uns.ac.rs; zoranbobic@uns.ac.rs; zagoricnik@uns.ac.rs; palterek@uns.ac.rs

PhD Aljaž Drnovšek, PhD Miha Čekada, Jožef Stefan Institute, Department of Thin Films and Surfaces, Jamova 39, Ljubljana, 1000, Slovenia, Phone.: +386 1 477 39 00.
E-mail: aljaz.drnovsek@ijs.si; miha.cekada@ijs.si

MMA 2024
FLEXIBLE TECHNOLOGIES

15th INTERNATIONAL SCIENTIFIC CONFERENCE
NOVI SAD, SERBIA, SEPTEMBER 24-26, 2024

Original research paper https://doi.org/10.24867/MMA-2024-05-003

Panić, M., Smiljić, Đ., Movrin, D., Milutinović, M.

ANALYSIS OF THE INFLUENCE OF RING DIMENSION RATIO ON FRICTION IN UPSETTING TESTS

Abstract: *Friction, as an indispensable phenomenon, greatly affects the deformation process and, as such, is an important research factor. In this work, the ring compression test was used to determine the value of the friction factor and to examine how changes in the dimensions of the ring influence its value. A specimen made of C45e steel with the standard dimensions' ratio of 6:3:2 was used to obtain the friction factor. Samples with non-standard geometric dimensions were compressed and compared with the standard sample to understand the friction deviations. The compression test was carried out in segments, where the stroke value for each phase was 0.5 mm, while a certain amount of lubricant of 0.25 ml was dosed on the tool and the workpiece. The obtained friction factor was further applied in numerical simulations, where a more detailed analysis of the most influential parameters of the process was performed.*

Key words: *Ring, Compression test, Friction factor,*

1. INTRODUCTION

Plastic deformation of materials is a technology in which, under the influence of a sufficiently high load, the shape of the starting material is permanently changed. The most important factor in plastic deformation processes is the amount of contact friction, which significantly affects the quality of the final product. The method of determining friction on contact surfaces is based on experimental research, where the ratio of the workpiece dimensions is determined, which indicates the size of the contact friction [1].

Contact friction measurement methods can be divided as follows:

- Methods for measuring the effect of friction during rolling;
- Methods for measuring the effect of friction during drawing;
- Methods for measuring the impact of friction during upsetting;
- Methods for measuring the effect of friction during extrusion [2].

In addition to all the methods that can be applied to determine the value of contact friction experimentally, one of the most used is the ring compression test. It is a multi-phase process based on monitoring the changes in dimensions of the workpiece, i.e., the ring [2].

The following factors have a significant influence on the value of the friction coefficient:

- Type of process,
- Lubrication,
- Type of tool and workpiece material,
- Processing temperatures,
- Deformation rate,
- The condition of the tool-material contact surfaces.

The lubricant is one of the factors that shows the most significant influence on the friction on the contact surfaces and, as such, has a role in separating the surface of the tool and the material during the upsetting process. In order for the lubricant to justify its purpose, it must have the following characteristics:

- Resistant to high pressures,
- To dissipate heat and cool the tool,
- To have adequate stability.

2. FREE RING COMPRESSION

Free ring compression is a bulk deformation process reflected in the reduction or increase of the internal diameter, depending on the coefficient of friction on the contact surfaces. When the workpiece is compressed between two flat plates, an increase in friction leads to an inward flow of the material, while on the other hand, a decrease in friction affects the outward flow of the material, as shown in Fig. 1 [3].

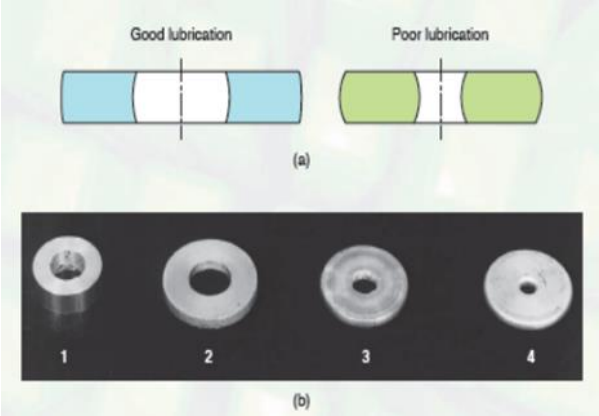


Fig. 1. Material flow during the compression test a) graphical interpretation, b) example of the specimen's shape and material flow during the testing

As can be seen in Fig. 1, with good lubrication, both the inner and outer diameters increase as the specimen is

compressed, and with poor lubrication, friction is high, and the inner diameter decreases [3].

2.1 Calibration curve

The principle of determining the friction coefficient using the ring compression method is based on the calibration curve (Fig. 2) [4,5].

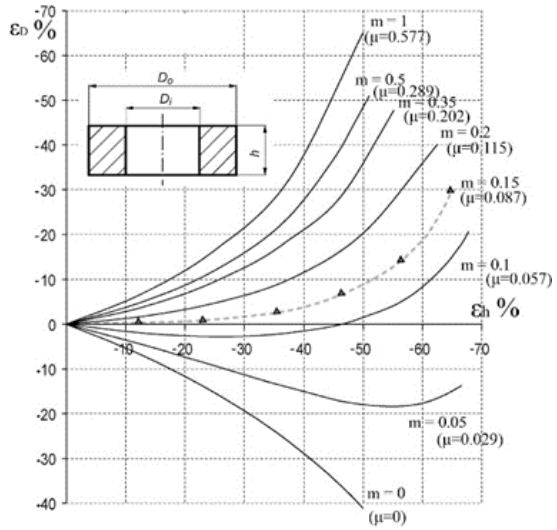


Fig. 2. Calibration curve for determining the friction factor in free ring compression [4,5]

The condition for using the calibration curve when determining the coefficient of friction for a specific type of material is a standardized ratio of the dimensions of the ring, i.e., outer diameter, inner diameter, and height, where the value of the ratio must be 6:3:2. The ring is lubricated with a suitable lubricant and compressed into segments, where at each stroke increase, the process is interrupted and the value of the current height of the ring (h) and the value of the inner diameter (Du) are measured. If the internal diameter of the sample increases during deformation, the friction is low, and if the internal diameter of the sample decreases, the friction value is high [4,5].

The relation used for calculating the inner diameter deformation:

$$\varepsilon_{Du} = \frac{D_{uo} - D_{u1}}{D_{uo}} \qquad (1)$$

The relation used for calculating the height deformation:

$$\varepsilon_h = \frac{h_o - h_1}{h_o} \qquad (2)$$

For each stroke, the values are calculated, and a curve is formed after the upsetting process is completed. Comparing the calibration curve with the curve obtained experimentally enables the determination of the value of the friction coefficient [4,5].

Fig. 3 shows the workpiece before and after the upsetting process, where the change in the shape of the workpiece can be observed. The workpiece takes on a barrel-like shape resulting from friction, which affects the flow of the material, causing tangential stresses to appear on the surfaces between the tool and the workpiece, which causes a change in shape.

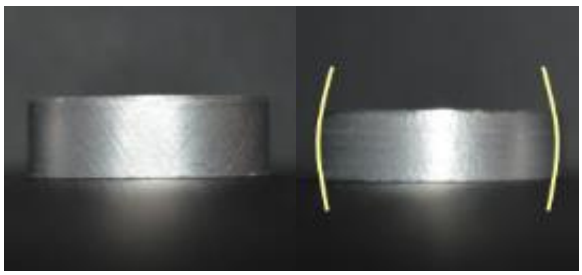


Fig. 3. Appearance of the workpiece before and after the upsetting process [6]

2. EXPERIMENTAL RESEARCH

In this paper, the magnitude of contact friction was examined through experimental research using the simplest method of ring compression. The experiment was performed on a Sack & Kiesselbach hydraulic press with a maximum force of 6.3 MN. As already stated, the upsetting process is based on the variation of the workpiece dimensions under different lubrication conditions. Mineral oil Molub HK, used as the lubricant, was used in concentrations of 0.25 ml on the workpiece and tool. During the research, samples of standard and non-standard dimensional ratios made of C45E steel were used to show their relation, as well as the difference in the magnitude of friction on the contact surfaces. The dimensions of the samples and their ratios are shown in Table 1, where the samples are classified into five groups.

group	D_{0s}	D_{0u}	h_0	Ratio
1	30	15	8	6 : 3 : 1.6
2	30	15	10	6 : 3 : 2
3	30	15	12	6 : 3 : 2.4
4	30	12	10	6 : 2.4 : 2
5	30	18	10	6 : 3.6 : 2

Table 1. Overview of dimensions and ratios of samples classified by groups

One sample from each group was tested in order to determine the change in dimensions and the impact of the change in dimensions on the friction manifested on the contact surfaces.

Overview of steps used in the experimental research:

- Measurement of initial sample dimensions used caliper;
- Dosing the lubricant of 0.25 ml on the surface of the workpiece and the surface of the tool;
- Compression of samples, whereby the process is iteratively stopped at every 0.5 mm stroke, with the removal of lubricant, measuring and recording the dimensions;
- Reapplying the same volume of lubricant and continuing the compression process, whereby the compression process of each sample is based on ten stages of 0.5 mm stroke each;
- Based on the obtained results, a curve was formed for each of the samples, where each was compared with the calibration curve to determine their mutual dependence and the value of the coefficient of friction.

Fig. 4 shows a sample of dimensions:

- Ds = 30 mm,
- Du = 15 mm and
- h = 10 mm,

and the standard ratio (6:3:2) provides the possibility of using the calibration curve.

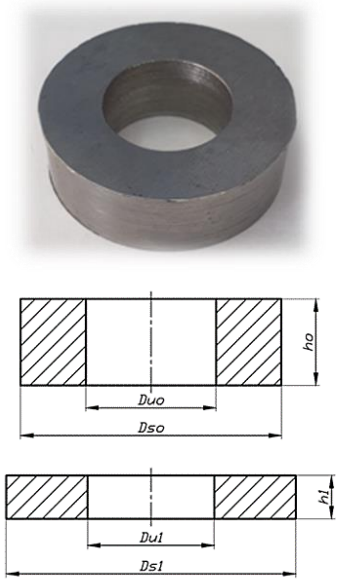


Fig.4. Standard ring dimensions with indicated sizes before and after the compression process

In Fig. 5, the calibration curve diagram is shown alongside the experimentally obtained calibration curve, represented by a broken line. Based on their relationship, the friction coefficient was determined to be 0.1.

On the other hand, based on the experimental values and the measured friction coefficient, the friction factor can be determined using analytical calculations:

$$m = \mu \cdot \sqrt{3}$$

The obtained value of the friction factor is 0.17.

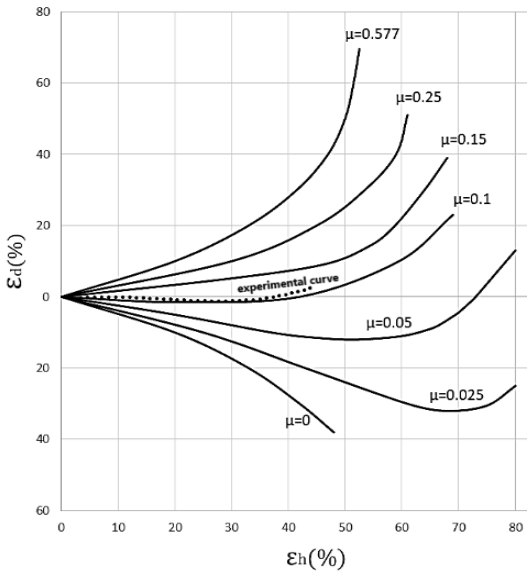


Fig. 5. Comparison of the experimental calibration curve with the calibration curve diagram

Figs. 6, 7, 8, and 9 show a comparison of the obtained experimental calibration curve represented by group 2 and indicated by a broken line on each of the diagrams, with the curves of non-standard samples of groups 1, 3, 4, and 5.

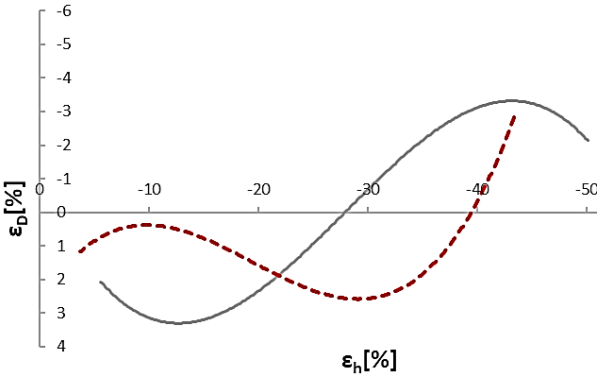


Fig. 6. Comparison of the non-standard sample curve of group 1 with the experimental calibration curve

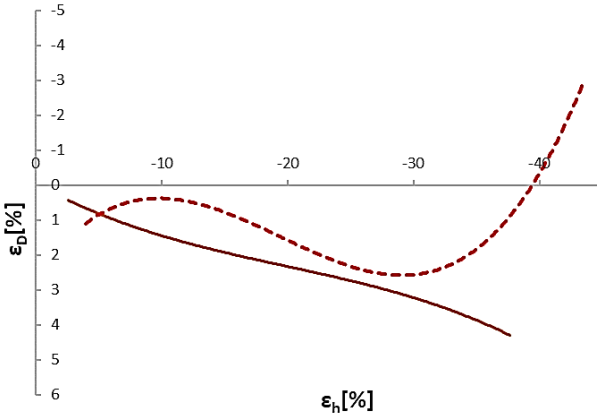


Fig. 7. Comparison of the non-standard sample curve of group 3 with the experimental calibration curve

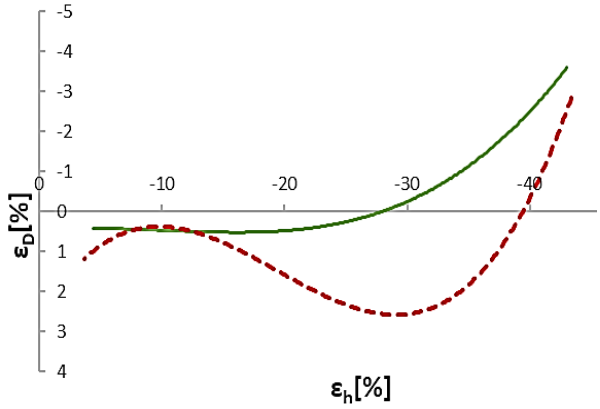


Fig. 8. Comparison of the non-standard sample curve of group 4 with the experimental calibration curve

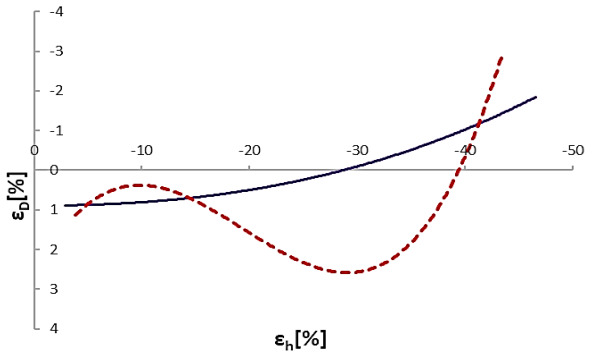


Fig. 9. Comparison of the non-standard sample curve of group 5 with the experimental calibration curve

3. CONCLUSION

Friction is one of the most important factors that manifest on contact surfaces between the tool and the workpiece. The coefficient of friction can be determined in various ways. The paper conducted the ring compression test as one of the simplest methods.

The geometry of the sample has a significant impact on determining friction. The standard ratio of the sample dimensions is 6:3:2. However, different ratios were used in the work: 6:3:1.6, 6:3:2.4, 6:2.4:2; 6:3.6:2.

Based on the calibration curve (standard specimen ratio), the value of the coefficient of friction was determined due to agreement with the curve obtained in the experimental part, and the determined value was 0.1. Also, as part of the experimental research, the relation of the experimental calibration curve with the curves of non-standard samples was shown, where a deviation was observed, caused by the geometry of the sample itself and the high surface roughness. The deviations of the inner diameter in groups 4 and 5 show a smaller offset from the experimental calibration curve than the height deviations in groups 1 and 3. Further research will be based on a repeated experiment, without stops between compression phases, and numerical simulations in order to compare the results and analyze the process itself.

4. REFERENCES

[1] V. Mandić, Fizičko i numeričko modeliranje procesa obrade deformisanjem, Kragujevac, Fakultet inženjerskih nauka, 2012.
[2] M. Plančak, D. Vilotić, Tehnologije plastičnog deformisnja, Novi Sad, Fakultet tehničkih nauka, 2012.
[3] E. Rajesh, M. Siva Prakash, Analysis of friction factor by employing the ring compression test under different lubricants, 2013.
[4] V. Vujović, Obrada deformisanjem I deo, FTN, Novi Sad, 1977.
[5] J. A. Schey, Metal deformation processes, Friction and lubrication, Marcel Dekker INC.,New York, 1970.
[6] F. Martína, M. J. Martína, L.Sevillaa, M. A. Sebastian, "The Ring Compression Test: Analysis of dimensions and canonical geometry", University of Malaga, 2015.

Authors:
MSc Milica Panić, MSc Đorđe Smiljić, PhD Dejan Movrin, PhD Mladomir Milutinović, University of Novi Sad, Faculty of Technical Sciences, Trg Dositeja Obradovica 6, 21000 Novi Sad, Serbia, Phone.: +381 21 485-23-34.
E-mail: milicapanic@uns.ac.rs; djordjesmiljic@gmail.com; movrin@uns.ac.rs; mladomil@uns.ac.rs

MMA 2024
FLEXIBLE TECHNOLOGIES

15th INTERNATIONAL SCIENTIFIC CONFERENCE
NOVI SAD, SERBIA, SEPTEMBER 24-26, 2024

Original research paper https://doi.org/10.24867/MMA-2024-05-004

Timotijević, M., Erić Cekić O., Janjatović, P., Rajnović, D.

THE INFLUENCE OF OVERHEATING TEMPERATURE ON THE MICROSTRUCTURE OF HP40 ALLOY

Abstract: *The study analyzed the microstructural changes of the heat-resistant centrifugally cast austenitic alloy HP40 Nb after overheating at temperatures of 950°C and 1150°C for 2 hours and 8 hours. For the microstructural analysis of the alloy in the as-received condition and after the thermal treatments, scanning electron microscopy (SEM) equipped with energy dispersive spectroscopy (EDS) was employed. Phase and precipitate analysis in the microstructure was conducted using scanning electron microscopy (SEM) via backscattered electron (BSE) imaging. Upon analyzing the results, a phase transformation of primary M_7C_3 carbides into $M_{23}C_6$ carbides and subsequent precipitation and dissolution of secondary carbides were observed in the microstructure. These microstructural changes resulted in alterations in the hardness values of the alloy.*

Key words: *Microstructure, overheating time, HP40-Nb alloy, secondary carbides*

1. INTRODUCTION

An HP alloy, denoted by 'H' for heat-resistance and 'P' indicating its Nickel content, primarily composed of Fe–25Cr–35Ni–0.4C (weight percent), is extensively utilized in petrochemical furnaces. The tubes in ethylene pyrolysis furnaces are a critical component of petrochemical industry plants. Tubes made from centrifugally cast austenitic HP40 Nb alloy steel have found applications in many industries, especially in the petrochemical industry, due to their good resistance to aggressive operating conditions [1-8]. A mixture of ethylene and steam passes through them under a pressure of about 2000 kPa, while burners heat the tube walls to temperatures above 750 ℃. The tubes are designed to operate for 100,000 hours, but their service life is often shorter due to instabilities in their microstructure [9].

Achieving good resistance of the tubes to working conditions is ensured by adding niobium, nickel, titanium, zirconium, tungsten, and cesium to the alloy. Nb, Ti, W, and Zn provide good resistance to creep because they form stable precipitates in the alloy at high temperatures. HP40 alloys are improved by adding a small amount of Nb, which leads to the precipitation of chromium carbides and the enhancement of the mechanical properties of the alloy [10].

It is known that the microstructure of the HP40-Nb alloy in the as-cast state consists of an austenitic matrix and a network of intergranular primary carbides rich in Cr and Nb. The chromium-rich carbides are of the M_7C_3 type, while the niobium-rich carbides are of the MC type [9,11-18]. Due to the exposure of the alloy to elevated temperatures, secondary carbides precipitate into the matrix, and the morphology of the carbides changes. The M_7C_3-type carbides transform into $M_{23}C_6$ carbides, and niobium-rich carbides transform into a very brittle G-phase. A large amount of secondary carbides is dispersed within the matrix. All these microstructural changes lead to changes in the mechanical properties of the alloy when exposed to various elevated temperatures [7,9,19].

Due to the aforementioned reasons, this study investigates the impact of different overheating temperatures (950-1150 ℃) on the microstructure and hardness of the HP40 Nb alloy.

2. METHODOLOGY

In this experiment, samples cut from centrifugally cast austenitic steel alloy HP40 Nb in the as-cast condition were examined. The chemical composition of the alloy was analyzed using Optical Energy Spectrometer (OES) type I Spark 8860, Thermo Scientific™, USA.

The samples were heated to 950 or 1150 ℃ for 2 or 8 hours, and then cooled to room temperature. The thermal treatment of the samples was conducted in a chamber-type laboratory furnace with a PID temperature controller. Thermocouples Pt-Pt13%Rh were placed above the samples to monitor the temperature inside the furnace.

After the thermal treatment, the samples were prepared for metallographic examination. The preparation technique included grinding with SiC papers (from 180 to 2400), polishing with diamond suspensions (with 6, 3, 1, and 1/4 μm particle size), and etching with a solution of 15 ml HCl, 10 ml glycerol, and 5 ml HNO3.

The microstructure of the samples was observed using a scanning electron microscope (JOEL JSM 6460 LV), and the observed phases were analyzed with an energy dispersive x-ray analyzer system (EDS) INCA Oxford Instruments in conjunction with the SEM.

The hardness of the samples was determined using a universal hardness tester, Dia Testor 2Rc-S3-E, Otto Wolpert, according to the standard procedure (ISO 6507-1) HV10.

3. RESULTS AND DISCUSSION

Fig. 1a shows the microstructure of the alloy sample in its initial state. From Fig. 1a, the austenitic matrix with a network of eutectic primary carbides along the

grain boundaries and between the dendrites can be observed. Fig. 1b indicates the presence of two types of carbides (dark and light phases): the dark phase—MC type carbide (MC=Nb, Ti) and the light phase—M_7C_3 type carbide (M=Cr, Ni, Fe). The Cr-rich carbides (Fig. 2b, Spectrum 1, Spectrum 4, Spectrum 5) and Nb-rich carbides (Fig. 2b, Spectrum 2, Spectrum 3).

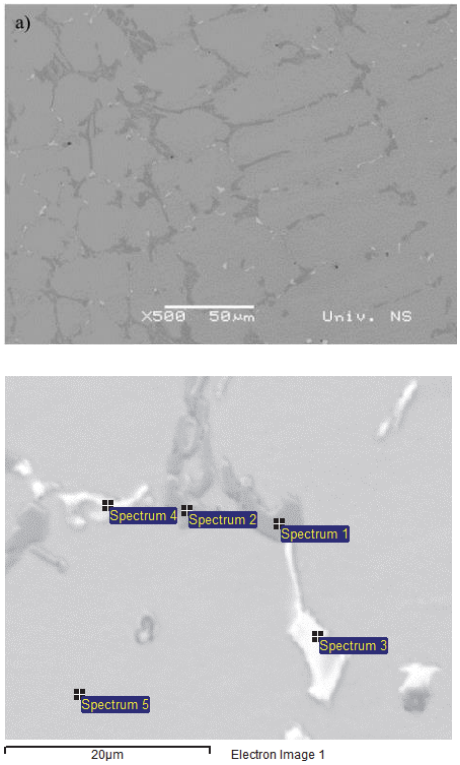


Fig. 1. Microstructure of alloy in its initial state: a) SEM micrograph, b) SEM micrograph (BSE) [20]

	C	Si	Cr	Ti	Fe	Ni	Nb
Spectrum 1	36.97		54.39		6.92	1.72	
Spectrum 2	15.83	3.41	28.73		27.11	24.93	
Spectrum 3	44.98		4.62	4.30	2.56	1.8	41.73
Spectrum 4	38.99	1.52	11.78	1.02	10.03	8.49	28.16

Table 1. Chemical composition (mass. %) of participate phases in HP40 Nb alloy, according to Fig 1b

Fig. 2a shows the microstructure of the sample after heat treatment at a temperature of 950℃ for 2 hours. After this thermal treatment, the presence of primary carbides with lamellar and plate-like shapes distributed along the dendrites in the form of discontinuous chains (marked in orange) and a large amount of precipitated fine secondary carbides in the austenitic matrix and in the zones around the dendrite boundaries (marked in red) can be observed.

Increasing the overheating time from 2 to 8 hours at 950 ℃ (Fig. 2b) reduced the amount of secondary carbides located around the primary carbides.

Fig. 2c shows the microstructure of the sample that was heat-treated at 1150 ℃ for 2 hours. After this thermal treatment, the amount of secondary carbides in the austenitic matrix and around the primary carbides was significantly reduced.

Fig. 2d shows the microstructure of the sample treated at 1150℃ for 8 hours. Increasing the overheating time at this temperature led to a further reduction in the amount of the secondary carbides and the appearance of carbide-free zones (marked in orange).

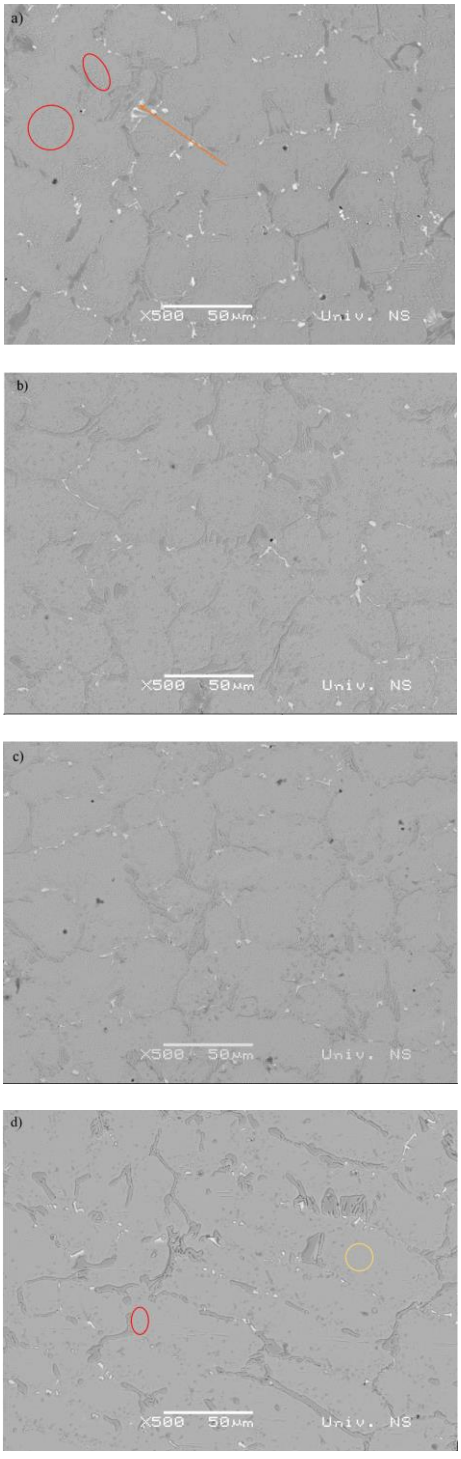


Fig. 2. SEM micrographs of a samples after heat treatment: a) 950℃ for 2h, b) 950℃ for 8h, c) 1150℃ for 2h, d) 1150℃ for 8h

Fig. 3 shows the EDS analysis of the microstructure of the sample thermally treated at 1150℃ for 8 hours. Dark gray phases, representing chromium-rich carbides, are visible. It can be observed that the Cr_7C_3 carbides have transformed into $Cr_{23}C_6$ carbides.

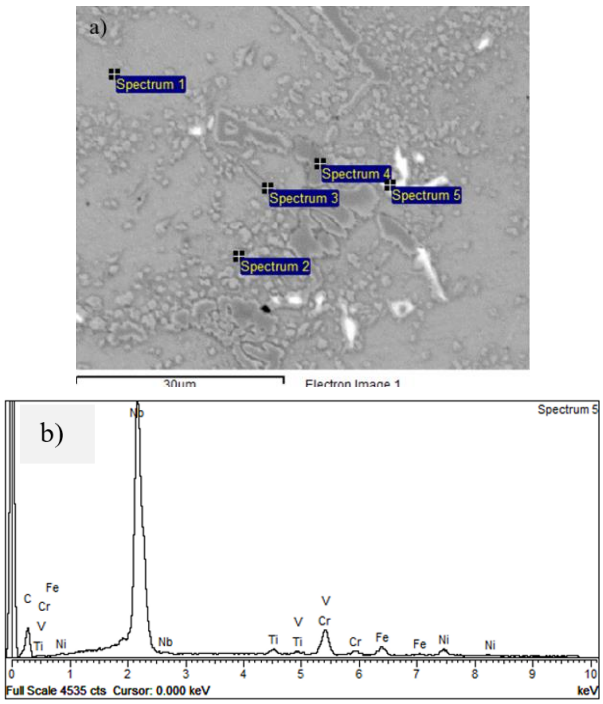


Fig. 3. Micrograph of present phases in alloy after heat treatment on 950 ℃ for 2h: a) SEM micrograph (BSE), b) EDS spectrum of Spectrum 5 - MC carbide (M=Nb, Ti)

Table 3 presents the hardness of HP-type heat-resistant alloy post-overheating at 950℃ and 1150°C.

Overheating temperature (℃)	Overheating time (hours)	Hardness (HV10)
950	2	207
	8	227
1150	2	206.7
	8	230

Table 3. The Vickers hardness test HV10 results for the samples post-overheating are as follows

Based on the measured hardness values of the samples after heat treatments (Table 3), we conclude the following: for the sample treated at 950 °C, increasing the overheating time from 2 to 8 hours resulted in an increase in hardness (from 207 to 227 HV10). It can be observed that increasing the overheating time also increased the hardness of the sample overheated at 1150 °C (from 206.7 to 230 HV10). The hardness increase is attributed to the reduction in the amount of secondary carbides, which dissolved, leading to carbon diffusion into the austenitic matrix. Different overheating temperatures had a negligible effect on hardness change.

Spectrum	C	Si	Ti	V	Cr	Mn	Fe	Ni	Nb
Spec. 1	8.91	1.38			21.1	1.31	34.29	33.01	
Spec. 2	12.24	1.65			28.39	1.25	26.88	29.58	
Spec. 3	23.67	1.02			24.24	1.37	24.69	25.01	
Spec. 4	26.36			0.39	60.68	1.08	8.68	2.81	
Spec. 5	37.15		0.84	0.51	6.34		2.68	2.76	49.72

Table 2. Corresponding chemical composition (mass%) of participate phases in HP40 Nb alloy (Fig.3a)

3. CONCLUSIONS

The microstructural analysis and hardness testing of HP40 Nb alloy after thermal treatments at 950 °C for 2 hours, 950 °C for 8 hours, 1150 °C for 2 hours, and 1150 °C for 8 hours, were investigated.

As-cast HP40 microstructure consists of an austenitic dendrite matrix and a network of primary carbides present in interdendritic areas.

Exposure to a temperature of 950 °C for 2 hours resulted in the transformation of primary M_7C_3 carbides into $M_{23}C_6$ carbides in the alloy microstructure.

Treatment at 950 °C for 2 hours led to the precipitation of a significant amount of secondary carbides in the austenitic matrix and in regions near the primary carbides.

The occurrence of secondary carbides and the alteration in precipitate shape in specimens subjected to overheating treatment at 950 and 1150 °C contributed to increased hardness levels.

4. REFERENCES

[1] Bonaccorsi, L., Guglielmino, E., Pino, R., Servetto, C., Sili, A.: *Damage analysis in Fe- Cr-Ni centrifugally cast alloy tubes for reforming furnaces*, Engineering Failure Analysis, Vol. 36, pp. 65-74, 2014.

[2] Swaminathan, J., Guguloth, K., Gunjan, M., Roy P., Ghosh, R.: *Failure analysis and remaining life assessment of service exposed primary reformer heater tubes*, Engineering Failure Analysis, Vol. 15, pp. 311-331, 2008.

[3] Andrade, A.R., Bolfarini, C., Ferreira, L.A.M., Vilar, A.A.A., Souz Filho, Bonazzi, L.H. C.: *Influence of niobium addition on the high temperature mechanical properties of a centrifugally cast HP alloy*, Material Science and Engineering A, Vol. 628, pp. 176–180, 2015.

[4] Soares, G.D.D.A., Almeida, L.H.D., Silveira, T.L.D., May, I.L.: *Niobium additions in HP heat-resistant cast stainless steels*, Material Characterization, Vol. 29, pp. 387–396, 1992.

[5] Ray, A.K., Kumar, Krishna, S. G., Gunjan, M., Goswami, Bose, B. S.C.: *Microstructural studies and remnant life assessment of eleven years service exposed reformer tube*, Material Science and Engineering A, Vol. 529, pp. 102–112, 2011.

[6] Alvino, A., Lega, D., Giacobbe, F., Mazzocchi, V., Rinaldi, A.: *Damage characterization in two reformer heater tubes after nearly 10 years of service at different operative and maintenance conditions*, Engineering Failure Analysis, Vol. 17, pp. 1526–1541, 2010.

[7] Liu, C.J., Chen, Y.: *Variations of the microstructure and mechanical properties of HP40Nb hydrogen reformer tube with time at elevated temperature*, Material Design, Vol. 32, pp. 2507–2512, 2011.
[8] Fuyang, C.M., Zhu, R., Zhang, P.P., Guo, X.F., Li, H., Geng, L.Y., Gong, J.M.: *Feasibility assessment of local repairment for reformer furnace tubes in service exposure*, International Journal of Pressure Vessels and Piping, Vol. 179, 2020.
[9] Picasso, A., Lanz, C., Sosa, M.: Microstructure *Evolution of a Nickel-Base Alloy Resistant to High Temperature during Aging*, Journal of Minerals and Materials Characterization and Engineering, Vol. 4, pp. 48-61, 2016.
[10] Fuyang, C-M., Chen, J-Y., Shao, B., Zhou, Gong, Y. J-M., Guo, X-F., Jiang, Y.: *Effect of microstructural evolution in thermal exposure on mechanical properties of HP40Nb alloy*, International Journal of Pressure Vessels and Piping, Vol.192, p. 104391, 2021.
[11] Kondrat'ev, S.Y., Kraposhin, V.S., Anastasiadi, G.P., Talis, A.L.: *Experimental observation and crystallographic description of M7C3 carbide transformation in Fe–Cr–Ni–C HP type alloy*, Acta Materialia, Vol. 100, pp. 275–281, 2015.
[12] Kondrat'ev, S.Y., Kraposhin, V.S., Anastasiadi, G.P., Talis, A.L.: *Fragmented structure of niobium carbide particles in as-cast modified HP alloys*, Acta Materialia, Vol. 127, pp. 267–276, 2017.
[13] Lanz, C., Brizuela, G., Juan, A., Simonetti, S.: *Microstructural evolution of a modified HP alloy: experimental and complementary computational study*, Journal of Advance Physics, Vol. 13(9), pp. 5141-5145, 2017.
[14] Wang, F., Northwood, D.O.: *The effect of carbon content on the microstructure of an experimental heat-resistant steel*, Material Characterization, Vol. 31(1), pp. 3–10, 1993.
[15] De Almeida Soares, G.D., de Almeida, L.H., da Silveira, T.L., Le May, I.: *Niobium additions in HP heat-resistant cast stainless steels*, Material Characterization, Vol. 29(3), pp.387-396, 1992.
[16] Voicu, R., Andrieu, E., Poquillon, D., Furtado, J., Lacaze, J.: *Microstructure evolution of HP40-Nb alloys during aging under air at 1000 ℃*, Material Characterization, Vol. 60(9), pp. 1020–1027, 2009.
[17] Chen, Q.Z., Thomas, C.W., Knowles, D.M.: *Characterization of 20Cr32Ni1Nb alloys in as-cast and ex-service condition by SEM, TEM and EDX*, Material Science and Engineering A, Vol. 374, pp. 398-408, 2004.
[18] Buchanan, K.G., Kral, M.V., Bishop, C.M.: *Crystallography and morphology of MC carbides in niobium-titanium modified as-cast HP alloys*, Metallurgical and Materials Transactions A, Vol. 45(8), pp. 3373–3385, 2014.
[19] Shen, L.M., Gong, J.M., Jiang, Y., Geng, L.Y.: *Effects of aging treatment on microstructure and mechanical properties of Cr25Ni35Nb and Cr35Ni45Nb furnace tube steel*, Acta Metallurgica Sinica, Vol. 24, pp. 235–242, 2011.
[20] Timotijević M., Erić Cekić O., Janatović P., Rajnović D.: *Microstructural analysis of a HP 40Nb alloy aged*, Vol.1, No.3. pp. 41-47, 2022.

ACKNOWLEDGMENTS

This work was supported by the Ministry of Science, Technological Development and Innovation of the Republic of Serbia, Contract No.: 451-03-65/2024-03/200108, Faculty of Mechanical and Civil Engineering in Kraljevo, University of Kragujevac; 451-03-66/2024-03/ 200213, Innovation Centre of the Faculty of Mechanical Engineering, Belgrade, University of Belgrade; 451-03-65/2024-03/200156 and No. 01-3394/1 by Faculty of Technical Science, University of Novi Sad.

Authors:
M.Sc. Milica Timotijević, University of Kragujevac, Faculty of Mechanical and Civil Engineering in Kraljevo, Department of General Engineering Education, Dositejeva 19, 36000 Kraljevo, Serbia.
E-mail: timotijevic.m@vakademija.edu.rs
Assoc. Prof. Olivera Erić Cekić, University of Kragujevac, Faculty of Mechanical and Civil Engineering in Kraljevo, Department of General Engineering Education, Dositejeva 19, 36000 Kraljevo, Serbia; University of Belgrade, Innovation Center of Mechanical Engineering Faculty, Kraljice Marije 16 11000 Belgrade, Serbia.
E-mail: olivera66eric@gmail.com
Assistant with PhD Petar Janjatović, Assoc. Prof. Dragan Rajnović, University of Novi Sad, Faculty of Technical Sciences, Department of Production Engineering, Trg Dositeja Obradovića 6, 21000 Novi Sad, Serbia, Phone.: +381 21 485-23-23.
E-mail: janjatovic@uns.ac.rs; draganr@uns.ac.rs

MMA 2024
FLEXIBLE TECHNOLOGIES

15th INTERNATIONAL SCIENTIFIC CONFERENCE
NOVI SAD, SERBIA, SEPTEMBER 24-26, 2024

Original research paper https://doi.org/10.24867/MMA-2024-05-005

Skakun, P., Janjatović, P., Dramićanin, M., Rajnović, D.

AN EXPERIMENTAL ASSESMENT OF DEFORMATION IN METAL FORMING PROCESSES

Abstract: *In this study an experimental method for estimation of plastic deformation within a bulk formed part is presented. The method is based on the principle that recrystallized grain size is a function of the degree of a prior deformation. This correlation is established through the experimentally determined calibration curve. The method was applied for assessment of plastic deformation and strain distribution in the cold formed part made of low carbon steel. Strain values were ascertained from calibration curve trough measurements of recrystallized grains size in deformed part. The size of grains varies through the cross section of specimen indicating different zones of deformation and the manner in which material flows. Furthermore, in the case of low carbon steel used, beside the size of the ferritic grains, analysis of the carbides and nonmetallic inclusions morphology further aided in determination of deformation zones.*

Key words: *metal forming, grain size, recrystallization*

1. INTRODUCTION

Strain state determination in metal forming helps to understand, analyze and optimize one process. Both experimental and numerical approaches are used, but numerical simulations are dominant nowadays [1, 2].

Additionally, there are not many experimental methods. One of the main reasons is that experiments usually require demanding and time-consuming procedures which, sometimes, are not affordable. Nevertheless, information about material flow, strain values and zones of critical values of deformation obtained through an experimental procedure are more accurate and realistic, helping to determine stress state in the forming zone.

One experimental method which is more suitable for sheet metal forming where plain strain state prevails is Digital Image Correlation (DIC) [3-5]. This method for strain and displacement measuring is based on optical non-contact technique.

Measuring material hardness (or microhardness) also can be used as an experimental method for strain determination. To apply this method, it is necessary do establish appropriate relationship [6, 7].

Another possibility is a metallographic method based on the relationship between recrystallized grain size and prior deformation of material. This method was used for determination of strain values and deformation distribution within cold formed parts made of single phase materials (e.g. pure aluminium) [8, 9].

In this paper application of metallographic method for strain distribution determination within a cold bulk formed part made of low carbon steel is presented. This steel consists of two micro-constituents, ferrite and pearlite. Therefore, the influences of multiphase microstructure on this method application is analyzed.

2. MATERIAL AND EXPERIMENT

2.1 Material

Material used in the forming experiment was a low carbon steel C10 (EN 10277-2: 2008), in the form of a bar. The chemical composition of the steel is presented in Table 1.

%Fe	%C	%Si	%Mn	%P
balance	0.123	0.165	0.504	0.012
%S	%Cr	%Ni	%Mo	%V
0.038	0.131	0.19	0.004	0.003

Table 1. The chemical composition of the steel C10

To apply this method for a specific material calibration curve needs to be determined experimentally. Both specimens used for the calibration curve and for forming experiment must have same initial microstructure. In order to achieve such microstructure all specimens should undergo the same initial preparation procedure. This procedure is consisted of:

- Soft annealing at 700 °C for 3.5 h,
- Slow cooling at 30 °C/h to 550 °C, and
- Air cooling to room temperature.

The microstructure obtained in this way consisted of ferritic grains with average size d_{av} = 18±0.8 μm and some strings of spheroidal carbides (Fig.1).

2.2 Calibration curve

To determine the degree of deformation within the cold formed part it is necessary to establish its relationship with the size of recrystallized grains. That relationship is presented in the calibration curve.

The calibration curve is determined experimentally, by upsetting cylindrical billets for the amount of true strain φ between 0.1 and 1.15. Each billet is deformed for different amount of strain. It was necessary to eliminate the influence of friction on the contact surfaces between billet and die to obtain uniform strain

distribution in the material. For that reason, Teflon foil was used.

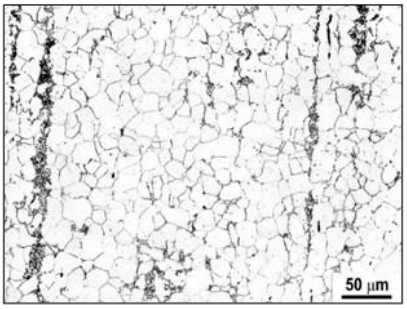


Fig. 1. Microstructure of the C10 specimens after initial heat treatment

After forming, all billets were heat treated at 690 °C for 5 hours followed by slow cooling in a furnace, to achieve recrystallized structure.

The size of recrystallized grains varies between billets as the result of different value of deformation. When subjected to minimal strain (φ=0.1), billets tend to develop fewer grains, but with larger diameters. Conversely, applying greater deformation-thus accumulating more energy during the forming process-results in a higher quantity of smaller grains after recrystallization. Additionally, there is a threshold of energy accumulation required to initiate the recrystallization process.

After metallographic examination and grain size measurement (described later) for each billet, a set of strain-recrystallized grain size values were obtained. According to this set of values calibration curve was approximated by the power function (1):

$$\boldsymbol{\varphi = 35.321 \cdot d^{-1.411}} \qquad (1)$$

where:

φ - is a true strain, and

d - is a grain diameter (in µm).

In Fig. 2 calibration curve used for strain values determination is presented.

If the forming load is measured in the upsetting experiment, the flow curve can also be obtained from this experiment. The flow curve can be used for stress calculation after strain state is determined.

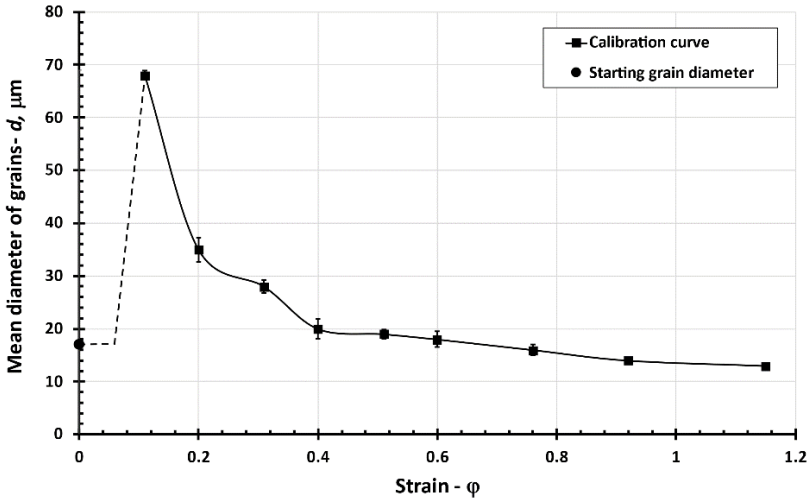


Fig. 2. Calibration curve [10]

2.3 Forming experiment

Experimental method presented in this paper was applied for strain values and deformation distribution determination within a bulk formed part made of low carbon steel. Two metal forming methods were combined in the experiment: upsetting and forward extrusion. The cylindrical piece (D=30 mm, H=38.5 mm) was pressed by a flat punch downwards (15 mm stroke) through the forward extrusion die. When material is formed in this way it could flow in two directions, radially, as in the upsetting, and axially as in the forward extrusion process.

Press used in experiment was hydraulic press Sack&Kiesselbach (F_{max}= 6.3 MN).

2.4 Metallographic examinations

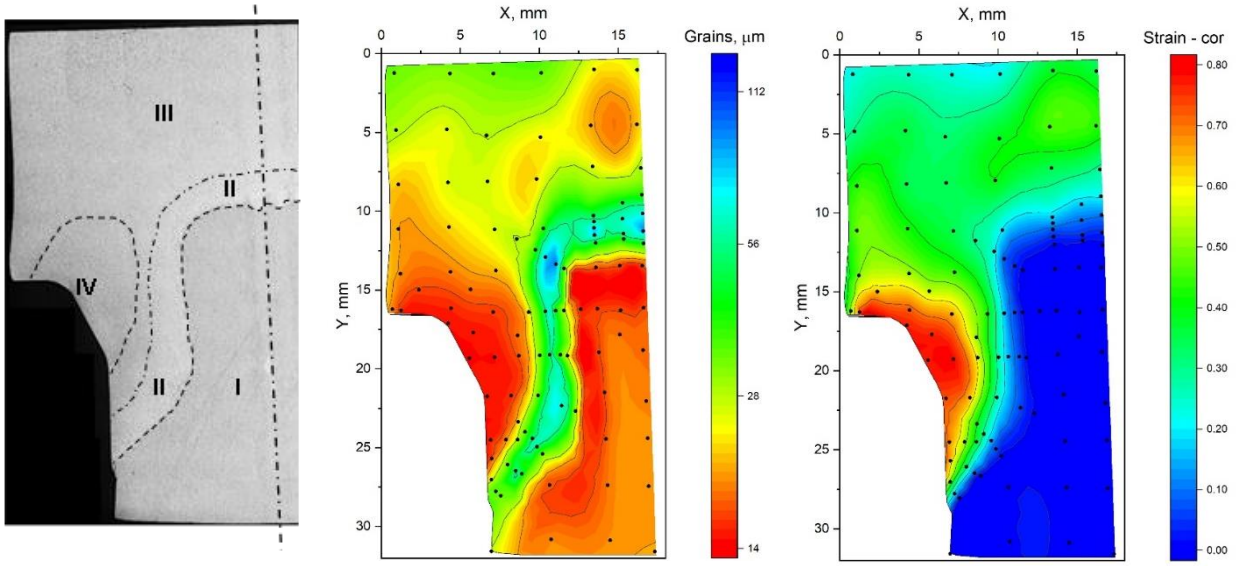
Prior to metallographic examination and analysis of recrystallized grain size, all specimens underwent metallographic analysis following conventional preparation procedures, which included grinding with silicon carbide (SiC) papers (ranging from a 220 to 2500 grit size) and subsequent polishing using a diamond suspension with particle sizes of 6, 3, 1, and 0.25 mm. The grains were revealed using a 3% nital solution, which is a mixture of nitric acid in alcohol. The detailed examination of each specimen was performed with a Orthoplan (Leitz, Germany) light microscope.

3. RESULTS AND DISCUSSION

On the cross section of the sample four distinctive macrostructure zones with different grain size could be observed, Fig. 3a. The grain size measured on corresponding places is given in Fig. 3b. The central lower section, (zone I) have grain sizes that are similar to the initial measurements, ranging from 17 to 19 µm. Further, in zone II, next to the border with zone I, the observed grain sizes are the largest, averaging around

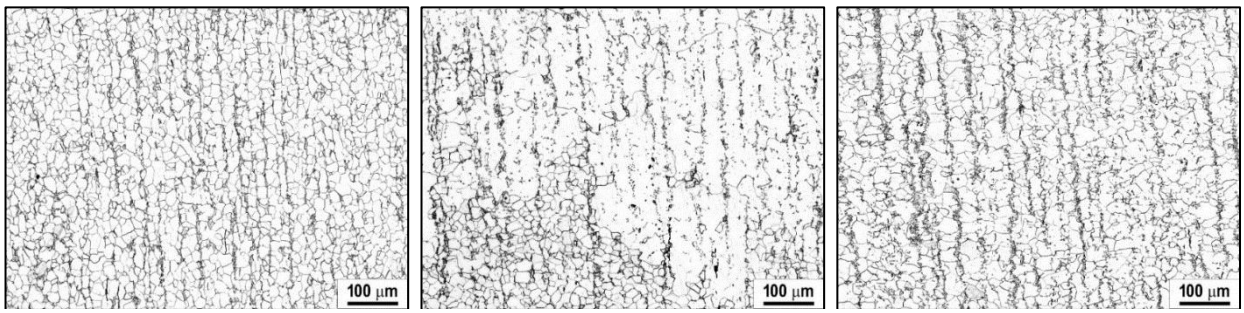
100 μm, while near border of zone III, there is a notable decrease in grain size, with diameters reducing to approximately 30 μm. Towards the top segment of the extruded material, zone III, the grains are measured to have diameters between 20 and 30 μm. The smallest grains are located in zone IV, situated near the die's slope, with their sizes reducing to 14-20 μm.

Fig. 4 illustrates the characteristic microstructures within the various zones. Small ferritic grains and strings of carbides are evident in zone I, Fig. 4a. The transition from small to large grains at the boundary between zones I and II is shown in Fig. 4b, where the carbides are more widely dispersed among the ferritic grains compared to zone I. Zone III has average size ferritic grains similar like zone I, and dispersed carbides similarly to zone II, Fig. 4c.



a) b) c)

Fig. 3. Grain size in the longitudinal half-section of the extruded element: a) Grain size zones; b) Mean grain diameter; c) Strain values – corrected (black dots on figures represent the position of grain diameter measurement or strain calculation) [10]



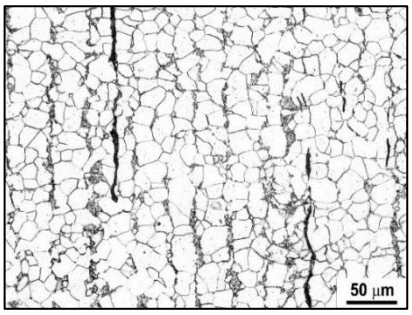
a) b) c)

Fig. 4. Characteristic microstructures of extruded element in the different zones: a) without significant deformation (zone I); b) transition from small to large grains (zone II); c) compression (zone III) [10]

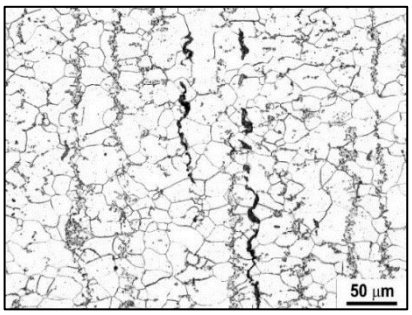
Further examination of the deformation can be conducted by analyzing the nonmetallic inclusions shown in Fig. 5. Within zone I, characterized by material extrusion, these inclusions exhibit an elongated form within a matrix of equiaxial ferritic grains and distinct carbide islands, Fig. 5a. Conversely, in zone III, the inclusions assume a zigzag pattern, a result of the radial material flow induced by compressive forces, Fig. 5b. This zigzag configuration is also evident in the carbide strings, which appear also in zigzag form, while carbide islands are more scattered throughout the matrix. In both cases, the orientation of inclusions and carbides is consistent with the direction of material flow.

The initial strain values in extruded element were calculated by using the calibration curve fitting equation (1) based on the grain size from Fig. 3a. However, it was observed that in zone I, where deformation is negligible, a high deformation values are obtained due to overlapping grain size of starting non-deformed material (d_{av} = 18±0.8 μm), and values of recrystallized grains in the same range after deformation which according to calibration curve should have strain of 0.56 to 0.63.

Thus, based on observed microstructure features of well-defined carbides strings and elongated nonmetallic inclusions which indicate negligible deformation of zone I, compared to zone III where a disperse carbides and zigzag nonmetallic inclusions appear indicating significant compression, a correction of strains given by calibration curve need to be performed. The final results of strain distribution are given in Fig. 3c



a)



b)

Fig. 5. Deformation of nonmetallic inclusions: a) elongated inclusions – zone I; b) compressed inclusions – zone III [10]

4. CONSLUSION

In summary, the described and used experimental metallographic technique offers dependable insights into the strain distribution present in extruded components, identifying various zones of deformation. Additionally, when applied to materials composed of two phases (or two micro-constituents), this technique leverages grain size and the deformation of carbides and non-metallic inclusions to realistically depict the material flow during the analyzed stage of element extrusion.

5. REFERENCES

[1] Lumelskyj, D., Rojek, J., Tkocz, M.: *Detection of Strain Localization in Numerical Simulation of Sheet Metal Forming*, Archives of Civil and Mechanical Engineering, 18, pp. 490–499, 2018.

[2] Gomez-Marquez, D., Ledesma-Orozco, E., Hino, R., Aguilera-Gomez, E., Korpała, G., Prahl, U.: *Numerical Study on the Hot Compression Test For Bulk Metal Forming Application*, SN Applied Sciences, 4:220, pp. 1-16, 2022.

[3] Gonzalez, M.M., Lutes, N.A., Fischer, J.D., Woodside, M.R., Bristow, D.A., Landers, R.G.: *Analysis of Geometric Accuracy and Thickness Reduction in Multistage Incremental Sheet Forming Using Digital Image Correlation*, Procedia Manufacturing, 34, pp. 950-960, 2019.

[4] Farahani, B.V., Belinha, J., Amaral, R., Tavares, P.J., Moreira, P.: *A Digital Image Correlation Analysis on a Sheet AA6061-T6 Bi-Failure Specimen to Predict Static Failure*, Engineering Failure Analysis, 90, pp. 179-196, 2018.

[5] Mashiwa, N., Furushima, T., Manabe, K.: *Novel Non-Contact Evaluation of Strain Distribution Using Digital Image Correlation with Laser Speckle Pattern of Low Carbon Steel Sheet*, Procedia Engineering, 184, pp. 16-21, 2017.

[6] Sundararajan, G., Tirupataiah, Y.: *The Hardness-Flow Stress Correlation in Metallic Materials*, Bulletin of Materials Science, 17, pp. 747–770, 1994.

[7] Alves, M.L., Rodrigues, J.M.C., Martins, P.A.F.: *Cold Forging of Gears: Experimental and Theoretical Investigation*, Finite elements in analysis and design, 37, pp. 549-558, 2001.

[8] Oyekanmi, B.O., Hughes, T.A., Bramley, A.N.: *A Microstructural Evaluation Technique for Deformation Studies in Metal Forming Processes*, Journal of Materials Processing Technology, 21, pp. 75-89, 1990.

[9] Skakun, P., Rajnovic, D., Janjatovic, P., Balos, S., Shishkin, A., Novak, P., Sidjanin, L.: *Metallographic Determination of Strain Distribution in Cold Extruded Aluminum Gear-Like Element*, Metals, 10:589, pp. 1-11, 2020.

[10] Skakun, P., Rajnovic, D., Janjatovic, P., Movrin, D., Dramicanin, M., Berus, L., Ficko, M.: *Experimental Determination of a Strain State in a Bulk Forming of a Low Carbon Steel*, Medziagotyra, 30 (1), pp. 40-46, 2024.

ACKNOWLEDGMENTS

The authors gratefully acknowledge research support by the project entitled "Interdisciplinarity in Materials Science and Joining Technologies" from the Department of Production Engineering, Faculty of Technical Sciences Novi Sad, Serbia.

FUNDING

This research has been supported by the Ministry of Science, Technological Development and Innovation (Contract No. 451-03-65/2024-03/200156) and the Faculty of Technical Sciences, University of Novi Sad through project "Scientific and Artistic Research Work of Researchers in Teaching and Associate Positions at the Faculty of Technical Sciences, University of Novi Sad" (No. 01-3394/1).

Authors:

Dr Plavka Skakun, Dr Petar Janjatović, Dr Miroslav Dramićanin, Dr Dragan Rajnović, University of Novi Sad, Faculty of Technical Sciences, Trg Dositeja Obradovica 6, 21000 Novi Sad, Serbia, Phone.: +381 21 485-23-17.

E-mail: plavkas@uns.ac.rs; janjatovic@uns.ac.rs; dramicanin@uns.ac.rs; draganr@uns.ac.rs

MMA 2024 FLEXIBLE TECHNOLOGIES

15th INTERNATIONAL SCIENTIFIC CONFERENCE
NOVI SAD, SERBIA, SEPTEMBER 24-26, 2024

Original research paper https://doi.org/10.24867/MMA-2024-05-006

Trivkovic, M., Maksimovic, N., Pecanac, M., Stojisic, N., Dramicanin, M., Rajnovic D., Balos, S.

LASER SHOCK PEENING OF AISI 316L AUSTENITIC STAINLESS STEEL WITH VARIOUS CONFINEMENTS

Abstract: *Laser shock peening (LSP) is a novel technology for the induction of compression stresses in the materials. The principle of LSP is based on the plasma imparted by the laser pulse impact, which influences the induction of compressive stresses in the material, which can be beneficial from different aspects: microhardness, corrosion and fatigue. It can be performed on virtually all alloys, including additively manufactured, and alloys that can not be successfully heat treated, such as ferritic and austenitic stainless steels. In this manuscript, the LSP of AISI 316L austenitic stainless steel was examined. In order to improve the effect of the LSP process, various solid confinements were used and the effect in terms of residual stresses and microhardness were applied to test the effect of LSP. It was found that solid confinement can be beneficial and that compressive stresses and microhardness are strongly related.*
Key words: *laser shock peening, residual stresses, microhardness*

1. INTRODUCTION

A significant number of production technologies induce relatively tensile residual stresses in the material that are added to the tensile stresses that come from the exploitation loads. This might lead to the premature failure due to overload, fatigue fracture or an increased sensitivity to corrosion. Tensile stresses are induced in a number of technologies, mostly those that use melting and crystallization. Some of those are casting, fuse welding processes and more recent, additive technologies such as selective laser melting (SLM) and wire arc additive manufacturing (WAAM). To reduce or convert tensile stresses into much more convenient compressive stresses, peening processes were developed, particularly the traditional shot peening. This technology uses steel or ceramic balls to strike the surface of the material and impart cold working and subsequently, compressive stresses. However, an alternative, promising a deeper effect in the material emerged as laser shock peening (LSP). This technology utilises pulsed laser impacts at the surface of the material, where hi-power plasma occurs [1]. Plasma induces stress waves in the material, where, as in shot peening, surface compression occurs [2]. In order to increase the effect through concentrating stress waves in the material, and thus make the process more efficient in view of compressive stresses, as well as hardness and depth, confinement is introduced. The traditional confinement is water [3, 4], however, other types of confinement emerged, predominantly solid; in form of of glass [5, 6] or polymer [7, 8]. The basic schematic depiction of LSP is shown in Fig. 1.

In this paper, a comparative study was done, encompassing the use of various confinements was used, to explore their effectiveness with 1064 nm laser pulse wavelength, on austenitic steel rolled base material.

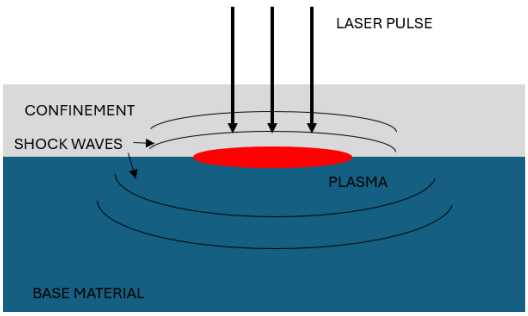


Fig. 1. Scheme of LSP process on the base material

2. EXPERIMENTAL PART

Base material used in this research was austenitic stainless steel EN X2CrNiMo17-13-2 (1.4404; AISI 316L). The results of chemical analysis, determined by G.N.R. MicroLab 150 optical emission spectrometer (OES) is given in Table 1.

C	Si	Mn	P	S	Cr	Ni	Mo
0.017	0.95	2.0	0.001	0.003	17.2	11.9	2.7

Table 1. Chemical composition of X2CrNiMo17-13-2, Fe balance (mass %)

LSP process was done by using the fixed Quantel Twins Nd:YAG 10 ns pulsed laser, coupled to a mirror and the lense. Wavelength used was 1064 nm, spot size Ø1 mm, ½ overlapping pattern was applied to form the treated area of 10x10 mm. The test sample was placed on a custom-built stage that provided movement, Fig. 2.

Specimens were LSP treated by using the following confinements:

- Specimen A: 2 mm commercial glass,
- Specimen B: 3 mm commercial glass,
- Specimen C: 3 mm commercial glass+15 μm stretch foil wrap,
- Specimen D: 3 mm commercial glass+25 μm stretch foil wrap.

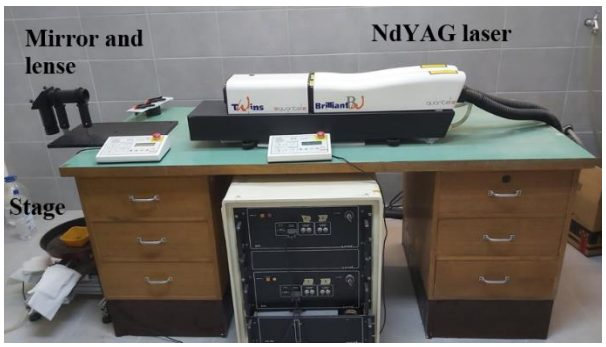


Fig. 2. LSP setup

Strech foil wrap was made of LLDPE (linear low-density polyethylene). Each specimen was treated with four laser cycles.

Characterization was aimed at exploring the effectiveness of proposed confinements. After the preparation, residual stresses were measured by Rigaku MiniFlex 600 device, with Cr-Kα tube, (220) diffracted plane, 128.8º Bragg angle of diffraction (2θ), 15 mA current and 40 kV voltage. After that, the specimens were sectioned and metallographically prepared on Struers equipment. This preparation encompassed cutting with cooling to avoid overheating, mounting into polyetylene, grinding with various SiC abrasive papers (P100 to P2000 grit, from coarse to fine) and finally, polishing (diamond suspensions 6, 3, 1 and ¼ μm). These steps were to prepare the cross section for microhardness measurement, which was performed on Wilson Tukon 1102 device, using 100 g loading. Measurements were done under the surface, through the cross section, at distance between identations of 0.1 mm, up to the depth of 1.5 mm to test the material response to LSP. Specimens A-D were compared to Specimen 0, which is control specimen, without any LSP treatment, for reference.

3. RESULTS AND DISCUSSION

A typical treated surface is shown in Fig. 3, while the corresponding effect on glass is shown in Fig. 4. It can be seen that the surface of the specimen is darker, as the result of the effect of plasma. Similarly, the effect on glass is that it also becomes darker in color, which, after four cycles becomes less effective and its transparency drops significantly, thus becoming unusable for further LSP process. This is in strong contrast with water, which locally evaporates, but its transparency and the transmittance of laser is not affected. However, the merit of using solid confinements is the application in components that are already mounted on aircraft. A typical example is landing gear components, since there is a number of sensors and electronic components, which can be sensitive to water (water LSP confinement). It is very inconvenient to disassemble these systems for maintenance and therefore solid confinement may be a better option. Also, another use id the marrying the LSP and selective laser melting (SLM) technology, in aim to produce all 3D compressive stressed parts [9].



Fig. 3. LSP effect in the Specimens B and C

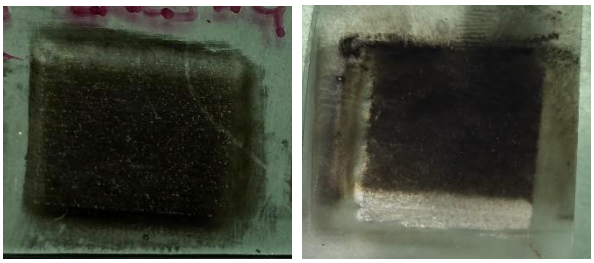

a) b)

Fig. 4. LSP effect on the: a-glass confinement in the Specimen A; b-foil wrap in Specimen D

The results of residual stresses are shown in Fig. 5. It can be seen that residual stresses are slight compressive in Specimen 0 (-20.22±5.51 MPa). However, by applying glass confinement, with wavelength of 1064 nm, these compressive stresses increase to -58.12±9.95 MPa and -82.99±12.26 MPa if 2- and 3-mm glass (Specimens A and B). This can be attributed to a more rigid and a thicker glass in Specimen B compared to Specimen A, which is more efficient in concentrating stress waves into the base material. If the foil is added, these stresses become tensile in nature and reach considerable values of 120.29±14.15 and 143.40±11.05 MPa (Specimens C and D). This is in contrast to Specimen A and particularly Specimen B. This effect can be attributed to two effects; a possible existence of gaps between the foil and base material and the foil and the glass, as well as the burning effect and heating of the foil which had to be replaced after each pass. The thicker foil proved to be even less effective than the thinner one.

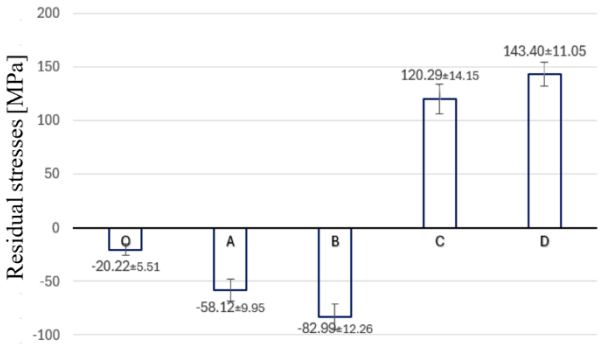


Fig. 5. Residual stresses in tested specimens: + values are tensile; - values are compression

Microhardness results are shown in Fig. 6 to 10. The values of base material (Specimen 0) are relatively consistent and reach 225.07±3.91 HV0.1, which is common for X2CrNiMo17-13-2 austenitic stainless steel [10]. A similar trend, without notable rise in microhardness in the surface layer, nor average microhardnesses was obtained in Specimens C and D, with values of 225.42±7.98 HV0.1 and 222.73±10.92 HV0.1. Although average values are similar, it can be seen that standard deviations are higher than in Specimen 0, which can be an indicator that LSP does influence some transformations in the material. Finally, in Specimens A and B, a significant rise in microhardness was measured particularly in the surface, where almost 300 HV0.1 was obtained (maximal values 275.2 and 282.7 HV0.1 in Specimen A and B). In deeper layers, values similar to Specimen 0 were obtained, which influenced not to high rise in average values up to the depth of 1.5 mm: 236.91±15.62 and 250.80±20.38 HV0.1 in Specimens A and B respectively. The depth do which the increase in microhardness in Specimens A and B can be detected is around 1 mm.

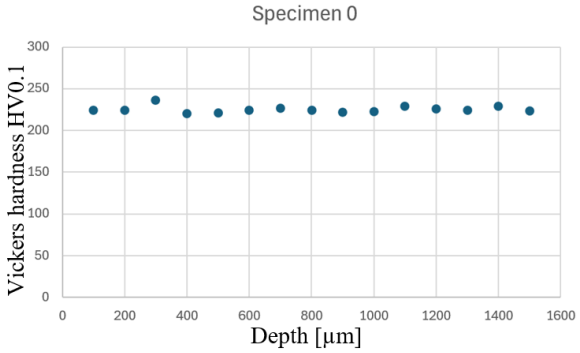


Fig. 6. Microhardness values in Specimen 0

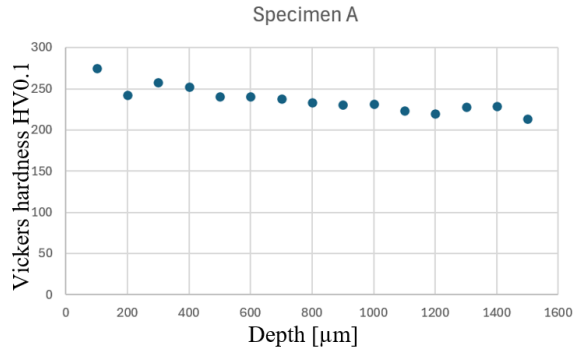


Fig. 7. Microhardness values in Specimen A

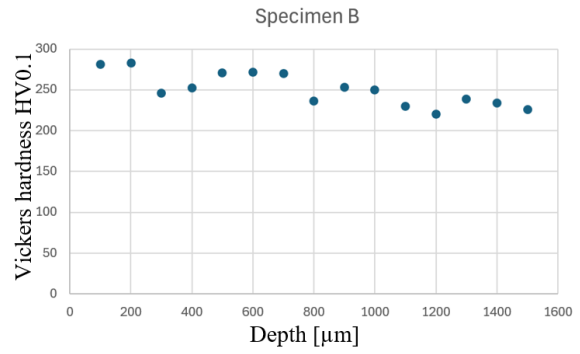


Fig. 8. Microhardness values in Specimen B

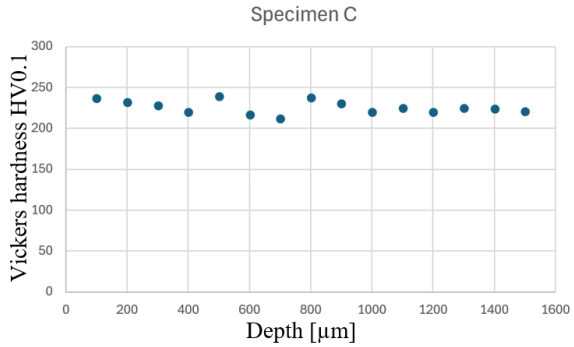


Fig. 9. Microhardness values in Specimen C

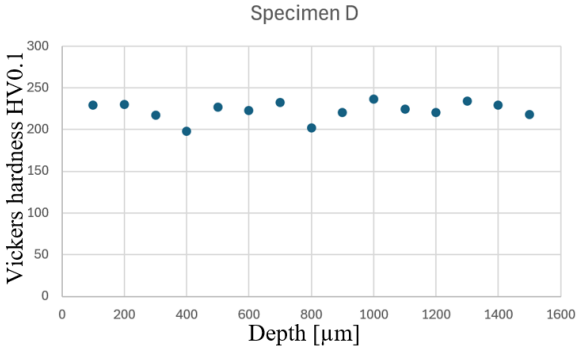


Fig. 10. Microhardness values in Specimen D

4. CONCLUSIONS

In the presented study, LSP of austenitic stainless steel was performed, with various solid confinements was performed. In accordance with the presented results, the following conclusions can be drawn:

- Commercial glass only confinement proved to be more effective than glass and foil.
- Glass confinement proved to be effective in increasing compression residual stresses, which is in contrast to the combined glass and polymer foil which induced tensile stresses.
- The main reason is the gap between the base material, foil and glass, which dissipates the laser energy.
- These results were also reflected on the microhardness, significantly increased in specimens laser treated with glass confinement.

5. REFERENCES

[1] Peyre, P., Fabbro, R. Laser shock processing: A review of the physics and applications, Optical and Quantum Electronics, Vol. 27, pp. 1213-1229, 1995.

[2] Ding K., Ye L. Laser Shock Peening: Performance and Process Simulation, Woodhead Publishing, 22, 2002.

[3] Martı-Lopeza, R., Ocanaa, E., Pineiroc, A. Asensio. Laser Peening Induced ShockWaves and Cavitation Bubbles in Water Studied by Optical Schlieren Visualization, Physics Procedia, Vol. 12, pp.442-451, 2011.

[4] Claudia, P., Glaser, D. Bedekar, R.D. Water Confinement Influences on the Laser Shock

Peening process Conference: Proceedings of the 30th International Congress on High-Speed Imaging and Photonics (ICHSIP30), At: CSIR International Conference Centre, Pretoria, South Africa, Volume: 978-0-620-56214-0.
[5] Sandmann, P., Keller, S., Kashaev, N., Ghouse, S., Hooper, P.A., Klusemann, B., Davies, C.M. Influence of laser shock peening on the residual stresses in additively manufactured 316L by Laser Powder Bed Fusion: A combined experimental–numerical study, Additive Manufacturing, Vol. 60, Part A, 103204, 2022.
[6] Wu, X., Duan, Z.,Song, H., Wei, Y., Wang, X., Huang C., Shock pressure induced by glass-confined laser shock peening: Experiments, modeling and simulation, Journal of Applied Physics, Vol. 110, 053112, 2011.
[7] Hong, X., Wang, S., Guo, D., Wu, H., Wang, J., Dai, Y., Xia, X., Xie, Y. Confining medium and absorptive overlay: Their effects on a laser-induced shock wave. Optics and Lasers in Engineering, Vol.29, pp. 447–455, 1998.
[8] Le Bras, C., Rondepierre, A., Seddik, R., Scius-Bertrand, M., Rouchausse, Y., Videau, L.; Fayolle, B., Gervais, M., Morin, L., Valadon, S. Laser Shock Peening: Toward the Use of Pliable Solid Polymers for Confinement. Metals Vol. 9, 793, 2019.
[9] Kalentics, N., Ortega Varela de Seijas M., Griffiths, S., Leinenbach, C., Logé, R.E., 3D laser shock peening – A new method for improving fatigue properties of selective laser melted parts, Additive Manufacturing, Vol.33, 101112, 2020.
[10] Zahoor, S., Qaiser Saleem, M., Abdul-Kader, W., Ishfaq, K., Shehzad, A., Ghani H.U., Hussain, A., Usman, M., Dawood, M., Improving surface integrity aspects of AISI 316L in the context, of bioimplant applications, The International Journal of Advanced Manufacturing Technology, Vol. 105, pp. 2857–2867, 2019.

FUNDING
This research has received funding from the regional project funded by the Provincial Secretary for Higher Education and Scientific Research, Vojvodina, Serbia with grant agreement no. 000838124 2024 09418 003 000 000 001 04 003. Also, this research has been supported by the Ministry of Science, Technological Development and Innovation (Contract No. 451-03-65/2024-03/200156) and the Faculty of Technical Sciences, University of Novi Sad through project "Scientific and Artistic Research Work of Researchers in Teaching and Associate Positions at the Faculty of Technical Sciences, University of Novi Sad" (No. 01-3394/1).

ACKNOWLEDGMENTS
The authors gratefully acknowledge research support by the project entitled "Interdisciplinarity in Materials Science and Joining Technologies" from the Department of Production Engineering, Faculty of Technical Sciences Novi Sad, Serbia.

Authors:
MSc Mirjana Trivkovic, BSc Nikola Maksimovic, MSc Milan Pecanac, BSc Nikolina Stojisic, PhD Miroslav Dramicanin, PhD Dragan Rajnovic, PhD Sebastian Balos, University of Novi Sad, Faculty of Technical Sciences, Trg Dositeja Obradovica 6, 21000 Novi Sad, Serbia, Phone.: +381 21 485-2055.
E-mail: mirjana.trivkovic@uns.ac.rs; maksimovic.nikola@uns.ac.rs; pecanac.milan@uns.ac.rs; nikolina.stojisic@uns.ac.rs; dramicanin@uns.ac.rs; draganr@uns.ac.rs; sebab@uns.ac.rs

MMA 2024 FLEXIBLE TECHNOLOGIES

15th INTERNATIONAL SCIENTIFIC CONFERENCE
NOVI SAD, SERBIA, SEPTEMBER 24-26, 2024

Original research paper https://doi.org/10.24867/MMA-2024-05-007

Vilotić, M., Dačević, N., Li, Y., Rynkovskaya, M., Alexandrov, S.

THE PREDICTION OF A STRAIN STATE IN THE MULTISTAGE SEVERE PLASTIC DEFORMATION

Abstract: *Cold metal forming processes cause specific changes in the material, leading to material strengthening and improved mechanical properties, but accompanied by a reduction in plasticity. In most forming processes, such as forging, drawing, rolling, and bending, the material's crystal grain size undergoes a slight change. For achieving significant property improvement through forming, it is necessary to substantially refine the grain, i.e., to create a submicron microstructure. It is possible to create such a microstructure through severe plastic deformation processes. The processes typically involve multiple stages, resulting in very high total effective strain. The new severe plastic deformation process is predicted using strain calculation through numerical simulation methods. The prediction is then experimentally verified. This paper outlines the results of the prediction and experimental validation of the strain state during multistage upsetting of a prismatic sample using V-shaped dies.*

Key words: *Severe plastic deformation, multistage upsetting, strain state, numerical simulation, experiment*

1. INTRODUCTION

Severe plastic deformation (SPD) is a metal forming process that creates ultrafine microstructure [1]. Valiev [2] formulated three essential conditions necessary for the creation of a fine-grained structure using SPD: (1) extremely high values of effective strain must not cause critical defects or cracks in the material, (2) the fine-grained structure must have high-angle grain boundaries, and (3) the structure must be uniform throughout the entire volume of the workpiece. Additionally, SPD processes should be carried out at a relatively low temperature and under high hydrostatic pressure conditions [2].

There are many different SPD methods [3]. Major among them are High-pressure torsion (HPT), Equal channel angular pressing (ECAP), Repetitive corrugation and straightening (RCS), Caliber rolling (CAROL), Multi-directional forging (MDF), Cyclic extrusion and compression (CEC), Twist extrusion (TE), and others. Other methods combine the principles of various SPD methods. Different criteria can be used to categorize these methods. One criterion is the shape of the workpiece, which can be either bulk or sheet metal, and another is how the load is applied to the workpiece – through upsetting (compression) or torsion, while the third criterion can be the continuity of the process, which can be cyclic or continuous.

To achieve the desired effects of severe plastic deformation, it is crucial to employ reliable methods for determining the total effective strain in the entire volume of the formed workpiece during the design phase. Numerical simulation methods based on the finite element method are utilized for this purpose.

This paper presents the results of determining the strain state in the workpiece during multistage upsetting of a prismatic workpiece using a V-shape dies (Fig. 1).

A billet with a square cross-section of a certain length is placed between two identical V-shape dies (Fig. 1a). The first upsetting stage begins with the upper tool's downward movement. The process continues until the dies are fully closed (Fig. 1b).

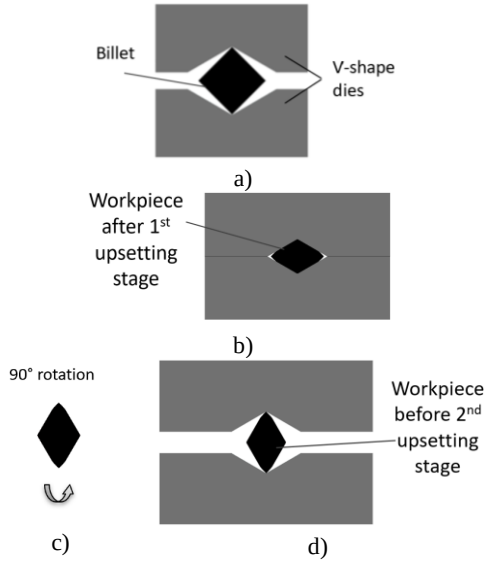


Fig. 1. Severe plastic deformation – multistage upsetting by V-shape dies: a) first stage – the beginning of the upsetting process, b) end of the first stage, c) workpiece rotation for 90° around the longitudinal axis, d) the die and workpiece at the beginning of the second (or n-th) upsetting stage [4]

After the first upsetting stage, the workpiece is removed from the dies, rotated 90° relative to the longitudinal axis (Fig. 1c), and then reinserted into the dies (Fig. 1d). Finally, the second and subsequent stages of upsetting can begin. Initial assessment of the strain state (and other process parameters) in the described multistage upsetting process was carried out using numerical simulation methods by finite element method (FEM), and the verification of these results was performed experimentally.

Experimental determination of the strain state at the

frontal (free) surface of the sample was conducted based on the change in the geometry (dimensions) of the grid elements applied to the billet (Fig. 2).

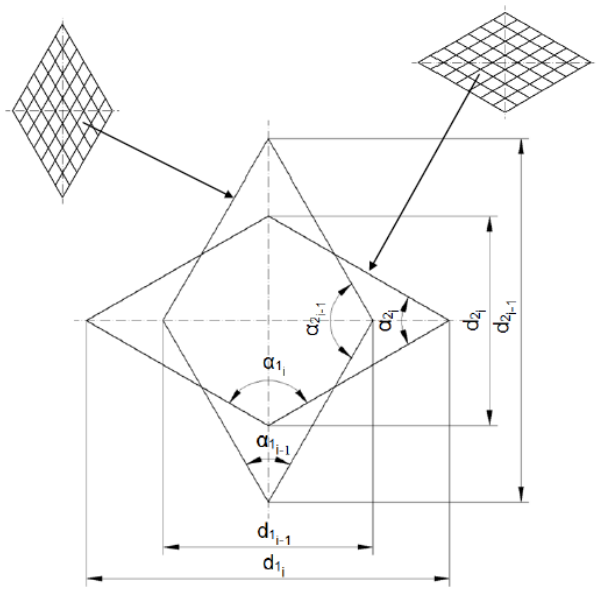


Fig. 2. The change of grid and cell shape between two upsetting stages [5]

To calculate the strains on the sample's frontal surface, a 2 × 2 mm grid was applied to the billet. The grid and its diagonals were scanned after each upsetting stage.

The components of logarithmic strain in the n-th stage were calculated using the length of the cell diagonals (Fig. 2) with the following formulas:

$$\varphi_{1i} = \ln \frac{d_{1i}}{d_{1i-1}} \quad (1)$$

$$\varphi_{2i} = \ln \frac{d_{2i}}{d_{2i-1}} \quad (2)$$

$$\varphi_{3i} = -\left(\varphi_{1i} + \varphi_{2i}\right) \quad (3)$$

The effective strain was calculated using the equation 4:

$$\varphi_{ei} = \frac{\sqrt{2}}{3}\sqrt{\left(\varphi_{1i} - \varphi_{2i}\right)^2 + \left(\varphi_{2i} - \varphi_{3i}\right)^2 + \left(\varphi_{3i} - \varphi_{1i}\right)^2} \quad (4)$$

The total strain per cell through the entire upsetting process is found as a sum of the strains at each upsetting stage (equation 5):

$$\varphi_e = \Sigma \varphi_{ei} \quad (5)$$

2. THE RESULTS OF NUMERICAL ANALYSIS AND EXPERIMENTAL VERIFICATION OF THE STRAIN STATE

The strain state of a C15 prismatic steel sample, with initial dimensions of 14 × 14 × 70 mm, during multistage upsetting was determined for 18 stages.

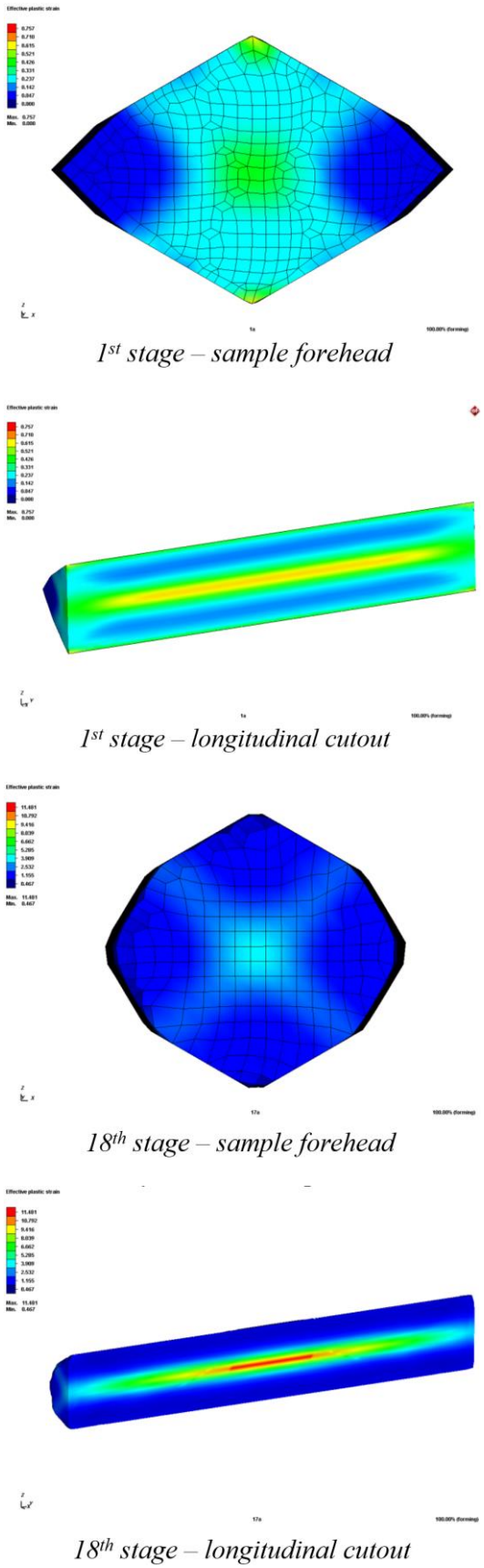


Fig. 3. Strain state at multistage upsetting obtained through numerical simulations [5]

The strain state was first obtained numerically and then experimentally. Part of the results are presented below.

To illustrate the potentials of numerical simulation

by Simufact.Forming V12, the results of predicting the strain state in the first and final upsetting stage by V-shape dies are presented in Fig. 3. A 3D simulation was set up for a rigid dies and deformable workpiece at room temperature. The friction factor between the dies and workpiece was m = 0.25. The size of a hexahedral element was about 0.8 mm, and 30000 elements were used to approximate the geometry of the workpiece. Ram speed was 1 mm/s. The flow curve of the workpiece material steel C15E EN 10084 (Č.1221 JUS) was obtained experimentally by the Rastegaev method:

$$k = 698,6841 \cdot \varphi_e^{0,1723} \left[MPa \right] \qquad (6)$$

The numerical simulation results were verified experimentally by calculating strains on the sample frontal surface with a grid applied (Fig. 4).

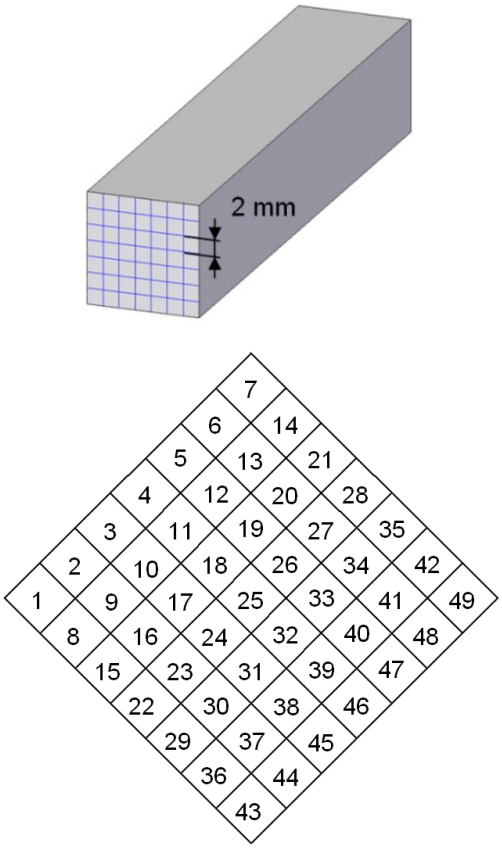


Fig. 4. Initial grid at the frontal surface: (a) grid dimensions, (b) position of grid cells [5]

Strain components and the total effective strain were calculated using measured diagonals at individual cells (Fig. 4) by equations 1, 2, 3, and 4. To illustrate the results of the experimental determination of effective strain, values for the first two (1 and 2) and the last two (17 and 18) upsetting stages are presented in Fig. 5.

Fig. 6 compares the effective strain values calculated by numerical simulation (right) and experimentally (left) for different upsetting stages (from 1 to 18). Fig. 7 displays the effective strain values in the central zone of the sample's free surface, where the highest values are observed.

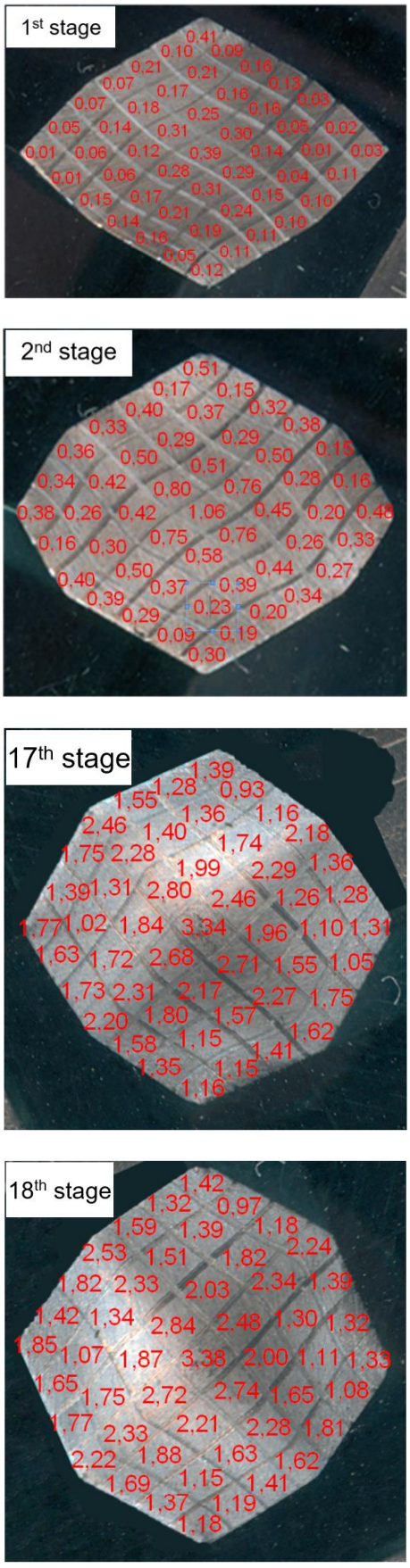


Fig. 5. Total effective strain for stages 1, 2, 17, and 18 [5]

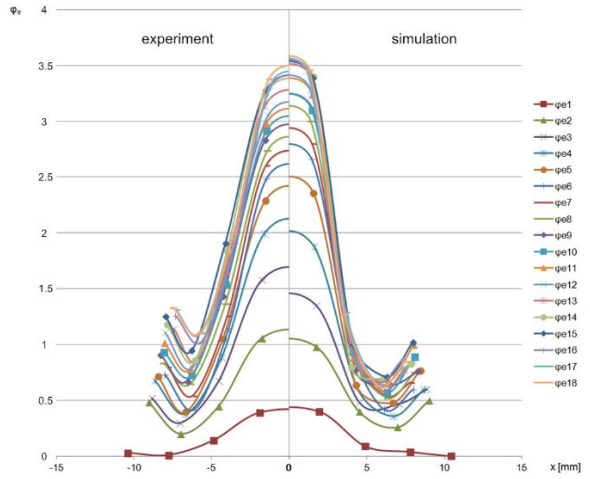


Fig. 6. Effective strain at the sample free surface calculated by numerical simulation (right) and experimentally (left) [5]

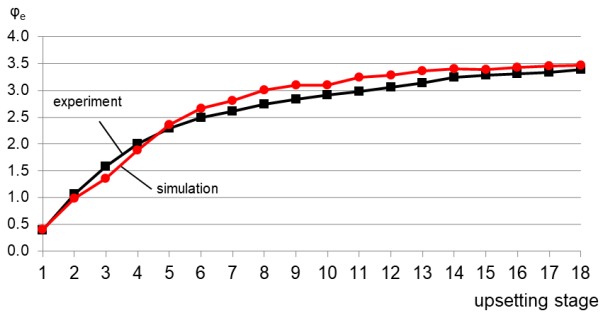


Fig. 7. Effective strain at the sample free surface calculated by numerical simulation and experimentally [5]

3. DISCUSSION

The amount of effective strain imposed through the upsetting process is the foundation for indicating the possibility of creating an ultrafine microstructure in the material and improving the mechanical properties of the produced parts. Therefore, determining the strain state is very important for SPD processes.

Numerical simulation of the multistage upsetting process of a prismatic sample by V-shape dies was used in the development step of this process to evaluate whether it meets the criteria of severe plastic deformation. The results of this analysis confirmed that the effective strain in the cross-sections of the sample is partially uneven. At the same time, it is more uniform along the longitudinal axis of the sample (Fig. 3). In the central zone of the sample with a diameter of about 6 mm, the effective strain is more uniform, and its highest value is 3.5, which indicates that the multistage upsetting process of the prismatic sample using V-shape dies meets the requirements of severe plastic deformation.

The results of the experimental determination of effective strain in the multistage upsetting process of the prismatic sample by V-shape dies using the grid measurement method also confirmed strain unevenness on the sample's frontal surface. The maximum value of effective strain is present in the central area of the frontal surface and is slightly lower than the value obtained by numerical simulation ($\varphi_{ie} < 3.56$). Additionally, the data from the experimental determination of strains served to consider the reliability of the numerical simulation method in predicting the strain state. The difference between the results of the applied methods is illustrated in the diagram in Fig. 6 and Fig. 7, which shows a high correlation between the change in effective strain in the central zone of the sample's frontal surface.

4. CONCLUSIONS

The results of effective strain obtained through numerical simulations and experiments have shown that the process of multistage upsetting of a prismatic sample using V-shape dies belongs to the category of severe plastic deformation processes. It is particularly important that this conclusion was reached during the preliminary phase of the process design through the application of numerical simulation methods.

The application of numerical simulations in metal forming provides the design of optimal technological processes and the reduction of production costs.

5. REFERENCES

[1] Segal, V.: *Materials processing by simple shear*, Materials Science and Engineering: A, Vol. 197, pp. 157-164, 1995.

[2] Valiev, R.Z., Islamgaliev, R.K., Alexandrov, I.V.: *Bulk nanostructured materials from severe plastic deformation*, Progress in Materials Science, Vol. 45, pp. 103-189, 2000.

[3] Estrin, Y., Vinogradov, A.: *Extreme grain refinement by severe plastic deformation: A wealth of challenging science*, Acta Materialia, Vol. 61, pp. 782-817, 2013.

[4] Vilotic, M., Sidjanin, L., Alexandrov, S., Lang, L.: *Effect of Rotation of the Principal Stress Axes Relative to the Material on the Evolution of Material Properties in Severe Plastic Deformation Processes*, Materials, Vol. 13, pp. 4667, 2020.

[5] Vilotic, M.: *Severe Plastic Deformation in Material Multistage Upsetting Processes*, PhD thesis, University of Novi Sad, Faculty of Technical Sciences, 2016.

Authors:

Professor Marko Vilotić PhD, assistant Nemanja Dačević MSc, University of Novi Sad, Faculty of Technical Sciences, Trg Dositeja Obradovica 6, 21000 Novi Sad, Serbia, Phone.: +381 21 485-24-76.
E-mail: markovil@uns.ac.rs; nemanja.dacevic@gmail.com

Professor Yong Li PhD, Professor Sergei Alexandrov, PhD, Beihang University, School of Mechanical Engineering and Automation, 39 Xueyuan Road, Haidian District, Beijing, China, Phone.: +86 10 82-317-114.
E-mail:liyong19@buaa.edu.cn; sergei_alexandrov@spartak.ru

Professor Marina Rynkovskaya PhD, associate professor, Department of Civil Engineering, RUDN University, 6 Miklukho-Maklaya St, Moscow, 117198, Russia. E-mail: rynkovskaya-mi@rudn.ru

MMA 2024
FLEXIBLE TECHNOLOGIES

15th INTERNATIONAL SCIENTIFIC CONFERENCE
NOVI SAD, SERBIA, SEPTEMBER 24-26, 2024

Original research paper https://doi.org/10.24867/MMA-2024-05-008

Petrovic, B., Pecanac, M., Hauck, A., Stojisic, N., Savkovic, B., Rajnovic, D., Balos S.

RESISTANCE ELEMENT WELDING OF AW6060 AND STRUCTURAL STEEL

Abstract: *Resistance Element Welding (REW) is a relatively new welding process that is used to join dissimilar materials, by using the basic principle of resistance welding, combined with the addition of the element that forms the mechanical joint with the base material that is more difficult to weld. One of the most attractive applications is the welding of aluminium alloys and steel, which, currently, represent the mainstay of automotive industry in terms of car body fabrication. For this purpose, AW6060 aluminium combined with structural steel is of great significance, where structural steel would be used for the parts that are designed to absorb kinetic energy of the eventual crash, while aluminium alloy parts save weight. In this research, AW6060 with structural steel was joined by REW, using one, two and three elements, with three different welding times, where shear testing, microhardness and metallographic examination were performed to test the welds.*

Key words: *welding, dissimilar materials, characterization*

1. INTRODUCTION

Automotive industry currently relies predominantly on structural steels and aluminium alloys, usually aluminium-silicon-magnesium (Al-Si-Mg, AW6000 series, such as AW6060). While steels are traditional materials for car bodies, aluminium alloys are only recently used on a larger scale by a relatively limited number of car brands, in a strive to reduce the weight of cars. This limitation is understandable, since aluminium alloys are several times more expensive than steels, which strongly reflects on the overall cost of the car, with adverse effect on competitiveness on the market. For that reason, there is a tendency to apply both materials, steels for segments that stress crash resistance, that is, around the occupant area, while aluminium alloy for other less stressed parts [1]. Such arrangement has been hampered by the inherent difficulty of joining these two materials. Namely, the most frequently used joining method is welding, of which, electric resistance welding (ERW), or simply called resistance welding (RW) is, due to its automation potential the most attractive [2]. However, the welding of ferrous alloys and aluminium, particularly fusion welding results in the formation of ferroaluminide intermetallic compounds, which can cause a drop in mechanical properties, to the point of some considering these two materials unweldable [3]. To address this, a variation of RW, called resistance element welding (REW) appeared. This process uses elements, made of structural steel, which are mechanically attached to the aluminium alloy (or other light alloy or material (such as composites) by insertion or punching. Subsequently, resistance spot welding is performed between steel element and steel base material, Fig. 1 [4].

In this paper, AW6060 with structural steel was joined by REW, using variations in the number of elements and welding time.

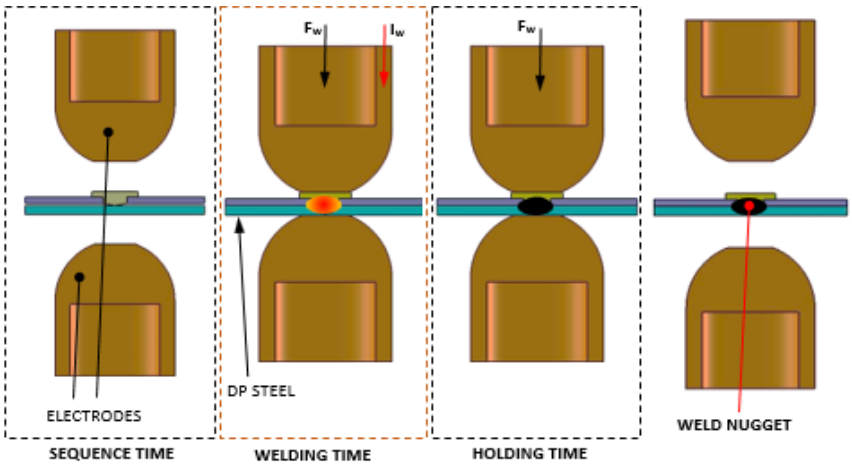


Fig. 1. Basic scheme of REW [5]

2. EXPERIMENTAL PART

Base materials used in this study are S235JR structural steel and AW6060 aluminium alloy, while elements were made of C20 carbon steel. Chemical compositions of these materials were determined by optical emission spectroscope (OES), G.N.R. MicroLab 150.

C	Si	Mn	P	S	Cr	Ni	Cu
0.07	0.18	0.55	0.003	0.003	0.018	0.03	0.04

Table 1. Chemical composition of S235JR steel, Fe-balance (mass %)

Si	Fe	Cu	Mn	Mg	Cr	Zn
0.51	0.20	0.043	0.056	0.4	0.011	0.028

Table 2. Chemical composition of AW 6060 aluminium alloy, Al-balance (mass. %)

C	Si	Mn	P	S	Cr	Ni	Cu
0.19	0.14	0.52	0.004	0.004	0.052	0.05	0.03

Table 3. Chemical composition of C20 steel, Fe-balance (mass %)

The scheme showing the overlapping weld and base material dimensions is shown in Fig. 2. In Fig. 3, element shape and dimensions are presented. Before welding, one, two or three elements were inserted in the pre-drilled aluminium sheets, 2 mm thick. After that, spot welding was performed on Schlatter T3111.5 machine, with 50, 60 and 70 ms current duration time.

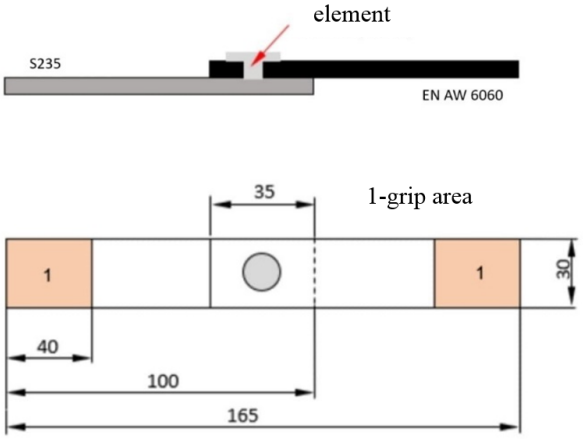


Fig. 2. Weld shape and base material dimensions

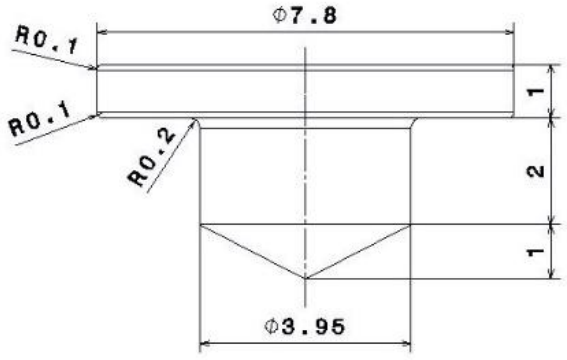


Fig. 3. Element shape and dimensions

Overall, eight specimens were welded, and specimens were designated in Roman numbers, I to VIII, Fig. 4. To reduce the number of specimens, experimental plan was devised, thoroughly explained in [6].

Characterisation was performed in several aspects: shear, microhardness and metallographic tests. Shear testing was done in specimens having dimensions as shown in Fig. 2. Testing was done using VEB 5/91 tensile testing machine. Microhardness was tested on Wilson Tukon 1102 device, using 100 g loading. Finally, microstructures were determined after a full metallographic preparation on Struers laboratory. Preparation consisted of cutting, mounting, grinding (P100 to P2000 grit abrasive papers), polishing (diamond suspensions 6, 3, 1 and ¼ μm) and etching with 3 % Nital (3 % HNO_3 in ethanol). Microstructure examination was done on Leitz Orthoplan light microscope.

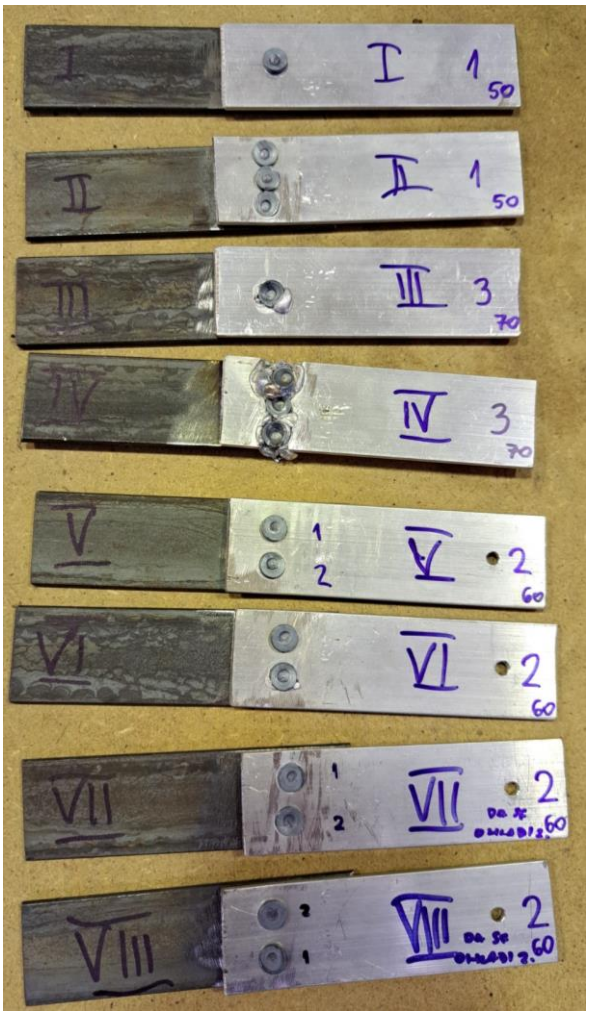


Fig. 4. Welded specimens marked by numbers I to VIII

3. RESULTS AND DISCUSSION

Tensile testing of welded specimens resulted in various modes of fracture, Fig. 5, while tensile testing results are given in Table 4. It can be seen that there are three modes of fracture: pulling the element (specimen III), fracture of aluminium alloy (specimen IV) and fracture at the weld. Data given in Table 4 show that the highest tensile force was obtained for the specimen III, fractured by pulling out the element from the aluminium alloy.

Microhardness testing results of the representative specimen III are shown in Fig. 6. It can be seen that the lowest hardness is obtained in the base material (structural steel), followed by steel/HAZ region and HAZ, spot and the element. This is the result of a

considerably higher carbon content in the element, which influences the rise in microhardness. The values reach almost 300 HV0.1, which is most probably higher than 300 HV10, due to the presence of reversed indentation size effect (RISE), which is inherent to metallic materials [7]. Values over 300 HV10 are the sign of the sporadic occurrence of martensite in the material, which is the result of rapid heating into austenitic area and rapid subsequent cooling, as the result of materials acting as heat sinks, particularly aluminium alloy. Finally, macro and microstructure analyses are given in Figs. 7 and 8.



Fig. 5. Tensile tested specimens

Specimen	Fm [N]
I	626.2
II	222.2
III	3555.2
IV	621.15
V	1939.2
VI	1494.8
VII	2706.8
VIII	1393.8

Table 4. Tensile testing results, maximum tensile forces

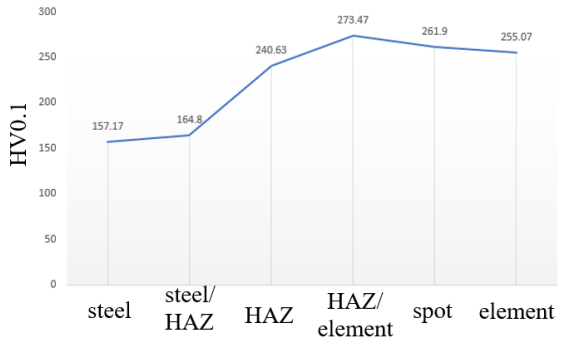


Fig. 6. Microhardness testing results

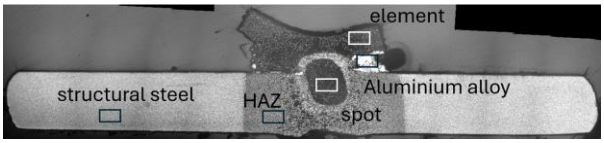


Fig. 7. Macro image of the welded specimen III

Microstructure of the base metal (structural steel) if ferrite-pearlite, typical for rolled material, Fig. 8a. This microstructure is in agreement with chemical composition of S235JR shown in Table 1.

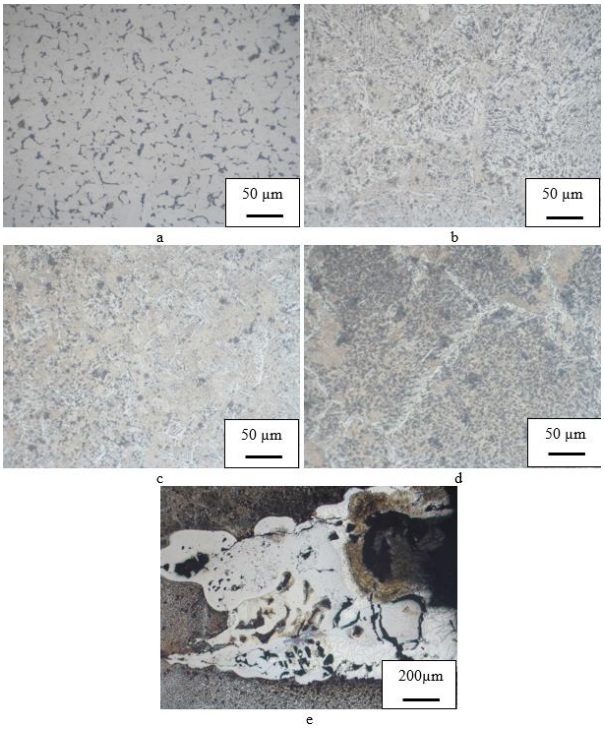


Fig. 8. Microstructures of areas shown in Fig. 7: a) structural steel; b) HAZ; c) spot; d) element; e) aluminium alloy

Fig. 8b shows the microstructure of HAZ, which contains various types of ferrite; Widmanstaetten, acicular and polygonal.

The spot is remelted, also with Widmanstaetten and acicular ferrite, Fig. 8c.

Finally, the element shows signs of overheating, with significant amount of Widmanstaetten ferrite especially at the previous austenitic grain boundaries. Within them are various microstructures: ferrite, pearlite and bainite. Also, within HAZ, spot and element, there could be islands of martensite, which is indicated by a relatively high hardnesses shown in Fig. 6.

In Fig. 8e the melted and subsequently solidified aluminium alloy coming from the other base metal is shown. Solidification is clearly shown by the un-homogenous morphology, especially the needle-like darker phases near the fracture to the right. Besides apparent segregation, there are cracks and gas pores present, which makes the material weaker and prone to failing, in this case, pulling the element out of the aluminium alloy base metal. In specimen IV, the fracture of aluminium alloy occurred due to this effect as well. The presence of three elements and melted and solidified

aluminium alloy containing cracks, pores and segregation instead of rolled heat-treated microstructure of AW6060 alloy.

4. CONCLUSIONS

Based on the results of this work and considering its limitations, the following conclusions can be drawn:

- Tensile strength is primarily influenced by welding time, where a longer time and a single element give the highest tensile force.
- Two or three elements give a relatively low tensile forces since there is considerable overheating of the aluminium alloy, its melting and solidification with cracks and pores.
- Fracture modes are related to pull-out of the element, aluminium alloy base material fracture and most frequently, fracture at the welds. The latter can be avoided with longer elements that will improve the quality of welded spots.
- Obtaining a relatively high hardness in HAZ and elements is of a secondary importance, meaning that a lower carbon steel for fabrication of elements can be used, improving the weldability and improving the overall weld quality.

5. REFERENCES

[1] Hirsch, J.R., Recent development in aluminium for automotive applications, Transactions of Nonferrous Metals Society of China Vol. 24, pp. 1995−2002, 2014.

[2] Banga, H.K., Kalra, P., Kumar, R., Singh, S., Pruncu, C.I., Optimization of the cycle time of robotics resistance spot welding for automotive applications, Journal of Advanced Manufacturing Processes, Vol.3, 10084, 2023.

[3] Kah, P., Rajan, R., Martikainen, J., Suoranta, R., Investigation of weld defects in friction-stir welding and fusion welding of aluminium alloys, International Journal of Mechanical and Materials Engineering, Vol.10, 26, 2016.

[4] Đurić, A, Milčić, D., Klobčar, D., Marković, M., Milčić, M., The analysis of the occurrence of defects and discontinuities in the REW weld of DP steel and alumionium alloy, Proceedings of the 2nd International scientific-professional conference SBW2023 "Engineering technologies in manufacturing technologies, constructions and products SBW 2023", pp. 158-166, Slavonski Brod, 26. i 27. 04. 2023. and Požega 28. 04. 2023.

[5] Đurić, A, Milčić, D., Burzić, Z, Klobčar, D., Milčić, M., Marković, B., Krstić, V., Microstructure and Fatigue Properties of Resistance Element Welded Joints of DP500 Steel and AW 5754 H22 Aluminum Alloy, Crystals, Vol. 12, No.2, 258, 2022.

[6] Petrović B., Zavarivanje električnim otporom sa elementima, Master rad, Fakultet tehničkih nauka, 2024.

[7] Balos, S., Pecanac, M., Trivkovic, M., Bojic, S., Hanus, P., Load-Independent Hardness and Indentation Size Effect in Iron Aluminides. Materials, Vol. 17, 2107, 2024.

FUNDING

This research has been supported by the Ministry of Science, Technological Development and Innovation (Contract No. 451-03-65/2024-03/200156) and the Faculty of Technical Sciences, University of Novi Sad through project "Scientific and Artistic Research Work of Researchers in Teaching and Associate Positions at the Faculty of Technical Sciences, University of Novi Sad" (No. 01-3394/1).

ACKNOWLEDGMENTS

The authors gratefully acknowledge research support by the project entitled "Interdisciplinarity in Materials Science and Joining Technologies" from the Department of Production Engineering, Faculty of Technical Sciences Novi Sad, Serbia.

Authors:

BSc Boban Petrovic, Bulevar company, Micurinova 30, 21000 Novi Sad, Serbia, Phone: 0381 21 544244
E-mail: boban.petrovic@bulevar-company.rs

MSc Milan Pecanac, BSc Albert Hauck, BSc Nikolina Stojisic, PhD Borislav Savkovic, PhD Dragan Rajnovic, PhD Sebastian Balos, University of Novi Sad, Faculty of Technical Sciences, Trg Dositeja Obradovica 6, 21000 Novi Sad, Serbia, Phone.: +381 21 485-2055.
E-mail: pecanac.milan@uns.ac.rs; albert.hauck@uns.ac.rs; nikolina.stojisic@uns.ac.rs; savkovic@uns.ac.rs; draganr@uns.ac.rs, sebab@uns.ac.rs

MMA 2024
FLEXIBLE TECHNOLOGIES

15th INTERNATIONAL SCIENTIFIC CONFERENCE
NOVI SAD, SERBIA, SEPTEMBER 24-26, 2024

Original research paper https://doi.org/10.24867/MMA-2024-05-009

Kostić, N., Ranđelović, S., Perić, M.

FEM SIMULATION AND VERIFICATION OF MECHANICAL PROPERTIES OF NONSYMMETRIC HOT FORGED PART

Abstract: *Hot forged parts are required to have high mechanical properties due to usage of those products as elements of machine that are under high loads and are required to be reliable and durable, making hot forged parts indispensable in various industrial applications. To obtain the desired geometry of forged part goes through high level of plastic deformation so it can fill the most outer parts of die cavities in its final stage. Hot forging of nonsymmetric parts requires different flow of material so it can fill die cavities and as such represents challenge to obtain desired material properties of part. Deformation behavior of material during hot forging is evaluated by finite element analysis (FEA) and arise that have shown the elevated levels of stress/strain rate are observed. Hardnes test of material at cross section in different areas of material flow are preformed to determine deformation behavior.*
Key words: *Hot forging, FEM, mechanical properties, hardness*

1. INTRODUCTION

Hot forging is a deformation process in which the work is compressed between two dies used to make a variety of high-strength components. Hot forging is one of the most performed forging type, because of complex geometry of the forge parts that require significant deformation and need to reduce strength during the process and increase durability of the material of forged parts.

During the planning of hot forging process principles and limitations of process must be taken into consideration. Die design plays a crucial role in the success of forging operations. During die design parts such as fillet and corner radii dictate how material flow with the purpose to fill die cavities in that way not to cause internal material defects such as inhomogeneity and laps of material of forged parts. Fillet and corner radius dimension are directing material flow by increasing radius in area that needs smoother transition of material and by reducing radius limits the flow but increases stresses. Pressure in die is controlled by designing a flash land and gutter into die. The land determines the surface area along which lateral flow of metal occurs, thereby controlling the pressure increase inside the die. The gutter permits excess metal to escape without causing the forging load to reach extreme values [1,2].

FEM simulations in hot metal forming have proven to have good results in prediction of forming loads, stresses and strain that can help to significantly improve product quality such as height strength and production rate of parts and decrease cost of production and material loss. Results that are obtained from FEA simulation such as effective stress, strain rate, material flow and temperature distribution can be used to predict mechanical properties of final products. Deformation flow pattern of grain can be examined by strain behavior obtained by FEM simulation. Large variation of strain is represented by reduced homogeneity and hence higher uniformity of grain refinement that is achieved [3]. Folds or laps are one of the most come defect that can occur during material flow on the sharp corners of the die cavity that can weaken the structural integrity of forged components and crate stress concentration points that lead to weak points in structure that lead to failure of component. FEM simulation can be used to observe complex material flow and predict material folds and be bases for the optimization of tool geometry so that laps do not occur during any steps of hot forging process [4,5].

Forging process at different temperatures and stage, the forged part shows various characteristics through its volume because the microstructure, temperature, and strain are not the same. Forged part especially non symmetric parts are submitted to a different deformation pattern so it can fill most outer die cavities and to grain fragmentation, to the stretching of ductile inclusions, and to the alignment of hard inclusions, resulting in heterogeneous grain flow patterns. The flow pattern predicted by FEM simulation can show heterogeneous material properties through material volume. Variances in the microstructure of the obtain forged part is indicated by differences in hardness values of hot forged parts material. By conducting Brinell hardness testing on forged parts, forging process can be better interpreted by hardness variations and make informed decisions regarding obtained material quality of hot forge part and its process [6,7].

2. FEM ANALYSIS OF NONSYMMETRIC HOT FORGING PART

Hot forging die (Fig. 1) has a negative shape of forge part which plays a decisive role in the process of shaping workpiece into the shape of forge part. The tool simulation model is generated as a one-piece rigid volume which will reduce computation time of simulation and have minimal impact on accuracy of the simulation results. The temperature of the dies was assumed at 200 °C, and material of dies H13 6408.



Fig. 1. Die design of non-isometric hot forging tool

The work piece is deformable in the simulation, and it is cylindrical in shape with a diameter of 65 mm and a length of 75 mm, made of steel S355J2. Workpiece temperature was assumed to be 1100 °C, and due to high temperature difference between workpiece and lower die in the contact zone program assume drop in temperature in some arias to 933.623 °C, indicating nonhemogenic of temperature in workpiece volume. The simulation was undertaken at a room temperature of 20 °C. The mechanical characteristics of the selected steel are given in the Table 1.

D [mm]	to 3mm	3-100	100-150
R_m [N/mm^2]	510-680	470-630	450-600
$R_{0.2}$ [N/mm^2]	355	320	280

Table 1. Mechanical characteristics of the selected steel S355J2

During Hot forging material undergoes simultaneous strengthening and softening phenomenon due material nature, which leads to certain microstructural changes and corresponding mechanical properties during process of hot forging. Those changes are considered during simulation and represented by table and figure. Flow stress is set by points, and it may depend on the temperature, accumulated strain and strain rate which is show at Table 2 [8, 11].

The values of peak stress and static flow stress increase with the increase of the strain rate and with the decrease of the deformation temperature. The higher deformation temperature is the greater the dynamic softening, and the lower the peak stress correspondingly. The higher the strain rate is, the higher the working hardening, and the higher peak stress and flow stress correspondingly [9]. The curve change in true flow stress of at elevated temperatures of S355J2 material 1100 °C is given by the curves of hardening (Fig. 2.).

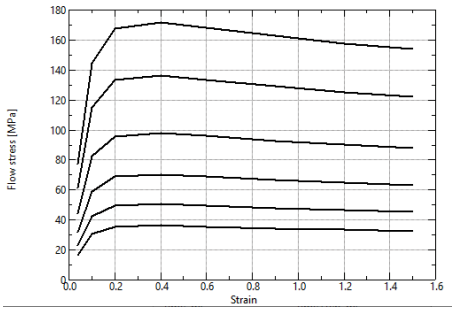


Fig. 2. Flow stress for material S355J2 on temperature 1100 °C

The lubricant used is a salt solution, which has the following characteristics: friction law according to Levanov, which coefficient is 1.25, heat transfer coefficient 45000 W/(m^{2}K), pause coefficient of 0.05, which is represented by next formula:

$$\tau = m \cdot \frac{\sigma_T}{\sqrt{3}} \cdot \left(1 - e^{-n \cdot \frac{\sigma_n}{\sigma_T}}\right) \qquad (1)$$

Levanov friction law is a generalization of Coulomb and Siebel friction models. When normal contact pressures are low, Levanov's shear stresses are close to Coulomb's ones, and when normal contact pressures are high, they are close to Siebel's shear stresses [10]. The figure below shows shear stresses versus normal contact pressure according to Siebel and Levanov friction laws (m = 0.8, σ_T = 300 MPa, n = 1.25), and as per the *Coulomb* (μ=0.4) [11].

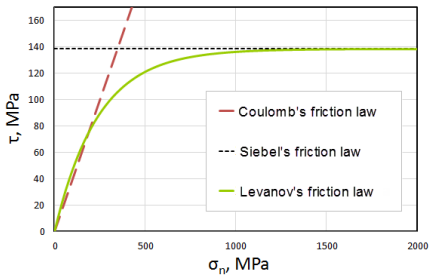


Fig. 3. Shear stresses versus normal contact pressure according to Siebel, Levanov and Coulomb friction law

		Strain-rate [1/s]					
	T = 1100 °C	0.01	0.1	1	10	100	500
Strain	0.03978087	16.42	22.85	31.79	44.24	61.56	77.56
	0.099820335	30.63	42.62	59.3	82.52	114.83	144.66
	0.199671195	35.53	49.44	68.8	95.74	133.23	167.84
	0.400477567	36.3	50.51	70.29	97.81	136.11	171.47
	0.599656837	35.6	49.54	68.94	95.93	133.48	168.16
	0.898942094	34.42	47.9	66.66	92.76	129.07	162.6
	1.200645014	33.41	46.5	64.7	90.03	125.28	157.83
	1.500583508	32.57	45.32	63.07	87.76	122.12	153.85

Table 2. Flow stress at 1100 °C of S355J2 material

3. FEM ANALYSIS RESULTS

The dies load increases evenly and slightly up to 6×10^{-3} s of the forming process at the amounts to 0.66 MN, after which it increases rapidly, until the end of the process when reaches its maximum value of 11.72 MN at the end of the forging process. Rapid increase in forging load can be attributed to the occurrence of height

level of deformation, work harding as the dominant deformation mechanism and increasing of interfacial friction between the workpiece and the die [12]. A plot of forging die load versus time is shown at Fig 4.

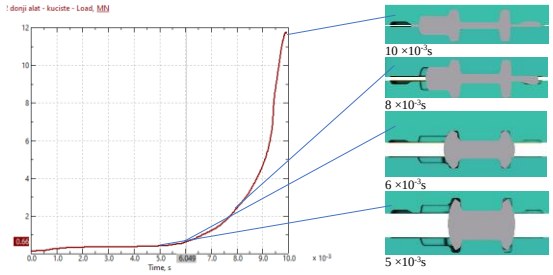


Fig. 4. Die load chart of hot forging

Based on the results obtained, it can be concluded that concentration of elevated stresses are in areas of flash formation and sudden changes in die geometry.

The regions where flash forms experience high stress due to excessive flow of material in its final stages as it interacts with the die surfaces leading to stress concentrations in these regions as well as material flows and fills out the die cavity can contribute to elevated stresses in the regions where flash is forming. Based on the obtained results, the maximum stress appears at the place where the flash is formed, and it is 181.537 MPa.

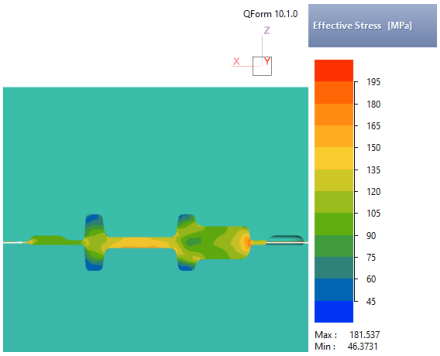


Fig. 5. Field of effective stress on the cross section of nonsymmetric hot forged part

Web part of the forging shows high stress. High level of stress in this region can be contributed to high compression rate by reducing workpiece from height of 70 mm, causing great level of deformation and high level of material flow in direction perpendicular to the parting line of forging part.

Ribs of forging are formed early stages of forging process. As material files die cavities in can be observed that in its most upper and lower parts of ribs we have occurrence of dead zone of material flow, where is observed minimum effective stress is 46.3731 MPa. As material flows in direction perpendicular to the parting line at the region of crossing for web to rib we have elevated stress of material, as material continues to flow in that direction we can observed significant drop in stress until it reaches area of transition bridge and forming of flash where we can observe a significant rise of stress in those region.

The plastic strain that occurs during hot forging proceses can be seen at Fig. 6, where the highest degree of plastic strain can be seen in the areas of the formation of the flash of the forged part and its value is is 13.4518. Areas where the flash forms experience the highest degree of plastic strain because material under significant deformation as it flows into gutter allowing it to fill the die cavity first. While in the upper areas of ribs where the material has filled the cavity of the dies the material is not in a plastic state.

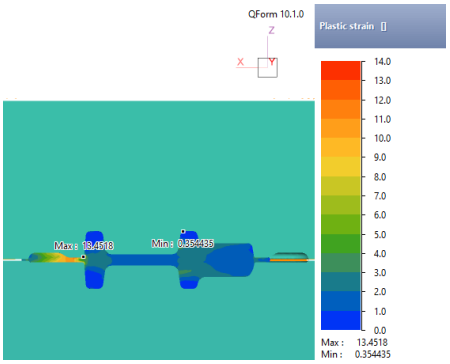


Fig. 6. Plastic strain in cross section of of nonsymmetric hot forged part

During simulation material flow has been observed in order to determine will there be any folds and there was no occurrence during any phase of simulation of hot forging. Absence of folds indicates that the material flow was unformal during simulation of deformation process. At the end of hot forging process simulation all die cavities were filled, indicating that the material has flowed properly and filled all intendent die cavities.

4. HARDNES TEST RESULTS

The Rockwell Hardness test is a widely used method due to its simplicity and effectiveness in determining the hardness of materials, and several enhancements over the years have made the test adaptable to a variety of materials making it valuable in various industries. Measurement was done in Rockwell Scale B (Hardness Symbol HRB) where indenter is pressed into the specimen using a minor load, thus seating the indenter in the material, then a major load of 100 dN is applied, causing the indenter to penetrate into the specimen a certain distance beyond its initial position. This additional penetration distance is converted into a Rockwell hardness reading by the testing machine shown in Fig. 7.



Fig. 7. The Rockwell Hardness test

Hardness measurement is performed at the approximate point of beginning, end and middle of filet region as well as along site perpendicular to the parting

line of forging part from the end region of web to the beginning of flash formation. Distance between measuring points are taken in such a way that hardening effect of material in points of measurement have no impact on obtain results. Obtained results and distribution of measuring points at cross section of hot forge part can be seen at Fig. 8.

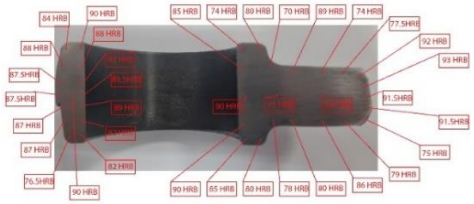


Fig. 8. Hardness of nonsymmetric hot forged part at cross section

Changes in hardness of material at the cross section of hot forged part indicates the degree of plastic deformation that's has occurred during the forging process. The parts of volume that have undergone highest degree of plastic deformation is indicated by increased hardness then the rest of forged volume and can be Sean at areas close to the end of web and at the beginning and in filet region of formation of flash. On the right side of the web region of hot forged part in area of formation of flash have tendencies of increasing of hardness of material as it gets close to transitioning bridge where the measured hardness value riches highest value of 93 HRB close to upper transition bridge. The same tendency of material hardness increase can be seen between web and rib. Area between rib and transition bridge on the right side of web are area where lowest hardness values appear as those regions have gone through lower level of deformation and FEM simulation have also shown lower stress values in those areas of material volume.

5. CONCLUSION

Hot forging is one of the commonly used technologies in metal forming industries used to get high quality near net shape products. Products obtained by hot forging technology have better mechanical characteristics than products obtained by other technologies making it indispensable in modern industries.

Software simulations today in hot forging technology is an indispensable tool that can help us to predict how material behaves during the process of forging in critical areas with relatively height accuracy.

In hot forging processes, variations in hardness can occur across different areas of the forged part due to the localized deformation, stress, and cooling rates occurring during forging. Due to high stress and deformation rates in areas such as web and flash shown at FEM simulation, occurrence of critical values are expected, and those areas cannot withstand any more deformation.

Obtained results show relative homogeneity of hardness values of material at cross section of hot forged part with no identified defects such as breaks in the material during flow, occurrence of material laps at simulation and examination physical examination of hot forged part.

6. REFERENCES

[1] T. Altan, T., Ngaile G., G. Shen: Cold and Hot Forging Fundamentals and Applications, ASM International, Materials Park, USA, 2005.

[2] Mikell P. Groover, Fundamentals of Modern Manufacturing Materials, Processes, and Systems Fifth Edition, John Wiley & Sons, Inc 2013.

[3] Wangchaichune, S., & Suranuntchai, S.: Finite Element Simulation of Hot Forging Process for KVBM Gear. Applied Mechanics and Materials, 875, 30–35, 2018.

[4] Behrens, B.-A., Nickel, R., & Stonis, M.: Simulation algorithm for the assessment and modification of multi-directional forging processes and tool geometries. Production Engineering, 6, 187–198, 2012.

[5] I. Balasundar, T. Raghu, Deformation behaviour of commercial pure copper during repetitive upsetting-extrusion (RUE) using a modified die design, Kovove Materialy, 49, 333-345, 2011.

[6] Rajendran, N., et al. "Hot Forging Die Design Optimization Using FEM Analysis for Near-Net Forming of 18CrNiMo7-6 Steel Pinion Shaft. Metals 2023, 13, 815, 2023.

[7] Wojtaszek, M., Śleboda, T., Rumiński, M., & Łuksza, J.: Design and Verification of the Parameters of Hot Forging of Ti10V2Fe3Al Alloy Compacts. Applied Mechanics and Materials, 606, 119–123, 2014.

[8] Mukherjee, M., Prahl, U., & Bleck, W.: Modelling of Microstructure and Flow Stress Evolution during Hot Forging. Steel Research International, 81, 1102–1116, 2010.

[9] SHI, R., & LIU, Z.: Hot Deformation Behavior of P92 Steel Used for Ultra-Super-Critical Power Plants. Journal of Iron and Steel Research, International, 18, 53–58, 2011.

[10] Bandini, C., Reggiani, B., Donati, L., & Tomesani, L.: Code Validation and Development of User Routines for Microstructural Prediction with Qform. Materials Today: Proceedings, 2, 4904–4914, 2015.

[11] QForm, Users Manual, V 10.1, 2021.

[12] Obiko, J. O., Mwema, F. M., & Bodunrin, M. O. (2019).Finite element simulation of X20CrMoV121 steel billet forging process using the Deform 3D software. SN Applied Sciences,doi:10.1007/s42452-019-1087-y

Authors:

PhD Nikola Kostić, PhD Saša Ranđelović, PhD Marko Perić, University of Niš, Faculty of Mechanical Engineering, Aleksandra Medvedeva 14, 18000 Niš, Serbia, Phone.: (+381 18) 588 255

E-mail: kostic94nikola@gmail.com; sasa.randjelovic@masfak.ni.ac.rs; marko.peric@masfak.ni.ac.rs

MMA 2024 FLEXIBLE TECHNOLOGIES

15th INTERNATIONAL SCIENTIFIC CONFERENCE
NOVI SAD, SERBIA, SEPTEMBER 24-26, 2024

Original research paper https://doi.org/10.24867/MMA-2024-05-010

Maksimovic, N., Hauck, A., Janjatovic, P., Pecanac, M., Savkovic, B., Rajnovic, D., Savic, V., Balos, S.

INFLUENCE OF BASE METAL ROUGHNESS ON ADHESION-JOINED ALUMINIUM ALLOY AND STEEL

Abstract: *Adhesion joining is an established, yet not fully exploited joining process that is often considerably less exploited in engineering compared to the more ubiquitous welding and brazing for structural purposes. It has considerable advantages over welding and brazing, which relate to the simplicity of application and personnel certification, joining speed and the total lack of microstructural alternation of the base material, leading to the possibility of joining virtually all materials, regardless of their properties. In this paper, epoxy, as one of the most widely used adhesives, was applied to join aluminium alloy with steel, two materials notoriously difficult to weld by conventional arc welding processes. Surface roughness was varied in both steel and aluminium alloy. It was proved that surface roughness was an important factor in producing strong welds in shear testing.*

Key words: adhesion joining, surface roughness, shear testing

1. INTRODUCTION

Adhesively bonded joints in its basic, consist of two adherents (joined components) and the adhesive between them [1]. Compared to other joining technologies, such as welding and soldering, adhesion has several advantages and drawbacks. Advantages are related to: simpler training of personnel, simple joining regardless of specimen thickness, as well as materials with good thermal conduction, coated surfaces need to be cleaned in welding, no distortion induced by heat input, vibration dampening, and no influence on the material microstructure, which, in welding, particularly of difficult to weld materials can have a detrimental effect on the weld performance. Finally, economic advantages are also significant; much lower energy consumption and lower equipment cost. On the other hand, there are certain drawbacks of adhesive bonding: relatively long cure time, and theoretically, for some materials, most commonly the most widely used structural steels, a significantly lower joint strength, particularly at relatively high temperatures and questionable durability of joints. Today, the most common type of adhesive is epoxy, due to its high strength and temperature resistance, high durability and resistance to environmental extremes, relatively low cure temperatures, easy to use and low cost. Furthermore, epoxy is suitable for various adherents, metals, ceramics, polymers and composite materials [2, 3]. As such, epoxy is suitable to be used as matrix, in a range of composite materials, usually reinforced by carbon or aramid fibers, or both. [4 - 6]. These properties of epoxy enabled its applicability in various industries: automotive, transportation, railway, civil engineering, military and aerospace. Mechanical properties of joints primarily depend on the adhesive type and its eventual modifications. One of the most prospective type of modification are nanoparticles, of which Al_2O_3 and SiO_2 have shown a relatively high improvement potential [7, 8], as well as NIMs (Nanoscale Ionic Materials) [9], which can improve bonding strength and reduce the curing time, making the adhesive more effective and easy to use in industrial conditions. However, a significant influence on the joint strength can be expected from the properties of the prepared surfaces of the adherents. As said, in case of epoxy, preparation is theoretically very simple and quick, adding to the popularity of epoxy in industrial use.

In this paper, an attempt was made to profound the knowledge base and investigate the effect of roughening of the surface of adherents, in this case, structural steel and aluminium alloy, materials notoriously difficult to weld.

2. EXPERIMENTAL PART

Adherents (base materials) used in this work were S235JR structural steel and AW6060 aluminium-silicon-magnesium alloy. Chemical compositions of adherents were tested by optical emission spectroscope (OES), G.N.R. MicroLab 150, in Materials Testing Laboratory of the Department of Production Engineering, Faculty of Technical Sciences.

C	Si	Mn	P	S	Cr	Ni	Cu
0.08	0.19	0.6	0.0021	0.0024	0.025	0.07	0.02

Table 1. Chemical composition of S235JR steel, Fe-balance (in mass %)

Si	Fe	Cu	Mn	Mg	Cr	Zn
0.5	0.16	0.047	0.058	0.41	0.013	0.03

Table 2. Chemical composition of AW 6060 aluminium alloy, Al-balance (in mass. %)

Adherent preparation was conducted in sense of cutting specimens to 30x100 mm dimensions and preparing the contact surface to which the adhesive will be applied (30x30 mm). Preparation consisted of grinding the area with SiC abrasive papers: P120, P500

and P1000 (specimens 2, 3 and 4; 1 was the unground specimen). The control specimens were left untreated. Surface roughness was measured by Mitutoyo SJ210 device.

Subsequently, an adhesion process was conducted, using Sika SikaPower 4720 epoxy adhesive, with glass beads for keeping the optimal distance between adherents. The adhesion process consisted of the following steps:

- Cleaning the surfaces with acetone,
- Assemble the gun, the cartridge and the mixer,
- Application of the adhesive onto both surfaces to be welded and smear the adhesive so that the surfaces will be primed and protected from corrosion,
- Application of the adhesive some 5 mm from the specimen edges in order to prevent excessive squeeze out,
- Aligning the joint within 60 min from the adhesive application,
- Clamping the joint with power grip plier,
- Cure time of at least must be allowed, but in this case, 24 h was used.

Testing was performed after 30 days, to enable obtaining mechanical properties as close to exploitation as possible, without achieving excessive study execution time. Specimen shape and size is shown in Fig. 1. It can be seen that spacers were used to enable the maintaining the testing axes of specimens when gripping in the machine. VEB ZDM 5/91 mechanical tensile testing machine was used.

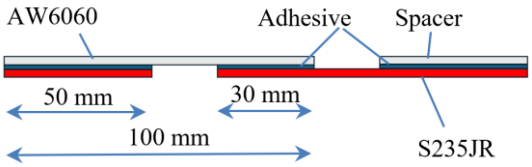


Fig. 1. Tensile test specimen (width 30 mm)

After tensile testing, visual check of the fracture surfaces was performed in order to determine fracture mode of specimens.

3. RESULTS AND DISCUSSION

The results showing average values of measured average roughness (Ra) are presented in Fig. 1. It can be seen that in specimen 1 (as received material, unground), the average roughness is the highest in specimen 0, structural steel, which becomes lower as the finer abrasive paper is applied. On the other hand, aluminium alloy AW6060 average roughness is the highest when the coarsest abrasive paper was applied (P120), followed by P500 treated specimen, unground specimen and finally the specimen ground with P1000 abrasive paper. These results suggest that by grinding by abrasive papers, average roughness of adherents becomes similar to each other, which is in strong contrast to control unground specimen, where average roughness of steel is significantly higher compared to aluminium alloy.

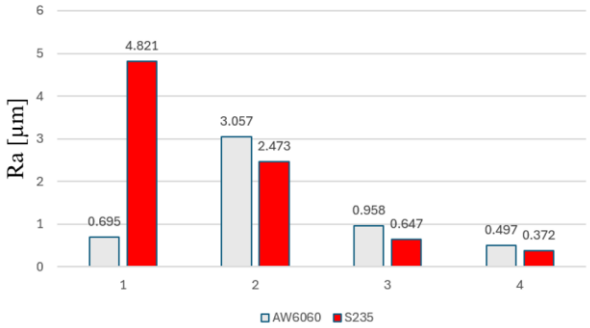


Fig. 2. Average roughness Ra of AW6060 aluminium alloy and S235 structural steel

Tensile testing results in the form of rupture force (maximum force, Fm) are shown in Fig. 3. It can be deducted that the rupture force in Specimen 1 (control) is the lowest of all tested, followed by Specimens 4, 3 and 2, which has the highest rupture force Fm. The results of specimens 2 to 4 can be well correlated to the average roughness in specimens prior to adhesive bonding, Fig. 2. As the average roughness of adherents is higher, maximum forces are also higher, which is probably the result of increasing the surface area that provides contact between adherents and the adhesive, where the adhesive fills the voids created by surface roughness, leading to improved bonding strength. However, specimen 1 exhibits the highest average roughness in the steel adherent, and still does not possess the highest rupture force. The answers to this phenomenon will be clarified after presenting macro images of fracture surfaces.

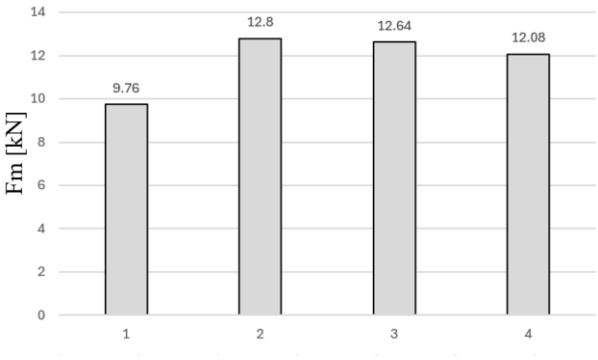


Fig. 3. Tensile forces obtained for tested specimens

Representative macro images of fracture surfaces are shown in Figs. 4–7. It can be seen that in Specimen 1 adhesive is completely detached from one adherent, in majority of cases, aluminium alloy, probably due to the presence of the very inert Al_2O_3 surface layer and corrosion. On the other hand, in Specimens 2 to 4, the adhesive suffered a cohesive failure, which is a more convenient case (acceptable failure mode) than detaching from the adherent. That means, the surface condition of the unground Specimen 1, although having a significant roughness, does not represent a suitable adherent, probably due to the partial surface corrosion that was removed by grinding, in Specimens 2 to 4. This leads to the fact that grinding is not only the way to increase the contact surface between the adherents and

adhesive, but also for cleaning the surfaces, where chemical means are not always entirely adequate.



Fig. 4. Fracture surfaces of Specimens 1



Fig. 5. Fracture surfaces of Specimens 2



Fig. 6. Fracture surfaces of Specimens 3



Fig. 7. Fracture surfaces of Specimens 4

4. CONCLUSIONS

In the presented study, adhesive joining of aluminium alloy to structural steel was performed and the influence of surface roughness was studied. In accordance with the presented results, the following conclusions can be drawn:

- Roughening the surfaces of adherents is necessary to increase the bond strength.
- The effectiveness of grinding the surfaces is higher if a coarser abrasive paper is used.
- The main reason for a higher effectiveness of coarser abrasive applied for preparing the surfaces is increasing, is related to increasing the contact surface between the adherents and adhesive.
- A relatively high roughness of unground specimens resulted in a lower rupture force, the main reason being corrosion.
- In these specimens, where unground specimens were adhesive bonded, the adhesive was completely detached from the adherent material, more often from aluminium alloy, probably due to its lower roughness, while corrosion is also present.
- In roughened specimens, a cohesive fracture of the adhesive occurs which is optimal case.

5. REFERENCES

[1] Shadlou, S., Ahmadi-Moghadam, B., Taheri, F., Nano-Enhanced Adhesives. Review of Adhesion and Adhesives, Vol. 2, pp.371–412, 2014.

[2] Ebnesajjad, S. Handbook of Adhesives and Surface Preparation: Technology, Applications and Manufacturing; Elsevier: Oxford, UK, 2011.

[3] Marques, A.C., Mocanu, A., Tomic, N.Z., Balos, S., Stammen, E., Lundevall, A., Abrahami, S.T., Günther, R., de Kok, J.M.M., de Freitas, S.T., Review on Adhesives and Surface Treatments for Structural Applications: Recent Developments on Sustainability and Implementation for Metal and Composite Substrates, Materials, Vol. 13, 5590, 2020.

[4] Han, Q., Sheng Y., Liu X., Zhang X., Chen, X. Li, B., Han Z., Carbon fiber reinforced epoxy composite combining superior electrochemical energy storage and mechanical performance, Chemical Engineering Journal, Vol. 437, 135228, 2022.

[5] Yan, R., Chen, X., Aramid/epoxy composites with angle-laid reinforcement constructions for ballistic protection, Journal of Industrial Textiles, Vol. 45, pp. 765–779, 2016.

[6] Çakir, M., Akin, E., Renda, G., Mechanical properties of carbon-aramid hybrid fiber-reinforced epoxy/poly(vinyl butyral) composites, Polymer Composites, Vol. 44, Issue 8, pp. 4826-4841, 2023.

[7] Zhai, L., Ling, G., Li, J., Wang, Y. The effect of nanoparticles on the adhesion of epoxy adhesive, Materials Letters, Vol. 60, pp. 3031–3033, 2006.

[8] Long, J., Li, C., Li, Y. Enhancement of Mechanical and Bond Properties of Epoxy Adhesives Modified by SiO_2 Nanoparticles with Active Groups, Polymers, Vol. 14(10), 2052, 2022.

[9] Farzanehfar, N., Taheri, A., Rafiemanzelat, F., Jazani, O.M:, High-performance epoxy nanocomposite adhesives with enhanced mechanical, thermal and adhesion properties based on new nanoscale ionic materials, Chemical Engineering Journal, Vol. 471, 144428, 2023.

FUNDING

This research has received funding from the regional project funded by the Provincial Secretary for Higher Education and Scientific Research, Vojvodina, Serbia with grant agreement no. 000838124 2024 09418 003 000 000 001 04 003. Also, this research has been supported by the Ministry of Science, Technological Development and Innovation (Contract No. 451-03-65/2024-03/200156) and the Faculty of Technical Sciences, University of Novi Sad through project "Scientific and Artistic Research Work of Researchers in Teaching and Associate Positions at the Faculty of Technical Sciences, University of Novi Sad" (No. 01-3394/1).

ACKNOWLEDGMENTS

The authors gratefully acknowledge research support by the project entitled "Interdisciplinarity in Materials Science and Joining Technologies" from the Department of Production Engineering, Faculty of Technical Sciences Novi Sad, Serbia.

Authors:

Nikola Maksimović, Albert Hauck, Petar Janjatovic, Milan Pecanac, Borislav Savković, Dragan Rajnovic, Sebastian Balos, University of Novi Sad, Faculty of Technical Sciences, Trg Dositeja Obradovica 6, 21000 Novi Sad, Serbia, Phone: +381 21 485-2055.
E-mail: maksimovic.nikola@uns.ac.rs; albert.hauck@uns.ac.rs; janjatovic@uns.ac.rs; pecanac.milan@uns.ac.rs; savkovic@uns.ac.rs; draganr@uns.ac.rs; sebab@uns.ac.rs

Vladimir Savic, Sika, Patrijarha Pavla 1, 22310 Simanovci, Serbia, Phone: +381222155777.
E-mail: savic.vladimir@rs.sika.com

MMA 2024
FLEXIBLE TECHNOLOGIES

15th INTERNATIONAL SCIENTIFIC CONFERENCE
NOVI SAD, SERBIA, SEPTEMBER 24-26, 2024

Original research paper https://doi.org/10.24867/MMA-2024-05-011

Karpe, B., Kosec, B., Gojic, M., Ivanic, I., Nagode, A., Cigic, L., Bizjak, M.

HEAT TRANSFER IN CHILLING WHEEL IN MELT-SPINNING PROCESS

Abstract: *In the case of continuous casting of metal ribbons with the melt-spinning process, larger quantity of melt could lead to a slow excessive warming of the chilling wheel, which would further lead to solidification of a ribbon at non-uniform conditions and increased wearing of the wheel. Primary goal of our work was to determine to what extent the release of heat during contact of the melt/ribbon on the circumferential surface of the chilling wheel affect its surface temperature rise, and inversely how much elevated temperature of the chill wheel surface affects on metal ribbon cooling rate and its solidification velocity. On the basis of developed mathematical model, a computer program was made and used for analyses of heat transfer in the melt-spinning process. The calculations show that contact resistance between metal melt and chilling wheel has a great influence on melt/ribbon cooling and chill wheel heating rate, and must not be neglected in numerical calculations, even if its value is very low. In the case of continuous casting, significant long term surface temperature increase may take place, if the wheel is not internally cooled. But inner cooling is effective only if wheel casing thickness is properly chosen. New method for determining contact resistance through variable heat transfer coefficient is introduced which takes into account physical properties of the casting material, process parameters and contact time/length between metal melt/ribbon and substrate and enables cooling rate prediction before the experiment execution. In the case of continuous casting, heat balance of the melt-spinning process is calculated, and influence of the chilling wheel cooling mode on cooling rate of metallic ribbon is analyzed.*

Key words: *Metallic Materials, Rapid Solidification, Melt-Spinning, Heat Transfer, Heat Transfer Coefficient, Modeling*

1. INTRODUCTION

Single roll melt spinning is the most commonly used process for the production of rapidly solidified thin metal foils or ribbons with amorphous, microcrystalline or even combined microstructure [1]. Two variants of this process are employed. Free jet melt spinning, where crucible nozzle is located relatively far away from the wheel and planar flow melt casting, where crucible nozzle is so close to the wheel circumferential surface, that it constrains the melt puddle. It is proved that small gap between nozzle and the wheel damps perturbations in the melt flow, improves stability of the melt puddle and enables production of wider ribbons [2]. In both types of a process, a molten material is introduced onto a surface of the spinning wheel, where melt puddle is formed (Fig. 1).

Material is then dragged out from the puddle by relative motion of the wheel. Usually thin ribbons are produced which can leave the wheel surface in solidified, semi-solidified or fully liquid form, depending on the thermal contact resistance between the melt and substrate, heat transfer in the melt and in the wheel, wetting between melt and wheel material, process parameters, and nucleation and crystal growth characteristics of the particular casting material [3]. With regard to the heat and momentum transport relative efficiency, two mechanisms of ribbon formation are distinguished. Thermal controlled mechanism, where solidification of the ribbon is completed in the puddle and dragged out in already solid form and momentum controlled mechanism, where solidification of the ribbon is delayed for some reason and solidification take place further downstream [4].

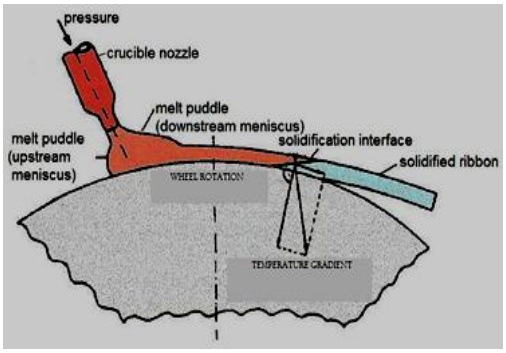


Fig.1. Scheme of a melt puddle development on the circumferential surface of the wheel at free jet melt-spinning process

The most important advantages of rapid solidification, which can be made with this process are extended solubility, refined microstructure, thermal stability at elevated temperatures, and improved magnetic and electrical properties [5,6].

2. HEAT TRANSFER CALCULATIONS

In the case of industrial casting of metal ribbons or foils with the chill block melt spinning processes, like free jet, planar flow or melt extraction, continuous solidification of larger quantities of melt and consecutive heat release could lead to a slow overheating of the chilling wheel [7]. This would further lead to solidification of a ribbon at non-uniform conditions, increased wearing of the wheel or even to the

contamination of the casting material with the wheel material. Primary objective of our work was to calculate the temperature field inside the chilling wheel during melt spinning process and to ascertain the influence of the chill wheel surface temperature on metal ribbon cooling rate and solidification velocity [8].

Because melt puddle is thin compare to its width and length we can make an assumption of two-dimensional (2D) transient heat transfer. Assuming 2D transient heat transfer with variable thermal properties and internal heat generation (latent heat of crystallization), general partial differential equation for the melt is reduced to:

$$\frac{1}{r}\cdot(\lambda_m\cdot\frac{\partial T}{\partial r})+\frac{\partial}{\partial r}\cdot(\lambda_m\cdot\frac{\partial T}{\partial r})+\frac{1}{r^2}\cdot\frac{\partial}{\partial\varphi}\cdot(\lambda_m\cdot\frac{\partial T}{\partial\varphi})+q'''=\rho_m\cdot c_m\cdot\frac{\partial T}{\partial t} \quad (1)$$

And for chill wheel, where no heat is released by wheel material:

$$\frac{1}{r}\cdot(\lambda_w\cdot\frac{\partial T}{\partial r})+\frac{\partial}{\partial r}\cdot(\lambda_w\cdot\frac{\partial T}{\partial r})+\frac{1}{r^2}\cdot\frac{\partial}{\partial\varphi}\cdot(\lambda_w\cdot\frac{\partial T}{\partial\varphi})=\rho_w\cdot c_w\cdot\frac{\partial T}{\partial t} \quad (2)$$

where:
- r, φ , z - cylindrical coordinate system [m; rad; m],
- T - temperature [ºC],
- ρ_m,ρ_w=ρ(T) - density of the melt and wheel material [kg/m^3],
- λ_m,λ_w= λ(T) - thermal conductivity of the melt and wheel material [W/m·K],
- c_m,c_w=c(T) - specific heat of the melt and wheel material [J/(kg·K)],
- q$'''$- volumetric heat generation rate [W/m^3].

For calculation of temperature distribution inside the melt puddle and chill wheel, we used explicit finite difference method (FDM) with cylindrical coordinate system. Thermal properties of the melt and wheel material are temperature dependant and are calculated for each iteration step with linear interpolation from tabulated values. Density in solidification interval of the casting material is changing linearly or parabolic, depending of the alloy solidification type [9], whereas density of the wheel material is approximated as constant.

In situations where a detailed description of thermal physics is very complicated, such as in melt-spinning process, where heat transfer between melt and substrate (wheel) is coupled with fluid flow which is further complicated by the presence of solidified region, combined modes of heat exchange are usually taken in to account with the overall heat transfer coefficient. Heat transfer coefficient (α) includes conduction and radiation of heat, as well as any convective effects and is defined as the ratio of the heat flux (q) from the liquid metal and solid ribbon across the interface with the wheel, to the temperature difference between molten metal or ribbon and the wheel [10].

Because the temperatures of the casting material and chill wheel are changing along contact length, numerical modeling of the heat transfer with constant heat transfer coefficient and nominal chill wheel temperature is not realistic. Actually, heat transfer coefficient is dependant by many factors which include physical and thermal properties of the melt and chill substrate, fluid velocity, state and geometry of the chill surface and its temperature. Moreover, molten material solidifies and shrinks, which changes the physical contact from liquid/solid to solid/solid or (solid+gas)/solid. Consequently, value of heat transfer coefficient over entire contact length can vary in wide range.

Furthermore, values of the heat transfer coefficient are difficult to measure with confidence. In literature you can find different techniques. From those based on pyrometric, photocalorimetric or wheel surface temperature measurements with embedded thermocouples, to those based on dendritic arm or interlamellar spacing, but none of them can predict the value of the local heat transfer coefficient particularly accurate.

To simplify the mathematical model, we considered number of assumptions. The local heat transfer coefficient α(x) is calculated with the integral method for liquid metals flow over flat plate. The approximation of the flat plate is reasonable, because of the large aspect ratio between puddle length and radius of the wheel. Another assumption in our model is to consider that there is no velocity gradient in the puddle. This is not completely true in the actual case, but when metallic materials are cast, we believe that velocity gradient can be neglected for thermal field calculation inside the chill wheel. Namely, metal melts have very low Prandtl number and consequently thermal boundary layer much thicker than velocity boundary layer [11]. Ribbon thickness is also found to be approximately proportional to circumferential velocity of the chill wheel (u_w^{-1}) and the pressure in the crucible ($p^{0.5}$), as predicted by continuity and Bernoulli equations [12]. Next assumption is that temperature of the melt in the puddle direct under the impinging jet stays equal to casting temperature, because strong turbulences in that region.

The equation for local heat transfer coefficient α(x) calculation, included in the numerical scheme is:

$$\alpha(x)=\alpha(R,\varphi_j)=\lambda_m\frac{\partial\theta}{\partial y}\Big|_{y=0}=\frac{3\cdot\lambda_m}{2\delta_t}=\frac{3\cdot\lambda_m}{2\cdot\sqrt{8}}\cdot\sqrt{\frac{u_w}{a\cdot x}} \quad (3)$$

where:
- u_w - circumferential velocity of the wheel [m/s],
- λ_m - thermal conductivity of the casting material (temperature dependent) [W/(m·K)],
- δ - thermal boundary layer thickness [m],
- a - temperature diffusivity [m^2/s],
- x - istance from the initial contact point to the actual calculation point [m].

3. RESULTS AND DISCUSSION

Fig. 2 represents calculated temperature cooling curves in Al ribbon and heating curves for Cu wheel surface, considering different modes of contact resistance: ideal contact, variable contact resistance (*α(x)=integral method*) and constant contact resistance through entire contact time/length ($\alpha(x)$=10^{6}W/(m^2·K)). Value for constant average heat transfer coefficient for aluminum reported by other authors, was obtained by subsequent microstructure analyses [13]. Reported contact times are usually calculated from observations of puddle length with the high speed frame camera and lie in the range between 0.2 and 1 millisecond [14] and

are dependent on wheel speed, wheel diameter and casting material properties. In our case, selected values for contact time represent limiting values for the analyses propose, and are calculated as a multiplication of iteration step time interval, restricted by the stability criteria of the numerical solution.

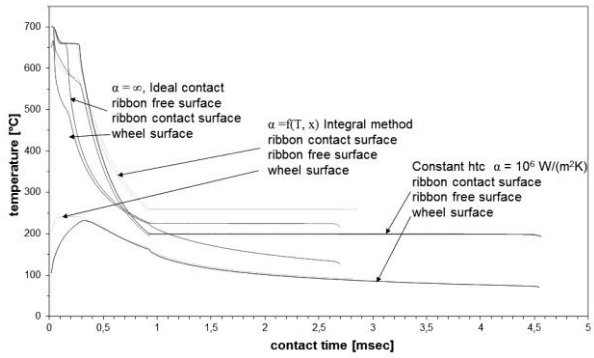


Fig. 2. Cooling curves of free and contact surface of Al ribbon and contact surface of the Cu wheel as a function of different contact resistance (u_w=18.9 m/s, ribbon thickness 66μm, contact time 0.923 msec)

Comparison of the contact and free ribbon surface temperature cooling curves, calculated with different approximation of heat transfer coefficient shows, that contact resistance should not be neglected, even if its value is very low. Calculated cooling rate of the melt is relatively much slower when some contact resistance is considered, although its value is very low (10^{-6} m^2·K/W). Integral method calculation of heat transfer coefficient gives the most logical results for entire duration of the contact. Calculated solidification time is practically the same to those obtained by overall heat transfer coefficient, but final temperature of the ribbon at the detachment point is much higher, especially for longer contact time, where constant contact resistance (10^{-6}(m^2·K)/W) approximation predicts lower ribbon temperature then ideal contact calculation, which is not possible. Cooling of the wheel surface in spite of contact with hotter ribbon seems unlikely, but considering the wheel as a whole, enthalpy of the wheel is increasing, because temperature more than 0.3 mm under the surface, is increasing entire contact time. Namely, conduction heat transfer rate into the wheel is faster than heat transfer rate across ribbon/wheel interface.

When thicker ribbons are cast or materials with low thermal conductivity, thermal resistance in already solidified region of the ribbon becomes the limiting factor of the heat transfer. High cooling and solidifying rates, through entire cross section of the ribbon, especially on its free surface, can be achieved only when very thin (< 30μm) ribbons are cast (Fig. 3).

Wheel material also has significant influence on the cooling rate of the ribbon. Fig. 4 shows calculated temperature profiles in steel or copper wheel, when aluminum is cast. As we can see, surface temperature will increase significantly, especially for a wheel of lower thermal diffusivity.

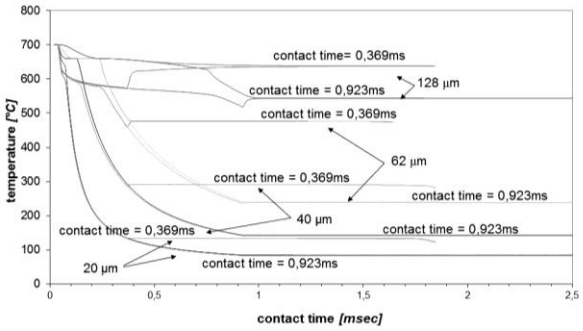


Fig. 3. Calculated cooling curves of contact and free surface of the Al ribbon as a function of its thickness and contact time (u_w=18.9 m/s, α(x) = integral method)

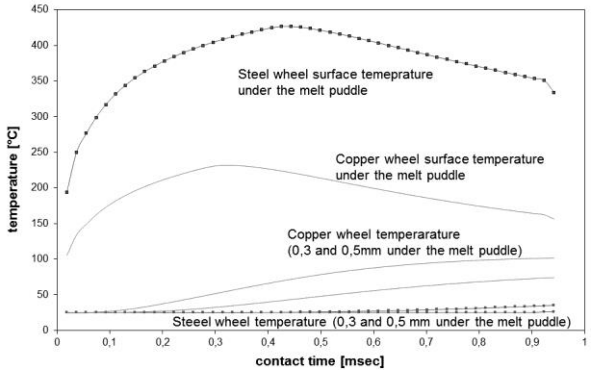


Fig. 4. Steel and copper wheel temperature increase as a function of contact time when aluminum ribbon is cast (u_w=18.9 m/s, ribbon thickness 66 μm, contact time 0.92 msec, α=10^6 W/m^2·K)

Because short duration of the contact (< 1 ms) and limited thermal diffusivity of the wheel material, the thermal energy can penetrate only a short distance in the wheel, which results in a higher temperature at the wheel surface. The magnitude of temperature increase depends on the wheel material. For steel wheel, which has much lower thermal diffusivity than copper, an increase of surface temperature is over 400 °C, and heat penetration depth about 0.5 mm. On contrary, copper wheel surface temperature increase is about 200 °C and penetration depth twice as much. Of course, when materials with higher melting point are cast, surface temperature of the wheel will increase much higher. Obviously, such a large deviation in surface temperature should not be neglected in calculation of cooling and solidification rate of the melt. Fig. 5 shows calculated temperature profiles in aluminum ribbon cast on the circumferential surface of steel or copper wheel as a function of contact time between metal melt/ribbon and surface of the chilling wheel. Importance of wheel material selection is evident. Because contact duration is so short, chilling wheel made from steel is much less effective heat sink than copper wheel and consequently, cooling rate of the ribbon significantly slower.

During continuous casting process, the wheel is not subjected only to heat transfer from the solidifying material, but also to radiation and convection heat transfer from the crucible. In the case of continuous casting, significant "long term" surface temperature

increase may take place, if the wheel in not externally or internally cooled. In calculations discussed above, we have assumed that the wheel surface is at room temperature at the beginning of the contact. For first ten to hundred revolutions surface temperature increase may indeed not be significant, but when continuous casting is performed, especially when materials with high melting point are cast, surface temperature of the wheel can increase in such an extent, that formation of the ribbon will be disturbed, because of decreased cooling and solidifying rate in the melt puddle.

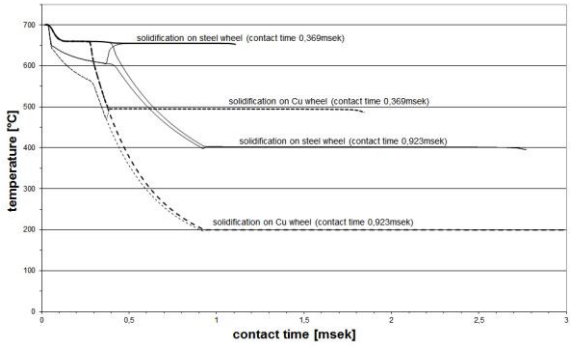


Fig. 5. Calculated cooling curves of Al ribbon as a function of wheel material and contact time (u_w=18.9 m/s, ribbon thickness 66 μm, contact time 0.923 msec, $\alpha=10^6$ W/m^2·K)

Fig. 6 shows the effect of the initial wheel temperature on calculated temperature profiles in the Al ribbon. As we can see, initial wheel temperature has substantial influence on ribbon cooling rate especially, if the contact time is short (high wheel speed). Because melt puddle formation is also momentum controlled, changing the cooling rate could alter solidification pattern in the melt puddle and cause its instability.

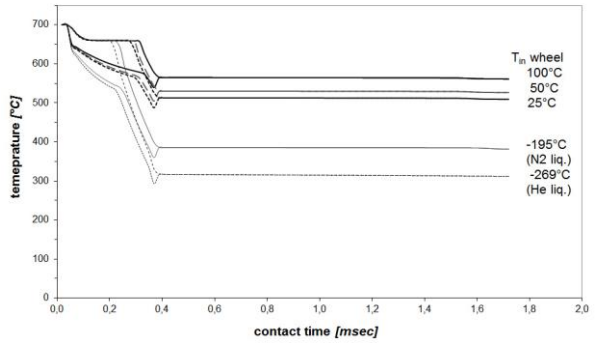


Fig. 6. Cooling curves for 66 μm thick Al ribbon as a function of initial wheel temperature and contact time (u_w=18.9 m/s, ribbon thickness 66 μm, contact time 0.369 msec, α(x)=integral method)

Because copper becomes super conductor of heat at cryogenic temperature ($\lambda_{Cu}\approx$20000 W/mK, a≈20 m^2/s at T=10 K), possibility of liquid gas cooling was analyzed. Calculations, based on the assumption of the same physical contact between the melt and wheel surface, irrespective of the wheel surface temperature indicate that cooling rate will increase substantially for the ribbon of the same thickness. But in spite of much lower wheel surface temperature, the influence of the wheel surface temperature is minor compared to the influence of the ribbon thickness, which mostly depends on the process parameters (Fig. 7). Very high cooling and solidification velocities of the melt will still be reached only if the ribbon is thin.

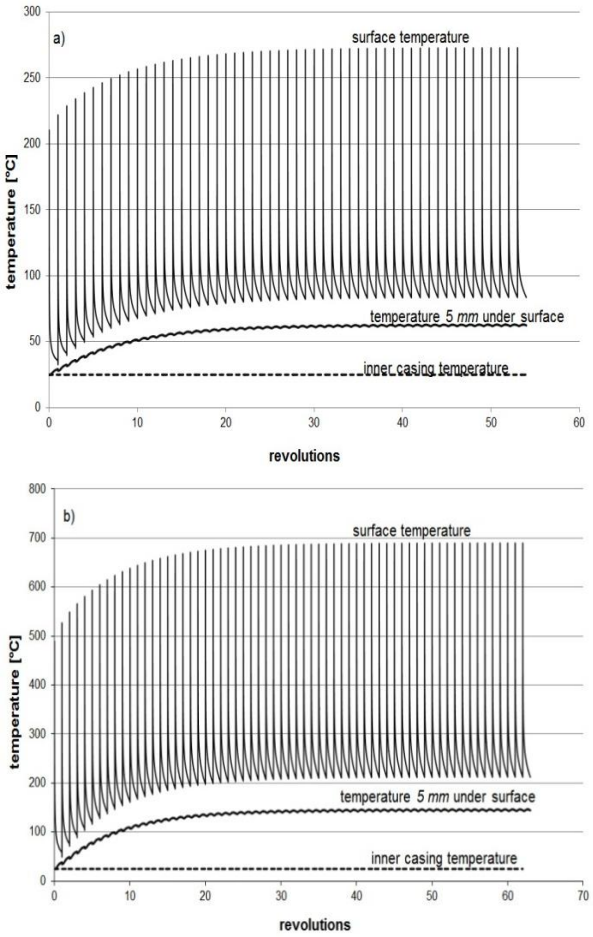


Fig. 7. Surface temperature of the internally water cooled wheel with casing thickness 10 mm and wheel radius 0.2 m a) aluminum casting; b) iron casting (u_w=18.9 m/s, α_{water}=5000 W/m^2·K), α_{air}=50W/m^2·K)

From economical point of view and design simplicity, cooling the wheel with external gas jets or inner rotating water stream is the most promising. For the purpose of the continuous casting on our laboratory apparatus, we calculated temperature heat balance for inner water cooled wheel (R_w=0.2 m) as a function of its casing thickness. From the outside, wheel is convectively cooled with surrounding atmosphere, and from the inside with water stream. In the mathematical model, convective heat transfer coefficients are taken as constants (α_{water}=5000 W/m^2·K) and α_{air}=50 W/m^2·K) and represent average values, calculated from forced convection correlation equations [9]. No radiation from the crucible is taking into account. To ascertain influence of external cooling with gas jets, we also made calculations, based on assumption of exaggerated value for convective heat transfer coefficient (α_{air}=1000 W/m^2·K), which is practically impossible to attain.

The calculated surface temperatures for 10 mm thick

wheel casing are shown in Fig. 8. Each saw tooth spike corresponds to the temperature of the wheel surface being underneath the puddle. As we can see, internally water cooled wheel will reach the periodic steady state after few revolutions. But still, long term surface temperature can increase significantly when iron is cast (>200 °C), although we assume exaggerated value (α_{air} = 1000 W/m^2·K) for convective heat transfer coefficient to the surrounding atmosphere. Namely, duration of one revolution of the wheel is so short that external gas convective cooling would have no significant influence on the wheel surface temperature. Conducting of heat into the wheel and cooling of the inner casing surface with water stream is much faster than external convective cooling with surrounding atmosphere or gas jets.

If we reduce wheel casing thickness up to 2 mm, internal water cooling will be more effective, and wheel surface temperature that melt will effectively "see" at the beginning of the next pass of the wheel under the puddle, will be practically the same as at the first revolution, even if high melting temperature materials are cast (Fig. 8, 9).

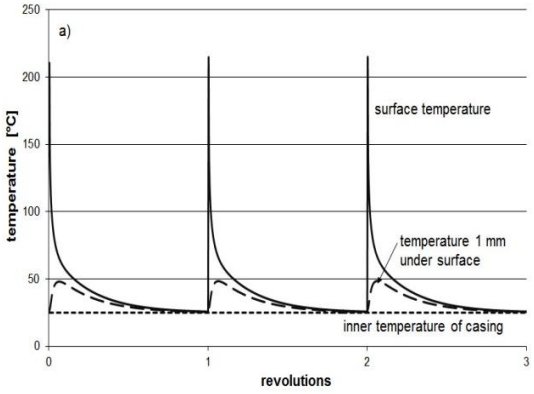


Fig. 8. Surface temperature of the internally water cooled wheel with casing thickness 2 mm and wheel radius 0.2 m, a) Aluminum casting (u_w = 18.9 m/s, α_{water} = 5000W/(m^2·K) and α_{ai} = 50W/m^2·K)

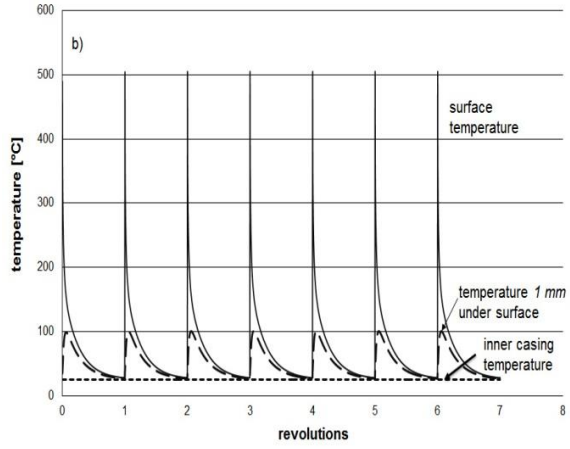


Fig. 9. Surface temperature of the internally water cooled wheel with casing thickness 2 mm and wheel radius 0.2 m, b) Iron casting (u_w = 18.9 m/s, α_{water} = 5000W/(m^2·K) and α_{ai} = 50 W/m2·K)

But if we reduce wheel casing even further, beneath the heat penetration depth under the melt puddle, convective heat resistance on the inner side (wheel – water interface) becomes significant. Even if we assume heat transfer coefficient value on inner side of a casing as high as 100000 W/m^2·K, which can be reached with high pressure impingement water jets [14], heat removal from the melt will be slower as in the case of full or internally water cooled wheel with 10 mm thick casing (Fig. 10).

Cooling the thin wheel casing with water stream, flowing between casing and the inner core of the wheel would be even less effective. Because high temperature difference between wheel casing and cooling media, peak heat flux would be exceeded and unstable vapour film formation on inner side of a casing would take place. This phenomenon is called unstable film boiling regime, where heat flux decreases as the surface temperature increases, because the average wetted area of the casing inner surface decrease. Consequently, the wheel casing temperature would increase even more. Reducing the thickness of the wheel casing is unsuitable, from rapid solidification and from steadiness point of view.

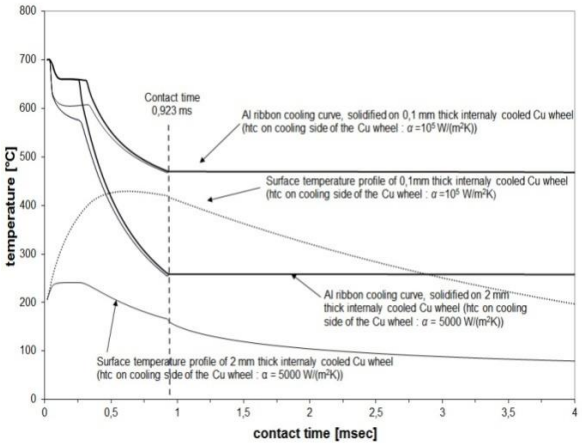


Fig. 10. Internally cooled copper wheel surface temperature increase as a function of contact time and thickness of wheel casing for aluminum casting. (R_w=0.2 m, u_w=18.9 m/s, ribbon thickness 66 μm, contact time 0,923 msec, htc on wheel-water side 100000 W/m^2·K)

4. CONCLUSIONS

An improved finite difference method (FDM) with variable heat transfer coefficient was used to calculate the heat balance of free jet melt-spinning process.

The mathematical model developed, includes the effect of the conduction heat transfer within the chilling wheel and allows us to investigate the influence of heat contact resistance between the melt and the chill wheel, wheel material, and inner wheel cooling. The fact that the wheel surface temperature is increasing significantly under the solidification melt puddle, selection of the wheel material is important. From rapid solidification point of view, materials with highest temperature diffusivity are preferable. Deoxidized copper has the highest thermal diffusivity between all commercially

useful materials, but low mechanical properties at elevated temperature. When wearing of the wheel surface is a problem, Cu-Be or ODS copper alloys are preferable.

For continuous casting internally cooled wheel is preferable, but only in the case when wheel casing thickness is correctly selected. When too thick casing is applied, water cooling will not have adequate influence on wheel surface temperature increase. When the casing of the wheel is too thin, thermal resistance on the cooling side (wheel-water interface) becomes the limiting factor, which decreases the heat transfer rate from the melt and consequently its cooling and solidifying rate.

5. REFERENCES

[1] Bizjak, M., Kosec, L., Kneissl, A.C., Kosec, B.: The characterisation of microstructural changes in rapidly solidified Al-Fe alloys through measurement of their electrical resistance, International Journal of Materials Research, Vol. 99, No. 1, pp. 101-108, 2008.

[2] Kosec, B.; Device for rapid solidifying of metal alloys, Euroteh, Vol. 3, pp. 32-33, 2004.

[3] Haga, T., Inoue, K., Watari, H.: Micro-forming of Al-Si foil, Journal of Achievements in Materials and Manufacturing Engineering, Vol. 40, No. 2, pp. 115 – 122, 2010.

[4] Dobrzanski, L.A.: Technical and Economical Issues of Materials Selection, Silesian Technical University, Gliwice, 1997.

[5] Praisner, T.J., Chen, J.S., Tseng, A.: An Experimental Study of Process Behavior in Planar Flow Melt Spinning, Metallurgical Trans. B, Vol. 26B, pp. 1199-1208, 1995.

[6] Collins, L.E.: Overview of rapid solidification technology, Canadian Metallurgy Quarterly, Vol. 25, No. 2, pp. 59-71, 1986.

[7] Lojen, G., Anzel, I., Kneissl, A.C., Unterweger, E., Kosec, B., Bizjak, M.: Microstructure of rapidly solidified Cu-Al-Ni shape memory alloy ribbons, Journal of Materials Processing Technology, Vol. 162/163, pp. 220-229, 2005.

[8] Karpe, B., Kosec, B., Kolenko, T., Bizjak, M.: Heat transfer analyses of continuous casting by free jet meltspinning device, Metallurgy, Vol. 50, No. 1, pp. 13-16, 2011.

[9] Stefanescu, D.M.: Science and Engineering of casting solidification, Kluwen Academic/Plenum Publishers, Kluewen, 2005.

[10] Carpenter, J.K., Steen, P.H.: On the Heat transfer to the Wheel in Planar – Flow Melt Spinning, Metallurgical Transactions B, Vol. 21B, No. 2, pp. 279-283, 1990.

[11] Karpe, B., Kosec, B., Bizjak, M.: Analyses of the melt cooling rate in the melt-spinning process. Journal of achievements in materials and manufacturing engineering, Vol. 51, No. 2, pp. 59-66, 2012.

[12] Libermann, H.H.: Rapidly solidified alloys, Marcel Dekker Inc., London, 1993.

[13] Ivanic, I., Kozuh S., Kosel, F., Kosec, B., Anzel, I., Bizjak, M., Gojic, M.: The influence of heat treatment on fracture surface morphology of the CuAlNi shape memory alloy. Engineering failure analysis. Vol. 77, pp. 85-92. 2017.

[14] Ciofalo, M., Di Piazza, I., Brucatto, V.: Investigation of the cooling of hot walls by liquid water sprays, International Journal of Heat and Mass Transfer, Vol. 42, pp. 1157-1175, 1999.

ACKNOWLEDGMENTS

The authors want to thank professor Ladislav Kosec+ (University of Ljubljana) and professor Anton Smolej (University of Ljubljana) for mentorship at study of rapid solidification and development of advanced shape memory materials.

Authors:

PhD Blaž Karpe, PhD Borut Kosec, PhD Aleš Nagode, MSc Lovro Cigic, PhD Milan Bizjak, University of Ljubljana, Faculty of Natural Sciences and Engineering, Aškerčeva 12, 1000 Ljubljana, Slovenia, Phone: +386 1 2000413.
E-mail: blaz.karpe@ntf.uni-lj.si; borut.kosec@ntf.uni-lj.si; ales.nagode@ntf.uni-lj.si; lovro.cigic@ntf.uni-lj.si; milan.bizjak@ntf.uni-lj.si

PhD Mirko Gojić, PhD. Ivana Ivanic, University of Zagreb, Faculty of Metallurgy, Aleja Narodnih heroja 3, 44103 Sisak, Croatia, Phone: +385 43 533 381.
E-mail: gojic@simet.hr; iivanic@simet.hr

MMA 2024
FLEXIBLE TECHNOLOGIES

Section F:
MECHANICAL ENGINEERING AND ENVIRONMENTAL PROTECTION

MMA 2024 FLEXIBLE TECHNOLOGIES

15th INTERNATIONAL SCIENTIFIC CONFERENCE
NOVI SAD, SERBIA, SEPTEMBER 24-26, 2024

Original research paper https://doi.org/10.24867/MMA-2024-06-001

Stanivuk, T., Dujmovic, M., Muslim, N., Dujmovic, M.

ELECTRICAL MACHINES AND CONTROLL SYSTEM FOR MANAGING BALLAST WATER OF SHIP

Abstract: *This paper defines ways of solving practical problems in managing ballast waters on ships. It presents different methods of solving the same problem through direct star connection, automatic star-delta connection with control and main circuit, frequency converters, soft starters, programmable logic controllers and microcontrollers with assembly language. With each method of problem solving, basic guidelines for their implementation have also been given, depending on the complexity of the practical problem. Application of the paper with minor modifications is possible in various fields of application. Analogue PID controller is also used to compare speed in eliminating error signal.*

Key words: *star–delta connection, starting method, automation, microcontroller*

1. INTRODUCTION

Ship ballast pump is most often centrifugal pump because they can satisfy these needs most effectively.

System automation is an essential precondition for improving the production process. In systems realized by electrical devices and programmable logic controller's automation can be realized in several ways. This paper presents some of the automation methods, precisely two control methods: PLC control automation with STEP 7 (Function Block Diagram) and microcontroller automation with assembly language. The application of a certain method depends on the environmental conditions and equipment used for system automation, as well as on the expertise of employees. The main feature of these systems is that they are modular and flexible, which means they can be easily adapted. The possibility of remote controlling via the PLC interface has become crucial and unavoidable for process automation.

2. SELECTION OF ELECTRICAL MOTOR TO DRIVE THE PUMP

Electrical machines are divided in 3 main groups: Three phase, single phase and DC machines. DC series motor has highest torque for the same shaft power (no eddy currents in the stator and no hysteresis) but DC drives require brushes and more maintenance than asynchronous squirrel cage induction motor. Synchronous motors and DC parallel are not recommended to use because they keep constant speed with variation of the load.

Single phase motors for the same power have bigger size and are creating unbalance on the secondary side of transformer Dy5. These are the main reason to select three phase asynchronous (induction) motor with squirrel cage rotor.

The magnetic flux generated in the stator winding of the three-phase asynchronous machine does not have a sine-wave form and is composed of a fundamental wave and several harmonic waves that cause an unwanted oscillating torque. The current, shaft (mechanical) power and torque values of the star connection amount to approximately one third of the values of the delta connection.

At no-load speed, the motor will only develop the torque that is required for bearing friction and ventilator.

For the selection of an asynchronous motor with squirrel-cage rotor, nominal speed must be taken into consideration. Characteristic of torque and speed of the motor must be adapted to the characteristic of load torque of the ballast pump and speed of the driven machine (pump).

The driven machine requires a torque from the driving motor that depends upon the load and the speed of the driven machine. Load torque of pump is proportional to speed square as is the case with other centrifugal drives. In case the starting torque of the driven machine is higher than the starting torque of the motor, the motor cannot start when switched-on. The current consumed by the motor amounts to approx. 6 times the nominal current and will result in the destruction of the windings upon a short time. Overload protection must switch of the motor in short time.

In case the starting torque of the motor is much higher than the load torque of the driven machine, high accelerating powers will develop at starting which may result in water hammering. Water hammering is caused by a rapid change in flow velocity in the pipeline and it reduce service life of the driven machine.

In case of direct start of the asynchronous motor approx. 6 times the nominal current will flow at the start. Voltage drop in the power lines from the bus bar is proportional to the current and that will result in a decrease of the terminal voltage. Since the torque of the motor is proportional to the square of the terminal voltage, the voltage decrease will result in a decrease of the starting torque.

2.1 Summary

In case a three-phase induction motor is too small, the torque is too low to guarantee the starting. In case the motor is too large, the high starting current could result

in a great voltage drop in the lines of the bus bar and in a very great decrease of the starting torque, so that heavy starting will not be guaranteed.

3. SPLINE AND BEZIER INTERPOLATION

The torque of a three-phase induction motor with squirrel-cage rotor is represented as a function of speed.

The characteristic of torque and speed as shown below will result (Fig. 1., Fig. 2., Fig. 3.).

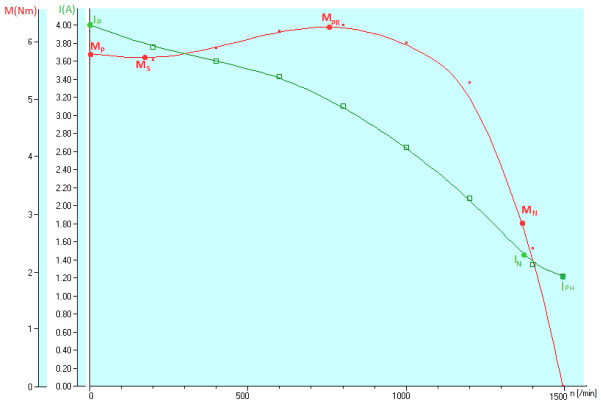


Fig. 1. Torque and current characteristics.

At the make instant, the motor will develop the starting torque MA. By increasing speed, the torque will first drop down to the pull-up torque MS and after torque will rise up to a maximum value, the breakdown torque MK, and will then very rapidly drop down.

The torque of the asynchronous motor depends upon the magnetic flux of the rotary field and the rotor current.

In case of synchronous speed, the rotary frequencies of rotary field and rotor will be identical and no voltage will be induced in the rotor so that no currents can flow in the cage bars and consequently no torque will be generated.

When motor is loaded, the speed of the rotor will decrease so that a voltage is induced in the cage of the rotor and currents will flow in the cage bars and a torque will be generated. Speed of the rotor will decrease until the torque of the motor and the load torque of the driven machine are balanced. Somehow the speed of the motor will decrease and adopt with increasing load of the motor.

3.1 Torque characteristic for star-delta starting

In case of direct-on starting of a three-phase induction motor, the high starting current will cause a voltage drop in the bus bar of power supply. For the limitation of the high starting current, the star-delta starting connection is often used because of its low cost comparing to soft starters and frequency converters.

First, the motor is connected in star and then reconnected to delta approximately at 75% of nominal speed. The only motors to be suitable for star-delta starting are those the permissible phase voltage of which corresponds with the phase-to-phase voltage of the supply system (lover level of voltage).

In case of starting in star connection, only 1/3 of the current will flow in the supply lines that would flow in case of direct-on starting in delta connection. The torque of starting in star connection only amounts to 1/3 of the torque of starting in delta connection, for the torque is proportional to the square of the phase voltage and therefore star-delta starting is not suitable for driven machines with full-load or heavy starting.

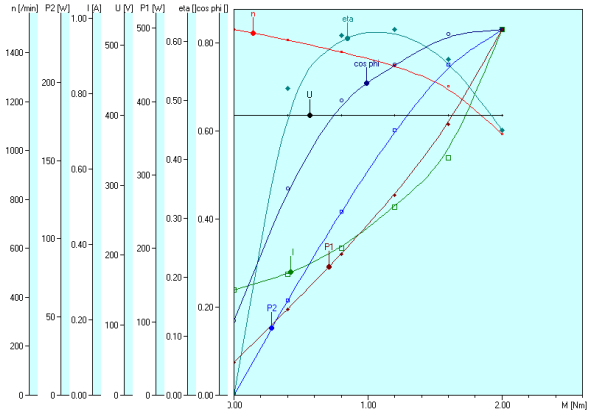


Fig. 2. Spline interpolation.

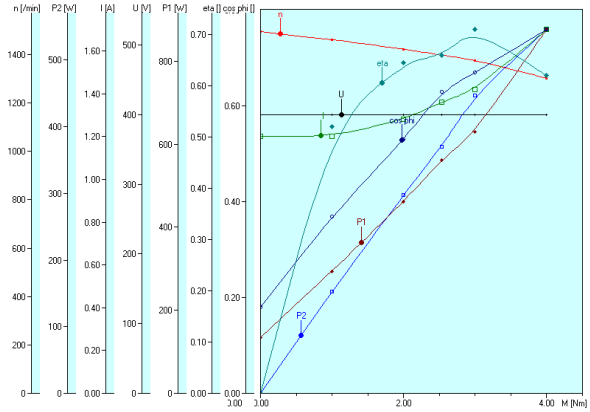


Fig. 3. Spline interpolation for delta connection.

3.2 Summary

The only three-phase induction motors suitable for star-delta starting are those the permissible phase voltage of which corresponds with the phase-to-phase voltage of the supply system (230/400 for automatic star delta can use only 230 V bus bar and 400/690 can use only 400 V bus bar).

In comparison to direct-on starting in delta connection, the starting current amounts to 1/3 of starting in star connection. The starting torque in star connection is 1/3 of the starting torque in delta connection. Recording characteristics with different interpolation methods are represented on pictures below (Fig. 4., Fig. 5.).

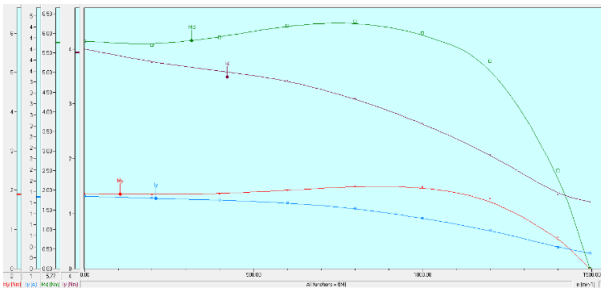


Fig. 4. Spline interpolation.

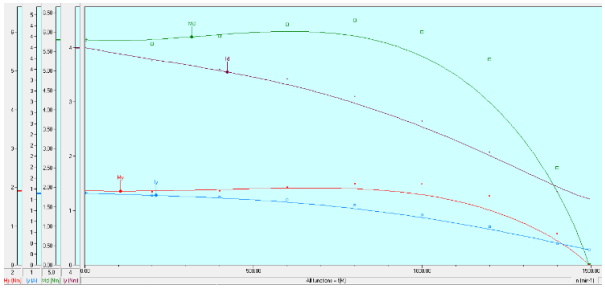


Fig. 5. Bezier Interpolation.

4. SIEMENS microcontroller CPU 80515

When using microcontrollers, we need to take great care on radio frequency interference (RFI) because one bit is of 5 V, so we need to take care for denouncing and bouncing of pushbuttons and for distance and protective elements connected from the I/O ports of microcontroller toward 5V relays that are controlling contactors in above current diagrams.

Alarms and protections are made with interrupt vector.

In case of fault (i.e. overload from NC 95 96) one port for interrupt will stop the main program and give approx. 20 seconds to the engineer to fix the problem. Alarm consists from red pilot lamp and buzzer that oscillate with frequency organized from the TIMER subroutine.

If engineer fix the problem electrical drive continue from the same state of work (program going back to the last instruction on RAM), but if not it will PUSH the first address on steak and program will trip the power supply.

Program is big so in this work only part of the program related to interrupt vector is presented.

```
ASSEMBLY LANGUAGE
; ------------------- Function Description -------------------
; The interrupt output on the Key-unit is connected to the
input
; for external interrupt 2 on P1.4. A LED in the LED-unit
is
; connected to P4.0 to provide a visual indication of the
; interrupt initiated by pressing a key.
; ------------------------------------------------------------
 --------- Declarations required for the Assembler ---------
  CPU     80515          ; Select microcontroller
  INCLUDE STDDEF51       ; SFR definitions
 SEGMENT Code            ; Code segment starts here
ORG      0000H          ; 1st. instruction, starts at address
0000H
; ------------------------------------------------------------
 jmp   START             ; Jump to main program
; ------------------------------------------------------------
; ---------------- Enter the IV in the IVT ---------------------
ORG   004BH             ; IV-position for external interrupt
2
JMP   ISR_INT2          ; Interrupt vector (IV)
; ------------------------------------------------------------
; ************************************************
; *       Main program, "Ext. Interrupt 2 from pressing a
key  *
; ************************************************
START:
CALL INIT_INT2        ; Initialize ext. Interrupt 2
************************************************
;                                                    y   d;
************************************************
MOV     A, #11111111B          ; Define bit pattern
MOV     P1, A                  ; Bit pattern to Port 1
JB   P4.3, ST7
JMP          START
INTERUPT SUB-ROUTINE
; ------------------------------------------------------------
;    Sub-routine for initializing external Interrupt 2
; ------------------------------------------------------------
INIT_INT2:
CLR   EAL           ; Global inhibit of interrupt acceptance
SETB I2FR             ; 0-1 edge initiates interrupt
SETB EX2              ; Allow interrupt from ext. Int 2
SETB EAL              ; Allow interrupt acceptance, global
RET
; ------------------------------------------------------------
;                ISR for ext. Interrupt 2
; ------------------------------------------------------------
ISR_INT2:
CALL     TIMERINTERUPT
CLR   IEX2            ; Reset interrupt request bit (*)
          JB P1.5, ST77
          JMP ST78
ST77:                PUSH 0000H
ST78:              RETI
; ------------------------------------------------------------
END
```

5. PLC – PROGRAM LOGIC CONTROLLER

A water tank is used as a reservoir for ballast water with an intermittent inflow via a pipeline that is opened and closed by means of a solenoid valve Y1.

PID controller can be made from PLC program block in STEP 7 or can be used external PID with 4-20mA input from level sensor (pressure transmitter).

Following graph shows the current consumption depending on the water in the tank (when SP = PV error is 0 and process is done) (Fig.6.).

When using PLC for controlling system of electrical motors we have to consider delay of the time PLC send order to contactor to connect and the time contacts connect. That's why we use one NO 13 14 contact from contactor back to the PLC.

Each bit is 24 V so the RFI are less problematic. Relays on the output must have protective diode parallel to the relay coil.

Full program and symbol table and hardware configuration are not involved in this work. Only main contactor protection, fault condition, hand/automatic start of the pumps and use of frequency converters (Fig.7.).

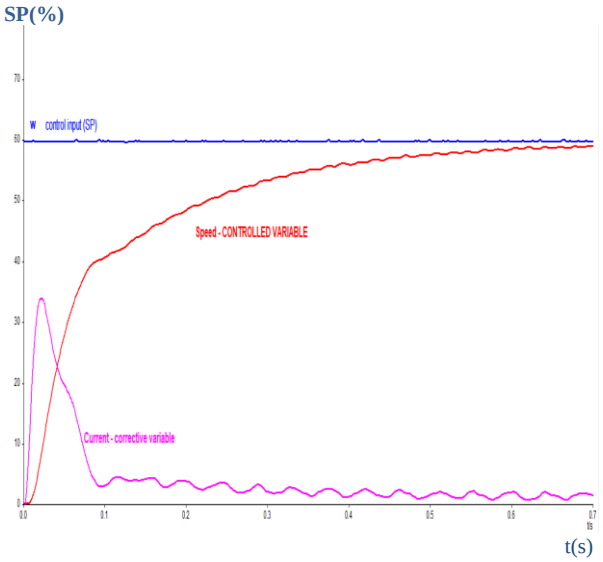


Fig. 6. Control characteristic.

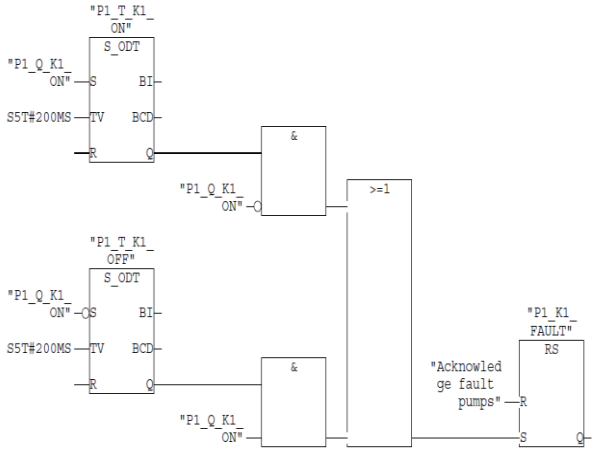


Fig. 7. Network for main contactor.

Fault of main contactor with OR logic gate (didn't close or didn't trip). Any contactor fault, MCB or emergency stop will trip breaker and make alarm (Fig.8.).

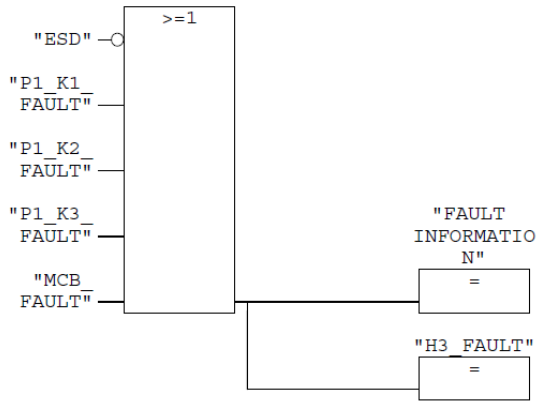


Fig. 8. Network for fault signalization.

6. CONCLUSION

On the example of using different methods of solving, we approached the way of realization of a specific practical problem depending on the available equipment, production conditions and staff training. It is easier to use FBD program than assembly language because the logic is more easy to monitor. On the other hand assembly programming provide precision and smaller hardware dimensions. For the most processes with feedback PLC control is the best solution. It provides the possibility of easy upgrading and control. Each of the methods can be applied in practice and are necessarily preconditioned by the production process itself and all its peculiarities.

7. REFERENCES

[1] Jureković, J.: Električni strojevi, Zagreb 2014.
[2] Nikolić, G.: Pneumatika, Školske novine, Zagreb, 1994.
[3] Planning and Design of Hydraulic Power Systems, Mannesmann Rexroth AG, 1998.
[4] Petrusella, F.: Electrical Machines and control systems, Published on Oct 19, 2016.
[5] Rabie, M.: Fluid Power Engineering, McGraw-Hill, 2009. 2. Lang, R.A. (ed.): Pneumatic Trainer 1
[6] Siemens STEP 7 help
[7] https://cache.industry.siemens.com/dl/files/551/45531551/att_56643/v1/S7gs___b.pdf
[8] Siemens – CPU 80515 https://www.keil.com/dd/docs/datashts/infineon/80x515_um.pdf

Authors:
Prof. Tatjana Stanivuk, Ph.D., student Marin Dujmović, University of Split, Faculty of Maritime Studies, Ruđera Boškovića 37, 21000 Split, Croatia.
E-mail: tstanivu@pfst.hr; mdujmovic@pfst.hr
Miroslav Dujmović, M.Sc., University Lecturer and High School Teacher, Nikola Muslim, B.Sc., High School Teacher, Electrotechnical School Split, Nikole Tesle 2, 21000 Split, Croatia.
E-mail: miroslav.dujmovic@skole.hr; nikola.muslim@skole.hr

MMA 2024
FLEXIBLE TECHNOLOGIES

15th INTERNATIONAL SCIENTIFIC CONFERENCE
NOVI SAD, SERBIA, SEPTEMBER 24-26, 2024

Original research paper https://doi.org/10.24867/MMA-2024-06-002

Jovanovic, S., Ranisavljev, M., Milosevic, A., Ilic Micunovic, M., Vukelic, D., Agarski, B.

LIFE CYCLE ASSESSMENT OF MACHINING PROCESSES: TURNING, MILLING, AND DRILLING

Abstract: *Machining is a widely utilized technique for producing various components, employing machine tools, cutting tools and fixtures to remove material via cutting, drilling, milling, turning, etc. However, these machining processes often generate significant amounts of waste material, contributing to environmental degradation. Furthermore, conducting Life Cycle Assessments on machining processes can provide valuable insights into their overall environmental impact, from raw material extraction to end-of-life disposal. The aim of the research is the analysis of generic data from the Life Cycle Inventory database that model machining processes, such as turning, milling and drilling and their impact on eutrophication, global warming potential acidification, abiotic depletion (fossil fuels), marine aquatic ecotoxicity and photochemical oxidation. The results indicate that the turning machining process significantly influences all six impact categories. Additionally, the materials aluminum and chromium steel exhibit higher impact values compared to conventional steel.*

Key words: *machining, life cycle assessment, global warming potential, acidification, eutrophication*

1. INTRODUCTION

The exponential rise in human population and industrialization over the past century has posed a significant challenge, escalating the environmental burden worldwide [1]. The industrial sector consumes approximately 54% of the world's total energy production [2], with manufacturing of metal-based durables alone accounting for about 25% of primary resource utilization and over one-third of global electricity consumption [3]. The significant energy and resource consumption by the industrial sector highlights the imperative for adopting sustainable manufacturing practices. Life Cycle Assessment (LCA) is a valuable tool for assessing the environmental impact of a product, process, or activity throughout its entire life cycle [4]. LCA is a widely recognized assessment tool that reveals the environmental impacts of products and services throughout their life cycles [5]. It enables a thorough analysis of environmental aspects and potential impacts across all stages of a product's life, spanning from raw material extraction through production, use, and disposal [6].

The machining process is critical for promoting sustainable production on factory floors. Processes such as turning, milling, grinding, and drilling are essential in manufacturing metal parts and components. However, these operations are energy-intensive and result in significant waste and emissions, contributing to various environmental concerns [7]. Sustainable machining can be defined as a process that can be sustained over an extended period without compromising its effectiveness. This approach aims to preserve the social, economic, environmental, and technological aspects of machining to ensure long-term sustainability [8]. Sustainable machining practices strive to mitigate the environmental impact of machining processes through strategies such as reducing energy consumption, optimizing material usage, and adopting cleaner production techniques [9].

The aim of this research is the analysis of datasets from the Life Cycle Inventory (LCI) database that model machining processes, such as turning, milling, and drilling, and their impact on eutrophication (EP), global warming potential (GWP), acidification (AP), abiotic depletion (fossil fuels) (AD (FF)), marine ecotoxicity (MAE), and photochemical oxidation (PO). The materials analysed in the research include steel, chromium steel, and aluminium.

2. METHODOLOGY

For this research, openLCA software (version 2.0) [10] and the Ecoinvent LCI database (version 3.7) [11] were utilized.

The methodology involved the following steps:

- Database selection: Ecoinvent version 3.7 was chosen for its comprehensive coverage of industrial processes and materials;
- Keyword search: Keywords "steel" "chromium steel" and "aluminium" were used to identify relevant datasets within the database;
- Process selection: Specific machining processes such as "turning" "milling" and "drilling" were searched within the material datasets. Dressing, small parts, large parts, and primarily roughing are excluded from the analysis; only 'average' processes are included;
- Analysis of impact category results: The selected datasets were analyzed for their contributions to GWP, EP, AP, AD (FF), MAE, and PO using the CML-IA baseline method in openLCA.

3. RESULTS

Fig. 1-4 show the impact of machining processes (turning, milling, and drilling) on EP, GWP, AP, AD (FF), MAE, and PO, calculated for 1 kg of material removed by that machining processes.

The processes selected from the database are: market for aluminium removed by drilling, computer numerical controlled (DRILL-ALU-CNC), market for aluminium removed by drilling, conventional (DRILL-ALU-CONV), market for chromium steel removed by drilling, computer numerical controlled (DRILL-CHR-STEEL-CNC), market for chromium steel removed by drilling, conventional (DRILL-CHR-STEEL-CONV), market for steel removed by drilling, computer numerical controlled (DRILL-STEEL-CNC), market for steel removed by drilling, conventional - steel removed by drilling, conventional (DRILL-STEEL-CONV), market for aluminium removed by milling, average (MILL-ALU-AVER), market for chromium steel removed by milling, average (MILL-CHR-STEEL-AVER), market for steel removed by milling, average (MILL-STEEL-AVER), market for aluminium removed by turning, average, computer numerical controlled (TURN-ALU-AVER-CNC), market for aluminium removed by turning, average, conventional (TURN-ALU-AVER-CONV), market for chromium steel removed by turning, average, computer numerical controlled (TURN-CHR-STEEL-AVER-CNC), market for chromium steel removed by turning, average, conventional (TURN-CHR-STEEL-AVER-CONV), market for steel removed by turning, average, computer numerical controlled (TURN-STEEL-AVER-CNC), market for steel removed by turning, average, conventional (TURN-STEEL-AVER-CONV).

On Fig. 1. the process with the greatest impact on all impact categories is DRILL-ALU-CNC. Fig 2 shows that the MILL-ALU-AVER process has the greatest impact on the impact categories. Fig. 3. shows that the TURN-ALU-AVER-CNC process has the greatest impact on all impact categories.

Fig. 4. shows comparative view of machining processes and their impact on GWP.

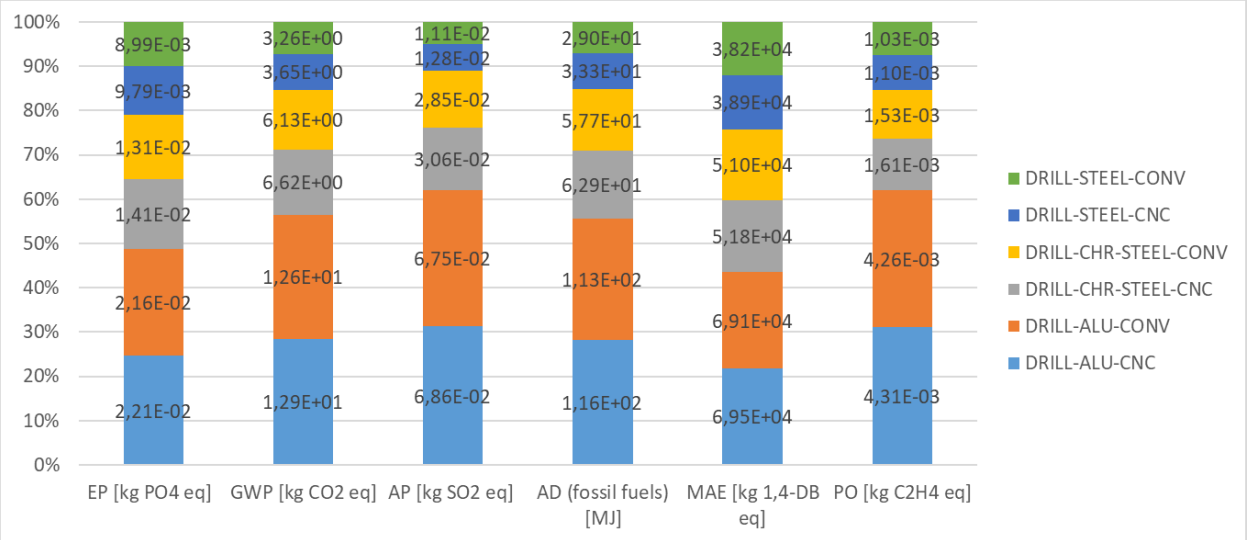


Fig. 1. The impact of the drilling machining processes on EP, GWP, AP, AD (FF), MAE and PO

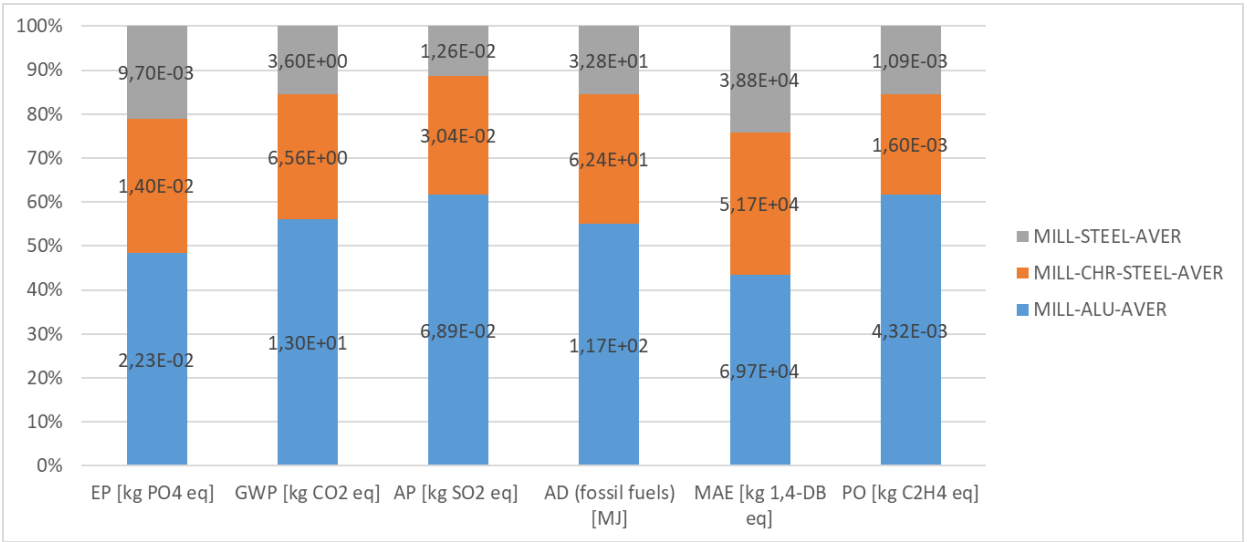


Fig. 2. The impact of the milling machining processes on EP, GWP, AP, AD (FF), MAE and PO

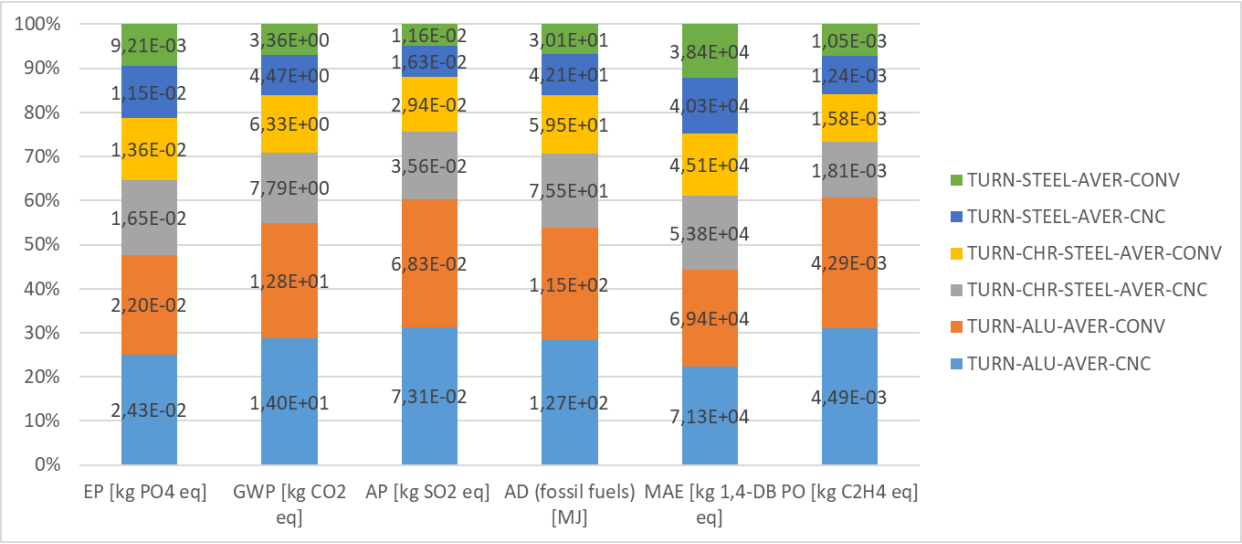


Fig. 3. The impact of the turning machining processes on EP, GWP, AP, AD (FF), MAE and PO

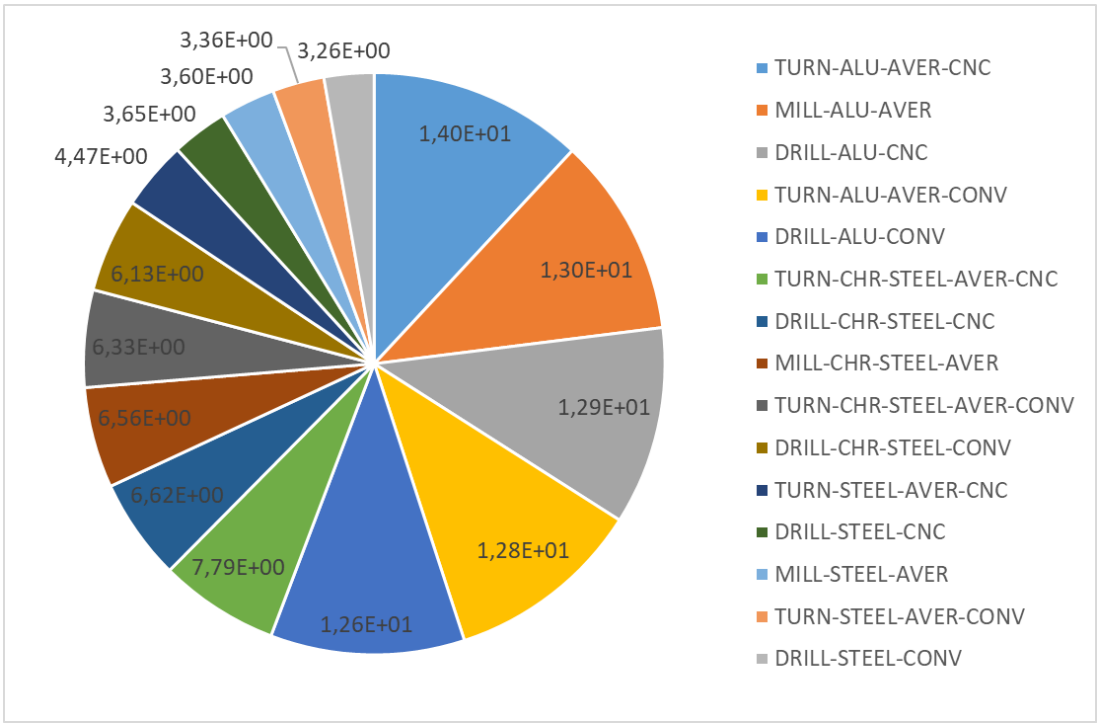


Fig. 4. Comparative view of GWP [kg - CO2 eq] for all machining processes

4. DISCUSSION AND CONCLUSION

The analysis of machining processes has revealed significant insights into their environmental impacts. In the drilling process, DRILL-ALU-CNC and DRILL-ALU-CONV have the greatest impacts on various impact categories (Fig. 1). In the milling process, the highest influences are associated with MILL-ALU-AVER and MILL-CHR-STEEL-AVER (Fig. 2). For the turning process, TURN-ALU-AVER-CNC and TURN-ALU-AVER-CONV are identified as having the greatest influence on the impact categories (Fig. 3).

The results indicate that conventional and CNC machining of aluminum have the most significant impacts across all evaluated categories. Specifically, the GWP is most affected by TURN-ALU-AVER-CNC, MILL-ALU-AVER, and DRILL-ALU-CNC (Fig. 4). Among the analyzed machining processes, turning is found to have the greatest overall impact on all environmental impact categories, including EP, AP, GWP, AD (FF), MAE, and PO.

The greater impact of the turning process can be attributed to several factors. Turning typically involves continuous contact between the cutting tool and the workpiece, resulting in higher energy consumption and greater tool wear, which in turn leads to increased emissions and resource use. Additionally, the turning process generates significant amounts of metal turnings and coolant waste, contributing to higher levels of MAE and PO. The energy-intensive nature of CNC turning further exacerbates these impacts, particularly in terms of AD (FF) and GWP.

Furthermore, the materials used in turning, such as aluminum and chromium steel, exhibit higher

environmental impact values compared to conventional steel. Aluminum, in particular, requires substantial energy for extraction and processing, leading to elevated levels of EP and AP.

Chromium steel, due to its alloying elements and complex manufacturing processes, also contributes significantly to these impact categories.

The findings of this research underscore that the generic data on the machining process from the database represent the mean values of the environmental impact results from those processing procedures. This approach highlights the importance of considering variations in machining parameters and material properties when assessing environmental impacts.

To further reduce the environmental impacts of machining processes, the following strategies are recommended:

- Energy Efficiency: Implement energy-efficient technologies and practices, such as high-efficiency motors, variable-frequency drives, and energy recovery systems, to reduce fossil fuel consumption in machining.
- Emission Control: Use advanced filtration and treatment systems, like High-Efficiency Particulate Air (HEPA) filters, electrostatic precipitators, and advanced coolant recycling systems, to minimize pollutants that contribute to EP, AP, and MAE.
- Sustainable Materials: Explore alternative materials and lubricants with lower environmental impacts, such as biodegradable lubricants and coolants.
- Process Optimization: Optimize process parameters and adopt cleaner production techniques, including precision machining, real-time monitoring, and lean manufacturing principles, to reduce waste and emissions.

By addressing these key areas, manufacturers can significantly reduce the environmental footprint of machining processes, foster more sustainable industrial practices, and protect the environment. Future research should prioritize the development of innovative technologies and methods to further mitigate the environmental impacts of machining. This includes the exploration of advanced materials, such as composites and nanomaterials, which offer the potential for enhanced performance with reduced environmental impact.

5. REFERENCES

[1] Khanna, N., Wadhwa, J., Pitroda, A., Shah, P., Schoop, J., Sarıkaya, M.: Life cycle assessment of environmentally friendly initiatives for sustainable machining: A short review of current knowledge and a case study, Sustainable Materials and Technologies, Vol. 32, 2022.

[2] Campitelli, A., Cristóbal, J., Fischer, J., Becker, B., Schebek, L.: Resource efficiency analysis of lubricating strategies for machining processes using life cycle assessment methodology, Journal of Cleaner Production, Vol. 222, No. 3, pp. 464-475, 2019.

[3] Roy, P., Nei, D., Orikasa, T., Xu, Q., Okadome, H., Nakamura, N., Shiina, T.: A review of life cycle assessment (LCA) on some food products, Journal of Food Engineering, Vol. 90, No. 1, pp. 1-10, 2009.

[4] Van der Giesen, C., Cucurachi, S., Guinée, J., Kramer, G. J., Tukker, A.: A critical view on the current application of LCA for new technologies and recommendations for improved practice, Journal of Cleaner Production, Vol. 259, pp. 120904, 2020.

[5] Soori, M., Jough, F.K.G., Dastres, R., Arezoo, B.: Sustainable CNC machining operations, a review, Sustainable Operations and Computers, Vol. 5, pp. 73-87, 2024.

[6] Guinée, J.B. (Ed.). Handbook on Life Cycle Assessment: Operational Guide to the ISO Standards. Springer, 2002.

[7] Dornfeld, D., Min, S., Takeuchi, Y.: Recent advances in green and sustainable manufacturing, International Conference on Competitive Manufacturing, pp. 13-20, Stellenbosch, South Africa, 2006.

[8] Duflou, J.R., Sutherland, J.W., Dornfeld, D., Herrmann, C., Jeswiet, J., Kara, S., Kellens, K.: Towards energy and resource-efficient manufacturing: A processes and systems approach, CIRP Annals, Vol. 61, No. 2, pp. 587-609, 2012.

[9] Jawahir, I.S., Dillon, O.W.: Sustainable manufacturing processes: New challenges for developing predictive models and optimization techniques, Proceedings of the First International Conference on Sustainable Manufacturing, Vol. 1, pp. 1-19, 2007.

[10] https://www.openlca.org/

[11] https://ecoinvent.org/database/

ACKNOWLEDGEMENTS

This research has been supported by the Ministry of Science, Technological Development and Innovation (Contract No. 451-03-65/2024-03/200156) and the Faculty of Technical Sciences, University of Novi Sad through project "Scientific and Artistic Research Work of Researchers in Teaching and Associate Positions at the Faculty of Technical Sciences, University of Novi Sad" (No. 01-3394/1).

Authors:

MSc Sladjana Jovanovic, MSc Milos Ranisavljev, MSc Aleksandar Milosevic, PhD Milana Ilic Micunovic, PhD Djordje Vukelic, PhD Boris Agarski, University of Novi Sad, Faculty of Technical Sciences, Trg Dositeja Obradovica 6, 21000 Novi Sad, Serbia, Phone.: +381 21 485-24-76.

E-mail: sladjanajovanovic76@yahoo.com; mranisavljev97@gmail.com; aleksandar.milosevic@uns.ac.rs; milanai@uns.ac.rs; vukelic@uns.ac.rs; agarski@uns.ac.rs

MMA 2024
FLEXIBLE TECHNOLOGIES

15th INTERNATIONAL SCIENTIFIC CONFERENCE
NOVI SAD, SERBIA, SEPTEMBER 24-26, 2024

Original research paper https://doi.org/10.24867/MMA-2024-06-003

Bošković, G., Stepanov, B., Bošković. M., Todorović, M., Čepić, Z.

THE PROCEDURE FOR CALCULATING INPUT PARAMETERS IN THE PROCESS OF DETERMINING POTENTIAL RISK ZONES IN WAREHOUSES

Abstract: *Taking into account that fire safety in warehouses is a serious challenge and has not been sufficiently investigated, this paper aims to present a new methodological approach concerning the mentioned issue. The COPRAS MCDM method was implemented in the aforementioned approach to determine the weight coefficients based on the emission and thermal characteristics of the materials placed in the high-bay warehouse. The mentioned coefficients represent input data for calculations and simulations related to determining potential fire risk zones. The effectiveness of the proposed approach was verified by a numerical example.*
Keywords: *Fire, High-bay warehouse, MCDM, COPRAS method, Fire risk zones*

1. INTRODUCTION

Bearing in mind that fire poses a serious threat to the safety of people and property, whether residential, warehouse, or industrial, managing the risk of fire outbreaks is a major challenge in urban and rural areas. [1]. Fires in warehouses have a small share in the total number of fires compared to other locations where fires occur. However, in terms of the release of heat, the size of the area affected by the fire, the degree of damage to the building itself, and material damage, these fires in warehouses have significant consequences compared to fires in other types of buildings.

Warehouses, which represent an integral part of logistics, are often exposed to various improvements and corrections in the development phase, all with the aim of better performance, capacity, and efficiency of the warehouses themselves. The aforementioned improvements result in larger and higher warehouses, the use of automated systems for storage and retrieval of storage units (AS/RS systems), increased storage density, and placement of storage units at higher heights [2]. The improvements above have made warehouses efficient, but they have also led to potential hazards in fire protection.

The analysis and modeling of fires in storage facilities, as well as the assessment of the risk of accidents, is attracting more and more attention from both researchers and engineers who design these facilities and systems. Fires in such buildings are characterized as very intense due to the high content of combustible matter per unit area about the volume of the building. Depending on the type of warehouse and the fuel in the warehouse, in the event of a fire, smoke and toxic combustion products (containing carcinogenic substances) are emitted intensively, which contributes to harming the health of people inside the facility as well as air pollution.

The main goal of the research in this paper is the development of a procedure for determining the input parameters necessary for the process of determining the potential risk zone of fire occurrence in high-bay warehouses. Compared to existing methods and approaches in the field of safety and risk assessment in warehouses, this procedure enables the precise determination of input parameters in the form of weight coefficients that are obtained based on the characteristics of the stored material. By using the multi-criteria decision-making method, weight coefficients are obtained for each material that is stored and which represents input data in the process of determining the specified location in the high-bay warehouse.

2. MATERIALS AND METHODS

The procedure for determining input parameters consists of two parts (Fig. 1). The first part refers to the selection of parameters used in fire risk assessment methods, necessary to obtain weighting coefficients necessary for determining fire danger zones using multi-criteria decision procedures [3, 4]. The second part presents the COPRAS method, which was chosen as relevant for obtaining the weight coefficients necessary for further calculation, as in the paper [5].

2.1 Selection of Parameters for Multicriteria Analysis

The basic concept in the development of the procedure was to combine factors related to the emission of harmful substances due to the frequency of poisoning in fires, as well as aspects related to the process of burning materials in a fire. To implement the procedure, 7 key parameters were selected based on the available literature, which at the same time represents a limitation of the COPRAS method to the number of criteria that can be applied. The mentioned parameters represent the criteria in the multi-criteria analysis procedure, which are divided into two groups: criteria related to the impact on human health and the thermal characteristics of the stored materials.

To determine potential fire risk zones based on data from the available literature [6, 7], 7 different parameters were selected: CO concentration [mg/g], CO_2 concentration [mg/g], Smoke density [kg/m^3], Ignition temperature [^{o}C], Thermal conductivity [V/mK], Specific heat capacity [J/(kgK)] and calorific value

[MJ/kg]. By increasing the number of criteria within the COPRAS method, the quality and precision of the results obtained by the multi-criteria decision-making process are reduced [8].

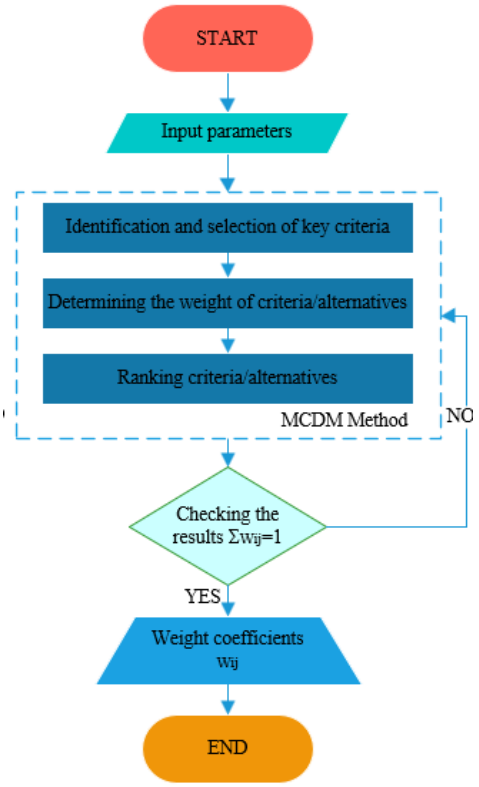


Fig. 1. Flowchart of the proposed procedure

2.2 Determination of Input Parameters Using the COPRAS Method

The COPRAS method is widely used in various fields. It was used for risk assessment in the construction industry, for the selection of the type of robotization in production, for the selection of mechanical processing of composite materials, for the selection of materials for solar panels, etc. In this paper, the COPRAS method was used to determine the weighting coefficients, which also represent input parameters for risk assessment in the case of a high-bay warehouse, as the authors presented in their paper [9]. The COPRAS method includes several steps:

- Step 1 - Creation of the initial decision matrix

In the first step, to create the initial decision-making matrix, 5 materials were selected to be stored: wood, cardboard, chipboard, PVC plastic, and rubber. These materials will represent alternatives in the process of multi-criteria decision-making using the COPRAS method in further steps. In a multi-criteria decision-making process, the criteria usually have different units of measure. In order to transform the performance of the considered alternatives, which represent the materials in the warehouse, into dimensionless values, the normalization procedure is used. For normalization in the COPRAS method, the following formula is used, which also represents the initial matrix containing the input data related to the *i-th* alternative and the *j-th* criterion:

$$X = \left[x_{ij} \right]_{m \times n} = \begin{bmatrix} x_{11} & \dots & x_{1j} & \dots & x_{1n} \\ \vdots & \ddots & \vdots & \ddots & \vdots \\ x_{21} & \dots & x_{ij} & \dots & x_{2n} \\ \vdots & \ddots & \vdots & \ddots & \vdots \\ x_{m1} & \dots & x_{mj} & \dots & x_{mn} \end{bmatrix}_{m \times n} \quad (1)$$

where alternatives are marked with *i=1, 2,...,m*, and criteria are marked with *j=1,2,...,n.*

- Step 2 - Normalization of the decision matrix

The normalization of the values of the elements of the decision matrix to remove the dimensionality is done by linear transformation with the mathematical form according to Eq. (2).

$$r_{ij} = \frac{x_{ij}}{\sum_{i=1}^{n} x_{ij}}, \; i = 1, \dots m, \; j = 1, \dots n \quad (2)$$

where: k_{ij} - performance of the *i-th* alternative in relation to the *j-th* criterion; *m* - number of alternatives; *n* - number of criteria.

- Step 3 - Forming the weighted normalized decision matrix $V = \left[V_{ij} \right]_{m \times n}$

The weight vector indicating the preference level is denoted by the weight vector represented in Eq. (3).

$$w_j = \left[w_1 \dots w_n \right] \text{ where } \sum_{i=1}^{n} \left(w_1 \dots w_n \right) = 1 \quad (3)$$

The weight-normalized value of the decision matrix V_{ij} is calculated using the weight vector and the normalized decision matrix, using Eq. (4):

$$V_{ij} = w_j \times r_{ij}, i = 1, \dots m, \; j = 1, \dots n \quad (4)$$

- Step 4 - Sum of the weighted normalized values of criteria V_{ij}

In this step, it is necessary to categorize the criteria into useful or useless criteria to maximize all those criteria that are useful and minimizing all those that are considered useless. To make it easier to calculate income S_{+i} (maximizing indices) and expenditure S_{-i} (minimizing indices), the decision matrix first places the income and then expenditure criteria, and S_{+i} and S_{-i} are calculated using expressions (5) and (6):

$$S_{+i} = \sum_{j=1}^{n} V_{ij} \Big| \; j \in j^{\max}, i = 1, \dots m \quad (5)$$

$$S_{-i} = \sum_{j=1}^{n} V_{ij} \Big| \; j \in j^{\min}, i = 1, \dots m \quad (6)$$

- Step 5 - Determining the relative importance (weight) of each alternative

Relative importance helps to compare different alternatives through a generalized metric. It can be calculated according to the following formula:

$$Q_i = S_{+i} + \frac{S_{-\min} \sum_{j=1}^{n} S_{-i}}{S_{-i} \sum_{j=1}^{n} \left(S_{-\min} / S_{-i} \right)}, i = 1, 2, \dots m \quad (7)$$

where S_{-min} is the minimum value of S_{-i}.

• Step 6 - Ranking the alternatives

The considered alternatives are ranked in ascending order, according to the value of Q_i, and the best alternative is determined using the following formula:

$$U_i = \left[\frac{Q_i}{Q_{\max}} \right] \times 100\% \qquad (8)$$

3. NUMERICAL EXAMPLE

In the numerical example shown in this section, the parameters of the high-bay warehouse related to dimensions and layout (see Fig. 2) given in the paper [9] were used. Based on the considerations given in Chapter 2, to obtain the most accurate data needed for further simulation, it was decided to select 5 types of solid materials (wood, cardboard, chipboard, PVC plastic, and rubber) as alternatives in the multi-criteria decision-making process, which will be the subject of further calculations.



Fig. 2. Layout of a high-bay warehouse with associated dimensions and materials (• wood, • cardboard, • chipboard, • PVC, and • rubber)

Material	CO [mg/g]	CO_2 [mg/g]	Smoke density [kg/m^3]	Ignition temperature [°C]	Thermal conductivity [W/mK]	Specific heat capacity [J/(kg K)]	Calorific value [MJ/kg]
Wood	6	1696	100	350	0.15	1360	14.4
Cardboard	0.1	1450	39.8	427	0.061	1400	13.5
Plywood	6	1774	400	150	0.13	2500	17
PVC	71	657	55.03	391	0.185	900	41
Rubber (tire)	600	1911	8000	315	1.85	1880	35

Table 1. Input parameters in the procedure of determining the weighting coefficients required for the simulation

Criterions	C1	C2	C3	C4	C5	C6	C7
Unit of measure	[mg/g]	[mg/g]	[kg/m^3]	[°C]	[W/mK]	[J/(kg K)]	[MJ/kg]
Goal	min	min	min	max	min	max	min
	Beneficial			Non-Beneficial			
Weights	0.2	0.2	0.2	0.1	0.1	0.1	0.1
A1	6	1696	100	350	14.4	1360	0.15
A2	0.1	1450	3.8	427	13.5	1400	0.061
A3	6	1774	400	150	17	2500	0.13
A4	71	657	55.03	391	41	900	0.185
A5	600	1911	8000	315	35	1880	1.85

Table 2. Decision matrix

The list of materials and the numerical values of the seven selected parameters are given in Table 1. The listed characteristics of materials related to combustion shown in the mentioned table represent criteria in the multi-criteria decision-making process and are taken from the literature [10, 11].

Table 2 presents the criteria in the order presented in section 2.1, of which C1, C2, and C3 are considered useful because they take into account the emission of harmful gases affecting human health, while the other criteria are C4, C5, C6, and C7 concerning combustion declared in the first case as useless.

Following all the steps provided by the COPRAS method (1-6) and based on equations (2-8), in step 6 the weights for each of the alternatives w_i and the corresponding ranking are obtained as shown in Table 3.

4. RESULTS

After the procedure was carried out, the individual results of each alternative for each criterion were obtained, which are shown in Fig. 3. Based on the obtained data from the table, it is seen that alternative A5, i.e. rubber has the highest weight coefficient.

w_i
0,14821
0,13642
0,15195
0,11238
0,45105

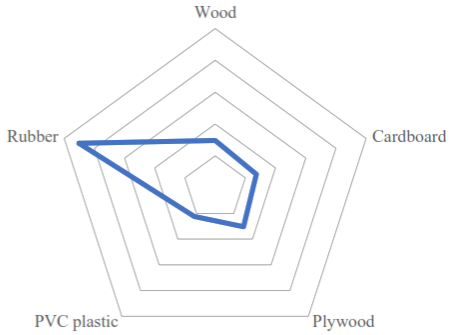


Fig. 3. Tabular and graphical representation of the results obtained using the procedure

5. FINAL REMARKS

Warehouses represent an important link in the supply chain. Warehouses that function efficiently allow the companies that own them to smoothly perform all the necessary operations within the warehouse itself. For the aforementioned reasons, a multi-criteria analysis using the COPRAS method was carried out in this paper, taking into account several criteria in the form of thermal characteristics of materials. The materials considered as alternatives in this procedure are wood, cardboard, plywood, PVC plastic, and rubber. The paper also shows that the COPRAS MCDM method is simple, easy to use, and can be applied to a wide range of decision alternatives. The relative weight coefficients obtained using the mentioned method will represent the input parameters for further simulations and mathematical models for fires in warehouses and storage systems. In future research, it is possible to compare the results of several multi-criteria methods and determine which of the methods provides more accurate data on the weight coefficients.

6. REFERENCES

[1] lkış, S., Aksoy, E., Akpınar, K.: *Risk Assessment of Industrial Fires for Surrounding Vulnerable Facilities Using a Multi-Criteria Decision Support Approach and GIS*, Fire, Vol. 4, No. 3, pp. 53, 2021.

[2] Dinaburg, J., Gottuk, D.T.: Fire Detection in Warehouse Facilities; Springer, New York, 2012.

[3] Bošković, G., Čepić, Z., Ubavin, D.: *Determination of Relative Weight Coefficients Based on Thermal Characteristics of Materials Using the F-AHP Method*, Engineering Today, Vol. 1, No.4, pp. 27–32, 2022.

[4] Chanthakhot, W., Ransikarbum, K.: *Integrated IEW-TOPSIS and Fire Dynamics Simulation for Agent-Based Evacuation Modeling in Industrial Safety*, Safety, Vol. 7, No. 2, pp. 47, 2021.

[5] Valipour, A., Yahaya, N., Md Noor, N., Antuchevičienė, J., Tamošaitienė, J.: *Hybrid SWARA-COPRAS Method for Risk Assessment in Deep Foundation Excavation Project: An Iranian Case Study*, Journal of Civil Engineering and Management Vol. 23, No. 4, pp. 524–532, 2017.

[6] Ju, W., Su, G., Wu, L., Oforiwaa, P.O.: *The 3D-Dynamic Fire Risk Evaluation Method of Modern Logistics Warehouses: A Modified Gustav Method*. Fire Technology, 2023.

[7] Hurley, M.J., Gottuk, D., Hall, J.R., Harada, K., Kuligowski, E., Puchovsky, M., Torero, J., Watts, J.M., Wieczorek, C., Eds.: SFPE Handbook of Fire Protection Engineering; Springer, New York, 2016.

[8] Alinezhad, A., Khalili, J.: *COPRAS Method. In New Methods and Applications in Multiple Attribute Decision Making (MADM)*, International Series in Operations Research & Management Science: CHAM, Vol. 277, pp. 87–91, 2019.

[9] Bošković, G., Todorović, M., Markovic, G., Čepić, Z., Mladenović, P.: *Multi-Aisle Automated Rack Warehouse Simulation for Average Travel Time*, Proceedings of XI International Conference "Heavy Machinery-HM 2023", Faculty of Mechanical and Civil Engineering in Kraljevo, pp. A53–A58, Vrnjačka Banja, 2023.

[10] Ch. Varada Rajulu, K., Nandanwar, A., C. Kiran, M.: *Evaluation of Smoke Density on Combustion of Wood Based Panel Products*, International Journal of Materials and Chemistry IJMC, Vol. 2, No. 5, pp. 225-228, 2013.

[11] Kutz, M.: Handbook of Environmental Degradation of Materials; Elsevier, Amsterdam, 2018.

ACKNOWLEDGMENTS

The authors wish to acknowledge the support of the Ministry of Science, Technological Development and Innovation of the Republic of Serbia, through the Contracts for the scientific research financing in 2024, 451-03-65/2024-03/200108 and 451-03-65/2024-03/200156.

Authors:

MSc Goran Bošković, PhD Marina Bošković, MSc Marko Todorović, University of Kragujevac, Faculty of Mechanical and Civil Engineering in Kraljevo, Dositejeva 19, 36000 Kraljevo, Serbia, Phone.: +381 36 38-32-69.

E-mail: boskovic.g@mfkv.kg.ac.rs; boskovic.m@mfkv.kg.ac.rs; todorovic.m@mfkv.kg.ac.rs

PhD Borivoj Stepanov, PhD Zoran Čepić, University of Novi Sad, Faculty of Technical Sciences, Trg Dositeja Obradovica 6, 21000 Novi Sad, Serbia, Phone.: +381 21 485-24-76.

E-mail: bstep@uns.ac.rs; zorancepic@uns.ac.rs

MMA 2024
FLEXIBLE TECHNOLOGIES

15th INTERNATIONAL SCIENTIFIC CONFERENCE
NOVI SAD, SERBIA, SEPTEMBER 24-26, 2024

Original research paper https://doi.org/10.24867/MMA-2024-06-004

Ćurčić, S., Milovančević, M., Šarenac, S.

APPLICATION OF MECHATRONIC STRUCTURES FOR THE PURPOSE OF ENVIRONMENTAL PROTECTION

Abstract: *The paper analyzes the issues related to harmful emissions of plastic into the atmosphere, i.e. describes plastic used for the formation of containers and bins. In addition, the harmfulness of producing the container itself in tools (molds) on robots based on the noise produced by the individual molds where they create a problem for the operators in the production is also described. Certain analyses are presented in which it is attached how these problems occur and then analyze how these problems are solved with various aids. These aids in our case are sensors, visual control and some other mechatronic structures that are the topic of this paper. Experimental analysis is done by changes in PLC applications where sensors give us certain signals for the action of our protection and thus with the help of these analyzes it is concluded how these problems are solved. Through calculations and certain measurements, which are based on previous experiences, these problems are solved using software that are destined for it, where changes in the sequence of obtaining bins are added to certain sub programs or structures for the purpose of solving this problem. The results of the analysis, give us information on how all these problems can be stopped and of course if they come to them and solve these problems.*

Key words: *harmful emissions, plastic containers, noise pollution, mechatronic solutions, experimental analysis*

1. INTRODUCTION

Plastic is a material derived from oil. After use, plastic products decompose in the country for a long time, over 100 years. Therefore, it should be known that plastic waste, in essence, does not have to be waste, but a group of new resources, that is, raw materials that can be reused. Plastic waste in landfills accounts for 9% of the total weight of waste, but by volume it occupies 32%. Recycling waste plastics contributes to reducing electricity consumption and thus reducing greenhouse gas emissions. In Serbia, about 10% of plastic waste is recycled. Plastic recycling is the separation and sorting of plastic materials from waste and its reuse. Plastic waste is a very complex substance, because its chemical composition varies depending on the type of plastic. Therefore, it is very important to first separate the plastic by type. There are seven types of plastic, which are most often recycled. Each of them has its own recycling marks, for ease of separation. It is best if there are opportunities to separate plastic waste at the place of its formation. Many plastic materials can be reused if they are properly sorted. In addition to the labels, plastic for recycling can be successfully classified by the ignition process. Different types of plastic when up there have a different smell and color of flame. Such a sorted plastic goes for further treatment, which consists in washing and cleaning sorted plastic. Washing and cleaning is carried out for more efficient use in further production. The next stage of plastic recycling is shredding in special mills for grinding this material. The larger pieces are cut into smaller pieces, for easy placement in the mill. Such ground plastic, known in jargon as "grinding", can be various granulations, which depends on the sieve on the mill. The resulting granulate can be used immediately in the process of manufacturing plastic items, and can also go through another stage, i.e. the reconstruction. This stage of re-grinding is carried out with regranulators. The resulting plastic regranulate is used directly in the process of manufacturing plastic items.

The physical properties of the plastic are: light weight, easy processing, properties can be modified, low permeability, chemical resistance.

Recycling: Plastic can be recycled using different methods. Plastic recycling is the process of reusing scrap and waste plastic and reprocessing materials into useful products, sometimes in completely different forms from the initial state. Since plastics are not usually biodegradable, recycling is part of a global effort to reduce the share of plastics in waste. This helps to reduce the high proportions of plastic in the accumulation of waste [1].

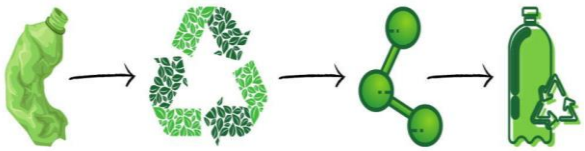


Fig. 1. Molecular plastic recycling [1]

2. ANALYSIS AND MEASUREMENTS

Analyses and measurements are described problems that arise in the company Inmold Group Požega.

Analyses are carried out on certain problems in the plant and along with the analysis and type of problem, the solution of that problem belongs to the given topic is also stated. Analyses of the problem will be presented, in order, in their entirety.

2.1 Solving the high temperature problem created by plastic injection molding machine

For the analysis, the measurement of air humidity and temperature in the working area for the production

of plastic packaging and products used in food industry was carried out. The measurement was carried out in the working area, the plant, where there are machines for the production and processing of plastic products. In the room there are large temperature variations during the production process that affect the quality of production of the product itself and the atmosphere in the plant itself where workers perform work in the production and maintenance of the machine. The machine that is the main cause of the temperature variation in operation is the plastic injection molding machine. There are other machines in operation, but they don't have too much influence. The plastic injection molding machine operates at high temperatures of over 120°C, which is necessary for melting plastic and injection molding. The main problem arises in the summer when the outside temperatures are over 30-35 °C, then the cooling and ventilation systems have to work continuously because otherwise due to excessive temperature, the product is deformed because the tool has a fixed cooling mode and due to excessive temperature inside the plant there is inadequate cooling in the tool so that there is inconsistent products in production as well as a more difficult working conditions for workers who serve the machine and work in the plant. Due to the high temperature in the plant, it becomes barely tolerable for workers because then the problem is not only heat but also toxic gases that are released due to the process of making from plastic that can be harmful in the long term. Specifically for the manufacture of the aforementioned plastic packaging, toxic gases are at a minimum because for the production of containers made of plastic used in the food industry, PS (polystyrene) is used, which is not as harmful as PVC plastic because polyvinyl chlorides release a large amount of toxic gases that are far more dangerous than polystyrene [6].

Troubleshooting devices

To solve the defined problem, the following components will be used:

- The RH520 is a portable temperature measuring device that is fixed in nature. It can be placed on a wall or a flat base. The device has power supply via AC adapter and can be inserted 3 AA-type batteries that serve as support in case of voltage drop or if the measurement is carried out in the field [5],
- Temperature sensor,
- Visual control camera with PLC PLC Schneider Modicon M241.

The principle of problem solving

The solution of the problem is based on the following:

- The sensor detects high temperatures,
- The type of nature of the problem (hardware or software) is revealed,
- The IML robot borrows visual inspection cameras, where you can see a higher percentage of scrap, which tells us that the problem is related in the insufficiently solid state of the vessel (the vessel does not have enough time to harden because the temperature of the mold is higher than the set),
- RH520 provides temperature and humidity values (along with the percentage of harmful ness of plastic in the air), i.e. data and reacts to the machine and robot to stop immediately,
- The workforce from this part is isolated for a while
- The problem is solved (analysis and the whole process of solving it below).

One of the main causes of this problem is that these high temperatures, which lead to air damage and intolerability, come from the mold of the machine in which the molten plastic is injected as well as the injector itself. The analysis leads to the conclusion that every time this problem occurs, it was in the 3rd shift or in the late hours in summer temperatures when the machine works non-stop for a large number of hours or at 3h, 4h when the temperatures in the summer are therefore huge.

The temperature of molten plastic becomes significantly high, where the molds become very hot and therefore do not get the given shape of the container. For some initial detection, a visual control on the robot is used, which immediately detects scrap with a given program. Confirmation of the problem comes from temperature sensors and later workers complain about the heat in the area. Then the alarm goes off that something is wrong.

Visual inspection of IML robots

The system performs a 360-degree inspection for all types of IML decorations – wrapping decorations as well as basic labels regardless of the orientation of the labels. Even unadorned surfaces can be inspected for a flawless look. IMLWatcher® is applicable in all areas of IML manufacturing design. It is usually used to control bowls, cups and lids. Depending on the requirements, the system can be equipped with multiple cameras and special lighting that are capable of detecting all typical IML defects such as the control of the edges of the bowl and whether the ethics are beautifulblind or melted (to us important because it is the main cause of temperature), blow-bis, offset etiquette and angular rotation. IMLWatcher® provides comprehensive quality control for the mold marking process. The advantage is obvious: the system can be integrated directly into automation robots and therefore especially saves space and efficient. It fits into the existing landscape without any difficulty and supports very fast cycle times.

In Fig. 2, you can see the camera scanning the vessels and looking at certain edges, thus detecting whether the vessel is good or not. On the right side you can see the scales where certain aspects are checked whether they meet the conditions that are given and that the bowl is classified as a non-compliant product or not.

These aspects are: the edges of the bowl, the position of the label (vertical, horizontal and label rotation), blow-encore, bubbles and folds that occur due to high temperature, contamination, errors in printing on the label and defect on the edge of the label.

In Fig. 3, we can see a classic example of error detection and that is poorly glued label and edges are not good. For both, the causative agent is high temperature. Later, this container is placed on a strip of bad pieces and we in the PLC program can see how this number grows,

already then it can be concluded what the problem is production stops. And in these diagrams you can clearly see the pattern of changing parameters. Fig. 4 clearly shows the drop in temperature caused by the cooling of the room during the adjustment of the machine because the people in charge of maintenance constantly entered and exited the plant to the workshop and the outer door was constantly open where the external temperature was about 10 degrees. After this, it is mandatory to check the condition in the drive, the temperature sensor, the condition around the machines, and the main thing is whether the operator felt any problem. The operator's request is more important than all of these because he is the main alarm that tells us that something is wrong. Then the RH520 instrument enters and the measurement is carried out. By measuring (attached graphic) you can see the temperature, humidity and harmful emission of plastic into the atmosphere. The measurement was carried out at the plant for the production of packaging and plastic products of polystyrene type (PS). In operation, the machine worked occasionally (you can see the graphics after the temperature jump). The average outdoor temperature is 16 °C.

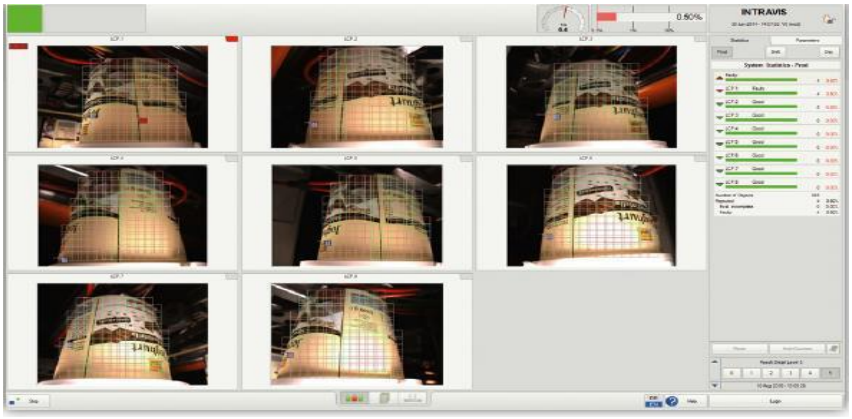


Fig. 2. Snippet from Visual Control

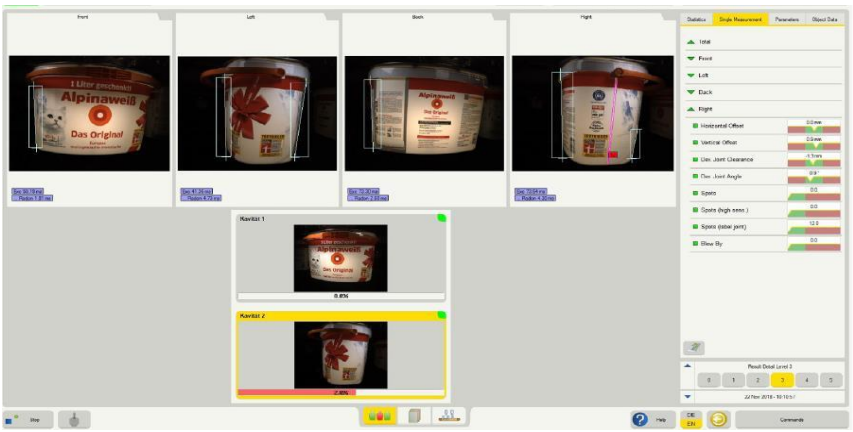


Fig. 3. Error detection

The RH520 stands on the protective cover of the machine above the plastic injection tool and the part over which the technician supervises the manufacturing process. The protective cover is automated so that when it is opened, the automatic stops the machine.

The first diagram is a diagram of the temperature in which see the jumps and falls that are described in the text above. The second diagram gives an increase in the value of plastic damage in that room at the moment of high temperatures. It can be seen that the damage has not reached great values, so in this case overhaul and cooling was carried out.

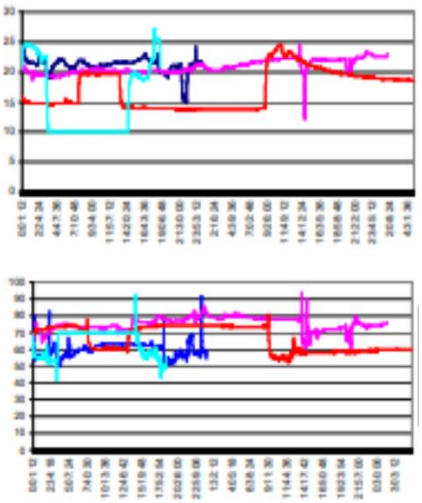


Fig. 4. Status diagrams RH520

Solution to the problem

The conditions in the production facility are tolerable in a measured period of time, but it is still necessary to better air condition the space in terms of cooling it when the machine is not working at the time of overhaul, servicing, maintenance, tool replacement, etc. Air conditioning and ventilation systems are now developed according to automation systems. A slight cooling is always present. When the temperature in the summer reaches great values the sensor gives a signal and begins a higher cooling. This is also true for ventilation and that is how this problem is solved.

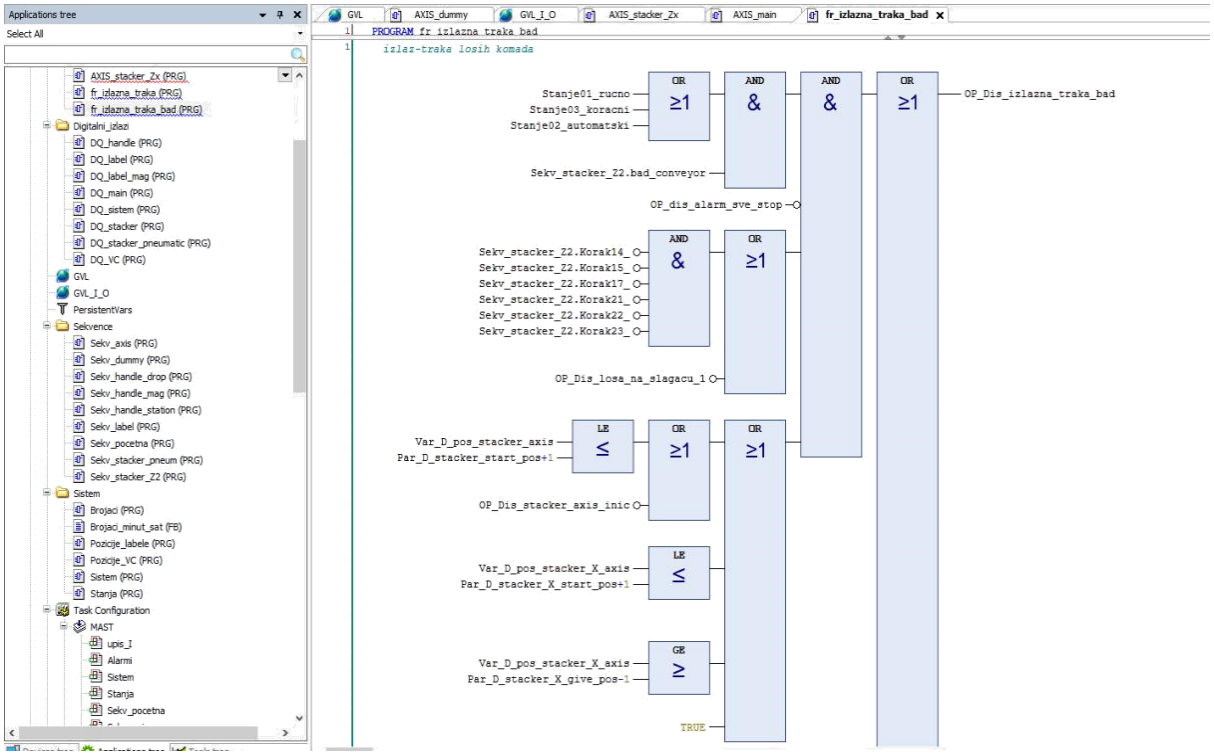


Fig. 5. PLC program related to counting non-compliant pieces

3. CONCLUSIONS

This paper initially describes specifically plastic and the great importance of recycling as well as some interesting facts about it. The introductory story is reduced to explaining the essential concepts related to plastic and injection into machines. This story is very important for this topic because it gives us some initial story about all the problems faced by companies engaged in the production of plastic products. It is described what kind of plastics are used, their characteristics and explanation of how plastic is inserted into the machine and the whole term is in some optimal way derived in this paper.

Next are given all the essential elements that help us solve the above problems. We have their characteristics and a detailed description of their application. The great importance of PLC and instruments that help us to conclude what kind of problems are present.

4. REFERENCES

[1] Recycling, Wikipedia, 2009.

[2] Herbert Rees, Injection Molding, Choice of Injection Molding Tools, Munich, 2006.

[3] Harry Pruner, Understanding Injection Molding Tools, HANSER, Lahr, 2011.

[4] IML robots characteristics, INMOLD GROUP Požega, 2019.

[5] Djordje Mirković, Automatic Safety Devices. work, 2020.

[6] Electric car noise, college tech. Science of Novi Sad, 2017.

ACKNOWLEDGMENTS

This study was supported by the Ministry of Science, Technological Development and Innovation of the Republic of Serbia, and these results are parts of the Grant No. 451-03-66 / 2024-03 / 200132 with University of Kragujevac - Faculty of Technical Sciences Čačak. Grant No. 41-03-65/2024-03/ 200122, Faculty of Science, University of Kragujevac

Authors:

PhD Srecko Ćurčić, University of Kragujevac, Faculty of Technical Sciences, Svetog Save 65, 6, 32000 Čačak, Serbia, Phone: +381 32 302 737.
E-mail: srecko.curcic.@ftn.kg.ac.rs

PhD Miloš Milovančević, University of Niš, Faculty Mechanical Engineering, Aleksandra Medvedeva 14, 14000 Niš, Serbia, Phone.: +381 64 1138300.
Email: milos.milovancevic@gmail.com

BSc Slobodan Šarenac, INMOLD Plast d.o.o. Serbia, Phone: +381 60 0517940
E-mail: slobodan.sarenac00@gmail.com

MMA 2024
FLEXIBLE TECHNOLOGIES

15th INTERNATIONAL SCIENTIFIC CONFERENCE
NOVI SAD, SERBIA, SEPTEMBER 24-26, 2024

Original research paper https://doi.org/10.24867/MMA-2024-06-005

Krstanoski, M.

STRATEGIES THAT CONTRIBUTE TO THE SUSTAINABLE DESIGN IN HURRICANE PRONE ENVIRONMENTS

Abstract: *Navigating the intersection of sustainable design, lean methods, site planning, project management, landscape ecology and business principles is a challenging process. Testing these principles of applied sustainability becomes a core for thoughtful and rational selection and development of the synergetic process between all elements that manifest the complexity of the design and human aspect of the land with a deeper approach in mind. Infrastructure strategies and indicators for efficient lean methods, sustainability characteristics, have an impact on the site development and interrelations between components that can reinforce the importance of the three fundamental elements of sustainability. They can influence performance, and ability to adapt and resist frequent nature challenges and its aftermath, hurricanes and site erosion. The growth in Florida's population increased the demand for new construction, primarily in the residential sector and commercial area in the past four years. Building along the coastline of Florida's requires resilient methods and lean principles to tackle coastline erosion that can endanger the resources, the land and the natural eco system. Construction without critical thinking can disrupt natural native habitats leading to the extinction of endangered species, affect the resources, may be a source of soil erosion, and flooding, affecting not only new, and but also existing structures as well. The destructive outcome of hurricane Ian that made a landfall in Florida tested all previously concluded approaches. With objective of the study to explore the unique challenges that Florida as a hurricane prompt area is experiencing, furthermore an overview of the ongoing recovery efforts on the communities, land, and regulatory requirements proposed because of the latest hurricane that affected construction are elaborated, along with proposed risk assessment study. Decision making principles such as SWIFT (Structured What-If Technique) is suggested to explore changing construction efforts along the coastline, erosion mitigation, known risks, previous experiences, regulatory requirements, existing controls, and its relationship with sustainability. Exploring the unique challenges that hurricane prompt areas are experiencing, holistically suggests an agile way of approach and specific mindset towards adopting and implementing sustainable environmental principles.*

Key words: *Wind velocity, Building Code, Total Quality Management, SWIFT*

1. INTRODUCTION

Hurricanes form over oceans beginning as a tropical wave, a low-pressure area that moves through warm high moisture tropics increasing precipitation and thunderstorm activity. They are a common occurrence in Florida, especially during the hurricane season from June until November, with the most active time from mid-August through mid-October. Hurricanes do not always make landfall, due to the geolocation of Florida, surrounded by water, but do have some residual effect on the area, depending on its path and landfall.

The origins of devastating storm Ian can be traced back on September 15th, 2022, starting as a tropical wave that moved off the African West Coast, increasing the activities while advancing across the Atlantic. Strengthened and developed as a hurricane in the last week of September 2022, reached Windward Islands on September 21st, made a landfall in western Cuba as category 3 intensity, causing damages and loss of power to the entire island. The hurricane made landfall as category 4 intensity in Southwestern Florida, south of Punta Gorda, Fort Myers and Cape Coral area, producing strong damaging winds 125 kt (144 mph) with some records showing 150 mph catastrophic storm surge (up to 18 ft)[11] and flooding, making the costliest, devastation storm with 150 direct and indirect casualties, over $112 billion in damages, causing devastation and flooding on large area.[3] Based on the NOAA meteorological data Ian's estimated peak intensity measured 140 kt (161 mph) and flight-level winds support a surface intensity estimate of 136 kt (157 mph), and an uncertainty of around ±10%, NHC advised on very little practical difference between a 140-kt category 5 and a 135-kt category 4 hurricane [3].

As a result of damage caused by the hurricanes, codes changes took effect in the past and at times, after devastating occurrences.

Back in 1992, hurricane Andrew with wind gusts up to 167 kt (192 mph), made a landfall in southern Miami-Dade County, near Eliot Key, Florida on August 24, 1992, creating storm surge of 9-13 feet. The aftermath left 63,000 residential structures destroyed and an additional 100,000 damaged, flattened entire neighborhoods [1], prior hitting Eleuthera and Berry islands in the Bahamas with similar intensity.

Hurricane Charley made landfall on August 13, 2004, near Cayo Costa as a category 4 hurricane. Hurricane Irma had devasting effects on the communities after making a landfall on September 10, 2017, as category 4 in Cudjoe Key.

In September 2017, Hurricane Maria, Category 4 cyclone, with observed maximum sustained winds of 155 mph, made a direct landfall in Puerto Rico prior

impacting the island of Dominica, galloping with intense winds, and causing massive destruction. The devastating effects of hurricane Maria destabilized the entire island for a long time. Impacted services electricity, water, infrastructure, medical sector, environmental, social, housing market, land and services.[9]

Estimated $354 million in damage to the housing sector, included replacement costs of destroyed houses and repair, with estimated ninety percent of the housing damaged, near 272,000 sustained moderate or major damage or were destroyed. [4]

In 1996 the Florida Building Code Study Commission was formed to update preventative measures, quality control on buildings and adopt building codes addressing buildings to withstand hurricane-force winds. 2001 FBC (abbrev. Florida Building Code) Code and 2002 began to focus on structural integrity, building envelope, roof, wall-to-roof connections and penetrations, to resist wind load and withstand impacts from wind-bone debris.

When the 2001 Florida Building Code (FBC) became effective, used codes dating back to 1997.[6] Wind resistive and design improvements were implemented in the FBC. From 2004 FBC and after, brought more standards, including existing buildings and residential standards. Structures built prior to 2001FBC or pre-FBC era, also became subject to improvements to comply with the new code. Hurricane Charley brought to light even more the need to develop standards based on Florida-specific issues. The 2017 FBC standard would be the last edition based on International Building Codes (IBC).

The 2020 FBC sets the standards for the entire state as a minimum with municipalities able to enhance the standards for each applicable region.

2. RESEARCH METHODOLOGY

Safety is the paramount objective, the most important principle of the stakeholders involved in evaluating the design intend. Also are cost-effectiveness, productivity and constructability. Before a decision is made design must first conform to the applicable codes and safety aspects.

Risk assessment study considering impact factors that affect the sustainability of the environment as well as SWIFT (Structured What-If Technique) can be conducted, as quantitative risk assessment method that identifies hazards and evaluates potential impacts by utilizing available published data. Ways are suggested to improve how design is approached in hurricane prone areas. This flexible risk identification technique can be utilized along with the environmental and design assessment study.

Root Cause Analysis (RCA) goal is to uncover the system level causes and factors that influence decision makers, by analysis of the impact factors. The root of the RCA is TQM (Total Quality Management) an approach that enhances quality endeavors, execute change and continuous improvement process.

Dr. Joseph Juran defines quality as “fitness for intended use”, “conformance to specifications”, and “conformance to requirements”.[7] Total Quality Management (TQM) approach has been mostly implemented in manufacturing and with limited application in the construction. Benefits of implementation of TQM include improvement of the quality and safety planning, strengthening of the front-end stakeholder collaboration, process management and research of the database and analysis. Continuous improvement can be achieved by defining step-by-step process to achieve the quality. Insufficient data collection, nonconformance, quality of performance and productivity, lack of preparation, planning and execution are a few elements that need to be answered.

Impact factors need to be measured as part of the TQM. By developing metrics as key performance indicators (KPI) and further with measurements and weighting of the factors - It is possible to reduce the critical links and to improve the process of analyzing elements that influence the design (Fig. 1). Note, Fig. 1 does not include applicable code and regulation. Meeting applicable Codes should be an integral part of the design and represent minimum design requirements.

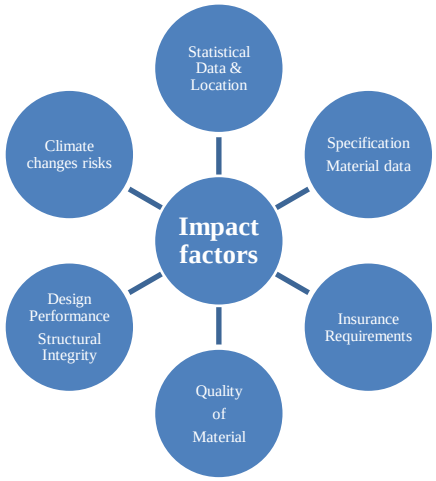


Fig. 1. Impact factors part of TQM in the initial study

Increasing wind velocity zones above what has been recorded in a region ensures that structures can withstand lower-rated wind speeds for longer times. This brings development in new building materials, design that would call for rated for impact resistance, resistant to a structural failure, or debris penetrating through it.

August 2022 Florida Building Commission and legislation changes started to enforce the 25 percent rule. Anything over 25 percent of the roof replacement owner will be required to replace the entire roof. This goes for all roof types, designs and roof ages. Upon replacement will have to meet the current building code.

Technology and advancements to predict better outcomes, hurricane projection paths, notifications, and building assessments to combat hurricane losses. FEMA (abbrev. Federal Emergency Management Agency) developed a vulnerability assessment tool for residential structures with that purpose [12]. The intent is to assist homeowners and contractors in better evaluating the weak points in a structure, by utilizing historical data from all past hurricanes and structure performances. FEMA’s technical paper for every major hurricane, suited to perform and produce realistic proven results to

understand the uncertainty and to serve a good resource. Prior hurricane impacts on the geographical area should reveal the geographical characteristic (population characteristics, socio-economic content, housing market, property insurance, construction specific, changes in design by clients, effects from the weather, contractor-subcontractor coordination).

SWIFT Technique is often used as part of a brainstorming process by facilitator, suggesting ideas presenting to a group for discussion. Access to the data and type of knowledge is essential. Analysis scope focuses on uncertainty and gives flexibility by:

- Discussing desirable options and outcomes;
- Items that did/did not worked in the past or present;
- Spatial components and Socio-economic status;
- Developing ideas about mitigation methods for undesirable outcomes and exploitation methods for desirable outcomes.

Human factors and stakeholders:

- Employment and education
- Infrastructure considerations, age of the existing structure, maintenance, housing market;
- Developing situations by implementing applicable network of "what ifs', effects and solutions;
- Implementing continuous improvement, measuring different processes and approaches;
- Identifying, measuring and continuously improving products and services while maintaining conformance with the specifications without compromising the quality;
- Defining measurable performance goals;
- Advancing the knowledge of coastal hazards and disasters and climate changes risks;
- Implementing root cause analysis.

3. DEFINITIONS AND DISCUSSION

Hurricane's high intense activity affects human safety, environment, the flora and fauna, and the coastal line causing soil erosion. Severe flooding that arises from heavy showers, lightning strikes, and thunders, affecting the community, infrastructure, causing damages on the properties, roads and bridges from flying debris or structure malfunction, power outages, also create state of emotional disturbance in the affected communities.

The devastation in 1992 by hurricane Andrew exposed significant challenges with the applicable building codes at the time, addressed the condition, necessity of change, as well as enforcement of the codes. Many homes had lost roof deck covering and gable ends; this often-caused truss failure and collapse of exterior walls. The second leading cause of damage to structures was wind-borne debris, flying objects catapulted by high wind forces, the leading cause of window and door opening failures [2] the roof structure faced increased roof uplift, creating more wind-borne debris.

Implementing and enforcing 2001 FBC and 2006 FBC and lessons learned from the past, addressed requirements for structures, to be designed to the intended wind velocity, wind-borne debris region and terrain exposure as defined in the FBC. This implementation refers to single family homes and multi-family homes (see Table. 1). 2004 FBC defines wind-borne debris region (Section 1609.2) and wind-borne debris impact resisting products whereas wind-resistant seismic section was reserved. Chapter 31 Special construction/3101.1 Scope defines or governs special building construction including membrane structures, temporary systems, pedestrian walkways and tunnels, awnings, and canopies, marquees, signs, and towers and antennas. Section 3109 provisions ensure that structures located seaward of the coastal construction control line are designed to resist the predicted forces associated with a 100-year storm event and elaborates further the application and exception. Coastal Construction Control Line is the line established by the State of Florida pursuant to section 161.053, Florida Statutes, and recorded in the official records of the county which defines that portion of the beach-dune system subject to severe fluctuations based on a 100-year storm surge, storm waves or other predictable weather conditions. The key word is "predictable".

Design grade was defined as predicted eroded grade caused by the 100-year storm.

Fifty-foot setback line, is defined as a line of jurisdiction, established pursuant to the provisions of Section 161.052 Florida Statutes, in which construction is prohibited within 50 feet (15.13 mm) of the line of mean high water at any riparian coastal location fronting the Gulf of Mexico or the Atlantic.

Group I	Group II	Group III
< 60 feet with wood roof decks	< 60 feet tall with non-wood roof decks	> 60 feet tall

Table 1. Three group classification of multi-family residences based on the building height

2004 FBC defines story above grade as any story having its finished floor surface entirely above grade plane, except a basement shall be considered as a story above grade plane where finished surface of the floor above basement is:

- More than 6 feet (1829 mm) above grade plane;
- More than 6 feet (1829 mm) above finished ground level for more than 50 % of the total building perimeter, or
- More than 12 feet (3658 mm) above finished ground level at any point.

Per the 2004 FBC in Section 102 Applicability, General 102.1 "Where, in any specific case, different sections of this code specify materials, methods of construction or other requirements, the most restrictive shall govern. Where there is a conflict between a general requirement and a specific requirement, the specific requirement shall be applicable.".

Construction documents are defined as written, graphic and pictorial documents, prepared or assembled for describing the design, location and physical characteristics of the elements of a project necessary for obtaining a building permit.

2004 FBC defines One-Hundred-Year Storm

Elevation, the height of the breaking wave crest or wave approach as superimposed on the storm surge with dynamic wave set-up of 100-year storm. This elevation is determined by the Florida Department of Environmental Protection based on studies published as part of coastal structural control line establishment process and an analysis of topographic and other site-specific data.

Experiences from the recent damage sustained from Hurricane Ian, will reflect in the next Code edition. The damage was recorded by FEMA reports. This enables the state to develop better plans for preparing and promoting more advanced codes. Documenting failures on existing buildings shows retrofits that still need further development and enforcement to protect older homes.

4. CONCLUSION

The FBC building codes and standards evolved from what they were in the early 1900s. Even with these advancements, there are still challenges that Florida is facing: flood, soil erosion and structural damage to the infrastructure and residential homes. Hurricanes, although traced with percentage of accuracy, still may have unpredictable paths and strengths. With Florida's ability to implement and change its building codes, advancements will continue to make buildings safer.

Florida Codes will continue to advance, and with the recent aftermath of Hurricane Ian this will have to come sooner than later. With the most considerable loss ever and highest death toll since 1935, the pressure is on to develop and push wind-borne debris zones to the future model to prevent future similar losses. FEMA's Mitigation Assessment Team Report sheds further light on the current standings of how the FBC 2020 code performed and what will have to change to prevent significant future losses. In addition, insurance companies pressure homeowners to meet codes and requirements outside and above current standards.

Insurance companies are becoming fewer in Florida due to significant losses like the aftermath of Hurricane Ian. With roof covering loss coupled with secondary membrane failure leads to water intrusion and large loss claims that the insurance company must pay for. The downside of the reduced number of available insurance companies is the high cost the homeowners to cover for roof replacement. Possible one way to option out of having to replace the roof, which required a qualified certified roofing company to sign off that the roof would last another five years, providing all investigation is conducted and insurance id provided. Most roofs were exempted lost the roof coverings, which will more than likely lead to removal of this exemption or shifting it onto the roofing companies to take full assumption of the risk in the event the roof does fail.

Spatial components remained understudied, herein including subarea within area of geography and specifics of that area. Site planners and landscape restoration specialists must play important role in considering rehabilitation via wetland restoration and revegetation projects, and reclamation projects by including rain gardens and by eliminating invasive exotic vegetation to encourage return of native species.

Construction site managers need to always ensure clear understanding of the site complexity and review the classification of site in the register if any, brownfield (smaller scale under jurisdiction of state and local authorities) or superfund site (handled by the federal government).

5. REFERENCES

[1] ABCNews: 25 Years Later: How Florida Buildings Are Better Able to Withstand Category 5 Storms. Retrieved August 04, 2024, from https://abcnews.go.com/US/25-years-florida-buildings-withstand-category storms/story?id=49649317, 2017.

[2] Applied Research Associates, Inc.: 2008 Florida Residential Wind Loss Mitigation Study. Retrieved August 3, 2024, from https://www.floir.com/sitedocuments/aralossmitigationstudy.pdf, 2009.

[3] Bucci, L, Alaka, L., Hagen, A., Delgado S., Beven, J.: National Hurricane Center Tropical Cyclone Report, Hurricane Ian, National Hurricane Center 3 April 2023, retrieved August 4, 2024, available at AL092022_Ian.pdf (noaa.gov), 2022.

[4] FEMA: Wind retrofit guide - FEMA. Successfully Retrofitting Buildings for Wind Resistance. Retrieved August 2, 2024,,from https://www.fema.gov/sites/default/files/2020-07/p-804_wind-retrofit-guide-residential.pdf, 2019.

[5] Federal Emergency Management Agency FEMA, available online at https://www.fema.gov

[6] Florida Building Commission: Florida Building Code (FBC). 7th edition, Florida Building Commission, 2019.

[7] Forbes, L.H., & Ahmed, S.M.: Lean Project Delivery and Integrated Practices in Modern Construction (2nd ed.). Routledge, 2020

[8] Florida Building Code, Building, International Code Council, 2004.

[9] Krstanoski, M. Melendez, R.: Exploring Methodology for Development of Sustainable Construction Management Processes in Puerto Rico, Nineteenth Annual Early Career Technical Conference, November 2-3, Birmingham, Alabama USA, 2019.

[10] NPR: Hurricane Ian makes landfall in Florida with catastrophic strength: Live updates, September 28, 2022, retrieved August 4, 2024, Hurricane Ian makes landfall in Florida with catastrophic strength: Live updates | NPR, 2022.

[11] Smith, D. J., Roueche, D. B., Thompson, A. P., and Prevatt, D. O.: A vulnerability assessment tool for residential structures and extreme wind events. Proceedings of the Second International Conference on Performance-Based and Life-Cycle Structural Engineering, 2015.

Authors:

PhD Magdalena Krstanoski, Everglades University, Sarasota, Florida, 34240 USA.

E-mail: mkrstanoski@yahoo.com

MMA 2024
FLEXIBLE TECHNOLOGIES

Section H:
ADDITIVE MANUFACTURING TECHNOLOGIES

MMA 2024
FLEXIBLE TECHNOLOGIES

15th INTERNATIONAL SCIENTIFIC CONFERENCE
NOVI SAD, SERBIA, SEPTEMBER 24-26, 2024

Original research paper https://doi.org/10.24867/MMA-2024-08-001

Vasileska E., Pandilov Z., Gecevska V., Tomov M.

EXPERIMENTAL DETERMINATION OF FLUENCE THRESHOLD AND MELT SIZE WITH D-SQUARED METHOD IN LASER POWDER BED FUSION

Abstract: *In Laser Powder Bed Fusion (LPBF), precise control over laser parameters is vital for achieving high-quality parts, especially in complex lattice structures where the optimal energy input is crucial to avoid defects. This study investigates the experimental determination of the irradiation fluence threshold required for material modification initiation and the heat source diameter using the so-called D-squared or Liu's method. Single point experiments with varying laser energy input were conducted on an LPBF platform employing three powder metal alloys. Microscope measurements were used to characterize the relationship between laser energy and material response. The results provide empirical calculation of the fluence threshold and melt spot resolution as a function of energy input for each tested material. These findings offer practical guidance for process optimization, facilitating quality fabrication of intricate geometries and lattice structures requiring melt spot resolution and controlled melting behavior.*

Key words: *Laser powder bed fusion, d-squared method, fluence, melt spot size*

1. INTRODUCTION

Laser Powder Bed Fusion (LPBF) has developed as a leading metal additive manufacturing technology, offering high flexibility in fabricating complex three-dimensional components with lattice structures. The selection of nominal process parameters is important factor in achieving the melt size needed and ensuring the quality of the fabricated part [1]. This aspect becomes even more crucial when printing intricate geometries characteristic for lattice designs. Hence, attention to the delivered laser energy input is crucial for achieving controlled melting dynamics and dimensional accuracy [2]. The fluence threshold, defined as the minimum energy per unit area required to initiate material modification or melting, represents a critical parameter in understanding the laser-material interaction dynamics during LPBF. By precisely characterizing the fluence threshold, researchers and engineers can optimize laser processing parameters to achieve desired material properties and part geometries while minimizing defects and process uncertainties [3]. However, the fluence cannot be directly measured and assessed, as it requires characterizing both the integrated laser pulse energy and its spatial distribution. Moreover, its theoretical calculation is challenging due to unknown parameters during laser irradiation, such as reflectivity, conductivity, dielectric constant, density, and expansion coefficient, which vary significantly during the laser irradiation and are difficult to quantify accurately [4]. The Liu's method, also known as the D-squared method, has become a powerful tool for experimentally determining the fluence threshold in laser processing applications [5]. The method interprets the material's threshold response to laser pulse irradiation as a direct reflection of the laser profile. By examining the melting shape of the modification due to laser-material interaction generated at various pulse energies, the method associates the modification limits to a local fluence, representing the fluence threshold for modification initiation. Although Liu originally developed this method to empirically determine the diameter of a Gaussian laser beam, its practical application extends to accurately determining the modification fluence threshold of any material exposed to laser pulses. Through single-point laser irradiation experiments, the method characterizes the relationship between laser energy input and material response, enabling determination of the fluence threshold and melt size of the material under consideration [6]. The melt size of the material modification induced by laser irradiation is critical in LPBF processes as it directly impacts the resolution, surface finish, and dimensional accuracy of the fabricated parts. Understanding and controlling the melt size are essential for achieving high-fidelity fabrication, particularly in applications requiring fine features, intricate geometries, or lattice structures [7]. Liu's method has been commonly used in research works for laser ablation process to investigate the ablation fluency threshold [8], and the interference diameter [9].

This paper shows the application of Liu's method for fluency threshold and heat source diameter estimation employed in LPBF. Firstly, a theoretical overview of the method is provided. Then, an experiment is proposed with varied energy input and measurements of the melt spot diameters were collected. The findings include the results of model fitting and discussions on fluence threshold and heat source diameter estimation.

2. THEORETICAL BACKGROUND OF D-SQUARED METHOD

Liu's method, also known as the D-square method, offers a straightforward experimental approach for determining the fluence modification threshold by measuring the sizes of induced modifications at various irradiation energies. An assumption for applying the

method is that the laser beam profile follows a Gaussian distribution. Mathematically, this methodology is expressed by the equation:

$$F(r) = F_0 \cdot e^{-2r^2/w_0^2} \qquad (1)$$

where $F(r)$ represents the local fluence at a radial position r, F_0 is the peak fluence value, and $2 \cdot w_0 = D_0$ denotes the heat source diameter at $1/e^2$ the peak value. The schematic depiction of a Gaussian laser beam profile with the designated measurement of the heat source diameter D_0 is illustrated in Fig. 1.

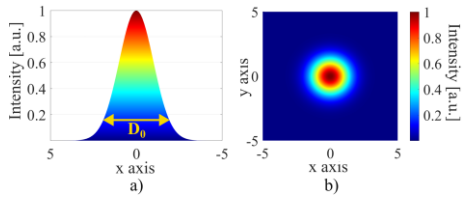


Fig. 1. Gaussian laser beam profile illustration: a) in x-z plane; b) in x-y plane

Liu's method, based on the assumption of a deterministic material modification behavior, defines the fluence threshold, F_{th}, as the local fluence corresponding to the border of the crater, where its radius is equal to R. Thus, the expression is given by:

$$F_{th} = F_0 \cdot e^{-2R^2/w_0^2} \qquad (2)$$

The expression that can be linearized by taking its logarithm, resulting in:

$$R^2 = \frac{w_0^2}{2} \cdot \ln\left(\frac{F_0}{F_{th}}\right) \qquad (3)$$

However, the experimental parameter typically measured is not the peak fluence but rather the integrated pulse energy delivered during the laser spot exposure on the material, denoted as E. In the case of typical squared wave emission profiles with modulated emission in the µs regime, the single pulse energy E corresponds to the product of the peak power P and the exposure time t_{on}:

$$E = P \cdot t_{on} \qquad (4)$$

Then, E can be derived from F_0 as follows:

$$F_0 = \frac{2 \cdot E}{\pi \cdot w_0^2} \qquad (5)$$

With the energy input threshold E_{th} defined as the minimum pulse energy required for material modification initiation, the calculation of the fluence threshold is conducted as follows:

$$F_{th} = \frac{2 \cdot E_{th}}{\pi \cdot w_0^2} \qquad (6)$$

By substituting Equation 5 and Equation 6 into Equation 3, the relationship between the observables R and E is established as follows:

$$R^2 = \frac{w_0^2}{2} \cdot \ln\left(\frac{E}{E_{th}}\right) \qquad (7)$$

When utilizing diameter values of the laser-induced melt spots on the material, the equation can be expressed in the following manner which constitutes the fundamental aspect of the Liu's method:

$$D^2 = 2 \cdot w_0^2 \cdot \ln\left(\frac{E}{E_{th}}\right) \qquad (8)$$

Liu's method suggests plotting $\ln(E)$ values on the x-axis and D^2 values on the y-axis. Consequently, the Gaussian beam waist diameter D_0 is determined through the slope of a linear regression. Moreover, the energy threshold value E_{th} can be obtained from the x-axis intercept. Subsequently, the laser fluence threshold value F_{th} is easily calculated by applying Equation 6 using these two obtained values.

3. EXPERIMENT METHODOLOGY

3.1 Experimental setup

The laser exposure experiments were carried out on an open LPBF platform employing a single-mode fiber laser (IPG Photonics YLR-300-AC-Y11, Cambridge, MA, USA), emitting at a wavelength of 1070 nm. The laser source can emit in pulse wave regime in order to obtain laser pulses with varying exposure times, with a peak power output of 300W.

3.2 Experiment

Three powder materials were tested: AISI316L, Ti-6Al-4V, and Zn-0.5Mg alloy. These metal alloys were deliberately selected due to their widespread industrial applications, as they are commonly utilized in critical sectors such as aerospace, automotive, and biomedical industries. Experiments were performed with six levels of laser energy (E), achieved by varying the peak power (P) across two levels (200 W and 150 W) and adjusting the pulse duration (ton) across three levels (800 µs, 400 µs, and 200 µs). This resulted in six energy levels (0.16, 0.12, 0.08, 0.06, 0.04, and 0.03 J). Each experimental condition was replicated three times, leading to a total of 18 laser spot exposures per material. The fixed and varied parameters are outlined in Table 1.

Fixed parameters	Values
Powder layer height [µm]	50
Variable parameters	Values
Material	AISI316L, Ti-6Al-4V, Zn-0.5Mg
Laser power, P [W]	150-200
Laser exposure time, t_{on} [µs]	200-400-800

Table 1. Fixed and variable parameters used in the experiment

The rationale for altering both parameters that influence the energy input (P and ton), rather than just to achieve the needed value of E by changing only one, was to investigate if either parameter individually influenced the outcome. However, the results indicated that whether the variation in E stemmed from changes of P or of ton, the response remained unaffected. Instead, the melting behavior of the material was influenced only by the collective energy input of the laser.

3.3 Measurement

The experimental samples were captured using an optical microscope, followed by automated estimation of the diameter using an algorithm written in the software MATLAB (The MathWorks, Inc., Massachusetts, USA). The algorithm first identifies the largest possible inscribed circle within the sample spot and then calculates its diameter. This automated measurement method reduces human error and excludes

stuck powder particles on the circumference of the melt spot. Examples of the laser melt spots for the three materials are presented in Table 2, showcasing spots obtained with maximum energy input (0.16 J) and minimum energy input (0.03 J).

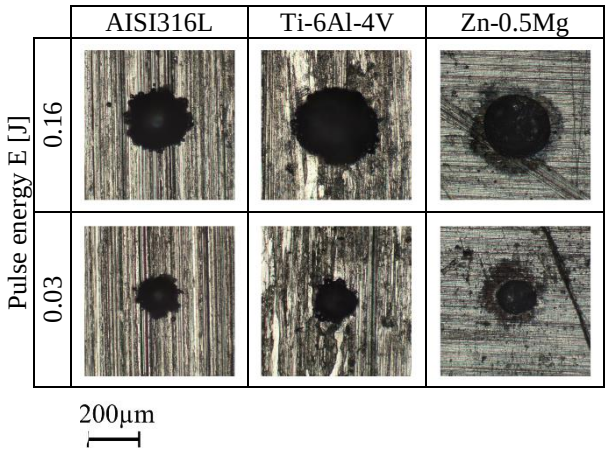


Table 2. Examples of melt spots dimensions as function of materials and energy input levels

4. RESULTS AND DISCUSSION

Employing Liu's method on the gathered experimental information, the graphs depicted in [10] show $\ln(E)$ values on the x-axis and D^2 values on the y-axis. The resulting graphical fitting of Liu's analytical model (Eq. 8) is displayed in the figure, along with the confidence interval (CI) and prediction interval (PI) of the fitting. It can be observed that the majority of data points belong within the prediction interval, validating the fitting of the regression model. Moreover, the figures illustrate the coefficients of determination R2 for the model fitting across the three materials, demonstrating a high goodness of fit. Additionally, the lack-of-fit test yielded non-significant results.

The regression line for AISI316L is as follows:

$$D^2 = 0.09903 + 0.02330 \cdot \ln E \qquad (9)$$

The regression line for Ti-6Al-4V is as follows:

$$D^2 = 0.1862 + 0.04622 \cdot \ln E \qquad (10)$$

The regression line for Zn-0.5Mg is as follows:

$$D^2 = 0.1066 + 0.02515 \cdot \ln E \qquad (11)$$

Based on the linear regression model fitting and Eq. 8, the model coefficients enable estimation of the energy threshold value E_{th}, as well as heat source diameter at $1/e^2$ the peak value D_0. Evidently, the linear regression lines of the three materials are different since the E_{th} as the minimum energy needed to start material modification is a characteristic dependent on the considered material. Moreover, the fluency threshold value F_{th} can be calculated from Eq. 6. The results for the three materials are shown in the following Table 3. It can be seen that Ti-6Al-4V exhibits a higher energy input threshold compared to the other materials, indicating that to start melting a higher laser energy is required. This disparity can be rationalized by the higher melting point of the titanium alloy compared to the other materials. Additionally, examining the fluency threshold shows that Ti-6Al-4V requires a lower fluence, implying less energy per unit area for initiating melting. When equivalent energy levels were applied, the Ti-6Al-4V alloy displayed a larger spot size compared to the other materials. This can be attributed to the fact that Ti-6Al-4V has higher absorption coefficient, meaning that it absorbs the laser energy more efficiently which in terms affects how it responds to laser irradiation. Consequently, this property impacts the heat distribution within the material, thereby affecting both the size of the melting spot and the energy per unit area required. Thus, while the Ti-6Al-4V alloy demands more total energy to start melting, it disperses this energy over a larger area, necessitating less energy per unit area for melting initiation compared to the other materials.

	AISI316L	TI-6AL-4V	ZN-0.5MG
D_0 $[\mu m]$	215.870	304.039	224.277
$E_{th}[J]$	0.014	0.018	0.014
$F_{th}[J/cm^2]$	77.970	49.059	73.081

Table 3. Results of E_{th}, D_0 and F_{th} estimation with Liu's method for the three materials

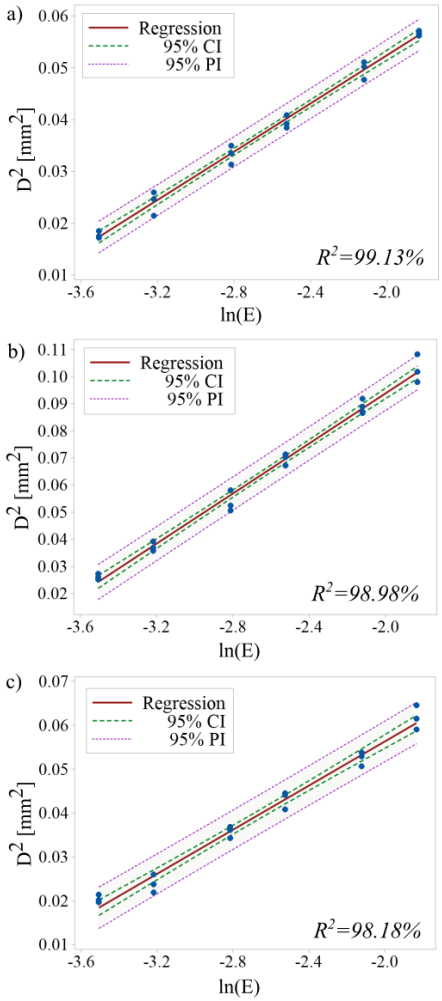


Fig. 2. Graphical representation of Liu's regression fit with 95% confidence (CI) and prediction intervals (PI) of the materials: a) AISI316L; b) Ti-6Al-4V; c) Zn-0.5Mg

By means of the regression equations, it is possible to calculate the predicted melting spot size attained with a specific energy input. Understanding the relationship

between melt size and energy input is particularly critical in the fabrication of intricate lattice structures, where precise spot resolution and controlled melting behavior are necessary.

It is worth noting that while Liu's method has been extensively used in literature, its validity hinges on the requirement that the laser interacting with the target has a perfectly Gaussian beam profile. Hence, an assumption for the fluence analysis is that the irradiation beam is perfectly Gaussian. However, imperfections in the beam from laser systems or practical optical setups can introduce dispersion in the fluence results obtained using this method [10]. Additionally, it is observed that the heat source diameter is estimated with different values for the three materials and is also estimated larger the laser beam diameter employed in the process. This observation suggests that heat transfer mechanisms during laser-material interaction may not be entirely negligible in the LPBF process. Moreover, sintered particles around the melted region can be present which may adhere to the neighboring particles. Despite these limitations, the method offers an analytical thermal model that has demonstrated its usefulness in empirically characterizing the laser beam profile and the material fluence thresholds.

5. CONCLUSION

The study provides practical insights into the determination of fluence threshold and melt size in LPBF using the Liu's or D-squared method, by analyzing the laser-material interactions in three powder metal alloys. A specifically designed experiment was conducted where the energy input was varied and measurements of the melt spot diameters were collected. The fitting of Liu's analytical model showed high accuracy. The material-specific characteristics, especially the material's melting point and absorption coefficient, led to variations in the model coefficients, affecting the resulting fluence threshold and the diameter of the heat source at 1⁄e2 of the peak value across different materials. The model furthermore offers a method to compute melt size as a function of the delivered laser energy, which is particularly important when producing intricate structures to ensure precise control over the melting spot. However, it's essential to acknowledge limitations when applying the method, including the assumption of a perfect Gaussian beam profile and the neglect of certain heat transfer mechanisms during laser-material interaction.

6. REFERENCES

[1] N. Ahmed, I. Barsoum, G. Haidemenopoulos, and R. K. A. Al-Rub, "Process parameter selection and optimization of laser powder bed fusion for 316L stainless steel: A review," J Manuf Process, vol. 75, pp. 415–434, 2022, doi: https://doi.org/10.1016/j.jmapro.2021.12.064.

[2] E. Vasileska, A. G. Demir, B. M. Colosimo, and B. Previtali, "A novel paradigm for feedback control in LPBF: layer-wise correction for overhang structures," Adv Manuf, vol. 10, no. 2, pp. 326–344, 2022, doi: 10.1007/s40436-021-00379-6.

[3] A. Großmann, J. Felger, T. Frölich, J. Gosmann, and C. Mittelstedt, "Melt pool controlled laser powder bed fusion for customised low-density lattice structures," Mater Des, vol. 181, p. 108054, 2019, doi: https://doi.org/10.1016/j.matdes.2019.108054.

[4] L. Torrisi, A. Borrielli, and D. Margarone, "Study on the ablation threshold induced by pulsed lasers at different wavelengths," Nucl Instrum Methods Phys Res B, vol. 255, no. 2, pp. 373–379, Feb. 2007, doi: 10.1016/j.nimb.2006.12.144.

[5] J. M. Liu, "Simple technique for measurements of pulsed Gaussian-beam spot sizes," 1982.

[6] G. Chang and Y. Tu, "The threshold intensity measurement in the femtosecond laser ablation by defocusing," Opt Lasers Eng, vol. 50, no. 5, pp. 767–771, May 2012, doi: 10.1016/j.optlaseng.2011.12.010.

[7] E. Vasileska, A. G. Demir, B. M. Colosimo, and B. Previtali, "Layer-wise control of selective laser melting by means of inline melt pool area measurements," J. Laser Appl., vol. 32, no. 022057, 2020, doi: doi.org/10.2351/7.0000108.

[8] F. Schell et al., "From infrared to ultraviolet: direct laser interference patterning of additively manufactured titanium alloy using a picosecond laser," in Proc.SPIE, Mar. 2022, p. 119890Q. doi: 10.1117/12.2610634.

[9] A. Hariharan et al., "Single- and Multiscale Laser Patterning of 3D Printed Biomedical Titanium Alloy: Toward an Enhanced Adhesion and Early Differentiation of Human Bone Marrow Stromal Cells," Adv Funct Mater, vol. 34, no. 8, Feb. 2024, doi: 10.1002/adfm.202310607.

[10] M. Garcia-Lechuga and D. Grojo, "Simple and robust method for determination of laser fluence thresholds for material modifications: an extension of Liu's approach to imperfect beams," 2021, doi: 10.12688/openreseurope.13073.1ï.

ACKNOWLEDGMENTS

The authors gratefully acknowledge Prof. Barbara Previtali and Prof. Ali Gökhan Demir at the Department of Mechanical Engineering - Manufacturing and Production Systems Division at the University Politecnico di Milano in Italy for providing equipment for the experimental work, and for their shared knowledge and continuous support throughout the research.

Authors:

MSc Ema Vasileska, PhD Zoran Pandilov, PhD Valentina Gecevska, PhD Mite Tomov

Ss. Cyril and Methodius University in Skopje, Faculty of Mechanical Engineering - Skopje, Ul. Ruger Boskovic 18, 1000 Skopje, North Macedonia, Phone: +38923099200, Fax: +38923099298.

E-mail: ema.vasileska@mf.edu.mk; zoran.pandilov@mf.edu.mk; valentina.gecevska@mf.edu.mk; mite.tomov@mf.edu.mk

MMA 2024
FLEXIBLE TECHNOLOGIES

15th INTERNATIONAL SCIENTIFIC CONFERENCE
NOVI SAD, SERBIA, SEPTEMBER 24-26, 2024

Original research paper https://doi.org/10.24867/MMA-2024-08-002

Cerjak, A., Fink, A., Jurečič, J., Zaviršek, N., Žalec, U., Hozdić, E., Rogelj, A., Hozdić, E.

EFFECT OF INFILL STRUCTURE SHAPE ON THE MECHANICAL PARAMETERS OF FDM 3D PRINTED PETG AND PETG+CF MATERIALS

Abstract: *The article addresses the topic of using additive manufacturing (AM), also known as 3D printing, for creating products directly from computer-generated 3D models. AM technologies are evolving as methods of material addition and play a significant role in the industry, with the ability to manufacture products, with almost complete material utilization. This research focuses specifically on Fused Deposition Modeling (FDM), a rapidly growing AM technology that utilizes thermoplastic polymers, such as PLA, ABS, PETG, and their composites with additives like glass or carbon fibers. The study examined the effects of different infill structures (hexagonal, triangular, linear) in 3D printing of polymeric materials and composites on various product properties, such as mechanical characteristics, weight, printing time, and material consumption. The research is based on the experimental testing of samples made from PETG and PETG+CF composites, analyzing how different geometric designs affect the mechanical properties of the printed products. The results provide insights into optimizing AM processes to enhance the quality of final products.*

Key words: *AM, FDM, infill patterns, mechanical properties, PETG, PETG+CF*

1. INTRODUCTION

Additive manufacturing (AM), also known as 3D printing, has catalyzed transformative shifts in the creation and fabrication of diverse products. This technology builds three-dimensional objects by sequentially adding material in layers according to designs from computer-aided design (CAD) models. Over the past ten years, 3D printing has seen substantial expansion and has become essential across multiple sectors, particularly in engineering and manufacturing. Its success is driven by its capacity for quick prototyping, its adaptability to various applications, and its cost-efficiency, which have all significantly boosted its adoption [1, 2].

Based on the classification provided by [1,3], additive manufacturing (AM) can be divided into three primary categories depending on the base material used: solid-based, powder-based, and liquid-based technologies. Solid-based AM comprises several processes, such as laminated object manufacturing (LOM), fused deposition modeling (FDM), wire and arc additive manufacturing (WAAM), and electron beam freeform fabrication (EBF3). Powder-based AM involves techniques like selective laser sintering (SLS), electron beam melting (EBM), selective laser melting (SLM), and laser metal deposition (LMD). Lastly, liquid-based AM is mainly represented by material jetting (MJ) and vat photopolymerization (VPP).

FDM is one of the methods of AM that is widely used due to its simplicity, efficiency, and accessibility [1]. FDM operates on the principle of melt extrusion, which means it builds three-dimensional objects layer by layer by extruding melted thermoplastic material through a precisely controlled nozzle. The object is gradually shaped by extruding and depositing in layers onto a movable platform. This platform is maintained at a lower temperature so that the thermoplastic quickly solidifies. This process is relatively simple but is limited to thermoplastic materials and wax for precision casting. Key parameters, such as nozzle temperature, bed temperature, and layer height, directly affect the fractional behavior of 3D printed parts and shape the quality of the object.

FDM technology is suitable for a wide range of materials, including acrylonitrile butadiene styrene (ABS), acrylonitrile styrene acrylate (ASA), polyamide (PA), polylactide (PLA), and polyethylene terephthalate glycol-modified (PETG). Among the various materials used in FDM 3D printing, PLA and PETG have become popular due to their favorable mechanical properties and ease of use. To further enhance their performance, reinforcing additives such as carbon fibers (CFs) have been incorporated into these materials, resulting in composites with superior mechanical strength and stiffness [4].

Numerous studies in the scientific community have assessed the mechanical behavior of materials fabricated using 3D FDM technologies. A comprehensive review of the literature suggests that research on the mechanical properties of 3D printed materials (including tensile, flexural, and torsional properties) branches into four primary areas. Initially, research centers on the influence of the characteristics of the input materials, such as their type and color. Subsequent studies focus on how the design of the infill affects the mechanical properties [5]. Another significant area of inquiry is the impact of various production process parameters, which include layer height, air gap, raster width, raster angle, build orientation, number of contours, floor/roof thickness, and deposition speed. Finally, research has also been conducted on how environmental conditions such as temperature, vibrations, and humidity affect the materials [4].

Further examination of the literature [5-7] reveals the critical role of the infill structure, an essential

component integrated into the interior of a 3D printed product during its creation. Infill typically refers to the internal framework within the printed material of a product, which in traditional manufacturing would be solid. Common infill patterns include rectangular, triangular, linear, hexagonal (honeycomb), and diamond-shaped structures.

Infill usage in FDM-printed materials primarily offers benefits, such as reduced material use, lighter product weight, and quicker production times, which collectively lower the overall cost of the final product. Nonetheless, it is crucial to acknowledge that the infill structure significantly affects not only the mechanical properties but also other characteristics of the printed materials [8].

The aim of this study is to thoroughly investigate and analyze the impact of different infill structure designs on the key mechanical parameters of 3D FDM printed materials PETG and PETG+CF. By analyzing the results, a more comprehensive understanding of how to adapt the infill structure design to meet the specific requirements of the final product will be gained. This contribution will help optimize the 3D printing process and achieve the desired mechanical properties of the products, which is essential for further advancements and innovations in this rapidly evolving field.

2. EXPERIMENTAL FRAMEWORK

In this paper, two types of commercial materials were used: PETG and PETG+CF. The specifications and mechanical parameters of both materials are presented in Table 1 and Table 2, as provided by the manufacturer [9].

Material Type	PETG	PETG+CF
Diameter (mm)	1.75	1.75
Color	green	black
Net filament weight (g)	1000	1000
Printing speed (mm/s)	60 – 90	60 – 90
Layer height (mm)	0.1 – 0.2	0.1 – 0.2
Extrusion temperature (°C)	240 – 250	230 – 250
Bed platform temperature (°C)	80 – 90	60 – 80

Table 1. PETG and PETG+CF filaments specifications [9].

Table 2 displays mechanical parameters provided by the filament manufacturer [9] associated with test samples that have a full infill density of 100%. The study utilized filaments with a circular cross-section, adhering to the specifications set by the manufacturer [9], which are defined by an average diameter of 1.75 mm and exhibit minimal variation in size.

Material Type	PETG	PETG+CF
Density (g/cm^3)	1.23	~1.28
Tensile Strength (MPa)	40-45	40-43
Flexural Strength (MPa)	50-55	75-85
Modulus of Elasticity (MPa)	1000-1100	2100-2400
Elongation at Break (%)	6.0-8.0	7.5-8.5
Heat Deflection Temperature (°C)	74	70

Table 2. Mechanical properties of PETG and PETG+CF filaments [9].

The specimen model for conducting the experiment in this article was designed in accordance with the ISO standard 527-2 [10] and prepared in the *SolidWorks 2020* software environment, see Fig. 1. After the design phase, the model was converted into STL format, which enables its use in software for generating *G-code*.

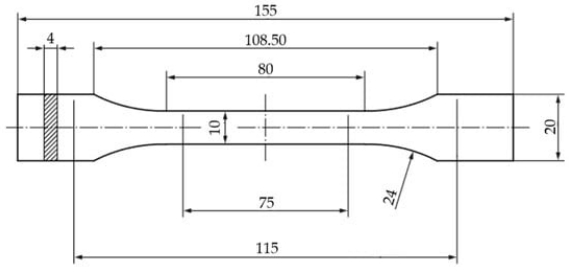


Fig. 1. 3D model of tensile test specimen according to ISO 527-2 standard [4].

All the tensile test specimens were printed using the *Adventure 4 Series 3D printer* by *FlashForge* [9].

The slicer *FlashPrint5* software enables adjusting printer parameters and managing and monitoring the print progress. Main printing parameters for both materials are presented in Table 3.

3D Printing parameter	PETG	PETG+CF
Filament diameter (mm)	1.75	1.75
Infill pattern	Hexagon / Triangle / Line	Hexagon / Triangle / Line
Infill density (%)	30	30
Nozzle diameter (mm)	0.4	0.4
Base print speed (mm/s)	60	60
Travel speed (mm/s)	100	100
First layer maximum (mm/s)	10	10
Top solid layers	4	4
Bottom solid layers	3	3
Layer height (mm)	0.2	0.2
First layer height (mm)	0.3	0.3
Extrusion temperature (°C)	240	245
Bed temperature (°C)	90	80

Table 3. Main printing parameters.

In slicer *FleshPrint5* software, the user has the option to select four different infill patterns: Line, Hexagon, Triangle, and 3D Infill. For this study, on all tensile test specimens, "Hexagon", "Triangle" and "Line" infill pattern was used with 30% fill density.

Once all parameters were set in the slicer *FlashPrint5* software (Table 3), the *G-code* was generated and transferred to the computer controlling the 3D printer.

For each material, nine identical tensile test specimens were printed, resulting in a total of 18 specimens being printed. All the tensile test specimens were built with 1000g spools of PETG and PETG+CF materials.

Specimens for tensile testing, created using FDM technology, served as the inputs for the process. These 3D-printed specimens from each material were categorized into three groups based on their infill structure shapes (hexagon, triangle, and line) and each group was tested. All the samples maintained a

consistent 30% infill density.

The tensile tests were performed on a Shimadzu AGS-X universal testing machine, which has a maximum loading capacity of 10 kN and operates at a testing speed of 6 mm/min, in accordance with ISO 527-2 standards. The TrapeziumX software, version 1.5.2, also from Shimadzu, was used to monitor and record the results of the tensile tests.

The outcomes of the tensile testing process included detailed data on tensile strength. This data was gathered and subsequently analyzed using Excel software, with the results discussed and examined in the subsequent section of the document.

The findings from the analysis of these mechanical parameters from the tensile tests on 3D-printed PETG and PETG+CF specimens are detailed in the following section.

3. RESULTS AND DISCUTION

The results of tensile tests for all tested samples of FDM 3D-printed PETG material, with respect to the infill structure shape, are divided into three groups of samples:

a) 3D printed PETG material with a hexagonal infill structure shape and 30% infill density (PETG_411, PETG_412 and PETG_413) – *Case 1*,
b) 3D printed PETG material with a triangular infill structure shape and 30% infill density (PETG_421, PETG_422 and PETG_423) – *Case 2*,
c) 3D printed PETG material with a linear infill structure shape and 30% infill density (PETG_431, PETG_432 and PETG_433) – *Case 3*.

The examination of data from tensile tests on specimens made with FDM 3D printing technology using PETG and various infill configurations reveals significant variations in the behavior of the material and in key measurable parameters.

The average maximum force and average maximum displacement for tested samples of FDM 3D-printed PETG material are depicted in Fig. 2.

The results of tensile tests for all tested samples of FDM 3D-printed PETG+CF material, with respect to the infill structure shape, are divided into three groups of samples:

a) 3D printed PETG+CF material with a hexagonal infill structure shape and 30% infill density (PETG+CF_711, PETG+CF_712 and PETG+CF_713) – Case 4,
b) 3D printed PETG+CF material with a triangular infill structure shape and 30% infill density (PETG+CF_721, PETG+CF_722 and PETG+CF_723) – Case 5,
c) 3D printed PETG+CF material with a linear infill structure shape and 30% infill density (PETG+CF_731, PETG+CF_732 and PETG+CF_733) – Case 6.

The average maximum force and average maximum displacement for tested samples of FDM 3D-printed PETG+CF material are depicted in Fig. 3.

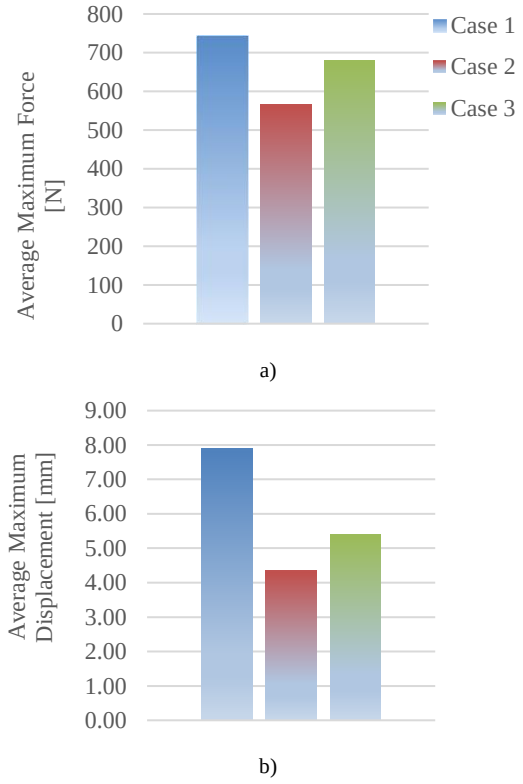


Fig. 2. Graphic representation of average values of tensile test results of FDM 3D printed PETG material specimens, based on the shape of the infill structure: a) average maximum force, b) average maximum displacement.

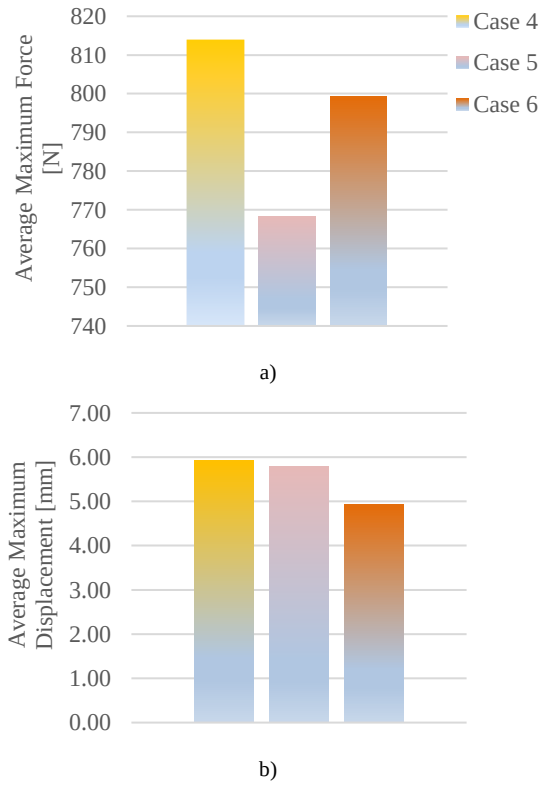


Fig. 3. Graphic representation of average values of tensile test results of FDM 3D printed PETG+CF material specimens, based on the shape of the infill structure: a) average maximum force, b) average maximum displacement.

4. CONCLUSION

In this study, we performed a comprehensive analysis of the mechanical properties of FDM 3D-printed PETG and PETG+CF materials, specifically focusing on the influence of infill structure shapes at a 30% infill density. The results underscore the significant impact that infill geometry has on the mechanical parameters.

Data analysis revealed that PETG specimens with a hexagonal infill structure (*Case 1*) showcased superior mechanical properties among the PETG-only group. These specimens not only withstood the highest forces but also exhibited the greatest elongation at break, indicating an optimal balance between strength and ductility. Specifically, the average maximum force and break force in this group were notably higher than those observed in other cases, with a remarkable elongation at break that surpassed *Case 2* by 44.96% and *Case 3* by 30.68%.

Conversely, the triangular and linear infill structures (*Cases 2* and *Case 3*) presented a trade-off between mechanical strength and elasticity, with the triangular structure notably displaying the lowest mechanical performance. This suggests a considerable sensitivity of PETG's mechanical properties to the infill geometry, highlighting the importance of careful design consideration in applications requiring specific strength or flexibility levels.

Transitioning to the PETG+CF composites, the enhancement in properties due to the addition of carbon fibers was evident across all infill designs. However, variations still persisted depending on the infill shape. For example, samples with a linear infill structure (*Case 6*) exhibited the highest modulus of elasticity, underscoring their ability to endure substantial loads without permanent deformation, an essential feature for high-stress structural applications.

In summary, the study not only emphasizes the importance of selecting appropriate infill patterns to optimize the mechanical properties of FDM 3D-printed materials but also illustrates the beneficial effects of carbon fiber reinforcements in enhancing these properties. These findings contribute significantly to the field of materials engineering, particularly in the context of FDM 3D printing where customization of material properties is paramount. Future work should further explore the interplay between different infill densities and the integration of other composite materials to broaden the application range of FDM 3D-printed polymers and composites.

5. REFERENCES

[1] I. Gibson, D. Rosen, B. Stucker, and M. Khorasani, *Additive Manufacturing Technologies*. Cham: Springer International Publishing, 2021.

[2] ISO/ASTM, ISO/ASTM 52900: Additive manufacturing - General principles - Terminology, Int. Stand. 2015.

[3] ASTM F42, Committee F42 on Additive Manufacturing Technologies. ASTM International. [Online]. Available: http://www.astm.org/-COMMITTEE/F42.htm.

[4] E. Hozdić, E. Hozdić, Comparative Analysis of the Influence of Mineral Engine Oil on the Mechanical Parameters of FDM 3D-Printed PLA, PLA+CF, PETG, and PETG+CF Materials. *Materials (Basel).*, vol. 16, no. 18, p. 6342, 2023.

[5] H. K. Dave, N. H. Patadiya, A. R. Prajapati, and S. R. Rajpurohit, Effect of infill pattern and infill density at varying part orientation on tensile properties of fused deposition modeling-printed poly-lactic acid part. *Proc. Inst. Mech. Eng. Part C J. Mech. Eng. Sci.*, vol. 235, no. 10, pp. 1811–1827, 2021.

[6] L. Bergonzi, M. Vettori, L. Stefanini, and L. D'Alcamo, Different infill geometry influence on mechanical properties of FDM produced PLA. *IOP Conf. Ser. Mater. Sci. Eng.*, vol. 1038, no. 1, p. 012071, 2021.

[7] M. R. Derise and A. Zulkharnain, Effect of infill pattern and density on tensile properties of 3d printed polylactic acid parts via fused deposition modeling (FDM). *Int. J. Mech. Mechatronics Eng.*, vol. 20, pp. 56–63, 2020.

[8] R. Srinivasan, W. Ruban, A. Deepanraj, R. Bhuvanesh, and T. Bhuvanesh, Effect on infill density on mechanical properties of PETG part fabricated by fused deposition modelling. *Mater. Today Proc.*, vol. 27, pp. 1838–1842, 2020.

[9] FASHFORGE, *Comparison between Flashforge PLA, PLA Pro, PLA-CF, ABS, ABS Pro, PETG, PETG Pro, PETG-CF*.

[10] ISO 527-2:2012, *Plastics - Determination of Tensile Properties - Part 2: Test Conditions for Moulding and Extrusion Plastics*. Geneva, Switzerland: International Organization for Standardization, 2012.

Authors:

BSc Andrej Cerjak, BSc Anja Fink, BSc Jaka Jurečič, BSc Nejc Zaviršek, BSc Urban Žalec, PhD Elvis Hozdić, University of Novo mesto, Faculty of Mechanical Engineering, Na Loko 2, 8000 Novo mesto, Slovenia.

E-mail:andrejc456@gmail.com; finkanja8@gmail.com; jaka.jurecic14@gmail.com; zavirseknejc@gmail.com; zalec.urban@gmail.com; elvis.hozdic@fs-unm.si

MSc Aljaž Rogelj, MSc Emine Hozdić, Kranj School Centre, Kidričeva cesta 55, 4000 Kranj, Slovenia.

E-mail: aljaz.rogelj@sckr.si; emine.hozdic@sckr.si

MMA 2024
FLEXIBLE TECHNOLOGIES

15th INTERNATIONAL SCIENTIFIC CONFERENCE
NOVI SAD, SERBIA, SEPTEMBER 24-26, 2024

Original research paper https://doi.org/10.24867/MMA-2024-08-003

Ilić, K., Banjanin, B., Spasojević, S., Adamović, S., Dramićanin, M.

EFFECT OF INFILL PATTERN ON THE TENSILE STRENGTH OF FDM 3D PRINTED PLA MATERIAL

Abstract: *Fused Deposition Modeling (FDM) is a widely used 3D printing technique that involves the layer-by-layer deposition of thermoplastic materials to create complex geometries. The infill pattern, a crucial parameter in FDM, significantly influences the mechanical properties of printed parts, particularly tensile strength. Research indicates that different infill patterns, such as rectilinear, honeycomb, and gyroid, affect the distribution of stress and strain within the material. Higher infill densities generally enhance tensile strength, but the relationship is nonlinear, with diminishing returns beyond certain thresholds. Optimizing infill patterns can lead to improved mechanical performance and reduced material usage, making FDM a versatile and efficient manufacturing method.*
Key words: *Fused Deposition Modeling, Polylactic acid, Infill Pattern, 3D Printing, Tensile strength*

1. INTRODUCTION

Fused Deposition Modeling (FDM), a popular 3D printing technology, has experienced a surge in popularity due to its ability to fabricate intricate and personalized parts [1]. One crucial aspect of FDM printing that has a significantly impacts the final product's mechanical properties is the infill percentage, which refers to the amount of material used to fill the interior of the printed object. The infill percentage can have a substantial effect on the mechanical characteristics of FDM-printed parts, as demonstrated by various studies [2]. Researchers have found that adjusting the infill percentage can lead to improvements in flexural strength, flexural modulus, and other key mechanical properties [3]. This is particularly important when the 3D printed components are intended to be integrated into functional devices, rather than serving solely as prototypes or models [4]. By carefully optimizing the infill percentage, along with other printing parameters such as bed temperature, nozzle temperature, and print speed, it is possible to tailor the mechanical performance of FDM-printed parts to meet the specific requirements of the application [2,5]. This allows designers and engineers to create 3D printed components that are not only visually appealing, structurally robust, and durable.

Another the key factor influencing the mechanical properties of 3D printed parts is the infill pattern, which determines the internal structure of the part. The infill pattern has an effect to the density and studies have shown that the infill percentage, which represents the amount of material used in the infill, can significantly impact the mechanical properties of the printed parts. [3].

Beyond just the percentage of infill, the specific geometric configuration of the infill pattern, such as rectilinear, honeycomb, or triangular designs, can also play a crucial role in determining the mechanical performance of the printed part [4,6]. The arrangement and orientation of the infill pattern can influence the load transfer and stress distribution within the part, ultimately affecting its overall tensile strength [6].

Higher infill percentages have been found to enhance the tensile and flexural strengths of 3D printed components, as the increased material density provides more excellent internal support and load-bearing capacity [3].

Beyond just the percentage of infill, the specific geometric configuration of the infill pattern, such as rectilinear, honeycomb, or triangular designs, can also play a crucial role in determining the mechanical performance of the printed part. [4,6]. The arrangement and orientation of the infill pattern can influence the load transfer and stress distribution within the part, ultimately affecting its overall tensile strength [6].

2. EXPERIMENT

2.1 Preprocessing

To examine the impact of infill patterns on 3D FDM printing, it was first necessary to design a tensile test specimen compliant with ASTM 790 (Parallel length 33 mm, width 6 mm, and thickness 3.4 mm). The specimen was modeled using the Creo 4.0 software, and at the end, the model was exported as an STL file to be imported into the Ultimaker CURA program. CURA is a slicer software that preprocesses the model to generate the output G-code. It is called a slicer because it arranges the model layer by layer by height, thus forming the 3D shape. CURA includes profiles for specific printers and materials. In our case, profiles for the Ender 3 Pro printer and Generic PLA (Polylactic acid) material were used. These profiles contain all the parameters regarding printing speed, temperature, density, and flow rate. These parameters can be adjusted, but they were not altered to represent the typical out-of-the-box user experience for this study. The infill percentage for all samples was 60%, and the key difference between the samples was the different predefined infill patterns in the software. For comparison purposes, samples were also printed with 100% infill and without any infill, meaning they consisted only of the outer wall (Fig. 1).

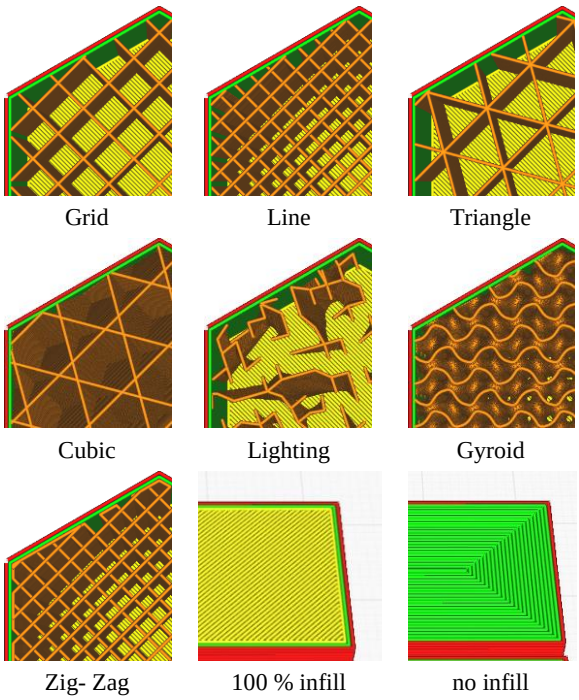


Fig 1. Type of infill pattern in Ultimaker Cura software

2.2 Printing

In this study, while keeping processing parameters constant, the infill pattern of the specimens has been changed. Nine different profiles of infill patterns have been selected for this study, shown in Figure 1: Grid, Line, Triangle, Cubic, Lighting, Gyroid, Zig-Zag, 100% infill, and 100% wall (no infill).

The material used for the test specimens is 1.75 mm CR-PLA Filament, with a density of 1.24 g/cm³. The filament production company gives the following mechanical properties: Tensile strength of 51 MPa, Bending strength of 86 MPa, and Impact strength of 10.5 J/m^2. The temperature range for processing of the material is 195°C to 210°C, hotbed temperature is not necessary but with the limit of 60°C and the required print speed is 40- 120 mm/s.

The Ender 3 Pro printer was used for producing the specimens (Fig. 2).

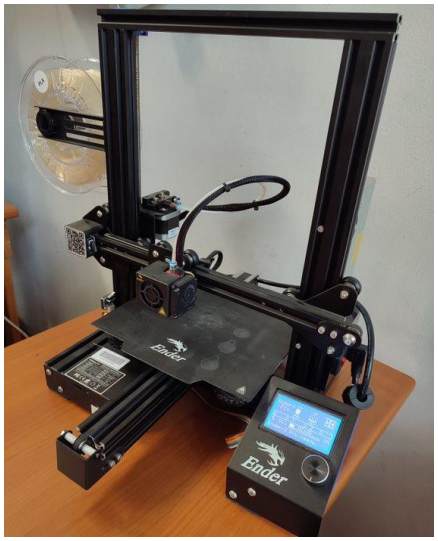


Fig 2. 3D printer Creality Ender 3 Pro

For each infill condition presented, three test specimens were printed at the same time (Fig. 3), which resulted in a total of twenty-seven produced specimens.

During the printing test specimens, the printing nozzle temperature was set at 210 °C, while the hotbed temperature was at 50 °C, and the printing speed was 60 mm/s.



Fig 3. Printing bench of specimen

2.3 Testing

The testing was carried out in conformity with ASTM D638 - *Standard Test Methods for Tensile Properties of Plastics.* The tensile testing of the 3D printed PLA specimens was carried out on a universal tensile tester UTS Shimadzu Compact Tabletop Testing Machine EZ-LX, with a load cell capacity of up to 5 kN (Fig. 4). The constant speed tensile test was set at 5 mm/min. The tensile properties were observed through the failure of the material and fracture propagation. With the results being digitally recorded.



Fig 4. UTS Shimadzu Compact Tabletop Testing Machine EZ-LX

3. RESULT

The tensile test gives output recorded as force-elongation, which is then, on the spot, transformed into engineering stress-strain curves for all specimens, with the tensile properties such as yield strength and tensile strength for all the specimens.

The results for nine patterns are summarized in Table 1. The values shown are yield strength, tensile strength, and strain, which are given as the average values of each specimen for nine profiles.

	Infill Pattern	Yield Strength [MPa]	Tensile Strength [MPa]	Strain [%]
1	Grid	29.5	30.0	2.8
2	Lines	30.1	30.2	2.3
3	Triangle	28.2	28.8	2.3
4	Cubic	30.0	30.1	2.6
5	Lighting	29.5	29.8	2.7
6	Gyroid	30.1	30.6	2.7
7	Zig-Zag	32.4	32.6	2.6
8	100% infill	46.3	46.9	2.6
9	100% wall	51.7	52.9	2.4

Table 1. Yield strength, Tensile strength and Strain from Tensile Testing

Additionally, the diagram containing stress-strain curves of all 9 tested patterns is presented in Figure 5. From this diagram, the referent tensile properties of every tested filling pattern can be observed and mutually compared with one another.

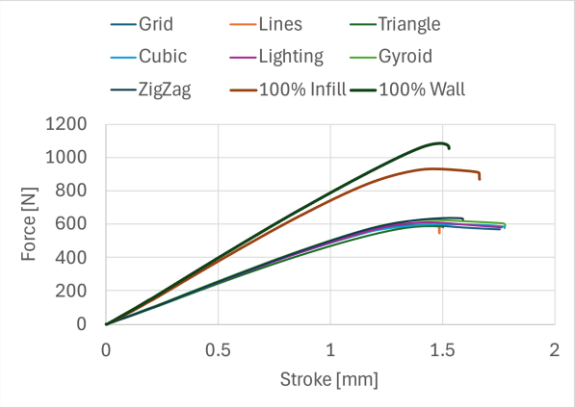


Fig. 5. Stress-strain curves

4. DISCUSSION

At first glance at the results presented, two infill patterns that can be considered benchmarks for the experiment have the highest tensile properties and are in accordance with the material specifications provided by the manufacturer. This is due to the specimens being 100% of the outer wall and having an infill of 100% in both cases this fill of 100% decreases the air gaps in the parts and increases cross-sectional area, giving the specimens the ability to bear higher tensile load. From this, it can be implied that not only infill pattern, which is the main topic of this study, but also infill density has a significant effect on the tensile properties of the material.

If we take into consideration only standard pattern profiles with the 60% infill, the Zig-Zag infill pattern showed both the highest yield strength of 32.4 MPa and the highest tensile strength of 32.6 MPa, while the strain was, on average, with a value of 2.6 %. This can be considered as a consequence of two interchanging directions of the infill layers, giving the printed part flexibility and the ability to compensate for the deformation. Under the same conditions, due to its interlocking geometry, the Gyroid infill pattern showed the second-highest tensile properties, especially the tensile strength. Lines and Cubic patterns have nearly the same level of values obtained from results, with the significant difference being a lower strain of Line infill pattern of 2.3% compared to 2.6% of Cubic.

Between the nine profiles, the infill pattern with the lowest tensile properties is a Triangular infill since it contains infill lines scattered in three directions, and thus the toleration of the tensile load is lowered. The average yield strength of the triangular infill pattern was 28.2 MPa, while the tensile strength was 28.8 MPa, and the strain was only 2.3%.

In the Grid pattern, due to the building nature of the material being printed in both directions, rotated by 90° in each layer, on the spots where the paths cross the occurrence of the material accumulation is present. With this phenomenon, we can explain the occurrence of the highest strain among all the patterns.

As seen in Figure 6. Lightning specimens didn't fully develop their structure due to their low height. This impacted the specimens, as this pattern had lower-than-expected tensile properties.



Fig. 6. Lighting undeveloped infill pattern in the tested specimens

The results shown that when printing parts that will be submitted to tensile load with FDM technology it is necessary to take into consideration the infill pattern selected for the print and its ability to withstand tensile load. This study may serve as a guide for engineers to simplify the choice of the correct infill pattern.

5. CONCLUSION

This research studied the impact of only different infill patterns while keeping the process parameters and infill percentage of Fused Deposition Modeling 3D printed parts constant.

The following remarks could be concluded from the

study presented in the work above:

Infill pattern directly impacts the tensile properties of the FDM printed specimens.

The Zig-Zag pattern showed the highest studied properties between 7 infill patterns with an infill percentage of 60%.

On the other hand, the lowest properties can be found in specimens with a triangular pattern, followed by a lighting pattern that didn't develop form completely.

It has been concluded that for specimens from whom it will be required to bear tensile load in their usage, required properties can be achieved through the optimization of infill patterns with respect to the process parameters.

Specimens with the infill percentage of 100%, and specimens of 100% wall infill showed the highest values of tensile properties, among all tested patterns. From these results is clear that the infill density has a significant impact on the tensile properties, and it is an area that holds promise for comprehensive investigation in future studies.

6. REFERENCES

[1] Wang S., Ma Y., Deng Z., Zhang S., Cai J.: Effects of fused deposition modeling process parameters on tensile, dynamic mechanical properties of 3D printed polylactic acid materials, Polymer Testing, Vol. 86, 2020.

[2] Diederichs, E., Picard, M., Chang, B. P., Misra, M., Mielewski, D. F., and Mohanty, A. K.: Strategy to improve printability of renewable resource-based engineering plastic tailored for FDM applications, ACS Omega, Vol. 4, No. 3, pp. 20297-20307, 2019.

[3] Kesavarma S., Kong C. K., Samykano M., Kadirgama K. and Pandeya. A.K: Bending properties of 3D printed coconut wood-PLA composite, IOP Conference Series: Materials Science and Engineering, Vol. 736, 2020.

[4] Ćwikła G., Grabowik C., Kalinowski K., IPaprocka I. and Ociepka P.:The influence of printing parameters on selected mechanical properties of FDM/FFF 3D-printed parts, IOP Conference Series: Materials Science and Engineering, Vol. 227, 2017.

[5] García Plaza, E., Núñez López, P.J., Caminero Torija, M.Á., Chacón Muñoz, J.M.: Analysis of PLA Geometric Properties Processed by FFF Additive Manufacturing: Effects of Process Parameters and Plate-Extruder Precision Motion, Polymers, Vol.11, No. 10, 2019.

[6] Lee, D., Wu, G.-Y.: Parameters Affecting the Mechanical Properties of Three-Dimensional (3D) Printed Carbon Fiber-Reinforced Polylactide Composites, Polymers, Vol. 12, No. 11, 2020.

[7] Eryildiz M.: The Effect of Infill Patterns on the Mechanical Properties of 3D Printed PLA Parts Fabricated by FDM, Ukrainian Journal of Mechanical Engineering and Materials Science, Vol. 7, No. 1, 2021.

[8] Lalegani Dezaki, M.; Ariffin, M.K.A.M.; Serjouei, A.; Zolfagharian, A.; Hatami, S.; Bodaghi, M.: Influence of Infill Patterns Generated by CAD and FDM 3D Printer on Surface Roughness and Tensile Strength Properties, Applied Sciences, Vol 11, No.16, 2021.

[9] Rismalia M., Hidajat S., Permana I., Hadisujoto B.: Infill pattern and density effects on the tensile properties of 3D printed PLA material, Journal of Physics: Conference Series, Vol. 1402, 2019.

[10] Ganeshkumar S., Kumar S.D., Magarajan U., Rajkumar S., Arulmurugan B., Sharma S., Li C., Ilyas R.A., Badran M.F.: Investigation of Tensile Properties of Different Infill Pattern Structures of 3D-Printed PLA Polymers: Analysis and Validation Using Finite Element Analysis in ANSYS. Materials (Basel), Vol. 15, No. 15, 2022.

ACKNOWLEDGMENTS

The authors gratefully acknowledge research support by the project entitled "Interdisciplinarity in Materials Science and Joining Technologies" from the Department of Production Engineering, Faculty of Technical Sciences Novi Sad, Serbia.

Authors:

BSc Katarina Ilić, Neofyton, Partizanska 27B, 21000 Novi Sad; Serbia, Phone: +381 69 1998-966
E-mail: kata.katarina.ilic@gmail.com

PhD Bojan Banjanin, MSc Stanko Spasojević, PhD Savka Adamović, PhD Miroslav Dramićanin, University of Novi Sad, Faculty of Technical Sciences, Trg Dositeja Obradovica 6, 21000 Novi Sad, Serbia, Phone.: +381 21 485-2055.
E-mail: bojanb@uns.ac.rs; stankos@uns.ac.rs; adamovicsavka@uns.ac.rs; dramicanin@uns.ac.rs

MMA 2024 FLEXIBLE TECHNOLOGIES

15th INTERNATIONAL SCIENTIFIC CONFERENCE
NOVI SAD, SERBIA, SEPTEMBER 24-26, 2024

Review paper https://doi.org/10.24867/MMA-2024-08-004

Tuteski, O., Kochov, A.

OVERVIEW OF THE APPLICATION OF STEREOLITHOGRAPHY IN ADDITIVE MANUFACTURING OF INJECTION MOLDING TOOL INSERTS

Abstract: *This paper provides a comprehensive overview of the application of Stereolithography (SLA) in the additive manufacturing of mold inserts. It explores the advantages and limitations of using the SLA technology for producing high-precision, intricate mold inserts compared to traditional manufacturing methods. Key benefits such as reduced lead times, cost-effectiveness for small production runs, and enhanced design flexibility are discussed. The paper also addresses the challenges related to material properties, thermal stability, and durability of SLA-produced inserts. Additionally, advancements in SLA materials and post-processing techniques are reviewed to showcase improvements in mechanical and thermal properties. The findings underscore the potential of SLA technology to revolutionize mold manufacturing, offering significant benefits in rapid prototyping and small to medium-scale production environments.*
Key words: *injection molding, additive manufacturing, rapid tooling, Stereolithography*

1. INTRODUCTION

Additive manufacturing (AM), commonly known as 3D printing, has revolutionized the manufacturing landscape by enabling the production of complex geometries with unprecedented precision and flexibility. Among the various AM technologies, Stereolithography (SLA) stands out due to its ability to produce highly detailed and accurate parts. Since its inception in the 1980s, SLA has evolved significantly, making it a viable option for a wide range of applications, including the production of injection molding tool inserts.

Injection molding is a predominant manufacturing process used to produce plastic parts in large volumes. Traditionally, the mold inserts used in injection molding are manufactured through conventional methods such as machining and electrical discharge machining (EDM). While these methods are effective, they often entail long lead times and high costs, especially for complex designs and small production runs. The integration of SLA in the production of mold inserts presents an opportunity to overcome these challenges.

This paper seeks to provide insights into how SLA can be effectively utilized in the production of injection molding tool inserts, offering a balanced view of its benefits and limitations while showcasing the latest advancements in the field.

2. RAPID TOOLING USING SLA

Additive manufacturing provides cost-effective solutions for small-scale or customized production runs [1], outperforming traditional injection molding in these scenarios. When it comes to tooling, additive manufacturing facilitates the swift introduction of new products and services to the market with minimal financial investment and low fixed costs. As a result, rapid tooling technology is crucial in accelerating the pace of tooling development [2]. Recognized as early as 1995 for its potential to substantially lower costs, rapid tooling continues to play a pivotal role in modern manufacturing processes.

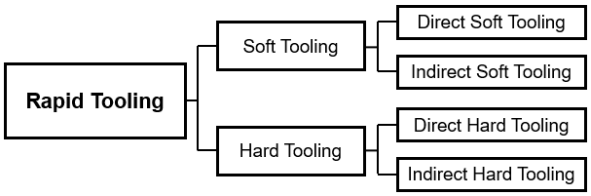
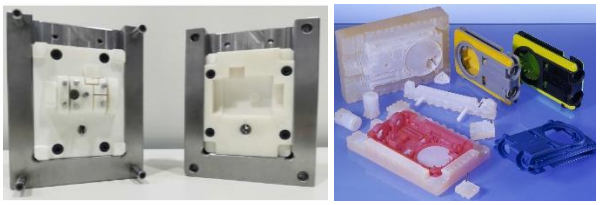


Fig. 1. Classification of rapid tooling [3]

It encompasses various applications of additive manufacturing used in the creation of tools, tool inserts, gauges, and molds [4], as outlined in Fig. 1. The core concept of rapid tooling is defined by the ability to produce multiple copies of a prototype with functional material properties in a short lead time.

Injection molding tooling inserts manufactured by SLA and other derivative processes under the same class fall into the direct soft tooling category. The term "soft tooling" refers to molds created from non-metal materials, primarily utilized for small batch production or even single-use applications. This includes the direct manufacturing of tools for injection molds using additive manufacturing technologies, such as light-reactive photopolymer curing. The primary advantages include rapid and cost-effective production of tooling equipment. However, the major drawback is the relatively poor thermal and mechanical properties of the produced tools.



a) b)

Fig. 2. Direct (a) and indirect (b) soft tooling; a) SLA molding inserts; b) silicon molds [5, 6]

The direct or indirect classification refers to whether AM is used to produce the entire mold geometry or only a master pattern that is used for mold manufacturing using some additional processes. An example of indirect tooling are epoxy or silicon tooling made by casting around the master pattern geometry (Fig. 2).

2. STEREOLITHOGRAPHY FUNDAMENTALS

Stereolithography (SLA) is one of the earliest and most widely adopted additive manufacturing technologies. It utilizes a vat of liquid photopolymer resin that is cured, layer by layer, by a UV laser to create a solid object (Fig. 3).

The SLA process begins with the creation of a 3D digital model using computer-aided design (CAD) software. The model is then sliced into thin layers using slicing software, which generates a set of instructions for the SLA machine. The machine's build platform is submerged in a vat of photopolymer resin, and a UV laser selectively cures the resin according to the sliced layers of the digital model. This process is repeated layer by layer until the entire object is formed.

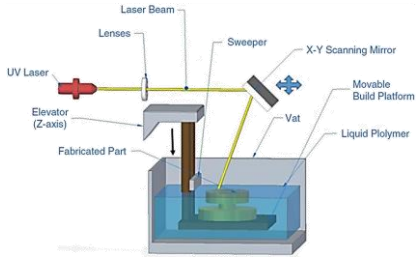


Fig. 3. Schematic of a stereolithography (SLA) process [7]

SLA technology utilizes photopolymerization, a process where liquid resin transforms into a solid polymer upon exposure to light. The 3D structure is created by selectively exposing layers of the photopolymer in a horizontal plane, followed by the downward movement of the build platform once each layer is cured or hardened. This method results in high-resolution prints with smooth surface finishes.

Since the material is liquid, the uncured resin cannot support the structure during the building process. Therefore, support structures are typically added. Similar processes in this category include digital light processing (DLP) and continuous liquid interface production (CLIP). Among these, SLA is the most commonly used, while CLIP, the latest development, is said to be 100 times faster than both SLA and DLP [8].

2.1 Materials Used in SLA

SLA uses a variety of photopolymer resins, each with specific properties suited to different applications. One of the primary challenges of using SLA for molding inserts is the inherent material properties of photopolymer resins. Compared to traditional mold materials such as steel and aluminum, SLA resins often exhibit lower mechanical strength and higher brittleness. These properties can limit the use of SLA-produced inserts in high-stress and high-wear applications.

Thermal stability is a critical factor for mold inserts used in injection molding, as they are subjected to high temperatures during the molding process. Many SLA resins have lower heat deflection temperatures compared to metals, making them susceptible to deformation or degradation under high thermal loads. This limitation can affect the performance and lifespan of SLA-produced mold inserts.

The durability of SLA-produced mold inserts is another concern. Photopolymer resins can wear out more quickly than traditional mold materials, particularly when used for high-volume production runs. This wear can lead to a loss of dimensional accuracy and surface finish quality over time, necessitating more frequent replacement or maintenance of the inserts.

Recent developments in SLA materials have led to the creation of high-performance resins with enhanced properties. These new resins offer improved mechanical strength, flexibility, and thermal stability, making them more suitable for demanding mold insert applications [9-11]. The ideal SLA material suitable for injection molding use must have a combination of strength, stiffness, and thermal resistance. The advanced strength ensures the mold can withstand the clamping and injection pressures without breaking, while the high stiffness enables the mold to maintain its shape under these pressures and produce accurate parts.

2.2 Design recommendations for SLA inserts

Previous experiences involving the use of SLA inserts in injection molding technology have shown that it is optimal to use a universal metal base that houses the core and cavity inserts. This modular approach affords the utilization of a master base for various inserts, minimizing the size of SLA inserts and thereby conserving time and material during their production (Fig. 4). The mold master in also supports the inserts against the injection pressure.

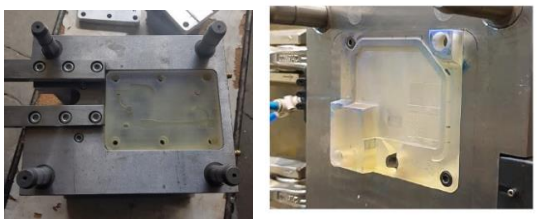


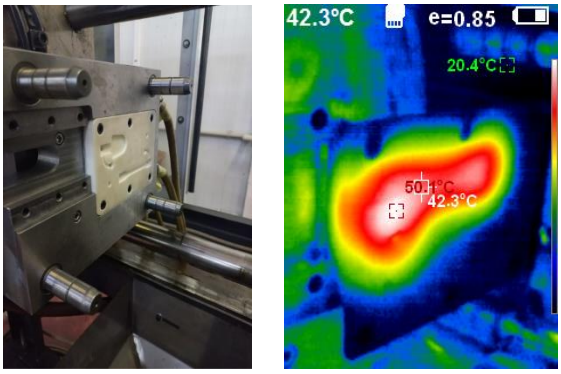
Fig. 4. Schematic of a stereolithography (SLA) process [12, 5]

Draft angle	Radii	Gate size	Runner size	Holes for sprue, ejectors etc.)	Cooling channels
Increase as much as possible	Increase as much as possible	increase by 2-3x	standard sizing recommendations apply	undersize by 0,2-0,3 mm and ream to size	standard sizing recommendations apply

Table 1. General design guidelines for an SLA molding insert

Furthermore, the geometry of the mold should be modified slightly to account for the mechanical, thermal, and dimensional properties of the soft tooling. In table 1 there are recommendation given for some of the mold features.

As far as the processing parameters, standard recommendation for industrial polymers apply but its always recommended to take the lower end values for both injection pressure and mold and melt temperatures. Since the cooling will inevitably be longer due to the lower heat conductivity pf the inserts, it's always recommended to control the inserts temperature until an acceptable cycle time is established (Fig. 5).



a) b)

Fig. 5. Temperature control of the stereolithographic inserts; a) the molding insert placed in the master housing; b) thermographic camera image of the insert with temperature distribution after injection [12]

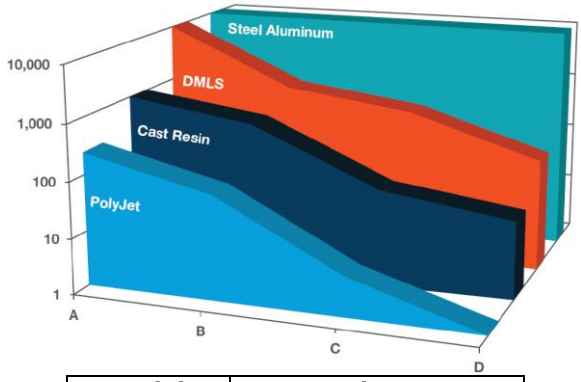
3. ADVANTAGES OF SLA FOR MOLD INSERTS

SLA can be used to replace the traditional machining of injection molds for prototyping in end-use plastics, especially prior to investing in production tooling. This method is particularly beneficial when working with injection molding thermoplastics that have reasonable characteristics, such as low to moderate melting points (below 300°C) and good flowability. Suitable polymer materials for use with SLA inserts include PE, PP, PS, ABS, TPE, PA, POM, PC-ABS, and glass-filled resins. SLA is ideal for small production runs, typically ranging from 5 to 100 molded parts, and for small to medium-sized parts, up to ~150 cm³, using 50- to 80-ton injection molding machines. This technology is also advantageous when design and functionality confirmation is required before proceeding to full-scale production.

SLA also offers significant benefits in the production of injection molds for prototyping end-use plastics. One of the primary advantages is the reduction in lead time, with average savings ranging from 50% to 90%. Additionally, SLA can lead to substantial cost reductions, with average savings between 50% and 70% [13, 14, 5]. It also allows for the functional evaluation of molds using production plastics, ensuring that the materials meet specifications. The efficiency gains are notable, as the automated tool-making process involves few steps. Furthermore, SLA enables early confirmation of part performance and tool design, as well as the validation of thermoplastic selection, ensuring that the chosen materials are suitable for the intended application.

4. LIMITATIONS AND CHALLENGES OF SLA FOR MOLD INSERTS

When using SLA molds, both tool life and part quality are influenced by the thermoplastic material used in the injection molding process. As melt temperature, viscosity, and abrasiveness increase, tool life tends to decrease. Highly viscous polymers can cause issues such as short shots and knit lines during injection molding. While high pressure can help prevent these problems, SLA molds cannot withstand extreme pressure, so it is recommended to use polymers with good flow characteristics. Additionally, part geometry affects the choice of injection molding material. When the design features do not hinder the flow of plastic, resins with higher viscosity and temperature may be used.



Material class	Polymer
A	PE, PP, PS, ABS, TPE
B	PP+G, PA, POM, PC+ABS
C	PA+G, PC, POM+G
D	PC+G, PPO, PPS

Fig. 6. Estimated number of parts obtained per tool, based on the polymer material used [15]

As seen in Figure 6, the number of obtained parts not only depends on the type of the tool used, but also from the specific polymer that's being injected. The lifetime of SLA molds and can vary from around 5 cycles to more than 1000 cycles [16].

Photopolymers used in injection molding require lower injection speed, pressure, and temperatures compared to metal tooling, allowing the plastic to freeze later due to photopolymers' heat transfer characteristics. The thermal properties of SLA molds can impact part morphology, crystallinity, shrinkage, and mechanical properties [17-19]. The cycle time is usually longer due to the lower heat conductivity of photopolymers. Longer cycle times reduce parts sticking to the insert [20], while shorter cooling times before ejection require less force and minimize the risk of tool failure. Different mold materials show varied thermal characteristics, and mold release agents can aid in part ejection [21].

The SLA molding inserts may not match the dimensional accuracy of a metal-machined tool. However, post-processing techniques like sanding or machining can be used to reduce size variations.

However, as we can see in current work ([5], [22]), the acceptable tolerances of plastic parts made in such tools is acceptable with more than 80% of produced parts having all dimensions in an acceptable tolerance range.

5. CONCLUSION AND FUTURE PROSPECTS

Stereolithography (SLA) in additive manufacturing offers significant benefits over traditional methods for producing injection molding tool inserts. SLA reduces lead times and costs, making it ideal for small production runs and rapid prototyping. It enables the creation of high-precision, intricate mold inserts with enhanced design flexibility.

However, SLA faces challenges such as lower mechanical strength and higher brittleness of photopolymer resins compared to traditional materials, limiting its use in high-stress applications. Additionally, SLA-produced inserts may deform under high thermal loads and wear out faster in high-volume production.

Despite these challenges, SLA is poised to revolutionize mold manufacturing. As material properties improve and technology becomes more accessible, SLA is expected to become standard for rapid prototyping and small to medium-scale production. Its significant advantages in cost, time, and design flexibility, along with continuous improvements, position SLA as a key technology for the future of mold manufacturing.

6. REFERENCES

[1] M. Franchetti and C. Kress, "An economic analysis comparing the cost feasibility of replacing injection molding processes with emerging additive manufacturing techniques," The International Journal of Advanced Manufacturing Technology, vol. 88, no. 9–12, pp. 2573–2579, Feb. 2017, doi: 10.1007/s00170-016-8968-7.

[2] A. Equbal, A. K. Sood, and M. Shamim, "Rapid tooling: A major shift in tooling practice," Manufacturing and Industrial Engineering, vol. 14, no. 3–4, Sep. 2015, doi: 10.12776/mie.v14i3-4.325.

[3] C. K. Chua, K. F. Leong, and Z. H. Liu, "Rapid Tooling in Manufacturing," in Handbook of Manufacturing Engineering and Technology, London: Springer London, 2015, pp. 2525–2549. doi: 10.1007/978-1-4471-4670-4_39.

[4] A. Gebhardt and J.-S. Heotter, Additive Manufacturing. 3D Printing for Prototyping and Manufacturing. Hanser Gardner Publications, 2016.

[5] FormLabs, "Low-Volume Rapid Injection Molding With 3D Printed Molds," Jul. 2022.

[6] Scott-AM, "https://www.scott-am.com/products/vacuum-casting/."

[7] A. Rashid, "Additive Manufacturing Technologies," in CIRP Encyclopedia of Production Engineering, Berlin, Heidelberg: Springer Berlin Heidelberg, 2019, pp. 39–46. doi: 10.1007/978-3-662-53120-4_16866.

[8] M. Layani, X. Wang, and S. Magdassi, "Novel Materials for 3D Printing by Photopolymerization," Advanced Materials, vol. 30, no. 41, Oct. 2018, doi: 10.1002/adma.201706344.

[9] FormLabs, "Formlabs Rigid 10k Resin Material Datasheet," 2022.

[10] DSM Somos, "Somos® NanoTool Material Safety Data Sheet," 2006.

[11] Stratasys, "Digital ABS PlusTM Material Data Sheet," 2021.

[12] O. Tuteski and A. Kočov, "Experimental research of the mechanical properties of the injection molded parts in molds produced by additive manufacturing," Mechanical Engineering-Scientific Journal, vol. 41, no. 2, pp. 131–140, 2023, doi: 10.55302/MESJ23412673131t.

[13] Stratasys, "Precision Prototyping - The role of 3d printed molds in the injection molding industry," 2017.

[14] Stratasys, "Demonstration of an Effective Design Validation Tool for 3D Printed Injection Molds (3DPIM)," 2017.

[15] Stratasys, "PolyJet For Injection Molding - Technical Application Guide," 2014.

[16] FormLabs, "Injection Molding with 3D Printed Molds: Process Conditions," Mar. 2020.

[17] P. J. Bartolo, Stereolithography: Materials, Processes and Applications. Boston, MA: Springer US, 2011. doi: 10.1007/978-0-387-92904-0.

[18] R. A. Harris, R. J. M. Hague, and P. M. Dickens, "Crystallinity control in parts produced from stereolithography injection mould tooling," Proceedings of the Institution of Mechanical Engineers, Part L: Journal of Materials: Design and Applications, vol. 217, no. 4, pp. 269–276, Oct. 2003, doi: 10.1177/146442070321700402.

[19] E. K. Dawson and J. D. Muzzy, "The effect of rapid tooling on mechanical polystyrene properties," in Proceedings of the Time Compression Technologies Conference, Nottingham, Oct. 1999, pp. 205–207.

[20] S. Rahmati and P. Dickens, "Rapid tooling analysis of Stereolithography injection mould tooling," Int J Mach Tools Manuf, vol. 47, no. 5, pp. 740–747, Apr. 2007, doi: 10.1016/j.ijmachtools.2006.09.022.

[21] N. Hopkinson and P. M. Dickens, "A comparison between stereolithography and aluminium injection moulding tooling," Rapid Prototyp J, vol. 6, no. 4, pp. 253–258, Jan. 2000.

[22] O. Tuteski, "Application of stereolithographic technologies in additive manufacturing for injection molding tool design," ss. Cyril and Methodius University, Skopje, 2024

Authors:

Ognen Tuteski, Atanas Kochov, SS. Cyril and Methodius University in Skopje, Faculty of Mechanical Engineering, Skopje, North Macedonia.

E-mail: ognen.tuteski@mf.edu.mk; atanas.kochov@mf.edu.mk

MMA 2024
FLEXIBLE TECHNOLOGIES

15th INTERNATIONAL SCIENTIFIC CONFERENCE
NOVI SAD, SERBIA, SEPTEMBER 24-26, 2024

Original research paper https://doi.org/10.24867/MMA-2024-08-005

Trontelj, K., Slak, D., Primožič, J., Božič, A., Hozdić, E., Rogelj, A., Hozdić, E.

IMPACT OF INFILL DENSITY ON THE MECHANICAL PROPERTIES OF FDM 3D PRINTED PETG AND PETG+CF MATERIALS

Abstract: *Additive manufacturing, also known as 3D printing, is a revolutionary approach that allows for rapid prototyping and the use of various materials. The article focused on analyzing the mechanical properties of polymer and composite materials created using Fused Deposition Modeling (FDM) technology and explored the impact of mineral engine oil on these properties. A comprehensive review of literature helped deepen the understanding of this topic. In the experimental section, the mechanical properties of glycol-modified polyethylene terephthalate (PETG) and carbon fiber reinforced PETG (PETG+CF) were examined. The study analyzed how different infill structure densities affected the mechanical properties of PETG and PETG+CF materials. Results indicated that infill structure densities impacted both materials similarly.*

Key words: *AM, FDM, infill structure density, mechanical properties, PETG, PETG+CF*

1. INTRODUCTION

In the 20th century, innovations in computer technology precipitated a paradigm shift in prototyping. Computer-Aided Design (CAD) became an essential tool in engineering design, enabling even more precise and rapid prototype production. This digitization led to the emergence of rapid prototyping and 3D printing, or additive manufacturing (AM), which revolutionized the industry by allowing the creation of complex parts directly from digital models [1].

Today, a wide array of AM technologies is available, including Fused Deposition Modeling (FDM), Selective Laser Sintering (SLS), Stereolithography (SLA), Powder Bed Fusion (PBF), Laminated Object Manufacturing (LOM), 3D plotting, Directed Energy Deposition (DED), Inkjet Printing (IJP), Direct Write technologies (DW), among others (Fig. 1) [2-5].

FDM ranks among the most widespread and accessible AM technologies. In this process, thermoplastic filaments are melted and deposited layer by layer to form the final product [6, 7]. FDM supports the use of a variety of materials, including acrylonitrile butadiene styrene (ABS), acrylonitrile styrene acrylate (ASA), polyamide (PA), polylactic acid (PLA), polycarbonate (PC), polyethylene terephthalate (PETG), and others. Understanding the mechanical properties of FDM-printed polymer and composite materials is crucial for proper dimensioning and the prevention of undesirable deformations and fractures under external loads. In analyzing mechanical properties, it is essential to differentiate between the filament and the printed material, where various factors influence the final properties of the material. The need for standardization of the mechanical properties of FDM-printed materials is critical to ensure quality and comparability among different materials and their performances. Current research focuses on the application of existing ISO and ASTM standards for polymeric materials, but the future will require the development and adoption of unified standards that will enable the advancement and reliable use of AM technologies.

One of the key advantages of AM, including FDM technology, is the ability to produce products with low mass while achieving desired mechanical properties, geometry, fit, function, and cost-effectiveness. In conventional manufacturing methods, it is well-known that products are typically made from solid (full, homogeneous) materials. FDM technology allows for the creation of hollow, completely enclosed geometric bodies (products). Whether this is sensible or not is dictated by the requirements of the product itself, but usually, a certain structural strength is required [8, 9].

Additionally, this technology enables the production of printed materials that are not completely hollow but contain infill of a specific shape and density. The infill is commonly defined as the internal structure within the printed material of a product, which would conventionally be manufactured as solid. Regarding the shapes of infill, there are various predefined forms, which depend on the software used to prepare 3D models for printing [10]. The most common infill shapes are rectangular, triangular, linear, hexagonal (honeycomb), and diamond.

The density of the infill structure of FDM 3D-printed polymer materials and composites are reflected in the internal geometric configuration of the product material, significantly impacting its mechanical properties, weight, duration of the printing process, and material consumption. Software for preparing 3D printing allows the selection among various infill patterns, ranging from simple linear structures to complex geometric configurations [3].

In this article, we focus on analyzing and comparing the mechanical properties of the polymer material PETG and its composite variant PETG+CF, utilizing FDM technology for the production of prototype specimens. We have investigated how changes in the linear infill during the AM process affect the mechanical properties of these specimens, particularly emphasizing infills of

30%, 60%, and 100%. Through the analysis of practical examples with different linear infills, we aim to contribute to more reliable and efficient use of FDM 3D-printed components in various practical applications.

2. FLOW OF THE EXPERIMENT

The experimental study utilized SolidWorks 2020 for designing the specimens, *FleshPrint5* slicer software (http://www.flashforge.com/ accessed on 18 August 2023) for adjusting printer parameters, and the *Adventurer 4 Series 3D printer* for manufacturing the tensile test specimens.

The tensile test specimen model was created in SolidWorks 2020 following the ISO 527-2 standard [11] (Fig. 1) and was then converted to STL format for use with the *FleshPrint5* software.

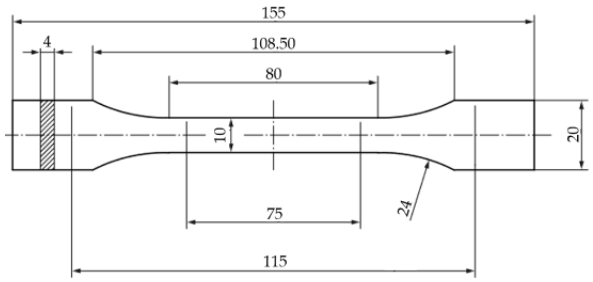


Fig. 1. Design of the tensile test specimen following the guidelines of the ISO 527-2:2012 standard [12]

The STL file serves as the input for configuring and adjusting the parameters for the 3D printing process. The primary printing parameters for PETG and PETG+CF materials are detailed in Table 1.

3D Printing parameter	PETG	PETG+CF
Filament diameter (mm)	1.75	1.75
Infill pattern	Line	Line
Infill density (%)	30 / 60 / 100	30 / 60 / 100
Nozzle diameter (mm)	0.4	0.4
Base print speed (mm/s)	60	60
Travel speed (mm/s)	100	100
First layer maximum (mm/s)	10	10
Top solid layers	4	4
Bottom solid layers	3	3
Layer height (mm)	0.2	0.2
First layer height (mm)	0.3	0.3
Extrusion temperature (°C)	240	245
Bed temperature (°C)	90	80

Table 1. Main printing parameters

The specifications and mechanical parameters for PETG and PETG+CF materials, as provided by the manufacturer, are detailed in Table 2 and Table 3 [13]. Table 3 outlines the mechanical parameters for test samples with a full infill density of 100%.

Once all parameters were configured in the *FlashPrint5* slicer software (Table 1), the *G-code* was generated and transferred to the computer that controls the 3D printer. All the tensile test specimens were printed using the *Adventure 4 Series 3D printer* by *FlashForge*. The FDM 3D-printed specimens from both materials were categorized into three groups based on their infill structure densities (30%, 60%, and 100%) and each group was tested. For all the tensile test specimens, the "Line" infill pattern was used.

Material Type	PETG	PETG+CF
Diameter (mm)	1.75	1.75
Color	green	black
Net filament weight (g)	1000	1000
Printing speed (mm/s)	60 – 90	60 – 90
Layer height (mm)	0.1 – 0.2	0.1 – 0.2
Extrusion temperature (°C)	240 – 250	230 – 250
Bed platform temperature (°C)	80 – 90	60 – 80

Table 2. PETG and PETG+CF filaments specifications [13]

Material Type	PETG	PETG+CF
Density (g/cm^3)	1.23	~1.28
Tensile Strength (MPa)	40-45	40-43
Flexural Strength (MPa)	50-55	75-85
Modulus of Elasticity (MPa)	1000-1100	2100-2400
Elongation at Break (%)	6.0-8.0	7.5-8.5
Heat Deflection Temperature (°C)	74	70

Table 3. Mechanical properties of PETG and PETG+CF filaments [13]

The input for the tensile testing is represented by the 3D-printed tensile test specimens. The testing procedure employed in this research is explained according to [11]. Tensile tests were performed using a Shimadzu AGS-X universal testing machine with a maximum load capacity of 10 kN and a testing speed of 6 mm/min, in compliance with the ISO 527-2 standard. All 3D-printed tensile test specimens were subjected to static loading.

After collecting the tensile test data, the results were processed using Excel and are presented in the following section.

4. RESULTS AND DISCUSION

The results of tensile tests for all tested specimens of FDM 3D-printed PETG material, with respect to the infill structure densities, are divided into three groups of specimens:

a) 3D printed PETG material with a line infill structure shape and 30% infill density (PETG_431, PETG_432, and PETG_433) – *Case 1*,
b) 3D printed PETG material with a line infill structure shape and 60% infill density (PETG_434, PETG_435, and PETG_436) – *Case 2*,
c) 3D printed PETG material with a line infill structure shape and 100% infill density (PETG_437, PETG_438 and PETG_439) – *Case 3*.

Based on the data obtained from tensile testing of PETG material samples, where we varied the density of the linear infill structure, we created a graphical representation of these results. The interpreted results are presented in Fig. 2.

The tensile test data for the 3D-printed PETG+CF material specimens, based on linear infill density, are divided into three groups of specimens:

a) 3D printed PETG+CF material with a line infill

structure shape and 30% infill density (PETG+CF_731, PETG+CF_732, and PETG+CF_733) – *Case 4*,

b) 3D printed PETG+CF material with a line infill structure shape and 60% infill density (PETG+CF_734, PETG+CF_735, and PETG+CF_736) – *Case 5*,

c) 3D printed PETG+CF material with a line infill structure shape and 100% infill density (PETG+CF_737, PETG+CF_738, and PETG+CF_739) – *Case 6*.

The interpreted results from tensile testing of PETG+CF material samples are presented in Fig. 3.

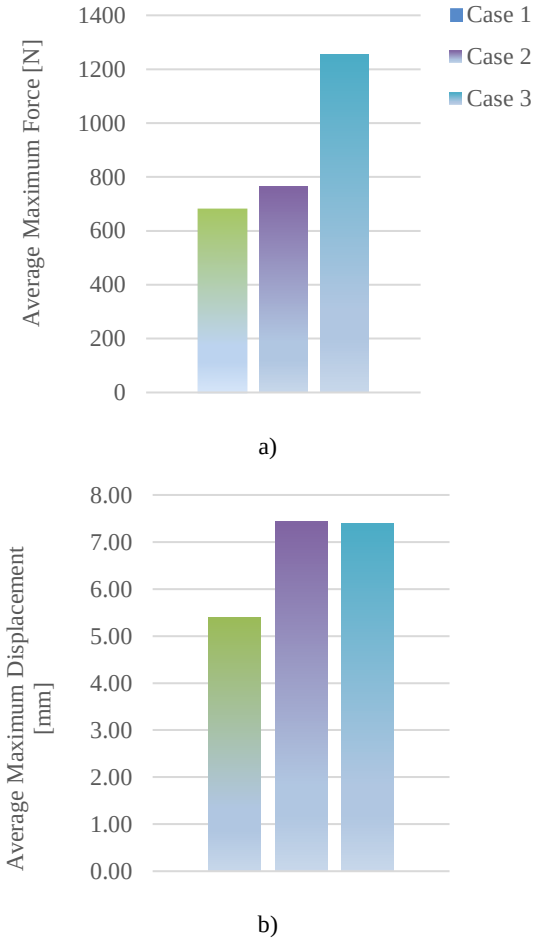


Fig. 2. Graphical representation of the average tensile test results for FDM 3D-printed PETG specimens based on linear infill structure densities: a) average maximum force, b) average maximum displacement.

5. CONCLUSION

This study comprehensively examined the mechanical properties of FDM 3D-printed PETG and PETG+CF materials with varying infill structure densities. Through meticulous tensile testing, we aimed to uncover how infill density influences the strength, durability, and overall performance of these commonly used FDM 3D-printing materials.

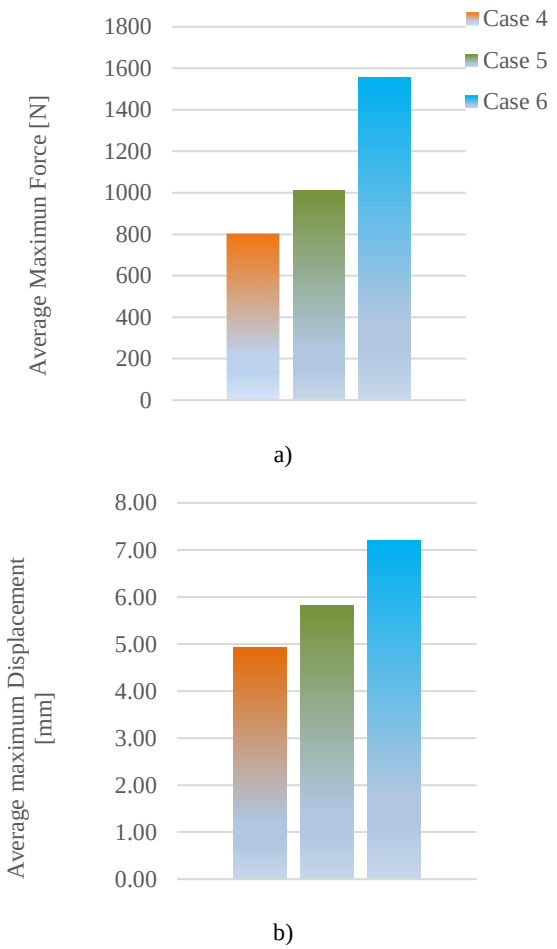


Fig. 3. Graphical representation of the average tensile test results for FDM 3D-printed PETG+CF specimens based on linear infill structure densities: a) average maximum force, b) average maximum displacement.

From the tensile tests, it was evident that the mechanical properties of the PETG specimens varied considerably with changes in infill density. Specimens with a 100% infill density, exhibited the highest average maximum force, showing a 44.54% increase over specimens with a 60% and a 45.11% increase over specimens with 30%. This indicates that a higher infill density significantly enhances the material's mechanical strength. Conversely, Specimens with 30% infill density showed the lowest values for maximum force, break force, maximum elongation, and break time, underscoring its inferior mechanical performance.

Interestingly, specimens with a 60% infill density stood out with the highest values for Young's modulus and maximum elongation, suggesting that this infill density offers a balance of strength and flexibility, enabling the material to withstand loads without permanent deformation. The minimal difference in break time and maximum elongation between specimens with a 60% and a 100% infill density suggests similar behavior under mechanical loads, indicating that both densities are effective in maintaining structural integrity.

The results for PETG+CF specimens mirrored the trends observed in the pure PETG samples, with specimens of the *Case 6* (with a 100% infill density) showing superior mechanical properties. These

specimens exhibited the highest values for most parameters, except for Young's modulus. It achieved a 69.13% higher maximum force compared to specimens with a 30% infill density and a 64.87% higher maximum force compared to specimens with a 60% infill density. This underscores the enhanced strength and durability provided by a 100% infill density.

The findings from this study provide valuable insights into the mechanical behavior of PETG and PETG+CF materials with varying infill densities, highlighting the critical role of infill density in determining the performance of 3D-printed components. The results suggest that higher infill densities generally lead to better mechanical properties, making materials more suitable for demanding applications.

Moreover, the study underscores the importance of selecting appropriate infill densities based on the specific requirements of the application. For instance, components requiring high strength and durability would benefit from higher infill densities, while those needing a balance of flexibility and strength might opt for intermediate densities.

Future research could further explore the microstructural changes induced by different infill patterns and post-processing techniques, such as annealing, to enhance the mechanical properties of FDM 3D-printed materials. Additionally, investigating the long-term effects of environmental factors, such as exposure to chemicals or extreme temperatures, could provide deeper insights into the durability and reliability of these materials in various practical applications.

In conclusion, this study has laid a robust foundation for understanding the mechanical properties of FDM 3D-printed PETG and PETG+CF materials, offering guidelines for optimizing the use of these materials in industrial and engineering applications. The insights gained here will undoubtedly contribute to advancing the field of additive manufacturing, enabling the production of more reliable and efficient 3D-printed components.

6. REFERENCES

[1] I. Gibson, D. W. Rosen, and B. Stucker, *Additive Manufacturing Technologies*. Boston, MA: Springer US, 2010.

[2] I. Gibson, D. Rosen, B. Stucker, and M. Khorasani, *Additive Manufacturing Technologies*. Cham: Springer International Publishing, 2021.

[3] ASTM F42, Committee F42 on Additive Manufacturing Technologies. ASTM International. [Online]. Available: http://www.astm.org/-COMMITTEE/F42.htm.

[4] S. D. Nath and S. Nilufar, An Overview of Additive Manufacturing of Polymers and Associated Composites. *Polymers (Basel).*, vol. 12, no. 11, p. 2719, 2020.

[5] Y. Zhang *et al.*, Additive Manufacturing of Metallic Materials: A Review. *J. Mater. Eng. Perform.*, vol. 27, no. 1, pp. 1–13, 2018.

[6] V. Mazzanti, L. Malagutti, and F. Mollica, FDM 3D Printing of Polymers Containing Natural Fillers: A Review of their Mechanical Properties. *Polymers (Basel).*, vol. 11, no. 7, p. 1094, 2019.

[7] S. Garzon-Hernandez, D. Garcia-Gonzalez, A. Jérusalem, and A. Arias, Design of FDM 3D printed polymers: An experimental-modelling methodology for the prediction of mechanical properties. *Mater. Des.*, vol. 188, p. 108414, 2020.

[8] D. Syrlybayev, B. Zharylkassyn, A. Seisekulova, M. Akhmetov, A. Perveen, and D. Talamona, Optimisation of Strength Properties of FDM Printed Parts—A Critical Review. *Polymers (Basel).*, vol. 13, no. 10, p. 1587, 2021.

[9] D. A. Prawel, Material Extrusion Additive Manufacturing Systems. In *Additive Manufacturing Processes*, ASM International, 2020, pp. 40–51.

[10] H. K. Dave and S. T. Patel, Introduction to Fused Deposition Modeling Based 3D Printing Process. In *Fused Deposition Modeling Based 3D Printing*, 2021, pp. 1–21.

[11] ISO 527-2:2012, *Plastics - Determination of Tensile Properties - Part 2: Test Conditions for Moulding and Extrusion Plastics*. Geneva, Switzerland: International Organization for Standardization, 2012.

[12] E. Hozdić, Characterization and Comparative Analysis of Mechanical Parameters of FDM- and SLA-Printed ABS Materials. *Appl. Sci.*, vol. 14, no. 2, p. 649, 2024.

[13] FASHFORGE, *Comparison between Flashforge PLA, PLA Pro, PLA-CF, ABS, ABS Pro, PETG, PETG Pro, PETG-CF*.

Authors:

BSc Klemen Trontelj, BSc David Slak, BSc Jaka Primožič, BSc Anton Božič, PhD Elvis Hozdić, University of Novo mesto, Faculty of Mechanical Engineering, Na Loko 2, 8000 Novo mesto, Slovenia.
E-mail: klemen99.trontelj@gmail.com; slak.david8@gmail.com; jaka.primozic@gmail.com; tone.bozic97@gmail.com; elvis.hozdic@fs-unm.si

MSc Aljaž Rogelj, MSc Emine Hozdić, Kranj School Centre, Kidričeva cesta 55, 4000 Kranj, Slovenia.
E-mail: aljaz.rogelj@sckr.si; emine.hozdic@sckr.si

MMA 2024
FLEXIBLE TECHNOLOGIES

15th INTERNATIONAL SCIENTIFIC CONFERENCE
NOVI SAD, SERBIA, SEPTEMBER 24-26, 2024

Original research paper https://doi.org/10.24867/MMA-2024-08-006

Bogojević, N., Ćirić-Kostić, S., Sinđelić, V., Olmi, G., Croccolo, D.

EFFECTS OF AGING AND SURFACE TREATMENTS ON THE FATIGUE STRENGTH OF STEEL COMPONENTS PRODUCED BY DMLS

Abstract: *Metal Additive Manufacturing (AM) processes offer advantages over traditional technologies, especially when it comes to shaping components with intricate designs. These processes boast high forming speeds and exceptional manufacturing flexibility, making them widely utilized in various industries. However, comprehending the fatigue characteristics of metal parts created through AM is vital for their successful integration across different sectors. Numerous factors play a crucial role in influencing the fatigue properties of metal parts manufactured through AM. This study explores the impact of heat treatment and surface treatment on the fatigue behavior of components made from marging steel (MS1) and stainless steel (PH1). After subjecting MS1 and PH1 steels to heat treatment, the fatigue limits are expected to increase compared to their as-built state. In addition, experimental findings show that not only do surface treatments significantly affect fatigue strength when used alone, but changing the sequence of subsequent treatments can increase or decrease fatigue strength.*
Key words: *fatigue strength, additive manufacturing, maraging steel, stainless steel*

1. INTRODUCTION

Additive manufacturing (AM) is a relatively young technology that, unlike conventional methods, is characterized by the production of parts by adding materials. With AM technologies, material is added only where needed, while forming parts are made layer by layer. Thanks to this production process, the technology itself allows the production of parts with very complex geometric shapes. Thanks to the possibility to make parts from complex shapes, optimization of mass and load capacity of parts, such as lattice structures, topological optimization [1], bionic optimization [2] can be easily achieved by applying AM.

AM includes a large number of different technologies and materials, which are classified into 7 groups. Due to the variety of production procedures, the variety of materials and the fact that this is a relatively young technology, there is not enough data to evaluate the fatigue life of the parts produced by AM. Fatigue life refers to the number of stresses cycles a material can withstand before it fails under repeated loading. This is a critical factor to consider, especially in industries where safety and reliability are very important.

Research has shown that parts produced by additive manufacturing may have different fatigue properties compared to traditionally manufactured parts [3]. The layer-by-layer deposition process in additive manufacturing can introduce microstructural defects and anisotropy, which can affect the fatigue behavior of the material [4]. These factors can lead to premature fatigue failure and compromise the integrity of the part. It is crucial for engineers and designers to have a understanding of the fatigue properties of parts produced by additive manufacturing techniques. Without this knowledge, components may fail prematurely in service, leading to safety hazards, costly repairs, and potential liabilities.

Within this paper, the focus will be given to metal parts produced by Direct Metal Laser Sintering (DMLS) and the assessment of post processing such as shot-peening, heat-treatment and machining on the fatigue behavior of steel parts.

DMLS, also known as Selective Laser Melting (SLM) belongs to the powder bed fusion (PBF) additive technologies, where the metal parts are produced in layers. Each layer of the part is created by melting of the metal powder by laser beam, which is guided by digital CAD file. After printing a layer, new layer of powder is spread over previous layer and the process is repeated.

The paper presents a part of research related to the Horizon 2020 project "Advanced design rules for optimal dynamic properties of additive manufacturing products - A_MADAM", which represents a systematic study of fatigue behavior of steel parts produced by Direct Metal Laser Sintering (DMLS) technology. The aim of the A_MADAM project is to establish design rules for the best fatigue performances of DMLS parts.

2. EXPERIMENT

2.1 Material and specimen

The testing was performed according to the ISO 1143 standard [5], where the geometry of the samples and the procedure for testing by rotational bending are defined. The geometry of the test samples is defined in the ISO 1143 as a cylindrical test tube with a diameter of 6 mm on the gauge and 10 mm on the end. A drawing of the specimen with indication of all its dimensions and tolerances is shown in Fig. 1.

The specimens were manufactured by DMLS machine EOSINT M280 equipped with Ytterbium fibre laser with 200 W power and emitting 0.1 mm thickness and 1064 mm wavelength infrared light beam. The process takes place in an inert environment, without Oxygen, and the scanning speed may range up to 7000 mm/s. The production chamber machine has a horizontal baseplate with dimensions 250×250 mm, and is capable

to produce part up to 325 mm of height.

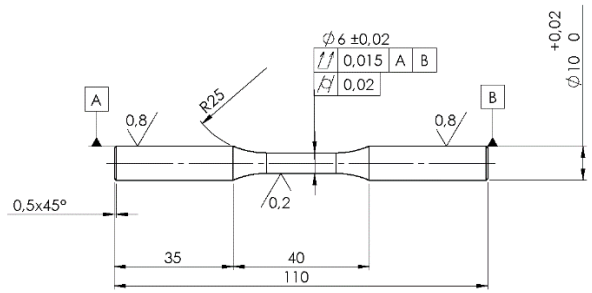


Fig. 1. Specimen with 6 mm diameter at gage in agreement with ISO 1143 standard [5]

It should be noted that the samples in this paper were examined in the form of "as built", whereby the standard was deviated from in the part that defines the roughness of the surface, all in order to examine the influence of various parameters on fatigue.

The specimens were made from two types of material: maraging steel (MS1) – equivalent to DIN 1.2709 shown in Fig. 2, and stainless steel (PH1) – equivalent to DIN 1.4540 shown in Fig. 2. b [6].

In order to the results of this research will applicable by all users of DMLS technology, the applied process parameters were selected according to the recommendations of manufacturer of the material. In particular, the layer thickness was set to 20 μm for the stainless steel – PH1 (EOS "Surface" set of the parameters) and 40 μm for maraging steel - MS1 (EOS "Performance" set of the parameters). A parallel scan strategy with alternating scan direction was adopted. Between the subsequent layers, the scanning direction was rotated by approximately 70°, in order to prevent or reduce in- plane property variations [7].

Five set of specimens from maraging steel MS1 were produced. Four sets of stainless steel PH1 specimens were made. Each set, MS1 and PH1 had 10 specimens.

Material	Specimens postprocessing methods				
MS1	P	PH	PM	PHM	MP
PH1	P	PH		PHM	HMP

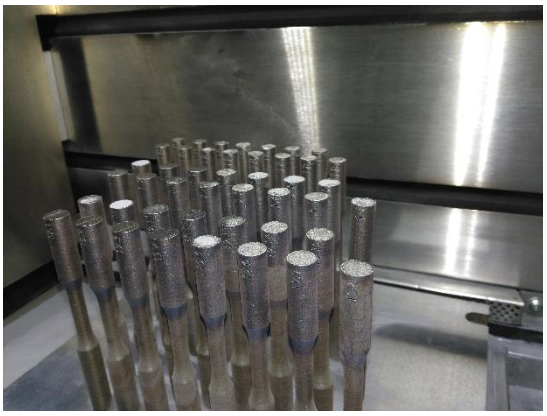
Table 1. Specimens postprocessing methods for fatigue testing

In order to investigate the influence of a shot-peening, heat treatment and machining each set had a different treatment. In the case that are applied two or more postprocessing treatments, than their order is described in the name of the set with letters, as it is shown in Table1.

Letter P means that specimens were treated with shot -peening, H specimens were exposed to heat treatment and letter M that describes those specimens had a machining.

All samples were treated by micro shot-peening by steel spheres with diameter of 0.7mm, under the 5-bar pressure.

Heat-treatment of maraging steel specimens was age-hardening at 490°C for 6 hours. The hardness of such thermally treated specimens was around 50 HRC. Stainless steel parts made from PH1 were exposed to 482 °C for 4 hours. Typical achieved hardness of the PH1 part, after heat treatment is 43 HRC. After cooling process in fresh air, the specimens were removed from the building plate using wire electro discharge machine, and then, underwent machining and refining by grinding with the aim of achieving the roughness, dimensional specifications and improving of the fatigue performance.



a) MS1



b) PH1

Fig. 2. Orientation of the samples in the EOS M270

It should be noted that with aging of specimens except hardness, also and tensile and yield strength of the specimens has been increased. For the specimens from MS1 tensile strength increased from 1100 MPa to 2050 MPa, and for specimens from PH1 the tensile strength increased from 1200 MPa to 1350 MPa [6].

2.2 Test procedures

To ensure the reliability and durability of produced samples, comprehensive fatigue testing and analysis has been conducted. This involves subjecting the parts to cyclic loading conditions that simulate real-world operating conditions and evaluating their performance over time.

The fatigue campaign made is possible to obtain the S-N curves and the fatigue limits. A staircase method was applied to determine the fatigue life: for this purpose, the series of failure and not-failure events were processed by the Dixon method [8]. A life duration of 10^7 cycles was set as run-out. The Dixon method is an

abbreviated staircase method that makes it possible to estimate fatigue life even from a short series of nominal trials at staircase (four to ten in this work).

The results in the finite life domain were analysed according to the Standard ISO 12107 standard [9]. The staircase method was then used to determine the fatigue limit of the specimens.

The specimens were tested under rotating bending fatigue by a rotary bending testing machine, where the specimen is loaded in the four-point bending configuration, so that bending moment keeps constant over the entire sample length, and in particular at its gage. The sample was pinched at its ends by a pressure of approximately 70 MPa [11]. All the tests were conducted under fully reversed bending load (stress ratio R =-1) at the frequency *f* of 60 Hz.

3. RESULTS AND DISCUSSION

During the test campaign some of the samples have runout the limit number of the cycles - 10^7. Those specimens did not take into account for creating S-N curves. Also, some of the samples, during test, have broken on the head of the sample, and those samples were not included in the results for determination of the S-N curves.

Based on the archived results of testing a S-N curves for MS1, shown in the Fig. 3, and SN curves for specimens from PH1, shown in Fig4, were created.

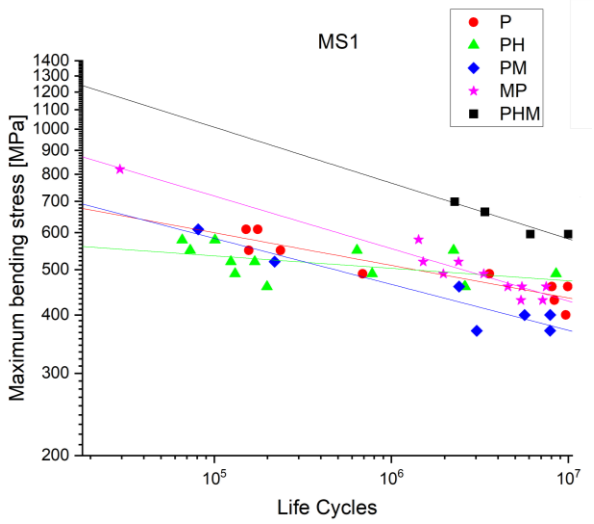


Fig. 3. S-N curves in the finite life domain for specimens made from MS1

Analysing the samples produced from MS1 material it can be seen that the lowest position of the S-N has samples subjected to shot-peening and after that to machining, as it is shown with blue squares in Fig. 3. This can be explained that after machining additional irregularities have been brought to the surface, which represent the source of the initial crack.

The S-N curve of the samples, where the first applied machining and then shot-peening, is little bit higher than previous set, as it is shown with violet stars – line in Fig. 3.

The same position of the S-N curve as previous set has the samples where only shot-peening is applied, but with lower slope.

The highest position of the S-N curve has the sample set, which treated with three procedures in next order: shot-peening, then aging (heat-treatment) and at the end the machining. This also mean that this set of the samples have and highest value of fatigue limit.

The P, MP, PM and PH sets have Fatigue limit ranging from 400 MPa to 550 MPa. The PHM set has fatigue limit of about 650 MPa.

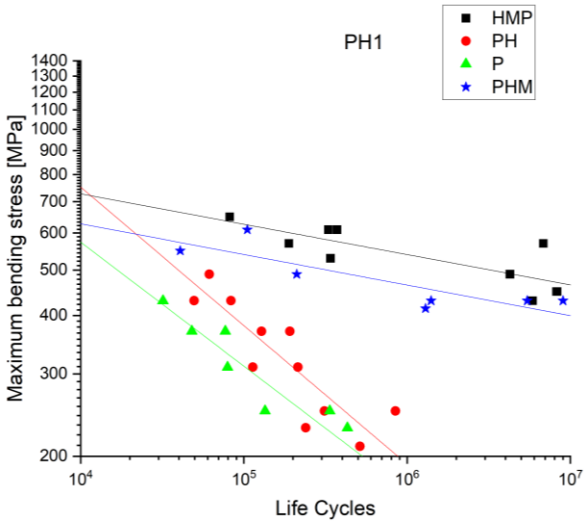


Fig. 4. S-N curves in the finite life domain for specimens made from PH1

From the Fig. 4 it can be seen that PH1 sets without machining have very big slope and relatively low values of the fatigue limits. The lowest S-N curve represent the set where only shot-peening is applied, curve denoted with green triangles. Appling the heat-treatment to the samples, curve denoted with red dots in Fig. 4, the S-N curve did not change the slope but it is moved to higher value, compared to samples where only shot-peening has been applied.

When the heat-treatment is applied to the samples, the S-N curves have changed the slope and moves to the higher levels.

For set where are applied the heat-treatment, from the Fig. 4, it can be noticed that order of the postprocessing operations have an influence on the S-N curves and the fatigue limits.

The highest S-N curve describes the set where the samples were first subjected to heat-treatment, after that machining and at the end to shot-peening, denoted with black squares in the Fig 4. This can be explained that shot-peening closes the irregularities which are brought to the surface after machining. The shot-peening applied at the end of the postprocessing treatment can decrease the surface quality, bat this is very small change compared to the benefit on the fatigue limit of the samples.

4. CONCLUSIONS

To improve the fatigue behaviour of parts produced by additive manufacturing, various methods can be employed. One approach is the use of post-processing

techniques such as shot peening or surface smoothing to eliminate surface irregularities and improve the overall surface quality, thereby enhancing the fatigue resistance of the parts. Heat-treatment processes like annealing or solution heat treatment can also be applied to relieve internal stresses, refine the microstructure, and improve the mechanical properties of the material, consequently increasing the fatigue life of the components. Furthermore, surface finishing operations such as polishing can provide an additional level of protection against fatigue failure.

In this paper is presented the experimental investigation of the influence of the post-processing techniques on the dynamic behavior of the part produced from maraging steel - MS1 and stainless steel - PH1 by additive manufacturing. From the obtained results it can be seen that heat treatment and machining have significant influence on the fatigue life and fatigue limit. Furthermore, the order of the post-processing techniques may have influence on the fatigue limit.

The fatigue life of parts produced by additive manufacturing is a critical consideration in ensuring the reliability and safety of components used in various industries. By understanding the factors influencing fatigue life, implementing methods to enhance durability, and utilizing experimental approaches to assess performance, manufacturers can optimize the design and production of additive manufacturing parts for improved longevity and performance. Continued research and development in this area are essential to further advance the capabilities and applications of additive manufacturing technology.

5. REFERENCES

[1] Jihong ZHU, Han ZHOU, Chuang WANG, Lu ZHOU, Shangqin YUAN, Weihong ZHANG, A review of topology optimization for additive manufacturing: Status and challenges, Chinese Journal of Aeronautics, Vol. 34, Issue 1, pp. 91-110, 2021. https://doi.org/10.1016/j.cja.2020.09.020

[2] Huang, Z.; Du, C.; Wang, C.; Sun, Q.; Xu, Y.; Shao, L.; Yu, B.; Ma, G.; Kong, X. Bionic Design and Optimization on the Flow Channel of a Legged Robot Joint Hydraulic Drive Unit Based on Additive Manufacturing. Biomimetics, 9, 13. 2024. https://doi.org/10.3390/biomimetics9010013

[3] Kempen, K.; Yasa, E.; Thijs, L.; Kruth, J.P.; Van Humbeeck, J. Microstructure and mechanical properties of Selective Laser Melted 18Ni-300 steel. Phys. Procedia, 12, 255–263, 2011.

[4] Yasa, E.; Kempen, K.; Kruth, J.P.; Thijs, L.; Van Humbeeck, J. Microstructure and mechanical properties of maraging steel 300 after selective laser melting. In Proceedings of the 21st International Solid Freeform Fabrication Symposium, Austin, TX, USA, 9–11 August 2010; pp. 383–396, 2010.

[5] International Organization for Standardization ISO 1143:2010, Standard - Metallic materials – Rotating bar bending fatigue testing, International Organization for Standardization (ISO), Geneva, Switzerland, 2010.

[6] https://www.eos.info/en-us/metal-solutions/metal-materials , last accessed 2024/07/10

[7] Croccolo, D.; De Agostinis, M.; Fini, S.; Olmi, G.; Vranic, A.; Ciric-Kostic, S. Influence of the build orientation on the fatigue strength of EOS maraging steel produced by additive metal machine. Fatigue Fract. Eng. Mater. Struct., 39, 637–647, 2016.

[8] W.J. Dixon, F. Massey Jr., Introduction to Statistical Analysis, McGraw-Hill, New York, United States, 1983.

[9] International organization for standardization ISO 12107:2012. Metallic Materials – Fatigue Testing – Statistical Planning and Analysis of Data. Geneva, Switzerland: International Organization for Standardization (ISO); 2012.

[10] G. Olmi, A. Freddi, "A new method for modelling the support effect under rotating bending fatigue: Application to Ti-6Al-4V alloy, with and without shot peening", Fatigue and Fracture of Engineering Materials and Structures, 36 (10), 981–993, 2013.

[11] D. Croccolo, M. De Agostinis, G. Olmi, "Fatigue life characterisation of interference fitted joints", Proc. 2013 ASME International Mechanical Engineering Congress and Exposition", in Proc. IMECE 2013, San Diego, CA, United States, Vol. 2B, V02BT02A015 (10 pages),2013. DOI: 10.1115/IMECE2013-63515

ACKNOWLEDGMENTS

The research presented in this paper has received funding from the European Union's Horizon 2020 research and innovation programme under the Marie Skłodowska-Curie grant agreement No. 734455.

The authors also wish to acknowledge the support of Ministry of Education, Science and Technology Development of Republic of Serbia through Grant 451-03-65/2024-03/200108

Authors:

Assoc. Prof. Nebojša Bogojević, Assoc. Prof. Snežana Ćirić-Kostić, M.Sc. Vladimir Sinđelić, University of Kragujevac, Faculty of Mechanical and Civil Engineering in Kraljevo, Dositejeva 19, 36000 Kraljevo, Serbia, Phone.: +381 36 383-380, Fax: +381 36 383-269.

E-mail: bogojevic.n@mfkv.kg.ac.rs; cirickostic.s@mfkv.kg.ac.rs; sindjelic.v@mfkv.kg.ac.rs

Full Prof. Dario Croccolo, Associate Prof. Giorgio Olmi, University of Bologna, Department of Industrial Engineering (DIN) Viale Risorgimento, 2 40136 BOLOGNA, Italy, Phone.: +390 51 20-93413, Fax: +390 51 20-93413.

E-mail:dario.croccolo@unibo.it; giorgio.olmi@unibo.it

MMA 2024

FLEXIBLE TECHNOLOGIES

AUTHOR INDEX

Author Index

A

Ačko Bojan 103
Adamović Savka 235
Agarski Boris 211
Alexandrov Sergei 185
Aleksić Anđelko 1, 21, 25
Anišić Zoran 47

B

Baloš Sebastian 181, 189, 197
Banjanin Bojan 235
Barač Željko 99
Baralić Jelena 9
Bizjak Milan 201
Bobić Zoran 165
Bogojević Nebojša 247
Borojević Stevo 151
Bošković Goran 215
Bošković Marina 215
Božić Dejan 135, 151
Božić Dubravka 111, 127
Božič Anton 243
Brenjo Katarina 71
Budimir Buda Alexander 63

C

Cajner Hrvoje 139, 143
Calin Andrei 75
Cerjak Andrej 231
Cigic Lovro 201
Croccolo Dario 247

Č

Čekada Miha 165
Čepić Zoran 215

Ć

Ćirić-Kostić Snežana 247
Ćorić Danko 115
Ćurčić Srećko 155, 219

D

Dačević Nemanja 185
Dakić Nikolina 59
Devedžić Goran 51
Dević Andrija 39
Dimić Zoran 63
Dramićanin Miroslav 177, 181, 235
Drnovšek Aljaž 165
Dudić Branislav 13
Dujmović Marin 207
Dujmović Miroslav 207
Džunic Dragan 51

Đ

Đorđevic Aleksandar 51
Đukić Goran 139

E

Erić Cekić Olivera 173

F

Fink Anja 231

G

Gečevska Valentina 227
Gojić Mirko 201
Gostimirović Marin 1, 21

H

Hadžistević Miodrag 43, 103, 147
Hauck Albert 189, 197
Hozdić Elvis 231, 243
Hozdić Emine 231, 243
Husak Ermin 31

I

Ilić Katarina 235
Ilić Mićunović Milana 211
Ivanic Ivana 201
Ivanov Vitalii 123

J

Jakovljević Živana 83
Janjatović Petar 173, 177, 197
Janković Predrag 5
Janjić Goran 91
Jevtić Đorđe 71
Jesić Dušan 13
Jokić Aleksandar 71
Jotić Goran 103
Jovanović Slađana 211
Jovanović Pešić Živana 51
Jovičić Aleksandar 9
Jurečič Jaka 231
Jurošević Vladimir 59

K

Karabegović Edina 31
Karabegović Isak 31
Karpe Blaž 201
Kasalica Vidoje 119
Knežev Miloš 35, 75
Kochov Atanas 239
Kočović Vladimir 51, 95
Kokotovic Branko 17
Konjević Predrag 79
Kosanović Aleksandra 1, 21, 25
Kosec Borut 201
Kostić Nikola 193
Kovač Pavel 13, 25
Kovačević Lazar 165
Krošnjar Aleksa 55
Krstanoski Magdalena 223

L

Li Yong 185
Lisjak Dragutin 111, 127
Lukić Dejan 135, 151
Lukšić Helena 115, 161

M

Madić Miloš 5
Mahmić Mehmed 31
Maksimović Nikola 181, 197
Makovec Igor 131
Maletić Julija 87
Marinković Dejan 35, 75
Marinović Budimirka 135
Matin Ivan 43
Mejić Luka 35
Miljković Zoran 71
Milošević Aleksandar 95, 123, 211
Milošević Mijodrag 135, 147, 151
Milovančević Miloš 155, 219
Milutinović Mladomir 169
Mlađenović Cvijetin 35, 75
Movrin Dejan 169
Muslim Nikola 207
Mustapić Miljenko 139

N

Nagode Aleš 201
Nedeljković Dušan 83
Nedić Bogdan 9
Nešovanović Ljubomir 79

O

Ognjenčić Krešimir 107
Olmi Giorgio 247
Opetuk Tihomir 139

P

Pačarek Goran 99
Pandilov Zoran 227
Panić Mićo 91
Panić Milica 169
Pavlović Dragan 55
Pećanac Milan 181, 189, 197
Peić Tukuljac Emil 47
Perić Marko 193
Petrović Boban 189
Petrović Milica 71
Petrović Savić Suzana 51
Ponjavić Milan 55
Primožič Jaka 243

R

Radovanovic Milica 135
Rajnović Dragan 173, 177, 181, 189, 197
Ranđelović Saša 193
Ranisavljev Miloš 43, 147, 211
Razumic Andrej 111, 127
Rede Vera 115, 161
Reljić Vule 59
Rogelj Aljaž 231, 243
Rodinger Tomislav 115
Rodić Dragan 1, 13, 21, 25
Rozing Goran 99
Runje Biserka 103, 111, 127
Rynkovskaya Marina 185

S

Santoši Željko 95, 123
Savković Bogdan 155
Savković Borislav 1, 13, 21, 25, 35, 189, 197
Savić Vladimir 197
Sekulić Milenko 1, 21, 25
Sinđelić Vladimir 247
Skakun Plavka 177
Slak David 243
Smiljić Đorđe 169
Spaić Obrad 135
Spasojević Stanko 235
Stanivuk Tatjana 207
Stepanov Borivoj 215
Stepanović Aleksandar 39, 55
Stojadinović Slavenko 119
Stojišić Nikolina 181, 189
Suvajac Zivojin 83

Š

Šarenac Slobodan 219
Šimunović Katica 99
Šimunović Goran 95, 107
Škorić Branko 165
Šokac Mario 95, 103, 123
Štrbac Branko 43, 103, 111, 127, 147
Štrbac Goran 147
Šulc Jovan 59

T

Tabaković Slobodan 63, 67
Tadić Branko 95
Tanasić Zorana 91, 103
Tarić Mirfad 13
Terek Vladimir 165
Terek Pal 165
Timotijević Milica 173
Todorović Marko 215
Trifunović Milan 5
Trivković Mirjana 181
Trontelj Klemen 243
Trstenjak Maja 139, 143
Tomov Mite 227
Tuteski Ognen 239

U

Ungureanu Nicolae 151

V

Vasileska Ema 227
Vidaković Ivan 99
Vidaković Jelena 39
Vilotić Marko 185
Vorkapić Nikola 17, 87
Vukelić Đorđe 43, 51, 95, 123, 211
Vukelic Željko 143
Vukman Jovan 151
Vuković Maja 91

Z

Zagoričnik Marko 165
Zaviršek Nejc 231
Zeljković Milan 63, 67

Ž

Žalec Urban 231
Živanović Saša 17, 63, 67, 79, 87, 119
Živković Aleksandar 35, 75
Živković Nikola 39, 55

IN MEMORIAM

IN MEMORIAM

Prof. Emeritus Dr. Leposava Šiđanin (1940-2023)



In Novi Sad, on November 10, 2023, our esteemed and beloved Professor Emeritus Dr. Leposava Šiđanin passed away at the age of 83.

She was a cherished educator whose wisdom and guidance touched the lives of many students and colleagues. Her dedication to teaching and her passion for knowledge left an indelible mark on the academic community. Professor Šiđanin's legacy will continue to inspire future generations, and her memory will be held in the highest regard by all who had the privilege of knowing her.

She was born on April 6, 1940, in Skopje, now North Macedonia. After completing high school in Skopje in 1959, she enrolled in the Faculty of Natural Sciences and Engineering, Department of Metallurgy, at the University of Ljubljana, Slovenia, where she was the only girl among 60 students in her generation. She graduated in June 1965.

In Ljubljana, at the Department of Metallurgy (now Metallurgy and Materials) of the Faculty of Natural Sciences and Engineering, she defended her Master's thesis titled "Research of Optimal Dimensions in Fine Wire Drawing" in January 1976, and her doctoral dissertation "Morphology and Mechanisms of Fracture of Low-Carbon Killed Steel" was defended in June 1983.

At the University of Ljubljana, she met her husband, Dušan Šiđanin, master engineer of metallurgy, and they were married until his passing in 2012. They had one daughter, Dr. Duška Šiđanin, Ph.D., who is a professor of Genetics at the Medical College of Wisconsin, Milwaukee, USA. She is married to Michael Maier, and they have two grandsons, Mark and Alex.

After her marriage, Professor Šiđanin moved to Novi Sad and began her teaching career on September 1, 1965, as a high school teacher at the Mechanical Technical School in Novi Sad, where she worked until August 30, 1972. Following her appointment as a teaching assistant, she joined the Faculty of Technical Sciences on September 1, 1972, where she worked until her retirement on September 30, 2007, after 42 years of employment.

At the Faculty, she become assistant professor in 1984, associate professor in 1989, and a full professor in 1994. On January 24, 2008, she was honored with the title of emeritus professor at the University of Novi Sad, becoming one of the inaugural six to receive this distinction.

Her scientific field was Material Science, Engineering Materials, and Microscopy.

Since 2008, as a professor emeritus at the Faculty of Technical Sciences, she teaches at master's and doctoral studies, passing on her knowledge to students until the very last moment.

She also formerly lectured at the Technical Faculty "Mihajlo Pupin" in Zrenjanin, and at the Faculty of Agriculture and the Faculty of Sciences in Novi Sad. At the University of California at Berkeley, Department of Material Science and Mineral Engineering, she held a portion of the laboratory exercises for the course Engineering Materials and their Applications under Prof. Gareth Thomas during the 1986/87 school year. Throughout her long teaching career, she was always highly esteemed and beloved by students.

At the Faculty of Technical Sciences, she introduces new subjects into the curriculum: Metallography, Fracture Mechanics of Materials, Microscopic Aspects of Fracture, Selected Chapters from Phase and Structural Transformations, Advanced Materials, Advanced Methods of Material Testing, Light and Electron Microscopy, and Electron Microanalysis. In 1975, at the Faculty she established a Metallographic Laboratory with high-quality equipment that is still in intensive use today and has been recognized as a reference laboratory by the Committee for Interlaboratory Material Testing (KOMIM) thanks to its successful work. At the University level, in 1978, she participated in the procurement of SEM and TEM microscopes and the establishment of an Electron Microscopy Laboratory. Through her tireless efforts and with the help of colleagues from the University, a new SEM microscope was acquired in 2003, and the University Center for Electron Microscopy - Novi Sad was formed. Since 2003, she has been the first President of the Center's Council.

In 2002, thanks to her dedication and the support of the Dean of the Faculty of Technical Sciences, Professor Ilija Ćosić, the Chair of Materials and Joining Technologies, at the Department of Production Engineering was established, and she was appointed as its first head. This highlighted the importance of materials in manufacturing technologies, which further contributed to the development of all interconnected areas of Production Engineering.

Throughout her scientific career, she participated in numerous scientific exchange programs, notably at the University of Birmingham, UK, and at the University of California, Berkeley, USA, where she specialized in electron microscopy. She spent a total of 20 months at the University of Birmingham from 1977 to 1995, under Professor Ray (Raymond Edward) Smallman. Initially supported by the University of Novi Sad, her training was later funded by the British Council, the Royal Society, and the University of Birmingham. In recognition of a long-standing successful collaboration, on the

recommendation of Prof. Šiđanin and members of the Department of Production Engineering, FTN, Novi Sad, the University of Novi Sad awarded Professor R.E. Smallman an honorary doctorate in 1990. She spent 13 months at Berkeley during the 1986/87 academic year as a recipient of the prestigious Fulbright Scholarship, under Professor Gareth Thomas.

She collaborates with Prof. Surya Kalindindi, head of the Department of Material Science and Engineering at Drexel University, USA. As part of this collaboration, four students from FTN were admitted to doctoral studies and successfully completed their PhDs.

Prof. Dr. Šiđanin has worked throughout her career on the advancement of many young individuals who are now eminent experts in their field, both in the country and abroad.

She participates as a mentor and as a member of committees in the creation of a large number of bachelor's, master's, and doctoral theses, not only at the Faculty of Technical Sciences but also at the Faculty of Sciences and the Faculty of Technology in Novi Sad; as well as at faculties in Belgrade, Podgorica, and Sarajevo.

The scientific work of Prof. Dr. Šiđanin was primarily focused on the characterization of microstructures, especially of metals and alloys, obtained through various processing technologies. For characterization, she utilizes advanced research techniques, among which the results achieved using electron microscopy (SEM and TEM) and electron microanalysis stand out. In the field of microscopy, she is recognized both domestically and internationally, and her involvement has been of great significance in affirming the University of Novi Sad as a leading center for microscopy in the region. Additionally, notable results have been observed in the characterization of the microstructure and mechanical properties of metallic glasses, traditional ceramics, and polymers. Her most significant contribution has been in the research of iron-based alloys, steels, cast irons, and particularly ADI materials.

Working with her was an exceptional experience; she knew all the microstructures, all the conditions of transformation, all the methods of preparation, etching, and had a photographic memory. She always shared her knowledge selflessly and was always there to help everyone.

Professor Dr. Šiđanin is the author of 430 scientific, review, and professional papers both domestically and internationally, including 70 works in prestigious international journals. He has authored several textbooks, books, and other professional literature, and has been a leader and participant in numerous scientific and professional workshops, conferences, and projects.

Within the scope of social activities, Prof. Dr. Šiđanin served in the Department of Production Machinery as a member of the executive board and assistant director. She was the president of the FTN union from 1994 to 2002, and the president of the University of Novi Sad union from 1998 to 2002. She was a member of the executive board of the Serbian Society for Electron Microscopy from 1992 to 2006, and the General Secretary of the Society, during which time the Society became a member of the European Microscopy Society, from 1996 to 2006. In 2011, the Accreditation Body of Serbia appointed Prof. Dr. Šiđanin as a member of the Sectoral Commission for the Accreditation of Material Testing Laboratories.

She was a member of professional associations: European Microscopy Society, European Ceramic Society, Serbian Society for Microscopy, Serbian Chemical Society, Serbian Society for Tribology, Society for the Advancement of Welding in Serbia, and the Committee for Interlaboratory Material Testing of Serbia.

Professor Šiđanin received various recognitions and awards, both national and international, among which are noteworthy: The Lifetime Achievement Award in the field of technical sciences by the Association of University Teachers and Scientists of Vojvodina, 2014, and The Award for exceptional results in science and 45 years of work at FTN, Novi Sad, 2016. As well as the selection for Honorary Senior Research Fellow, University of Birmingham, UK, 1993, and the Plaque for special contribution to the development of the Faculty of Technical Sciences Novi Sad on the occasion of the faculty's 50th anniversary in 2010.

As we bid farewell to Prof. Emeritus Dr. Leposava Šiđanin, we are reminded of the lasting mark she left in the world of academia and beyond, on to all of us who had the opportunity to meet her, to work with her, and to learn from her example. Her unwavering dedication to education, her pioneering research, and her compassionate mentorship have shaped countless minds and futures. Her spirit, preserved in her work and the people she influenced, will continue to guide the path of education and discovery.

Rest in peace, esteemed scholar and cherished friend.

MMA 2024

FLEXIBLE TECHNOLOGIES

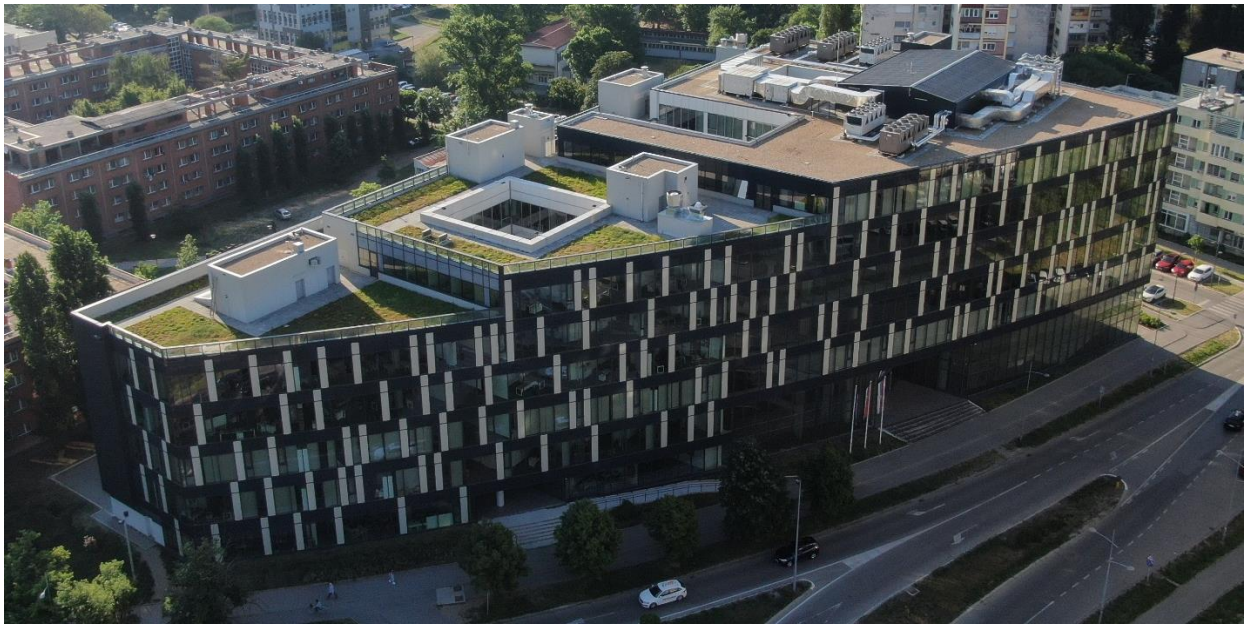
INFORMATION ABOUT VENUE

SCIENCE AND TECHNOLOGY PARK NOVI SAD

The Science and Technology Park Novi Sad was founded by the Autonomous Province of Vojvodina in order to provide support to its members, to commercialize innovative products and services, and implement the development and new technologies, as quickly as possible. Members of Science and Technology Park Novi Sad can be any technological company engaged in innovative activities, startup companies and startup teams, as well as research and development institutes.

In addition to spatial and infrastructural work conditions, Science and Technology Park Novi Sad will simultaneously provide scientific research, educational and other services to its members, in order to create ideas and ready-made solutions for the business world.

The Science and Technology Park Novi Sad is a place of connecting and exchanging with the economy, science and institutions, which with its activities, programs and services has one of the key influences on the development of a Serbian innovation ecosystem.



https://ntpns.rs
E-mail address: office@ntpns.rs
Phone: +381 62 792 056
Address: Fruškogorska 1, 21102 Novi Sad, Republic of Serbia

MMA 2024
FLEXIBLE TECHNOLOGIES

INFORMATION ABOUT SPONSORS AND DONATORS

MINISTRY OF SCIENCE, TECHNOLOGICAL DEVELOPMENT AND INNOVATION



https://nitra.gov.rs
kabinet@nitra.gov.rs
+381 11 363 37 01

Nemanjina 11
11000 Belgrade
Republic of Serbia

PROVINCIAL SECRETARIAT FOR HIGHER EDUCATION AND SCIENTIFIC RESEARCH





https://apv.visokoobrazovanje.vojvodina.gov.rs/
psnauka@vojvodina.gov.rs
+381 21 487 4641

Bulevar Mihajla Pupina 16
21101 Novi Sad
Autonomous Province of Vojvodina
Republic of Serbia

UNIVERSITY OF NOVI SAD

https://www.uns.ac.rs
rektorat@uns.ac.rs
+381 21 450 418

Dr Zorana Đinđića 1
21102 Novi Sad
Republic of Serbia

FACULTY OF TECHNICAL SCIENCES

http://ftn.uns.ac.rs
ftndean@uns.ac.rs
+381 21 450 810

Trg Dositeja Obradovića 6
21000 Novi Sad
Republic of Serbia

DEPARTMENT OF PRODUCTION ENGINEERING



http://www.dpm.ftn.uns.ac.rs
dpm@uns.ac.rs
+381 21 485 2320

Vladimira Perića Valtera 2
21102 Novi Sad
Republic of Serbia

LOLA INSTITUTE



https://www.li.rs/en/
+381 / 11 / 25 46 423; +381 / 11 / 25 41 303

Kneza Višeslava 70A
11030 Belgrade
Republic of Serbia

TEHNOEXPORT



https://tehnoexport.rs
office@tehnoexport.com
+381(0) 22 553 453
+381(0) 22 561 417

Jovana Popovića 43, Kralja Petra I bb
22320 Inđija
Republic of Serbia

MECAFOR PRODUCTS

nnedeljkovic@mecafor-lfa.com
+381 (0) 230315037

Vuka Karadžića 70
23300 Kikinda
Republic of Serbia